Quantification de l'évolution du relief Néogène et Quaternaire des Alpes occidentales. Apports de la thermochronologie basse-température couplée à la modélisation numérique

Pierre Valla

UNIVERSITÉ DE GRENOBLE

THÈSE

Pour obtenir le grade de

DOCTEUR DE L'UNIVERSITÉ DE GRENOBLE

Spécialité : **Terre, Univers, Environnement**

Arrêté ministériel : 7 août 2006

Présentée par

Pierre VALLA

Thèse dirigée par Peter VAN DER BEEK et codirigée par Jean BRAUN

préparée au sein du **Laboratoire de Géodynamique des Chaînes Alpines**
dans **l'École Doctorale Terre, Univers, Environnement**

Quantification de l'évolution du relief Néogène et Quaternaire des Alpes Occidentales

-

Apports de la thermochronologie basse-température couplée à la modélisation numérique

Thèse soutenue publiquement le **28 Janvier 2011**,
devant le jury composé de :

Mr. Todd EHLERS
Professeur, Universität Tübingen, Rapporteur
Mr. Bernard HALLET
Professeur, University of Washington, Rapporteur
Mr. Kerry GALLAGHER
Professeur, Université de Rennes 1, Président
Mr. Gweltaz MAHEO
Maître de conférences, Université Lyon 1, Examinateur
Mr. Fritz SCHLUNEGGER
Professeur, Universität Bern, Examinateur
Mr. Peter VAN DER BEEK
Professeur, Université de Grenoble, Directeur de thèse
Mr. Jean BRAUN
Professeur, Université de Grenoble, Directeur de thèse

« L'eau érode les montagnes et comble
les vallées, et si elle en avait le pouvoir, elle
réduirait la Terre à l'état de sphère parfaite »

LEONARD DE VINCI
[*CODEX ATLANTICUS, 185 v.c*]

Remerciements

Ce travail n'aurait jamais été mené à bien, et je n'en serais surement pas là, si je n'avais pas eu la chance de rencontrer bon nombre de personnes formidables que je tiens à remercier ici pour leur aide, leur soutien et leur présence durant ces longues années…

Tout d'abord, un grand merci à mes directeurs Peter et Jean pour leur aide et leur soutien tant au niveau scientifique qu'humain. Merci Peter de m'avoir pris sous ton aile dès mon Master, tu as su encadrer mon travail d'une manière efficace tout en me laissant la grande liberté de développer mes idées et pistes de recherche. Merci également pour ton optimisme perpétuel quant à mes idées parfois farfelues, et pour ton attention constante afin de me recadrer lors de mes (nombreux) éparpillements... Merci Jean de m'avoir suivi (plus ou moins à distance) depuis maintenant cinq longues années, d'avoir toujours été accessible et enthousiaste vis-à-vis de mes idées, et finalement de nous avoir rejoints à Grenoble pour le dernier sprint… Enfin, merci à Frédéric pour ton aide et ton soutien continu, malgré la distance, j'ai toujours pu bénéficier de ta grande ouverture scientifique et de ton grand potentiel à l'éparpillement (en ce sens je crois avoir bien suivi tes enseignements !).
J'ai beaucoup appris grâce à votre encadrement, tant sur le plan professionnel de par votre grande expertise et ouverture scientifique, que sur le plan humain de par votre disponibilité et les excellents rapports humains dont vous m'avez témoignés…

Je tiens à remercier les membres de mon jury, Todd Ehlers, Kerry Gallagher, Bernard Hallet, Gweltaz Mahéo et Fritz Schlunegger, qui m'ont fait l'honneur de bien vouloir évaluer mon travail. Un grand merci à Todd et Bernard pour avoir accepté de lire et décortiquer mon manuscrit pendant les fêtes de fin d'année, ainsi que pour leurs rapports pertinents et sincères. Merci à tous pour votre présence lors de ma soutenance, et pour les échanges scientifiques que nous avons pu avoir lors de cette discussion.

Merci également à toutes les personnes du "LGCA" et de l'OSUG qui ont participé à rendre cette expérience de thèse fructueuse. Tout d'abord, je tiens à remercier Claudine, Claudie et Christine pour leur aide et patience sans faille lorsqu'il s'agit de se plonger dans les labyrinthes de l'administration, ainsi que Pascale pour son aide dans la recherche bibliographique (ou comment dénicher l'introuvable !) et Maria pour ses agréables visites journalières… Merci à Rodolphe pour sa gestion quasi-virtuose de l'informatique et sa disponibilité aussi bien pour régler les problèmes techniques que pour faire le point sur la saison NBA ! Un grand merci à François et Francis pour votre disponibilité malgré les tonnes de cailloux que j'ai pu vous ramener au cours de cette thèse; votre expertise m'a toujours été d'une aide précieuse…

Merci à tous les "géo-scientifiques" que j'ai eu la chance de rencontrer et côtoyer au LGCA : Catherine, Pascale, Matthias, Alex, Pierre, Stéphane(s), Etienne, Christophe, Arnaud, Manu(s), Olivier, Eric, Thierry, Jean-Louis… Je tiens à vous remercier pour cette bonne ambiance, quasi-familiale, et l'atmosphère (de travail mais pas que !) qui m'ont accompagné durant ces quatre années ! Merci aux diverses personnes que j'ai également eu la chance de rencontrer au sein de l'OSUG, et notamment les glacios : Catherine, Delph, Manu, Vincent et Buno…

Cette expérience de thèse, ainsi que ma formation universitaire en général, a été l'occasion de nombreuses rencontres et collaborations lors de séjours dont je garde un excellent souvenir. Je tiens par conséquent à remercier un grand nombre de personnes dont la rencontre a été une opportunité unique pour l'ours sédentaire que je suis… Merci à Eric et François, ainsi qu'à toute l'équipe de l'OVSG, pour ces superbes vacances (oups, ce stage) en Guadeloupe durant l'été 2005, première approche du monde de la recherche, mais également de la bouffe créole et du rhum Bologne (pas vrai Polo ?). Un grand merci à Jean-Philippe, Frédéric (à l'époque postdoc mais déjà super encadrant !) et Mathieu pour m'avoir fait profiter du soleil californien et de la culture ouïghoure durant l'été 2006. Ces expériences commencent à dater, pourtant elles ont grandement participé à mon apprentissage du métier de chercheur et au développement de mon intérêt pour les rencontres…

Ma thèse a été le moteur de nombreuses collaborations aussi bien en France qu'à l'étranger, me permettant ainsi de partager mon travail avec des personnes qui sont pour la plupart devenues des collègues et amis. Merci à Dimitri pour nos longues discussions sur les rivières, aussi bien à Rennes qu'au bar du Marriott SF; merci à David et Vivi pour mon expérience danoise (malgré la pluie et le poisson!); un grand merci à Jeff, Sylvain et Luc pour les balades géomorpho glaciaire et les discussions qui s'en sont suivies. Un immense merci à David (et Erin…) pour son accueil à Berkeley, son aide et expertise durant mon apprentissage de la géochimie des gaz nobles (ce qui n'était pas gagné par avance), et enfin sa grande générosité humaine ! Merci également à Greg et toute l'équipe du BGC pour leur accueil chaleureux, et notamment Brian pour les séances de picking et de shuffleboard… Enfin, mes divers séjours à l'ETH Zürich ont été agréablement agrémentés par la présence de nombreuses personnes : Fred, JD (en souvenir de la Topalihütte…), Matt, Pietro, Rebecca, Rasmus et Pipo avec qui je ne comptent plus les bières partagées au Kulturcafé et Bar Andorra…

Voilà que je m'attaque aux personnes maîtresses de mon expérience de thèse, à savoir les forces vives que sont (ex-)thésards du LGCA ou l'ensemble des (ex-)étudiants qui m'ont accompagné au cours de mon cursus universitaire… Un grand merci aux potes de galère (pardon prépa !) : Bruno (et son attrait pour les drosophiles…), David & Amélie (désormais si proches de Swissland !), mais également Côme et Manue. Merci également aux potes de l'ENS : Emi, Côme et Polo (Riders on the storm…), Clément, Fanny, Christophe, Damien, Frod, Tom et bien d'autres…

Voici venus les derniers amis en date, mais avec qui j'ai partagé (et je l'espère, partagera !) des moments énormes qui sont partie entière de mon expérience de thèse… Je me dois de commencer par les deux affreux jojos qui m'ont lâchement abandonné après trois années d'intense cohabitation au bureau 349 (souvent non-productive, parfois houleuse, mais tellement extra !), véritable auberge espagnole du ex-LGCA… Merci Chichi et Gordo pour votre présence, votre aide, nos affaires non-résolues (les méandres ardéchois, la vinification, les champignons…) et nos journées mises à contribution dans le développement et le test des plateformes ArmorGames ou Kongregate ! Un grand merci aux compères de fin de rédaction qui ont partagé leurs week-ends et vacances avec moi : merci Tibo (pour ton expérience free-lance du magmatisme, ton optimisme et bonne humeur à toute épreuve, et pour cette nouvelle cohabitation), Clém (pour la météo en temps réel, les bons moments passés et le temps que je t'ai fait perdre en trois ans à discuter de tout et rien autour d'un café…) et enfin le grand Thibault (pour son hygiène de vie irréprochable, ses goûts musicaux tellement éclectiques… une vraie mine d'or pour mes soirées de rédaction !). Merci également aux anciens (avec parfois une thèse quasi-concordante avec mon Bac !), aussi bien ceux qui ont définitivement élu domicile au LGCA (n'est-ce pas Jéjé, Juju et Schwartzy ?), les anciens profs devenus collègues et potes (Pierrot, Nico, Fredo !), et les ex-thésards qui sont partis pour de nouvelles aventures : Antoine, Bobby, Jérémie, Marion, Romain, Shazo, Xav… Merci pour tous ces bons moments ! Enfin, merci et bon courage aux suivants sur la liste : Chacha, Vio, Morgane (merci le bureau des filles d'à côté pour votre patience, on n'a pas toujours été des voisins très discrets !), Marion, Christophe, Yohann, Nico et Pierre…

Enfin, je tiens à remercier ici les personnes les plus importantes à mon cœur et qui m'ont soutenu tout au long de ma scolarité… Un grand merci à mes amis de longue date, qui n'ont pas toujours compris ce que je faisais mais ont toujours été là pour moi, surtout pour m'aider à relativiser et sortir du monde des cailloux : futurs Dr. Mat & Zab (cool encore des thèses à arroser !), Dr. Ben (thèse déjà bien arrosée !), Guigui & Cécile, Isa & Timm, Math & Marie-Anaïs, Bruno & Marie, mais également Tom & Elsa ! Enfin, je ne saurai jamais assez remercier mes soutiens de toujours, ceux qui m'ont toujours poussé dans mes choix souvent sans savoir totalement dans quelle aventure je m'embarquais : merci Maman et Papa, merci Popo, et un grand merci à toute ma formidable famille et belle famille pour avoir participer à la construction de la personne que je suis aujourd'hui ! Enfin, un immense merci à ma supportrice des bons comme des mauvais moments. Merci Marine pour ton soutien constant, ton optimiste et ta patience pourtant mise à rude épreuve ces derniers mois (années ?); une grande partie de ce travail n'aurait jamais vu le jour si tu n'avais pas été à mes côtés et je te dois beaucoup dans la réussite de cette expérience…

Pierre (Totoro), Printemps 2011

Résumé

L'évolution topographique des chaînes de montagne résulte d'interactions complexes entre la tectonique et le climat via l'action des processus de surface. La quantification de l'évolution du relief passe par le développement d'outils méthodologiques permettant d'identifier les processus mis en jeu pour des échelles de temps (10^3-10^6 années) et d'espace (1-100 km) caractéristiques de contextes orogéniques. Dans cette étude, l'évolution Néogène et Quaternaire du relief des Alpes Européennes est abordée à partir d'une approche couplant la thermochronométrie basse-température *in-situ* (essentiellement (U-Th-Sm)/He et $^4He/^3He$ sur apatite) et la modélisation numérique.

Le développement d'une méthode numérique associant la modélisation thermo-cinématique (*Pecube*) à un algorithme d'inversion (*Neighbourhood Algorithm*) permet l'interprétation quantitative de données thermochronologiques en termes d'histoires d'exhumation et d'évolution du relief. La quantification de l'évolution du relief reste néanmoins problématique et fortement dépendante du contexte géomorphologique étudié. Cette étude implique la nécessité de repenser *a priori* la stratégie d'échantillonnage et d'interprétation des données suivant le contexte géomorphologique considéré et le signal d'exhumation que l'on cherche à quantifier via la thermochronologie. Enfin, l'application de cette approche à un jeu de données thermochronologiques échantillonnées dans le massif des Ecrins-Pelvoux (Alpes françaises) révèle l'existence d'un épisode d'exhumation rapide cessant autour de ~5-6 Ma, encadré par des taux d'exhumation plus modérés. Cependant, les données ne permettent pas de conclure quant à l'évolution tardi-Néogène du relief dans le massif des Ecrins-Pelvoux.

L'application de la thermochronométrie $^4He/^3He$ dans la vallée du Rhône (Alpes suisses), couplée à des données thermochronologiques issues de la littérature, confirme un épisode d'exhumation rapide jusqu'à ~5-7 Ma, et révèle une augmentation majeure du relief local (~1-1.5 km) associée au creusement des vallées par d'importants appareils glaciaires. Le début de cette phase de creusement correspond à la transition climatique Mi-Pléistocène (~1 Ma) depuis des cycles glaciaires symétriques de 40 ka vers des cycles asymétriques (100 ka) de plus forte amplitude. Ces données permettent également de reconstruire la topographie pré-glaciaire du bassin versant du Rhône, et ainsi d'évaluer, à une échelle plus globale, l'impact des glaciations Pléistocènes sur l'évolution du relief.

Des résultats préliminaires issus de la modélisation numérique des processus glaciaires mettent en évidence le potentiel d'une telle approche afin de tester quantitativement l'influence de la transition climatique Mi-Pléistocène sur le développement du relief alpin, ouvrant de nouvelles perspectives de recherche. Enfin, l'étude de l'évolution topographique post-glaciaire dans le massif des Ecrins-Pelvoux (modélisation numérique et utilisation du ^{10}Be cosmogénique produit *in-situ*) met en évidence une dynamique d'érosion fluviale pouvant atteindre localement des vitesses de l'ordre du cm an^{-1}, illustrant l'évolution géomorphologique rapide en réponse à la transition climatique entre le tardi-Pléistocène et l'Holocène.

Abstract

The topographic evolution of mountain belts results from complex couplings between tectonics, climate and surface processes. Quantifying landscape evolution requires methodological tools to constrain forcing processes over temporal (10^3-10^6 years) and spatial (1-100 km) scales characteristic of orogenic systems. This thesis investigates the Neogene and Quaternary relief evolution of the European Alps using *in situ* low-temperature thermochronometry (mostly apatite (U-Th-Sm)/He and ^{4}He/^{3}He) and numerical modeling.

A novel numerical approach combining thermal-kinematic modeling (*Pecube*) with an inversion scheme (*Neighbourhood Algorithm*) allows extracting quantitative information on exhumation and relief histories from thermochronological datasets. Quantifying relief evolution remains problematic, however, and strongly depends on the geomorphic setting. Our results show that both thermochronology data sampling and modeling strategies have to be considered *a priori*, in function of the geomorphic setting and the spatial/temporal scale of the exhumation signal to be constrained. This approach has been applied on a thermochronological dataset collected in the Ecrins-Pelvoux massif (French Alps). The results show a pulse of rapid exhumation until ~5-6 Ma, preceded and followed by more moderate rates of exhumation. However, the data cannot resolve the late-Neogene relief evolution in the Ecrins-Pelvoux massif.

New ^{4}He/^{3}He thermochronometry data from the Rhône valley (Swiss Alps), combined with thermochronological data from the literature, also point out an episode of rapid exhumation until ~5-7 Ma, and reveal a major increase in local topographic relief (~1-1.5 km) linked to valley carving by large mountain glaciers. The onset of this phase of relief carving corresponds to the Mid-Pleistocene transition from symmetric 40-ka to asymmetric and high amplitude 100-ka glacial/interglacial oscillations. The new data also permit to reconstruct the pre-glacial topography of the Rhône basin, and to evaluate the net effect of Pleistocene glaciations on relief evolution at the basin scale.

Preliminary results from numerical modeling of glacial dynamics highlight the potential opportunity of using such an approach to quantitatively assess the impact of the Mid-Pleistocene climate transition on Alpine relief development, leading to new research avenues. Finally, the post-glacial topographic evolution of the Ecrins-Pelvoux massif has been studied using numerical modeling and *in situ* cosmogenic ^{10}Be analyses. The results suggest efficient fluvial incision at rates of cm yr^{-1}, illustrating the efficient landscape response to late-Pleistocene/Holocene climate change.

Table des matières / Table of contents

Table des figures et tableaux / List of figures and tables

Chapter I :

Chapter II :

Chapter III :

Chapter IV :

Avant propos - Foreword

Le manuscrit présent regroupe l'ensemble des travaux de recherche que j'ai réalisés durant ma thèse de Doctorat au Laboratoire de Géodynamique des Chaînes Alpines (Université de Grenoble) sous la direction des Prs. Peter van der Beek et Jean Braun. Il rassemble également une partie du travail effectué au cours de mon Master de recherche (Université de Grenoble) sous la direction du Pr. Peter van der Beek.

Ce mémoire est organisé selon cinq chapitres indépendants. Dans une première partie, rédigée en français, je présente le contexte scientifique et géodynamique de mon étude et expose la problématique à l'origine de mes travaux, avant de synthétiser les approches méthodologiques développées au cours de ma thèse. Les trois chapitres suivants, rédigés en anglais, synthétisent les résultats originaux de mes travaux faisant l'objet de publication dans des revues scientifiques internationales (exceptés les résultats de la partie IV.2 qui restent préliminaires). Ces trois chapitres sont par conséquent organisés sous la forme d'articles publiés, en révision ou prêts à être soumis. Le dernier chapitre synthétise en français les principales avancées scientifiques résultant de mon étude et clôt ce manuscrit par la proposition d'éventuelles perspectives de recherche.

*****

This manuscript gathers the research work I have realised during my PhD thesis at the Laboratoire de Géodynamique des Chaînes Alpines (Université de Grenoble) under the supervision of Profs. Peter van der Beek et Jean Braun. This manuscript also encompasses preliminary work I have done during my Master thesis (Université de Grenoble) under the supervision of Prof. Peter van der Beek.

This memoir is organised following five independent chapters. The first part (in French) presents the scientific and geodynamic context of this study and exposes the scientific questions at the base of my PhD work; it then summarizes the methodological approaches I developed. The three following chapters (in English) expose original results of my work organised in different papers that are either published, in revision or ready to be submitted to international scientific journals (except preliminary results presented in section IV.2). The final chapter (in French) summarizes the main scientific outcomes of my work and presents potential future research avenues.

Chapter I :

Introduction et Méthodologie

I.1 - Introduction

I.1.1 - Motivations de cette étude

La topographie des chaînes de montagne résulte des interactions entre les processus "internes" (*i.e.*, la tectonique, *Gilbert*, 1897; *Davis*, 1899) et "externes" ou "exogènes" (*i.e.*, le climat, *Tricart and Cailleux*, 1965) via l'action des processus de surface. La description des différents processus internes/externes ne peut pas être considérée de façon indépendante et nécessite la prise en compte de ces interactions et couplages complexes autour de l'évolution du relief [*e.g.*, *Willett*, 1999; *Whipple*, 2009].

La tectonique agit sur l'érosion, d'une part en créant de la topographie (pente et relief) par accumulation différentielle de masse (chevauchements, plis, failles normales), et d'autre part en contrôlant la localisation initiale des vallées le long d'accidents tectoniques majeurs [*e.g.*, *Kühni and Pfiffner*, 2001a]. Le climat agit également de façon directe et indirecte sur les processus d'érosion, conditionnant les agents érosifs principaux ainsi que les vitesses d'érosion locale/régionale: processus de versants, fluviaux ou glaciaires en fonction de la température, des précipitations ou encore de la végétation. Les interactions climat/tectonique sont plus subtiles et passent par des rétroactions faisant également intervenir l'érosion. Les processus d'érosion agissent en effet sur la redistribution de masses à la surface de la lithosphère par transport de sédiments érodés depuis les chaînes de montagne vers les bassins de dépôts périphériques [*e.g.*, *Allen*, 2008] et modifient par conséquent l'état de contrainte gravitationnelle de la lithosphère [*e.g.*, *Koons*, 1989; *Willett*, 1999]. L'érosion limite ainsi l'extension latérale et verticale des chaînes de montagne en localisant la déformation tectonique dans les zones internes [*Avouac and Burov*, 1996; *Willett*, 1999]. Par ailleurs, la décharge de masse induite par l'érosion dans une chaîne de montagne entraine une réponse isostatique de la lithosphère qui se traduit par un rebond flexural et donc un soulèvement de la chaîne [*e.g.*, *Stewart and Watts*, 1997; *Watts*, 2001]. Ainsi, les paramètres climatiques et leur évolution spatio-temporelle, ayant une influence sur les processus d'érosion, participent à la modulation de l'activité tectonique au sein d'une chaîne de montagne [*e.g.*, *Molnar and England*, 1990]. D'un autre côté, les processus d'érosion entrainent une consommation plus ou moins importante de dioxyde de carbone atmosphérique par les processus d'altération des silicates et d'enfouissement du carbone organique [*e.g.*, *Galy et al.*, 2007], et peuvent potentiellement engendrer un refroidissement global du climat [*e.g.*, *Raymo and Ruddiman*,

1992], illustrant ainsi l'effet rétroactif de l'activité tectonique sur le climat via l'action des processus de surface.

L'évolution spatio-temporelle du relief dans les chaînes de montagne reflète donc l'expression morphologique des processus tectoniques et/ou climatiques [*e.g.*, *Gilbert*, 1897; *Penck*, 1924; *Hack*, 1957], permettant une quantification plus ou moins aisée de ces processus via l'analyse de la topographie. Cependant, le besoin de compréhension des interactions complexes entre tectonique, climat et érosion passe notamment par une meilleure connaissance des processus de surface, de leur efficacité relative dans l'évolution du relief, mais également des échelles spatiales et temporelles auxquelles ces processus agissent sur la topographie. Ces nouvelles problématiques ont donné le jour à une évolution progressive de la géomorphologie classique basée sur l'observation des morphologies et des processus vers une approche plus quantitative des processus de surface, de l'évolution du relief ainsi que des différents forçages internes/externes associés [*e.g.*, *Kirby*, 1994; *Summerfield*, 2000].

Le développement de la géomorphologie quantitative est en partie lié au débat, initié dans les années 1990 et se perdurant aujourd'hui, portant sur l'évolution tardi-Cénozoïque des chaînes de montagne, leur dynamique d'érosion et le changement climatique global synchrone [*Molnar and England*, 1990; *Raymo and Ruddiman*, 1992]. D'une part, *Molnar and England* [1990] proposent une théorie expliquant l'augmentation globale au Miocène-Pliocène des vitesses de sédimentation [*e.g.*, *Davies et al.*, 1977; *Hay et al.*, 1988; *Métivier et al.*, 1999; *Zhang et al.*, 2001; *Kuhlemann et al.*, 2002; *Molnar*, 2004] par un refroidissement global observé durant la transition Miocène-Pliocène (Figure I.1.1A) et le développement d'oscillations entre des périodes glaciaires et interglaciaires (Figure I.1.1B). En effet, ces auteurs proposent une théorie selon laquelle l'augmentation à l'échelle du globe des vitesses d'érosion au sein des chaînes de montagne (et le soulèvement associé par rebond isostatique) serait une réponse au refroidissement climatique global, à une augmentation des précipitations, et à une plus grande variabilité du climat depuis le tardi-Cénozoïque. D'autre part, *Raymo and Ruddiman* [1992] proposent une explication alternative à l'augmentation des flux de sédiments selon laquelle une plus forte activité tectonique aurait favorisé l'intensification des processus d'érosion, et ainsi la consommation de dioxyde de carbone atmosphérique (altération des silicates), entrainant ainsi un refroidissement global du climat.

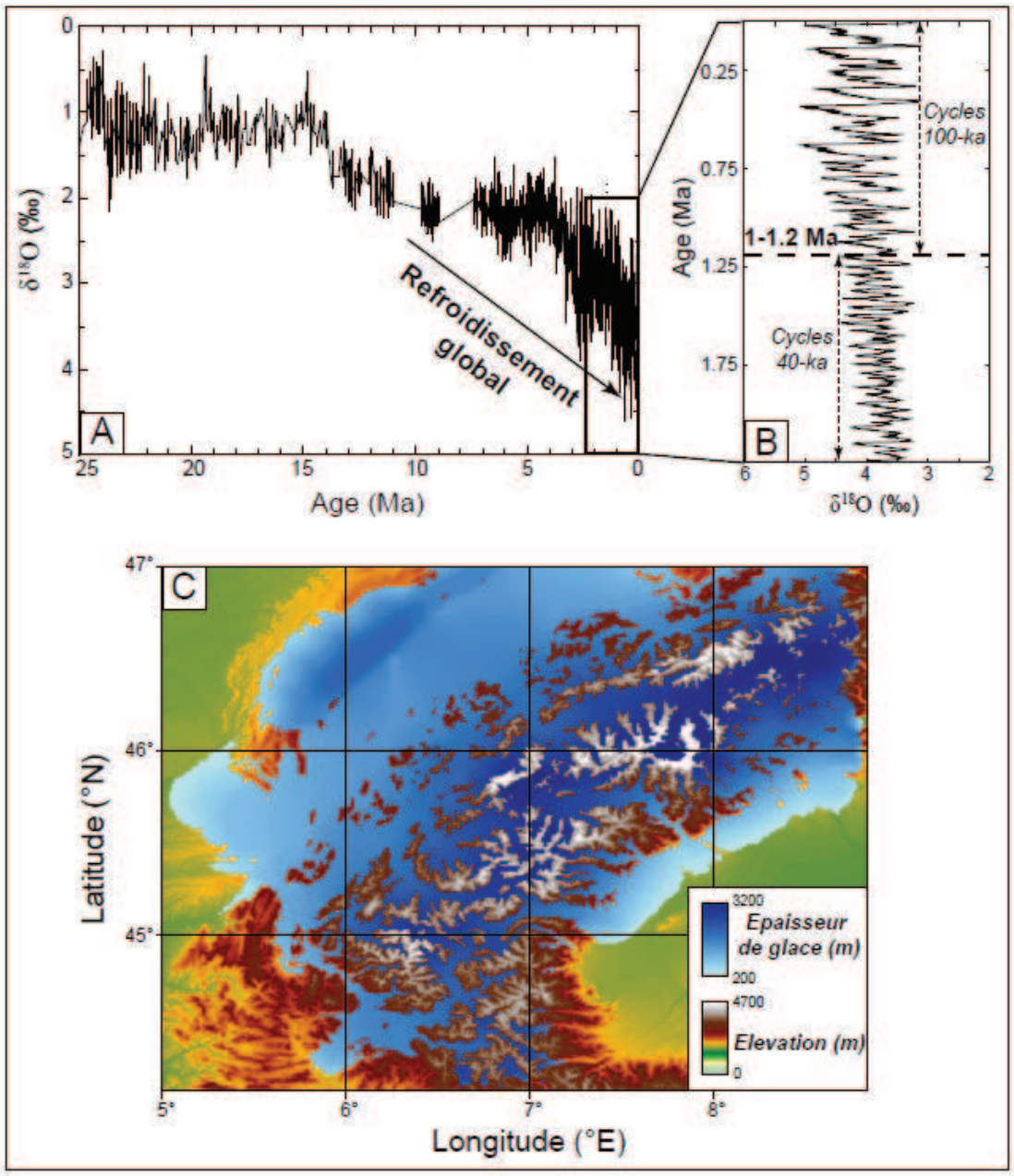

Figure I.1.1. *A) Evolution du $\delta^{18}O$ des sédiments marins, proxy de l'évolution du climat global (refroidissement global et augmentation de la variabilité climatique depuis ~5 Ma). B) Zoom sur la courbe d'évolution du $\delta^{18}O$ des sédiments marins pour les derniers 2 Ma, illustrant la transition climatique mi-Pléistocène. Modifiées d'après Zhang et al. [2001] et Lisiecki and Raymo [2005]. C) Englacement des Alpes Européennes occidentales lors du Dernier Maximum Glaciaire (DMG ~20 ka). Modifiée d'après Ehlers and Gibbard [2004].*

Enfin, une étude récente de *Willenbring and von Blanckenburg* [2010] remet potentiellement en cause le signal global d'une augmentation des vitesses de sédimentation, démontrant que l'altération des silicates et la teneur atmosphérique globale en dioxyde de carbone n'avaient que très peu variées au Miocène-Pliocène. Ainsi, la transition Miocène-Pliocène ne serait pas

associée à un changement climatique global, et l'augmentation Pliocène des flux sédimentaires proviendrait d'un effet d'échelle, les enregistrements sédimentaires récents étant potentiellement mieux conservés que les archives anciennes [*Sadler*, 1981; *Willenbring and von Blanckenburg*, 2010]. Ce débat, toujours d'actualité, a soulevé de nombreuses études afin de vérifier ou d'imputer ces hypothèses et a progressivement favorisé le développement de la géomorphologie quantitative au cours des dernières décennies.

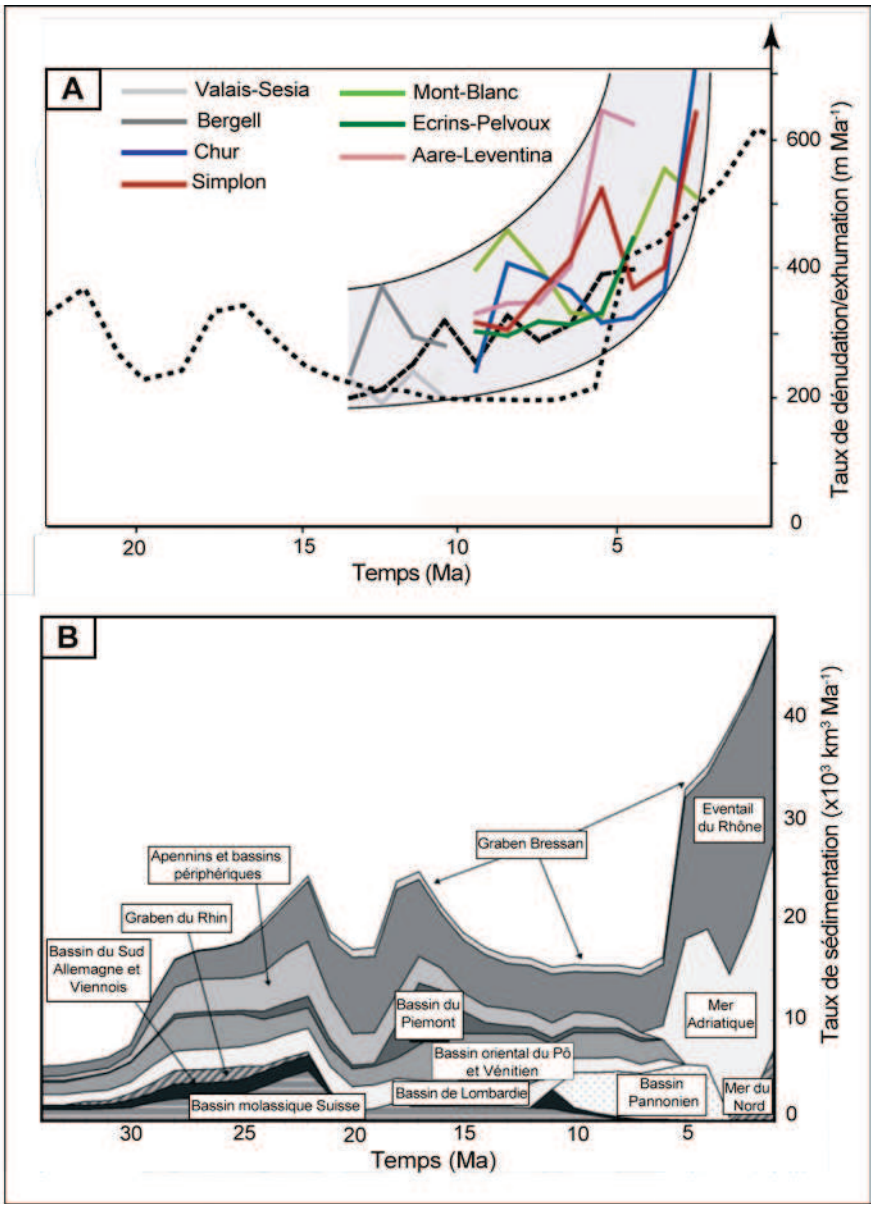

Figure I.1.2. *A) Taux de dénudation (exhumation) moyennés à partir d'une compilation de données traces de fission sur apatite (surfaces isoages, couleurs représentant les zones étudiées); et taux de sédimentation moyens enregistrés dans les bassins périphériques (courbe pointillée). B) Taux de sédimentation dans les bassins de dépôts autour des Alpes Européennes Occidentales. Modifiées d'après Vernon et al. [2008] et Kuhlemann et al. [2002].*

Ce débat est parfaitement illustré par l'évolution des Alpes Européennes depuis le Miocène (Figure I.1.2). En effet, *Kuhlemann et al.* [2002] rapportent une augmentation majeure (d'un facteur deux à trois) des vitesses de sédimentation au sein des bassins périphériques alpins (Figure I.1.2B) depuis la transition Miocène-Pliocène (~5 Ma). Pour la même période, *Vernon et al.* [2008] proposent une augmentation des vitesses d'exhumation des principaux massifs alpins (Figure I.1.2A) et *Cederbom et al.* [2004] démontrent l'initiation du soulèvement du bassin d'avant-pays au nord de la chaîne (associé selon ces auteurs au rebond isostatique en réponse à la décharge érosive au sein de la chaîne, Figure I.1.3A). Cependant, ces études sont partiellement remises en cause par les travaux de *Bernet et al.* [2001] et *Glotzbach et al.* [2011] qui rapportent une exhumation constante des Alpes Occidentales depuis le Miocène, sans accélération nette au cours des derniers ~5 Ma.

L'apport de nouveaux arguments à ce débat de longue date passe par l'acquisition de données quantitatives et temporelles quant à l'évolution du relief des chaînes de montagne au cours du tardi-Cénozoïque, notamment lors de la transition Miocène-Pliocène et durant le Quaternaire. Une question majeure, et relative à cette problématique, est la chronologie de la formation du relief des chaînes de montagne tel que nous pouvons l'observer aujourd'hui : formation continue et progressive du relief topographique depuis le début de la construction de l'orogène, ou au contraire transition brutale au Pliocène-Quaternaire associée au développement de la topographie dans les chaînes de montagne telle qu'elle apparait aujourd'hui.

Un des arguments majeurs de *Molnar and England* [1990] repose sur l'impact du changement climatique global, et notamment un refroidissement progressif depuis le Pliocène (associé à une forte augmentation de la variabilité climatique, Figure I.1.1A) sur la dynamique d'érosion au sein des chaînes de montagne, avec le développement de périodes glaciaires récurrentes et une augmentation de la fréquence oscillatoire des cycles glaciaire/interglaciaire (Figure I.1.1B). Cet effet, s'il est avéré, doit avoir été enregistré dans l'évolution du relief et la transition depuis des processus d'érosion fluviaux et de versants vers une alternance avec des processus glaciaires/périglaciaires. Par ailleurs, ces mêmes auteurs [*Molnar and England*, 1990] considèrent le soulèvement des chaînes de montagne au cours du Pliocène comme une réponse isostatique à l'augmentation des taux d'érosion (Figure I.1.3A), et avancent même l'hypothèse selon laquelle les sommets, relativement moins érodés comparé au creusement

des vallées, pourraient avoir connu une augmentation de leur élévation par rebond isostatique [*e.g.*, *Small and Anderson*, 1998].

Enfin, l'ensemble de cette théorie couplant l'activité tectonique Pliocène, l'augmentation de la dynamique érosive et des flux sédimentaires dans les chaînes de montagne à la transition climatique Miocène-Pliocène et/ou Quaternaire [*e.g.*, *Whipple*, 2009] repose sur l'hypothèse d'un impact fort des oscillations climatiques glaciaire/interglaciaire sur le développement du relief topographique (*i.e.*, différence d'élévation entre les fonds des vallées et les sommets, aussi appelé "relief géophysique", *Small and Anderson*, 1998; *Brocklehurst and Whipple*, 2002). Ainsi, plusieurs questions apparaissent : (1) l'érosion glaciaire (taux et répartition spatiale) diffère-t-elle significativement de la dynamique érosive fluviale?; (2) quel est l'impact des oscillations climatiques Pliocène et des glaciations Quaternaires sur le relief topographique, à la fois pour une échelle locale (vallée) et globale (bassin versant, chaîne de montagne)?; et (3) quelle est la chronologie de l'initiation des glaciations majeures dans les chaînes de montagne?

Quelques études ont montré que, dans des cas spécifiques, l'érosion glaciaire était plus efficace que les processus fluviaux dans l'évolution de la topographie [*e.g.*, *Hallet et al.*, 1996; *Montgomery*, 2002; *Naylor and Gabet*, 2007; *Dowdeswell et al.*, 2010]; en revanche, *Koppes and Montgomery* [2009] ont démontré que, au niveau global et sur plusieurs échelles de temps (*i.e.*, de la centaine aux millions d'années), l'efficacité érosive des processus glaciaires et fluviaux est sensiblement du même ordre de grandeur.

L'impact de l'érosion glaciaire au long terme sur le relief topographique est un sujet également très controversé (Figure I.1.3B). Plusieurs études ont récemment démontré l'efficacité des processus glaciaires dans le développement du relief, le creusement de vallées [*e.g.*, *Montgomery*, 2002; *Shuster et al.*, 2005; *Haeuselmann et al.*, 2007] et l'érosion de cirques glaciaires [*e.g.*, *Oskin and Burbank*, 2005; *Naylor and Gabet*, 2007] participant à l'augmentation locale et globale du relief topographique. Au contraire, des auteurs avancent une théorie opposée selon laquelle les glaciers, dont l'efficacité érosive et donc l'impact sur la topographie sont maximum au niveau de la ligne d'équilibre glaciaire [*e.g.*, *Anderson et al.*, 2006], limitent l'élévation moyenne des chaînes de montagne et par conséquent participent à la réduction du relief topographique [*e.g.*, *Brozovic et al.*, 1997; *Whipple et al.*, 1999; *Egholm et al.*, 2009]. Enfin, *Thomson et al.* [2010] illustrent dans le cas des Andes la préservation

potentielle de la topographie par des glaciers à base froide [*e.g.*, *Bo et al.*, 2009], limitant l'érosion et favorisant ainsi l'expansion (latérale et verticale) de la chaîne Andine. Ainsi, la controverse liée à l'impact des glaciations sur le relief et la transition topographique depuis un paysage purement fluvial vers une topographie plutôt glaciaire (Figure I.1.3B) reste ouverte.

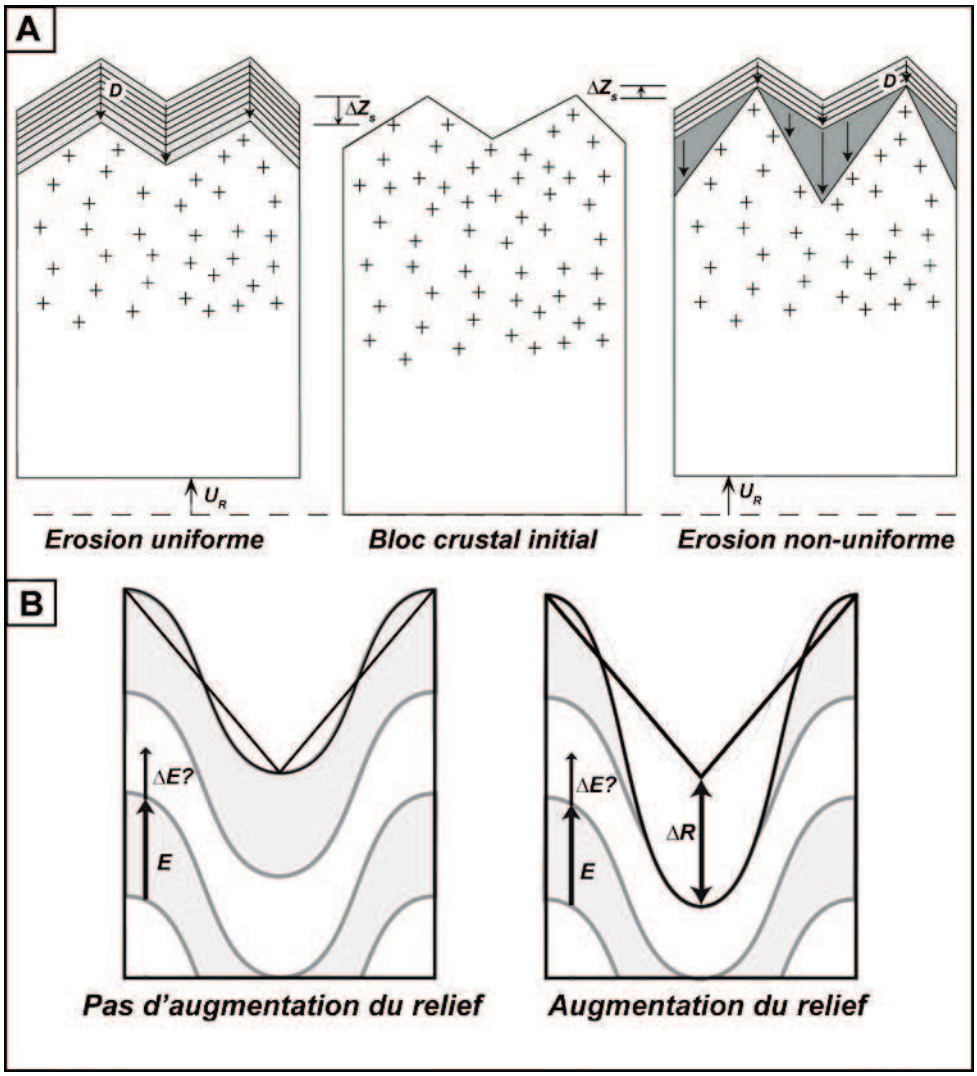

Figure I.1.3. *A) Evolution schématique d'une chaîne de montagne (état initial au centre) suivant le mode d'érosion (D) : spatialement uniforme (gauche) ou variable avec un creusement préférentiel des vallées (droite). La réponse isostatique étant similaire (U_R), l'évolution de l'élévation des sommets (ΔZ_s) est différente suivant les cas : diminution dans le cas d'une érosion uniforme (gauche) et au contraire augmentation si l'érosion est spatialement variable (droite). Modifiée d'après Small and Anderson [1998]. B) Evolution de l'exhumation (E) et du relief (R) lors d'une transition climatique vers une période glaciaire : augmentation potentielle de l'exhumation générale (ΔE?); et transition depuis un paysage fluvial (vallée en V) vers une morphologie glaciaire (vallée en U) associée (droite) ou non (gauche) à une augmentation du relief local (ΔR). Modifiée d'après une figure réalisée par F. Herman.*

La chronologie de l'initiation des périodes glaciaires, et de l'impact glaciaire sur le relief des chaînes de montagne, est également un paramètre qui reste mal contraint. Les archives climatiques (Figure I.1.1A) semblent démontrer un refroidissement global initié à ~5 Ma [*e.g.*, *Maslin et al.*, 1996; *Zhang et al.*, 2001], associé à plusieurs épisodes d'intensification du refroidissement au cours du Pliocène interprétés comme marquant l'entrée en glaciation de l'Hémisphère Nord (~3.5 et 2.7 Ma, respectivement selon *Mudelsee and Raymo*, 2005 et *Haug et al.*, 2005). Cependant, les évidences des premières glaciations (~2.5-2 Ma) en Amérique du Nord [*Balco and Rovey*, 2010] et dans les Alpes Européennes [*e.g.*, *Schlüchter*, 1986; *Haeuselmann et al.,* 2007] sont postérieures à ces chronologies de refroidissement global. Pareillement, la réponse topographique semble postdater l'entrée en glaciation de l'Hémisphère Nord : évidences d'une érosion glaciaire à ~1.8 en Amérique du Nord [*Shuster et al.*, 2005] et à ~0.9-0.8 Ma pour les Alpes Européennes [*Muttoni et al.*, 2003; *Haeuselmann et al.*, 2007]. Ce décalage temporel entre l'entrée en glaciation et les premiers indices de l'impact glaciaire sur le relief topographique reflète potentiellement, d'une part un temps de réponse du système géomorphologique au forçage climatique, et d'autre part un effet de seuil dans l'érosion glaciaire. Cette seconde hypothèse relie les premières évidences morphologiques d'une érosion glaciaire à la transition climatique Mi-Pléistocène (~1.2-1 Ma, *Lisiecki and Raymo*, 2005; *Lisiecki*, 2009) associée au passage depuis des cycles glaciaire/interglaciaire symétriques d'une période de 40-ka vers des cycles fortement asymétriques de 100-ka (Figure I.1.1B).

Mon travail de thèse provient par conséquent de la nécessité d'apporter des contraintes temporelles et quantitatives à la fois sur l'exhumation tardi-Néogène des chaînes de montagne et sur la quantification de l'évolution du relief topographique depuis la transition climatique Miocène-Pliocène. Je me suis essentiellement focalisé sur l'évolution des Alpes Européennes occidentales, pour lesquelles d'une part des données d'exhumation au cours du Néogène sont abondantes grâce à l'acquisition de données thermochronologiques réparties sur l'ensemble de la chaîne [*e.g.*, *Wagner and Reimer*, 1972; *Glotzbach et al.*, 2008; 2010; *Reinecker et al.*, 2008; *Vernon et al.*, 2008; 2009; *van der Beek et al.*, 2010], et d'autre part l'évolution de la topographie et des vitesses d'érosion au cours du Quaternaire/Holocène, bien que documentée par plusieurs études, restent mal contraintes de par leurs liens complexes avec les cycles climatiques glaciaire/interglaciaire [*e.g.*, *Hinderer*, 2001; *Brocard*, 2002; *Schlunegger and Hinderer*, 2003; *Kelly et al.*, 2004; *Champagnac et al.*, 2007; *Haeuselmann et al.*, 2007; *Wittmann et al.*, 2007; *Norton*, 2008; *van der Beek and Bourbon*, 2008; *Delunel*, 2010; *Norton et al.*, 2010a].

I.1.2 - Contexte géodynamique et géomorphologique

Les Alpes Européennes, chaîne de montagne arquée, résultent de la collision entre les continents Européen et Africain ainsi que des unités océaniques de l'ancienne Neothetys [*e.g.*, *Schmid et al.*, 2004]. Cette chaîne de montagne est formée de diverses unités tectono-lithologiques [*e.g.*, *Debelmas and Lemoine*, 1970; *Schmid et al.*, 1996; 2004] avec principalement (Figure I.1.4): (1) les socles Européen et Africain (massifs cristallins externes Européens et socle Apulien, respectivement) formés au cours de l'orogénèse Varisque (Carbonifère), et (2) les unités sédimentaires déposées lors de l'ouverture de la Neothetys et provenant également des couvertures de marges continentales (couverture sédimentaire Européenne, unités Océaniques, Autroalpines et Lepontines). Mon travail de thèse étant centré sur les parties occidentale et centrale de la chaîne, la description suivante est focalisée sur ces zones géographiques.

La convergence entre les continents Européen et Africain s'initie au cours du Crétacé [*Schmid et al.*, 2004], liée à la rotation anti-horaire de la plaque Africaine; et la subduction océanique s'étend jusqu'à environ 65-35 Ma selon les zones [*e.g.*, *Rosenbaum and Lister*, 2005]. La collision continentale, débutant dès le Crétacé et continuant durant tout le Cénozoïque, entraine l'accrétion progressive des différentes unités qui sont déformées et métamorphisées [*e.g.*, *Abrecht*, 1994; *Frey et al.*, 1999; *von Raumer et al.*, 1999]. Durant l'Oligocène, la poursuite de la convergence initie la phase constructive de l'orogène [*Willett et al.*, 2006] associée à des chevauchements par nappes de charriage dans les zones internes et externes [*e.g.*, *Schmid and Kissling*, 2000], ainsi qu'une migration progressive du front de déformation vers les zones externes. Ainsi, autour de la transition Oligocène-Miocène, l'exhumation des massifs cristallins externes (Figure I.1.4) s'accélère [*von Blanckenburg and Davies*, 1995], et au cours du Miocène le chevauchement du Jura se met en place [*Schmid and Kissling*, 2000]. Au même moment, le bassin périphérique nord (Bassin Molassique, Figure I.1.4) est progressivement rempli de par l'érosion de la chaîne [*e.g.*, *Schlunegger et al.*, 1997] avant d'être également exhumé vers la fin du Miocène [*Cederbom et al.*, 2004].
Autour de la transition Miocène-Pliocène (Figure I.1.2), les Alpes Européennes semblent connaitre une accélération des vitesses d'exhumation [*Vernon et al.*, 2008] synchrone d'une augmentation des flux sédimentaires vers les bassins de dépôts [*Kuhlemann et al.*, 2002]; de plus l'activité tectonique cesse dans les zones externes et la déformation se concentre dans les zones internes, l'orogène passe ainsi en phase destructive [*e.g.*, *Willett et al.*, 2006].

L'évolution tardi-Néogène des Alpes est contrôlée par un régime post-collisionel extensif [*e.g.*, *Champagnac et al.*, 2004; *Sue et al.*, 2007] de par la cinématique stable et faiblement extensive de la rotation anti-horaire Europe/Afrique [*Calais et al.*, 2002; *Nocquet and Calais*, 2004]; néanmoins certaines zones enregistrent encore aujourd'hui un soulèvement pouvant atteindre ~1 mm an^{-1} [*e.g.*, *Jouanne et al.*, 1995; *Kähle et al.*, 1997; *Schlatter et al.*, 2005].

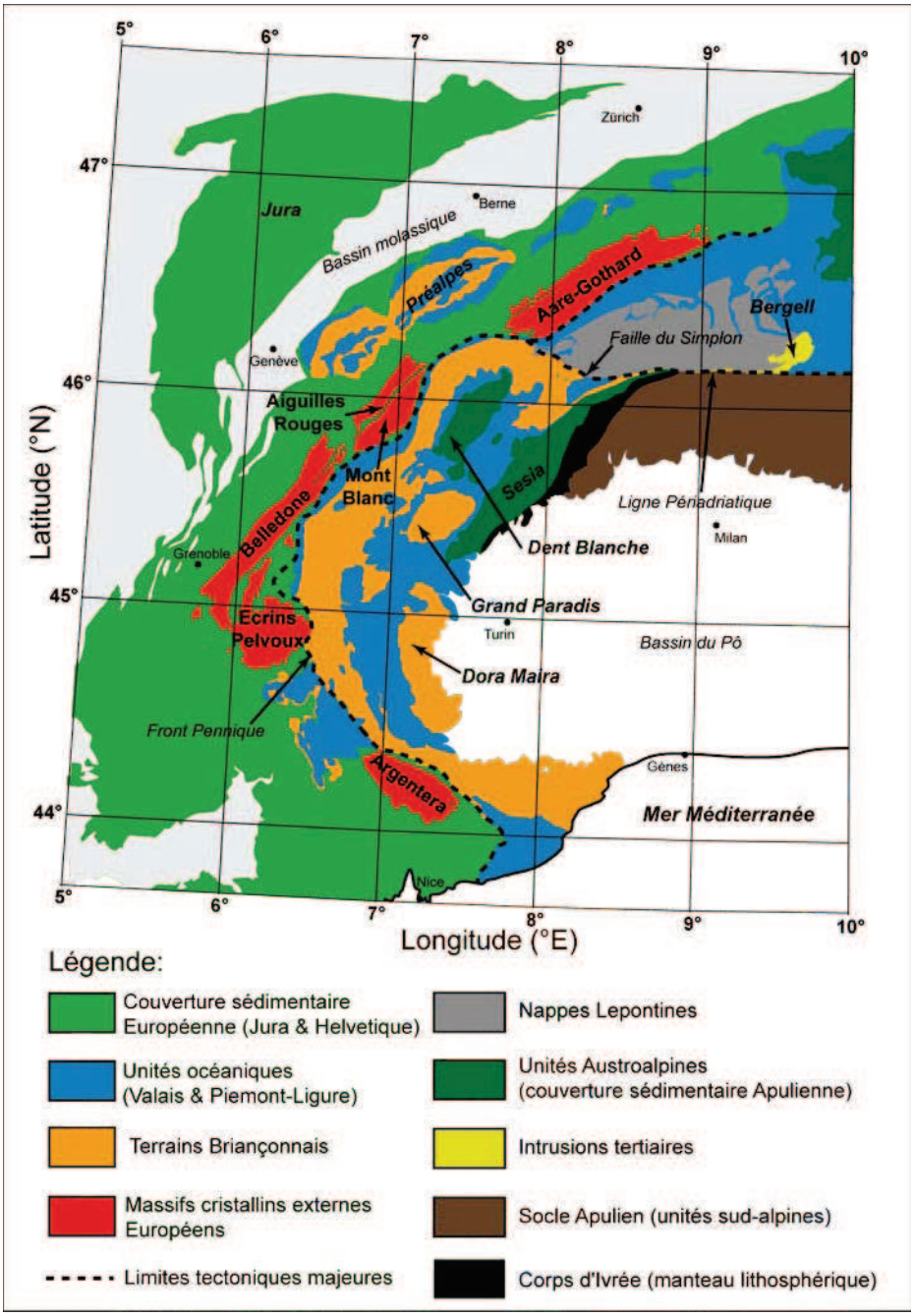

Figure I.1.4. *Carte géologique simplifiée des Alpes Européennes occidentales et centrales, représentant les différentes unités lithologiques/tectoniques ainsi que les contacts tectoniques majeurs. Les différents massifs cristallins externes (rouge) étudiés lors de cette étude (Figure I.1.5) sont indiqués sur la carte. Modifiée d'après Schmid et al. [2004].*

Le relief alpin actuel reflète l'intégration complexe de morphologies glaciaires (vallées en U et surcreusements glaciaires, *e.g.*, *van der Beek and Bourbon*, 2008), fluviales (cascades, rivières en tresses, gorges de raccordement, *e.g.*, *Montjuvent*, 1978), ainsi que les processus de versants (éboulements rocheux, *e.g.*, *Delunel et al.*, 2010a). Le paysage alpin actuel révèle également un fort relief topographique avec des sommets culminant à plus de 4000 m et des vallées profondément creusées à des altitudes de 200-1000 m (Figure I.1.5).

Les Alpes ont été extensivement englacées au cours du Pléistocène-Quaternaire lors de périodes glaciaires récurrentes et entrecoupées d'événements interglaciaires [*e.g.*, *Penck*, 1905]. La chronologie des premiers englacements alpins est assez mal connue de par le peu d'archives disponibles, cependant plusieurs études montrent la présence de glaciers alpins à partir de la fin du Pliocène [*Schlüchter*, 1986; *Haeuselmann et al.*, 2007]. Les premières évidences nettes de l'impact des glaciations sur le relief alpin sont datées à ~0.9-0.8 Ma et proviennent de : (1) l'enregistrement sédimentaire dans le bassin du Pô (Figure I.1.4) marquant la transition entre des dépôts de sédiments purement fluviaux et des granulométries sédimentaires plus grossières d'origine glaciaire [*Muttoni et al.*, 2003]; et (2) la quantification de l'incision de la vallée de l'Aar (Alpes suisses) par datations cosmogéniques de sédiments enfouis dans des karsts [*Haeuselmann et al.*, 2007]. Cependant, ces études ne donnent pas de détails précis sur les périodes glaciaires/interglaciaires successives au cours du Quaternaire, l'extension des glaciers alpins au cours des diverses périodes "froides" ou encore sur l'évolution progressive du relief au cours des stades glaciaire/interglaciaire individuels [*van der Beek and Bourbon*, 2008].

L'épisode d'englacement alpin le mieux documenté spatialement et temporellement est le Dernier Maximum Glaciaire (DMG ou en anglais "Last Glacial Maximum", LGM). A partir des archives sédimentaires déposées par les glaciers à l'extérieur de la chaîne [*e.g.*, *Buoncristiani and Campy*, 2004; *Coutterand*, 2010], et des traces d'érosion glaciaires (roches moutonnées, polis glaciaires) et périglaciaires [*e.g.*, *Thorp*, 1981], plusieurs études locales [*e.g.*, *Montjuvent*, 1978; *Florineth and Schlüchter*, 1998; *Kelly et al.*, 2004; *Coutterand and Buoncristiani*, 2006; *van der Beek and Bourbon*, 2008; *Delunel*, 2010] et à l'échelle des Alpes [*e.g.*, *Jäckli*, 1970; *Bini et al.*, 2009; *Coutterand*, 2010] ont constitué des reconstructions paléogéographiques glaciaires lors du DMG (Figure I.1.1C). La chronologie du DMG a été extensivement débattue au cours des dernières décennies [*e.g.*, *Coutterand*, 2010]. L'initiation du retrait glaciaire dans les bassins périphériques (Bassin Molassique, Bassin du Pô…) est daté autour de 21 ka [*e.g.*, *Ivy-Ochs et al.*, 2004; 2009] tandis que la déglaciation des massifs

alpins internes est plus tardive, datée autour de 15-12 ka [*Kelly et al.*, 2006; *Ivy-Ochs et al.*, 2006; *Delunel*, 2010] et intègre des périodes courtes de refroidissement tel le Dryas ancien [*e.g.*, *Ivy-Ochs et al.*, 2006]. La période Holocène (10 ka à l'actuel) connait également de nombreuses fluctuations glaciaires de faible amplitude [*e.g.*, *Joerin et al.*, 2006; *Delunel*, 2010] se terminant avec l'épisode du Petit Age de Glace (du 17ème au 19ème siècle, *e.g.*, *Nesje and Dahl*, 2003; *Vincent et al.*, 2005).

Depuis le retrait glaciaire, la topographie alpine reflète un ajustement topographique progressif de par l'action érosive des processus fluviaux et de versants [*e.g.*, *Schlunegger and Schneider*, 2005]. Le retrait glaciaire fin-Pléistocène induit au cours de l'Holocène une relaxation des versants et par conséquent de nombreux éboulement rocheux [*e.g.*, *Cossart et al.*, 2008; *Le Roux et al.*, 2009; *Delunel et al.*, 2010a; *Sanchez et al.*, 2010]. Par ailleurs, le réseau fluvial, fortement perturbé par l'action des glaciers [*e.g.*, *Montjuvent*, 1978; *Norton et al.*, 2010a], présente des zones de déséquilibre associées à des vitesses d'érosion importantes telles les gorges de raccordement (gradins de confluence entre une vallée principale et ses affluents, *e.g.*, *MacGregor et al.*, 2000; *Amundson and Iverson*, 2006).
Actuellement, les vitesses d'érosion mesurées à l'échelle de bassins versants sont de l'ordre du mm an^{-1} [*e.g.*, *Hinderer*, 2001; *Wittman et al.*, 2007; *Norton et al.*, 2010b; *Delunel et al.*, 2010b] et traduisent une réponse postglaciaire du relief à la transition glaciaire/interglaciaire depuis le DMG [*Schlunegger and Hinderer*, 2003; *Norton et al.*, 2010a]. Cette transition géomorphologique est associé à des vitesses de soulèvement importantes également de l'ordre du mm an^{-1}, notamment pour les massifs cristallins externes [*e.g.*, *Jouanne et al.*, 1995; *Kähle et al.*, 1997; *Schlatter et al.*, 2005]. Ce soulèvement, en l'absence d'évidence actuelle d'une convergence active [*Nocquet and Calais*, 2004; *Champagnac et al.*, 2009], est expliqué à la fois par un phénomène de rebond isostatique en réponse au retrait glaciaire depuis le DMG [*Gudmundsson*, 1994; *Barletta et al.*, 2006], et par une réponse isostatique de plus long terme reflétant la décharge érosive et le développement du relief (Figure I.1.3A) au cours des oscillations glaciaire/interglaciaire Quaternaires [*e.g.*, *Schlunegger and Hinderer*, 2001; *Champagnac et al.*, 2007; *van der Beek and Bourbon*, 2008]. Ainsi, la concordance spatiale et temporelle entre les vitesses de soulèvement et d'érosion illustre selon plusieurs auteurs [*e.g.*, *Wittmann et al.*, 2007; *Champagnac et al.*, 2008; 2009] l'existence d'un couplage actuel érosion/tectonique; ce couplage, ainsi que le déséquilibre du relief topographique et la réponse érosive postglacaire, étant entretenu par les oscillations récurrentes entre périodes glaciaires/interglaciaires durant le Quaternaire [*e.g.*, *Norton et al.*, 2010a].

I.1.3 - Problématique et organisation du manuscrit

Les Alpes occidentales et leur évolution tardi-Néogène sont propices à l'étude des couplages entre les processus climatiques, tectoniques et de surface dans la dynamique orogénique et notamment le développement du relief topographique. Mon travail de thèse, rapporté dans ce présent manuscrit, vise à la fois à apporter des contraintes temporelles sur l'exhumation Miocène-Pliocène des Alpes occidentales, mais également à quantifier le développement et l'évolution du relief alpin au cours du Pliocène-Pléistocène. En effet, le lien entre la mise en place des glaciations Quaternaires et l'évolution du relief alpin reste mal contraint, et mes travaux de recherche se sont particulièrement focalisés sur la réponse de la topographie alpine aux cycles glaciaire/interglaciaire successifs durant les derniers millions d'années de l'histoire des Alpes occidentales. Ainsi, ce travail a pour objectif deux attentes principales : (1) quantifier l'influence des changements climatiques sur l'évolution du relief; et (2) mieux comprendre l'histoire d'exhumation récente des Alpes occidentales afin d'évaluer l'importance relative des processus d'érosion dans la dynamique actuelle (notamment le soulèvement) de l'orogène.

La quantification de l'exhumation tardi-Néogène des Alpes occidentales et de l'évolution du relief topographique Pliocène-Quaternaire nécessite des outils méthodologiques permettant de contraindre les vitesses d'exhumation, d'érosion et l'évolution du relief. Ainsi, ce manuscrit est basé sur l'utilisation de : (1) la thermochronologie basse température (*i.e.*, méthode de géochronologie quantifiant le chemin thermique d'une roche lors de son exhumation au sein de la lithosphère vers la surface topographique, *e.g.*, *Gallagher et al.*, 1998; *Farley*, 2002; *Ehlers and Farley*, 2003; *Shuster and Farley*, 2005) via les méthodes (U-Th-Sm)/He et $^{4}He/^{3}He$ sur apatite; ainsi que la datation par nucléides cosmogéniques (^{10}Be produit *in situ* dans le quartz, *e.g.*, *Gosse and Philips*, 2001); et (2) la modélisation numérique afin, d'une part d'interpréter quantitativement les données thermochronologiques en terme de vitesses d'exhumation et d'évolution de la topographie [*e.g.*, *Braun*, 2002a; *Gallagher et al.*, 2005a, b], et d'autre part de contraindre l'impact sur le relief des processus de surface fluviaux et glaciaires [*e.g.*, *Kooi and Beaumont*, 1994; *Braun et al.*, 1998; *Whipple and Tucker*, 1999].

Suite à cette introduction du contexte scientifique et l'exposition de ma problématique, je présente dans la suite de ce chapitre la méthodologie des techniques analytiques (thermochronologie basse température et nucléides cosmogéniques) et numériques

(interprétation de données thermochronologiques et modélisation des processus de surface) que j'ai utilisées durant ma thèse.

Le second chapitre présente une approche numérique inverse développée afin d'interpréter quantitativement des données thermochronologiques et de contraindre indépendamment des histoires complexes d'exhumation et d'évolution du relief. Ce chapitre est basé sur deux études synthétiques et rapporte également l'application de cette méthode sur un jeu de données thermochronologiques réelles récoltées dans le massif des Ecrins-Pelvoux (Figure I.1.5).

Le troisième chapitre est consacré à l'exposition des résultats (U-Th-Sm)/He et $^{4}He/^{3}He$ (en collaboration avec D. Shuster du Berkeley Geochronology Center) obtenus dans la vallée du Rhône (Alpes suisses, Figure I.1.5) ainsi que leur interprétation en terme d'évolution Pléistocène du relief topographique. De plus, mes données sont complétées par des données thermochronologiques issues de la littérature afin de contraindre l'histoire d'exhumation Néogène de cette zone d'étude. Enfin, j'utilise les contraintes sur l'évolution topographique Pléistocène obtenues via la thermochronologie afin de proposer une reconstruction numérique de la topographie pré-glaciaire de la vallée du Rhône, estimant ainsi l'érosion totale à l'échelle du bassin versant au cours du Quaternaire et son impact sur le soulèvement actuel de la zone.

Le quatrième chapitre est consacré à la modélisation numérique des processus de surface fluviaux et glaciaires afin de quantifier leur action respective sur le relief alpin. Dans un premier temps, je présente le résultat de modélisations glaciaires préliminaires ainsi que des perspectives de recherche concernant l'impact sur le relief des oscillations climatiques entre périodes glaciaires et interglaciaires au cours du Quaternaire. Par la suite, je propose une étude combinant analyse morphométrique, modélisation numérique et datation par nucléides cosmogéniques, afin de quantifier l'évolution fluviale postglaciaire des gorges de raccordement (massif des Ecrins-Pelvoux, Figure I.1.5), étude débutée au cours de mon stage de Master 2 et achevée durant ma thèse.

Dans un dernier chapitre, je synthétise les principaux résultats de mes travaux de thèse sur : (1) les apports de la thermochronologie basse température et de l'approche numérique inverse dans la quantification d'histoires d'exhumation complexes combinant dénudation régionale et évolution du relief topographique; et (2) les nouvelles contraintes temporelles sur l'exhumation Néogène-Quaternaire des Alpes occidentales et le développement du relief alpin tel qu'il est observable aujourd'hui. Enfin, je propose une conclusion générale de mes travaux de thèse et mets en avant les ouvertures et perspectives scientifiques ressortant de mon étude

au sujet des interactions entre les changements climatiques, l'activité tectonique et l'évolution du relief.

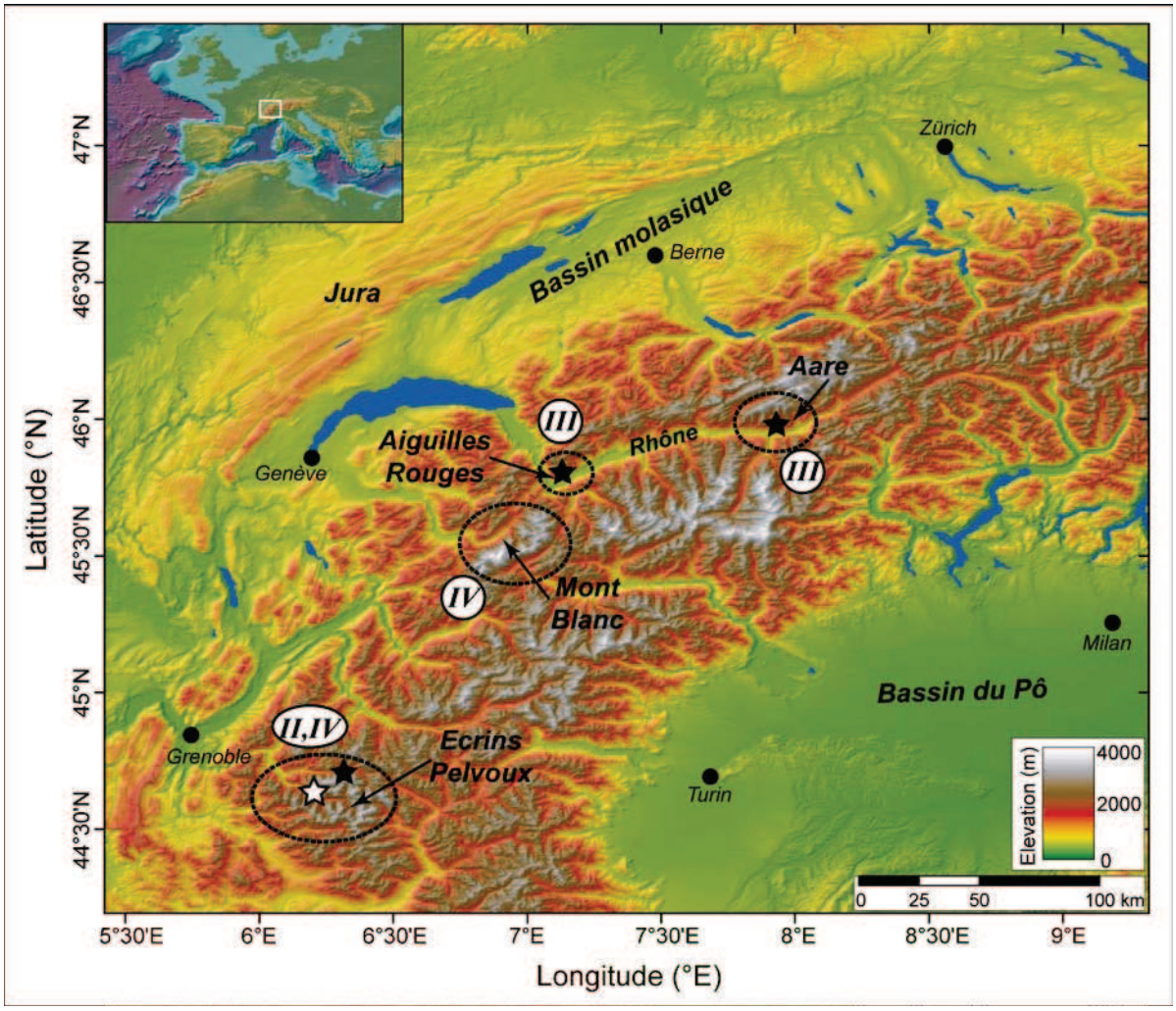

Figure I.1.5. *Modèle Numérique de Terrain des Alpes Européennes occidentales et centrales (l'encart localise la zone d'étude au sein du continent Européen). Les cercles pointillés indiquent les différentes zones d'étude respectivement pour les chapitres II, III et IV (numéros indiqués sur la carte). Les étoiles correspondent aux localisations des sites d'échantillonnage pour les données : traces de fission et (U-Th)/He sur apatite et zircon (chapitre II, étoile noire au sein du massif des Ecrins-Pelvoux; van der Beek et al., 2010), (U-Th-Sm)/He et $^{4}He/^{3}He$ sur apatite (chapitre III, étoiles noires le long de la vallée du Rhône correspondant aux massifs des Aiguilles Rouges et de l'Aar; Valla et al., submitted, a), et ^{10}Be cosmogénique produit in situ (chapitre IV, étoile blanche au sein du massif des Ecrins-Pelvoux; Valla et al., 2010a). Modifiée d'après une figure réalisée par J.-D. Champagnac.*

I.2 - Méthodologie

I.2.1 - Méthodes de géochronologie

I.2.1.1 - Thermochronométrie (U-Th-Sm)/He et $^4He/^3He$ sur apatite

Principes de Thermochronométrie

La thermochronométrie, méthode relative à la géochronologie radio-isotopique, est un ensemble de méthodologies se basant sur des mesures géochimiques d'une roche afin d'en contraindre l'histoire thermique au cours des temps géologiques (cette histoire thermique est aussi appelée thermochronologie; *Reiners and Ehlers*, 2005). La plupart de ces méthodes implique la mesure de la production d'isotopes radiogéniques (éléments "fils") issus de la désintégration d'isotopes radioactifs (éléments "père"), ce couple père/fils formant un système thermochronométrique spécifique à un minéral donné (*i.e.*, défini ci-après comme un thermochronomètre). Cependant, l'accumulation de l'élément "fils" dans un minéral est sujette aux processus de diffusion depuis le réseau cristallin vers l'extérieur du minéral. Les processus de diffusion d'un élément (N) au sein d'un minéral et au cours du temps (t) peuvent être décrits par l'équation de diffusion simple suivante :

$$\frac{\partial N}{\partial t} = D(T)\nabla^2 N + P \qquad \text{(I.2.1)}$$

avec P (atomes an^{-1}) le taux de production de l'élément N (*i.e.*, production par désintégration radioactive), ∇^2 l'opérateur laplacien (dérivée spatiale de second ordre) et D (m^2 an^{-1}) le coefficient de diffusivité de l'élément N dans un minéral donné. D est fonction de la température (T), et suit une loi d'Arrhenius du type [*e.g.*, *Dodson*, 1973; *Braun et al.*, 2006] :

$$\frac{D(T)}{a^2} = \frac{D_0}{a^2} e^{-E_a/RT} \qquad \text{(I.2.2)}$$

avec D_0 (m^2 an^{-1}) le coefficient de diffusivité de l'élément N à une température infinie, a (m) la dimension du domaine de diffusion (souvent approximée par la taille du grain, *i.e.*, son rayon spécifique), E_a l'énergie d'activation (J mol^{-1}) et R la constante des gaz parfaits (~8.314 J mol^{-1} K^{-1}). Les coefficients de diffusion E_a, D_0 et a sont caractéristiques du thermochronomètre et varient également grain à grain selon la structure, la composition et

éventuellement les défauts du minéral. Ces constantes sont généralement déterminées expérimentalement (Figure I.2.1) au cours d'expériences de diffusion [*e.g.*, *Farley*, 2000].

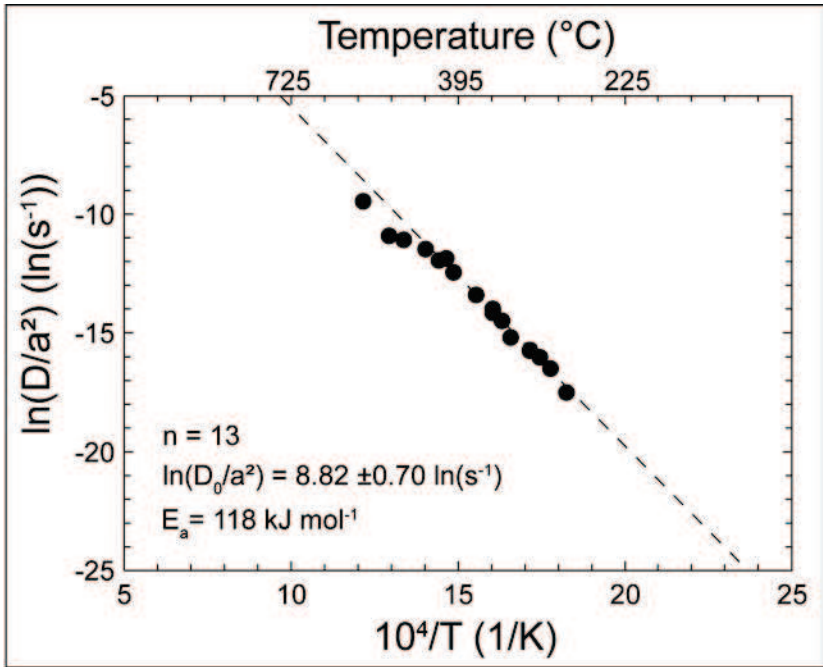

Figure I.2.1. *Détermination expérimentale des coefficients de diffusion D_0/a^2 et E_a (diffusion d'hélium dans un minéral d'apatite). Le diagramme d'Arrhenius présente les différentes mesures de diffusivité (n=13) pour une gamme variable de températures (~200-600 °C). La droite de régression (pointillés) permet l'obtention des paramètres de diffusivité D_0/a^2 et E_a.*

L'évolution d'un système thermochronométrique donné au cours du temps est par conséquent fortement dépendante de la température et varie suivant 3 différents états : (1) à hautes températures, le système est dit "ouvert", *i.e.*, tout élément radiogénique "fils" produit est exporté hors du minéral du fait d'une diffusivité extrêmement élevée; (2) au cours du refroidissement, la diffusivité de l'élément radiogénique diminue et une partie de la production de l'élément "fils" est conservée dans le minéral; et (3) en dessous d'une certaine température, la diffusivité devient si faible que tout élément radiogénique produit est retenu dans le réseau cristallin du minéral, le système devient alors "fermé". L'intervalle de températures entre les états (2) et (3) est défini comme la zone partielle de rétention (en anglais : Partial Retention Zone, PRZ; *Braun et al.*, 2006).

La mesure de l'abondance actuelle en éléments "père" et "fils" au sein d'un minéral permet la définition d'un âge de refroidissement, impliquant la définition de la notion de température de fermeture T_c d'un minéral vis-à-vis d'un système thermochronomètrique donné [*Dodson*,

1973]. La température de fermeture, comme définie par *Dodson* [1973], correspond à la température à laquelle la rétention de l'élément "fils" au sein du réseau cristallin devient effective.

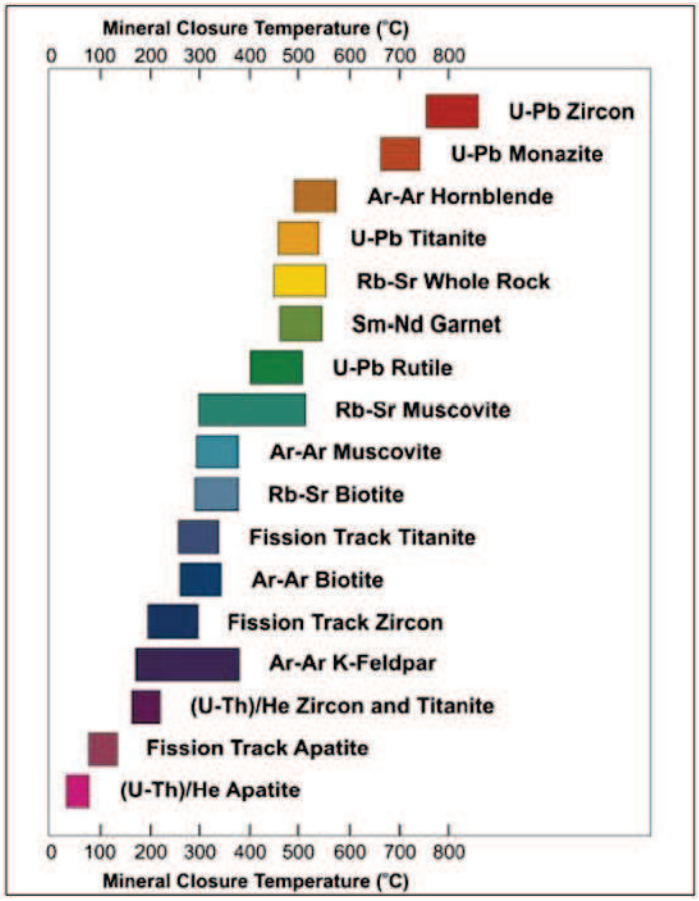

Figure I.2.2. *Estimations de la gamme de températures de fermeture effectives T_c pour différents systèmes thermochronométriques et divers minéraux. Ces gammes prennent en compte la variabilité des paramètres de diffusivité (E_a, D_0) pour un type de minéral, ainsi que l'influence de la vitesse de refroidissement sur la température de fermeture. Modifiée d'après une figure disponible via http://su-thermochronology.syr.edu*

Dodson [1973] propose une solution analytique pour T_c (voir *Braun et al.*, 2006, pour une démonstration complète) présentée sous la forme suivante :

$$T_c = \frac{E_a}{R \ln(A \tau D_0 / a^2)} \qquad \text{avec} \quad \tau = \frac{R T_c^2}{E_a \dot{T}} \tag{I.2.3}$$

avec A une constante de diffusion sans unité dépendante du système géométrique considéré (A = 25 pour une sphère, 27 pour un cylindre et 8.7 pour une surface plane), τ une constante de temps (an) traduisant la diminution de la diffusivité du minéral d'un facteur exponentiel, et $\dot{T}$

la vitesse de refroidissement (°C an^{-1}). La notion de température de fermeture n'est donc pas une constante fixée mais recouvre une gamme de températures dépendante d'une part des propriétés caractéristiques du minéral et de l'élément diffusif considéré (a, E_a, D_0), et d'autre part de la vitesse à laquelle la roche est refroidie, et par conséquent du contexte géologique (Figure I.2.2).

Durant ma thèse, je me suis principalement intéressé au système thermochronométrique (U-Th-Sm)/He [*e.g.*, *Farley*, 2002] et à la thermochronométrie $^4He/^3He$ [*e.g.*, *Shuster and Farley*, 2005] dans le minéral d'apatite ($Ca_5(PO_4)_3(OH,Cl,F)$). Dans la suite de cette partie, je vais tout d'abord présenter les principe et protocole analytique de la thermochronométrie (U-Th-Sm)/He avant de préciser les spécificités de la thermochronométrie $^4He/^3He$.

Thermochronométrie (U-Th-Sm)/He sur apatite

Le système (U-Th-Sm)/He sur apatite [*Hurley et al.*, 1956; *Zeitler et al.*, 1987; *Wolf et al.*, 1996; 1998] est un thermochronomètre de basse température (Figure I.2.2, $T_c \approx 75 \pm 15$°C, *Farley*, 2000; *PRZ* ≈ 40-85 °C, *Wolf et al.*, 1996) utilisé afin contraindre les processus d'exhumation récente ou encore l'évolution du relief [*Elhers and Farley*, 2003].

La thermochronométrie (U-Th-Sm)/He est basée sur : (1) la production d'hélium (^4He) par les réactions de désintégration radioactive (décroissance alpha, en anglais "α -decay") de certains éléments de la série des actinides (respectivement 8, 7 et 6 particules α produites pour la désintégration d'un atome d'^{238}U, ^{235}U et ^{232}Th) et en moindre importance du ^{147}Sm (1 particule α produite pour une réaction de désintégration) ; et (2) la diffusion du ^4He produit au travers du minéral selon une diffusion simple de type Arrhenius [*Dodson*, 1973]. La production de ^4He par décroissance radioactive des éléments ^{238}U, ^{235}U, ^{232}Th et ^{147}Sm est donnée par l'équation suivante :

$$^4He = 8\ ^{238}U\,(e^{\lambda_{238}t} - 1) + 7\ \frac{^{238}U}{137.88}\,(e^{\lambda_{235}t} - 1) + 6\ ^{232}Th\,(e^{\lambda_{232}t} - 1) + ^{147}Sm\,(e^{\lambda_{147}t} - 1) \qquad \text{(I.2.4)}$$

avec ^4He, ^{238}U, ^{232}Th et ^{147}Sm les abondances actuelles mesurées dans le minéral, t l'âge thermochronométrique de l'échantillon, et λ la constante de désintégration des divers éléments "pères" ($\lambda_{238} = 1.511\ 10^{-10}$ an^{-1}, $\lambda_{235} = 9.849\ 10^{-10}$ an^{-1}, $\lambda_{232} = 4.948\ 10^{-11}$ an^{-1}, $\lambda_{147} = 6.540\ 10^{-12}$ an^{-1}). Le rapport (1/137.88) représente le rapport actuel entre les isotopes $^{235}U/^{238}U$. La détermination de l'âge thermochronométrique (référé ci-après par l'expression "âge He")

requière par conséquent la mesure des abondances respectives en éléments "fils" (^{4}He) et "pères" (^{238}U, ^{232}Th et ^{147}Sm) et ainsi une préparation et analyse des échantillons selon un protocole analytique précis. La constante de désintégration du ^{147}Sm (λ_{147}) étant faible par rapport aux autres constantes, l'isotope ^{147}Sm est important dans la détermination d'un âge He seulement pour des échantillons présentant de fortes concentrations en ^{147}Sm.

Les échantillons ont été dans un premier temps broyés et tamisés (collaboration F. Cœur, Laboratoire de Géodynamique des Chaînes Alpines, LGCA) puis triés par séparation magnétique (Frantz) et densimétrique au moyen de liqueurs denses (collaboration F. Senebier, LGCA) afin d'isoler la fraction contenant les minéraux d'apatite (fraction diamagnétique et de densité 3.1-3.2). J'ai ensuite sélectionné les grains d'apatite à l'aide d'un microscope binoculaire à polariseur et équipé d'un appareil photo numérique (LGCA et Berkeley Geochronology Center, BGC) afin de ne conserver que des grains de taille acceptable (>60 µm), de forme euhédrique, non cassés et sans inclusion visible (*e.g.*, zircon, monazite) [*Farley*, 2002]. Après cette étape sélective, les grains d'apatite sont isolés et mesurés (largeur et longueur) avant d'être placés individuellement dans des tubes de platine (Pt) de taille millimétrique.

L'extraction du ^{4}He, ainsi que la mesure des abondances en ^{238}U, ^{232}Th et ^{147}Sm ont été réalisées au Caltech Noble Gas Laboratory (Pasadena, USA) en collaboration avec L. Hedges et K. Farley, selon un protocole décrit par *Farley* [2002]. L'extraction du ^{4}He est réalisée sous vide par chauffage laser à une température de 1000 ±50°C (contrôle de température par pyrométrie optique) pendant une durée de 5-8 minutes [*House et al.*, 2000; *Farley*, 2002]. La taille et la nature des tubes Pt permet une répartition rapide et homogène de la chaleur et par conséquent un chauffage sur un temps suffisamment court pour ne pas engendrer de perte d'U, Th ou Sm [*House et al.*, 2000]. Le gaz extrait est ensuite mélangé à une solution avec entraineur de concentration connue en ^{3}He. Ce mélange est concentré par adsorption cryogénique avant d'être admis dans un spectromètre de masse quadripôle où le rapport ^{4}He/^{3}He est mesuré pendant une durée d'environ 2 minutes. L'opération d'extraction par chauffage est répétée sur le même échantillon, une fois le vide rétabli, afin de contrôler si une quantité non négligeable du ^{4}He (parfois >5 % de la quantité de ^{4}He extraite durant la première opération) peut provenir d'inclusions minérales (du type zircon ou monazite) non détectées lors de l'étape de sélection, et dans ce cas d'écarter l'analyse.

L'échantillon est ensuite retiré de la chambre d'extraction puis dissous dans une solution d'acide nitrique (HNO_3) à ~90 °C pendant une heure avant l'ajout d'une solution entraineur de ^{235}U-^{230}Th-^{145}Nd-^{51}V de concentration connue. La solution obtenue est analysée à l'aide d'un spectromètre de masse à plasma (Agilent ICP-MS, Caltech Noble Gas Laboratory) par dilution isotopique afin de déterminer les abondances en ^{238}U, ^{232}Th et ^{147}Sm, ainsi que la masse du grain d'apatite (détermination de l'abondance en calcium Ca). L'incertitude analytique liée à l'extraction du ^{4}He et aux mesures d'abondance en ^{238}U, ^{232}Th et ^{147}Sm est quantifiée via l'analyse de standards [*Farley*, 2002] et est évaluée à environ 6 % pour la détermination de l'âge He (la plus grande part d'incertitude provenant de la mesure du ^{4}He). Au cours des mesures de mes échantillons, la reproductibilité du standard Durango apatite [*Farley*, 2000] a été estimée à ~5 % et reflète la reproductibilité analytique de l'âge He. Cependant, la précision obtenue sur l'âge He final n'est généralement pas limitée par l'incertitude analytique, mais par la reproductibilité du protocole expérimental sur plusieurs grains d'un même échantillon. En effet, le protocole décrit ci-dessus est réalisé individuellement pour 3-5 grains d'apatite provenant d'un même échantillon, et l'âge He final est obtenu en moyennant arithmétiquement chacun des âges He individuels. L'incertitude finale sur l'âge He moyen est variable d'un échantillon à l'autre (de l'ordre de 10-20 %).

Plusieurs effets peuvent potentiellement induire des biais dans la détermination d'un âge He et doivent être corrigés ou au minimum considérés dans l'interprétation de cet âge. Tout d'abord, la présence de micro-inclusions (zircon, monazite), non visibles au microscope binoculaire (et n'étant pas dissoutes par la suite) et ne produisant pas une quantité significative de ^{4}He lors de la seconde étape de réextraction, peut engendrer un âge He plus vieux que l'âge réel de refroidissement depuis la température de fermeture. De plus, il est connu que la désintégration radioactive des noyaux U, Th et Sm produit des particules de fortes énergies (4-8 MeV; *Ziegler*, 1977) qui ont un trajet moyen d'environ 20 µm au sein du réseau cristallin (respectivement 19.68, 22.83 et 22.46 µm pour ^{238}U, ^{235}U et ^{232}Th; *Farley et al.*, 1996]. Les particules α produites (^{4}He) peuvent par conséquent transiter d'un minéral à un autre (Figure I.2.3), entrainant des pertes d'^{4}He au sein d'un grain d'apatite donné et donc un biais dans la détermination de l'âge He. Ce biais est amplifié si le grain d'apatite est de taille réduite (probabilité plus importante de perte de particules α); néanmoins il peut être partiellement corrigé via le facteur de correction F_T [*Farley et al.*, 1996]. Ce facteur considère la perte de ^{4}He par éjection α et fait l'hypothèse d'une répartition homogène des éléments "pères" dans l'apatite [*Farley*, 2002]. Par ailleurs, ce facteur prend en compte la géométrie du

grain (assimilé à un prisme hexagonal) ainsi que les contributions relatives de l'U et Th dans la production du ^{4}He. Un autre biais difficilement quantifiable [*Spiegel et al.*, 2009] est l'assimilation de ^{4}He depuis un minéral voisin du type zircon ou monazite (production de particules α plus importante, Figure I.2.3).

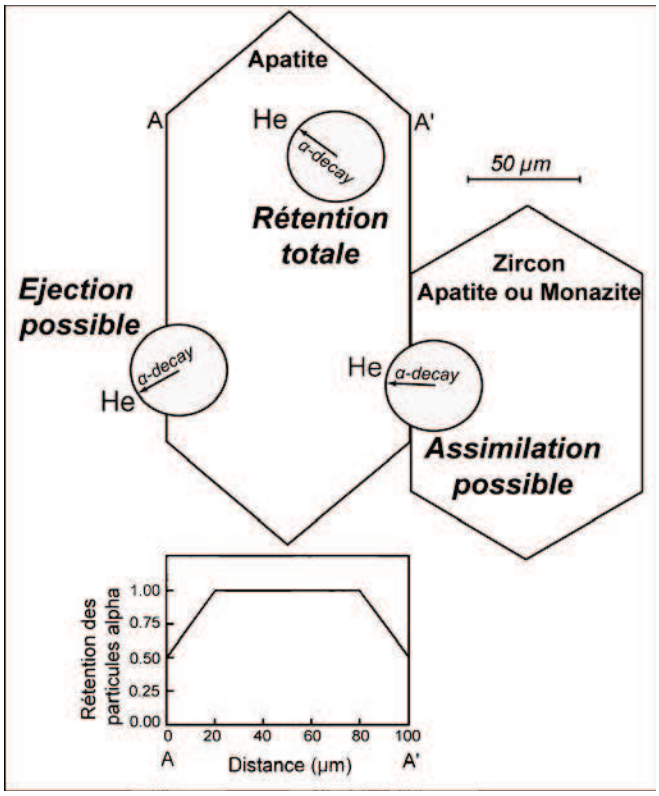

Figure I.2.3. *Effet de l'éjection α sur l'accumulation d'He dans un grain d'apatite. Trois situations sont potentiellement envisageables : rétention totale d'He dans le grain d'apatite, éjection vers un minéral voisin et enfin assimilation depuis un voisin. Le centre du cercle (rayon = trajet moyen d'une particule α) représente la position de l'élément "père" (U ou Th). Le graphe représente de manière schématique la rétention des particules α dans un grain d'apatite. Modifiée d'après Farley [2002].*

Le facteur de correction F_T est calculé de la façon suivante [*Farley*, 2002] :

$$^{238U/232Th}F_T = 1 + a_1\beta + a_2\beta^2 \qquad et \qquad \beta = (2.31L + 2R)/(RL) \tag{I.2.5}$$

avec L la longueur (µm), R la demi-largeur (µm, demi-distance entre 2 apex opposés), et β le rapport surface/volume (µm^{-1}) d'un grain d'apatite, a_1 et a_2 des constantes caractéristiques pour la correction respective de l'^{238}U/^{235}U et ^{232}Th [*Farley*, 2002]. Le facteur de correction moyen est calculé suivant l'équation :

$$^{mean}F_T = a_{238}\,{}^{238U}F_T + (1 - a_{238})\,{}^{232Th}F_T \tag{I.2.6}$$

avec $a_{238} = (1.04+0.245(Th/U))^{-1}$ obtenu directement à partir du rapport U/Th mesuré [*Farley*, 2002]. Les âges He individuels sont donc systématiquement corrigés par ce facteur en divisant l'âge He obtenu via l'équation (I.2.4) par le facteur de correction moyen ${}^{mean}F_T$. Ce facteur permet également de calculer pour chaque grain d'apatite un rayon de sphère équivalente, *i.e.*, l'approximation géométrique de l'apatite selon une sphère [*Farley et al.*, 1996] :

$$ {}^{mean}F_T = 1 - \frac{3S}{4a} + \frac{S^3}{16a^3} \qquad \text{(I.2.7)} $$

avec a le rayon de la sphère équivalente (µm) et S le trajet moyen des particules α (~20 µm). Cette caractéristique géométrique sera utilisée lors des modélisations thermiques (cf. partie I.2.2.1).

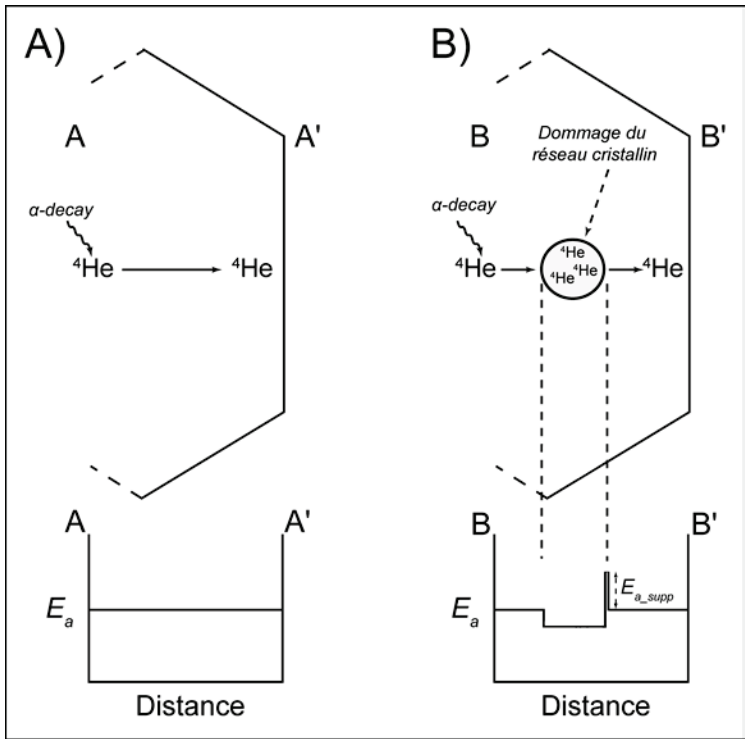

Figure I.2.4. *Modèle schématique représentant les effets potentiels des dommages du réseau cristallin sur la diffusion d'He dans un grain d'apatite. A) Diffusion d'un atome de ^{4}He sans dommage du réseau cristallin. Le graphe représente l'énergie d'activation (E_a = constante, suivant la loi d'Arrhenius) nécessaire à la diffusion de l'atome de ^{4}He au travers du minéral. B) Même situation de diffusion d'un atome de ^{4}He, mais cette fois-ci à travers un dommage du réseau cristallin (représenté par un cercle contenant plusieurs atomes de ^{4}He). Le graphe associé représente l'énergie d'activation effective en fonction de la position de l'atome de ^{4}He dans le minéral d'apatite. Le dommage du réseau agit comme un "piège" à atomes de ^{4}He (minimum local d'énergie d'activation), ainsi une énergie supplémentaire (E_{a_supp}) est nécessaire afin que l'atome de ^{4}He puisse sortir de ce dommage. Modifiée d'après Shuster et al. [2006].*

Un dernier effet pouvant entrainer un biais dans la détermination d'âge He est le dommage du réseau cristallin engendré par les réactions de désintégration radioactive (ce dommage peut être partiellement à totalement recouvré à hautes températures selon une cinétique identique au recuit des traces de fission; *Flowers et al.*, 2009; *Gautheron et al.*, 2009). L'accumulation de dommages au cours du temps (fonction de la concentration en U et Th) modifie les paramètres cinétiques de diffusion au sein d'un grain d'apatite [*Shuster et al.*, 2006] et rend le réseau cristallin plus rétentif à la diffusion d'^{4}He (Figure I.2.4). Ce processus a une influence non négligeable sur la température de fermeture du grain d'apatite en augmentant la limite supérieure de la PRZ (*i.e.*, rétention partielle du ^{4}He à plus haute température). Plusieurs études récentes ont proposé l'utilisation de simulations numériques afin de modéliser la création/réparation des dommages du réseau cristallin lors de désintégrationsα, et ainsi de quantifier, à partir des concentrations en U et Th et de l'histoire de refroidissement, l'impact de ces dommages sur la diffusion et la rétention du ^{4}He dans un grain d'apatite [*Flowers et al.*, 2009; *Gautheron et al.,* 2009].

Thermochronométrie ^{4}He/^{3}He sur apatite

La thermochronométrie ^{4}He/^{3}He est principalement basée sur la méthode (U-Th-Sm)/He (voir partie ci-dessus) et considère par conséquent les mêmes principes et hypothèses de base. Cependant, au contraire du thermochronomètre (U-Th-Sm)/He, cette technique ne prédit pas seulement un âge de refroidissement, mais elle apporte également des contraintes sur la distribution spatiale du ^{4}He radiogénique dans le grain d'apatite [*Shuster and Farley*, 2004; 2005]. En effet, la répartition du ^{4}He au sein d'un grain d'apatite évolue lors du passage de l'échantillon au travers de la PRZ mais également pour des températures plus basses (jusqu'à ~20 °C) : des expériences de diffusion ont montré que le ^{4}He pouvait être mobile et toujours diffuser au sein et partiellement au travers d'un minéral d'apatite pour des températures de l'ordre de 20-30 °C [*Green and Duddy*, 2006]. La distribution du ^{4}He est par conséquent une fonction de l'histoire temps/Température de l'échantillon (chemin *t-T*) et peut être schématiquement décrite par l'équation suivante [*Shuster and Farley*, 2005] :

$$\int_{t_0}^{actuel} [\mathrm{Pr}\,oduction(x,y,z,t) - Perte(x,y,z,T,t)]dt = Distribution(x,y,z,actuel) \qquad \text{(I.2.8)}$$

où le terme *Distribution* représente la distribution spatiale du ^{4}He radiogénique mesurée aujourd'hui (actuel) dans un grain d'apatite (de dimensions *x*, *y* et *z*), le terme *Production* correspond à la production au cours du temps (depuis un temps t_0) du ^{4}He par désintégration

radioactive des éléments U, Th et Sm (décroissance α, Eq. (I. 2.4)), et enfin le terme *Perte* décrit la diffusion du ^{4}He au sein et au travers du grain d'apatite (dépendante de la température *T*). Le terme *Production* est donné par la mesure des abondances actuelles en éléments "pères" selon le protocole identique à celui décrit précédemment [*Farley*, 2002].

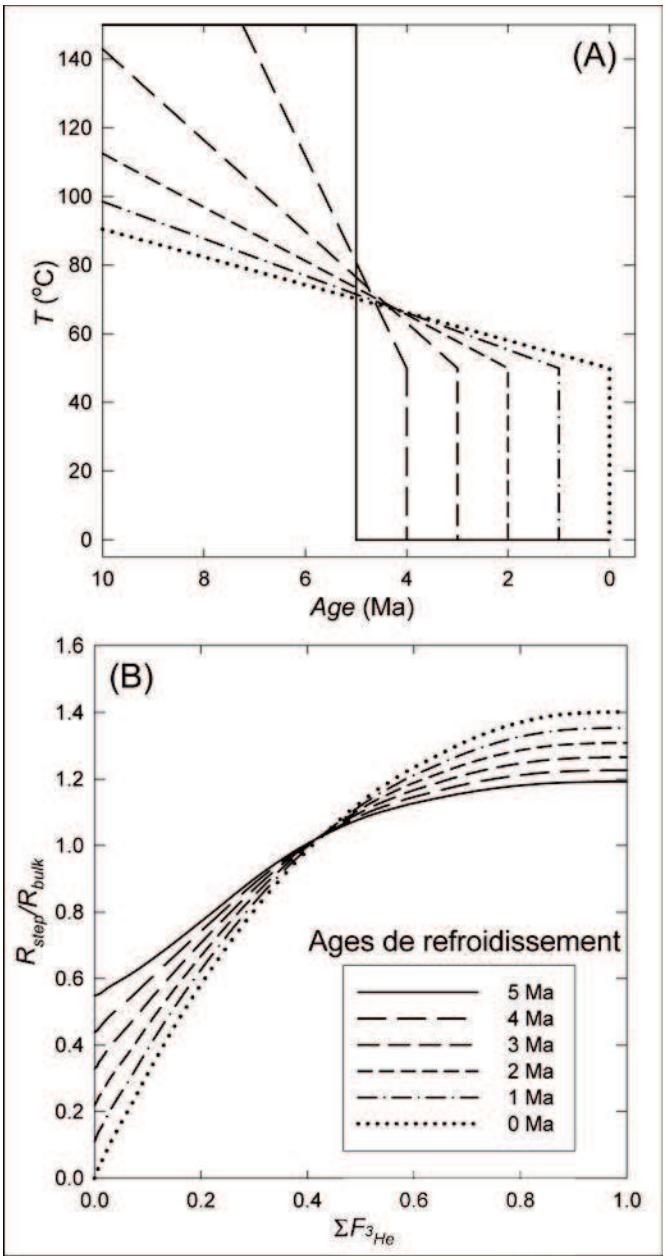

Figure I.2.5. *Exemple théorique de la thermochronométrie $^4He/^3He$. A) Six histoires t-T synthétiques donnent un âge He similaire (~5 Ma), cependant le refroidissement terminal de l'échantillon intervient à des périodes différentes (de 5 Ma à l'actuel). B) La distribution spatiale du ^4He (R_{step} = rapport $^4He/^3He$ mesuré pour chaque étape de chauffage; R_{bulk} = rapport $^4He/^3He$ moyen du grain d'apatite) au sein du grain d'apatite ($\sum F_{3He}$ = 0 pour le début et 1 pour la fin de l'extraction de l'He) pour chaque chemin t-T est différente. Modifiée d'après Shuster and Farley [2005].*

L'apport inédit de la thermochronométrie $^4He/^3He$ est de donner des contraintes à la fois sur la distribution spatiale du ^4He au sein d'un grain d'apatite (fonction *Distribution*) mais également de quantifier via l'analyse du même grain le terme *Perte* en contraignant les paramètres cinétiques de diffusion. Ainsi la thermochronométrie $^4He/^3He$, complétée par la détermination classique d'un âge He [*Farley*, 2002], apporte des contraintes quantitatives sur le chemin *t-T* depuis ~80 °C (*i.e.*, limite supérieure de la PRZ où la rétention d'^4He devient quantifiable) jusqu'à des températures de surface (~20-30 °C) et par conséquent des informations non disponibles via la méthode (U-Th-Sm)/He telle la vitesse de refroidissement terminal de l'échantillon ou encore celle du franchissement de la température de fermeture (Figure I.2.5). Ainsi, la thermochronométrie $^4He/^3He$ fait le lien entre des thermochronomètres de plus hautes températures (*e.g.*, mesure des traces de fission sur apatite, $T_c \approx 110 \pm 10°C$, *Gleadow and Duddy,* 1981) et l'utilisation des isotopes cosmogéniques (cf. partie I.2.1.2).

Le protocole analytique utilisé pour la thermochronométrie $^4He/^3He$ est assez similaire à celui adopté pour la méthode (U-Th-Sm)/He, cependant il comporte un certain nombre de variantes développées ci-après. Tout d'abord, la préparation et le tri des échantillons sont similaires à la méthode (U-Th-Sm)/He (broyage, tamisage et séparation magnétique puis densimétrique). Cependant, les apatites séparées (~50 mg) sont ensuite conditionnées dans une capsule d'étain (Sn) puis soumises à une irradiation protonique (~5.10^{15} protons cm^{-2} et ~220 MeV d'énergie incidente) pendant une période de sept heures (Francis H. Burr Proton Therapy Center, Boston, USA). Cette irradiation permet la production par spallation du ^3He réparti de façon homogène dans le grain d'apatite indépendamment de la concentration spatiale en U et Th [*Shuster et al.*, 2004]. Cette étape produit également du ^4He par spallation, cependant la quantité produite reste infime comparée au ^4He radiogénique produit par désintégration radioactive des éléments U et Th [*Shuster et al.*, 2004]. La production *a priori* uniforme du ^3He par irradiation protonique permet de contraindre les paramètres cinétiques de diffusion d'He lors de l'étape d'extraction par chauffage, les isotopes ^4He et ^3He ayant un comportement diffusif similaire [*Shuster and Farley*, 2005]. Suite à trois à quatre mois d'attente afin que la radioactivité diminue à un niveau acceptable, les capsules de Sn sont ouvertes et les grains d'apatite sont sélectionnés à l'aide d'un microscope binoculaire à polariseur (pas d'inclusion, forme euhédrique…), mesurés (longueur et largeur) puis placés individuellement dans des tubes de Pt.

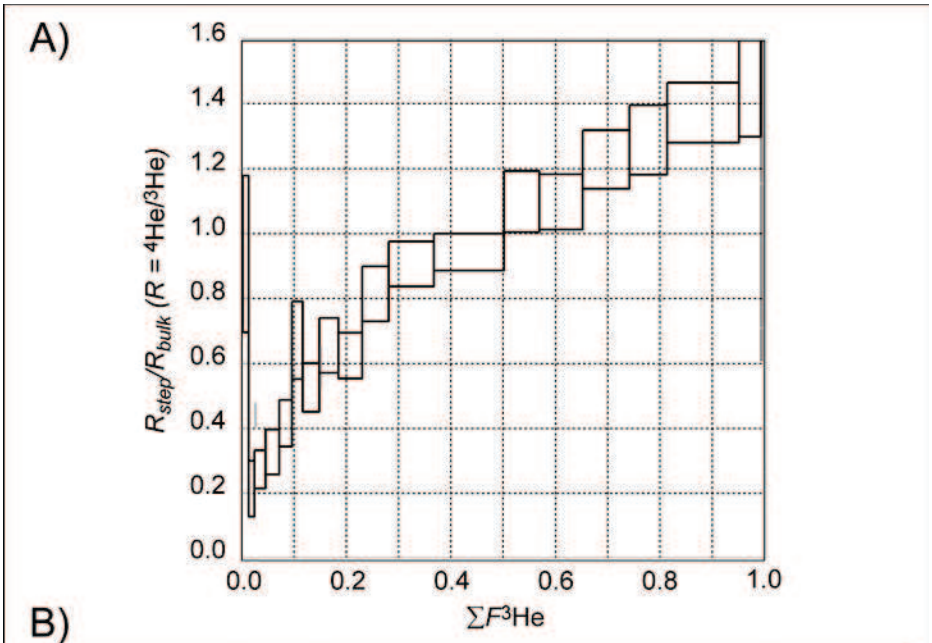

B)

Palier	Temp (°C)	Durée (heures)	^{3}He (x 10^6 atomes)	(+/-) (x 10^6 atomes)	^{4}He/^{3}He	(+/-)
1	260	0.38	0.035	0.007	1392	356
2	275	0.38	0.036	0.007	326	127
3	290	0.51	0.067	0.010	414	87
4	300	0.66	0.082	0.011	492	102
5	310	0.66	0.076	0.011	623	106
6	330	0.46	0.065	0.010	1001	176
7	340	0.45	0.100	0.013	785	110
8	350	0.48	0.114	0.014	977	125
9	350	0.66	0.144	0.016	930	104
10	370	0.53	0.158	0.016	1211	125
11	400	0.48	0.272	0.022	1347	102
12	410	0.63	0.420	0.027	1401	84
13	420	0.50	0.213	0.019	1630	139
14	440	0.50	0.261	0.021	1629	126
15	475	0.50	0.280	0.022	1821	133
16	500	0.50	0.227	0.020	1910	158
17	550	0.50	0.431	0.028	2034	136
18	700	0.50	0.131	0.015	2165	240
19	900	0.50	0.009	0.003	2704	1797
20	950	0.50	0.002	0.001	539	2744

Figure I.2.6. *Exemple pratique d'une expérience de dégazage par paliers successifs de température pour un échantillon d'apatite. Le tableau (B) présente les abondances mesurées en ^{3}He, le rapport mesuré ^{4}He/^{3}He et les incertitudes associées, ainsi que des informations sur le déroulement de l'expérience (nombre de paliers, température et durée pour chacun d'eux). Le graphe (A) illustre l'évolution du rapport mesuré ^{4}He/^{3}He (R_{step} = rapport ^{4}He/^{3}He mesuré pour chaque étape de chauffage; R_{bulk} = rapport ^{4}He/^{3}He moyen du grain d'apatite; et incertitudes analytiques 1σ données par la hauteur de chaque rectangle) au cours de l'expérience de dégazage (chaque palier est quantifié par la fraction du ^{3}He extrait, $\sum F_{3He}$).*

Le protocole d'extraction d'He a pour objectif d'une part de contraindre l'évolution du rapport ^{4}He/^{3}He au sein de l'échantillon afin de déterminer la distribution spatiale du ^{4}He (répartition spatiale uniforme du ^{3}He produit par irradiation protonique), mais également de

quantifier la fonction d'Arrhenius ($D(T)/a^2$, cf. Eq. (I.2.2)) via la mesure de la diffusivité du ^{3}He [*Shuster and Farley*, 2005]. Le protocole d'extraction (partiellement automatisé au BGC Noble Gas Thermochronometry Lab, collaboration D. Shuster et B. Lum) est basé sur les travaux réalisés pour la mesure du ^{40}Ar/^{39}Ar [*McDougall and Harrison*, 1999] et implique un dégazage par paliers successifs de température (de ~250 à 950 °C, Figure I.2.6). L'échantillon, placé dans la chambre d'extraction en condition "d'ultravide", est maintenu à une température donnée (diode laser 70 W contrôlée par un thermocouple) pendant une durée d'extraction préalablement déterminée (Figure I.2.6B). Ensuite, le gaz extrait est concentré par adsorption cryogénique et les abondances respectives en ^{4}He et ^{3}He sont mesurées à l'aide d'un spectromètre de masse à secteur magnétique pour l'analyse des gaz rares (MAP 215) avec détection par multiplicateur d'électrons [*Shuster et al.*, 2004].

Ce système analytique permet d'une part d'obtenir des mesures très précises (respectivement 0.5-5 % et ~0.5 % d'incertitude sur les abondances en ^{3}He et ^{4}He) à partir d'abondances très faibles et autorise par conséquent la mesure pour chaque palier de température à la fois des abondances en ^{3}He (~1-500 coups par seconde) et en ^{4}He (10^4-10^6 coups par seconde).

Durant chaque expérience de dégazage (environ 24 heures pour un échantillon), des standards dont le rapport ^{4}He/^{3}He est connu sont analysés (toutes les sept à douze heures) afin de vérifier la stabilité de la mesure par spectrométrie de masse; et plusieurs analyses de "blancs" sont programmées avant et pendant chaque expérience. Ces analyses permettent de quantifier la sensitivité de l'extraction par chauffage et de la mesure par spectrométrie de masse; typiquement les valeurs obtenues pour les "blancs" ^{3}He et ^{4}He sont respectivement <0.2 et <1500 coups par seconde [*Shuster et al.*, 2004]. Chaque mesure du rapport ^{4}He/^{3}He d'un échantillon est *a posteriori* corrigée à partir des rapports mesurés pour les "blancs" ainsi que des déviations analytiques potentielles lors de l'analyse des standards.

A la fin de l'expérience de dégazage, l'échantillon est dissous afin de mesurer les abondances en U, Th et Sm comme décrit précédemment pour la méthode (U-Th-Sm)/He [*Farley*, 2002]. Un âge He peut également être calculé en sommant les abondances en ^{4}He mesurées à chaque palier de dégazage. Traditionnellement, un échantillon est séparé en deux parties : (1) une première partie va être utilisée pour la thermochronométrie ^{4}He/^{3}He (irradiation protonique et expérience de dégazage par paliers de température successifs); et (2) l'autre partie de l'échantillon est analysée via la thermochronométrie classique (U-Th-Sm)/He. Ainsi, chaque

échantillon est contraint par : (1) un âge He moyen suite à l'analyse de plusieurs réplicas individuels et associé à une estimation des abondances moyennes en U, Th et Sm ; et (2) un diagramme de l'évolution du rapport $^4He/^3He$ lors d'une expérience de dégazage quantifiant la distribution spatiale d'^4He au sein du grain d'apatite.

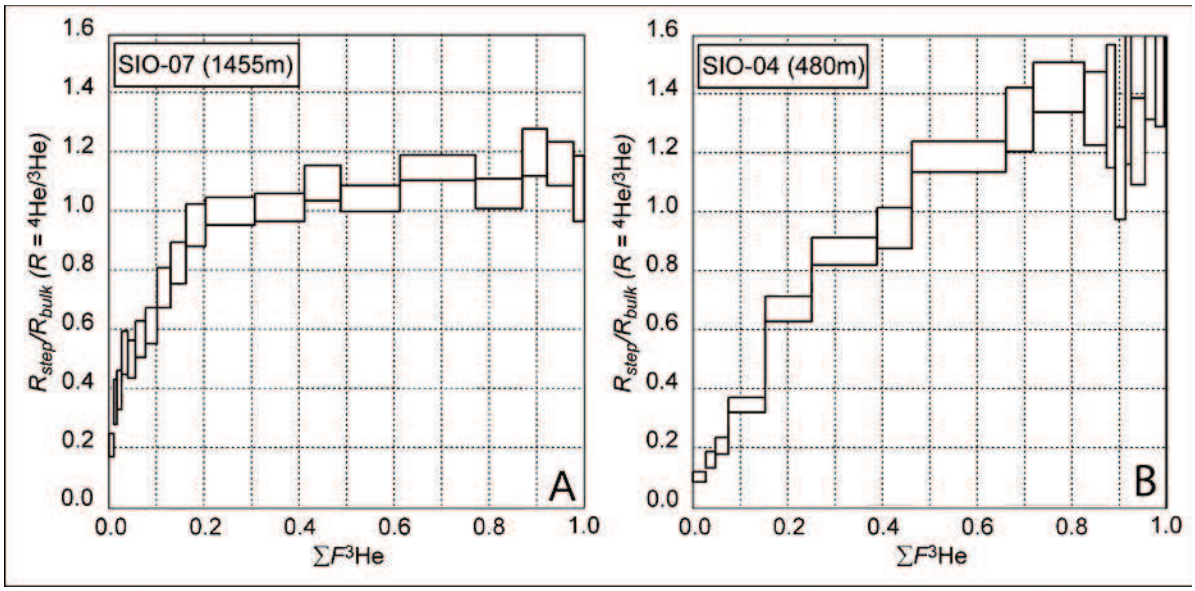

Figure I.2.7. *Comparaison de deux diagrammes (SIO-07 et SIO-04, cf. Chapitre III) illustrant l'évolution du rapport $^4He/^3He$ lors d'une expérience de dégazage (R_{step} = rapport $^4He/^3He$ mesuré pour chaque étape de chauffage; R_{bulk} = rapport $^4He/^3He$ moyen du grain d'apatite; et incertitudes analytiques 1σ données par la hauteur de chaque rectangle). L'échantillon SIO -04 (B, échantillon récolté au fond d'une vallée) présente une distribution d'^4He beaucoup plus diffusive que SIO-07 (A, échantillon récolté au sommet adjacent) et témoigne d'un refroidissement final plus rapide pour SIO-04. Modifié d'après Valla et al. [submitted, a].*

L'interprétation de ces données en termes d'histoires *t-T* nécessite l'utilisation de simulations numériques [*Shuster and Farley*, 2004; 2005; *Schildgen et al.*, 2010] et sera développée dans la partie suivante de ce chapitre. Cependant, une estimation qualitative des modalités de refroidissement d'un échantillon peut être établie en analysant la forme du diagramme de l'évolution du rapport $^4He/^3He$ (Figure I.2.7, *Shuster and Farley*, 2004; 2005).

I.2.1.2 - Datations à partir des isotopes cosmogéniques ^{10}Be produits *in-situ*

Une partie de ma thèse a été consacrée à la quantification de l'incision fluviale post-glaciaire à partir de l'étude d'une gorge de raccordement (Gorge du Diable, massif des Ecrins-Pelvoux) située dans les Alpes occidentales françaises (cf. Chapitre IV, partie IV.3.2 ; *Valla et al.*, 2010a). Pour ce travail, j'ai récolté et préparé une douzaine d'échantillons au LGCA afin d'en mesurer la concentration en ^{10}Be produit *in-situ* (instrument national ASTER au CEREGE, Aix en Provence; collaboration J. Carcaillet). Cette partie rappelle brièvement le principe des nucléides cosmogéniques et leurs applications en géomorphologie, avant de synthétiser les différentes étapes depuis l'échantillonnage des surfaces rocheuses jusqu'à l'interprétation des données géochronologiques en termes de processus d'érosion et d'évolution du relief.

Nucléides cosmogéniques produits *in-situ*

Les nucléides cosmogéniques, ou cosmonucléides, résultent de réactions nucléaires (spallation et capture neutronique) entre les particules chargées du rayonnement cosmique (les particules primaires, ainsi que les particules secondaires formées lors d'interactions de particules primaires avec l'atmosphère) et des éléments cibles présents dans l'atmosphère (*e.g.*, O et N) ou la lithosphère, dits "*in-situ*" (*e.g.*, Si, O, Mg…). Dans cette étude, je m'intéresse au ^{10}Be (béryllium-10), un nucléide cosmogénique dont la production *in-situ* [*e.g.*, *Lal*, 1991; *Gosse and Philips*, 2001] s'effectue principalement par spallation (~1-100 atomes g^{-1} an^{-1}) entre une infime partie des particules issues du rayonnement secondaire (~0.1 %) et certains éléments cibles présents dans la lithosphère (atomes de silicium Si). Du fait de ces interactions, la production de nucléides cosmogéniques décroît exponentiellement avec la profondeur [*Gosse and Philips*, 2001; *Braucher et al.*, 2003]; la signature en ^{10}Be est par conséquent acquise dans les premiers ~60 cm de la croûte terrestre. D'autre part, le ^{10}Be est un élément radioactif, caractérisé par une demi-vie $T_{1/2}$ = 1.36 ±0.07 10^6 ans [*Nishiizumi et al.*, 2007]. Ainsi, la concentration en ^{10}Be d'une surface rocheuse soumise au rayonnement cosmique et à l'érosion (érosion physique et/ou altération chimique) atteint théoriquement un équilibre stationnaire, où la production d'atomes ^{10}Be par spallation égale les "pertes" dues d'une part à la décroissance radioactive et d'autre part à l'ablation de matière par érosion (Figure I.2.8).

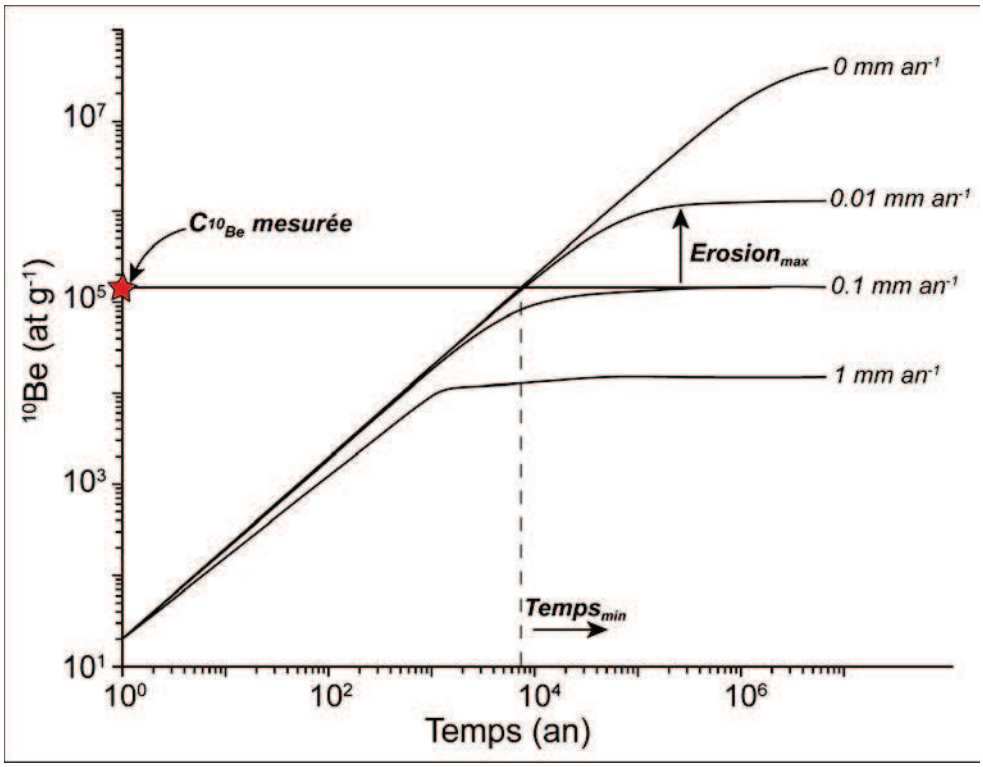

Figure I.2.8. *Evolution temporelle de la concentration en ^{10}Be d'une surface exposée de façon continue au rayonnement cosmique et soumise à différentes intensités d'érosion (0-1 mm an^{-1}). Chaque courbe représente un scénario d'érosion, et la concentration en ^{10}Be atteint l'équilibre séculaire (représenté graphiquement par un plateau) plus ou moins rapidement selon l'intensité de l'érosion. A partir de la concentration mesurée en ^{10}Be ($C_{^{10}Be}$ mesurée), il est possible de déterminer quantitativement : (1) un âge d'exposition minimum ($Temps_{min}$); ou (2) une vitesse d'érosion maximum ($Erosion_{max}$). Modifiée d'après Delunel [2010].*

Les caractéristiques du ^{10}Be produit *in-situ*, décrites ci-dessus, en font un excellent outil géochronologique pour quantifier les processus de surface et l'évolution du relief sur des échelles temporelles de 10^3-10^6 ans. La concentration en ^{10}Be mesurée au sein d'une surface rocheuse peut être interprétée suivant deux approches différentes (Figure I.2.8; *Balco et al.*, 2008) : (1) un âge d'exposition minimum de la surface, considérant que cette dernière est préservée de l'érosion [*e.g.*, *Brown et al.*, 1991; *Briner et al.*, 2005; *Schaller et al.*, 2005; *Ivy-Ochs et al.*, 2009]; ou (2) une vitesse d'érosion maximum de la surface considérée [*e.g.*, *Bierman*, 1994; *Small et al.*, 1997]. Plus récemment, la notion d'équilibre stationnaire a été utilisée à des échelles spatiales plus grandes afin de quantifier les vitesses d'érosion moyennées sur des bassins versants à partir de la mesure des concentrations en ^{10}Be dans des matériaux détritiques [*e.g.*, *Granger et al.*, 1996; *von Blanckenburg*, 2006; *Codilean et al.*, 2008; *Delunel et al.*, 2010b].

Dans cette étude, j'ai utilisé le ^{10}Be produit *in-situ* afin de dater la formation d'une gorge de raccordement et de quantifier la dynamique d'incision fluviale de cette gorge (cf. Chapitre IV, partie IV.3.2; *Valla et al.*, 2010a). La suite de cette partie méthodologique présente de façon synthétique les différentes étapes de préparation des échantillons, de mesure des concentrations en ^{10}Be et de calcul des âges d'exposition et/ou vitesses d'érosion (développées de manière exhaustive par *Braucher et al.* [2000] et *Delunel* [2010]).

Protocole d'échantillonnage et analytique

L'échantillonnage de la gorge du Diable a été réalisé durant l'automne 2007 (collaboration R. Delunel et X. Robert). Nous avons récolté une dizaine d'échantillons le long des parois de la gorge, ainsi que quelques échantillons dans le lit actif de la rivière. Afin de respecter les hypothèses évoquées précédemment, nous avons échantillonné les parois de la gorge en nous focalisant sur les morphologies fluviales (*i.e.*, ne présentant pas d'évidence d'une érosion postérieure à l'incision). Enfin, les surfaces sélectionnées dans le lit actuel de la rivière ne présentaient pas d'indice de couverture récente par des alluvions, même si nous ne pouvons pas exclure une histoire d'exposition complexe avec un ou plusieurs enfouissements dans un passé plus ou moins proche.

La préparation des échantillons et l'extraction du ^{10}Be ont été effectuées au LGCA. Dans un premier temps, les échantillons rocheux ont été broyés (broyeuse à mâchoires, collaboration F. Cœur) avant d'être tamisés pour en conserver la fraction granulométrique 250-1000 µm. J'ai réalisé un tri préliminaire des échantillons tamisés en séparant les fractions magnétiques et diamagnétiques (séparateur magnétique Frantz, CEREGE) afin de ne conserver que la fraction diamagnétique car, dans mon étude, seul le quartz (SiO_2) est utilisé pour la mesure du ^{10}Be.

L'extraction du ^{10}Be produit *in-situ* a été réalisée au LGCA, suivant le protocole décrit par *Brown et al.* [1991]. Les différentes étapes du protocole d'extraction utilisé au LGCA ont été décrites de manière exhaustive par *Braucher et al.* [2000] et *Carcaillet* [2003]. Une synthèse des principales étapes est présentée ci-après. Tout d'abord, les échantillons sont purifiés afin de ne conserver que les grains de quartz par ajout d'acides chlorhydrique (HCl) et hexafluorosilicique (H_2SiF_6) pendant plusieurs cycles de dissolution. Une fois les échantillons purifiés, ils sont soumis à trois étapes de dissolution séquentielle par acide fluorhydrique (HF) afin d'éliminer le ^{10}Be atmosphérique présent à la surface des grains de quartz [*Brown et al.*,

1991]. Suite à cette purification, les échantillons sont rincés et séchés à l'étuve et ~50 g de quartz sont prélevés pour la suite du protocole.

La dissolution du quartz est opérée en utilisant de l'acide fluorhydrique (HF), et l'ajout d'une solution d'entraineur de ^{9}Be (300 µl à une concentration connue 10^{-3} g g^{-1}) est effectué afin de pouvoir mesurer ultérieurement un rapport $^{10}Be/^{9}Be$ des échantillons par spectrométrie de masse par accélérateur. Lors de cette étape, un échantillon "blanc" est également réalisé par ajout de la même solution entraineur de ^{9}Be dans ~50 ml d'HF; ce "blanc" va subir les mêmes étapes analytiques afin de quantifier les éventuelles pollutions engendrées lors du protocole d'extraction. Le HF est ensuite substitué par de l'acide nitrique (HNO_3), ce dernier étant moins toxique pour l'homme. Les éléments, autres que le Be, présents en solution sont complexés via l'utilisation d'éthylènediaminetétraacétique (EDTA). L'ajout d'acétylacétone ($C_5H_8O_2$) permet de complexer le béryllium, celui-ci étant ensuite extrait par décantation grâce à l'ajout de tétrachlorure de carbone (CCl_4) suivant la formation d'un complexe organique ($Be(C_2H_7O_2)_2$; *Braucher et al.*, 2000). La solution extraite est successivement évaporée et reprise à chaud avec de l'HCl, HNO_3, puis de l'acide perchlorique ($HClO_4$) avant de rajouter de l'HNO_3 et de rincer [*Braucher et al.*, 2000; *Carcaillet*, 2003]. Cette opération est répétée une seconde fois (sans passer par l'ajout d'$HClO_4$), puis la solution est reprise dans de l'HCl. Celle-ci est ensuite amenée à pH 8-9 par ajout d'ammoniaque (NH_4OH) afin de précipiter le béryllium ($Be(OH)_2$) et d'éviter un précipité de bore ($B(OH)_2$, précipitation à pH plus basique). Après centrifugation, le surnageant est jeté et le précipité rincé puis remis en solution par ajout d'HCl. Cette opération de purification est répétée trois fois et le précipité est enfin solubilisé dans de l'HNO_3. Le béryllium est ensuite oxydé à ~800 °C en oxyde de béryllium (BeO).

Les mesures du rapport $^{10}Be/^{9}Be$ ont été effectuées par spectrométrie de masse par accélérateur (SMA, instrument national ASTER au CEREGE, Aix en Provence; collaboration J. Carcaillet). Le principe de la mesure par SMA permet de quantifier le nombre d'atomes de chaque isotope d'un élément, ces derniers étant caractérisés par une masse atomique propre (pour une description complète de l'instrument ASTER, cf. *Delunel*, 2010). Pour la mesure du ^{10}Be, l'utilisation du SMA permet de séparer ce dernier de son isobare naturel plus abondant, le ^{10}B (bore-10). Le rapport $^{10}Be/^{9}Be$ est donc quantifié pour l'ensemble des échantillons par comptage successif des atomes ^{10}Be et ^{9}Be et corrigé par l'utilisation d'un standard au rapport $^{10}Be/^{9}Be$ connu (NIST standard reference material 4325, rapport $^{10}Be/^{9}Be$ de 2.79 ±0.03 10^{-11}

et période de demi-vie du ^{10}Be ($T_{1/2}$) de 1.36 ±0.07 10^6 ans; *Nishiizumi et al.*, 2007). La mesure par SMA du rapport ^{10}Be/^{9}Be pour chaque échantillon, corrigée de la mesure effectuée pour le "blanc", peut être convertie en concentration de ^{10}Be; le nombre d'atomes ^{9}Be étant connu grâce à l'ajout d'une quantité connue d'entraineur ^{9}Be pour chaque échantillon.

Interprétation de la mesure ^{10}Be *in-situ*

L'interprétation des concentrations en ^{10}Be en termes d'âges d'exposition ou de vitesses d'érosion est basée sur l'équation suivante [*Braucher et al.*, 2003; *Delunel*, 2010]:

$$C_{(x,\varepsilon,t)} = C_i e^{-\lambda t} + \frac{P_{spal}}{\frac{\varepsilon}{\Lambda_n} + \lambda} e^{-\frac{x}{\Lambda_n}} \left[1 - e^{-t\left(\frac{\varepsilon}{\Lambda_n} + \lambda\right)} \right] + \frac{P_{\mu s}}{\frac{\varepsilon}{\Lambda_{\mu s}} + \lambda} e^{-\frac{x}{\Lambda_{\mu s}}} \left[1 - e^{-t\left(\frac{\varepsilon}{\Lambda_{\mu s}} + \lambda\right)} \right] + \frac{P_{\mu f}}{\frac{\varepsilon}{\Lambda_{\mu f}} + \lambda} e^{-\frac{x}{\Lambda_{\mu f}}} \left[1 - e^{-t\left(\frac{\varepsilon}{\Lambda_{\mu f}} + \lambda\right)} \right] \quad \text{(I.2.9)}$$

où la concentration mesurée en ^{10}Be produit *in-situ* (C) est fonction de la profondeur (x), du temps d'exposition au rayonnement cosmique (t) et de la vitesse d'érosion (ε). Cette concentration dépend également d'un héritage éventuel (histoire d'exposition complexe, C_i) ainsi que de la constante de désintégration radioactive du ^{10}Be ($\lambda = 1/T_{1/2}$).

La production totale en ^{10}Be fait intervenir des contributions diverses [*Braucher et al.*, 2003], dont celle des neutrons ($P_{spal,}$ longueur d'atténuation Λ_n = 150 g cm^{-2} et contribution relative ~97.85%), des muons lents ($P_{\mu s,}$ longueur d'atténuation $\Lambda_{\mu s}$ = 1500 g cm^{-2} et contribution relative ~1.5%), et des muons rapides ($P_{\mu f,}$ longueur d'atténuation $\Lambda_{\mu f}$ = 3000 g cm^{-2} et contribution relative ~0.65%).

La détermination des taux de production en ^{10}Be *in-situ* est spécifique à un site d'échantillonnage et aux caractéristiques propres à chaque échantillon (taille), cette étape importante requière la quantification de nombreux paramètres : production locale en surface, écrantage topographique et correction de l'épaisseur de roche prélevée [*Delunel*, 2010].

La production locale en ^{10}Be dépend principalement de l'altitude et de la latitude du site d'échantillonnage. J'ai utilisé un taux de production standard, défini au niveau de la mer et pour des hautes latitudes à une valeur de 4.5 ±0.3 atomes g^{-1} (quartz) an^{-1} [*Balco et al.*, 2008], et ai calculé la production locale en ^{10}Be à partir des polynômes de correction déterminés par *Stone* [2000]. La réduction du taux de production local par le relief avoisinant est prise en compte via l'utilisation du facteur d'écrantage [*Dunne et al.*, 1999], facteur discrétisant le relief environnant en un masque topographique [*Delunel*, 2010]. Finalement, le rayonnement cosmique étant exponentiellement atténué lors de son parcours dans la roche, la production en ^{10}Be *in-situ* doit être corrigée de l'épaisseur de l'échantillon prélevé. Cette correction, ainsi que le calcul des facteurs d'écrantage locaux, ont été réalisés via le calculateur CRONUS développé par G. Balco [*Balco et al.*, 2008].

A partir des considérations évoquées ci-dessus et de l'équation (I.2.9), il est possible d'interpréter les concentrations mesurées en ^{10}Be produit *in-situ* en termes d'âge d'exposition (t) ou de vitesse d'érosion (ε). Lors de mon étude, j'ai considéré les échantillons prélevés le long des parois de la gorge en terme d'âges d'exposition, tandis que les échantillons prélevés dans le lit actuel de la rivière ont permis de quantifier les vitesses d'incision fluviale actuelles [*Valla et al.*, 2010a].

L'incertitude des résultats obtenus est quantifiée en propageant les différentes incertitudes relatives associées d'une part à la mesure en ^{10}Be produit *in-situ*, et d'autre part dans l'estimation de la production locale en ^{10}Be. Les incertitudes liées à la mesure analytique par SMA comprennent d'une part l'incertitude sur le "blanc", l'incertitude analytique standard (<1 %) et celle sur la mesure de l'échantillon (tenant compte du nombre de coups comptabilisés lors de la mesure par SMA).

Pour mon étude, l'incertitude relative sur la production locale prend en compte l'incertitude sur le facteur d'écrantage qui, du fait des parois quasi-verticales de la gorge, est difficile à estimer (ajout d'une incertitude relative de ±5° lors du calcul de l'écrantage topographique, *Valla et al.*, 2010a). Finalement, je n'ai pas considéré dans les calculs de production locale en ^{10}Be *in-situ* l'atténuation potentielle par la neige [*Shildgen et al.*, 2005; *Delunel et al.*, in preparation] ainsi que la modulation de la production globale de par les variations du champ géomagnétique terrestre [*Carcaillet*, 2003]. Par conséquent, les âges d'exposition calculés sont des âges non-corrigés de ces effets et sont reportés en ^{10}Be-ka [*Valla et al.*, 2010a].

I.2.2 - Modélisations thermique et thermo-cinématique

I.2.2.1 - Modélisation thermique des données $^4He/^3He$

L'interprétation quantitative de données thermochronométriques $^4He/^3He$ (Figure I.2.7) nécessite l'utilisation de la modélisation numérique afin de contraindre les chemins *t-T* (temps-température) de refroidissement compatibles avec les données mesurées. J'ai utilisé un modèle numérique développé par G. Balco (BGC, *Shildgen et al.*, 2010) qui modélise au cours d'une histoire thermique la production du ^4He radiogénique dans une apatite de géométrie sphérique avant de simuler numériquement une expérience de dégazage par paliers successifs de température et ainsi de prédire un spectre d'évolution du rapport $^4He/^3He$. Ce modèle est couplé à un algorithme d'inversion [*Ketcham*, 2005] afin de contraindre de manière quantitative les chemins *t-T* compatibles avec un spectre $^4He/^3He$ mesuré dans un échantillon naturel (Figure I.2.7). L'ensemble des détails du modèle, ainsi que les paramètres utilisés sont décrits de manière exhaustive par *Schildgen et al.* [2010]. Dans la suite de cette partie, j'en résume les principales caractéristiques.

Avant de lancer la procédure d'inversion, le cadre temps/température doit être défini avec des températures initiale et finale données. La température initiale doit être fixée au dessus de la PRZ et est typiquement choisie autour de ~150°C pour un âge deux fois plus vieux que l'âge He mesuré [*Schildgen et al.*, 2010], à moins que des contraintes *t-T* supplémentaires soient disponibles à partir d'autres systèmes thermochronométriques (*e.g.*, un âge traces de fission sur apatite). La température finale correspond à la température actuelle (moyenne annuelle) de la région où a été récolté l'échantillon. A partir de ces deux points dans l'espace *t-T*, un algorithme Monte-Carlo [*Ketcham*, 2005] génère aléatoirement des chemins *t-T* (refroidissement uniquement) plus ou moins complexes (gamme de points d'inflexion fixée au début de l'inversion, typiquement de 3 à 10 points).

Chaque histoire thermique est par la suite utilisée pour modéliser la production-diffusion-éjection du ^4He radiogénique par différences finies dans une apatite de géométrie sphérique [*Ketcham*, 2005]. Cet algorithme est basé sur le modèle RDAAM (Radiation Damage Accumulation and Annealing Model) développé par *Flowers et al.* [2009]. Ce modèle considère l'effet de la formation de dommages du réseau cristallin lors de désintégrations radioactives [*Flowers et al.*, 2009; *Gautheron et al.*, 2009] et de leur recuit sur la cinétique de

diffusion de l'He dans et au travers le grain d'apatite [*Shuster et al.*, 2006]. Par ailleurs, ce modèle nécessite d'une part les caractéristiques géométriques du grain d'apatite (longueur/largeur du cristal) approximées par le rayon de la sphère équivalente moyen (*a*, Eq. (I.2.7)) des réplicas utilisés pour calculer l'âge He de l'échantillon; et d'autre part la concentration moyenne en U et Th (répartition *a priori* uniforme dans le grain d'apatite) de ces mêmes réplicas. Un âge (U-Th)/He est numériquement prédit et comparé à l'âge He mesuré. Si cet âge prédit n'est pas en accord avec l'âge mesuré (considérant une incertitude ±1σ sur l'âge He mesuré, cf. partie I.2.1.1), le chemin *t-T* est rejeté et une nouvelle histoire thermique est générée.

Dans le cas contraire, un algorithme de dégazage simule une expérience de chauffage par paliers de température selon le protocole fixé lors de l'analyse de l'échantillon (paliers de température et durées de chauffage identiques à l'expérience, Figure I.2.6), considérant une approche numérique par différences finies (ici, les caractéristiques géométriques correspondent à celles du grain d'apatite utilisé lors de l'analyse ^{4}He/^{3}He) ainsi qu'une diffusivité *a priori* similaire pour le ^{3}He et ^{4}He [*Shuster et al.*, 2004] et déterminée via le dégazage du ^{3}He uniformément réparti dans le grain d'apatite.

Un spectre d'évolution du rapport ^{4}He/^{3}He est ainsi prédit et peut être quantitativement confronté au spectre mesuré via le critère statistique suivant [*Schildgen et al.*, 2010]:

$$M = \frac{1}{n}\sum_{j=1}^{n}\frac{(R_{j,\mathrm{mod}} - R_{j,dat})^2}{\sigma_j{}^2} \qquad \text{(I.2.10)}$$

où $R_{j,mod}$ correspond au rapport ^{4}He/^{3}He calculé numériquement lors du palier de chauffage *j*, $R_{j,dat}$ est le rapport expérimentalement mesuré au cours du même palier *j*, *n* est le nombre total de paliers de chauffage et σ_j est l'incertitude associée au rapport ^{4}He/^{3}He mesuré lors du palier *j*. *Schildgen et al.* [2010] ont estimé que pour une expérience classique de dégazage par paliers successifs de température (~20 à 25 paliers), M ~2 correspond à l'intervalle de confiance à 99%.

Cette approche permet de déterminer quantitativement (Figure I.2.9) quels chemins *t-T* sont compatibles avec les données ^{4}He/^{3}He mesurées expérimentalement ($M < 2$) et ainsi d'écarter

les histoires thermiques incompatibles ($M > 4$, limite imposée de manière arbitraire) ou expliquant seulement partiellement les données ($2 < M < 4$).

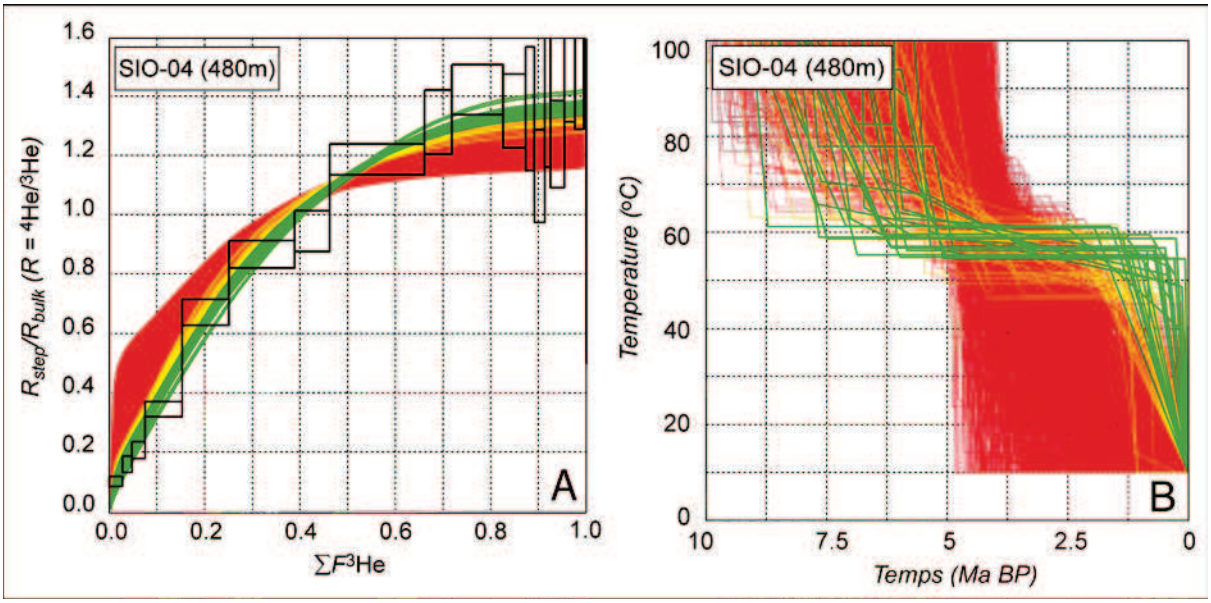

Figure I.2.9. *Exemple d'un spectre d'évolution en $^4He/^3He$ lors d'une expérience de dégazage (A, rectangles ouverts indiquant l'incertitude sur la mesure) et prédictions obtenues par modélisation thermique inverse (courbes colorées). Chaque histoire thermique (B) est associée à un spectre d'évolution en $^4He/^3He$ (les courbes vertes représentent des chemins t-T compatibles avec les données mesurées, tandis que les courbes jaunes et rouges illustrent respectivement les histoires de refroidissement partiellement et non compatibles avec les rapports $^4He/^3He$ mesurés. Modifié d'après Valla et al. [submitted, a]*

Lors de certaines expériences de dégazage, quelques paliers peuvent présenter des rapports $^4He/^3He$ éloignés de la tendance générale, ces derniers peuvent être exclus lors de la modélisation inverse afin de minimiser leur influence sur les prédictions du modèle. Plusieurs explications possibles pour ces rapports anormaux incluent : (1) des erreurs dans la correction liée au blanc ^4He pour un palier de température spécifique, (2) des inclusions et/ou fractures microscopiques à l'intérieur du cristal qui n'ont pas été détectées lors de l'étape de sélection, (3) une forte zonation spatiale de l'apatite en U et Th [*Farley et al.*, 2010].

I.2.2.2 - Modélisation thermo-cinématique: *Pecube*

Le développement des méthodes thermochronométriques [*e.g.*, *Gallagher et al.*, 1998; *Reiners et al.*, 2005] a permis d'ouvrir de nouvelles possibilités quant à la quantification des processus d'exhumation et d'évolution du relief [*e.g.*, *Ehlers and Farley*, 2003]. Cependant, apporter des contraintes sur les processus géodynamiques internes et/ou externes via l'utilisation de la thermochronologie nécessite, d'une part l'acquisition d'un large jeu de données thermochronologiques spatialement réparties et combinant plusieurs systèmes thermochronométriques, et d'autre part des outils méthodologiques pour interpréter quantitativement ces données.

L'échantillonnage de données thermochronologiques le long de profils âge-altitude (jeu de données thermochronologiques collectées à diverses altitudes dans une région spatialement restreinte) a été largement utilisé dans les dernières décennies afin de déterminer les histoires d'exhumation dans les chaînes de montagnes [*e.g.*, *Wagner et al.*, 1972; *Hurford*, 1991; *House et al.*, 1997; *Reiners et al.*, 2002]. Cependant, excepté dans des situations précises (*e.g.*, exhumation d'une Partial Annealing Zone, PAZ, ou d'une PRZ pour respectivement les systèmes thermochronométriques traces de fission et (U-Th-Sm)/He sur apatite; *e.g.*, *Fitzgerald et al.*, 1995; 2006), cette méthode considère l'hypothèse d'une exhumation constante au cours du temps et ne peut quantifier des variations temporelles dans l'histoire d'exhumation. Le développement de modèles numériques tels *HeFTy* [*Ketcham*, 2005] permet de prendre en compte la variation temporelle des vitesses d'exhumation et apporte des contraintes sur le chemin *t-T* d'un échantillon individuel à partir de données thermochronologiques. Néanmoins, l'utilisation de *HeFTy* ne permet pas d'exploiter la cohérence spatiale existant entre les données thermochronologiques. D'autres modèles ont été développés pour inclure cet effet dans l'interprétation de données thermochronologiques, utilisant la variation spatiale de ces données pour mieux contraindre leur histoire *t-T* [*Gallagher et al.*, 2005a, b].

Par ailleurs, la quantification des processus géodynamiques externes et/ou internes nécessite la conversion du chemin *t-T* d'un échantillon en vitesse d'exhumation (*i.e.*, la vitesse à laquelle les roches sont amenées à la surface, *England and Molnar*, 1990) qui combine à la fois : (1) des processus de dénudation en réponse à un soulèvement régional (tectonique ou isostatique); et (2) l'évolution du relief, ajoutant une composante locale à l'exhumation totale.

Les effets potentiels de la topographie sur la distribution des isothermes au sein de la croûte terrestre doivent par conséquent être pris en compte dans l'interprétation de données thermochronologiques [*Braun,* 2002a]. L'intensité de la perturbation topographique sur les isothermes est assez bien comprise pour une topographie à l'état d'équilibre [*Stüwe et al.*, 1994; *Manktelow and Grasemann*, 1997] et dépend de l'amplitude et la longueur d'onde de cette topographie. Cependant, l'influence sur les isothermes crustales d'une topographie évoluant au cours du temps reste mal contrainte [*Braun,* 2002a], malgré son importance non négligeable dans l'interprétation de données thermochronologiques [*Foeken et al.*, 2007].

Durant ma thèse (cf. Chapitres II et III), j'ai utilisé le modèle numérique en éléments finis *Pecube* [*Braun*, 2003] afin d'interpréter des données thermochronologiques en termes de scénarios tectono-géomorphiques. *Pecube* permet la simulation de la structure thermique d'un bloc crustal ainsi que la détermination d'histoires *t-T* à partir de la résolution de l'équation de chaleur [*Carslaw and Jaeger*, 1959] en trois dimensions :

$$\rho c \left(\frac{\partial T}{\partial t} + v \frac{\partial T}{\partial z}\right) = \frac{\partial}{\partial x} k \frac{\partial T}{\partial x} + \frac{\partial}{\partial y} k \frac{\partial T}{\partial y} + \frac{\partial}{\partial z} k \frac{\partial T}{\partial z} + H \qquad \text{(I.2.11)}$$

où $T(x,y,z,t)$ représente le champ de température au cours du temps (°C), ρ est la densité du matériau rocheux considéré (kg m^{-3}), c est la capacité de chaleur (J kg^{-1} K^{-1}), $v(t)$ correspond à la vitesse de soulèvement des roches et/ou dénudation (variable au cours du temps) des roches par rapport à la base du bloc crustal (m an^{-1}), k est la conductivité du matériaux rocheux (W m^{-1} K^{-1}) et H la production de chaleur par désintégration radioactive (W m^{-3}).

L'exhumation locale des roches est définie par des scénarios temporels (Figure I.2.10) et est modélisée selon deux processus indépendants dans *Pecube* : (1) une vitesse de soulèvement des roches *v* qui peut varier dans l'espace et au cours du temps, nommée par la suite vitesse de dénudation [*England and Molnar*, 1990] car dans *Pecube* la modélisation de l'exhumation des roches considère l'hypothèse d'un régime d'équilibre, *i.e.*, la vitesse de dénudation est égale au soulèvement des roches en tout point à la surface du modèle ; (2) l'évolution de la topographie au cours du temps qui engendre une composante de l'exhumation spatialement variable et permet un écart du régime d'équilibre. *Pecube* a récemment été complété par différents algorithmes [*Braun et al.*, 2010] permettant l'advection des roches le long de failles (*i.e.*, exhumation par advection verticale et horizontale des roches, *Robert et al.*, 2009;

Herman et al., 2010a) et ainsi des vitesses de soulèvement/dénudation spatialement variables au sein de blocs crustaux délimités.

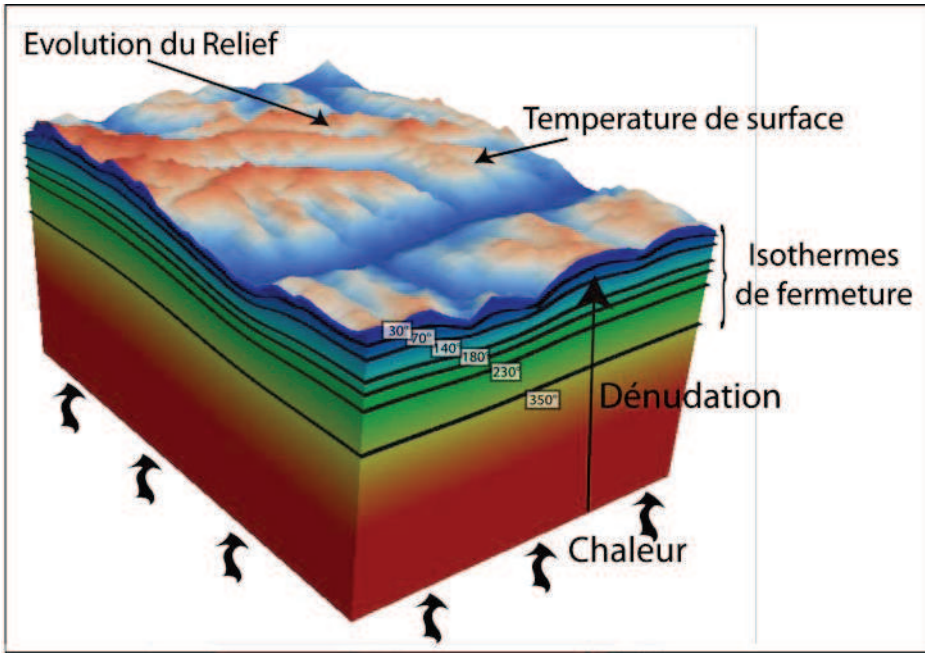

Figure I.2.10. *Présentation schématique du modèle numérique Pecube [Braun, 2003] reprenant les composantes thermo-cinématiques et élastiques (production de chaleur, évolution du champ de température et rebond isostatique) ainsi que les modalités d'advection des roches vers la surface (exhumation par soulèvement/dénudation et évolution de la topographie). Les isothermes de fermeture des principaux systèmes thermochronométriques sont représentées. Modifiée d'après une figure réalisée par F. Herman.*

L'évolution de la topographie au cours du temps est modélisée dans *Pecube* suivant l'équation suivante :

$$z_{x,y,t} = z_{x,y,actuel}\ R(t) + (z_{\max}\ (1 - R(t)) \qquad \text{(I.2.12)}$$

où z représente l'altitude en tout point à la surface du modèle au cours du temps (t) et à l'actuel (*actuel*), z_{max} est l'altitude maximale de la topographie actuelle (fixée) et R (variable au cours du temps) représente le facteur d'amplification du relief permettant une interpolation linéaire de la topographie entre chaque scénario. Ce facteur considère différentes configurations de la paléo-topographie : si $R = 0$, la paléo-topographie est un plateau (*i.e.*, pas de relief) à l'altitude maximale actuelle ; si $R < 1$ le paléo-relief est moins prononcé qu'à l'actuel et inversement si $R > 1$ [*Valla et al.*, 2010b]. D'autres approches ont plus récemment couplé *Pecube* avec des modèles d'évolution de la topographie simulant les processus de

surface [*Herman et al.*, 2010a; *Pedersen et al.*, 2010] afin de modéliser directement les interactions tectonique/processus de surface et leur enregistrement dans les données thermochronologiques. Par ailleurs, un module permet le calcul du rebond isostatique en réponse à l'évolution de la topographie, cette composante étant ajoutée à la dénudation régionale [*e.g.*, *Braun and Robert*, 2005].

L'utilisation du modèle *Pecube* implique également la définition de nombreuses constantes thermiques, mécaniques et élastiques, ainsi que des contraintes plus régionales suivant la zone géodynamique considérée : l'épaisseur crustale et la température en base de croûte [*e.g.*, *Vigano and Martin*, 2007; *Tesauro et al.*, 2008], la température au niveau de la mer et le gradient atmosphérique de température [*e.g.*, *Delunel et al.*, 2010b], l'épaisseur élastique de la lithosphère crustale [*e.g.*, *Stewart and Watts*, 1997] ou encore la production radiogénique de chaleur au sein de la croûte [*Jaboyedoff*, 1999].

Les histoires *t-T* prédites par *Pecube* sont utilisées pour calculer les données thermochronologiques via l'utilisation : (1) d'un modèle sphérique de production-diffusion-éjection pour l'hélium sur apatite et zircon [*Farley*, 2002; *Meesters and Dunai*, 2002], (2) d'un modèle de production et de recuit des traces de fission sur apatite [*Green et al.*, 1989; *Stephenson et al.*, 2006] et zircon [*Rahn et al.*, 2004]. De nouveaux algorithmes sont en cours d'implémentation dans *Pecube* pour la prédiction des âges traces de fission [*Ketcham*, 2005] et He [*Shuster et al.*, 2006; *Flowers et al.*, 2009; *Gautheron et al.*, 2009] sur apatite.

I.2.2.3 - Modélisation inverse de données thermochronologiques

Une partie de ma thèse [cf. Chapitre II, *Valla et al.,* 2010b; *van der Beek et al.*, 2010] a été consacrée à l'interprétation quantitative de données thermochronologiques via l'utilisation de *Pecube* [*Braun*, 2003] couplé à une méthode inverse [*Tarantola*, 2005] afin de contraindre des histoires de dénudation et d'évolution du relief topographique [*e.g.*, *Braun and Robert*, 2005; *Glotzbach et al.*, submitted; *Herman et al.*, 2007; 2010].

J'ai utilisé pour cela la procédure d'inversion NA (*Neighbourhood Algorithm*; *Sambridge*, 1999a, b) qui permet : (1) d'effectuer une recherche multidimensionnelle dans un espace de paramètres complexe (scénarios de dénudation et d'évolution de la topographie, paramètres thermo-cinématiques et élastiques…) afin d'extraire un jeu de paramètres reproduisant au

mieux les données thermochronologiques (première étape, appelée "*sampling stage*"); (2) de quantifier la résolution avec laquelle les données contraignent les paramètres recherchés à partir de l'ensemble des modèles générés (seconde étape, appelée "*appraisal stage*").

La première étape de la procédure ("*sampling stage*") explore l'espace multidimensionnel des paramètres sur plusieurs itérations et concentre la génération de modèles dans des régions où le jeu de paramètres va minimiser l'écart entre les âges thermochronologiques prédits et les données observées (Figure I.2.11). NA utilise une approche géométrique basée sur la répartition des modèles dans l'espace multidimensionnel des paramètres selon un diagramme de Voronoi (discrétisation de l'espace afin de trouver pour chaque modèle son plus proche voisin; *Sambridge*, 1999a). A chaque itération, NA reconstruit un diagramme de Voronoi et génère un modèle centré sur chaque cellule afin de calculer une fonction d'évaluation (Ψ) de la pertinence du modèle par rapport au données observées, de la forme :

$$\psi = \sqrt{\sum_{i=1}^{N}\sum_{j=1}^{M}\frac{({}^{i}\alpha_{j,\mathrm{mod}} - {}^{i}\alpha_{j,dat})^2}{{}^{i}\sigma_{j}{}^{2}}} \qquad \text{(I.2.13)}$$

où N est le nombre de systèmes thermochronométriques utilisés, M est le nombre d'échantillons pour chaque système, ${}^{\mathrm{i}}\alpha_{j,\mathrm{mod}}$ and ${}^{\mathrm{i}}\alpha_{j,dat}$ sont les données respectivement modélisées et observées, ${}^{\mathrm{i}}\sigma_{j}$ sont les incertitudes sur les données.

Les itérations NA suivantes utilisent cette fonction Ψ afin d'échantillonner de façon aléatoire les régions de l'espace des paramètres où Ψ est optimisée. Comme présentée par *Sambridge* [1999a], cette procédure inverse permet la convergence de *Pecube* vers un ou plusieurs jeux de paramètres permettant une prédiction optimale des données observées (Figure I.2.11). Cette première étape est fortement dépendante du nombre total d'itérations produites par NA, du nombre de modèles (*Pecube*) générés à chaque itération ainsi que du pourcentage de modèles acceptés/rejetés afin de reconstruire le diagramme de Voronoi. Ces paramètres vont influencer NA selon que la procédure d'inversion sera plus exploratoire (peu de modèles rejetés et un grand nombre d'itérations afin d'assurer la convergence de l'inversion) ou exploitante (taux de rejet important et convergence plus rapide) de l'espace multidimensionnel des paramètres [*Sambridge*, 1999a].

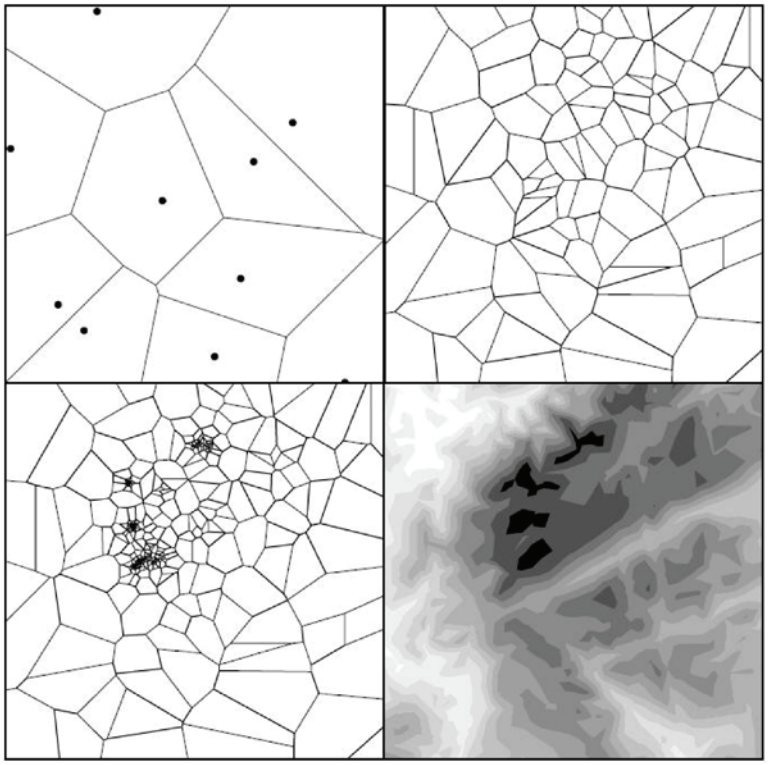

Figure I.2.11. *Exemple schématique du déroulement de la première étape NA ("sampling stage") pour un espace à deux paramètres. Le graphe en haut/gauche de la figure représente l'organisation du diagramme de Voronoi, chaque point illustrant un modèle (Pecube) généré aléatoirement dans chacune des cellules. Les graphes en haut/droite et bas/gauche représentent l'organisation de ce même diagramme après plusieurs itérations (respectivement 10 et 50 itérations). Les régions optimales de convergence apparaissent progressivement, validées par la distribution de la fonction d'évaluation Ψ (bas/droite). Modifiée d'après Sambridge [1999a].*

La seconde étape de la procédure ("*appraisal stage*") utilise l'ensemble des modèles générés lors de l'étape précédente afin de dériver des estimations quantitatives (Figure I.2.12) de la résolution sur chaque paramètre sous la forme de PDFs (fonctions de densité de probabilité *L*, *Sambridge*, 1999b) de la forme :

$$L = \prod_{i=1}^{N} \exp\left(-\frac{1}{2}\sum_{j=1}^{M} \frac{({}^{i}\alpha_{j,\mathrm{mod}} - {}^{i}\alpha_{j,dat})^2}{{}^{i}\sigma_{j}{}^{2}}\right) \qquad \text{(I.2.14)}$$

avec les même indices utilisés dans l'équation précédente (Eq. (I.2.13)).

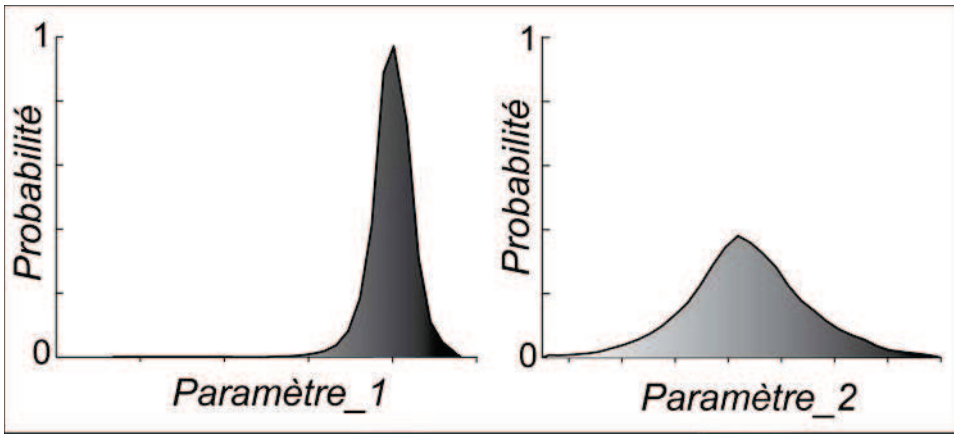

Figure I.2.12. *Représentation schématique des résultats obtenus après la seconde étape de la procédure NA ("appraisal stage"). L'exemple présenté ici concerne deux paramètres (Figure I.2.11) pour lesquels sont rapportées les valeurs optimales et les incertitudes associées selon une PDF (meilleure résolution sur le paramètre n°1).*

L'utilisation de modèles numériques complexes (*Pecube*) avec un grand nombre de paramètres, dont certains sont "libres" et contraints à partir de l'approche inverse NA, nécessite l'estimation de la dimensionnalité la mieux appropriée à l'interprétation des données observées [*e.g.*, *Akaike*, 1974; *Schwartz*, 1978; *Gallagher et al.*, 2005a]. Le principal problème lié à la modélisation numérique est de potentiellement sur-complexifier le modèle utilisé (*e.g.*, complexité du scénario d'exhumation et d'évolution du relief défini dans *Pecube*) alors que les données disponibles ont une résolution limitée. Pour limiter ce biais potentiel, il est possible d'utiliser un critère d'évaluation de la complexité du modèle employé appelé *BIC* (Bayesian Information Criterion, *Schwartz*, 1978) et défini par :

$$BIC = -2\ln(F) + k\ln(n) \qquad \text{et} \qquad \ln(F) = -\psi \tag{I.2.15}$$

avec k et n respectivement le nombre de paramètres "libres" et de données observés, et Ψ le critère d'évaluation de la pertinence du modèle par rapport au données observées (Eq. (I.2.13)). L'objectif du *BIC* est d'optimiser la fonction Ψ (et ainsi minimiser le *BIC*) tout en ne complexifiant pas le modèle (k) au-delà de la résolution des données (n). Ainsi, plus un modèle permet la prédiction quantitative d'un nombre important de données observées n avec un nombre limité de paramètres "libres" k, plus le *BIC* sera minimisé et les prédictions du modèle acceptables. Le *BIC* peut être par conséquent considéré comme un indicateur de la balance entre : (1) la capacité d'un modèle défini à expliquer les données observées, et (2) sa complexité.

I.2.3 - Modélisation des processus de surface

I.2.3.1 - Modélisation de l'incision fluviale en 1-D

La dynamique fluviale est une composante majeure de l'évolution des reliefs car les rivières jouent à la fois le rôle de niveau de base vis-à-vis des processus de pente en incisant le substratum rocheux, mais elles permettent également le transport et le transfert de sédiments au sein des bassins versants [*e.g.*, *Whipple*, 2004]. L'incision fluviale d'un substratum rocheux s'opère via des processus d'abrasion, de détachement de bloc ou encore des phénomènes de cavitation [*Howard*, 1998 ; *Whipple et al.*, 2000] et requiert d'une part que le substratum soit exposé aux flux d'eau et de sédiments, et d'autre part que la rivière transporte des particules sédimentaires en suspension ou par saltation/charriage [*Sklar and Dietrich*, 1998]. La formulation de l'incision fluviale communément utilisée considère l'hypothèse selon laquelle la vitesse d'incision est proportionnelle à la contrainte cisaillante basale, la puissance unitaire ou totale fournie par le flux d'eau [*e.g.*, *Howard*, 1994; *Whipple and Tucker*, 1999; *Lague*, 2003], selon l'équation suivante :

$$\dot{E} = k(\tau - \tau_c)^a \qquad \text{(I.2.16)}$$

où $\dot{E}$ correspond à la vitesse d'incision fluviale du substratum rocheux, k est une constante reflétant entre autre l'érodabilité du substrat, τ_c est un seuil critique d'incision et τ est l'intensité du flux d'eau (correspondant à la contrainte cisaillante basale, la puissance unitaire ou totale fournie par le flux d'eau) et a est un exposant positif [*e.g.*, *Lague*, 2003]. A partir de cette formulation, et considérant plusieurs hypothèses dont (1) le seuil critique souvent négligé (pourtant non négligeable dans certains cas; *e.g.*, *Lavé*, 1997); (2) l'utilisation de l'aire drainée comme proxy de la répartition des débits; et (3) plusieurs relations empiriques entre le débit, la géométrie hydraulique du chenal fluvial et la vitesse du flux d'eau [*e.g.*, *Hack*, 1957; *Howard et al.*, 1994; *Whipple and Tucker*, 1999; *Lague*, 2003], l'incision fluviale peut être synthétisée suivant la loi communément utilisée ("stream power law") :

$$\dot{E} = K A^m S^n \qquad \text{(I.2.17)}$$

où $\dot{E}$ correspond à la vitesse d'incision fluviale du substratum rocheux (m an^{-1}), K est une constante reflétant l'érodabilité du substrat ($m^{(1-2m)}$ an^{-1}), S est la pente locale (m m^{-1}), A est l'aire drainée (m^2), et n/m sont des constantes adimensionnées qui représentent la physique de l'incision fluviale [*e.g.*, *Whipple et al.*, 2000; *Lague*, 2003; *van der Beek and Bishop*, 2003],

ainsi que la variabilité des débits [*Lague et al.,* 2005]. Cette formulation de l'équation fluviale, utilisée dans de nombreux modèles, ne prend pas en compte le rôle des sédiments dans l'érosion du substratum et considère que toute particule sédimentaire érodée est transportée au dehors du système. La vitesse d'incision du substratum rocheux est par conséquent uniquement limitée par la capacité du flux d'eau à éroder le substrat; les modèles utilisant cette formulation sont communément appelés modèles limités par le détachement ("detachment-limited" models; *Whipple and Tucker*, 2002). Par ailleurs, ces modèles ne prennent pas en considération la dynamique du chenal fluvial dans le calcul de l'incision du substratum [*e.g.*, *Lavé*, 1997; *Finnegan et al.*, 2005; *Snyder and Krammer*, 2008], les variations potentielles de la largeur du chenal étant implicitement considérées comme uniquement dépendantes de l'aire drainée ($W \sim A^{0.5}$), même si des formulations récentes permettent une considération explicite [*e.g.*, *Whittaker et al.*, 2007].

Une formulation équivalente peut être dérivée concernant le transport sédimentaire [*Howard*, 1998] et est généralement simplifiée suivant les mêmes hypothèses afin de constituer les modèles d'incision fluviale dits limités par le transport ("transport-limited" models; *Willgoose et al.*, 1991; *Whipple and Tucker*, 2002]. Ces modèles considèrent la capacité de transport sédimentaire le long d'une rivière (Q_c) suivant une loi de puissance équivalente à la "stream power" :

$$Q_c = K_s A^{m_s} S^{n_s} \tag{I.2.18}$$

où K_s est également une constante reflétant dans ce cas la physique du transport ainsi que la nature/taille des sédiments ($m^{(3-2m_s)}$ an^{-1}), S est la pente locale (m m^{-1}), A est l'aire drainée (m^2), et n_s/m_s sont des constantes adimensionnées. Cette formulation pose l'hypothèse selon laquelle la rivière est en tout point à sa capacité de transport, et ainsi les processus de dépôt de sédiments ou d'incision du substratum sont uniquement engendrés par les variations spatiales de la capacité de transport le long du chenal selon :

$$\dot{E} = \frac{1}{W}\frac{\delta Q_c}{\delta \vec{x}} \tag{I.2.19}$$

où $\dot{E}$ correspond dans ce cas à la vitesse d'incision fluviale du substratum rocheux ($\dot{E}>0$) ou de dépôt des sédiments ($\dot{E}<0$) (m an^{-1}), W est la largeur du chenal (m), et $\vec{x}$ la direction d'écoulement de la rivière. Ces modèles prennent donc en compte, d'une part les variations

spatiales de la largeur du chenal explicitement dans le calcul de l'érosion/dépôt, et d'autre part ils assurent la prise en compte et le suivi du transport des sédiments le long de la rivière, ce phénomène réduisant ainsi la capacité effective d'incision du substratum rocheux de par la dissipation d'énergie nécessaire à la mobilisation et au transport des sédiments.

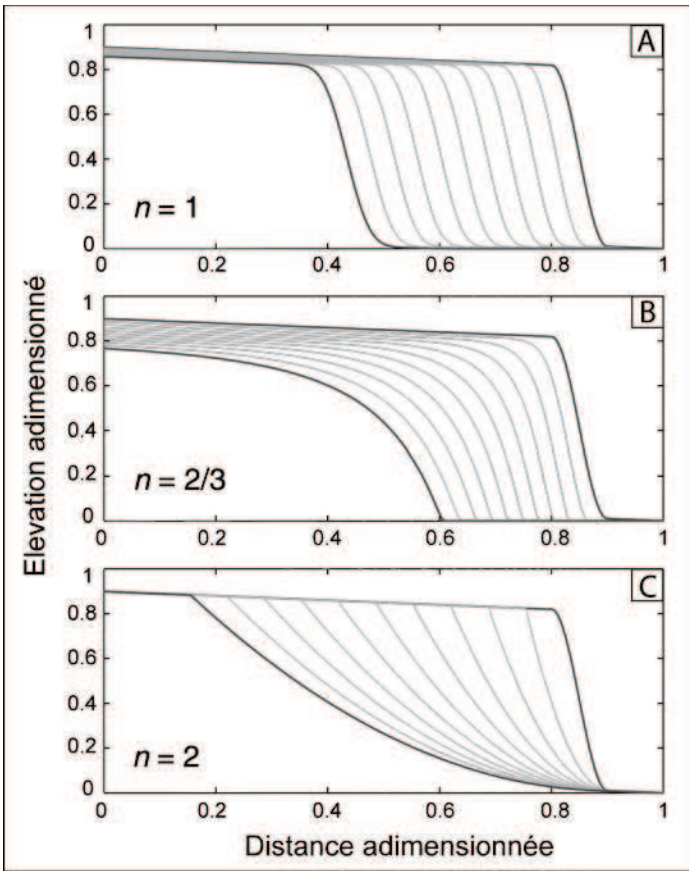

Figure I.2.13. *Exemple de simulations numériques en différences finies reproduisant la réponse d'un modèle limité par le détachement à une chute rapide du niveau de base (profil initial présentant un saut d'élévation dans sa partie inférieure). Chaque graphe (A, B et C) présente une simulation pour un exposant de pente (n) différent et illustre les réponses d'incision extrêmement variables suivant la valeur de cet exposant. Modifiée d'après Tucker and Whipple [2002].*

Au cours de ma thèse, j'ai principalement utilisé ces deux types de modèles afin de contraindre la dynamique d'incision de gorges post-glaciaires dans les Alpes occidentales françaises (cf. Chapitre IV, partie IV.3.1; *Valla et al.*, 2010c). La principale difficulté dans l'utilisation de ces modèles est la calibration des différents paramètres *n/m/K* ou $n_s/m_s/K_s$ régissant l'incision fluviale limitée par respectivement le détachement ou le transport sédimentaire. Plusieurs études [*e.g.*, *Tucker and Whipple*, 2002; *Tomkin et al.*, 2003; *van der Beek and Bishop*, 2003] ont tenté de calibrer ces paramètres et ont proposé des gammes

extrêmement variables selon les sites d'étude. Pour mon étude, j'ai également dû calibrer ces paramètres en me basant sur les profils longitudinaux initial et final de chaque rivière considérée. En effet, la réponse de l'incision fluviale va être extrêmement dépendante des facteurs K/K_s (facteurs contrôlant la vitesse de l'incision fluviale) mais également des exposants n/m (ou n_s/m_s) qui vont définir la répartition de l'incision le long de la rivière (Figure I.2.13).

J'ai uniquement réalisé des simulations numériques en une dimension (1-D, Figure I.2.13) au cours de ma thèse en utilisant des codes en différences finies basés sur l'étude de *van der Beek and Bishop* [2003] et reprenant les formulations simples d'incision fluviale limitée par le détachement du substratum rocheux ou le transport de sédiments. Cependant, mon approche comporte deux importantes simplifications : (1) la modélisation 1-D de l'incision fluviale ne permet pas de coupler dynamiquement la réponse érosive d'une rivière avec les processus de surface environnants tels les processus de pentes (éboulements, glissements de terrain et autres processus de versants…); (2) les modèles d'incision fluviale utilisés sont extrêmement simplifiés et ne rendent pas compte de la complexité liée à la variabilité des débits et donc des flux d'eau et de sédiments, au transport sédimentaire, et à l'adaptabilité du chenal à moduler sa géométrie, pour le calcul de l'incision fluviale. Dans la suite de cette partie, je vais présenter rapidement quels sont les différents modèles développés ces dernières années afin d'intégrer les complexités évoquées ci-dessus.

Plusieurs formulations ont été intégrées dans les modèles 1-D afin de prendre explicitement en compte les notions de seuils critiques dans l'incision fluviale (Eq. (I.2.16)) ainsi qu'une meilleure représentativité de la distribution stochastique des débits [*e.g.*, *Tucker*, 2004; *Lague et al.*, 2005], et également l'évolution dynamique du chenal, à partir de lois empiriques [*e.g.*, *Finnegan et al.*, 2005] ou en modélisant explicitement l'incision verticale et latérale du chenal [*Stark*, 2006; *Wobus et al.*, 2006; *Lague*, 2010]. Une simplification majeure des modèles considérant l'incision fluviale limitée par le transport ou le détachement concerne la non prise en compte de la complexité des interactions entre les sédiments transportés et le substratum rocheux [*e.g.*, *Sklar and Dietrich,* 1998; 2006; *Johnson et al.*, 2009]. Le flux de sédiments transportés par l'écoulement possède deux effets opposés sur l'incision du substratum : (1) à faibles concentrations en sédiments, ces derniers vont impacter le substratum lors de phénomènes de saltation, charriage ou encore cavitation, produisant un effet "outil" et par conséquent l'augmentation de la capacité d'incision de la rivière; au contraire (2) de fortes

concentrations en sédiments vont entraîner la formation d'une "couverture" sédimentaire plus ou moins transitoire protégeant le substratum rocheux de l'incision fluviale [*e.g.*, *Sklar and Dietrich*, 2004].

Ces effets "outil" et "couverture" des sédiments sur la capacité d'incision fluviale ont été intégrés dans les modèles 1-D par de nombreux auteurs, certains ne considérant que l'effet "couverture" selon une fonction linéaire (Figure I.2.14A; *Kooi and Beaumont*, 1994) tandis que d'autres tels *Sklar and Dietrich* [1998; 2004] ont proposé une formulation combinant en même temps les deux effets (Figure I.2.14A) selon une fonction parabolique basée sur le rapport entre capacité de transport de la rivière (Q_c) et le flux sédimentaire local (Q_s):

$$\dot{E} = k_s \frac{Q_s}{W}(1 - \frac{Q_s}{Q_c}) \qquad \text{(I.2.20)}$$

où $\dot{E}$ correspond à la vitesse d'incision fluviale du substratum rocheux ou de dépôt des sédiments (m an^{-1}), W est la largeur du chenal (m), et k_s est une constante. Cette approche, basée sur le flux de sédiments transportés (effet de couverture dynamique) diffère de celle proposée par *Howard* [1998] qui considère uniquement l'épaisseur de sédiments déposés (effet de couverture statique) dans le calcul de la capacité d'incision du substratum.
Lague [2010] a récemment développé un algorithme d'incision qui prend en compte ces deux effets de "couverture" (mais ne modélise pas l'effet "outil") suivant l'expression suivante :

$$\dot{E} = k_r \exp(-\upsilon \frac{Q_s}{Q_c}) \exp(-\frac{h_s}{\xi D_s})(\tau - \tau_c) \qquad \text{(I.2.21)}$$

où $\dot{E}$ correspond toujours à la vitesse d'incision fluviale du substratum rocheux ou de dépôt des sédiment (m an^{-1}), k_r est une constante liée à la vitesse d'incision (différente pour l'incision latérale et verticale), Q_s et Q_c sont respectivement le flux de sédiments et la capacité de transport, h_s est l'épaisseur moyenne de sédiments, D_s représente un facteur granulométrique, υ et ξ sont les facteurs de couverture dynamique est statique, et enfin τ et τ_c correspondent respectivement à la contrainte cisaillante basale et au seul critique d'incision. J'ai eu la possibilité d'utiliser ce modèle d'incision fluviale durant ma thèse (collaboration D. Lague, Université de Rennes; *Valla et al.*, 2010c). Une des principales innovations de cet algorithme est la prédiction d'un comportement hybride de la rivière au cours du temps (Figure I.2.14B; *Lague*, 2010) : suivant la distribution temporelle des débits, le système fluvial va se comporter soit selon un système où l'incision est limitée par le détachement du

substratum, soit dans le cas où l'incision est réduite par la nécessité de transporter et d'exporter les sédiments produits. Sur des modélisations au long-terme (*i.e.*, plusieurs milliers à millions d'années), ce modèle va par conséquent simuler l'alternance du système fluvial suivant ces deux états et permet par conséquent de mieux appréhender des effets transitoires tels une chute du niveau de base ou un changement du taux de soulèvement [*Lague*, 2010].

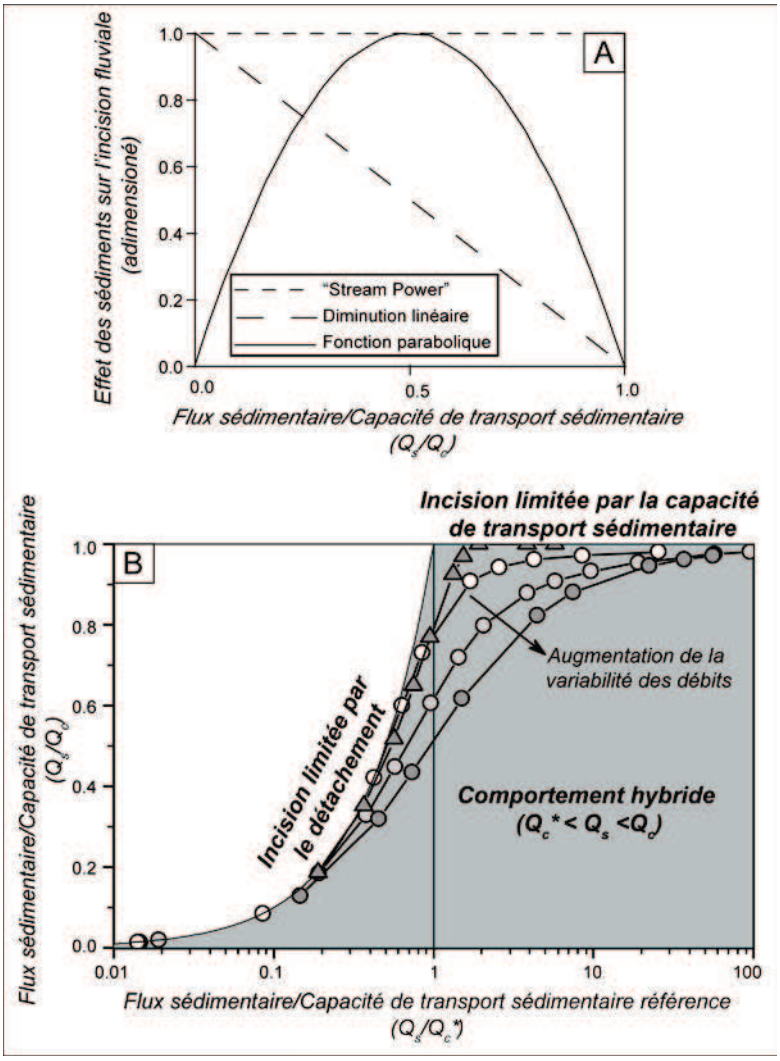

Figure I.2.14. *Effets "outil" et "couverture" des sédiments sur la capacité d'incision fluviale du substratum rocheux. A) Schéma de l'influence des sédiments transportés sur l'incision dans le cas où : (1) l'incision est limitée par le détachement du substratum ("stream power"), (2) uniquement l'effet "couverture" sédimentaire est considéré ("diminution linéaire"), et enfin (3) les effets "outil" et "couverture" des sédiments sont pris en compte ("fonction parabolique"). Modifiée d'après Whipple and Tucker [2002]. B) Illustration du comportement hybride de la rivière en fonction du flux sédimentaire, de la capacité de transport et de la variabilité des débits. Modifiée d'après Lague [2010].*

Enfin, il existe un grand nombre de modèles numériques permettant de modéliser les processus de surface et par conséquent l'évolution des paysages en deux dimensions (2-D) sur des échelles de temps variables (de l'échelle de la journée au million d'années). Ces modèles simulent d'une part les processus d'incision fluviale de manière diversifiée (plusieurs algorithmes d'incision fluviale selon les différents modèles présentés ci-dessus), mais ils considèrent également le couplage avec d'autres processus de surface tels les processus de versants (souvent représentés par un algorithme de diffusion simple ou incluant une pente de stabilité; *Roering et al.*, 2007). Ainsi, plusieurs modèles tels *Cascade* [*Braun and Sambridge*, 1997], *Eros* [*Crave and Davy*, 2001] ou encore *Child* [*Tucker et al.*, 2001] considèrent le système géomorphologique dans son ensemble et les couplages potentiels entre processus de versants d'une part, et la dynamique fluviale d'autre part, capturant de manière plus réaliste que l'approche 1-D les phénomènes naturels mais d'un autre côté complexifiant leur modélisation (Figure I.2.15).

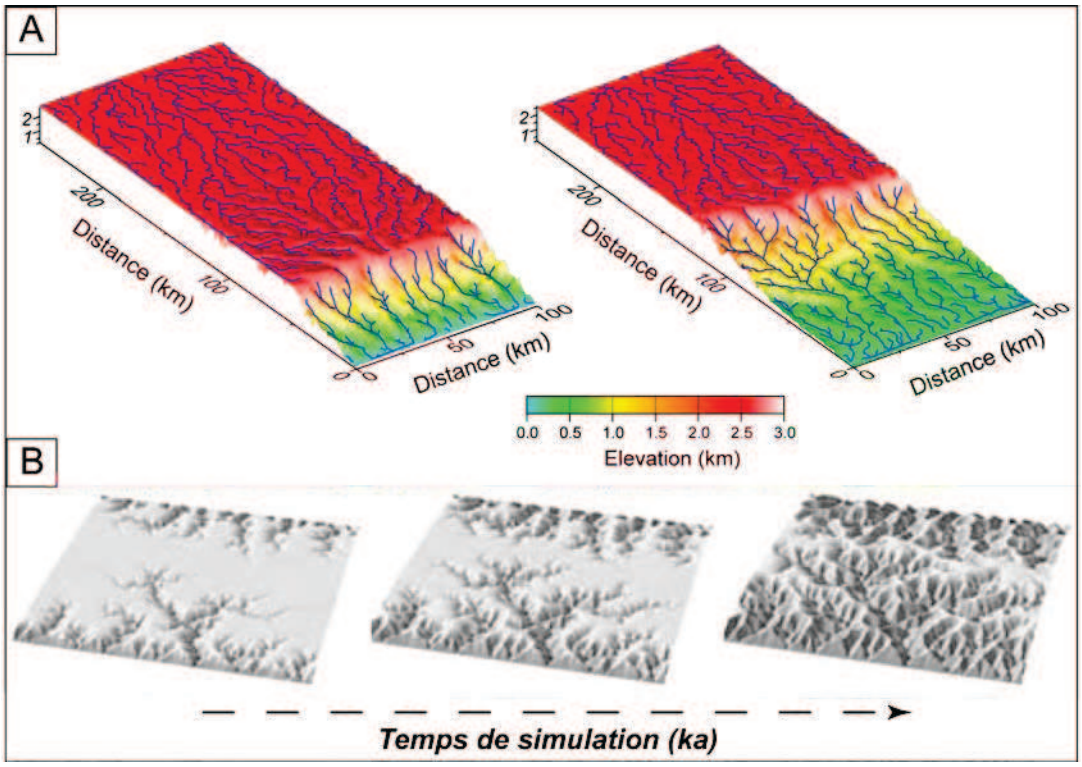

Figure I.2.15. *Illustration de modélisations 2-D de l'évolution de la topographie suivant deux différents modèles et deux situations considérées. A) Modélisation d'un retrait d'escarpement (topographie initiale à gauche, à la fin de la simulation à droite) à l'aide du modèle Cascade. Modifiée d'après van der Beek et al. [2002]. B) Réponse érosive d'un plateau en soulèvement à l'aide du modèle Eros. Modifiée d'après Crave and Davy [2001].*

I.2.3.2 - Modélisation 2-D de la dynamique et l'érosion glaciaire

La modélisation 2-D de la dynamique glaciaire a tout d'abord été développée pour l'étude de la dynamique et l'évolution des calottes polaires [*e.g.*, *Ritz et al.*, 2001; *Pattyn*, 2003; *Rutt et al.*, 2009] et les premiers modèles numériques 1-D ou pseudo 2-D pour les glaciers de montagne et l'érosion glaciaire se développent suite aux travaux de *Oerlemans* [1984] et de *Harbor* [1992a, b]. Cependant, le développement des modèles 2-D simulant les processus de surface et l'évolution de la topographie sur des échelles de temps géologiques a mené à l'adaptation progressive des algorithmes utilisés pour les calottes afin de pouvoir les appliquer aux conditions de glaciers de montagnes (aussi appelés glaciers de vallées) et de modéliser les processus d'érosion glaciaire [*e.g.*, *Braun et al.*, 1998; *Tomkin and Braun*, 2002; *Kessler et al.*, 2006; *Herman and Braun*, 2008; *Egholm et al.*, 2009].

La modélisation de l'épaisseur d'un glacier, de son évolution spatiale (2-D) et temporelle est basée sur la dynamique d'écoulement de la glace et une composante de bilan de masse (Figure I.2.16) selon l'équation suivante :

$$\frac{\partial H}{\partial t} = \nabla q + M \quad ; \quad q = Hu \quad \text{et} \quad M = M_s + M_b \tag{I.2.22}$$

où H représente l'épaisseur de glace (m), q est le flux de glace (m^3 an^{-1}) et M le bilan de masse annuel (m an^{-1}, *i.e.*, la quantité de glace qui est d'une part gagnée par accumulation de neige, et d'autre part perdue par la fonte de surface et basale). Le flux de glace q est calculé par le produit de l'épaisseur de glace H et de la vitesse moyenne d'écoulement u (m an^{-1}), tandis que le bilan de masse M est la somme des bilans de masse basal (M_b) et en surface (M_s).

La vitesse d'écoulement d'un glacier est définie par deux composantes : (1) la vitesse de déformation u_d (Eq. (I.2.23)) régie par la loi de déformation de Glen [*e.g.*, *Hooke*, 1981; *Paterson*, 1994]; et (2) la vitesse de glissement du glacier sur le socle rocheux u_s (Eq. (I.24)) définie selon la loi de Weertman [*Paterson*, 1994] :

$$\varepsilon_{ij} = A\,\tau_e^{n-1}\tau_{ij} \quad ; \quad \varepsilon_{ii} = \frac{\partial u_{d_i}}{\partial i} \;\; et \;\; \varepsilon_{ij} = 1/2\left(\frac{\partial u_{d_i}}{\partial j} + \frac{\partial u_{dj}}{\partial i}\right) \tag{I.2.23}$$

$$u_s = \frac{B_s \tau_b^n}{P_e^r} \tag{I.2.24}$$

où ε_{ij} (an^{-1}) et τ_{ij} (Pa) sont des composantes (selon x, y ou z) des tenseurs respectivement du taux de déformation et du déviateur des contraintes, τ_e (Pa) est la contrainte effective [*Barral et al.*, 2001], n est le paramètre de la loi de Glen (compris entre 1 et 3) et A (Pa^{-n} an^{-1}) est la constante de déformation de la glace [*Hooke*, 1981] pour le calcul de la vitesse de déformation u_d. Pour la vitesse de glissement u_s, τ_b (Pa) correspond à la contrainte basale, B_s est une constante de glissement (m $Pa^{-(n-r)}$ an^{-1}), et P_e représente la pression effective (Pa) avec un exposant positif r (communément égal à 1).

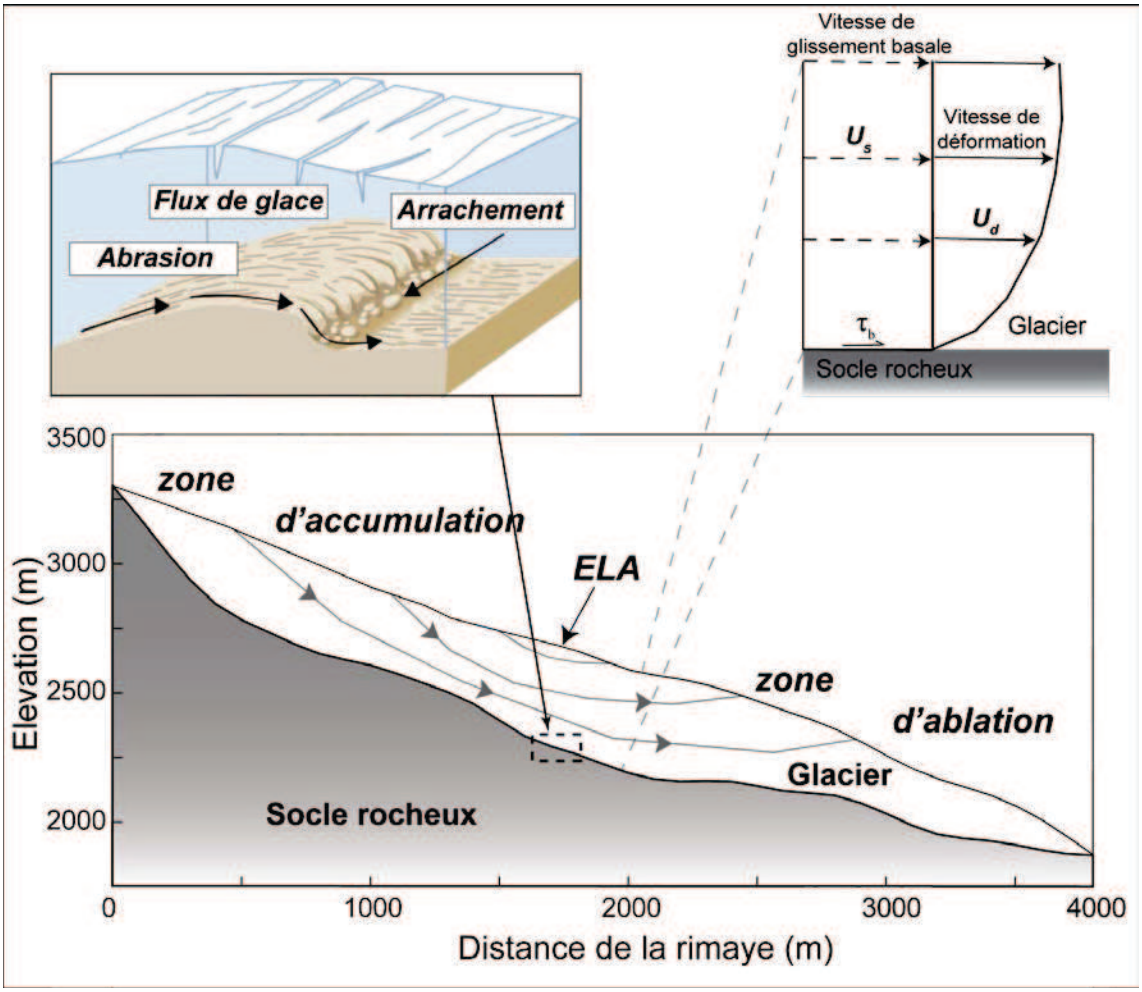

Figure I.2.16. *Coupe schématique d'un glacier, montrant les processus d'écoulement du glacier et d'érosion glaciaire. La coupe (bas) représente le fonctionnement dynamique d'un glacier (lignes de courant de l'écoulement interne de la glace). Le schéma (haut/droite) illustre les composantes de la vitesse d'écoulement d'un glacier : déformation interne (u_d) et glissement à l'interface glace/roche (u_s). L'illustration (haut/gauche) représente les processus d'érosion mécanique dominants à l'interface glace/roche.*

Tandis que la détermination de la vitesse de glissement (u_s) est assez directe, le calcul de la vitesse de déformation (u_d) nécessite le développement d'un système complexe d'équations reliant des équations de mécanique ainsi que les principes : (1) de conservation de la masse, et (2) d'incompressibilité de la glace (je ne développerai pas ces équations ici car le raisonnement serait assez long, cf. *Schäfer*, 2007). Afin de résoudre numériquement et de façon efficace ce système d'équations (temps de calcul raisonnable sur des temps géologiques), plusieurs simplifications ont été proposées par *Hutter* [1983] sous la forme de l'approximation de la couche mince ("Shallow Ice Approximation", référée ci-après par le terme SIA; *Le Meur et al.*, 2004; *Schäfer*, 2007). Cette approximation, provenant de la modélisation de calottes polaires, considère que la déformation est parallèle au substratum rocheux (*i.e.*, la déformation de la glace dans le plan horizontal est négligeable) et que les gradients de la surface de glace et du substratum rocheux sont faibles. Ces hypothèses sont vérifiées lorsque le rapport d'aspect ϕ est faible :

$$\phi = \frac{[H]}{[L]} << 1 \tag{I.2.25}$$

avec *[H]* et *[L]* les dimensions caractéristiques respectivement horizontale et verticale du système considéré. Les calottes polaires étant des objets glaciaires très étendus (*[H]<<[L]*), ce rapport d'aspect est de l'ordre de $\sim 10^{-3}$ [*Paterson*, 1994] et l'hypothèse est vérifiée. La situation est différente pour les glaciers de montagne car ceux-ci sont confinés dans des vallées de dimension finie et ont une épaisseur potentiellement importante au regard de leur étendue spatiale (rapport d'aspect de $\sim 10^{-1}$ à 1). Ainsi, toute variable approximée selon la SIA doit être suivie par un développement en série du rapport d'aspect, le degré de développement en série de cette perturbation va déterminer la précision de l'approximation selon :

$$G = \sum_{\upsilon=0}^{\infty} \phi^{\upsilon} G(\upsilon) = \phi^0 G(0) + \phi^1 G(1) + \phi^2 G(2) + \ldots \tag{I.2.26}$$

avec G la variable approximée, ϕ le rapport d'aspect et υ le degré de perturbation considéré (*i.e.*, le degré de précision vis-à-vis de l'approximation SIA). Ainsi, plusieurs modèles de dynamique des glaciers de montagne existent et diffèrent selon le degré de correction retenu pour l'approximation selon la SIA : modèles utilisant la SIA à l'ordre 0 [*e.g.*, *Braun et al.*, 1998; *Tomkin and Braun*, 2002; *Herman and Braun*, 2008]; simulations utilisant la SIA au premier ordre ("First Order Approximation", FOA; *Blatter*, 1995; *Greve and Blatter*, 2009] ou

encore la SIA développée au second ordre ("Second Order Shallow Ice Approximation", SOSIA; *Egholm et al.*, 2009).

Durant ma thèse, j'ai eu l'opportunité d'utiliser deux modèles numériques simulant les processus de la dynamique glaciaire. Le premier, développé par *Braun et al.* [1998] et récemment modifié et amélioré par *Herman and Braun* [2008], est basé sur la SIA développée à l'ordre 0 (ce modèle est appelé *ICECascade*) ; tandis que le second a été récemment développé par *Egholm et al.* [2009] et n'a été disponible qu'au cours de ma thèse (appelé ci-après *SPMIce*). Ces deux modèles sont très similaires; leur seule différence réside dans le calcul des vitesses de déformation et de glissement. Dans la suite de cette partie, je vais donc exposer les divers algorithmes de ces modèles permettant de simuler la dynamique glaciaire et plus concrètement de : (1) reconstruire les extensions glaciaires lors de périodes passées, et (2) contraindre l'impact de ces glaciations sur l'évolution des paysages en modélisant l'érosion glaciaire.

ICECascade est un modèle en différences finies [*Hindmarsh and Payne*, 1996; *Herman and Braun*, 2008] basé sur la SIA développée à l'ordre zéro. Cette approche permet une simplification avancée des équations régissant la dynamique glaciaire (vitesses de déformation et de glissement) et ainsi une résolution numérique efficace des vitesses, des gradients de surface et enfin de la variation temporelle et spatiale de l'épaisseur de glace. Ainsi, les vitesses de glissement (u_s) et déformation (u_d) sont calculées en chaque point d'une grille régulière selon les équations suivantes [*Hutter*, 1983] :

$$u_d = \frac{2A}{n+1}(\rho g)^n H^{n+2} \left|\nabla(H+z)\right|^{n-1} \nabla(H+z) \qquad \text{(I.2.27)}$$

$$u_s = \frac{B_s}{P_e}(\rho g)^n H^{n+1} \left|\nabla(H+z)\right|^{n-1} \nabla(H+z) \qquad \text{(I.2.28)}$$

avec la même terminologie utilisée pour les équations (I.2.23) et (I.2.24), et z (m) la topographie du substratum rocheux.

Comme expliqué précédemment, l'utilisation de la SIA développée à l'ordre zéro ne prend pas en compte les gradients de déformation dans le plan horizontal et n'est par conséquent pas adaptée à la modélisation d'écoulement glaciaire dans des vallées alpines souvent étroites

(*i.e.*, forts gradients dans le plan horizontal). Pour limiter ce biais, un facteur de constriction du flux de glace (β) est incorporé dans le calcul des vitesses de glissement et de déformation [*Svennson*, 1958] :

$$\beta = (1 + k_c \frac{\partial^2 z}{\partial x_c^{\,2}})^{-1} \qquad \text{(I.2.29)}$$

avec k_c (m) une constante empirique et x_c la direction normale aux flux d'écoulement de la glace. Ainsi, les vitesses d'écoulement de la glace sont numériquement diminuées afin de modéliser les phénomènes de friction du glacier sur les bordures de la vallée.

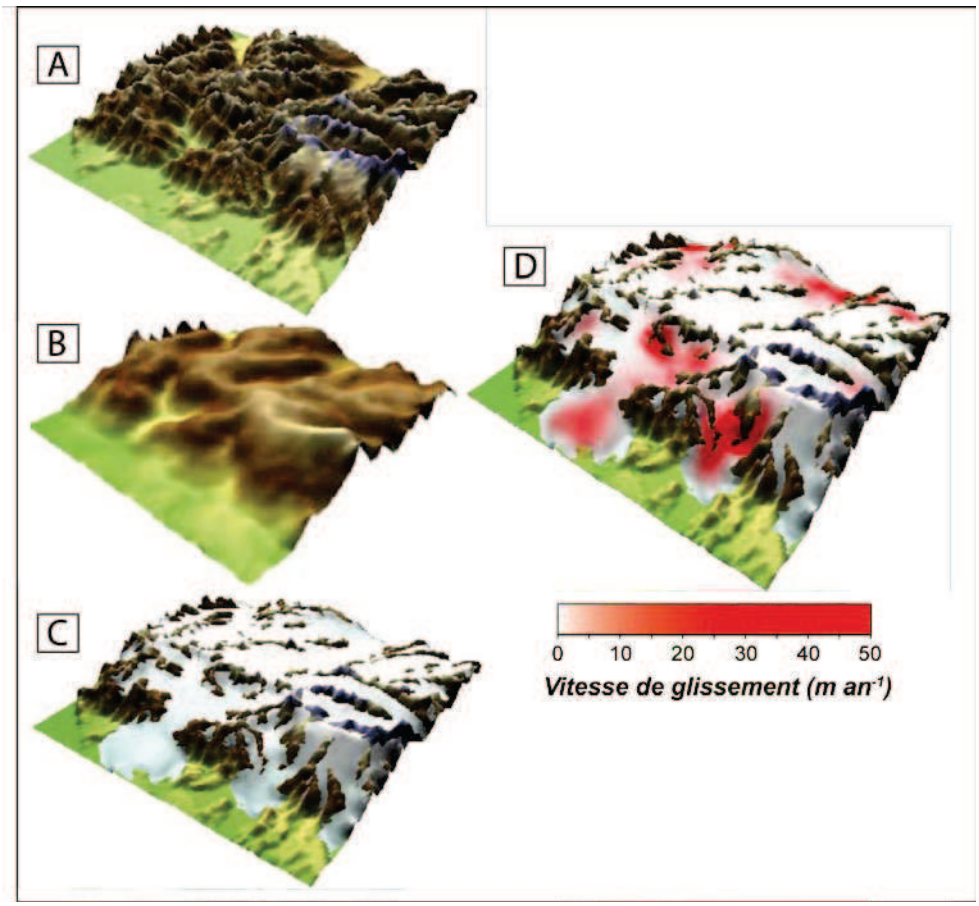

Figure I.2.17. *Exemple de l'approche numérique employée dans ICECascade. La topographie est représentée selon une grille régulière (A) dont la résolution est dégradée (B). Cette grille basse résolution est utilisée afin de déterminer les vitesses de glissement/déformation de la glace (C) et ainsi de calculer l'épaisseur de glace (C). Ces variables sont ensuite interpolées sur la grille haute résolution (A) pour le calcul de l'érosion glaciaire. Modifiée d'après Herman and Braun [2008].*

Enfin, l'utilisation de la SIA à l'ordre zéro limite la résolution de la grille de modélisation, et ne permet pas de simuler les phénomènes de dynamique glaciaire à petite échelle (résolution moyenne ~1-3 km; *Tomkin and Braun*, 2002). *Herman and Braun* [2008] ont adopté une approche différente avec l'utilisation de deux grilles régulières (Figure I.2.17) : (1) une première grille de basse résolution (~2 km) sur laquelle les vitesses de déformation et de glissement sont calculées suivant les équations (I.2.27) et (I.2.28); et (2) une grille de plus haute résolution (~250 m) sur laquelle sont interpolées les vitesses d'écoulement glaciaire ainsi que l'épaisseur de glace. Cette seconde grille est par la suite utilisée pour calculer l'érosion glaciaire et périglaciaire, avant de modéliser sur la grille basse résolution le rebond isostatique en réponse à, d'une part l'extension/retrait des glaciers, et d'autre part l'érosion glaciaire [*Herman and Braun*, 2008].

Le second modèle glaciaire utilisé (*SPMIce*, Figure I.2.18; *Egholm et al.*, 2009) est basé sur le développement de la SIA au second ordre et ainsi intègre de façon explicite des termes supplémentaires de correction dans le calcul des vitesses de déformation et de glissement. La vitesse de déformation (u_d) est calculée suivant l'équation [*Egholm et al.*, 2009] :

$$u_{d\,x,y} = 2A\,\tau_e^{n-1}\,(-\frac{1}{3}\frac{\partial(H+z)}{\partial x, y}H^2 + \Theta_{x,y} + \Omega_{x,y}) - \Lambda_{x,y} \qquad \text{(I.2.30)}$$

avec la même terminologie utilisée pour les équations (I.2.23), (I.2.24), (I.2.27) et (I.2.28), et l'ajout de termes correctifs supplémentaires : (1) $\Theta_{x,y}$ dans le cas de forts gradients et concavités de la surface de glace; (2) $\Omega_{x,y}$ afin de prendre en compte les gradients de contraintes dans le plan horizontal; et (3) $\Lambda_{x,y}$ représentant l'écoulement vertical de la glace [*Egholm et al.*, 2009]. La vitesse de glissement (u_s) est calculée à partir de l'équation (I.2.29) avec la prise en compte supplémentaire des composantes parallèle et transverse [*Egholm et al.*, 2009] dans la détermination de la contrainte cisaillante basale (τ_b, Eq. (I.2.24)). L'approche numérique diffère également de *ICECascade* et utilise une grille irrégulière (de résolution variable 100-1000 m, Figure I.2.18A). La topographie est ici discrétisée via la définition d'un diagramme de Voronoi [*Braun and Sambridge*, 1997] qui permet de suivre quantitativement les flux d'écoulement glaciaire depuis chaque cellule de Voronoi vers ces voisins directs [*Egholm and Nielsen*, 2010].

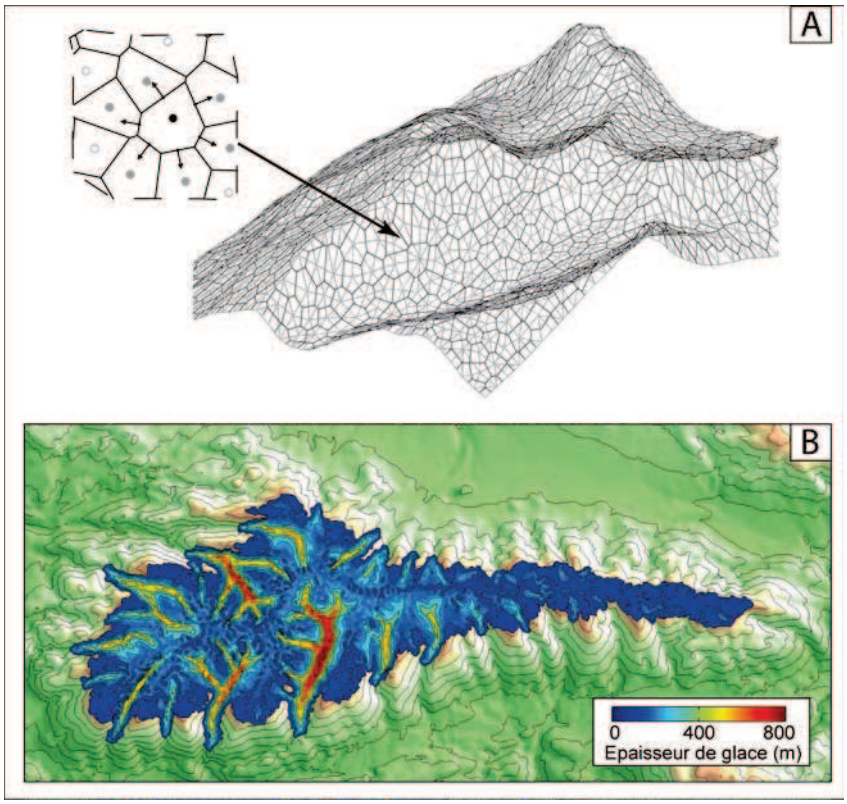

Figure I.2.18. *Exemple de l'approche numérique employée dans SPMIce. La topographie est interpolée selon une grille irrégulière (A) dont chaque nœud correspond à une cellule de Voronoi. Cette architecture permet un suivi efficace des flux de glace depuis une cellule vers ses voisins directs et ainsi le calcul des vitesses de glissement/déformation intervenant dans l'évolution spatio-temporelle de l'épaisseur de glace (B). Modifiée d'après Egholm et al. [2009].*

Les deux modèles numériques utilisés adoptent la même approche pour la détermination du bilan de masse (Eq. (I.2.22), Figure I.2.16). Concernant le bilan de masse en surface (M_s), un glacier est délimité suivant deux zones (la limite entre ces deux zones est la ligne d'équilibre glaciaire, ou "Equilibrium Line Altitude" : ELA) : (1) une zone dite d'accumulation où le bilan de surface net est positif, *i.e.*, la perte par fonte estivale est inférieure aux précipitations nivales; et (2) une zone dite d'ablation où le bilan de surface net est négatif, *i.e.*, la perte par fonte estivale est supérieure aux précipitations nivales.

Le bilan de masse en surface (M_s) peut être décrit à partir des équations suivantes :

$$M_s = -\gamma_s(T_s) \quad ; \quad T_s = T_0 - \alpha(H + z) \tag{I.2.31}$$

avec γ_s une constante positive (m an^{-1} °C^{-1}), T_s la température à la surface du glacier ou du substratum rocheux (°C), T_0 la température au niveau de la mer, α le gradient atmosphérique de température (°C m^{-1}), enfin H et z sont respectivement l'épaisseur de glace et l'altitude du substratum rocheux (m).

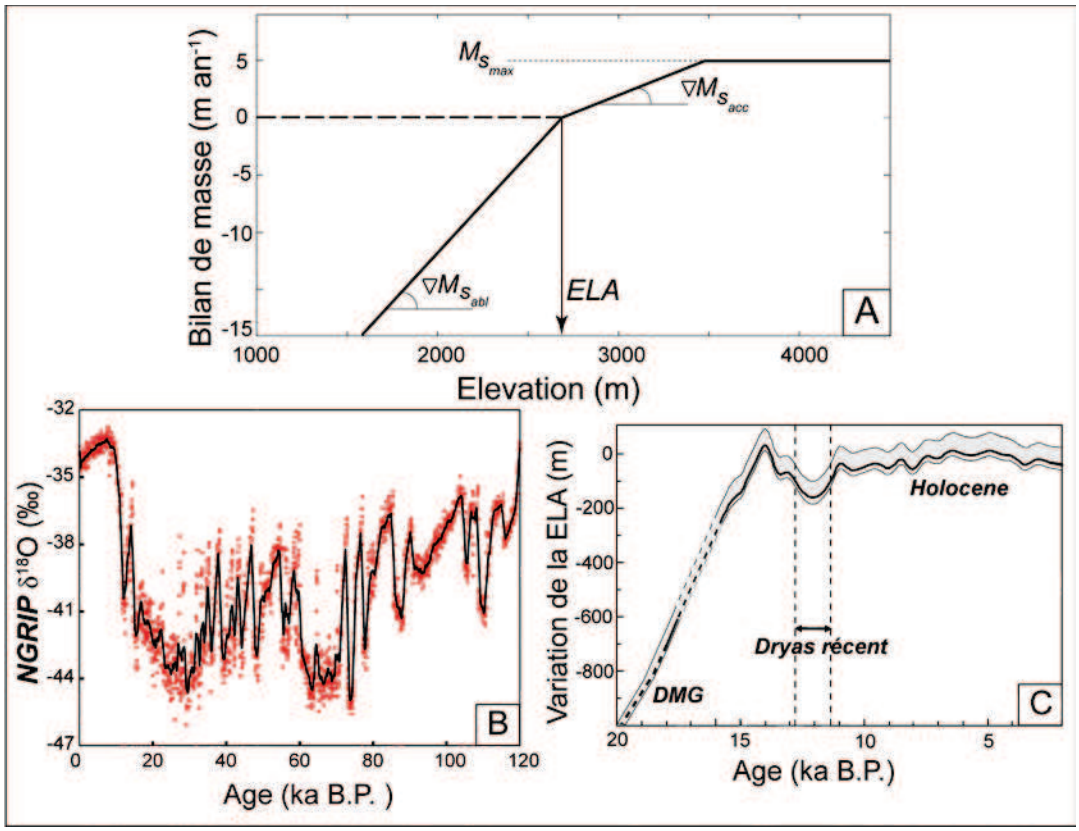

Figure I.2.19. *Définition et calibration du bilan de masse glaciaire en surface. (A) Représentation schématique de la définition du bilan de masse en surface pour les zones d'accumulation/ablation, et caractérisation de la ligne d'équilibre glaciaire (ELA). Modifiée d'après Kessler et al. [2006]. (B) Variations en $\delta^{18}O$ des glaces polaires (NGRIP), proxy des variations de température lors du dernier cycle glaciaire/interglaciaire. Modifiée d'après NGRIP members [2004]. (C) Estimations des variations de la position de la ELA (par rapport à l'actuel) depuis la fin du dernier maximum glaciaire (LGM). Modifiée d'après Norton and Hampel [2010].*

La modélisation et la calibration de l'évolution spatio-temporelle du bilan de masse en surface sont des étapes importantes dans la simulation de la dynamique glaciaire; cependant elles varient assez fortement d'une étude à l'autre (Figure I.2.19). En effet, La constante γ_s peut être similaire ou différente selon la zone d'accumulation ou d'ablation (Figure I.2.19A), et le bilan de masse en surface peut être potentiellement limité par une constante supplémentaire (*e.g.*, la quantité annuelle de précipitations). Par ailleurs, les variations au cours du temps de l'extension d'un glacier sont fortement conditionnées par les variations de températures (Figure I.2.19B), et par conséquent les variations dans la position de la ELA (Figure I.2.19C). Cependant, les variations climatiques, souvent enregistrées dans les archives polaires [*NGRIP members*, 2004] ou sédimentaires [*e.g.*, *Fauquette et al.*, 1999; *Zachos et al.*, 2001], sont difficilement interprétables en termes de variations de la position de la ELA [*Maisch*, 2000;

Vincent, 2002; *Norton and Hampel*, 2010], complexifiant la modélisation du bilan de masse en surface. Enfin, plusieurs effets locaux mais non négligeables ne sont pas pris en compte dans la modélisation du bilan de masse en surface : exposition Nord/Sud du glacier, redistribution de neige par le vent, avalanches depuis les sommets rocheux etc [*MacGregor et al.*, 2009].

La détermination du bilan de masse basal (M_b) nécessite l'estimation de la température basale (T_s) selon l'équation d'advection de chaleur suivante [*Braun et al.*, 1998]:

$$T_b = T_s + \frac{G}{K}\frac{\sqrt{\pi}}{2}\sqrt{\frac{2H\kappa}{M}}erf(H\sqrt{\frac{M}{2H\kappa}}) \qquad \text{(I.2.32)}$$

avec K la conductivité de la glace (W m^{-1} $°C^{-1}$), κ la diffusivité thermique (m^2 an^{-1}), G le gradient géothermique (W m^{-2}), H l'épaisseur de glace (m), et M le bilan de masse (m an^{-1}) calculé au pas de temps précédent. Cette équation n'est valable que pour la zone d'accumulation (M>0); ainsi, la température basale est linéairement intégrée depuis la surface du glacier dans la zone d'ablation (M<0). Le bilan de masse basal (M_b) est estimé à partir de l'équation suivante :

$$M_b = -\gamma_m(T_b - T_m) \;\; ; \;\; T_m = -8.7\times10^{-4}H \qquad \text{(I.2.33)}$$

avec γ_m une constante positive (m an^{-1} $°C^{-1}$), et T_m la température du point de fusion de la glace, dépendante de la pression exercée par l'épaisseur de glace sus-jacente [*Hooke*, 1998].

Plusieurs améliorations sont en cours d'implémentation dans ces modèles afin de mieux prendre en compte : (1) l'hydrologie sous-glaciaire [*Egholm et al.*, 2009] et son influence sur la vitesse de glissement (et donc sur l'érosion glaciaire); ainsi que (2) le transport sédimentaire sous-glaciaire et son influence sur l'érosion du substratum rocheux [*Hagdorn and Boulton*, 2004]. Par ailleurs, ces modèles sont couplés avec les algorithmes simulant les processus de surface tels l'incision fluviale ou encore les processus de versant (cf. partie I.2.3.1, *Braun and Sambridge*, 1997), et intègrent également la possibilité de modéliser des processus de soulèvement tectonique et/ou rebond isostatique [*Tomkin and Braun*, 2002; *Herman and Braun*, 2008; *Egholm et al.*, 2009].

L'érosion glaciaire intègre une combinaison de processus complexes comprenant [*e.g.*, *Boulton*, 1974; *Lliboutry*, 1994] : (1) l'érosion sous-glaciaire par les eaux de fonte circulant sous le glacier, (2) l'altération chimique du substratum rocheux, et (3) des phénomènes d'érosion mécanique (Figure I.2.16) tels l'abrasion par frottements du substratum rocheux en contact avec les sédiments enchâssés dans le glacier [*Hallet*, 1979] ou encore le détachement de blocs du substratum sous l'effet cisaillant de l'écoulement glaciaire [*Hallet*, 1996]. Plusieurs formulations théoriques ont été développées afin de quantifier ces phénomènes complexes et leurs interactions [*e.g.*, *Hallet*, 1979; 1996], cependant l'ensemble de ces processus érosifs glaciaires présente une similarité commune : tous sont dépendants de la vitesse de glissement (u_s) du glacier à l'interface glace-roche, et peuvent être représentés à partir de l'équation suivante [*Hallet*, 1979] :

$$\dot{E} = K_g \left| u_s \right|^l \tag{I.2.34}$$

avec $\dot{E}$ la vitesse d'érosion (m an^{-1}), K_g une constante (m^{1-l} an^{l-1}) reflétant entre autres l'érodabilité du substrat [*e.g.*, *Boulton*, 1979], et l un exposant variant théoriquement entre respectivement 1-2 et 1-4 pour respectivement les processus d'abrasion [*Hallet*, 1979] et de détachement de blocs [*Hallet*, 1996]. Peu de contraintes empiriques sont disponibles pour la calibration de cet exposant, ainsi, dans la majorité des études [*Harbor*, 1992a, b; *Herman and Braun*, 2008; *Egholm et al.*, 2009] celui-ci est choisi égal à 1. Cette approche (Eq. (I.2.34)) ne considère l'érosion glaciaire que dans le cas où le glacier est tempéré (*i.e.*, la température basale est supérieure au point de fusion, Eq. (I.2.32)) où l'eau disponible favorise le glissement à l'interface glace-roche. Ainsi, les modèles utilisés ne prédisent aucune érosion pour les glaciers dits "froids" (écoulement de la glace seulement dû à la déformation interne), cohérent avec des observations en Fennoscandie [*e.g.*, *Stroeven et al.,* 2002].

Chapter II :

Quantitative thermochronology: constraining exhumation and relief histories using thermochronological data

II.1 - Chapter II overview (Présentation du Chapitre II)

II.1.1 - Introduction

Le développement des méthodes thermochronométriques [*e.g.*, *Gallagher et al.*, 1998; *Reiners et al.*, 2005] a permis d'ouvrir de nouvelles possibilités quant à la quantification des processus d'exhumation et d'évolution du relief [*e.g.*, *Ehlers and Farley*, 2003]. Cependant, l'utilisation de la thermochronologie dans la quantification des processus tectono-géomorphiques nécessite, d'une part l'acquisition d'un large jeu de données thermochronologiques spatialement bien réparties [*Gallagher et al.*, 2005b] et combinant plusieurs systèmes thermochronométriques, et d'autre part des outils méthodologiques pour interpréter quantitativement ces données [*e.g.*, *Gallagher et al.*, 2005a; *Ketcham*, 2005; *Braun et al.*, 2006]. Dans ce chapitre, je présente les résultats d'interprétation quantitative de données thermochronomogiques à partir de la modélisation numérique (*Pecube*, *Braun*, 2003) couplée à une approche inverse (*Neighbourhood Algorithm*; *Sambridge*, 1999a, b) afin de contraindre des histoires d'exhumation et d'évolution du relief. Dans une première partie, je présente un article publié dans la revue *Earth and Planetary Science Letters* [*Valla et al.*, 2010b] décrivant l'utilisation de données thermochronologiques basse-température (traces de fission et (U-Th)/He sur apatite) collectées le long de profils "altitudinaux" synthétiques afin de contraindre des scénarios d'exhumation et/ou d'évolution du relief. Nos résultats montrent que les âges traces de fission sur apatite, malgré leur utilisation très répandue dans l'étude des chaînes de montagne, n'apportent que peu d'informations indépendantes sur les histoires d'exhumation et l'évolution du relief. La combinaison de plusieurs thermochronomètres (*e.g.*, traces de fission et (U-Th)/He sur apatite) et/ou l'inclusion d'information sur les longueurs de traces de fission permet une meilleure quantification des vitesses d'exhumation et de leurs changements au cours de l'évolution d'une chaîne de montagne. Cependant, l'évolution de la topographie est beaucoup plus difficile à contraindre et ne peut être quantifiée via la thermochronologie basse-température que pour des scénarios où la vitesse de développement du relief est au moins 2 à 3 fois supérieure à la vitesse d'exhumation régionale.

Dans une deuxième partie, je présente l'application de l'approche numérique inverse développée précédemment à un jeu de données thermochronologiques collectées le long d'un profil altitudinal au Pic de la Meije (massif des Ecrins-Pelvoux, Alpes occidentales, France).

Ces résultats ont également fait l'objet d'une publication dans la revue *Earth and Planetary Science Letters* [*van der Beek et al.*, 2010] et confirment les conclusions précédentes sur la nécessité de combiner plusieurs thermochronomètres afin de contraindre quantitativement les histoires d'exhumation. Par ailleurs, nos modèles d'exhumation sont en accord avec de récentes études sur différents massifs cristallins alpins [*e.g.*, *Glotzbach et al.*, 2008; submitted; *Vernon et al.*, 2009] et illustrent une histoire d'exhumation contrastée du massif des Ecrins-Pelvoux : une phase d'exhumation rapide entre 6 et 5.5 Ma (~1-2 km Ma^{-1}), précédée et suivie d'une exhumation plus modérée (~0.3-0.4 km Ma^{-1}). La détermination de l'évolution de la topographie, tout comme dans le cas de l'étude synthétique, reste mal contrainte et ne permet pas de conclure quant à un éventuel développement Pliocène-Quaternaire du relief dans cette zone. La résolution limitée de nos données provient de la relative faible augmentation du relief comparée à la vitesse d'exhumation régionale, les deux signaux d'exhumation ne pouvant pas être indépendamment quantifiés [*Valla et al.*, 2010b].

La troisième partie de ce chapitre reprend une étude, soumise à *Earth and Planetary Science Letters*, complétant les précédentes parties. Cependant, ce travail est ici basé sur la cohérence spatiale de données thermochonologiques et illustre l'importance, d'une part de la stratégie d'échantillonnage sur le terrain, et d'autre part des biais potentiels induits par la modélisation de ces données. En effet, la plupart des études thermochronologiques sont basées sur la collecte d'échantillons le long de profils "altitudinaux", même si, dans les deux parties précédentes de ce chapitre, nous avons montré l'apport limité de ce type de stratégie, particulièrement dans la quantification de l'évolution de la topographie. A partir d'une étude synthétique et du modèle numérique *Pecube*, nous avons testé l'efficacité relative de stratégies d'échantillonnage différentes (profil(s) "altitudinal(aux)", fond(s) de vallées…) et de leurs combinaisons optimales en vue de déterminer des histoires d'exhumation et de développement du relief. Nos résultats montrent qu'un échantillonnage réparti dans l'espace (plusieurs profils "altitudinaux", combinaison d'un profil avec des échantillons en fonds de vallées) produisent de meilleures estimations à la fois sur le relief et sur les vitesses d'exhumation. Par ailleurs, l'approche numérique dans l'interprétation de ces données influence également la précision des estimations sur les histoires tectono-géomorphiques. Ainsi, la résolution spatiale du modèle (*Pecube*) utilisé peut résulter en la perte d'informations quantitatives sur les vitesses d'exhumation et l'évolution de la topographie. Notre étude apporte de nouvelles contraintes sur la nécessité de définir *a priori* une stratégie précise pour l'échantillonnage et l'interprétation de données thermochronologiques.

II.1.2 - Presentations at international meetings

- December 2008, American Geophysical Union, Fall meeting, San Francisco (USA):

Valla, P.G., van der Beek, P.A., Herman, F., Braun, J. Extracting exhumation and relief history from thermochronological data: can we really quantify relief changes using age-elevation profiles? *Eos Trans. AGU, 89*(53), Fall Meet. Suppl., Abstract T53A-1917.

- **April, 2009**, European Geosciences Union, General assembly, Vienna (Austria):

Valla, P.G., van der Beek, P.A., Herman, F., Braun, J. Inversion of thermochronological data to extract independent constraints on denudation and relief evolution. *Geophysical Research Abstracts*, Vol. 11, EGU2009-3394.

van der Beek, P.A., Valla, P.G., Herman, F., Braun, J., Persano, C., Labrin, E., Dobson, K.J., Stuart, F. Extracting quantitative information on denudation and relief history from thermochronological age-elevation profiles: an example from the French Western Alps. *Geophysical Research Abstracts*, Vol. 11, EGU2009-3670.

- **August 2010**, Thermo2010, 12th International conference on thermochronology, Glasgow (United Kingdom):

van der Beek, P.A., Glotzbach, C., Valla, P.G., Bernet, M. The elusive 5-Ma increase in denudation rates of the European Alps. *Extended Abstract Volume, p.314*.

Braun, J. and members of the Low-T Thermochonology Team. Numerical modeling as an essential tool for the interpretation of thermochronological datasets. *Extended Abstract Volume, p.213*.

II.1.3 - Publications and contributors to Chapter II

This chapter presents two papers published in *Earth and Planetary Science Letters* (2010): Vol. 295, 511-522 (submitted September 18th 2009, accepted April 16th 2010) and Vol. 296, 9-22 (submitted September 18th 2009, accepted April 16th 2010). The 3rd part of this chapter reports a study submitted to *Earth and Planetary Science Letters*. P. van der Beek and J. Braun designed the study of the 1st paper. I personally produced all the results (collaboration F. Herman). P. van der Beek collected the samples presented in the 2nd paper. P. van der Beek and E. Labrin produced apatite/zircon fission track data, while C. Persano and K. Dobson provided zircon/apatite (U-Th)/He data. My contribution to this study was to interpret the data using numerical modelling (collaboration F. Herman). I personally designed the study and produced all the results presented in the 3rd part of this chapter.

II.2 - Inversion of thermochronological age-elevation profiles to extract independent estimates of denudation and relief history - I: Theory and conceptual model

Pierre G. Valla [1], Frédéric Herman [2], Peter A. van der Beek [1], and Jean Braun [1]

[1] *Laboratoire de Géodynamique des Chaînes Alpines, Université Joseph Fourier, BP 53, 38041 Grenoble, France*

[2] *Geologisches Institut, ETH Zürich, 8092 Zürich, Switzerland*

Abstract

We determine to what extent low-temperature thermochronology data, in particular from age-elevation profiles, provide independent and quantitative estimates on denudation rates and relief development. Thermochronological age-elevation profiles have been widely used to infer exhumation histories. However, their interpretation has remained inherently one-dimensional, neglecting potential effects of lateral offsets between samples. Furthermore, the potential effects of transient topography on crustal isotherms and consequently on thermochronological data have not yet been addressed in detail. We investigate this problem with the aim of deriving independent estimates of both denudation rates and relief history from low-temperature thermochronometers, measuring the relative uncertainties on these parameters and finally constraining the timing of potential variations in denudation rate and/or relief development. We adopt a non-linear inversion method combining the three-dimensional thermal-kinematic model *Pecube*, which predicts thermal histories and thermochronological ages from an input denudation and relief history, with an inversion scheme based on the neighbourhood algorithm. We use synthetic data predicted from imposed denudation and relief histories and quantitatively assess the resolution of thermochronological data collected along an age-elevation profile. Our results show that apatite fission-track (AFT) ages alone do not provide sufficient quantitative information to independently constrain denudation and relief histories. Multiple thermochronometers (apatite (U-Th)/He (AHe) ages and/or track-length measurements combined with AFT ages) are generally successful in constraining denudation rates and timing of rate changes, the optimum combination of thermochronometers varying with the input scenario (relief change or varying denudation rates). However, relief changes can only be quantified and precisely constrained from

thermochronological age-elevation profiles if the rate of relief growth is at least 2-3 times higher than the background denudation rate. This limited resolution is due to the depth of the closure isotherm (between ~70 and 110 °C) for the AFT and AHe systems, which only partly record topographic change. New thermochronometers (such as $^{4}He/^{3}He$ or OSL) that are sensitive to lower temperatures may be the key for resolving this issue.

II.2.1 - Introduction

Understanding the formation and evolution of orogenic topography requires a better comprehension of the couplings between climate, tectonics and surface processes [*e.g.*, *Beaumont et al.*, 1992; *Willett*, 1999; *Zeitler et al.*, 2001]. However, direct evidence of these couplings remains elusive and quantitative data are needed to better constrain the denudation and relief evolution of mountain belts. These are traditionally studied independently and only few methods such as low-temperature thermochronology [*e.g.*, *Gallagher et al.*, 1998; *Braun*, 2005; *Reiners and Brandon*, 2006; *Reiners*, 2007] may enable us to quantitatively assess both the denudation history and paleo-relief of mountain belts [*Braun*, 2002a, b].

Here, we explore to what extent low-temperature thermochronology (apatite fission-track and (U-Th)/He) data, in particular from age-elevation profiles, can provide such constraints on denudation history and paleo-relief of mountain belts. Apatite fission-track (AFT) age-elevation profiles, *i.e.*, sets of AFT ages collected from different elevations within a spatially restricted domain, have been widely used to infer exhumation histories of specific areas [*e.g.*, *Wagner and Reimer.*, 1972; *Hurford*, 1991; *Fitzgerald et al.*, 1995]. More recently, apatite (U-Th)/He (AHe) data have also been used in similar sampling schemes [*House et al.*, 1997; *Reiners et al.*, 2002; *Clark et al.*, 2005]. However, age-elevation relationships (AER) have generally considered the problem as one-dimensional, neglecting horizontal offsets between different samples of an elevation profile and therefore the potential effects of topography [*Braun*, 2002a; *Gallagher et al.*, 2005a; *Foeken et al.*, 2007]. Topographic effects on thermochronological age-elevation profiles result from the fact that near-surface isotherms are not horizontal but are deflected by the topography [*e.g.*, *House et al.*, 1998; *Braun*, 2002a]. The intensity of this perturbation and its depth of penetration are governed by the amplitude and wavelength of the topography. The influence of temporally steady-state topography on thermochronological age-elevation profiles is relatively well understood [*Stüwe et al.*, 1994; *Manktelow and Grasemann*, 1997]. However the potential effects of temporally varying

topography have not yet been addressed, although *Braun* [2002a] has shown conceptually what kind of patterns can be expected in AER and has highlighted the potential misinterpretation of AER slopes in terms of long-term denudation rates.

This study thus aims at: (1) deriving quantitative and independent estimates of both denudation and relief histories (rate and timing) from AER and (2) measuring the relative uncertainties on these parameters and thus the resolution of the data, which is very difficult to determine with current methods. Recent studies [*e.g.*, *Braun and van der Beek*, 2004; *Braun and Robert*, 2005; *Herman et al.*, 2007] have tackled similar problems by combining the three-dimensional thermal-kinematic model *Pecube* [*Braun*, 2003], which predicts thermal histories and thermochronological ages from an input denudation and relief history, with an inversion scheme based on the neighbourhood algorithm [*Sambridge*, 1999a] to search the parameter space and extract best-fitting scenarios for denudation and relief histories from the data. We adopt a similar method here but (1) specifically address the problem of interpreting age-elevation profiles and (2) add a model-appraisal stage [*Sambridge*, 1999a; *Herman et al.*, 2010a] to fully resolve the inverse problem and derive quantitative measures of the resolution with which we infer denudation and relief histories.

Here, we use synthetic data predicted from imposed denudation and relief histories, enabling us to quantitatively assess what constraints on denudation and relief history we can extract from low-temperature thermochronology data. In a companion paper [*van der Beek et al.*, 2010], we apply the same methodology on a real age-elevation profile in order to investigate the potential of AER in constraining the recent evolution of the western Alps in terms of temporally varying denudation rates and/or relief development [*e.g.*, *Glotzbach et al.*, 2008; *Vernon et al.*, 2009].

In the following, we first outline our conceptual model and present the synthetic data we will use in subsequent inversions. We then introduce our numerical approach and show to what extent predictions of denudation rates, timing and relief evolution can quantitatively be estimated from AER. We finally discuss the implications of our results for the use of thermochronology data in constraining tectonic and climatic controls on the evolution of orogenic topography.

II.2.2 - Conceptual model

II.2.2.1 - Modelling approach

In our conceptual model, outlined in Figure II.2.1, local exhumation rates at any point in the landscape result from two independent processes: regional denudation (which in the case of steady-state topography is equal to rock uplift as defined by *England and Molnar*, 1990) and temporal changes in topography. As thermochronology does not provide any constraints on surface uplift, topographic changes are expressed as changes in relief, defined as the difference in elevation Δh between the highest and lowest points in the area under consideration. A temporal change in local exhumation rate at any point, as recorded by a thermochronometer, may thus result from any combination of varying regional denudation rates ($E_1 \rightarrow E_2$; Figure II.2.1a) and/or varying relief ($\Delta h_1 \rightarrow \Delta h_2$; Figure II.2.1b).

We use a numerical approach with simple and imposed exhumation scenarios to assess to what extent both denudation rates and relief development can be constrained independently from thermochronological data. Based on this conceptual model (Figure II.2.1), we predict thermochronological ages for samples along an age-elevation profile spanning the ridge to valley relief, for three different end-member models: (1) both denudation rate and topography are constant through time; (2) topography is steady-state but denudation rates increase through time; (3) background denudation rates are constant but relief increases through time. In the latter case, we assume that relief increase results from preferential valley incision; *i.e.*, ridges remain at a constant elevation with respect to an exterior reference frame but valley bottoms are lowered, implying spatially varying exhumation rates with higher rates in the valleys than on the ridges (Figure II.2.1b).

We compute the thermal structure through time and thermal histories for material points now at the surface using the three-dimensional thermal-kinematic model *Pecube* [*Braun*, 2003]; a finite element code that solves the heat transfer equation [*Carslaw and Jaeger*, 1959] in 3D (Figure II.2.2):

$$\rho c \left(\frac{\partial T}{\partial t} + v \frac{\partial T}{\partial z}\right) = \frac{\partial}{\partial x} k \frac{\partial T}{\partial x} + \frac{\partial}{\partial y} k \frac{\partial T}{\partial y} + \frac{\partial}{\partial z} k \frac{\partial T}{\partial z} + H \qquad \text{(II.2.1)}$$

where $T(x,y,z,t)$ is temperature (°C), ρ is rock density (kg m^{-3}), c is heat capacity (J kg^{-1} K^{-1}), v is the vertical velocity of rocks with respect to the base of the model (mm yr^{-1}); k is conductivity (W m^{-1} K^{-1}) and H is radioactive heat production (W m^{-3}).

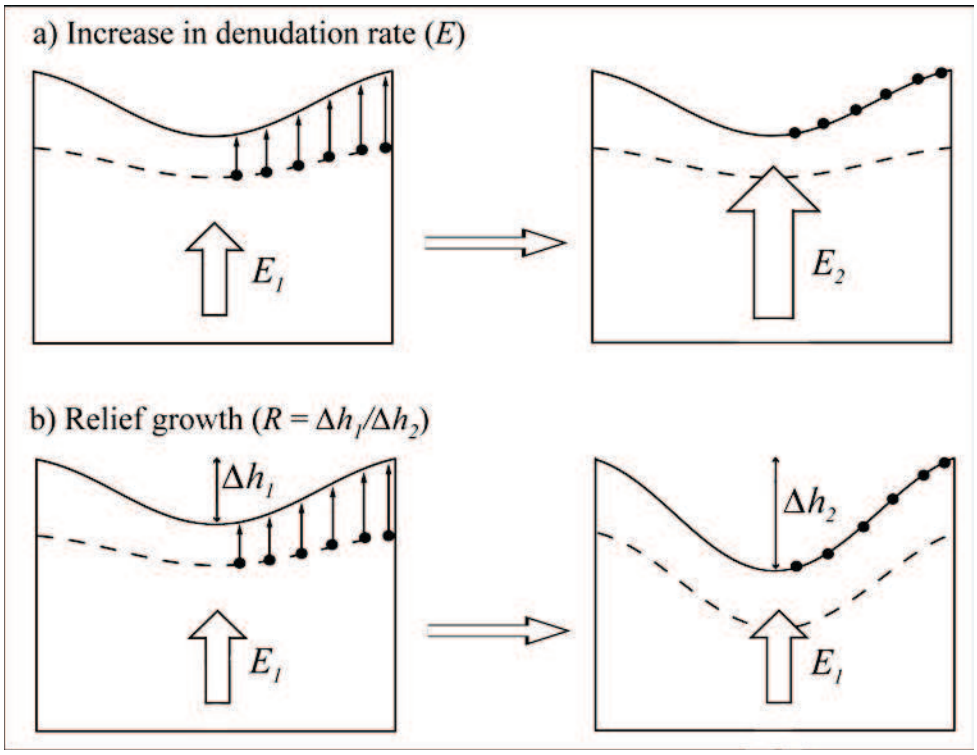

Figure II.2.1. *Conceptual model showing two end-members exhumation scenarios. Samples (black dots) are collected along an age-elevation profile spanning the ridge-to-valley relief; their thermochronological ages reflect, to a first order, the time since they passed the closure isotherm for the system considered (dashed line). (a) Increase in exhumation rate from an initial rate E_1 to a final rate E_2, under constant relief. (b) Regional exhumation rates remain constant (E_1) but ridge to valley relief increases from Δh_1 to Δh_2 through time. We assume relief increase to take place by valley incision; the amount of relief increase is quantified by the parameter $R = \Delta h_1 / \Delta h_2$.*

Pecube is able to solve Equation (II.2.1) for a time-varying surface topography, thus permitting to model transient relief. Relief evolution is incorporated here using the relief factor R, defined as the ratio between the initial (Δh_1) and present-day relief (Δh_2) :

$$R = \frac{\Delta h_1}{\Delta h_2} \qquad \text{(II.2.2)}$$

If $R = 0$, there is no initial relief (*i.e.*, the initial landscape is a plateau at the maximum present-day elevation); if $R < 1$ paleo-relief is lower than today (*e.g.*, Figure II.2.1b); if $R = 1$ relief is constant through time (*e.g.*, Figure II.2.1a); finally, if $R > 1$ paleo-relief is higher than

at present. Note that this approach supposes that the planform pattern of ridges and valleys is fixed, only the relief changes with time.

Predicted thermal histories are used to calculate AFT and AHe age-elevation profiles; these are currently the most commonly used thermochronometers for assessing late-stage exhumation and relief development in mountain belts. Thermal histories are translated into AHe ages using a simple forward model for He production-diffusion-ejection [*Farley*, 2000]. AFT ages are calculated using a forward model for AFT annealing [*Green et al.*, 1989] with a new parameter fit to the laboratory annealing data (MAP3; *Stephenson et al.*, 2006), which takes into account uncertainties in laboratory annealing temperatures as well as independent geological data. More elaborate forward models have recently been developed for both fission-track annealing [*e.g.*, *Ketcham*, 2005] and He diffusion in apatite [*Shuster et al.*, 2006; *Flowers et al.*, 2009; *Gautheron et al.*, 2009], which would predict slightly different effective closure temperatures depending on exhumation scenarios. However, forward models used for AFT and AHe age predictions are similar for both generating the synthetic data and resolving the inverse problem; the results shown here are thus largely independent of the age-prediction models we use in *Pecube*.

II.2.2.2 - Age-elevation relationships

We use a synthetic relief model characterised by a 2D sinusoidal topography with a wavelength of 20 km and amplitude of 4 km (Figure II.2.2a). These values were chosen to allow sufficient denudation of valley samples for models with relief increase only; they are also characteristic of the topography observed in the western Alps study area of the companion paper. Such topography strongly perturbs low-temperature isotherms and specifically the effective AHe and AFT closure isotherms (respectively ~70 °C and ~110 °C; cf. Figure II.2.2a). All models are run over 30 Myr, with a late-stage change in exhumation rate or relief (Figure II.2.2b-e); all samples are exhumed from temperatures above the AFT and AHe closure temperature.

Figures II.2.2b and c show synthetic AER for scenarios with steady-state topography and varying denudation rates (Model 1). In all cases, denudation rates are 1000 m Myr^{-1} since 4.8 Ma; denudation rates prior to that time vary between 0 and 1000 m Myr^{-1} for the different models. The two end-member scenarios (*i.e.*, constant denudation rate versus discrete denudation event; respectively Model 1a and Model 1e) have widely been discussed

previously in the literature [*e.g.*, *Fitzgerald et al.*, 1995; *Gallagher et al.*, 1998; *Braun et al.*, 2006]; we will start by discussing these end-member cases since they provide a framework in which to discuss the other model results.

The constant-rate denudation case (Figure II.2.2, Model 1a) leads to perfectly linear AFT and AHe AER (r^2 = 1.00), the slopes of which, however, are 1430 m Myr^{-1} and 1740 m Myr^{-1} respectively (*i.e.*, they overestimate the denudation rate by ~40 to 70%) due to the perturbation of isotherms under the sinusoidal topography [*e.g.*, *Stüwe et al.*, 1994; *Manktelow and Grasemann*, 1997]. The opposite case where denudation only occurs since 4.8 Ma (Figure II.2.2, Model 1e) leads to AFT AER containing both a convex-up and concave-up break-in-slope (a convex-up break-in-slope only for the AHe AER). These breaks-in-slope represent the base and top, respectively, of the pre-exhumation AFT partial annealing zone or AHe partial retention zone and provide valuable constraints on the timing of onset and the total amount of exhumation [*Fitzgerald et al.*, 1995, 1999; *Gleadow and Brown*, 2000].

Intermediate (and possibly more realistic) cases (Figure II.2.2, Models 1b, c, d), where denudation rates increase at 4.8 Ma but were non-zero before that time, lead to more-or-less linear to broadly convex-up AER from which it would be difficult to intuitively infer a sudden increase in denudation rates, especially when relative errors in AFT or AHe ages of the order of 10% are taken into account. Thus, even a five-fold increase in denudation rate (from 200 to 1000 m Myr^{-1}, Model 1c, Figure II.2.2b) may go unnoticed with AFT data only; the AER predicted by this scenario would most probably be interpreted as indicating constant exhumation at a rate ~550 m Myr^{-1} (r^2 = 0.95 for a linear fit). This "mean" exhumation rate integrates exhumation at a rate of 1000 m Myr^{-1} during the last 5 Myr after initial exhumation at 200 m Myr^{-1}. The AHe AER (Figure II.2.2c, Model 1c) better reflects the recent denudation history, with a linear slope of ~1300 m Myr^{-1} that overestimates the true denudation rate by ~30%, but contains no record of the previous lower exhumation rates. Of course, additional constraints can be placed on the denudation histories by measuring confined fission-track length distributions [*Gallagher et al.*, 1998; *Gleadow and Brown*, 2000]. The above models, however, predict little variation in mean confined track lengths (MTL) for the different samples and scenarios; MTL is typically in the range 10.5-12 μm regardless of the pre-4.8 Ma denudation rate, except for very slow rates (*i.e.*, ≤ 200 m Myr^{-1}). The latter scenarios predict a decrease in MTL with age and elevation, typical of age-elevation profiles containing an exhumed AFT partial annealing zone [*Fitzgerald et al.*, 1995, 1999; *Gleadow and Brown*, 2000].

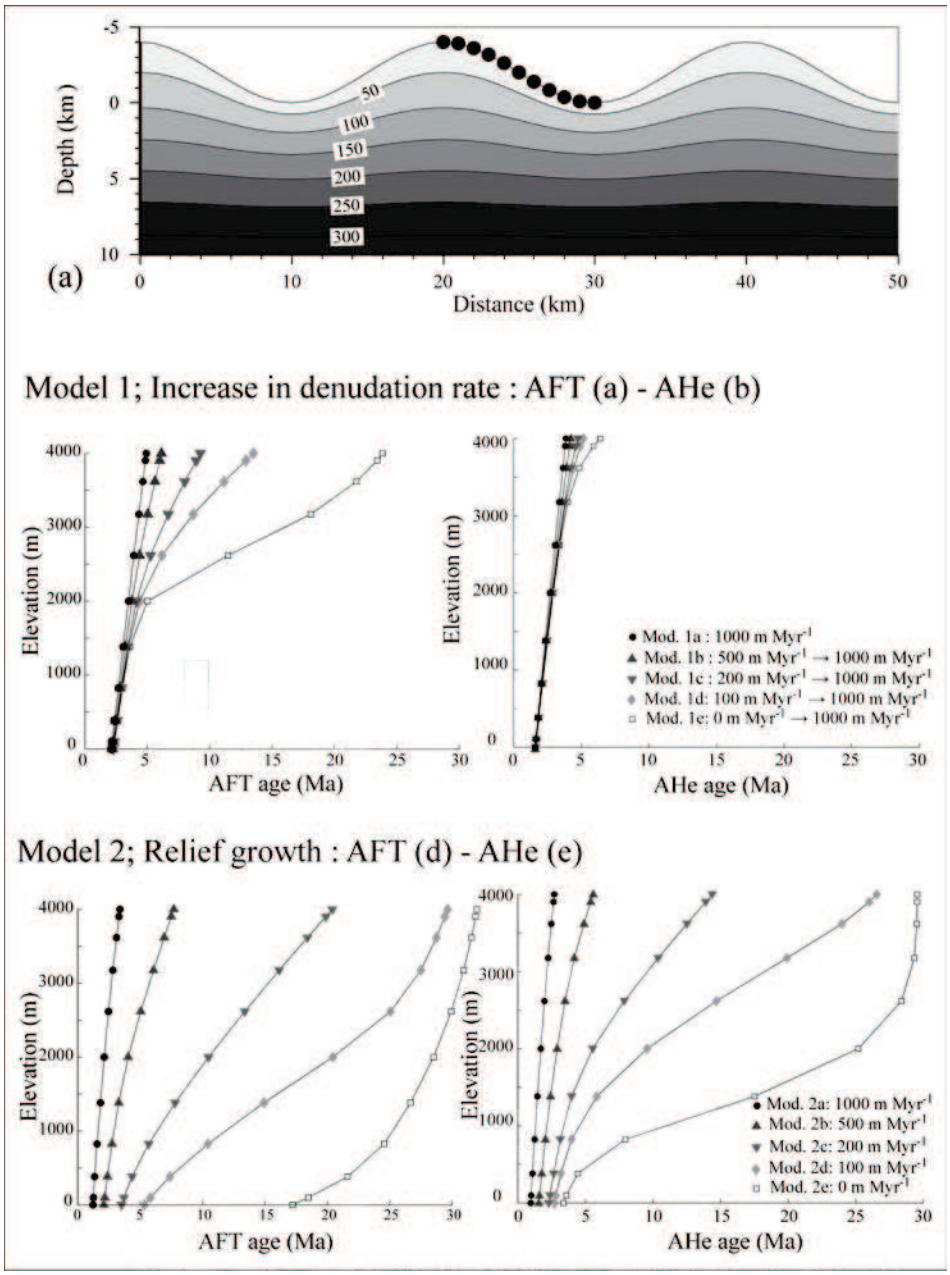

Figure II.2.2. *Predicted thermal structure and AFT and AHe age-elevation profiles for different denudation and relief history scenarios. (a) Model thermal structure (isotherms annotated in °C) for a steady-state sinusoidal topography with wavelength λ = 20 km, amplitude A = 4 km and a constant 1 km Myr^{-1} denudation rate. See Table II.2.1 for other thermo-kinematic parameters used in Pecube modelling. (b)-(c) Predicted AFT (b) and AHe (c) age-elevation profiles for a family of scenarios characterised a change in exhumation rate at 4.8 Ma: E_2 = 1000 m Myr^{-1} and E_1 varying between 0 and 1000 m Myr^{-1} as indicated in the legend, under steady-state topography (R = 1). (d)-(e) Predicted AFT (d) and AHe (e) age-elevation profiles for a family of scenarios characterized by valley carving since 4.8 Ma (R = 0) combined with temporally constant regional denudation rates varying between 0 and 1000 m Myr^{-1} as indicated in the legend.*

Models including relief growth (Model 2) are illustrated in Figures II.2.2d and e. For these models, valleys are supposed to have been carved since 4.8 Ma from a pre-existing horizontal plateau (*i.e.*, $R = 0$, see equation II.2.2). This relief-growth model is combined with constant denudation, at rates between 0 and 1000 m Myr^{-1}, over the modelled 30 Myr timespan (Figure II.2.2d, e; Model 2a to 2e). Resulting AFT and AHe AER are close to linear for denudation rates ≥ 200 m Myr^{-1} ($r^2 > 0.95$ for linear fits to the predicted age-elevation profiles). The AER slopes overestimate the input regional denudation rates; for instance, the slope is 230 m Myr^{-1} (AFT) or 310 m Myr^{-1} (AHe) for an input rate of 200 m Myr^{-1}; but 1840 m Myr^{-1} (AFT) or 2310 m Myr^{-1} (AHe) for an input rate of 1000 m Myr^{-1}. The reason for this overestimation is twofold. First, exhumation rates are not constant along the profile but vary from the background denudation rate at the summits to that rate augmented by the rate of valley carving (~830 m Myr^{-1}) at the valleys bottoms. On the other hand, since there is no relief before 4.8 Ma, isotherms are horizontal until that time and only become disturbed as valleys are carved, thus limiting the topographic effects on age-elevation profiles. For moderate to high background denudation rates, isotherms are advected to the surface, allowing to better record post-4.8 Ma relief development. However, for denudation rates < 200 m Myr^{-1}, heat advection is minor and erosion in the valleys is insufficient to expose samples exhumed from below the AFT partial annealing zone (for rates < 100 m Myr^{-1} the AHe partial retention zone is not exposed either), leading to distinctive concave-up AER. Such profiles might be interpreted as representing exhumation at rates that diminish through time or, if track-length data are taken into account, as limited and slow long-term denudation [*e.g.*, *Glotzbach et al.*, 2008; *Reiners and Brandon*, 2006].

Differences between age-elevation profiles predicted by very different scenarios may be subtle and the predicted patterns counter-intuitive. As shown in Figure II.2.2, scenarios with (Model 2) or without (Model 1) topographic change can be interpreted in the same way, judging from the pattern and slope of the AER. As discussed above, implicitly one-dimensional interpretation of such profiles is limited because of horizontal offsets between profile samples (up to 10 km in our simulations, Figure II.2.2) and topographic disturbance of isotherms. For example, Model 1c simulates an increase in denudation rate from 200 m Myr^{-1} to 1000 m Myr^{-1} with constant topography; whereas Model 2b combines topographic change with a regional exhumation rate of 500 m Myr^{-1}. Although these two scenarios are completely different, AFT AERs (Figure II.2.2b, d) have indistinguishable slopes of ~660 m Myr^{-1} (Model 1c) and ~700 m Myr^{-1} (Model 2b) respectively. AHe patterns (Figure II.2.2c, e) are

slightly different (~1300 m Myr^{-1} for Model 1c and ~1000 m Myr^{-1} for Model 2b); however the difference remains subtle and does not resolve the input denudation and relief histories. Straightforward interpretation of these two age-elevation profiles will lead to inferred spatially and temporally averaged exhumation rates that have no simple relation to the true exhumation history and do not address potential topographic changes.

II.2.3 - Inversion method and results

II.2.3.1 - Methodology: *Pecube* coupled to the *Neighbourhood Algorithm*

We choose two end-member scenarios to test whether numerical inversions can fully retrieve denudation and relief histories from AER (Figure II.2.2, respectively Models 1c and 2c): (1) constant topography (R = 1) but an abrupt change in denudation rates (E_1 = 200 m Myr^{-1}; E_2 = 1000 m Myr^{-1}) 4.8 Ma ago (referred to in the following as Scenario 1); and (2) a constant denudation rate $E_1 = E_2$ = 200 m Myr^{-1} but 4 km of relief growth (R = 0) since 4.8 Ma (Scenario 2). Thermo-kinematic data used as input parameters in *Pecube* are given in Table II.2.1; the simulation was run over 30 Myr to ensure that samples are exhumed through their closure isotherm and that isotherms are at steady state before increasing denudation or relief.

Parameter (unit)	Value
Crustal density (kg m^{-3})	2700
Sublithospheric mantle density (kg m^{-3})	3200
Equivalent elastic thickness (km)	25
Young's modulus (Pa)	1.10^{11}
Poisson ratio	0.25
Crustal thickness (km)	20
Thermal diffusivity ($km^2 Myr^{-1}$)	25
Basal crustal temperature (°C)	520
Sea-level temperature (°C)	15
Atmospheric lapse rate (°C km^{-1})	6
Crustal heat production (°C Myr^{-1})	0

Table II.2.1. *Thermo-kinematic and elastic parameters used in Pecube. Crustal thickness and basal temperature are set to obtain a geothermal gradient of 25 °C km^{-1}. Poisson ratio, Young's modulus and equivalent elastic thickness are used for calculating the isostatic rebound in response to relief change. Equivalent elastic thickness is set to a value that simulates moderate isostatic rebound.*

Figure II.2.3 shows the synthetic datasets used for inverse modelling; they consist of AFT and AHe ages as well as mean fission-track lengths (MTL). AER for AHe and AFT are quite similar for the two scenarios except that the age contrast between ridge and valley samples is

higher for Scenario 2. The main difference between the two scenarios is found in the MTL pattern, with an inverse (Scenario 1) versus normal (Scenario 2) correlation between MTL and elevation.

Using these predicted "perfect" data data, we explore for both Scenarios 1 and 2 what quantitative constraints can be set on denudation rates, timing and relief evolution. To do this, we first define for each parameter a specified range that will be searched by the inverse algorithm (uniform distribution for the priors): for the denudation rate of the first phase (E_1): 0-1000 m Myr^{-1}; denudation rate of the second phase (E_2): 0-1000 m Myr^{-1}; transition time (T): 0-30 Ma; and relief factor (R): 0-2. Since we wish to test to what extent a specific thermochronological dataset can provide independent estimates on those four parameters, we have run four inverse simulations (Table II.2.2) for both Scenarios 1 and 2 using: (1) AFT ages only (inversions 1-A and 2-A); (2) AFT + AHe ages (inversions 1-B and 2-B); (3) AFT ages + MTL (inversions 1-C and 2-C); and finally AFT + AHe + MTL (inversions 1-D and 2-D).

The Neighbourhood Algorithm (NA) is a two-stage numerical approach to derive Bayesian estimates on input parameters for non-linear inverse problems [*Sambridge*, 1999a, b]. The first or sampling stage is an iterative search method during which sampling gradually concentrates on regions of the multidimensional parameter space where the misfit function is optimised (*i.e.*, sets of parameters values that minimize the misfit to the data).

The parameter space is divided into Voronoi cells, centred on each sampled model, that represent the nearest neighbourhood about each point. A certain amount of best-fitting forward models (here 50%) is used to define new Voronoi cells and thus to fix a new parameter space. This new parameter space is then sampled during the next iteration in a random fashion, eventually converging towards one or several sets of parameters that minimize the misfit function to the data. In our approach, we use a weighted least-squares misfit function ψ:

$$\psi = \sqrt{\sum_{i=1}^{N}\sum_{j=1}^{M}\frac{({}^{i}\alpha_{j,\mathrm{mod}} - {}^{i}\alpha_{j,dat})^2}{{}^{i}\sigma_{j}{}^{2}}} \qquad \text{(II.2.3)}$$

where N is the number of datasets (1 for inversions A; 2 for inversions B and C; 3 for inversions D), M is the number of samples in each dataset (11), ${}^{i}\alpha_{j,\mathrm{mod}}$ and ${}^{i}\alpha_{j,dat}$ are predicted and observed values for AFT/AHe ages or MTL, respectively, and ${}^{i}\sigma_{j}$ is the uncertainty on the data.

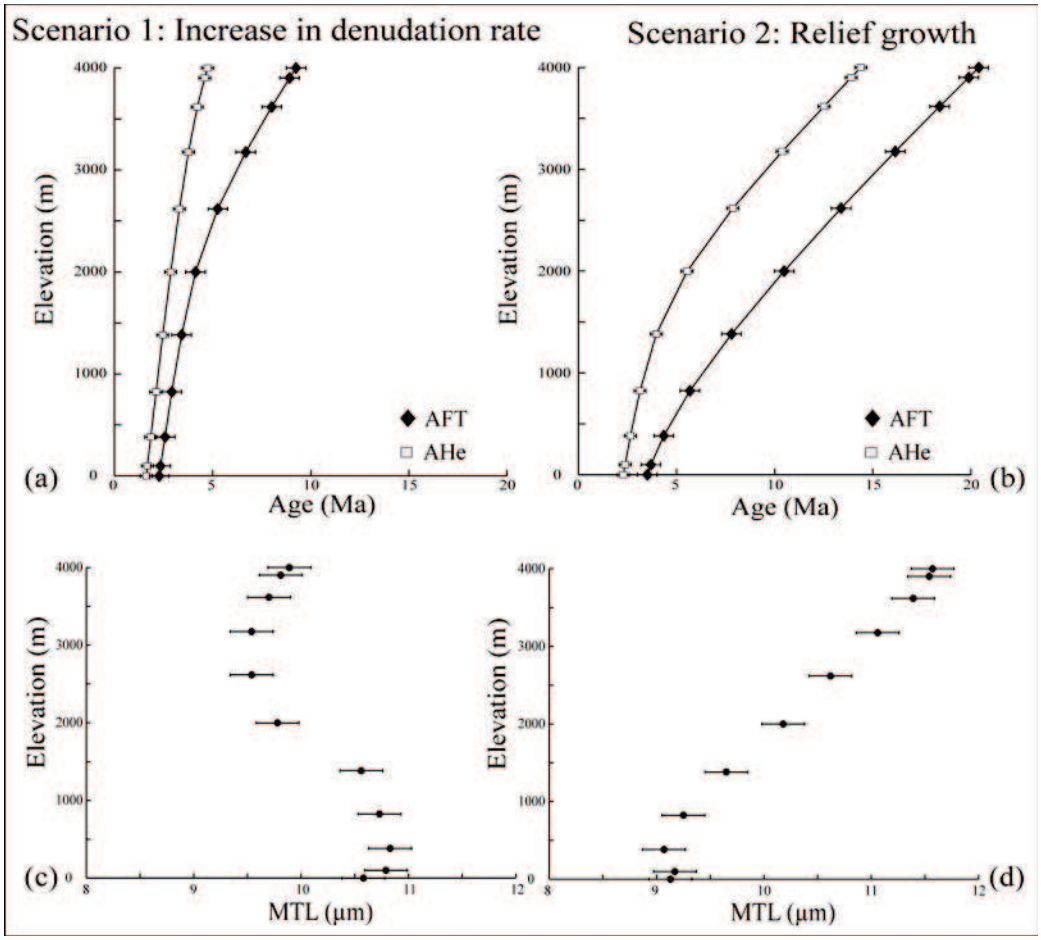

Figure II.2.3. *Synthetic thermochronological data used for the inverse modelling. (a)-(b) AFT and AHe ages versus elevation for Scenarios 1 and 2, respectively (error bars of ±0.5 Ma for AFT and ±0.3 Ma for AHe). (c)-(d) Mean fission-track length (MTL) versus elevation for Scenarios 1 and 2, respectively (error bars are ±0.2 μm).*

Here, we choose to use constant synthetic uncertainties (σ_j) of ±0.5 Ma, ±0.3 Ma and ±0.2 μm for AFT, AHe and MTL, respectively, to provide an equal weight on all samples for misfit calculations. We choose to fit the mean track length (MTL) rather than the full track-length distribution for computational convenience and because we can simply define an uncertainty on MTL that is comparable to the age uncertainty. Note that we do not use a reduced misfit, *i.e.*, the misfit function will be higher when we use a larger number of data. Using a high

performance cluster, we perform a large amount of forward model runs (~5000 per inversion), necessary to obtain a statistically significant result given the number of free parameters.

During the second or appraisal stage, the algorithm resamples the entire ensemble of models that were generated during the first stage to provide Bayesian measures of resolution in the form of marginal probability density functions (PDF) L for each parameter, following the equation :

$$L = \prod_{i=1}^{N} \exp\left(-\frac{1}{2}\sum_{j=1}^{M} \frac{({}^{i}\alpha_{j,\mathrm{mod}} - {}^{i}\alpha_{j,dat})^2}{{}^{i}\sigma_{j}{}^{2}}\right) \qquad \text{(II.2.4)}$$

II.2.3.2 - *NA* sampling stage results

We first present the results of the sampling stage, *i.e.*, the parameter optimisation, for Scenarios 1 (Figure II.2.4) and 2 (Figure II.2.5). Each forward model is represented by a dot, the colour of which depicts the value of the misfit function ψ for the associated model (Equation II.2.3), reduced by the number of data. The use of a reduced misfit function in Figures II.2.4 and II.2.5 allows us to directly compare inversion runs with different numbers of data. Parameter estimates are determined graphically, arbitrarily considering models represented by misfit values < 0.3 as "satisfying". We only represent scatter plots for inversions 1-A/2-A (AFT ages only) and 1-D/2-D (full dataset) since they illustrate how coupling different thermochronometers may provide better predictions on input parameters. Intermediate inversion results combining AFT ages with either MTL or AHe ages will be shown for the appraisal stage.

For Scenario 1 (Figure II.2.4), using AFT ages only (inversion 1-A, Figure II.2.4a, b) provides accurate but imprecise predictions for E_1 (0.2-0.5 km Myr^{-1}) and T (7-3 Ma). However, Run 1-A leads to erroneous estimates for both E_2 and R, suggesting a minor increase in denudation rate ($E_2 \approx$ 0.4-0.7 km Myr^{-1}) compared to the input value (E_{2input} = 1 km Myr^{-1}) but converging toward significant relief increase ($R \leq 0.4$) instead of a constant topography (R_{input} = 1). Adding MTL and AHe ages to AFT ages (inversion 1-D; Figure II.2.4c, d) leads to much better predictions. The precision of the estimated E_1 and T is improved ($E_1 \approx$ 0.15-0.25 km Myr^{-1}; $T \approx$ 4-6 Ma). Moreover, estimates on E_2 ($\approx$ 0.7-1 km Myr^{-1}) and R ($\approx$ 0.5-0.9) are much closer to the input values for inversion 1-D than for inversion 1-A.

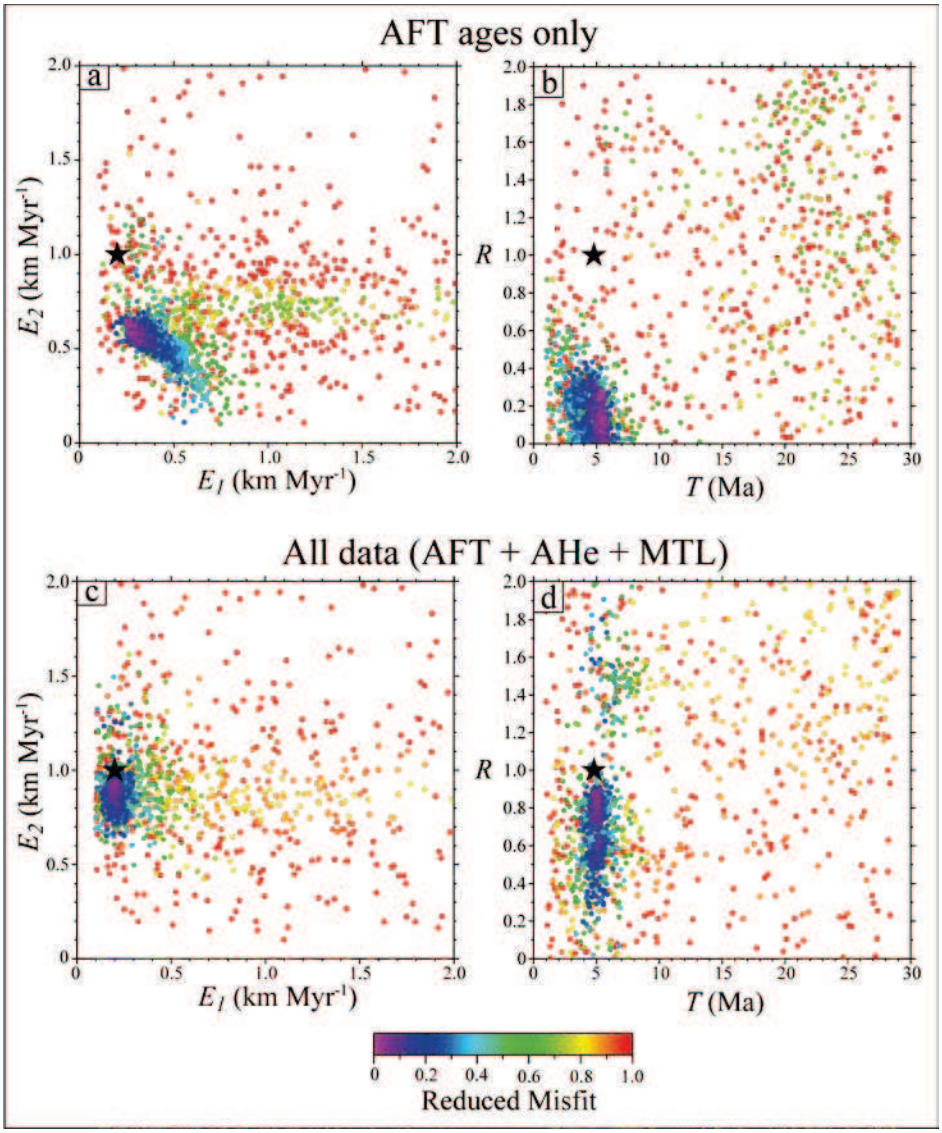

Figure II.2.4. *Scatter diagrams showing results of the NA inversion for Scenario 1. Each dot corresponds to a forward model; its colour is proportional to the value of the reduced misfit between predictions and the input data (misfit function ψ reduced by the number of data). Each diagram is the projection onto a plane defined by two of the four parameters (denudation rates E_1 and E_2; transition time T and relief factor R); horizontal and vertical axes define the parameter space. Note that violet/pink corresponds to low misfits and red corresponds to high misfits. Results are only shown for end-member inversion experiments with AFT ages alone (inversion 1-A, a-b) and AFT + AHe ages combined with MTL (inversion 1-D, c-d). Black stars show the "true" value of parameters used to calculate the input thermochronological data.*

We adopt the same methodology for Scenario 2 (Figure II.2.5), presenting first inversion results using AFT ages only (inversion 2-A; Figure II.2.5a, b) and then for AFT ages combined with both MTL and AHe ages (inversion 2-D; Figure II.2.5c, d). Using AFT ages

only in Scenario 2 provides different results than for Scenario 1: both E_1 and E_2 are predicted correctly ($E_1 \approx$ 0.15-0.25 km Myr^{-1} and $E_2 \approx$ 0.1-0.4 km Myr^{-1}) whether we use AFT ages alone (inversion 2-A) or the full dataset (inversion 2-D). The main differences between inversions 2-A and 2-D lie in the predictions for T, which are much less precise and accurate for inversion 2-A ($T \leq 5$ Ma) than for inversion 2-D ($T \approx$ 4-5 Ma; $T_{input} = 4.8$ Ma). Predictions on R suggest a lower relief increase than the input value ($R \leq 0.4$; $R_{input} = 0$) whether we use AFT ages alone (inversion 2-A) or the full dataset (inversion 2-D).

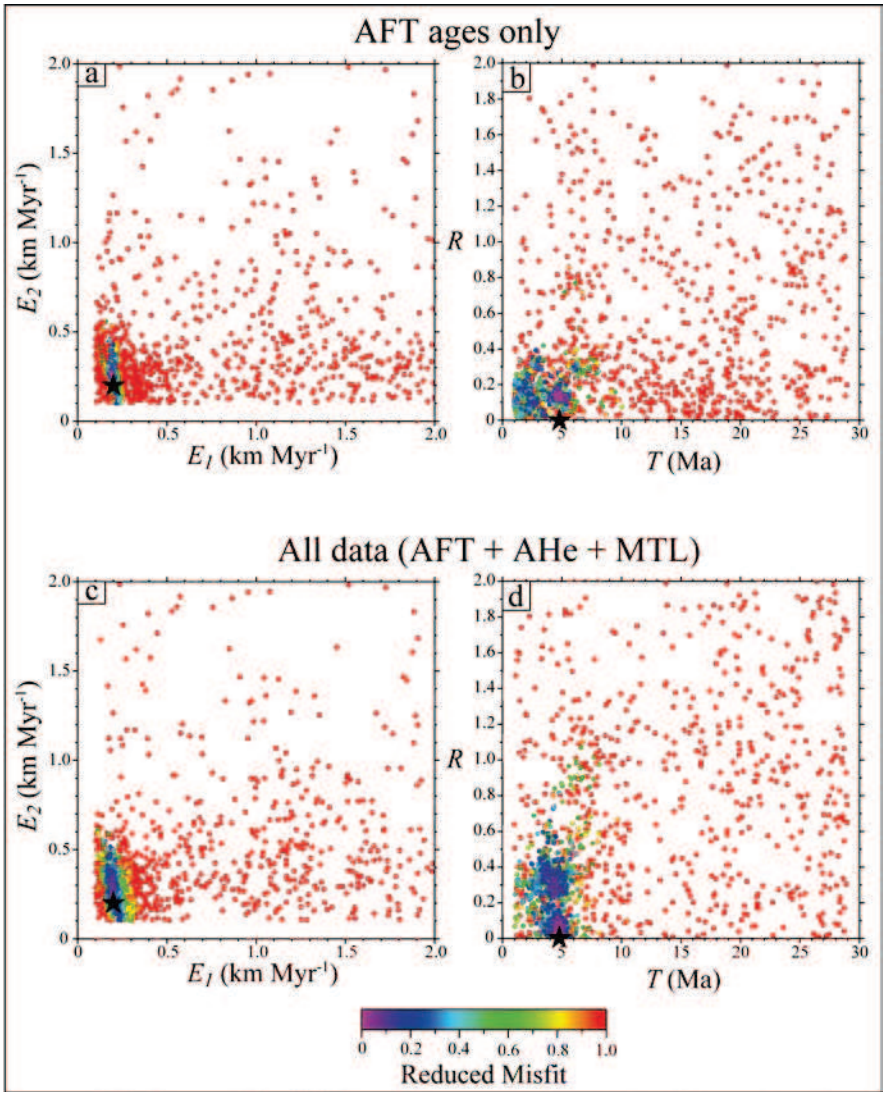

Figure II.2.5. *Same as Figure II.2.4 for Scenario 2. Results are only shown for end-member inversion experiments with AFT ages alone (inversion 2-A, a-b) and AFT + AHe ages combined with MTL (inversion 2-D, c-d). Note the positions of the black stars that define the "true" parameters used to calculate the input thermochronological data.*

These results show that the two input scenarios (increase in denudation rate versus relief growth) do not lead to the same inversion results. Although our graphical interpretation of these scatter plots (Figures II.2.4 and II.2.5) remains qualitative, these results strongly suggest that an AFT AER alone is not sufficient to provide quantitative independent estimates on denudation and relief histories; AHe and MTL datasets are needed to constrain the input scenario, leading to much better parameter estimates when using all the available data even in relatively simple cases with only a single change in relief or denudation rate.

II.2.3.3 - *NA* appraisal stage results

Results from the *NA* appraisal stage differ from the sampling stage since we do not focus on "satisfying" models via graphical inspection but investigate the statistical properties of the model ensemble. Posterior PDF's of parameter values for Scenarios 1 and 2 are plotted in Figures II.2.6 and II.2.7, respectively. Table II.2.2 reports both the most probable value and the estimated uncertainty, defined respectively by the mode and standard deviation of the marginal PDF, for each parameter (E_1, E_2, T and R) and all inversions (1-A to 1-D and 2-A to 2-D).

	Prior Pdf	Input value	AFT (inversion 1-A/2-A)	AFT+AHe (inversion 1-B/2-B)	AFT+MTL (inversion 1-C/2-C)	AFT+AHe+MTL (inversion 1-D/2-D)
Scenario 1						
E_1 (km Myr^{-1})	1.1 ± 0.6	0.2	0.9 ± 0.6	0.9 ± 0.5	0.2 ± 0.1	0.2 ± 0.1
E_2 (km Myr^{-1})	1.1 ± 0.6	1.0	0.7 ± 0.3	0.9 ± 0.3	0.9 ± 0.2	0.9 ± 0.3
T (Ma)	15 ± 8.1	4.8	13.9 ± 8.5	13.6 ± 8.3	4.9 ± 1.6	5.1 ± 1.6
R	1.0 ± 0.6	1.0	0.9 ± 0.6	1.1 ± 0.5	0.7 ± 0.4	0.9 ± 0.5
Scenario 2						
E_1 (km Myr^{-1})	1.1 ± 0.6	0.2	0.2 ± 0.1	0.2 ± 0.05	0.2 ± 0.05	0.2 ± 0.04
E_2 (km Myr^{-1})	1.1 ± 0.6	0.2	0.4 ± 0.1	0.4 ± 0.2	0.5 ± 0.2	0.3 ± 0.1
T (Ma)	15 ± 8.1	4.8	4.2 ± 3.2	3.6 ± 1.4	3.5 ± 1.3	4.0 ± 1.1
R	1.0 ± 0.6	0.0	0.3 ± 0.2	0.2 ± 0.2	0.6 ± 0.4	0.3 ± 0.2

Table II.2.2. *Bayesian estimates after the NA appraisal stage for input parameters E_1, E_2, T and R (see text for description and discussion). First column defines the parameters for the two scenarios. Second column gives prior PDF, i.e., the PDF describing the input parameter range for the inversion. Third column reports the parameters used to calculate the input thermochronological data (Figure II.2.3). Optimal values and estimated uncertainties of parameters are given in following columns for all inversion simulations (inversions 1-A/2-A, 1-B/2-B, 1-C/2-C and 1-D/2-D).*

For Scenario 1, the different inversions (1-A, 1-B, 1-C and 1-D) do not lead to similar quantitative predictions for the 4 parameters (E_1, E_2, T and R). E_1 and T estimates are not better resolved than the prior estimates (*i.e.*, a uniform distribution within the imposed limits) when using AFT ages only or AFT + AHe ages (Figure II.2.6a-c). Adding MTL to these datasets provides predictions that are closer to the input values and have lower uncertainties (inversions 1-C or 1-D). Including MTL thus appears to be more important than AHe ages to optimize predictions on these two parameters (E_1 and T). In contrast, accurate estimates for E_2 (Figure II.2.6b) requires AFT + AHe ages (inversion 1-B), MTL (inversion 1-C) or both (inversion 1-D), even though the resolution is similar whatever the input data. Finally, Bayesian estimates for R (Figure II.2.6d) are poor for all runs, with high uncertainties (± 50%) even when we combine AFT and AHe ages with MTL (inversion 1-D).

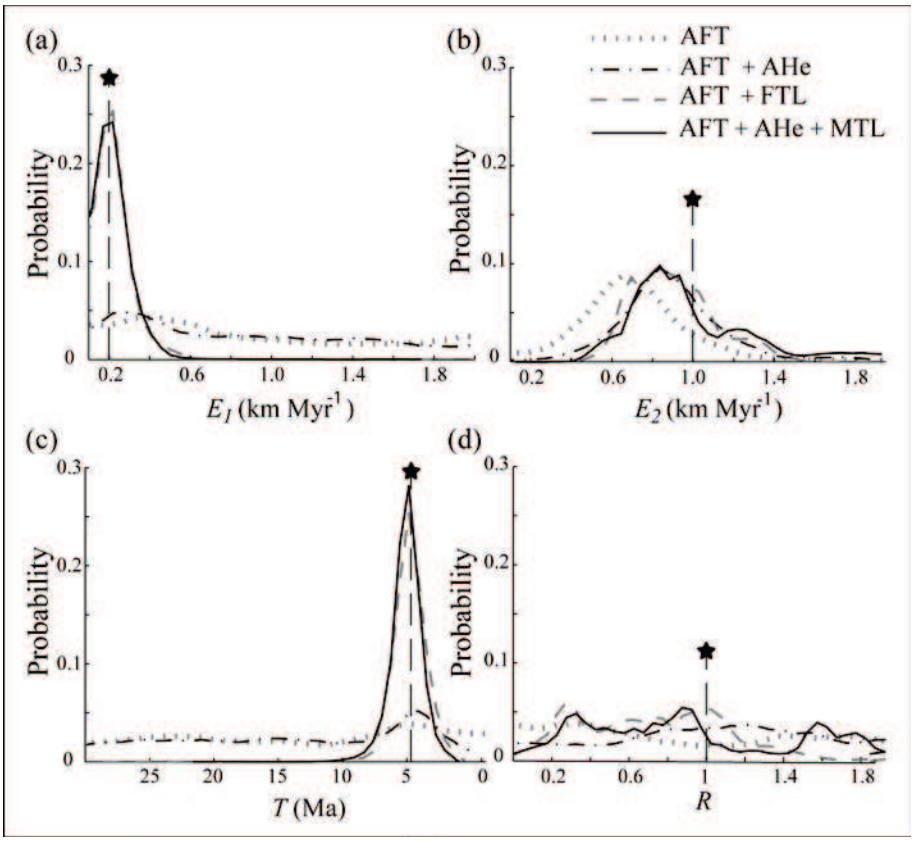

Figure II.2.6. *1D posterior PDF's for Scenario 1 parameters obtained after the NA appraisal stage: (a) denudation rate of the first exhumation phase (E_1); (b) denudation rate of the second exhumation phase (E_2); (c) transition time between the two exhumation phases (T); and (d) relief factor between the paleo-relief and the final relief (R). Each line defines an inversion experiment with a given set of thermochronological data (inversions 1-A, 1-B, 1-C and 1-D). Vertical dashed lines and black stars represent the "true" parameter values.*

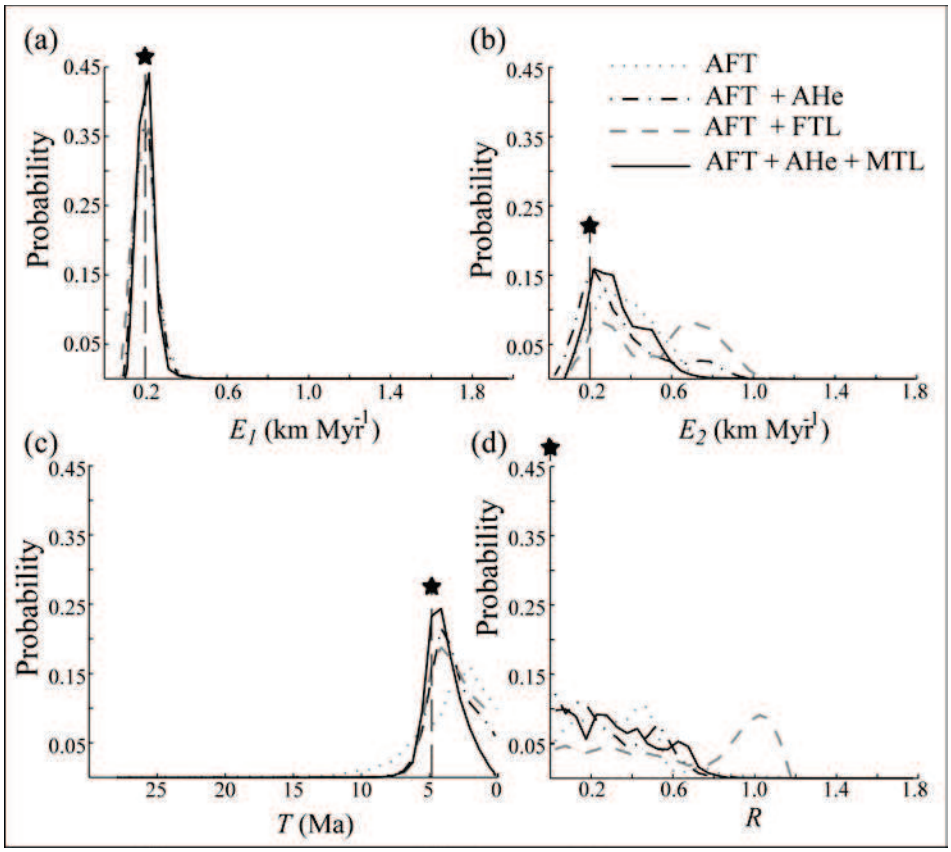

Figure II.2.7. *Same as Figure II.2.6 for Scenario 2: (a) denudation rate of the first exhumation phase (E_1); (b) denudation rate of the second exhumation phase (E_2); (c) transition time between the two exhumation phases (T); and (d) relief factor between the paleo-relief and the final relief (R). Each line defines an inversion experiment with a given set of thermochronological data (inversions 2-A, 2-B, 2-C and 2-D). Vertical dashed lines and black stars represent the "true" parameter values*

For the relief-growth experiment (Scenario 2; Figure II.2.7), Bayesian results show that we provide tight constrains on E_1 (Figure II.2.7a) even when using AFT ages only (inversion 2-A). Only the resolution of E_1 is improved by adding more information (0.2 ±0.1 km Myr^{-1} for inversion 2-A compared to 0.2 ±0.04 km Myr^{-1} for inversion 2-D). Predictions for E_2 and T are also quite similar for all the inversions (2-A to 2-D; Figure II.2.7b, c): they all underestimate the age of relief change ($T<T_{input}$) and overestimate the denudation rate ($E_2>E_{2input}$) of the second phase. Inversion 2-D, which combines AFT + AHe ages with MTL, leads to E_2 and T predictions (E_2 = 0.3 ±0.1 km Myr^{-1}; T = 4.0 ±1.1 Ma) that are closer to the input values (E_{2input} = 0.2 km Myr^{-1}; T_{input} = 4.8 Ma). In this case, AHe ages seem to be as important as MTL and AFT ages for providing reliable estimates of E_2 and T. Finally, predictions of R (Figure II.2.7d) with AFT ages only (R = 0.3 ±0.2) or AFT + AHe ages (R = 0.2 ±0.2) are close to the input value (R_{input} = 0) even though they consistently underestimate

the relief increase by ~20-30%. Adding MTL to AFT + AHe ages (inversion 2-D) does not improve the prediction (R = 0.3±0.2). Using AFT ages and MTL without AHe data (inversion 1-C) clearly underestimates the relief increase by ~60%.

Our results show that inverse numerical modelling of thermochronological AER combining various thermochronometers is an efficient tool for extracting quantitative information on denudation and relief histories. In the following, we will discuss our numerical results and their implications concerning the use of low-temperature thermochonometers for quantifying denudation histories and relief changes.

II.2.4 - Discussion

II.2.4.1 - Direct interpretation of AER

Our results show that even simple tectono-morphic scenarios such as a single increase in denudation rate (Model 1) or relief (Model 2) provide AER that may be problematic to interpret at face value (Figure II.2.2). AER may be powerful tools to detect first-order tectonic or geomorphic changes, such as a pulse of denudation after a long period of quiescence (Model 1e; Figure II.2.2b, c) or relief carving with a low background denudation rate (< 200 m Myr^{-1}; Models 2d and 2e, Figure II.2.2d, e). This exhumation pulse is recorded by AFT and AHe thermochronometers via exhumation of the Partial Annealing Zone (PAZ) for FT and Partial Retention Zone (PRZ) for He, which imprints a clear signal in the AER [*e.g.*, *Fitzgerald et al.*, 1995; 1999]. More subtle changes in denudation rates and/or relief changes do not have such a clear signal in AER, in particular because elevation profiles are not vertical and samples are laterally offset. Furthermore, direct interpretation is difficult since AER are often close to linear; the associated slope only provides a spatially and temporally averaged exhumation rate through the sampled time window. More information can be retrieved when including AHe data; however, we have seen that except in specific cases (*i.e.*, denudation rates < 200 m Myr^{-1}), AHe profiles resemble AFT AER and do not provide sufficient additional information to derive independent estimates on denudation and relief histories. The usefulness of track-length measurements for constraining relief growth is limited by their correlation with elevation (Figure II.2.3d) that is similar to the correlation observed for denudation scenarios under steady-state topography, except where denudation rates increase

by at least a factor of 5. In the latter scenarios, MTL patterns show a clear inverse correlation with elevation (Figure II.2.3c).

II.2.4.2 - Quantitative inversion of thermochronological data: multiple datasets

Using *Pecube* with an inverse approach (*NA* algorithm), we have analysed to what extent a specific dataset can provide quantitative estimates on denudation rates, timing and relief history. Before discussing the results, we should point out some limitations associated with our modelling approach. First, we have implemented relief changes in such a way that the planform topographic pattern does not change with time. This is not a limitation of the *Pecube* code, which can handle any arbitrary topographic change, but permits us to simply parameterize relief change through a single parameter *R*. We note, however, that evidence for relative longevity of drainage patterns exists in many mountain belts and present such evidence for the Western Alps study area in the companion paper. Second, the scenarios we have run, which all involve a recent increase in relief and/or denudation rate, are somewhat contextual and obviously only address a limited number of exhumation and relief scenarios from the infinite choice available. However, such recent changes in exhumation rate and/or relief in mountain belts have been investigated by many studies using thermochronological AER in recent years [*e.g.*, *Fitzgerald et al.*, 1995; 1999; *Densmore et al.*, 2007; *Gibson et al.*, 2007; *Whipp et al.*, 2007; *Glotzbach et al.*, 2008; *Vernon et al.*, 2009]. Third, our inferences are obviously somewhat dependent on the age-prediction model for AFT and AHe that we have chosen to implement, as well as on the fact that we only use MTL instead of the full track-length distribution.

Keeping the above caveats in mind, we focus here on predictions concerning denudation history (E_1 and E_2) and timing (T); quantitative estimates on relief evolution (R) will be discussed in the next section. In the case of an increase in denudation rate under steady-state topography (Scenario 1), parameter estimates from AFT ages alone are poor (Figure II.2.6; Table II.2.2). The inability of AFT ages alone to retrieve denudation and timing parameters explains why the inversion algorithm converges towards a parameter set that is different from the input values (Inversion 1-A, Figure II.2.4a, b). We have performed two tests to ascertain that it is the data and not the inversion procedure that leads to this erroneous prediction (See Supplementary Figures II.2.9 and II.2.10). Resampling a much larger proportion of models

between different generation leads to slower convergence but the same predicted optimal parameter values. In contrast, setting R=1 and only solving for denudation rates and timing leads to correct parameter predictions. These tests show that AFT data on their own do not have sufficient resolution to constrain the denudation and relief history and also that care should be taken when interpreting the optimisation results from *NA* on their own, without considering the resolution of the parameter predictions.

In contrast, AFT data alone lead to good predictions for the input parameters in a relief-growth context (Scenario 2), even though resolution is relatively low (Figure II.2.7). We thus suggest that, in the cases studied here, AFT data are more useful for studying relief growth than for quantifying variations in denudation rate under constant topography. This may be explained by the shape of the AER, which is less linear in the relief growth case (Figure II.2.3b) and shows a higher contrast in AFT ages between ridge and valley-bottom samples than in the denudation increase scenario (Figure II.2.3a).

In Scenario 1, AHe ages combined with AFT ages do not add more information than AFT ages alone and predictions of all parameters except E_2 remain poor (Table II.2.2). The AHe system has a lower closure temperature than AFT (respectively ~75 °C and ~110 °C), which explains why AHe ages provide better constraints on the recent denudation history (E_2). Adding MTL data leads to better constraints on both exhumation rates and timing. Quantitative estimates of the exhumation history under steady-state topography thus require both AFT ages and MTL measurements, whereas AHe ages do not seem to improve parameter predictions. The reason for this lies in the AHe and MTL profiles (Figure II.2.3): the AHe AER is very similar to the AFT profile whereas the MTL pattern is strongly contrasted between ridge (short MTL) and valley-bottom (longer MTL) samples.

Scenario 2 (*i.e.*, relief growth) shows completely different results. In this case, AHe ages combined with AFT ages provide much better estimates of E_1 and T (Table II.2.2 and Figure II.2.7a-c), E_2 being already well constrained by AFT ages alone (Figure II.2.7b). In contrast, using MTL measurements with AFT ages leads to both an overestimation of E_2 and an underestimation of T. This difference with Scenario 1 may be due the MTL pattern (Figure II.2.3d), which is characterized by a normal correlation between MTL and elevation in all relief-growth scenarios. Moreover, the AHe AER shows a higher contrast between ridge and valley-bottom samples than the AFT AER (Figure II.2.3b), since AHe has a lower closure

temperature and thus more potential to record changes in either exhumation rates or relief close to the surface. We thus suggest that in the case of relief change studied here, AHe data provide more information than MTL measurements.

The problem of course is that in a real-world study, one usually does not know *a priori* what scenario (varying denudation rates or relief change) to expect, and this will probably be the objective of the study. Therefore, the best approach appears to be to collect as much independent thermochronometry data as possible and typically to combine AFT and AHe ages with track-length measurements along altitudinal profiles. The fundamental reason for applying multiple thermochronometers is that AER sample the topography at a single wavelength (20 km in our case), which is problematic for extracting independent information on denudation and relief evolution [*Braun*, 2002b]. However, using different thermochronometers characterized by different closure temperatures can be interpreted as sampling different critical topographic wavelengths [*Braun*, 2002b] and thus may allow extracting independent information on denudation rate and relief change in favourable circumstances.

II.2.4.3 - Relief evolution

The aim of our study was to determine to what extent AER can provide quantitative estimates on relief evolution. However, we have shown that estimates for R are typically not as well constrained as estimates for denudation rates or timing. In Scenario 1, estimates of R have ~50% uncertainty (Table II.2.2) and thus lie between 0.5 (*i.e.*, 50% relief *increase*) and 1.5 (*i.e.*, 50% relief *decrease*), whether we use AFT ages only or a combination of AFT ages with AHe ages and/or MTL (Figure II.2.6d).

We suggest that, since samples record ~5 km of rapid denudation during the last 5 Myr in this scenario, they are insensitive to relief changes. Scenario 2 provides quite different results since it models major relief growth (4 km valley carving) with relatively minor background denudation. Quantitative estimates of R predict relief increase ($R < 0.5$ except for inversion 2-C, Table II.2.2), although predictions are 30-50% lower than the input value ($R_{input} = 0$). Adding AHe to AFT ages does not improve the estimate of R; including MTL measurements leads to higher uncertainties on R (Table II.2.2).

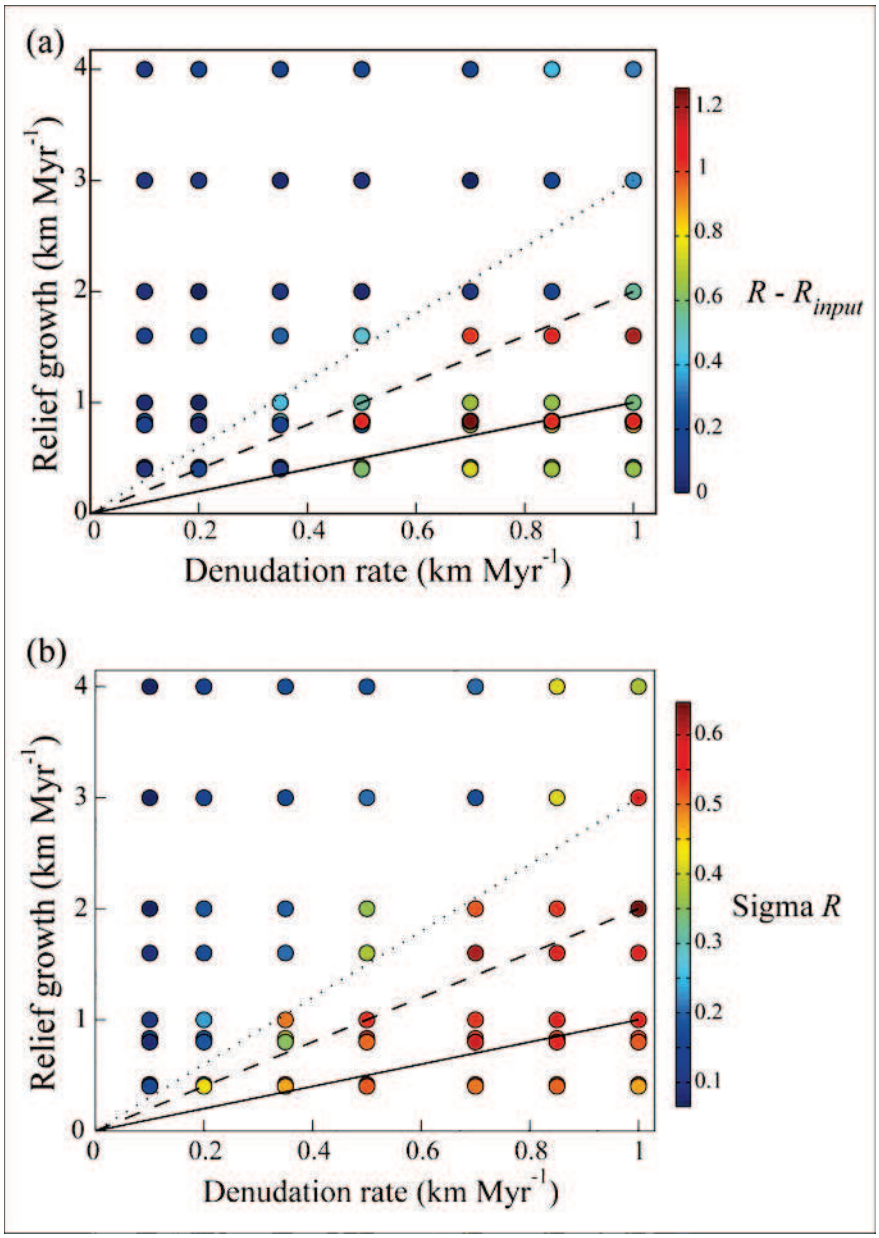

Figure II.2.8. *Scatter plots showing the quality of relief-change predictions (R) by the inversion approach developed here as a function of both denudation and relief-growth rates. Each dot results from an inverse model with a specified input denudation rate and relief evolution scenario. a) Absolute difference between predicted and "true" R (the latter indicated by R_{input}). b) 1σ uncertainty on predicted R (defined as the standard deviation of the PDF of R from its mean value). 1:1 (solid line), 1:2 (dashed line) and 1:3 (dotted line) ratio of relief-growth rate vs. denudation rate are indicated (see Supplementary Table II.2.3 for numerical results).*

We thus suggest that quantitative estimates on *R* may depend on the background denudation rate as well as the amplitude of relief growth and the time of relief change. We have run ~70 inversions (Supplementary Table II.2.3 for details) simulating relief-growth like in Scenario 2 and using AFT, AHe and MTL. For each inversion, we vary the input background denudation

rate (E: 0.1 to 1 km Myr^{-1}), the time of onset of relief change (T: 1 to 4.8 Ma) and the amplitude of relief growth (R: 0 to 0.9). We then compare R estimates (optimal values and uncertainties) with the ratio between denudation (E) and relief-growth rates (*i.e.*, $\Delta h/T$ with $\Delta h = (1\text{-}R) \times \Delta h_{present}$ and $\Delta h_{present}$= 4 km). Results show that the quality of predictions for R depends on the ratio between the background denudation rate and the relief-growth rate (Figure II.2.8). Our inversion approach leads to relatively accurate predictions on R (*i.e.*, < 50% error between R and R_{input}) for scenarios where the relief growth rate is at least 2 times higher than the background denudation rate (Figure II.2.8a). However, obtaining satisfactory resolution on R (*i.e.*, uncertainty < 0.4) requires a relief growth rate that is at least 3 times higher than the background denudation rate (Figure II.2.8b).

This sensitivity analysis suggests that relief development must be significantly more rapid than the background denudation rate to be quantitatively extracted from thermochronology data, which strongly reduces the number of suitable orogenic settings for this kind of investigations.

In effect, we suggest that this approach may be most successful in settings with low background denudation rates and potentially major recent relief increase, such as the Sierra Nevada (California) or the Pyrenees (Spain, France). Interestingly, in both settings contrasting conclusions have been drawn concerning recent relief change from the interpretation of thermochronological AER (*e.g.*, *House et al.*, 2001 *vs*. *Clark et al.*, 2005 for the Sierra Nevada; *Fitzgerald et al.*, 1999 *vs*. *Gibson et al.*, 2007 for the Pyrenees). In contrast, it does not appear very well suited to constrain potential relief changes in high-exhumation-rate settings such as the Himalaya [*Whipp et al.*, 2007] or the Southern Alps of New Zealand [*Herman et al.*, 2007]. New thermochronometers and models based on the He distribution within single apatite grains ($^4He/^3He$ thermochronology; *Shuster et al.*, 2005) or OSL-thermochronometry [*Herman et al.*, 2010b] may provide more precise information on relief changes, especially if they occurred during Quaternary times.

II.2.5 - Conclusions

This study shows that thermochronological age-elevation profiles may be used to quantitatively define denudation and relief histories in certain cases. We have used the thermal-kinematic 3D model *Pecube* to predict AFT and AHe AER and MTL patterns from imposed input scenarios with varying denudation or/and relief histories. Predicted AFT AER

mostly define linear trends that are delicate to interpret, even though AHe ages or MTL can help to define denudation and relief histories. In most cases, direct 1D analysis of these profiles would lead to infer temporally averaged exhumation estimates and no independent constraints on relief history. Combining *Pecube* with an inverse method (*NA*), we have run numerical experiments for synthetic datasets to determine to what extent denudation rates, relief development and the timing of change can be independently extracted from thermochronological data. Inversion results show that AFT ages alone do not provide tight constrains on the denudation or relief histories. Depending on the input scenario (relief change or varying denudation rates), adding other data (AHe ages and/or MTL measurements) to the AFT ages leads to generally accurate predictions of denudation rates and timing of change. In contrast, relief changes can only be precisely constrained in specific settings where relief growth is at least 2-3 times higher than the background denudation rate. New thermochronometers (such as $^{4}He/^{3}He$ or OSL) may be the key for resolving this issue as they more precisely record denudation rates and/or geomorphic changes close to the surface.

Acknowledgments

This study is supported by INSU-CNRS through the European Science Foundation Eurocores Topo-Europe programme 07-TOPO-EUROPE-FP-023 “Coupled climatic/tectonic forcing of European topography revealed through thermochronometry (Thermo-Europe)” and the Agence Nationale de la Recherche project N° ANR-08-BLAN-0303-01 “Erosion and Relief Development in the Western Alps”. It forms part of PV’s PhD project at Université Joseph Fourier, supported by the French Ministry for Research and Higher Education. Computations were performed on *Brutus*, the high performance computing facilities at ETH Zürich. The codes are available at http://svn-geo.ethz.ch after registering at this site. Thorough and constructive reviews by Mark Brandon and Richard Ketcham significantly improved the manuscript.

II.2.6 - Supplementary data

This section reports one supplementary table and two supplementary figures associated to the study presented above. The supplementary table (Table II.2.3) provides details of the numerical inversions for quantifying in which scenarios the relief prediction is optimal. All parameters reported in Table II.2.3 are associated with Figure II.2.8 in the main text.

	E_{input} (km Myr^{-1})	T_{input} (Ma)	R_{input}	*Relief growth* (km Myr^{-1})	$R_{predicted}$
Run 1	0.1	4.8	0	0.8	0.9 ± 0.13
Run 2	0.2	4.8	0	0.8	0.24 ± 0.20
Run 3	0.35	4.8	0	0.8	0.48 ± 0.41
Run 4	0.5	4.8	0	0.8	1.03 ± 0.61
Run 5	0.7	4.8	0	0.8	1.26 ± 0.53
Run 6	0.85	4.8	0	0.8	1.03 ± 0.53
Run 7	1	4.8	0	0.8	1.03 ± 0.53
Run 8	0.1	4.8	0.5	0.4	0.56 ± 0.09
Run 9	0.2	4.8	0.5	0.4	0.56 ± 0.21
Run 10	0.35	4.8	0.5	0.4	0.78 ± 0.54
Run 11	0.5	4.8	0.5	0.4	1.21 ± 0.60
Run 12	0.7	4.8	0.5	0.4	1.16 ± 0.54
Run 13	0.85	4.8	0.5	0.4	1.27 ± 0.50
Run 14	1	4.8	0.5	0.4	0.98 ± 0.52
Run 15	0.1	2.5	0	1.6	0.13 ± 0.09
Run 16	0.2	2.5	0	1.6	0.24 ± 0.18
Run 17	0.35	2.5	0	1.6	0.29 ± 0.21
Run 18	0.5	2.5	0	1.6	0.46 ± 0.38
Run 19	0.7	2.5	0	1.6	1.01 ± 0.61
Run 20	0.85	2.5	0	1.6	1.11 ± 0.59
Run 21	1	2.5	0	1.6	1.19 ± 0.59
Run 22	0.1	1	0	4.0	0.09 ± 0.07
Run 23	0.2	1	0	4.0	0.18 ± 0.14
Run 24	0.35	1	0	4.0	0.18 ± 0.18
Run 25	0.5	1	0	4.0	0.21 ± 0.18
Run 26	0.7	1	0	4.0	0.21 ± 0.20
Run 27	0.85	1	0	4.0	0.40 ± 0.41
Run 28	1	1	0	4.0	0.33 ± 0.37
Run 29	0.1	1	0.5	2.0	0.56 ± 0.07
Run 30	0.2	1	0.5	2.0	0.49 ± 0.19
Run 31	0.35	1	0.5	2.0	0.42 ± 0.20
Run 32	0.5	1	0.5	2.0	0.52 ± 0.36
Run 33	0.7	1	0.5	2.0	0.56 ± 0.51
Run 34	0.85	1	0.5	2.0	0.70 ± 0.53
Run 35	1	1	0.5	2.0	1.05 ± 0.65
Run 36	0.1	1	0.75	1.0	0.77 ± 0.09
Run 37	0.2	1	0.75	1.0	0.75 ± 0.23
Run 38	0.35	1	0.75	1.0	1.18 ± 0.49
Run 39	0.5	1	0.75	1.0	1.27 ± 0.55
Run 40	0.7	1	0.75	1.0	1.41 ± 0.53
Run 41	0.85	1	0.75	1.0	1.39 ± 0.56
Run 42	1	1	0.75	1.0	1.32 ± 0.58
Run 43	0.1	2.5	0.5	0.8	0.65 ± 0.08
Run 44	0.2	2.5	0.5	0.8	0.53 ± 0.19
Run 45	0.35	2.5	0.5	0.8	0.65 ± 0.35
Run 46	0.5	2.5	0.5	0.8	0.78 ± 0.51

Run 47	0.7	2.5	0.5	0.8	1.20 ± 0.59
Run 48	0.85	2.5	0.5	0.8	1.30 ± 0.55
Run 49	1	2.5	0.5	0.8	1.33 ± 0.52
Run 50	0.1	2.5	0.75	0.4	0.77 ± 0.16
Run 51	0.2	2.5	0.75	0.4	0.60 ± 0.30
Run 52	0.35	2.5	0.75	0.4	1.19 ± 0.53
Run 53	0.5	2.5	0.75	0.4	1.36 ± 0.53
Run 54	0.7	2.5	0.75	0.4	1.50 ± 0.48
Run 55	0.85	2.5	0.75	0.4	1.41 ± 0.50
Run 56	1	2.5	0.75	0.4	1.38 ± 0.50
Run 57	0.1	1	0.9	0.4	0.96 ± 0.17
Run 58	0.2	1	0.9	0.4	0.71 ± 0.43
Run 59	0.35	1	0.9	0.4	0.98 ± 0.47
Run 60	0.5	1	0.9	0.4	1.22 ± 0.52
Run 61	0.7	1	0.9	0.4	1.29 ± 0.49
Run 62	0.85	1	0.9	0.4	1.22 ± 0.51
Run 63	1	1	0.9	0.4	1.39 ± 0.47
Run 64	0.1	1	0.25	3.0	0.32 ± 0.07
Run 65	0.2	1	0.25	3.0	0.31 ± 0.16
Run 66	0.35	1	0.25	3.0	0.28 ± 0.17
Run 67	0.5	1	0.25	3.0	0.30 ± 0.21
Run 68	0.7	1	0.25	3.0	0.23 ± 0.18
Run 69	0.85	1	0.25	3.0	0.42 ± 0.38
Run 70	1	1	0.25	3.0	0.61 ± 0.58

Table II.2.3. *Input parameters (denudation rate E_{input}, timing T_{input} and relief change R_{input}) and Bayesian estimates of the relief change ($R_{predicted}$) for all the inversion runs.*

Supplementary figures have been added to the paper in order to show how our modelling strategy may (or not) influence the numerical predictions (Figures II.2.9 and II.2.10).

In the *Neighbourhood Algorithm* [*Sambridge*, 1999a, b], the inversion procedure is mainly controlled by the number of iterations, the number of models generated and the number of Voronoï cells that are re-sampled at each iteration. Increasing the ratio between the number of samples and the number of re-sampled Voronoi cells leads the sampling algorithm to be more exploitative (Figure II.2.4); on the contrary, the inversion procedure is more explorative if we increase the number of re-sampled Voronoï cells (Figure II.2.9). The test shows that the non-convergence towards true input parameters is not due to our modelling strategy, but rather to the limitations in the AFT data resolution (Figure II.2.9). In the main text (Figure II.2.4), we report that both the exhumation history (E_1 and E_2) and the relief evolution (R) are not resolved by the inversion. In this supplementary section (Figure II.2.10), we show that the exhumation history is much better resolved when fixing the relief parameter (R), highlighting that the model complexity is limited by the resolution of the AFT data.

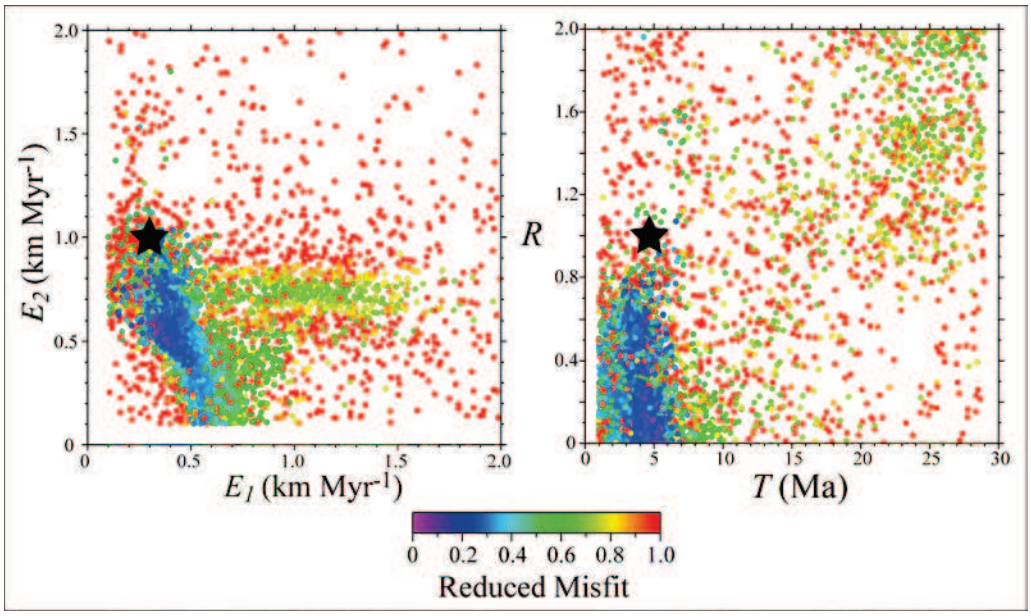

Figure II.2.9. *Scatter diagrams showing results of the NA inversion for Scenario 1 but with a different sampling scheme (85% resampled models compared to 50% in our analysis). See legend of Figure II.2.4 for explanation of colour coding and axis labels. This sampling scheme leads to much slower convergence (it is more comparable to Monte Carlo sampling which would be attained with 100% resampled models) but converges to the same optimal parameter combinations, which are different from the input parameters. This test shows that the convergence to an erroneous parameter set is independent of the sampling scheme.*

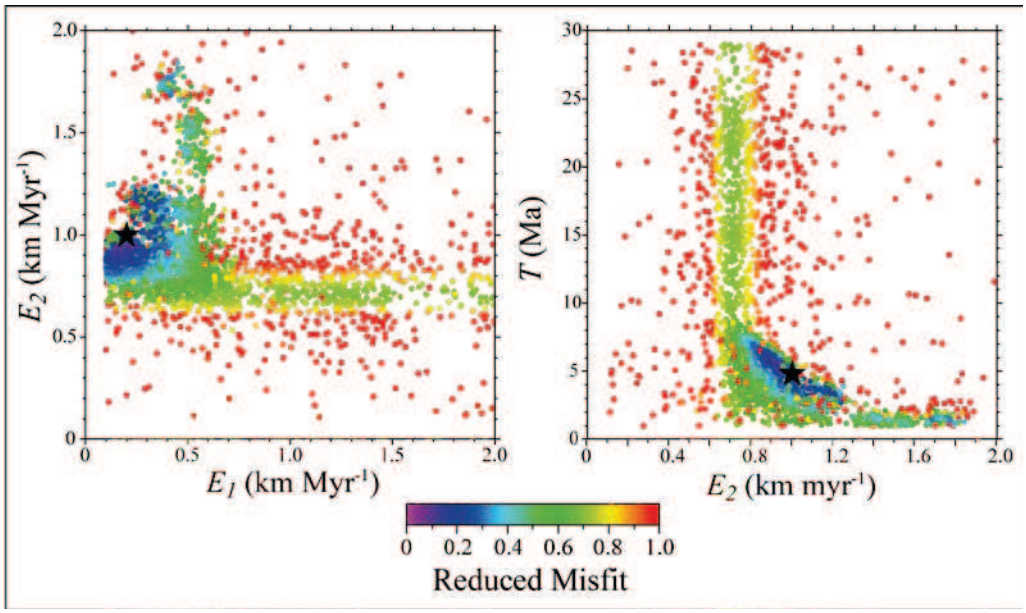

Figure II.2.10. *Scatter diagrams showing results of the NA inversion for Scenario 1 but fixing the relief ratio R = 1. See legend of Figure II.2.4 for explanation of colour coding and axis labels. This test shows that when reducing the degree of freedom for the inversion (R is fixed to the input value), the sampling stage converges towards the input set of parameters even though we used AFT data alone, with a similar sampling scheme as Scenario 1.*

II.3 - Inversion of thermochronological age-elevation profiles to extract independent estimates of denudation and relief history - II: Application to the French Western Alps

Peter A. van der Beek [1], Pierre G. Valla [1], Frédéric Herman [2], Jean Braun [1], Cristina Persano [3], Katherine J. Dobson [3], and Erika Labrin [1]

[1] *Laboratoire de Géodynamique des Chaînes Alpines, Université Joseph Fourier, BP 53, 38041 Grenoble, France*

[2] *Geologisches Institut, ETH Zurich, 8092 Zürich, Switzerland*

[3] *Department of Geographical and Earth Sciences, University of Glasgow, Glasgow G12 8QQ, United Kingdom*

Abstract

Thermochronologic data collected along age-elevation profiles are commonly interpreted as recording temporally variant but spatially constant exhumation rates. However, thermochronologic age-elevation relationships are known to be perturbed by topographic effects and potential changes in relief, which are neglected in the inherently 1-D interpretation commonly applied. Such data thus potentially record both the denudation and relief history of the sampled region but extracting this information is challenging. In a companion paper, we develop a methodology for rigorously interpreting thermochronologic age-elevation profiles in terms of exhumation rates and relief development through time, and to independently quantify the resolution of these constraints. Here we test this approach using a thermochronological dataset consisting of apatite and zircon fission-track and (U-Th)/He data, collected at La Meije Peak in the Ecrins-Pelvoux massif (French Western Alps). Our data and models suggest a three-phase exhumation history in the Pelvoux-Ecrins massif, including a pulse of rapid exhumation at ~6-5.5 Ma, preceded and followed by more moderate rates of denudation in the order of 0.3-0.4 km Myr^{-1}. This rapid exhumation event appears to occur coevally in other external crystalline massifs in the Alps but is not detected by qualitative inspection of the age-elevation relationships. Both our synthetic results and inversion of the La Meije data strongly suggest that apatite fission-track age-elevation relationships alone cannot resolve both denudation and relief histories independently and that multiple

thermochronometers are required. Combining apatite fission-track and (U-Th)/He ages and, particularly, including fission-track length data greatly improves the resolution of the inferred exhumation histories. Although denudation rates through time and the timing of rate changes are generally well resolved, our data have insufficient resolution to satisfactorily constrain the relief history. Synthetic results reported in the companion paper suggest that the reason for this limitation is that relief increase through valley carving has been insufficient with respect to the regional denudation rates to be unambiguously extracted from the data.

II.3.1 - Introduction

One of the key questions in the debate on the causal links between late Cainozoic climate change and the uplift of mountain belts is whether the Late Pliocene-Quaternary climate, characterized by high-frequency oscillations between glacial and interglacial conditions and significantly increased global denudation rates [*Zhang et al.*, 2001; *Molnar*, 2004], can lead to isostatic uplift of mountain peaks [*Molnar and England*, 1990]. Such climate-induced mountain-peak uplift requires isostatic rebound to outstrip erosion on the peaks [*Montgomery*, 1994; *Small and Anderson*, 1998; *Champagnac et al.*, 2007]. Erosion must therefore be concentrated in the valleys, increasing mountain-belt relief. It remains unclear if this is the case, particularly in response to the glaciation of mountain ranges. While several studies have indicated that glaciation leads to an increase in relief [*Montgomery*, 1994; *Small and Anderson*, 1995; *Kirkbride and Matthews*, 1997; *Montgomery*, 2002], theoretical considerations, numerical experiments and observations in the Himalaya suggest that increased glacial denudation rates may lead to a decrease in relief [*Brozovic et al.*, 1997; *Whipple et al.*, 1999; *Tomkin and Braun*, 2002]. The development of methods enabling us to quantitatively assess paleo-relief in mountain belts is required to resolve this apparent controversy.

We explore the capacity of low-temperature (apatite and zircon fission-track and (U-Th)/He) thermochronometric data, in particular thermochronological age-elevation profiles, to constrain the paleo-relief of mountain belts. Thermochronological analyses have generally considered the problem as one-dimensional [*e.g.*, *Fitzgerald et al.*, 1995], neglecting potential effects of temporally varying topography or laterally varying denudation rates on age-elevation profiles [*Braun*, 2002a]. Only recently have some studies interpreted thermochronological age-elevation profiles in terms of relief development [*Clark et al.*, 2005;

Schildgen et al., 2009; *Richardson et al*., 2010]. In this study, we quantify the extent to which such topographic effects may be extracted from thermochronological datasets, and determine if it is possible to differentiate regional changes in denudation rate from relief development by analyzing thermochronological age-elevation profiles.

We use a recently developed inverse method that combines the three-dimensional thermal-kinematic model *Pecube* [*Braun*, 2002a; 2003], with an inversion scheme based on the neighbourhood algorithm [*Sambridge*, 1999a, b]. We do not only search for best-fitting model parameters [*Braun and van der Beek*, 2004; *Braun and Robert*, 2005; *Herman et al.,* 2007], but also derive Bayesian probability-density functions for parameter values [*Herman et al.*, 2010a]. This approach allows best-fitting scenarios for denudation and relief histories to be extracted from the data and their resolution to be assessed. In a companion paper [*Valla et al*., 2010b], we fully describe the inverse method and use synthetic data from imposed denudation and relief histories to quantitatively assess the constraints on denudation rates, timing of rate changes and relief evolution that we can extract from typical low-temperature thermochronological datasets.

Here, we apply this method to a new thermochronological (apatite and zircon fission-track and (U-Th)/He) dataset collected along an age-elevation profile in the French western Alps (La Meije peak; Pelvoux-Ecrins massif), a region that has experienced modest tectonic activity but intense glaciation during the last few million years. We aim to quantify both the timing of denudation and relief development in this massif, in particular to detect the potential topographic effect of Quaternary glaciations (*i.e.*, relief increase due to glacial erosion) on the cooling histories derived from the thermochronological dataset.

In the following, we first introduce the study area and then present the thermochronological data and their qualitative interpretation regarding the evolution of exhumation rates through time. We briefly summarize our modelling approach, employ it to extract the resolvable denudation and relief histories from the data, and discuss its implications for our understanding of the tectonic and climatic controls on this history.

II.3.2 - The Pelvoux-Ecrins massif

The "External Crystalline Massifs" (ECM) of the western and central Alps consist of blocks of European crystalline basement exhumed from ~15 km depth along crustal-scale thrusts since Oligocene-Early Miocene times [*Schmid and Kissling*, 2000; *Leloup et al.*, 2005; *Simon-Labric et al.*, 2009]. The ECM are characterised by some of the highest topography and relief of the Alpine orogen, with many ≥ 4000-m-high peaks, although the main Alpine drainage divide is located more internally within the belt. Several recent studies of the denudation history of these massifs have suggested peak exhumation rates of >1 km Myr^{-1} around 6-7 Ma, followed by Pliocene-Quaternary rates of 0.5-1 km Myr^{-1}, *e.g.*, in the Argentera [*Bigot-Cormier et al.*, 2006], Mont Blanc [*Leloup et al.*, 2005; *Glotzbach et al.*, 2008] and Aar [*Vernon et al.*, 2009] massifs, although contrasting denudation histories have been inferred for the latter [*e.g.*, *Reinecker et al*., 2008; *Glotzbach et al*., 2010]. In contrast, sediment flux to the peri-Alpine basins [*Kuhlemann et al.*, 2002], and apatite fission-track (AFT) data from the North Alpine Foreland Basin [*Cederbom et al*., 2004] suggest significantly increased erosion of the belt since ~5 Ma. However, neither the history of relief development nor the potential effect of widespread glaciations on the relief history has been studied in detail.

We focus on the Pelvoux-Ecrins Massif in southeastern France (Figure II.3.1). This ECM is made up of several basement blocks with intervening inverted Mesozoic basin remnants. Basement blocks have been thrust up along steeply dipping faults with variable trends, which result from a complex polyphase history during both Early Mesozoic rifting and Alpine convergence phases [*Ford*, 1996; *Dumont et al.*, 2008]. Morphologically, the massif forms a NNW-SSE oriented elongated dome that has been deeply incised by tributaries of the Romanche, Drac and Durance rivers to the north, west, and southeast, respectively (Figure II.3.1). Glacial imprints on the morphology are widespread [*Montjuvent*, 1974; *van der Beek and Bourbon*, 2008; *Valla et al.*, 2010c] and consist of numerous hanging valleys, valley steps and overdeepenings. However, Miocene fluvial deposits surrounding the massif demonstrate that the planform drainage pattern is pre-glacial [*Montjuvent*, 1978].

Paleomagnetic, Ar-Ar and zircon fission-track (ZFT) data suggest that denudational cooling of the Pelvoux-Ecrins massif started ≥24 Ma from Alpine syn -tectonic temperatures of ~300°C [*Crouzet et al.*, 2001; *Simon-Labric et al*., 2009].

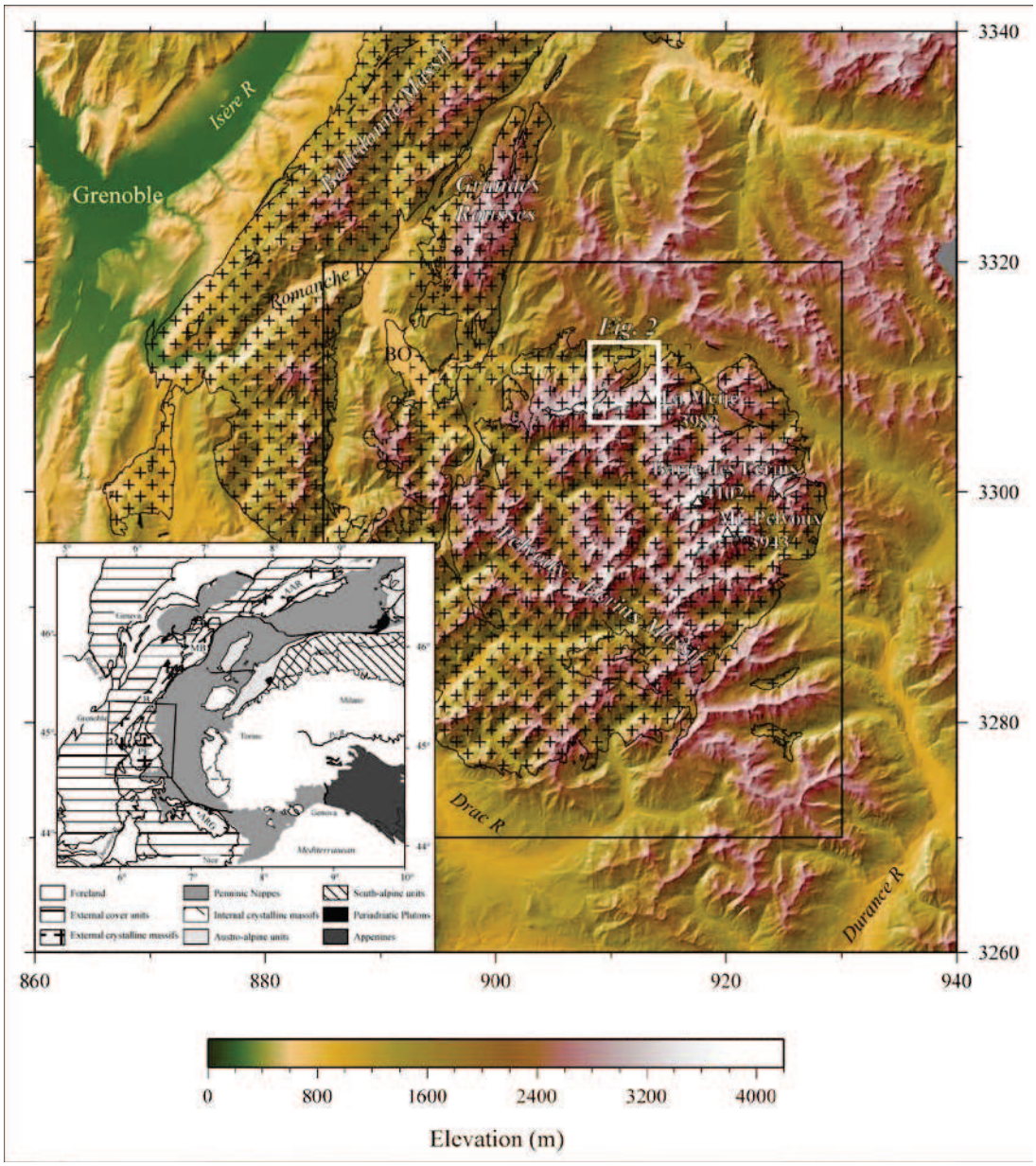

Figure II.3.1. *Digital Elevation Model of the Pelvoux-Ecrins massif and surrounding areas based on Institut Géographique National (IGN) 50-m resolution digital topography data. Cross pattern indicates extent of crystalline basement outcrop within External Crystalline Massifs. Eastings and northings follow the IGN Lambert-III grid, in kilometers. Large black box indicates extent of modelling domain; smaller white box location of Figure II.3.2. BO: Bourg d'Oisans. Inset shows simplified tectonic map of western and central Alps (modified from Schmid et al., 2004) with location of study area and other External Crystalline Massifs (Aar; MB: Mont Blanc; B: Belledonne, PE: Pelvoux-Écrins; ARG: Argentera).*

AFT ages from the massif and the contiguous Grandes Rousses (Figure II.3.1) are between ~3 and ~14 Ma [*Sabil*, 1995, *Seward et al.*, 1999], showing relatively large scatter and no clear age-elevation relationships (although neither study systematically sampled age-elevation

profiles). The youngest AFT ages are encountered at valley bottoms in the centre of the massif and require several kilometres of denudation since the Late Pliocene. Geodetic measurements suggest present-day uplift rates of up to 1 mm yr^{-1} (with respect to the foreland) within the Belledonne Massif to the north of the study area [*Jouanne et al.*, 1995]. However, these massifs are currently seismically inactive, except for modest transpressive activity within the Belledonne Massif [*Thouvenot et al.*, 2003], and continuous GPS measurements suggest minimal present-day deformation [*Calais et al.*, 2002; *Delacou et al.*, 2004].

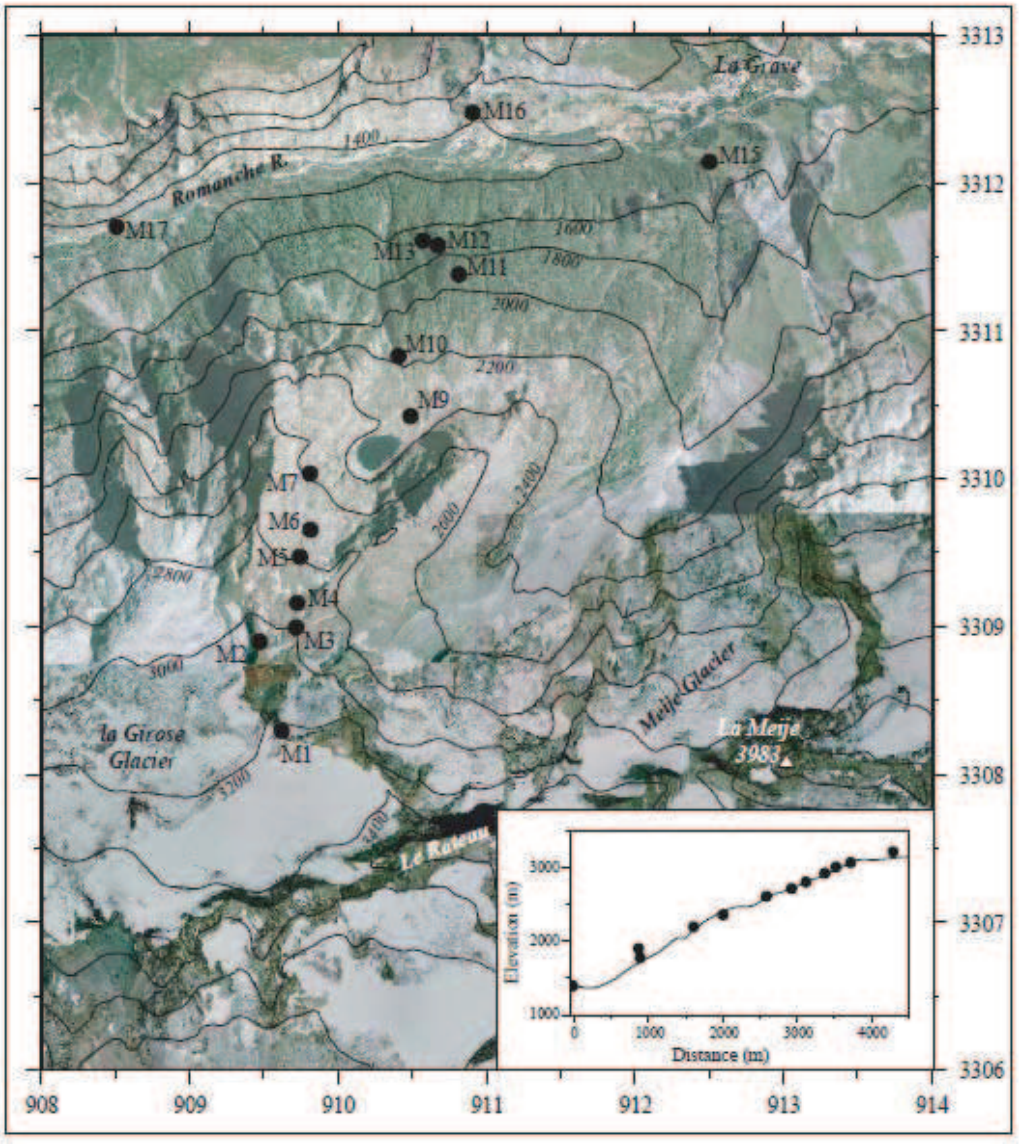

Figure II.3.2. *Topographic map of the sampling region (elevation contours from IGN 50-m resolution digital topography) overlain on orthorectified aerial photo mosaic from the Institut Géographique National Géoportail website (http://www.geoportail.fr), showing sample locations. Eastings and northings follow the IGN Lambert-III grid, in kilometers. Inset shows topography (no vertical exaggeration) and sample locations projected onto a N027E profile across the sampling sites.*

II.3.3 - Thermochronology data

Samples were collected in the upper Romanche valley and along a roughly north-south transect up the north-western flank of La Meije peak, between 1310 and 3215 m elevation (Figure II.3.2). La Meije peak consists of basement rocks (gneiss, schist and granite) thrust northwards over Mesozoic sediments that crop out at the base of the profile. Samples were collected every ~100 m along the profile where possible. Samples were initially prepared for AFT and ZFT thermochronology, following standard laboratory procedures (as described, for instance, in *Tricart et al*., 2007). 15 samples yielded sufficient apatite for AFT analysis and 6 proved suitable for ZFT analysis (Table II.3.1). Samples with high yields of good-quality apatite and zircon were prepared for (U-Th)/He analysis on apatite (AHe, 4 samples) and zircon (ZHe, 3 samples), following procedures outlined previously [*Persano et al*., 2002; *Foeken et al*., 2006; *Dobson et al*., 2009].

Sample	Elev. (m)	Easting (m)	Northing (m)	AHe Age ± 1σ (Ma)	AFT Age ± 1σ (Ma)	MTL ± 1σ (μm)	ZHe Age ± 1σ (Ma)	ZFT Age ± 1σ (Ma)
M1	3215	284,413	4,987,425		6.3 ± 0.4			
M2	3065	284,325	4,988,150	(12.0 ± 0.7)	7.7 ± 0.5		12.5 ± 2.2	27.2 ± 1.2
M3	3005	284,575	4,988,225		7.8 ± 0.4			
M4	2920	284,600	4,988,388		8.0 ± 0.5			
M5	2805	284,638	4,988,663		5.3 ± 0.3	13.5 ± 0.2		
M6	2715	284,725	4,988,838		7.0 ± 0.4			21.6 ± 1.7
M7	2610	284,752	4,989,217	6.2 ± 0.6	6.9 ± 0.4	14.4 ± 0.1	13.7 ± 1.6	20.3 ± 1.0
M9	2360	285,450	4,989,475		4.7 ± 0.7			
M10	2200	285,413	4,989,963		6.0 ± 0.2			
M11	1900	285,868	4,990,552		3.5 ± 0.2			
M12	1780	285,730	4,990,614		5.7 ± 0.4			
M13	1720	285,588	4,990,647		6.8 ± 0.4			16.3 ± 1.1
M15	1480	287,600	4,991,025		4.3 ± 0.3			
M16	1400	286,038	4,991,488	(8.5 ± 0.8)	3.2 ± 0.4			16.3 ± 1.1
M17	1310	283,588	4,990,975	4.0 ± 0.3	4.4 ± 0.5		12.5 ± 1.5	13.0 ± 1.0

Table II.3.1. *Thermochronology data from La Meije peak, French western Alps. Apatite (AFT) and zircon (ZFT) fission-track ages are central ages [Galbraith, 2005]; Apatite (AHe) and zircon (ZHe) (U-Th)/He ages are weighted mean averages from 2-4 duplicate measurements; the reported error is either the standard deviation of the sample, or the reproducibility of the age standard, whichever is greater. AHe ages given in parentheses are not used in inversion. Details for age determinations are provided in Supplementary Tables II.3.2 to II.3.5.*

II.3.3.1 - Apatite fission-track data

AFT ages vary between 3.2 ±0.8 and 8.0 ±1.0 Ma (±2σ, Tables II.3.1and II.3.5). Ages correlate reasonably well with elevation (Pearson correlation coefficient r = 0.73). The slope of the age-elevation profile (Figure II.3.3) is 542^{+51}_{-43} m Myr^{-1}, as given by the inverse of the weighted least-squares regression [*Williamson*, 1968], where the variation in slope represents

the 1-σ error in the estimate. In detail, however, the data show relatively large scatter, with several samples lying outside the age-elevation relationship at the 1-σ level (Figure II.3.3). The data appear to form two parallel age-elevation relationships, with samples M1, M5, M9, M11 and M16 defining the younger trend. Etch-pit widths parallel to the C-axis (D_{par}) can be used to monitor the annealing kinetics of apatite [*Carlson et al.*, 1999; *Barbarand et al.*, 2003]; in our samples D_{par} varies between 1.08 and 1.66 μm (standard deviations of 0.2-0.3 μm, Table II.3.5), indicating F-rich apatite that is not very resistant to annealing, and little compositional variation within individual samples. There is no systematic variation between D_{par} and AFT age of a sample at a given elevation; it is therefore unlikely that compositional control, leading to variable annealing kinetics, accounts for the observed trends. Two samples contained sufficient confined tracks to permit measuring statistically significant confined track-length distributions (Figure II.3.3b). Both show relatively long mean track lengths (MTL) indicative of rapid cooling. M5 has a MTL of 13.5 μm and mean D_{par} of 1.36 ±0.03 μm, whereas M7 has a MTL of 14.4 μm and mean D_{par} of 1.66 ±0.03 μm. The difference between the MTL distributions and the younger age of M5 with respect to M7, despite its higher elevation, may reflect slightly different annealing kinetics of these samples.

II.3.3.2 - Zircon fission-track data

ZFT ages increase monotonously with elevation from 13.0 ±2.0 Ma at 1310 m (M17) to 27.2 ±2.4 Ma at 3065 m (M2) (Tables II.3.1 and II.3.4). The age-elevation correlation is very good (Pearson correlation coefficient $r = 0.94$) and the slope of the age-elevation profile is 158^{+19}_{-15} m Myr^{-1}; significantly less steep than for the AFT data (Figure II.3.3). Single-grain ZFT ages for the upper three samples (M2, M6, M7) show very low dispersions ($D << 1\%$; $P(\chi^2) > 98\%$). In contrast, the lower three samples (M13, M16, M17) have dispersed single-grain ages ($D > 12\%$) and two of these fail the χ^2-test, suggesting that these samples have been exhumed from within the ZFT partial annealing zone, and that the lower three ZFT ages should be interpreted with caution. Binomial peak-fitting [*Stewart and Brandon*, 2004] of the single-grain ages from these three samples (a combined total of 38 dated zircon grains) suggests they contain a young age population of 12.2 ±1.1 Ma, made up by 65% of the grains, with the rest of the grains defining a population of 19.3 ±1.8 Ma.

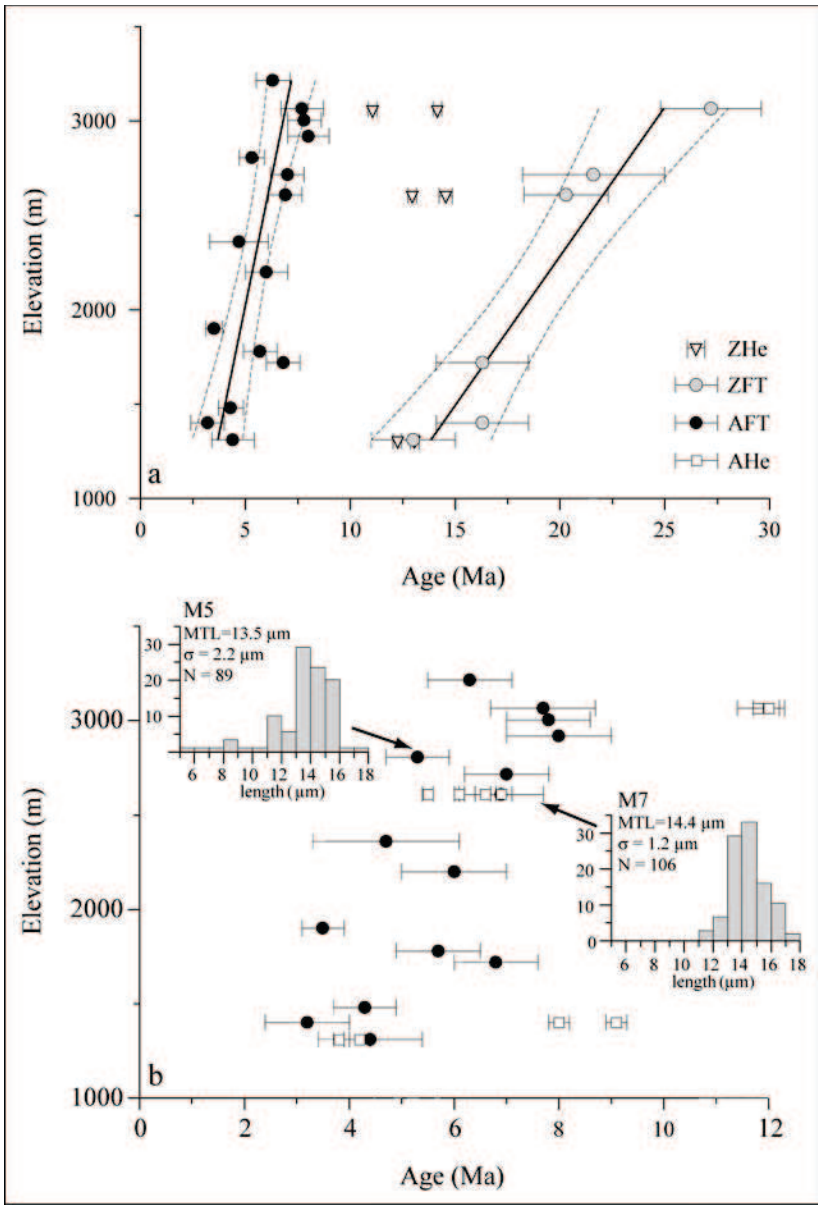

Figure II.3.3. *Thermochronological data from the La Meije age-elevation profile. (a) Age-elevation plots for ZFT and AFT data with weighted linear fit to the data (thick line: best-fit, dashed lines: ±1σ variation) and ZHe data. Note that AHe data are not plotted to avoid clutter. (b) Age-elevation plots for AFT and AHe data (note change in age-scale). Insets show horizontal confined track-length distributions for samples M5 and M7.*

II.3.3.3 - Apatite (U-Th)/He data

Of the four samples analysed, two have AHe ages that are consistent with the AFT ages, whereas two have AHe ages that are significantly older than the corresponding AFT ages (Tables II.3.1 and II.3.2; Figure II.3.3b) even though replicate measurements lie within the 8% standard-age reproducibility. M2 yields a weighted-mean AHe age of 12.0 ±1.0 Ma (2σ),

whereas the AFT age from the same sample is 7.7 ±1.0 Ma. Likewise, the weighted-mean AHe age of M16 (8.5 ±1.6 Ma) is significantly older than the corresponding AFT age (3.2 ±0.8 Ma).

In contrast, M7 and M17 yield mean AHe ages (6.2 ±1.2 Ma and 4.0 ±0.6 Ma, respectively) within error of the respective AFT ages (6.9 ±0.8 Ma and 4.4 ±1.0 Ma). The fact that two samples have AHe ages older than the corresponding AFT ages, and that all samples replicate only moderately well, leads us to consider the AHe ages with care. All samples were thoroughly screened for inclusions; however minute U and Th bearing inclusions may cause a problem of excess He in these relatively young samples. He implantation from surrounding phases [*Spiegel et al.*, 2009] is less likely to be a problem since U-concentrations of the analyzed apatites are between 30-90 ppm. Likewise, rapid cooling of these samples precludes significant radiation-damage control on He-retention [*e.g.*, *Flowers et al*., 2009; *Gautheron et al*., 2009]. The AHe ages of samples M2 and M16 are excluded from our analysis, and the possibility that the AHe ages of samples M7 and M17 may contain a component of excess He is noted.

II.3.3.4 - Zircon (U-Th)/He data

Two replicate single-grain age determinations were run for each of the 3 samples selected for ZHe analysis (Tables II.3.1 and II.3.3). Weighted-mean ages of all 3 samples are within error, varying from 12.5 ±1.5 Ma to 13.7 ±1.6 Ma, even though two samples (M2 and M7) were collected close to the top of the profile, and the third (M17) at its base. Samples M7 and M17 replicate within the age reproducibility of 11.9% but the variation in ages for M2 is slightly larger than that, possibly reflecting different U and Th zonation [*e.g.*, *Hourigan et al*., 2005], and/or potential variability in diffusion kinetics due to radiation-damage or anisotropy effects [*e.g.*, *Guenthner and Reiners*, 2009] within the analyzed crystals.

A weighted least-squares regression provides a slope of the age-elevation profile of 1710 ±1220 m Myr^{-1}, with a very low correlation coefficient (r = 0.11) due to the large dispersion in ages. The steep age-elevation profile suggested by these samples may indicate a pulse in exhumation rate around 12-14 Ma, in accord with the young age population encountered in the lower three ZFT samples.

II.3.3.5 - Qualitative interpretation

At face value, the variable slopes of the different age-elevation relationships (AER) can be interpreted as reflecting a pulsed exhumation history. The ZFT data suggest relatively slow denudation from within or below the ZFT partial annealing zone (~200-240 °C for α-damaged zircon; *Brandon et al.*, 1998) between ~27 and ~13 Ma, at a rate of ~160 m Myr^{-1}. Timing of this initial cooling is consistent with earlier estimates from Ar-Ar [*Simon-Labric et al.*, 2009] and paleomagnetic [*Crouzet et al.*, 2001] data obtained to the west and south of our profile.

The steeper age-elevation relationship from the AFT data implies an increase in regional denudation rates to ~500 m Myr^{-1} some time between ~13 and ~8 Ma. Varying denudation rates are also suggested by the ZHe data, which could be interpreted as implying a phase of rapid denudation (>1 km Myr^{-1}) at around 13 Ma (Figure II.3.3), even though the ZHe data must be interpreted with caution because of the small number of samples and relatively low reproducibility of ZHe ages.

The ZHe and AFT data together may indicate a regional increase in exhumation rate that started ~13 Ma, as also suggested by the relatively young age population (~12 Ma) within the lowermost ZFT samples (see section II.3.3.2). This timing correlates with the onset of deformation within the subalpine thrust belts to the northwest of the ECM [*Beck et al.*, 1998; *Burkhard and Sommaruga*, 1998]. Finally, the partial overlap between AFT and AHe ages could indicate rapid final cooling to surface temperatures at ~4-6 Ma.

This interpretation is, however, inherently one-dimensional and neglects the possible effects of surface topography on underlying isotherms, which could explain, for instance, part or all of the difference in slope between the high-temperature ZFT and low-temperature AFT AER's [*e.g.*, *Braun*, 2002a]. It also neglects the possible effects of relief development.

In the following, we will analyse our data more quantitatively using the inverse approach developed in *Valla et al.* [2010b], in order to analyse to what extent we can extract quantitative information on exhumation and relief history from this age-elevation profile.

II.3.4 - Inverse modelling of thermochronological data

A full description of the numerical methodology combining *Pecube* with the inverse algorithm *NA* is provided in the companion paper [*Valla et al.*, 2010b]. Thermo-kinematic and elastic parameters used for modelling are identical to those used by *Valla et al.* [2010b, see Table II.2.1]. We use the annealing algorithm of *Stephenson et al.* [2006] to predict AFT ages and mean fission-track lengths (MTL), the annealing model of *Tagami et al*. [1998] for ZFT ages and the diffusion models of *Farley* [2000] and *Reiners et al*. [2004] for AHe and ZHe ages, respectively. More sophisticated age-prediction models have been proposed in recent years, which take into account kinetic effects due to chemical variability for AFT annealing [*e.g.*, *Ketcham*, 2005] and radiation damage for AHe diffusion [*e.g.*, *Flowers et al*., 2009; *Gautheron et al*., 2009]. However, given the chemical composition of our samples (F-rich apatite, U-content ~30-90 ppm) and the expected cooling rates ≥10 °C Myr^{-1} through the AFT and AHe closure temperatures, these effects are expected to lead to only minor deviations from the predictions used by our models.

II.3.4.1 - Numerical approach

NA constitutes a two-stage inversion method [*Sambridge*, 1999a, b]: the first or sampling stage involves an iterative search in the multidimensional parameter space in order to find sets of input parameters that minimize the misfit between the modelled and observed data, based on a weighted least-squares function:

$$\psi = \sqrt{\sum_{i=1}^{N}\sum_{j=1}^{M}\frac{({}^{i}\alpha_{j,mod} - {}^{i}\alpha_{j,dat})}{{}^{i}\sigma_{j}}} \qquad \text{(II.3.1)}$$

where N is the number of datasets (up to 5 in our case, see below), M is the number of samples in each dataset, ${}^{i}\alpha_{j,mod}$ and ${}^{i}\alpha_{j,dat}$ are the predicted and observed values, respectively, and ${}^{i}\sigma_{j}$ is the error on the data. During the second or appraisal stage, the model ensemble is resampled to provide Bayesian measures of marginal probability-density functions (PDF's) for all parameters, allowing a quantitative assessment of the extent to which these parameters are resolved (see *Valla et al.*, 2010b, for full details).

We have an extended thermochronological dataset consisting of AFT and AHe ages and MTL measurements, as well as ZFT and ZHe ages. In order to evaluate to what extent apatite data alone can provide estimates of denudation and relief histories, and to determine what supplementary constraints zircon data impose on the tectonic-geomorphic history, we run models with the apatite data alone before the ZFT and ZHe data is incorporated. This allows us to interpret denudation and relief evolution since ~10 Ma before investigating a longer period (since ~30 Ma). The apatite-only scenario (hereafter referred to as Scenario Ap) was run over 15 Myr and describes a two-stage exhumation and relief history. This model combines four parameters: (1) denudation rate during the first phase (E_1: 0-4000 m Myr^{-1}); (2) denudation rate during the second phase (E_2: 0-2000 m Myr^{-1}); (3) transition time (T: 1-14 Ma); and (4) relief factor (R: 0-2). The relief factor R is defined as: $R = \Delta h_1 / \Delta h_2$; for Scenario Ap, relief is constant during the first phase (Δh_1) and then linearly evolves towards Δh_2 (the present-day relief; extracted from a 90-m Digital Elevation Model) at the end of the second phase. In our models, relief changes through valley incision; *i.e.*, peaks remain at constant elevation (see *Valla et al.*, 2010b for details).

For all parameters, this specified range will be considered as a uniform prior distribution during the appraisal stage (see *Valla et al.*, 2010b, for details). Four numerical inversions used AFT ages alone, AFT + AHe ages, AFT + MTL and finally all apatite data, allowing quantitative assessment of the combination of low-temperature thermochronometers that provides the tightest constraints on denudation rates and/or relief evolution through time.

The second scenario (hereafter referred to as Scenario Ap + Zr) includes both apatite and zircon data. This was run over 40 Myr, in order to assure that all points that end up at the surface cool through the ZFT closure temperature during the model run, and includes three phases with seven associated parameters (again assuming uniform prior distributions within the specified ranges): (1) denudation rate during the first phase (E_0: 0-2000 m Myr^{-1}); (2) denudation rate during the second phase (E_1 : 0-4000 m Myr^{-1}); (3) denudation rate during the third phase (E_2 : 0-2000 m Myr^{-1}; note that these phases are numbered so as to be comparable to those of Scenario Ap); (4) transition time between first and second phase (T_1 : 1-39 Ma); (5) transition time between second and third phase (T_2 : 1-39 Ma; with $T_1 > T_2$); (6) relief factor of the first phase (R_1 : 0-2); and (7) relief factor at the end of the second phase (R_2 : 0-2), the relief tending linearly toward the modern value (R = 1) during the third phase.

II.3.4.2 - Quantitative interpretation of apatite data

Inversion results using AFT ages only as well as the full apatite dataset (AFT ages, MTL and AHe ages) are reported in Figure II.3.4. The inversion based on the AFT ages alone (Figure II.3.4a, b) does not resolve a unique set of parameters for either denudation rates ($E_1 \approx$ 300-4000 m Myr^{-1}; $E_2 \approx$ 300-1800 m Myr^{-1}), timing ($T \approx$ 2-6 Ma) or relief evolution ($R \approx$ 0.3-1.8). The plots suggest significant tradeoff between parameters and show that the AFT ages alone do not have the resolution to independently predict denudation or relief development.

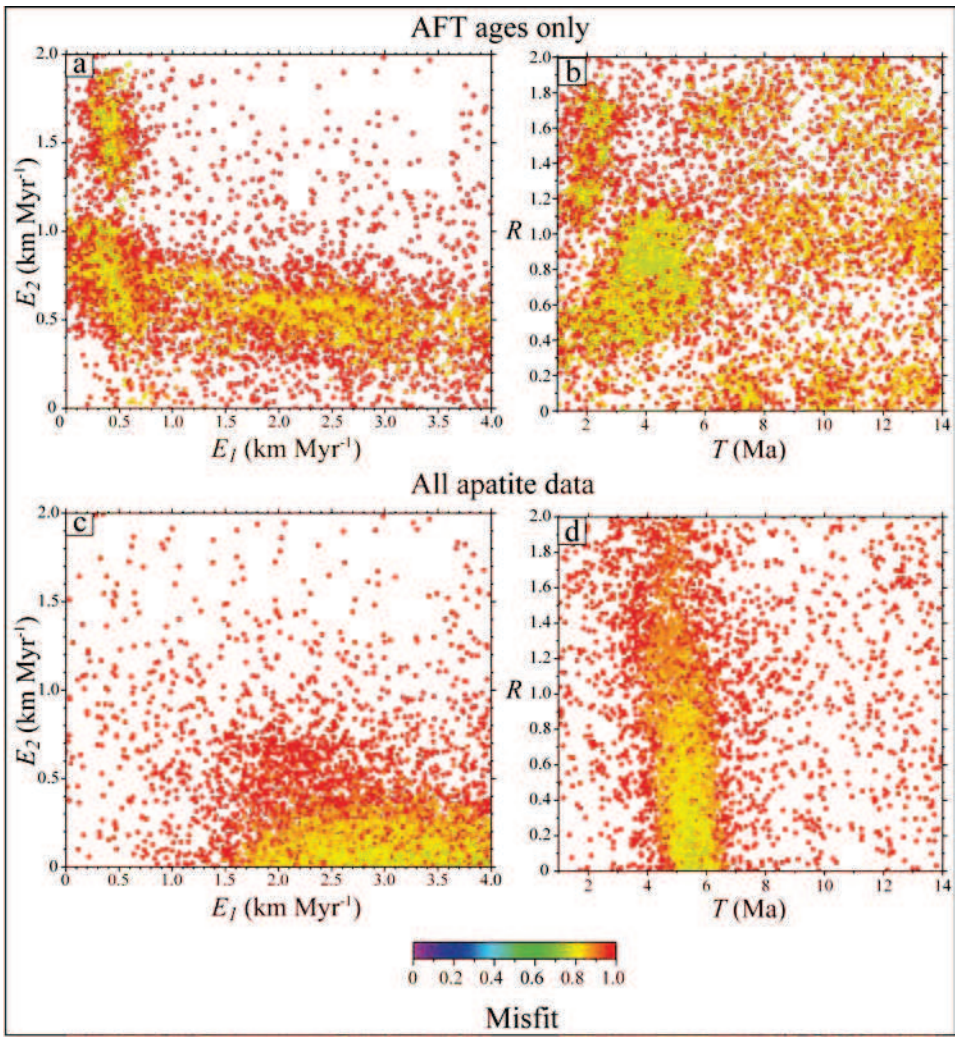

Figure II.3.4. *Scatter diagrams showing results of NA inversions for Scenario Ap. Each dot corresponds to a forward model; its colour is proportional to the value of the reduced misfit between predictions and data (misfit function ψ reduced by the number of data; blue to green corresponds to low misfits, red corresponds to mean misfits larger than the mean standard error on the data). Each diagram is the projection onto a plane defined by two of the four parameters (denudation rates E_1 and E_2; transition time T and relief factor R); horizontal and vertical axes define the parameter space. Results are only shown for end-member inversion experiments with 15 AFT ages only (a-b) and 15 AFT + 2 AHe ages combined with 2 MTL measurements (c-d).*

Addition of the two AHe ages and two MTL measurements significantly improves model convergence (Figure II.3.4c, d) and the sampling stage suggests high denudation rates (E_1 >1500 m Myr^{-1}) before 6.5-5 Ma followed by much slower denudation rates (E_2 <300 m Myr^{-1}) until present. The time of change is well constrained ($T \approx$ 5-6.5 Ma) and predictions for relief evolution suggest between 10 to 100% relief increase between the two phases ($R \leq 0.9$; Figure II.3.4d). Note that this optimum history deduced from the NA sampling stage differs significantly from that inferred qualitatively in the previous section: exhumation rates before 5 Ma are higher than inferred from the AFT AER and decrease sharply after that, which was not obvious from inspection of the AER. Furthermore, NA results provide independent information on relief evolution, suggesting that during this slow denudation phase, relief has dramatically increased.

Posterior probability-density functions (PDF's) for parameter values, derived from the appraisal stage, confirm most of these estimates (Figure II.3.5). The most important data for model convergence are the MTL measurements, especially for predictions of denudation rates (E_1 and E_2) and timing (T). While predictions for E_1 and E_2 from the AFT ages or AFT + AHe inversions are 600^{+1800}_{-600} and 700 ±200 m Myr^{-1} respectively, the inclusion of the MTL data yields values of 2400 ±900 and 130^{+180}_{-130} m Myr^{-1} (Figure II.3.5a, b; the quoted numbers are the mode and 1-σ dispersion around the mode of the PDF). The timing of change (T) is also better constrained, improving from 9.0 ±3.3 Ma (AFT + AHe) to 5.1 ±0.9 Ma when the MTL measurements are included (Figure II.3.5c). The Bayesian predictions for relief evolution, in contrast, are not improved by adding AHe and/or MTL data to the AFT ages (Figure II.3.5d); parameter PDF's show that our data has insufficient resolution to constrain the relief-ratio parameter (R = 1.1 ±0.6; since the distribution has no clear mode this value corresponds to its weighted mean). We thus have good constraints on both denudation rates and timing but not on relief development: our apatite data strongly suggest a sharp change from high (E_1 = 2400 ±900 m Myr^{-1}) to moderate (E_2 <310 m Myr^{-1}) denudation rates at 5.1 ±0.9 Ma. However, although the inversion suggests that relief may have increased since this time, the apatite data do not resolve relief evolution over the last ~15 Myr. The fit to both the AFT and AHe AERs for this "most probable" model is illustrated in Figure II.3.8a and shows how the inversion attempts to simultaneously optimise the fit to the relatively scattered AFT ages and the overlapping AHe ages.

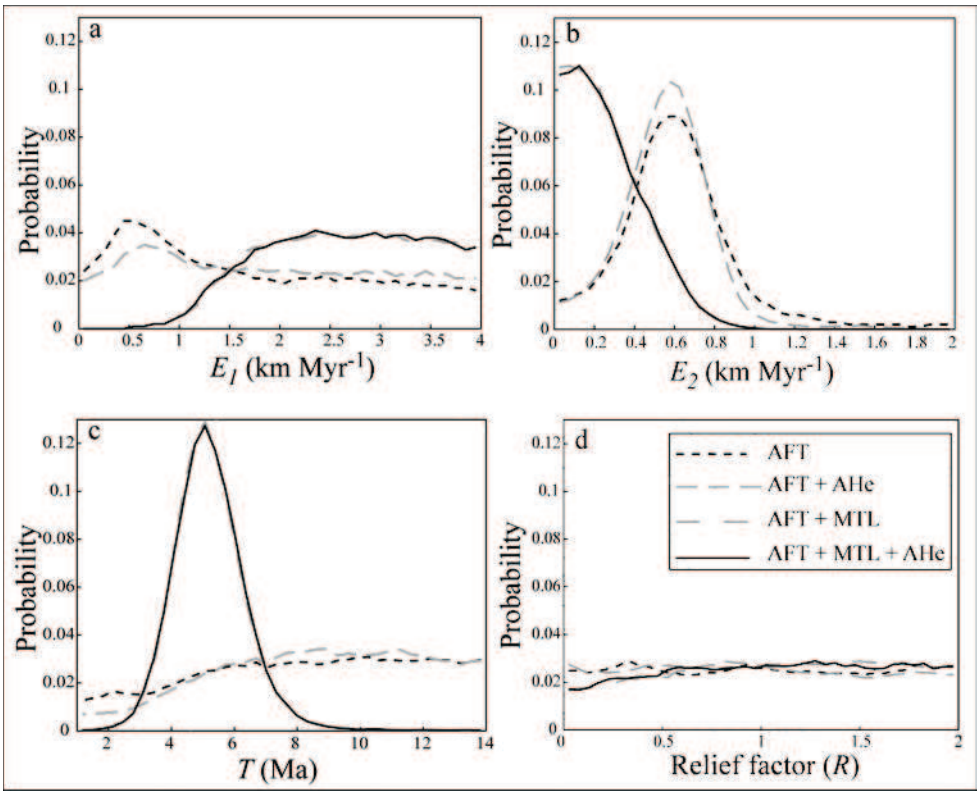

Figure II.3.5. *Posterior PDF's for Scenario-Ap parameters, obtained from the NA appraisal stage: (a) denudation rate of the first exhumation phase (E_1); (b) denudation rate of the second exhumation phase (E_2); (c) transition time between the two exhumation phases (T); and (d) relief factor between the paleo-relief and the present-day relief (R). Each line defines an inversion experiment with a given set of thermochronological data (see key in panel d).*

II.3.4.3 - Quantitative interpretation of apatite + zircon data

Sampling-stage results using all the data (Figure II.3.6) complete the results from Scenario Ap. The inversions suggest that moderate denudation rates (E_2 < 700 m Myr^{-1}; Figure II.3.6b) during the last 3-7 Ma (Figure II.3.6c) were preceded by a phase of rapid denudation (E_1 ≈ 1200-2500 m Myr^{-1}; Figure II.3.6a) between 5-11 and 3-7 Ma (Figure II.3.6c). Addition of the zircon data enables us to constrain an older phase of relatively low denudation rates of (E_0 < 500 m Myr^{-1}; Figure II.3.6a) from 30 to 5-11 Ma. Relief predictions are quite different from Scenario Ap; they suggest an increase in relief before 5-11 Ma (R_1 < 1, Figure II.3.6d) but a decrease since that time (R_2 > 0.8; Figure II.3.6d), even though again the relief parameters do not seem to converge very well.

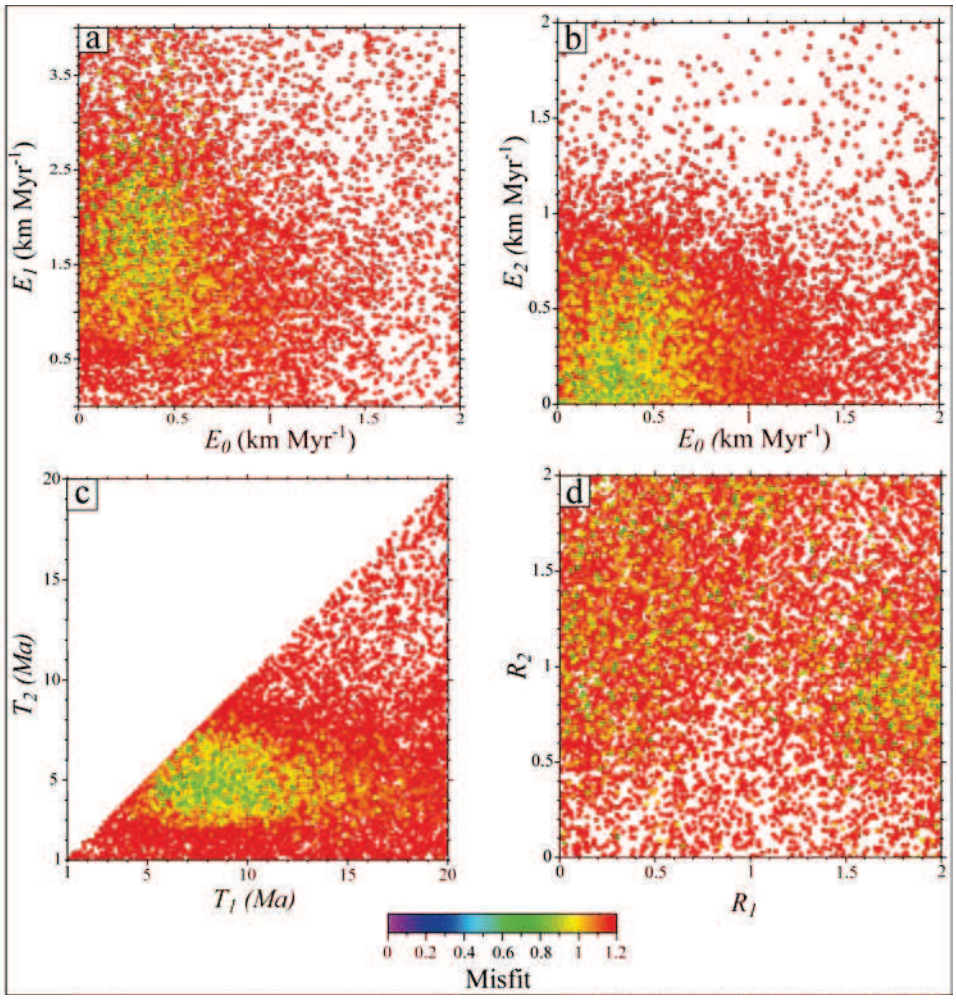

Figure II.3.6. *Scatter diagrams showing results of the NA inversion for Scenario Ap + Zr. Same plots as Figure II.3.4 but for seven parameters (denudation rates E_0, E_1 and E_2; transition times T_1 and T_2; relief factors R_1 and R_2); horizontal and vertical axes define the parameter space for given parameters. Note misfit function ψ is reduced by the number of data (i.e., 28); blue to green corresponds to low misfits, yellow corresponds to acceptable misfits (mean misfit smaller than the mean standard error on the data), and red corresponds to high misfits (larger than the mean standard error on the data).*

Parameter PDF's derived from the appraisal stage confirm that the exhumation history may be divided into 3 contrasting phases: moderate denudation rates (E_0 = 400 ±300 m Myr^{-1}; Figure II.3.7a) between 30 and 6.0 ±3.3 Ma (T_1; Figure II.3.7e); a pulse of rapid denudation (E_1 = 2600 ±1100 m Myr^{-1}; Figure II.3.7b) between 6.0 ±3.3 and 5.5 ±3.3 Ma (T_2; Figure II.3.7f); and finally moderate denudation rates (E_2 = 600 ±300 m Myr^{-1}; Figure II.3.7c) from 5.5 ±3.3 Ma to the present. Relief-parameter predictions remain relatively unconstrained and do not show a clear indication for relief increase (Figure II.3.7d), although relief before ~6.0 Ma may have been lower than today ($R_1 = 0.03^{+0.94}_{-0.03}$) and the inferred pulse of rapid denudation may

have been associated with higher relief ($R_2 = 1.98^{+0.02}_{-0.97}$). However, these estimates are not better resolved than the priors, implying that our data do not have sufficient resolution to constrain the relief history.

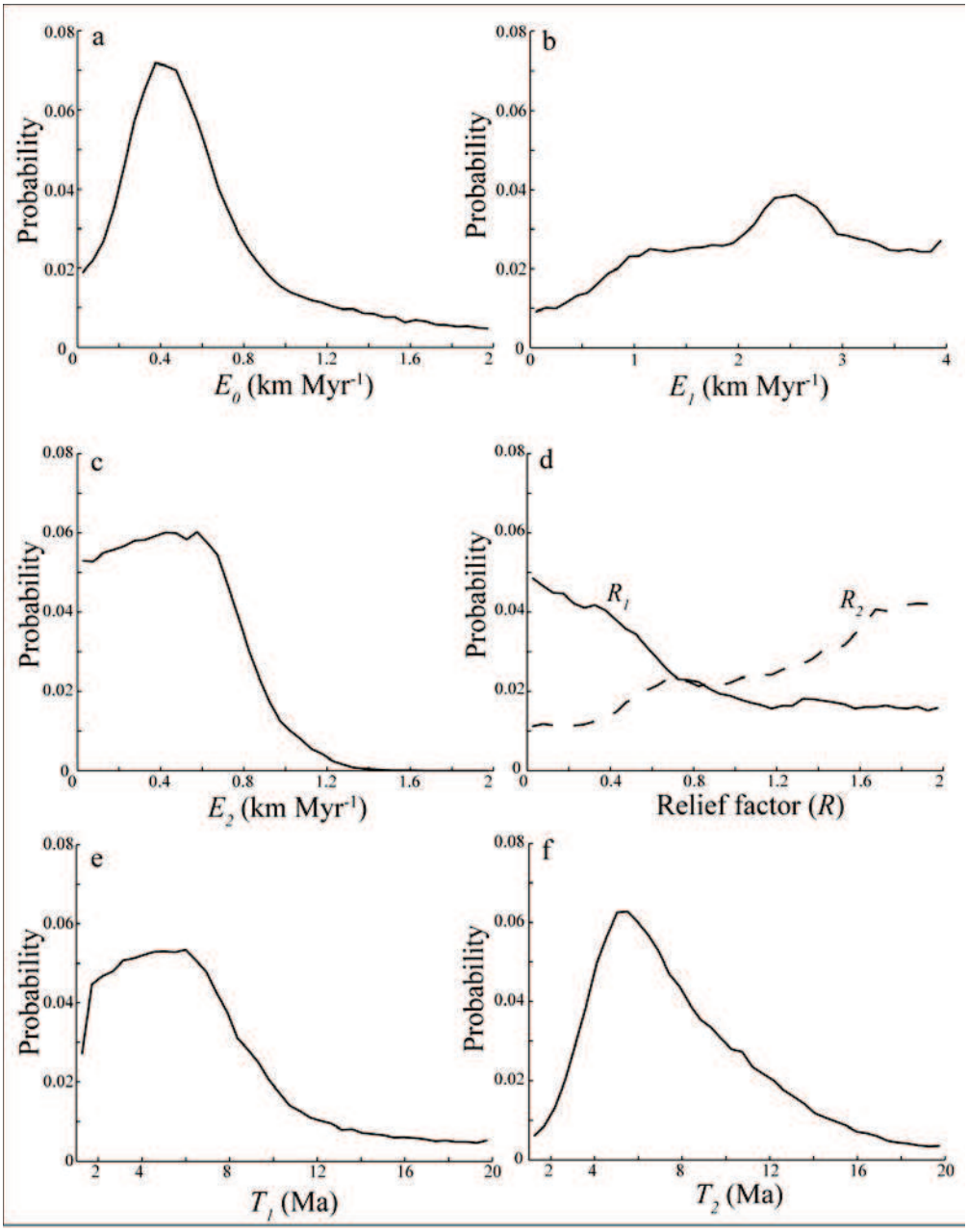

Figure II.3.7. *Posterior PDF's for Scenario Ap + Zr parameters, obtained from the NA appraisal stage: (a) denudation rate of the first exhumation phase (E_0); (b) denudation rate of the second exhumation phase (E_1); (c) denudation rate of the third exhumation phase (E_2); (d) relief factor for the first (R_1, solid line) and the second (R_2, dashed line) exhumation phases; (e) transition time between the first and second exhumation phases (T_1); and (f) transition time between the second and third exhumation phases (T_2).*

II.3.5 - Discussion

Our quantitative analysis of thermochronological data from an elevation profile at La Meije has important implications, both for the exhumation and relief history of the western Alps, and more generally for the interpretation of thermochronology data, in particular age-elevation relationships.

Our initial qualitative and inherently one-dimensional interpretation of the data suggested slow exhumation of ~150 m Myr^{-1} from ~30 to ~13 Ma (from the ZFT AER), increasing to ~540 m Myr^{-1} after ~8 Ma (from the AFT AER). Depending on how much confidence one places in the ZHe data, a phase of rapid exhumation may have intervened and the AHe ages that overlap with AFT ages suggest rapid exhumation around ~4 Ma (Figure II.3.9). In contrast, the inversions suggest a sharp decrease in exhumation rate at ~5 Ma and Scenario Ap+Zr implies a rapid pulse of exhumation between 6.0 ±3.3 and 5.5 ±3.3 Ma. Relief evolution remains essentially unconstrained, although an inversion using all data would suggest that the pulse of exhumation was associated with relief increase. A similar conclusion was recently reached by *Vernon et al*. [2009], who compared qualitative and forward-modelled exhumation and relief histories derived from two age-elevation profiles in the central Alps.

Best-fit scenarios from the inversions fit the age-elevation relationships reasonably well (Figure II.3.8), although there is significant scatter in the AFT age-elevation relationship (AER) as discussed previously, and the models have difficulty in simultaneously fitting the gentle slope of the ZFT AER, the very steep slope of the ZHe AER and the overlapping AFT and AHe ages. The overall fit to the data may appear disappointing: the "most probable" inversion scenarios fit the AER's less well than simple linear regressions. However, in contrast to the direct approach, the inversion does attempt to fit the entire dataset using an internally consistent and physically-based model. The model results can therefore be used not only to infer a regional exhumation history from the dataset, but also to identify potentially problematic data and limits to the model. In our case, exclusion of the potentially suspect ZHe data did not significantly change the inversion outcome. However, potential improvements to our approach could be provided by more sophisticated age-prediction models or more realistic relief-evolution scenarios (instead of simple linear valley carving as imposed here).

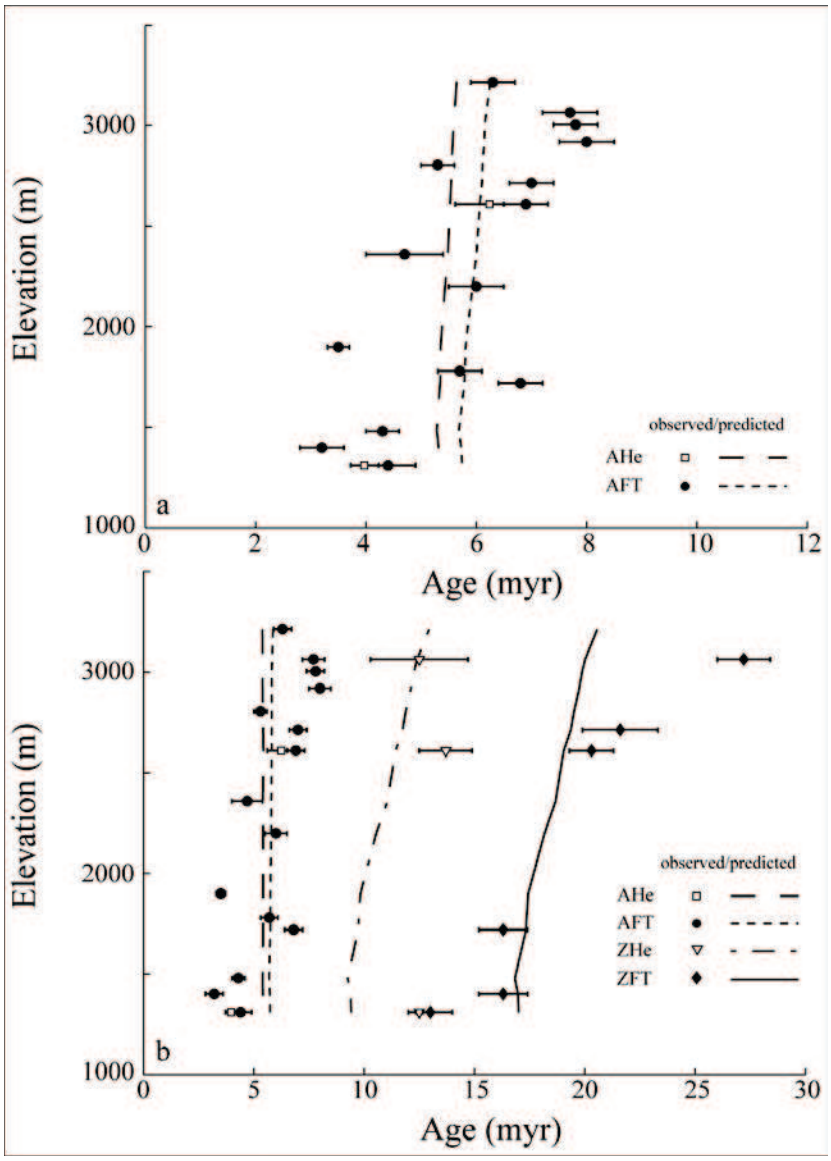

Figure II.3.8. *Comparison of observed (symbols) and predicted (lines) age-elevation relationships (AER's) for the different datasets (circles: AFT; diamonds: ZFT; squares: AHe; inverted triangles: ZHe). Note that weighted-mean ages are plotted for the He data. (a) Zoom on the AFT and AHe AER's for "most probable" model of Scenario Ap (i.e., a model defined by a combination of parameters corresponding to the modes of the posterior parameter PDF's; E_1 = 2.4 km Myr^{-1}; E_2 = 0.13 km Myr^{-1}; T = 5.1 Ma; R = 1.28); (b) AER's for all data. Predicted data are from the "most probable" model of Scenario Ap + Zr (E_0 = 0.4 km Myr^{-1}; E_1 = 2.6 km Myr^{-1}; E_2 = 0.6 km Myr^{-1}; T_1 = 6.0 Ma; T_2 = 5.5 Ma; R_1 = 0.03; R_2 = 1.98).*

In a regional context, our data support a major pulse of exhumation in the Pelvoux-Ecrins massif around 6.0-5.5 Ma. This event appears to be regionally significant, as exhumation phases that overlap in timing have recently been reported in the Argentera [*Bigot-Cormier et al.*, 2006], Mont Blanc [*Glotzbach et al.*, 2008] and Aar [*Vernon et al.*, 2009] massifs. The

transient nature of the erosion and relief signal may suggest it is climatically controlled [*e.g.*, *Whipple*, 2009]; its timing is consistent with Messinian climate change as recently proposed by *Willett et al*. [2006]. However, the fairly low resolution in timing (±3.3 Ma) does not allow ruling out other proposed climatic mechanisms, such as onset of Gulf Stream circulation at ~4.6 Ma [*Cederbom et al*., 2004] or alpine glaciation since ~3 Ma [*e.g.*, *Champagnac et al*., 2007]. Nor do these results rule out a possible tectonic control. In effect, underplating of normal-thickness continental crust below the ECM (as opposed to previously thinned continental margin), coincident with deformation stepping out into the Jura fold-and-thrust belt and aided by rapid exhumation is believed to have occurred sometime between ~12 and ~5 Ma [*e.g.*, *Burkhard and Sommaruga*, 1998; Bonnet *et al*., 2007]. A full understanding of the late Miocene-Pliocene evolution of the Alps, and its overriding tectonic and climatic controls, therefore appears beyond the current resolution of thermochronology data.

The data presented here cannot resolve the significant recent increase in Alpine relief that has been suggested from morphological analyses, and linked to major Quaternary glaciations [*Champagnac et al*., 2007; *Hauselmann et al.*, 2007, *van der Beek and Bourbon*, 2008]. Perhaps this is not surprising: in the companion study, *Valla et al*. [2010b] show that in order for relief increase to be detected, rates of local valley carving should be 2-3 times greater than background denudation rates, which would require recent rates of valley carving >1500 m Myr^{-1} in the Ecrins-Pelvoux massif.

More generally, our analysis supports the finding of the companion paper [*Valla et al*., 2010b] that an AFT age-elevation profile alone does not provide sufficient resolution to independently constrain denudation and relief histories. Potential reasons for this include (1) the large relative uncertainty often associated with AFT ages; (2) the non-unique nature of AFT ages: similar ages may result from widely varying cooling histories; and (3) the complex interplay between regional exhumation and relief development in setting local denudation and cooling histories. Adding AHe data and especially track-length measurements is required if tightly constrained exhumation scenarios are to be obtained from age-elevation profiles. Unfortunately, track-length data are not easily obtained in young and/or low-U samples because of low track numbers, although Cf-irradiation may help to limit this problem [*Donelick and Miller*, 1991].

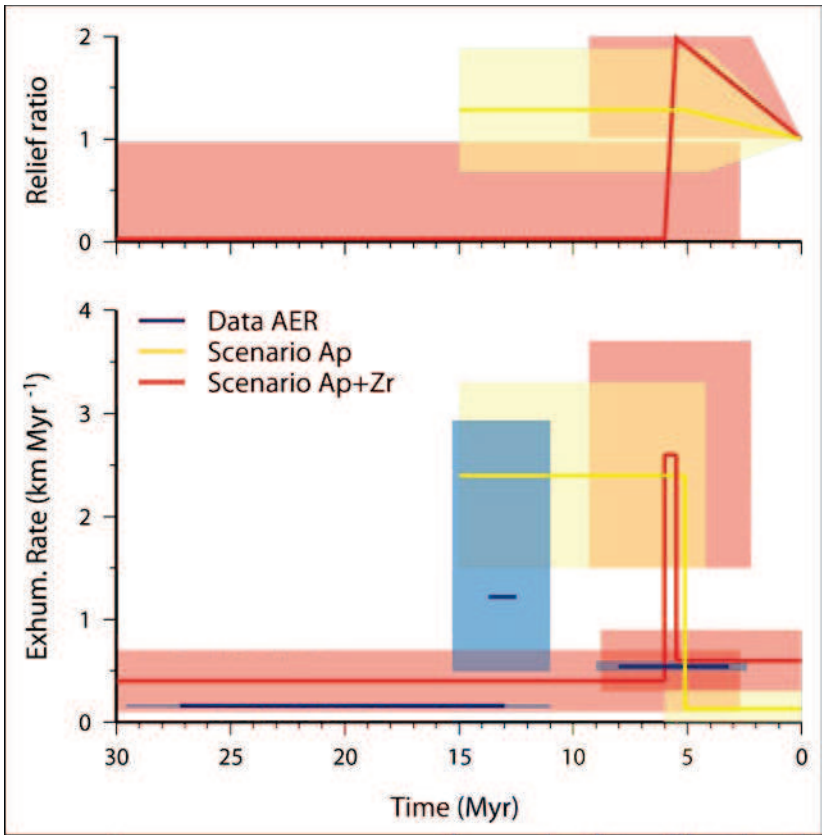

Figure II.3.9. *Exhumation and relief histories inferred from direct inspection of AER's (blue) and from the inversion of apatite (yellow) and apatite + zircon (red) data. Note that relief evolution cannot be inferred directly from AER's. Continuous lines show best-fit slope of AER or "most probable" value for exhumation rate or relief ratio (resulting from the NA appraisal stage, cf. Figures II.3.5, II.3.7 and II.3.8); shaded boxes indicate 1-σ uncertainty on these estimates.*

Relief development is hard to constrain using thermochronological age-elevation profiles. The relief ratio is clearly the least resolved parameter in all of the inversions we have run (both using synthetic and real data). There are several potential reasons for this: (1) on the scale of the topography studied here, the temperatures affected by relief development are below the thermal sensitivity of the thermochronometers used, even though relief is significant in both amplitude (~3 km) and wavelength (~15 km); (2) the age-elevation sampling scheme employed, in which topography was sampled at a single, relatively short wavelength, is not optimal for constraining relief change [*Braun*, 2002b]. Consequently, more promising approaches would be to employ recently developed thermochronometers that are sensitive to lower temperatures (*e.g.*, $^{4}He/^{3}He$ thermochronometry; *Shuster et al.*, 2005) and/or to sample topography at variable wavelengths along a transect [*e.g.*, *House et al.*, 1998; *Foeken et al.*, 2007; *Herman et al.*, 2007; *Glotzbach et al.*, 2008]. Such data can be analysed using either the approach developed here or by direct spectral analysis [*Braun*, 2002b; *Herman et al.*, 2007].

In a recent study, *Glotzbach et al.* [submitted] show that a similar analysis of data collected along a transect across the Mont Blanc massif allows detecting a recent increase in relief. In that case, the analysis is helped by the fact that relief change is very recent (~1 Ma) and rapid, largely outpacing the background denudation rate in the massif.

II.3.6 - Conclusions

We have developed a novel methodology to interpret thermochronological age-elevation profiles in terms of denudation and relief histories, and have applied this approach to a dataset collected in the Pelvoux-Ecrins massif, French Western Alps. Our results have both regional and more general implications. Our data and models suggest a three-phase exhumation history in the Pelvoux-Ecrins massif including a pulse of rapid exhumation between 6.0±3.3 and 5.5±3.3 Ma, which appears consistent with inferences from other external crystalline massifs in the Alps (Aar, Mont Blanc, Argentera). This rapid exhumation event was preceded and followed by more moderate rates of denudation, in the order of 0.3-0.4 km Myr^{-1}. The potential tectonic and/or climatic controls on these denudation histories remain unclear and need to be studied further. We have not obtained sufficient resolution on the history of relief development in the massif; the synthetic results reported in the companion paper suggest that the reason for this is that potential relief increase through valley carving has been insufficient with respect to the regional denudation rates to be unambiguously extracted from the data. Thus, other sampling schemes and/or thermochronometers that are sensitive to lower temperatures are required to constrain the relief history in this case. Finally, both our synthetic results and inversion of the La Meije data strongly suggest that AFT ages alone have insufficient resolution for resolving the exhumation history from age-elevation relationships and that multiple thermochronometers are required. Combining AFT and AHe ages and, particularly, including track-length data greatly improves the resolution of the inferred exhumation histories.

Acknowledgements

This study is supported by INSU-CNRS through the European Science Foundation Eurocores Topo-Europe programme 07-TOPO-EUROPE-FP-023 “Coupled climatic/tectonic forcing of European topography revealed through thermochronometry (Thermo-Europe)” and the *Agence Nationale de la Recherche* project no. ANR-08-BLAN-0303-01 “Erosion and Relief

Development in the Western Alps". PV is supported by a PhD grant from the French Ministry for Research and Higher Education. AFT and ZFT analyses were performed at the Grenoble thermochronology lab; AHe and ZHe at the Scottish Universities Environmental Research Centre (SUERC). We thank Christine Authemayou, Vincent de Andrade and Thierry Dumont for assistance with sampling, and Francis Coeur and François Senebier for sample preparation. Computations were performed on Brutus, the high-performance computing facilities at ETH Zürich. Codes are available on http://svn-geo.ethz.ch after registering at this site. Thorough and constructive reviews by M. Brandon and R. Ketcham significantly improved the manuscript.

II.3.7 - Supplementary data

This section reports four supplementary tables associated to the study presented above. Supplementary tables II.3.2 and II.3.3 provide (U-Th)/He data for respectively apatite and zircon samples. Supplementary tables II.3.4 and II.3.5 provide fission-track data for respectively zircon and apatite samples.

Sample	Elev. (m)	no crystals	He (cc)	^{238}U (ng)	^{232}Th (ng)	Th/U	Raw He age (Ma)	F_T	Corr. He age (Ma)	Error (Ma)
M2-1	3065	1	4.380×10^{-10}	0.19	0.05	0.25	9.7	0.82	11.8	0.4
M2-2	3065	1	5.384×10^{-10}	0.23	0.52	2.25	9.5	0.79	12.0	0.3
									12.0	**± 0.7**
M7-1	2610	3	6.322×10^{-10}	0.95	0.36	0.38	5.0	0.72	6.9	0.2
M7-2	2610	4	3.662×10^{-10}	0.61	0.27	0.44	4.5	0.74	6.1	0.1
M7-3	2610	4	6.103×10^{-10}	0.94	0.41	0.43	4.9	0.74	6.6	0.2
M7-4	2610	3	2.151×10^{-10}	0.39	0.17	0.43	4.1	0.74	5.5	0.1
									6.2	**± 0.6**
M16-1	1400	4	3.567×10^{-10}	0.38	0.14	0.38	7.0	0.77	9.1	0.2
M16-2	1400	4	3.483×10^{-10}	0.43	0.18	0.43	6.1	0.77	8.0	0.2
									8.5	**± 0.8**
M17-1	1310	1	8.620×10^{-11}	0.17	0.03	0.18	2.6	0.68	3.8	0.1
M17-2	1310	1	4.860×10^{-11}	0.03	0.03	0.95	2.8	0.67	4.2	0.2
									4.0	**± 0.3**

Table II.3.2. *Apatite (U-Th)/He data from La Meije peak, French western Alps. Age determinations by C. Persano. Analytical uncertainty on U and Th determinations is ~2%. Abbreviations: Raw He age: grain age before applying the F_T alpha-ejection correction factor; F_T: correction factor for alpha ejection [Farley, 2002]; Corr He age: grain age after applying the F_T alpha-ejection correction factor; Corrected ages are shown with 6% uncertainties as calculated from the reproducibility of Durango apatite. The weighted-mean age for each sample is given in bold together with the error calculated from the 1σ standard deviation of the sample, or from the Durango standard, whichever is greater.*

Sample	Elev. (m)	He (cc)	^{238}U (ng)	^{232}Th (ng)	Th/U	Raw He age (Ma)	F_T	Corr. He age (Ma)	Error (Ma)
M2-1	3065	7.395E-09	5.81	1.57	0.28	9.8	0.70	14.1	0.2
M2-2	3065	8.632E-09	7.09	2.18	0.32	9.3	0.85	11.0	0.2
								12.5	**± 2.2**
M7-1	2610	4.276E-08	25.92	14.22	0.55	12.0	0.83	14.5	0.3
M7-2	2610	2.772E-08	19.28	9.11	0.48	10.6	0.82	12.9	0.2
								13.7	**± 1.6**
M17-1	1310	7.827E-09	6.49	2.09	0.33	9.2	0.75	12.2	0.2
M17-2	1310	7.690E-09	6.29	0.87	0.15	9.7	0.75	13.0	0.2
								12.5	**± 1.5**

Table II.3.3. *Zircon (U-Th)/He data from La Meije peak, French western Alps. Age determinations by K. Dobson. All aliquots were single crystals. U and Th measurements are corrected for a Pt blank of 0.1067 ng U and 0.0997 ng Th. Analytical uncertainty is ~2-3%. Abbreviations as for Table II.3.2.* F_T *calculated after Hourigan et al. [2005], assuming homogenous U and Th distribution. Uncertainties on individual* F_T *corrected ages are 11.9 %, calculated from the age reproducibility of the FCT (Fish Canyon Tuff) age standard. Weighted-mean ZHe ages are shown with 1σ sample-specific age reproducibility or 11.9% FCT reproducibility, whichever is greater.*

Sample	Elev. (m)	N	ρ_s ($\times10^6$ cm^{-2})	N_s	ρ_i ($\times10^6$ cm^{-2})	N_i	ρ_d ($\times10^6$ cm^{-2})	N_d	$P(\chi^2)$ %	D %	Age (Ma)	± 2σ
M2	3065	15	5.396	2009	2.713	1010	0.193	15597	98.2	<<1	27.2	2.4
M6	2715	5	5.329	462	3.380	293	0.193	15597	98.8	<<1	21.6	3.4
M7	2610	12	2.738	1170	1.832	783	0.192	15597	99.9	<<1	20.3	2.0
M13	1720	8	4.385	1145	3.665	957	0.194	15597	4.6	12	16.3	2.2
M16	1400	12	7.021	888	5.701	721	0.194	15597	13.0	13	16.3	2.2
M17	1310	18	2.596	1501	2.592	1499	0.194	15597	<<1	25	13.0	2.0

Table II.3.4. *Zircon fission-track data from La Meije peak, French western Alps. All age determinations were performed by E. Labrin with* $\zeta = 142 \pm 3$ *for glass dosimeter CN1; all ages are reported as central ages [Galbraith and Laslett, 1993].*

Sample	Elev. (m)	Easting (m)	Northing (m)	N	ρ_s ($\times 10^5$ cm^{-2})	N_s	ρ_i ($\times 10^5$ cm^{-2})	N_i	ρ_d ($\times 10^5$ cm^{-2})	N_d	$P(\chi^2)$ %	D %	Age ± 2σ (Ma)	MTL ± 1σ (µm) (# measured)	SD (µm)	D_{par} ± 1σ (µm) (# measured)	SD (µm)
M1	3215	284413	4987425	19	0.334	319	2.920	2789	0.320	14121	97.5	<<1	6.3 ± 0.8			1.17 ± 0.03 (54)	0.24
M2	3065	284325	4988150	20	0.176	336	2.006	3827	0.512	15671	>99.9	<<1	7.7 ± 1.0				
M3	3005	284575	4988225	20	0.219	422	1.560	3014	0.322	14121	>99.9	<<1	7.8 ± 0.8			1.20 ± 0.04 (64)	0.31
M4	2920	284600	4988388	20	0.208	372	2.302	4109	0.512	15671	48.2	6	8.0 ± 1.0				
M5	2805	284638	4988663	20	0.242	455	2.560	4798	0.324	14121	>99.9	<<1	5.3 ± 0.6	13.5 ± 0.2 (89)	2.2	1.36 ± 0.03 (62)	0.20
M6	2715	284725	4988838	20	0.533	389	6.754	4926	0.512	15671	>99.9	<<1	7.0 ± 0.8				
M7	2610	284752	4989217	20	0.303	395	2.470	3219	0.326	14121	99.8	<<1	6.9 ± 0.8	14.4 ± 0.1 (106)	1.2	1.66 ± 0.03 (87)	0.32
M9	2360	285450	4989475	8	0.062	49	0.759	604	0.336	14121	47.3	2	4.7 ± 1.4				
M10	2200	285413	4989963	20	0.075	138	0.736	1353	0.339	14121	>99.9	<<1	6.0 ± 1.0			1.21 ± 0.03 (47)	0.21
M11	1900	285868	4990552	20	0.013	357	0.205	5866	0.334	14121	99.8	<<1	3.5 ± 0.4				
M12	1780	285730	4990614	19	0.173	207	2.687	3224	0.512	15671	99.0	<<1	5.7 ± 0.8			1.08 ± 0.03 (37)	0.18
M13	1720	285588	4990647	20	0.209	354	2.749	4655	0.512	15671	>99.9	<<1	6.8 ± 0.8				
M15	1480	287600	4991025	20	0.124	229	2.566	4726	0.512	15671	99.2	<<1	4.3 ± 0.6				
M16	1400	286038	4991488	20	0.044	83	1.230	2308	0.512	15671	>99.9	<<1	3.2 ± 0.8				
M17	1310	283588	4990975	20	0.059	97	1.195	1963	0.512	15671	>99.9	<<1	4.4 ± 1.0				

Table II.3.5. *Apatite fission-track data from La Meije peak, French western Alps. All age determinations were performed by E. Labrin with ζ = 346.6 ± 6.3 for glass dosimeter NBS962; all ages are reported as central ages [Galbraith, 2005]. All samples were etched in 5 M HNO_3 at 20 °C for 20 s. Eastings and Northings in Insitut Géographique National Lambert-III reference frame. N = number of grains counted; ρ_s = spontaneous track density; ρ_i = induced track density; ρ_d = dosimeter track density; N_s, N_i, N_d = number of tracks counted to determine the reported track densities; $P(\chi^2)$ = Chi-square probability that the single grain ages represent one population; D = age dispersion. Note that due to relatively low numbers of track counts (≤ 5 in several grains for all samples except M2, M3, M4), $P(\chi^2)$ may be overestimated [Galbraith, 2005]. MTL = mean confined horizontal track length; D_{par} = etch-pit width parallel to the C-axis; StDev = Standard Deviation; numbers in parenthesis in MTL and D_{par} columns are number of track lengths / widths measured.*

II.4 - Rethinking low-temperature thermochronology data sampling and modelling strategies for denudation and relief histories quantification

Pierre G. Valla [1], Peter A. van der Beek [1], and Jean Braun [1]

[1] LGCA-OSUG, Université de Grenoble, CNRS, BP 53, F-38041 Grenoble, France

Abstract

We assess the importance of thermochronology data sampling and modelling strategies for correctly estimating mountain belt exhumation. Thermochronological age-elevation profiles have been widely used to infer exhumation histories; however, recent studies have shown that age-elevation relationships may not be the most pertinent for quantifying both denudation and relief evolution. Here, we investigate the potential ability of combining different thermochronology data sampling schemes with numerical modelling to better constrain denudation rates and relief changes. We produce synthetic thermochronology datasets on a real topography under a specific exhumation and relief scenario using the thermal-kinematic model *Pecube*. We then adopt an inverse approach based on the *Neighbourhood Algorithm* to quantitatively assess the resolution of different thermochronology datasets collected following elevation profiles, long transect and valley bottom sampling. We also test the effect of the modelling approach on denudation and relief predictions, especially the influence of the topographic grid resolution and of potential constraints on the geothermal gradient. Our results first show that thermochronological sampling along a single elevation profile does not allow to quantitatively constrain both denudation and relief histories. Numerical outputs are highly improved when combining elevation profiles along different valleys, when using long transect or combining valley bottom samples with an elevation profile. The resolution with which relief evolution can be constrained may be increased by a factor of 2 when using dense spatial datasets. Results of thermal parameter inversions suggest that the geothermal gradient may be better estimated using elevation profiles or long transect sampling rather than using valley bottom samples. Simulations with different model topography resolutions show that degrading the resolution for computational efficiency may result in a loss of quantitative information on denudation rates and relief. In summary, we highlight that both thermochronological sampling strategies and modelling approach concerning thermal parameters or model topography resolution could have an important effect on predicted

denudation and relief histories. Care should thus be taken when designing such studies and interpreting their results in terms of mountain belt evolution.

II.4.1 - Introduction

Low-temperature thermochronology has been widely used to quantitatively study exhumation evolution of mountain belts [*e.g.*, *Gallagher et al.*, 1998; *Braun*, 2005; *Reiners and Brandon*, 2006]. Apatite fission track (AFT) [*e.g.*, *Hurford*, 1991; *Fitzgerald et al.*, 1995; *Gallagher et al.*, 1998] and (U-Th)/He (AHe) [*Farley*, 2002; *Ehlers and Farley*, 2003] data have been traditionally reported in the last decades to infer exhumation histories in specific areas. Moreover, low-temperature thermochronology may provide useful constraints for assessing paleo-topography and relief development [*e.g.*, *Clark et al.*, 2005; *Reiners*, 2007]. Many studies have shown the effect of steady-state topography on thermochronology data [*e.g.*, *Stüwe et al.*, 1994; *Mancktelow and Grasemann*, 1997]; however, potential effects of time-varying topography on age-elevation relationships are more difficult to assess [*Braun*, 2002a; *Foeken et al.*, 2007].

Thermochronology data sampling has been widely focused on obtaining age-elevation profiles, *i.e.*, datasets of either AFT or AHe ages (or both) collected along a steep elevation transect [*e.g.*, *Wagner and Reimer*, 1972; *Fitzgerald et al.*, 1995]. Age-elevation relationships allow inferring one-dimensional apparent exhumation rates over a specific time window, and are in theory independent of any assumed geothermal gradient. One-dimensional consideration of age-elevation relationships thus remains the most direct way to interpret thermochronology data; however, topographic effects on thermochronology data cannot be easily extracted from age-elevation relationships [*Braun*, 2002a], and recent modelling studies suggest that constraining mountain belt paleo-relief proved to be difficult when using age-elevation profiles [*Vernon et al.*, 2009; *van der Beek et al.*, 2010], even when combining large datasets and multiple thermochronometers [*Valla et al.*, 2010b].

Recent developments in numerical modelling offer tools for interpreting low-temperature thermochronology data, either considering each sample individually [*e.g.*, *Ketcham*, 2005] or exploiting the spatial correlation between samples [*Gallagher et al.*, 2005a, b; *Braun et al.*, 2006] to quantitatively derive thermal histories and eventually constrain both denudation and relief development. *Braun* [2002b] also recently proposed a novel approach to assess paleo-

relief by considering thermochronological sampling along a horizontal transect, using the spatial coherence between topography and thermochronology data to determine both a regional denudation rate and a rate of relief change [*Herman et al.*, 2007; 2010b; *Beucher et al.*, submitted]. However, the main limitation of this spectral method is that it assumes a spatially and temporally constant denudation history, and it only provides an upper bound on this denudation timing or on the age of relief change.

Numerical modelling thus offers the unique possibility to exploit dense spatial datasets either with or without any specific spatial relationship [*Braun and van der Beek*, 2004; *Gallagher et al.*, 2005a, b]. In this study, we want to assess under what sampling and modelling conditions quantitative constraints on denudation rates and relief evolution can be best extracted from low-temperature thermochronology. We define different 3D sampling strategies within a specified topography and test whether each sampling scheme permits deriving denudation rates, but also relief history. Moreover, our objective is to measure to what extent the modelling approach, especially the spatial resolution of the model grid or any imposed constraint on the geothermal gradient, can bias predicted estimates on denudation and relief histories.

Similar studies [*Valla et al.*, 2010b; *van der Beek et al.*, 2010; *Glotzbach et al.*, submitted] have recently attempted to extract denudation and relief independent information from thermochronology data by combining the three-dimensional thermal-kinematic model *Pecube* [*Braun*, 2003], which predicts thermal histories and thermochronological ages from an input denudation and relief history, with an inversion scheme based on the *Neighbourhood Algorithm* [*Sambridge*, 1999a, b] to search the parameter space, extract best-fitting scenarios from the data and derive quantitative estimates for the parameters (rates, timing and relief ratios) describing denudation and relief histories.

Here, we adopt a similar numerical approach as *Valla et al.* [2010b]; however, that study specifically focused on the problem of interpreting age-elevation profiles whereas here we consider various 3D spatial sampling strategies [*Gallagher et al.*, 2005b]. Moreover, instead of building a synthetic topography for inverse modelling [*Valla et al.*, 2010b], we use a real topography for predicting synthetic thermochronology data (Figure II.4.1a). We focus on the Ecrins-Pelvoux massif [*van der Beek et al.*, 2010], one of the External Crystalline Massifs (ECMs) within the Western European Alps [*e.g.*, *Dumont et al.*, 2008]. The Neogene

exhumation history of the ECMs has been widely studied in the last few years with contracting views regarding timing, exhumation rates, and the impact of Pliocene-Quaternary climate change on late stage exhumation [*Glotzbach et al.*, 2008; *Reinecker et al.*, 2008; *Vernon et al.*, 2009; *Glotzbach et al.*, 2010; *van der Beek et al.*, 2010]. Furthermore, our synthetic approach is motivated by recent predictions for the exhumation history of the Ecrins-Pelvoux massif from thermochronology data collected along either an elevation profile [van *der Beek et al.*, 2010] or a long transect [*Beucher et al.*, submitted]; both these studies provided precise constraints on denudation histories but could not resolve relief evolution quantitatively.

In the following, we first outline our numerical approach, show the synthetic data we will use for inverse simulations and present the inverse method. We then show inversion results and present to what extent predictions of denudation rates, relief change and near-surface thermal structure can be quantitatively determined by various thermochronological sampling strategies. We subsequently present the potential effects of varying the model grid resolution on inversion results, and finally discuss the implications of our findings for thermochronology data sampling strategies in constraining regional denudation rates and/or topographic evolution of mountain belts.

II.4.2 - Modelling approach

II.4.2.1 - Thermal-kinematic modelling and synthetic thermochronology data

The Ecrins-Pelvoux massif topography is characterized by a principal North-South topographic wavelength of ~10 km (Figure II.4.1a) organized around four major valleys (for details and locations see *van der Beek et al.*, 2010). This region comprises ~3 km of relief with summits around 4000 m and valley bottoms at ~1000 m (Figure II.4.1a). The Ecrins-Pelvoux massif has been chosen for our study as it forms a homogeneous area regarding Neogene exhumation and recent denudation histories [*Delunel et al.*, 2010b; *van der Beek et al.*, 2010], *i.e.*, no major active fault structure crosses the massif and consequently its exhumation history can be assumed to be spatially uniform [*van der Beek et al.*, 2010].

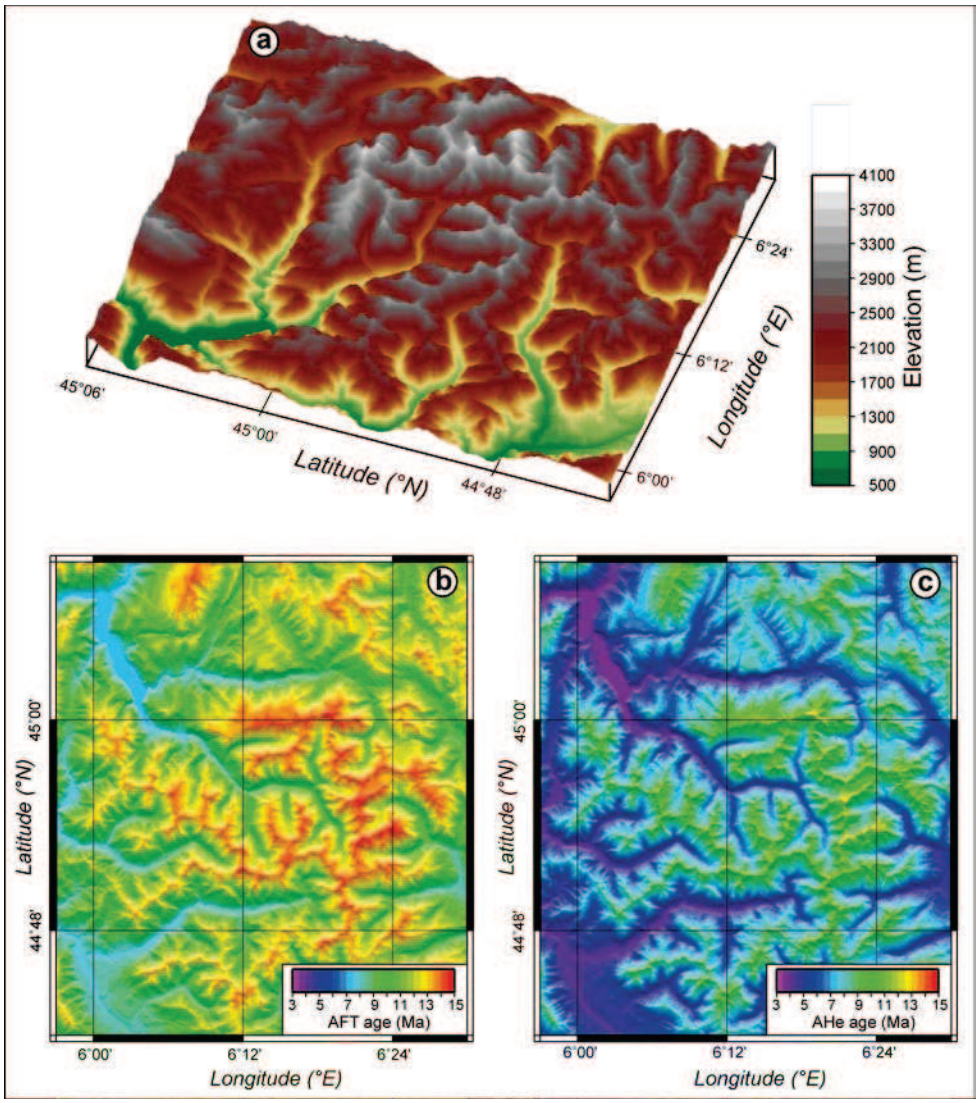

Figure II.4.1. *a) 3D map view of the modelling area (90-m resolution SRTM of the Ecrins-Pelvoux massif, Western Alps, France) used to produce AFT and AHe ages maps (b, c). This area shows a high-relief landscape, with valley bottoms at around 500-1000 m and summits over 4000 m elevation. b-c) Apatite fission track (b) and (U-Th)/He (c) age map produced using Pecube [Braun, 2003; Table II.4.1] and simulating a relief increase scenario of 50% (R_{input} = 0.5) during the last 3 Ma (T_{input}). The constant background denudation rate is 0.3 km Myr^{-1} (E_{1input} = E_{2input}) and resulting maximum rate of relief increase over the last 3 Ma is ~0.5 km Myr^{-1} (see text for discussion).*

Based on this topography, we predicted synthetic thermochronology data using the *Pecube* model [*Braun*, 2003]. *Pecube* is a 3D thermal-kinematic model that calculates the thermal structure through time within a crustal block (Table II.4.1) and provides thermal histories for rock particles that will end up at the surface of the model, taking into account the effects of an evolving topography (for modelling details, see *Braun*, 2003; *Valla et al.*, 2010b). The *Pecube*

finite-element code allows constraining exhumation scenarios through time, described as discrete phases with imposed denudation rates and paleo-reliefs.

Relief evolution is described in *Pecube* using the relief ratio *R* that quantifies the rate of relief change between two phases (*R* = 0: no relief, *i.e.*, the paleo-relief is a plateau at maximum elevation; *R* = 1: the paleo-relief is equal to present-day conditions; and *R* = 2: the paleo-relief is twice as large as the present-day relief) and is simulated through preferential valley incision; *i.e.*, ridges remain at a constant elevation but valley bottoms are lowered, implying spatially varying exhumation rates (see *Valla et al.*, 2010b for a complete description of *R*). Isostatic rebound in response to this crustal unloading is numerically calculated (Table II.4.1) and provides spatially variable additional exhumation rates.

Parameter (unit)	*Inversions value*
Crustal thickness (km)	40
Crustal density (kg m^{-3})	2700
Sublithospheric mantle density (kg m^{-3})	3200
Young's modulus (Pa)	1.10^{11}
Poisson ratio	0.25
Equivalent elastic thickness (km)	25
Thermal diffusivity (km^2 Myr^{-1})	25
Basal crustal temperature (°C)	600
Crustal heat production (°C Myr^{-1})	0.8
Sea-level temperature (°C)	15
Atmospheric lapse rate (°C km^{-1})	6

Table II.4.1. *Thermal-kinematic and elastic parameters used in Pecube. Crustal thickness and basal temperature are set to obtain a geothermal gradient of ~20-25 °C* km^{-1}*. Poisson ratio, Young's modulus and equivalent elastic thickness are used for calculating the isostatic rebound in response to relief change. Equivalent elastic thickness is set to a value that simulates moderate isostatic rebound [Valla et al., 2010b; van der Beek et al., 2010].*

Predicted thermal histories are then used to calculate cooling ages for model nodes that lie at the topographic surface at the end of the model experiment. In this study, we focus on late-stage exhumation histories and thus only compute low-temperature thermochronology data such as apatite fission-track (AFT) and (U-Th)/He (AHe) ages, as well as mean confined track lengths (MTL).

Thermal histories are translated into AHe ages using a simple forward model for He production-diffusion-ejection [*Farley*, 2000]. AFT ages are calculated using a forward model for AFT annealing [*Green et al.*, 1989; *Stephenson et al.*, 2006]. We acknowledge that using these simple algorithms does not completely reflect the complex annealing and diffusion processes included in low-temperature thermochronology [*Ketcham*, 2005; *Flowers et al.*, 2009; *Gautheron et al.*, 2009]. However, as discussed in *Valla et al.* [2010b], forward models used for AFT and AHe age predictions are similar for both generating the synthetic data and resolving the inverse problem; the results shown here are thus largely independent of the specific age-prediction models.

To produce the synthetic datasets that we will use to constrain our inversion procedure, we define a 2-phase exhumation scenario in *Pecube* with steady-state denudation (0.3 km Myr^{-1}) over 15 Myr and a 50% relief increase (R = 0.5) since 3 Ma (T = 3 Ma). This exhumation scenario simulates a moderate relief increase (~1.5 km of relief development over the last 3 Myr, *i.e.*, a mean relief growth rate of ~0.5 km Myr^{-1}) associated with a relatively low and constant background denudation rate (0.3 km Myr^{-1}). Thermochronology data are predicted following this input scenario on a very high resolution grid (90-m, Figures II.4.1b, c) to ensure that the finite amplitude topography effects on the crustal thermal structure are properly resolved by the numerical model. AFT and AHe maps show a significant age-contrast between valley bottoms (AFT ~7 Ma and AHe ~3-4 Ma) and ridges (AFT ~15 Ma and AHe ~12-13 Ma). Moreover, synthetic AFT and AHe data plotted against elevation provide a constant apparent exhumation rate of ~0.34 and 0.43 km Myr^{-1}, respectively (correlation coefficient $R^2 \approx 0.96$ and 0.99, respectively) that slightly overestimates the input background denudation rate due to recent local additional exhumation following topographic amplification. Note that our synthetic AFT and AHe data are in agreement with observed thermochronological ages in the area [*van der Beek et al.*, 2010; *Beucher et al.*, submitted], confirming that the imposed tectono-geomorphic scenario we define may be consistent with observed case studies [*van der Beek et al.*, 2010; *Beucher et al.*, submitted].

We sampled both AFT (and associated MTL) and AHe maps following five different strategies: (1) a single elevation profile (Figure II.4.2a, yellow circles: *1_Profile*), partly based on data locations reported by *van der Beek et al.* [2010]; (2) 3 elevation profiles sampling the three main valleys of the massif (Figure II.4.2a, black circles: *3_Profiles*); (3) valley bottom samples along the major valleys (Figure II.4.2a, white circles: *Valleys*); (4) an elevation

profile combined with valley bottom samples (Figure II.4.2b, yellow circles: *Profile + Valleys*); and finally (5) a long transect across the massif [*Beucher et al.*, submitted] following the sampling strategy recommended by *Braun* [2002b] (Figure II.4.2b, red circles: *Transect*). All sampling schemes combine 20 samples in total with both AFT, AHe and MTL data to allow comparisons on predictions for different sampling strategies but a similar quality dataset.

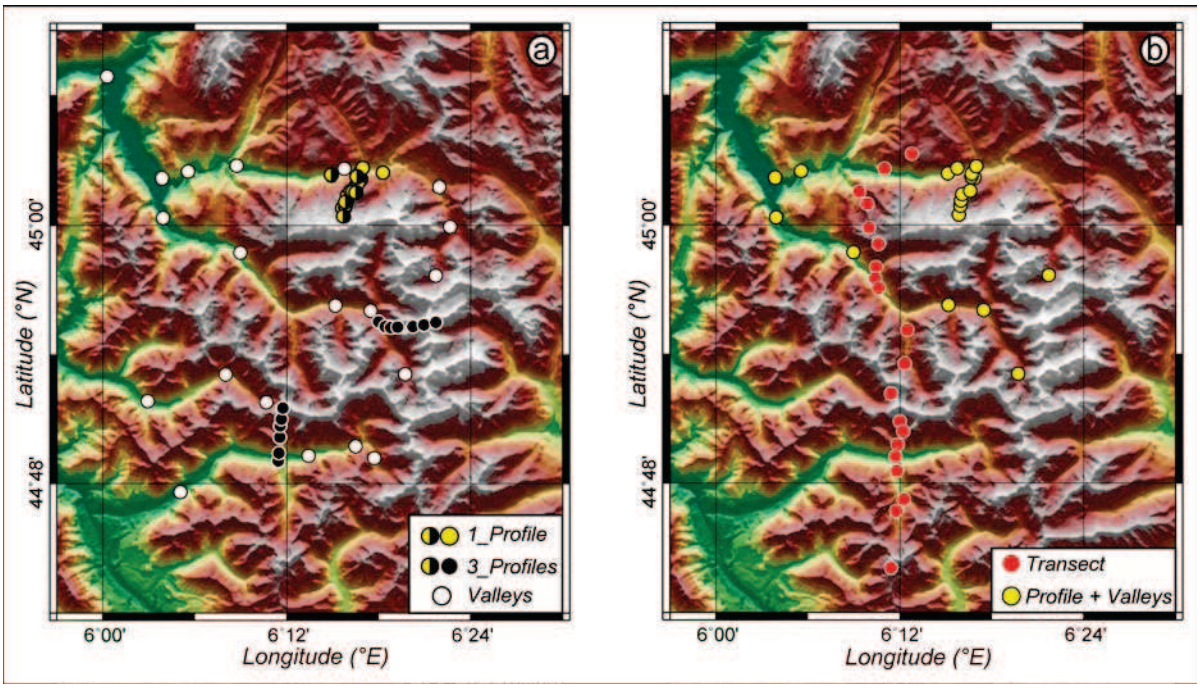

Figure II.4.2. *Sample location maps for the 5 different sampling schemes. a) Sample locations for sampling schemes 1_Profile (yellow circles, based on van der Beek et al., 2010), 3_Profiles (black circles) and Valleys (white circles). b) Sample locations for sampling schemes Transect (yellow circles, based on Beucher et al., submitted) and Profile + Valleys (yellow circles, partly based on van der Beek et al., 2010). Age predictions for each location are provided by AFT (and associated MTL) and AHe 90-m resolution grids (Fig. II.4.1).*

We wish to test the influence of the model resolution on relief and denudation predictions. For this, we repeat all inversions using four different resolution grids based on the interpolation of the initial topography at resolutions ranging between 500-m and 2-km (Figure II.4.3). We progressively degrade the topographic model from quite "high-resolution" grids (500- and 750-m, respectively Figure II.4.3a and b) including all information on relief details, to "low-resolution" grids (1- and 2-km, Figures II.4.2c and d) where only the main relief features remain.

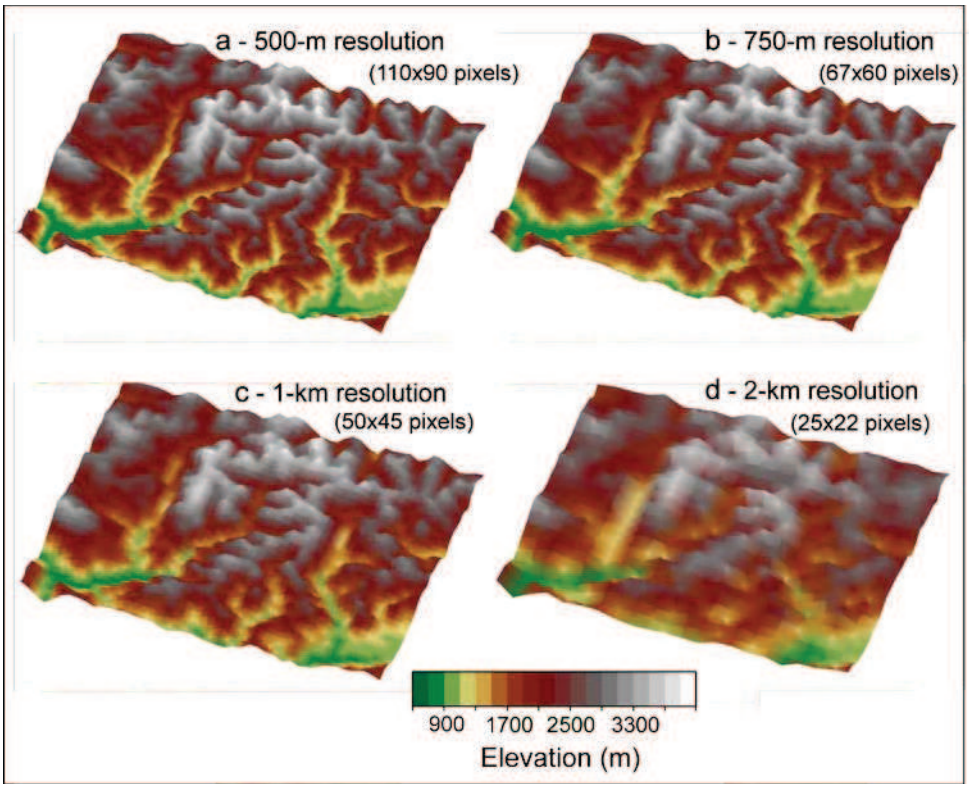

Figure II.4.3. *3D views of the modelling area for different grid resolution (a: 500-m; b: 750-m; c: 1-km and d: 2-km, number of pixels is indicated for each grid). Those grids are used as a sensitivity analysis for Profile + Valleys sampling scheme (Fig. II.4.2b) using AFT + AHe + MTL data (Table II.4.4 and Fig. II.4.5).*

II.4.2.2 - Inverse thermal-kinematic modelling

We first test the importance of the thermochronological sampling strategy for constraining relief and denudation histories. Thermal-kinematic data used as input parameters in *Pecube* are given in Table II.4.1; the geothermal gradient (defined by the basal crustal temperature *Temp* and the crustal heat production *H_prod*, see Table II.4.1 for values) is fixed to produce a geothermal gradient of ~20-25 °C km^{-1}, and each inverse simulation is run over 15 Myr. For each sampling scheme, we run inversions to recover 4 parameters (E_1, E_2, T, and R) used to describe the imposed tectono-geomorphic scenario of the input thermochronology datasets (AFT, AHe, AFT + AHe, AFT + MTL, and AFT + AHe + MTL data), and test what type of thermochronometer is more or less useful to quantify relief and denudation histories in different sampling situations. We also define a range for each parameter, in which the inversion procedure will search: (1) denudation rate of the first phase (E_1 : 0-2 km Myr^{-1}); (2) denudation rate of the second phase (E_2 : 0-2 km Myr^{-1}); (3) transition time (T : 0.5-14.5 Ma); and (4) relief factor (R : 0-2).

In a second set of inversions, we test the ability of the five different sampling schemes to constrain not only relief and denudation histories, but also to retrieve the geothermal gradient (*Temp* and *H_prod* parameters, Table II.4.3). To achieve this, we run five additional inverse simulations with AFT + AHe + MTL dataset and 6 inverted parameters (E_1, E_2, T, and R as described previously; and *Temp* : 500-800 °C, and *H_prod* : 0-3 °C Myr^{-1}).

Finally, we test the influence of the grid resolution on relief and denudation predictions. We select only one sampling scheme (*Profile* + *Valleys*, Figure II.4.2b), and one dataset (AFT + AHe + MTL data) to run five inverse simulations (4 inverted parameters: E_1, E_2, T, and R as initially described) for the different model grid resolutions (from 500 m to 2 km, Figure II.4.3 and Table II.4.4).

To perform the inversions, we use the *Neighbourhood Algorithm* (*NA*) of *Sambridge* [1999a, b]. *NA* is a two-stage numerical procedure for non-linear inverse problems, and allows to: (1) efficiently explore a multi-dimensional parameter space to find best-fitting models to an input dataset (*NA* sampling stage); (2) derive Bayesian estimates on inverted parameters from the ensemble of models run during the sampling stage (*NA* appraisal stage).

The sampling stage iteratively explores the multi-dimensional parameter space and concentrates on regions where parameter values minimize the misfit to the data. *NA* makes use of simple geometrical concepts by dividing the entire parameter space into a set of Voronoi cells, which represent the nearest neighbourhood about each point. At each step, *NA* samples a forward model centred on each Voronoi cell and calculates a misfit surface. Subsequent iterations make use of this misfit surface to randomly sample in regions of the parameter space where the misfit function is minimized. This numerical approach ensures optimised values of the misfit function in an iterative scheme. The sampling stage is controlled by tuning parameters determining the number of iterations, the number of forward models generated at each iteration, and the number of Voronoi cells to re-sample after each iteration. Varying these parameters will make the *NA* method either more explorative of the multi-dimensional parameter space, or more exploitative and faster in converging towards potential misfit minima [*Sambridge*, 1999a]. Based on previous studies [*Valla et al.*, 2010b; *Glotzbach et al.*, submitted], we choose to run for each inversion ~5000 models distributed in 35 iterations, and 50% of models re-sampling at each iteration.

In our approach, we use a weighted least-squares misfit function ψ:

$$\psi = \sqrt{\sum_{i=1}^{N}\sum_{j=1}^{M}\frac{({}^{i}\alpha_{j,\mathrm{mod}} - {}^{i}\alpha_{j,dat})^2}{{}^{i}\sigma_{j}{}^{2}}} \qquad \text{(II.4.1)}$$

where N is the number of datasets (AFT, AHe, AFT + AHe, AFT + MTL, or AFT + AHe + MTL data), M is the number of samples in each dataset (20 samples in total for each sampling scheme), ${}^{i}\alpha_{j,\mathrm{mod}}$ and ${}^{i}\alpha_{j,dat}$ are respectively predicted and observed values for AFT/AHe ages or MTL, and ${}^{i}\sigma_{j}$ is the uncertainty on the data. Here, we choose to use constant synthetic uncertainties (σ) of ±0.5 Ma and ±0.5 µm for AFT/AHe ages and MTL, respectively, to provide an equal weight on all samples for misfit calculations [*Valla et al.*, 2010b].

During the second or *NA* appraisal stage [*Sambridge*, 1999b], the algorithm resamples the entire ensemble of models that were generated during the first stage to provide Bayesian measures of resolution in the form of marginal probability density functions (PDFs) for each parameter.

II.4.3 - Inversion results

All inverse simulations provided best misfits close to zero as we used synthetic data, consequently the *NA* sampling stage results do not contain enough resolution to discriminate between different topographic sampling and modelling strategies. This is why we focus on 1D PDFs (Bayesian estimates and associated uncertainties compared to the input parameter values) to explore these potential differences. We first present results of each sampling scheme to assess differences in using various combinations of low-temperature thermochronometers. We then compare the different sampling schemes to discuss how best to predict denudation and relief histories. Finally, we show modelling results for inverting the geothermal gradient and testing model grid resolution. We would discuss the reasons for the observed differences in modelling results (resolution and errors on parameters estimates) in the next section.

II.4.3.1 - Sampling strategy results

The first sampling scheme (*1_Profile*, Table II.4.2) combines 20 samples along an elevation profile. Inversion results yield accurate predictions for E_1 (E_1 = 0.23-0.28 km Myr^{-1}; E_{1input} = 0.3 km Myr^{-1}) for all input thermochronological datasets with uncertainties ~20-40% except when using AHe data alone, for which the uncertainty rises to ~80%. Estimates on E_2 are less precise (uncertainties ~30-80%) and slightly overestimated when using AFT data alone or AFT + MTL data (E_2 ~0.4 km Myr^{-1}; E_{2input} = 0.3 km Myr^{-1}). Only AHe data alone or combined with AFT ages provide accurate predictions for E_2 (respectively E_2 = 0.33 ±0.11 and 0.28 ±0.18 km Myr^{-1}). However, adding MTL data does not improve inversion predictions (Table II.4.2).

Timing predictions are underestimated when using AFT alone, AFT + MTL or AFT + AHe + MTL data (T = 1-1.4 Ma) and clearly overestimated for AHe alone (T = 12.2 Ma). Only the AFT + AHe inversion (T = 2.8 Ma) gives predicted value of T close to the input value (T_{input} = 3 Ma). However, in all cases uncertainties on T predictions are very high (>100% for all inversions).

Relief predictions are in agreement with the input value (R_{input} = 0.5) when we use AHe data alone or combined with AFT ages (respectively R = 0.53 ±0.58 and 0.63 ±0.55). In contrast, using AFT ages alone or combined with MTL measurements predicts respectively an underestimated (R = 0.93 ±0.59) and overestimated (R = 0.18 +0.93/-0.18) relief increase. Combining both AFT and AHe ages with MTL does not provide accurate estimate on R (R = 1.08 ±0.55; *i.e.*, between ~50% increasing and 50% decreasing topographic relief). Moreover, as for T predictions, uncertainties on R are higher than 100% for all inversions.

In summary, inverse simulations using thermochronology data along a single elevation profile provide quite accurate estimates on denudation histories (E_1 and E_2) with moderate to high uncertainties depending on the dataset (~30 to 80%). In contrast, T and R estimates are not in agreement with input values and systematically present uncertainties >100%. Furthermore, best estimates are generally obtained when using AHe ages alone or combined with AFT data, and adding MTL measurement does not improve denudation and relief predictions.

Parameter (unit)	***E_1 (km Myr^{-1})***	***E_2 (km Myr^{-1})***	***T (Ma)***	***R***
Range / Input	0-2 / 0.3	0-2 / 0.3	0.5-14.5 / 3	0-2 / 0.5
1_Profile				
AFT	0.28 ±0.13	0.38 ±0.26	1.4 +5.3/-0.9	0.93 ±0.59
AHe	0.28 ±0.23	0.33 ±0.11	12.2 +2.3/-5.2	0.53 ±0.58
AFT + AHe	0.28 ±0.06	0.28 ±0.18	2.8 +3.9/-2.3	0.63 ±0.55
AFT + MTL	0.23 ±0.1	0.43 ±0.24	1.0 +8/-0.5	0.18 +0.93/-0.18
AFT + AHe + MTL	0.28 ±0.06	0.28 ±0.27	1.0 +6.4/-0.6	1.08 ±0.55
Best Estimate (%Input)	***-7% ±20%***	***+10% ±37%***	***-7% ±130%***	***+6% ±116%***
Data	***AFT + AHe***	***AHe***	***AFT + AHe***	***AHe***
3_Profiles				
AFT	0.28 ±0.12	0.28 ±0.21	2.1 +5.5/-1.6	0.38 ±0.41
AHe	0.23 ±0.1	0.28 ±0.13	6.9 ±3.8	0.53 ±0.32
AFT + AHe	0.28 ±0.3	0.28 ±0.14	1.0 +3.9/-0.5	0.58 ±0.29
AFT + MTL	0.28 ±0.08	0.33 ±0.19	1.4 +5.9/-0.9	0.58 ±0.40
AFT + AHe + MTL	0.28 ±0.05	0.28 ±0.15	1.7 +3.8/-1.2	0.18 +0.30/-0.18
Best Estimate (%Input)	***-7% ±17%***	***-7% ±43%***	***-43% ±127%***	***+6% ±64%***
Data	***AFT + AHe + MTL***	***AHe***	***AFT + AHe + MTL***	***AHe***
Valleys				
AFT	0.33 ±0.29	0.28 ±0.11	11.9 +2.6/-5.1	0.08 +0.37/-0.08
AHe	0.33 +0.56/-0.33	0.23 ±0.12	6.6 ±3.0	0.03 +0.50/-0.03
AFT + AHe	0.28 ±0.05	0.23 ±0.11	0.7 +4.8/-0.2	0.48 ±0.25
AFT + MTL	0.28 ±0.06	0.33 ±0.10	2.1 +5.3/-1.6	0.33 ±0.21
AFT + AHe + MTL	0.28 ±0.01	0.28 ±0.11	3.5 ±2.3	0.38 ±0.22
Best Estimate (%Input)	***-7% ±3%***	***-7% ±37%***	***-17% ±77%***	***-4% ±50%***
Data	***AFT + AHe + MTL***	***AFT + AHe + MTL***	***AFT + AHe + MTL***	***AFT + AHe***
Profile + Valleys				
AFT	0.23 ±0.12	0.28 ±0.13	3.8 +5.0/-3.3	0.03 +0.55/-0.03
AHe	0.23 ±0.11	0.28 ±0.14	2.8 +3.7/-2.3	0.03 +0.56/-0.03
AFT + AHe	0.28 ±0.04	0.28 ±0.14	0.7 +3.6/-0.2	0.38 ±0.24
AFT + MTL	0.28 ±0.08	0.33 ±0.12	1.0 +6.5/-0.5	0.28 ±0.23
AFT + AHe + MTL	0.28 ±0.01	0.23 ±0.11	2.1 +2.6/-1.6	0.28 ±0.21
Best Estimate (%Input)	***-7% ±3%***	***-7% ±47%***	***-30% ±87%***	***-24% ±48%***
Data	***AFT + AHe + MTL***	***AFT + AHe***	***AFT + AHe + MTL***	***AFT + AHe***
Transect				
AFT	0.23 ±0.12	0.28 ±0.17	2.1 +7.0/-1.6	0.18 +0.44/-0.18
AHe	0.28 ±0.15	0.43 ±0.18	1.7 +6.4/-1.2	0.48 +0.65/-0.48
AFT + AHe	0.28 ±0.32	0.43 ±0.22	1.0 +3.4/-0.5	0.58 ±0.39
AFT + MTL	0.28 ±0.07	0.43 ±0.21	6.3 ±3.8	0.38 ±0.62
AFT + AHe + MTL	0.28 ±0.03	0.28 ±0.2	0.7 +4.71/-0.2	0.48 ±0.37
Best Estimate (%Input)	***-7% ±10%***	***-7% ±57%***	***-67% ±113%***	***-4% ±74%***
Data	***AFT + AHe + MTL***	***AFT***	***AFT + AHe***	***AFT + AHe + MTL***

Table II.4.2. *Bayesian estimates after the NA appraisal stage for input parameters E_1, E_2, Time and R (see text for description and discussion). The second line reports parameters range and input values to calculate the input thermochronology data (Fig. II.4.1b, c). Parameters optimal values and associated uncertainties (mode ±1σ) are given in the following lines for various sampling schemes (Fig. II.4.2) and different input thermochronology datasets. Best parameter estimates (and associated input thermochronology dataset) are also reported as percentage errors and uncertainties regarding input values (%Input).*

Thermochronological sampling along three different elevation profiles (*3_Profiles*, Table II.4.2) provides similar predictions for E_1, even though the mean uncertainty is slightly reduced (~20-40%, except for AFT + AHe data for which the uncertainty rises to 100%). E_2 estimates are accurate for all inversions, but uncertainties remain quite high (~30-80%). T predictions are the same as previously, with systematic underestimates (T = 1.0-2.1 Ma) except for the AHe inversion (T = 6.9 ±3.8 Ma); all inversions uncertainties also remain higher than 100%. Relief predictions are much better than previous simulations using a single age-elevation profile. All inversions predict a relief increase (R = 0.18-0.58), and the inverse simulation combining all thermochronometric systems clearly overestimates the R input value (R = 0.18 +0.30/-0.18). Uncertainties on R predictions are also reduced (~65-90%, Table II.4.2). As when using a single elevation profile, best estimates on E_2 and R (recent exhumation history) are provided using AHe data; however, for both timing T and E_1 the most accurate predictions are obtained when using the whole thermochronological dataset (AFT + AHe + MTL data, Table II.4.2).

Sampling along valley bottoms (*Valleys*, Table II.4.2) provides accurate predictions for E_1 and E_2. Predicted uncertainties on E_1 are low only when using at least two thermochronometers (~3-20% for AFT + AHe, AFT + MTL and AFT + AHe + MTL data) but are much higher when using AFT or AHe data alone (~100-200%). In contrast, uncertainties on E_2 are fairly constant, whatever the dataset we use (~40-60%). Similarly, constrains on T are very poor using AFT or AHe data alone (T = 11.9 +2.6/-5.1 and 6.6 ±3.0 Ma, respectively) and are better when combining thermochronometers (best estimate T = 3.5 ±2.3 Ma for AFT + AHe + MTL data). Uncertainties on T are variable depending on the dataset we use (>100% for all inversions except for AFT + AHe + MTL for which the uncertainty is ~80%). Finally, relief increase is highly overestimated when using AFT or AHe data alone (R = 0.03-0.08) and predictions are not precise (uncertainties ~100%); however, combining the thermochronometers provides accurate values of R and reduced uncertainties (R = 0.33-0.48 and uncertainties are ~50%). In summary, this specific sampling scheme provides precise estimates on denudation history (E_1 and E_2) and satisfying predictions on T and R; however this requires combining at least two different thermochronometers (best estimates for AFT + AHe + MTL dataset).

Combining valley bottom samples with an elevation profile (*Profile + Valleys*, Table II.4.2) provides accurate and precise predictions for both E_1 and E_2 (E_1 = 0.23-0.28 ±0.01-0.12 km Myr^{-1} and E_2 = 0.23-0.33 ±0.11-0.14 km Myr^{-1}). T estimates are similar for all inversions and mostly underestimate the timing of change (T = 0.7-3.8 Ma), uncertainties on T are around or above 100%. Similarly to the *Valleys* sampling, the relief change R is highly overestimated when using AFT or AHe data alone (R = 0.03 +0.55/-0.03). Combining thermochronometers still overestimates the relief change (R = 0.28-0.38) but uncertainties on R are reduced to ~50%. Combining valley bottom samples with an elevation profile (still 20 samples in total) thus provides good estimates on E_1, E_2 and T for nearly all thermochronometer combinations even though best estimates on inverted parameters, especially on relief change, are obtained when using two or more thermochronometers.

The last inversion simulates sampling a long transect (*Transect*, Table II.4.2). This sampling scheme allows obtaining accurate estimates on E_1 with uncertainties around 10-40% (except for AFT + AHe data, for which the uncertainty rises to ~100%); however, E_2 predictions are slightly overestimated for AHe, AFT + AHe and AFT + MTL datasets (E_2 ~0.4 km Myr^{-1}, associated uncertainties ~60%). The timing parameter is also not well resolved (T = 0.7-6.3 Ma) with prediction uncertainties higher than 100-200%. Finally, relief estimates are quite accurate (R = 0.18-0.58) but associated uncertainties are between 75 and 130%. In summary, sampling a long transect provides accurate predictions on denudation rates (E_1 and E_2), however, timing is not well constrained and relief estimates are accurate but associated with quite high uncertainties. Moreover, our inversions results show that in this sampling configuration, using at least two thermochronometers also seems to enhance predictions on denudation rates and relief evolution.

To better explore the potential differences between the sampling strategies, we now present 1D PDFs of inverted parameters (E_1, E_2, T and R) for each sampling strategy (using the AFT + AHe + MTL dataset, Figure II.4.4). Inverse simulations provide accurate E_1 predictions for all sampling schemes (Figure II.4.4a), even though more precise estimates (uncertainties <10%) are obtained when sampling a long transect, valley bottoms or an elevation profile combined with valley bottoms (respectively *Transect*, *Valleys* and *Profile + Valleys*); uncertainties following sampling along elevation profiles (*1_Profile* and *3_Profiles*) are twice higher (uncertainties ~20%). The accuracy on E_2 estimates is also similar for all sampling schemes and only predicted uncertainties differ. Figure II.4.4b shows that lowest uncertainties

on E_2 predictions are obtained when sampling along valley bottoms (uncertainties are ~40% for *Valleys* and *Profile + Valleys*), the *3_Profiles* sampling scheme provides an uncertainty on E_2 of ~50% while the *Transect* and *1_Profile* sampling strategies yield uncertainties of ~70-90%. Figure II.4.4c confirms that timing (T) is the least resolved parameter with predicted uncertainties of 80-90% for *Valleys* and *Profile + Valleys* sampling schemes, and uncertainties on T higher than 100% for *Transect*, *3_Profiles* and *1_Profile* sampling schemes. Finally, constraints on R (Figure II.4.4d) slightly overestimate the relief increase for *3_Profiles*, *Valleys* and *Profile + Valleys* sampling schemes but provide acceptable uncertainties on R (~50-60%). *Transect* sampling also provides an accurate estimate for R but the associated uncertainty is high (~75%) whereas *1_Profile* does not provide any constraint on R (*i.e.*, it predicts either 50% increasing or decreasing topographic relief).

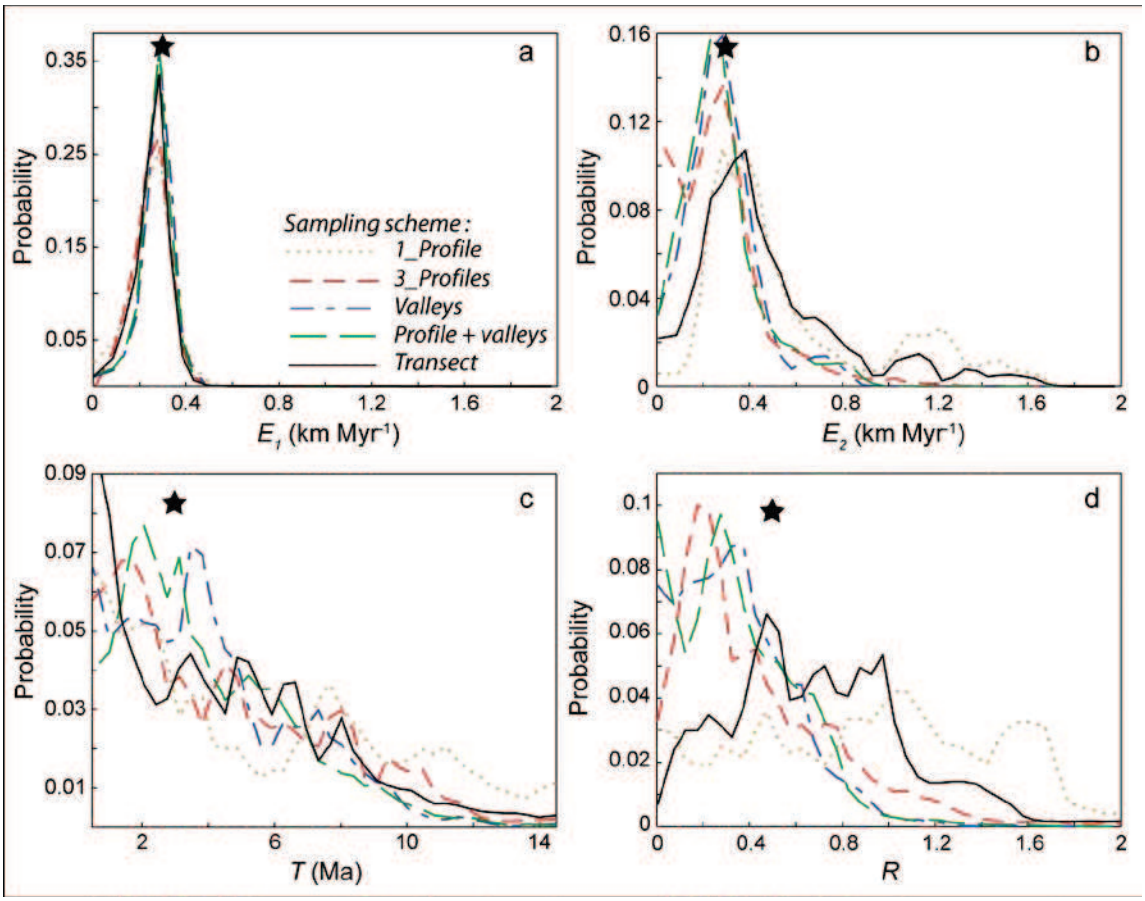

Figure II.4.4. *1D posterior parameter PDF's obtained after the NA appraisal stage for the five different sampling schemes (AFT + AHe + MTL dataset): (a) denudation rate of the first exhumation phase (E_1); (b) denudation rate of the second exhumation phase (E_2); (c) transition time between the two exhumation phases (T); and (d) relief factor between the paleo-relief and the final relief (R). Each line defines an inversion experiment with a sampling scheme (see figure for colour legend and Fig. II.4.2 for sampling locations). Black stars represent the input parameter values.*

II.4.3.2 - Modelling approach results

In all previous inverse simulations, our modelling strategy was to impose both the geothermal gradient (~20-25 °C km^{-1}, Table II.4.1) and the model grid resolution (750-m). In this section, we test how predictions for denudation and relief histories may differ when setting no constraint on the geothermal gradient or changing the model grid resolution.

We first present simulations results inverting both denudation/relief histories (E_1, E_2, T and R) and the geothermal gradient (*Temp* and *H_prod*). We run inversions for all five sampling schemes and use AFT + AHE + MTL data to compare output predictions (Table II.4.3) with previous outcomes (Figure II.4.4). Inverse results on the basal crustal temperature (*Temp*) provide similar underestimates for most of sampling schemes (*Temp* ~520-565 °C; $Temp_{input}$ = 600 °C) except for *3_Profiles* sampling that overestimates the basal temperature (*Temp* = 714 ±80 °C). Moreover, associated uncertainties on *Temp* are very close for all inversions (~11-16%, Table II.4.3). Constraints on the crustal heat production parameter (*H_prod*, Table II.4.3) are less tight. *Profile + Valleys*, *1_Profile* and *3_Profiles* sampling strategies provide accurate estimates (*H_prod* = 0.56-0.94 °C Myr^{-1}; H_prod_{input} = 0.8 °C Myr^{-1}) but estimated uncertainties are relatively high (~80-110%). *Valleys* sampling clearly does not resolve the heat production parameter (*H_prod* = 0.04 +0.65/-0.04 °C Myr^{-1}) whereas best predictions on *H_prod* are provided by the *Transect* inversion (*H_prod* = 1.16 ±0.44 °C Myr^{-1}).

Predictions for E_1 are slightly underestimated for *Transect*, *3_Profiles* and *1_Profile* samplings (E_1 = 0.23 ±0.1 km Myr^{-1}) and all results provide higher uncertainties on E_1 (~30%) compared to imposed geothermal gradient inversions (~3-20%). Output constraints on E_1 are best estimated using *Valleys* and *Profile + Valleys* sampling schemes. Results for E_2 are variable with best predictions for the *3_Profiles* inversion (E_2 = 0.28 ±0.14 km Myr^{-1}). Constrains on E_2 are slightly overestimated for the *Transect* sampling scheme (E_2 = 0.43 ±0.21 km Myr^{-1}) and underestimated for *Valleys* and *Profile + Valleys* sampling schemes (E_2 = 0.23 ±0.19 km Myr^{-1}). However, estimated uncertainties on E_2 are very similar to those obtained when imposing the geothermal gradient (~50-100%, maximum uncertainty for *1_Profile* sampling scheme). Timing predictions are all underestimated (T ~0.7-1.7 Ma) and associated uncertainties are similar to those found during imposed geothermal gradient inversions (~70-230%). Moreover, best estimates on T is given by *Valleys* inversion (T = 1.7 +2.0/-1.2 Ma), in agreement with previous results. Finally, setting no constrain on the

geothermal gradient does not have any effect on relief evolution predictions as *R* estimates are very close to values obtained with an imposed geothermal gradient, and optimal predictions are obtained for *3_Profiles*, *Valleys* and *Profile + Valleys* sampling schemes.

Parameter (unit) Range / Input	E_1 (km Myr^{-1}) 0-2 / 0.3	E_2 (km Myr^{-1}) 0-2 / 0.3	*T (Ma)* 0.5-14.5 / 3	*R* 0-2 / 0.5	*Temp (°C)* 500-800 / 600	*H_prod (°C Myr^{-1})* 0-3 / 0.8
1_Profile						
Mode ±1σ	0.23 ±0.1	0.33 ±0.29	0.7 +3.1/-0.2	1.08 ±0.52	549 +98/-49	0.64 +0.82/-0.64
%Input	(-23% ±33%)	(+10% ±97%)	(-77% ±103%)	(+116% ±104%)	(-9% ±16%)	(-20% ±103%)
3_Profiles						
Mode ±1σ	0.23 ±0.1	0.28 ±0.14	0.7 +6.9/-0.3	0.48 ±0.27	714 ±80	0.94 ±0.66
%Input	(-23% ±33%)	(-7% ±47%)	(-77% ±230%)	(-4% ±54%)	(+19% ±13%)	(+18% ±83%)
Valleys						
Mode ±1σ	0.33 ±0.1	0.23 ±0.19	1.7 +2.0/-1.2	0.33 ±0.21	519 +74/-19	0.04 +0.65/-0.04
%Input	(+10% ±33%)	(-23% ±63%)	(-43% ±67%)	(-34% ±42%)	(-14% ±12%)	(-95% ±81%)
Profile + Valleys						
Mode ±1σ	0.28 ±0.1	0.23 ±0.19	0.7 +5.1/-0.3	0.48 ±0.26	534 +95/-34	0.56 +0.85/-0.56
%Input	(-7% ±33%)	(-23% ±63%)	(-77% ±170%)	(-4% ±52%)	(-11% ±16%)	(-30% ±106%)
Transect						
Mode ±1σ	0.23 ±0.09	0.43 ±0.21	1.4 +4.4/-0.9	0.48 ±0.4	564 ±66	1.16 ±0.44
%Input	(-23% ±30%)	(+43% ±70%)	(-53% ±147%)	(-4% ±80%)	(-6% ±11%)	(+45% ±55%)

Table II.4.3. *Bayesian estimates after the NA appraisal stage for input parameters E_1, E_2, Time, R, Temp and H_prod. The second line reports parameters range and input values for the input thermochronology data generation (Fig. II.4.1b, c). Parameters optimal values and associated uncertainties (mode ±1σ) are given in the following lines for various sampling schemes (Fig. II.4.2; AFT + AHe + MTL dataset). Inversions results are also reported as percentage errors and uncertainties regarding input values (%Input).*

To summarize, numerical inversions with no imposed constraint on the geothermal gradient provide less accurate and precise estimates on E_1 and E_2 parameters, but output results for *T* and *R* parameters are very close to those found with an imposed geothermal gradient. Concerning thermal parameters (*H_prod* and *Temp*), best estimates are given by the *Transect* sampling, while inversions including at least one elevation profile (*Profile + Valleys*, *1_Profile* and *3_Profiles*) provide accurate estimates but associated with relatively high uncertainties; and valley bottom sampling (*Valleys*) does not resolve thermal parameters.

Finally, we present inversion results when varying the topographic grid resolution of the *Pecube* model (Figure II.4.3). We use the *Profile + Valleys* sampling scheme and AFT + AHe + MTL dataset for inverse simulations. Bayesian estimates on E_1, E_2, *T* and *R* parameters are reported in Table II.4.4 and associated 1D PDFs are shown in Figure II.4.5.

Parameter (unit)	***E_1 (km Myr^{-1})***		***E_2 (km Myr^{-1})***		***T (Ma)***		***R***	
Range / Input	**0-2 / 0.3**		**0-2 / 0.3**		**0.5-14.5 / 3**		**0-2 / 0.5**	
Grid_(nx/ny)	***Mode ±1σ***	***%Input***	***Mode ±1σ***	***%Input***	***Mode ±1σ***	***%Input***	***Mode ±1σ***	***%Input***
500-m_(110/90)	0.28 ±0.01	(-7% ±3%)	0.23 ±0.13	(-23% ±43%)	3.1 ±1.9	(+3% ±60%)	0.58 ±0.29	(+16% ±58%)
750-m_(67/60)	0.28 ±0.005	(-7% ±2%)	0.23 ±0.11	(-23% ±37%)	2.1 +2.6/-1.6	(-30% ±87%)	0.28 ±0.21	(-44% ±42%)
1000-m_(50/45)	0.28 ±0.04	(-7% ±13%)	0.23 ±0.12	(-23% ±40%)	1.4 +3.8/-0.9	(-53% ±127%)	0.33 ±0.21	(-34% ±42%)
1500-m_(33/30)	0.28 ±0.06	(-7% ±20%)	0.28 ±0.13	(-7% ±43%)	1.4 +4.9/-0.9	(-53% ±163%)	0.08 +0.43/-0.08	(-84% ±86%)
2000-m_(25/22)	0.33 ±0.14	(+10% ±47%)	0.33 ±0.12	(+10% ±40%)	14.3 +0.2/-9.0	(+376% ±300%)	0.43 ±0.38	(-14% ±76%)

Table II.4.4. *Bayesian estimates after the NA appraisal stage for input parameters E_1, E_2, Time and R. The second line reports parameters range and input values for the input thermochronology data generation (Fig. II.4.1b, c). Parameters optimal values and associated uncertainties (mode ±1σ) are given in the following lines for various grid resolutions (nx/ny: number of pixels in longitude and latitude, respectively, Fig. II.4.3) for Profile + valleys sampling scheme (Fig. II.4.2b; AFT + AHe + MTL dataset). Inversions results are also reported as percentage errors and uncertainties regarding input values (%Input).*

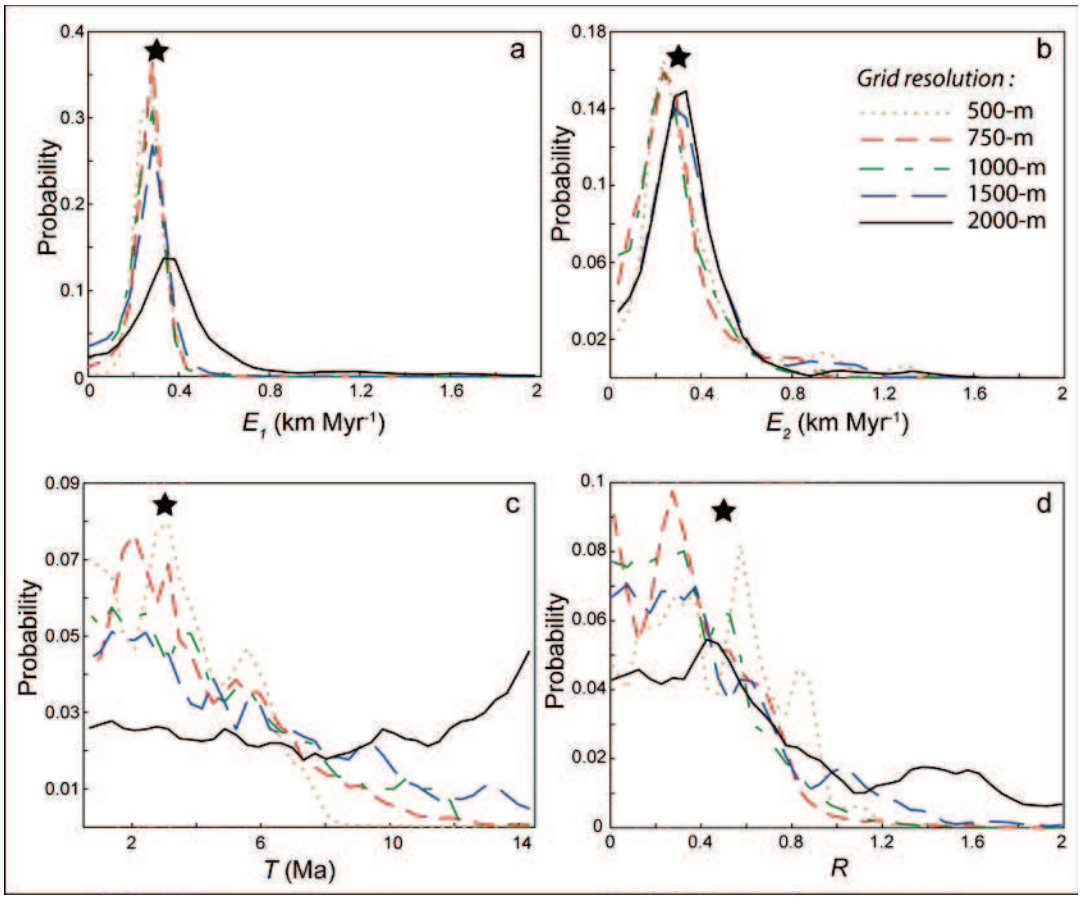

Figure II.4.5. *1D posterior parameter PDF's obtained after the NA appraisal stage for the sampling scheme Profile + valleys (AFT + AHe + MTL dataset) and different model grid resolutions: (a) denudation rate of the first exhumation phase (E_1); (b) denudation rate of the second exhumation phase (E_2); (c) transition time between the two exhumation phases (T); and (d) relief factor between the paleo-relief and the final relief (R). Each line (see figure for colour legend) defines an inversion experiment with a given grid resolution (from 500-m to 2-km, see Fig. II.4.3). Black stars represent the input parameter values.*

Predictions for E_1 are similar for 500-m and 750-m resolution topographies (E_1 = 0.28 ±0.005/0.01 km Myr^{-1}). Using lower resolution grids provides accurate values of E_1, associated uncertainties, however, increase from 13% (1000-m) to ~50% (2000-m, Figure II.4.5a). Output results are different for E_2 (Figure II.4.5b) as all resolution inversions lead to similar estimates of E_2 (E_2 = 0.28-0.33 ±0.11-0.13 km Myr^{-1}). Timing predictions T are accurate and quite precise with grid resolutions of 500-m and 750-m (respectively T = 3.1 ±1.9 and 2.1 +2.6/-1.6 Ma) and are degraded when lowering the grid resolution (T = 1.4-14.3 Ma, Figure II.4.5c). Finally, the relief increase R is overestimated for all inversions (R = 0.08-0.43, Table II.4.4) except when using the high-resolution topography (500 m) for which the R estimate is slightly underestimated (R = 0.58 ±0.29). Uncertainties associated with R

predictions are similar for the mid-resolution grids (*i.e.*, 750-m and 1000-m, uncertainties ~45%) and the 500-m resolution model (uncertainty ~55%). Low-resolution grids (1500-m and 2000-m) provide much higher uncertainties on *R* estimates (~75-85%).

In summary, we have shown that model grid resolution has little effect on predictions regarding denudation rates (E_1 and E_2); however, we demonstrate that timing and relief evolution (respectively *T* and *R*) are only poorly constrained when using low-resolution topographies (*i.e.*, pixel size greater than ~1 km).

II.4.4 - Discussion and conclusions

Before interpreting our results on thermochronology data sampling and modelling strategies for quantitatively assessing denudation and relief histories, we have to highlight some shortcomings associated with our numerical modelling approach.

First of all, the exhumation scenario we choose is quite simple with only two exhumation phases, a constant regional denudation rate over ~15 Myr and a single episode of relief development. We could have performed similar approach on various and contrasted exhumation scenarios (steady-state exhumation and relief, denudation pulse under steady-state (or varying) topography…). However, quantifying both timing and amplitude of topographic relief changes in mountain belts, even though it retained much attention from recent thermochronological studies [*e.g.*, *Ehlers et al.*, 2006; *Glotzbach et al.*, 2008; *Vernon et al.*, 2009; *van der Beek et al.*, 2010; *Glotzbach et al.*, submitted], has proved to be very elusive [*e.g.*, *Valla et al.*, 2010b], consequently motivating us to focus our study on this specific exhumation scenario.

Second, the way we define relief changes in *Pecube* remains fairly simplistic and does not capture the complexities of landscape evolution processes. Some limitations include the constant planform drainage pattern assumed in our numerical approach, and a geometric relief evolution approach in which peaks are fixed to their present-day value and relief evolves through valley carving only. Recent studies have used numerical modelling to better predict topographic evolution in *Pecube* by either considering different relief evolution geometries (*e.g.*, constant mean relief elevation, either fixed peaks or valley bottoms; *Whipp et al.*, 2009),

or by using a landscape evolution model to fully simulate landscape changes with surface process modelling [*Herman et al.*, 2010a].

Third, we assumed in our modelling approach that the crustal block we used has a uniform exhumation history, *i.e.*, there are no faults crossing the topography that may induce spatial exhumation differences. Similarly, we also assumed the geothermal gradient to be spatially uniform, although studies have shown that local fluid circulations along faults can induce large spatial variations in thermal properties [*Whipp and Ehlers*, 2007]. Moreover, we only tested one geothermal gradient scenario (~20-25 °C km^{-1}) and cannot therefore assess if our output results may apply in different settings with much lower or higher geothermal gradients.

Keeping these limitations in mind, we have shown that sampling and modelling strategies have a non-negligible effect on numerical predictions for denudation and relief histories from thermochronology data.

Our inversion results for a single elevation profile (*1_Profile*) show that although denudation rates may be quite accurately estimated by this sampling approach, it does not constrain relief evolution satisfactorily (uncertainties >100%, Table II.4.2). This finding is similar to the conclusion of *Valla et al.* [2010b] who also performed a sensitivity analysis and showed that relief evolution can only be precisely predicted from thermochronological age-elevation profiles if the rate of relief change is at least two to three times higher than the regional denudation rate. In our case, the regional denudation rate is kept constant at 0.3 km Myr^{-1} and the relief evolution scenario induces a maximum relief growth rate ~0.5 km Myr^{-1} for the last 3 Myr (*i.e.*, ~60% higher than the background denudation rate). Under this configuration, our inverse results are in good agreement with *Valla et al.* [2010b]; moreover, we suggest that the inability of a single age-elevation profile to constrain relief evolution may come from the insufficient spatial spacing of this specific sampling scheme, *i.e.*, thermochronology data sampling along a single elevation profile does not fully capture the topographic effects on near-surface isotherms [*Braun*, 2002a, b].

Sampling along three different elevation profiles (*3_Profiles*) provided similar results for denudation rates, but estimates of relief evolution are better constrained (uncertainties ~65%) and all predict a relief increase (R<1, Table II.4.2). This result may be explained by the sampling organization along three different valleys (Figure II.4.2) that allows sampling

different topographic wavelengths. As explained previously and by *Braun* [2002a], crustal isotherms are influenced by different topographic wavelengths and this effect can be used to constrain topographic changes using either a spectral method along a long transect [*Braun*, 2002b] or in our case by combining several elevation profiles along different valleys. This effect is also captured when sampling along several valley bottoms (*Valleys* and *Profile + Valleys*), which explains why optimal values for both denudation rate, timing and relief increase are all more accurate and precise (uncertainties on E_1, T and R are 2 to 6 times lower than for *1_Profile* inversion results).

Thermochronological sampling along a long transect allows applying spectral analysis [*Braun*, 2002b] to constrain both denudation rate over short topographic wavelengths and relief evolution over long topographic wavelengths. However, this method considers temporally constant denudation rates and allows neither determining precisely the timing of relief change nor estimating the uncertainties on optimal values for denudation and relief change. Inversion results using the *Transect* sampling (Table II.4.2) predict denudation and relief histories close to *3_Profiles* predictions, *i.e.*, accurate estimates on denudation rates (E_1 and E_2) and relief change (R); however, the uncertainties on these parameters are higher than those obtained with *Valleys* and *Profile + Valleys* sampling strategies. These differences may also come from the spatial configuration of the *Transect* sampling scheme. Although it covers a larger topographic area than *1_Profile* and *3_Profiles* sampling schemes, *Transect* data only sample one spatial direction (roughly North-South in our case, Figure II.4.2b) and may not fully record the 2D topographic perturbations of isotherms compared to thermochronology data spatially distributed along different valleys (*Valleys* or *Profile + Valleys* sampling scheme). Combining a long transect with at least one altitudinal profile would have allowed to best capture both short and long topographic wavelengths effects on the thermal structure [*Braun*, 2002a, b], simultaneously providing accurate and precise information on both denudation and relief predictions.

Inversions for which the thermal parameters are supposed unknown lead to the same accuracy but higher uncertainties for denudation and relief predictions than when imposing a specific geothermal gradient (Table II.4.3). These differences in predicted uncertainties highlight the classic problem of determining an appropriate dimensionality for a numerical problem (*i.e.*, the number of inverted parameters compared to the intrinsic data resolution; see *Gallagher et al.*, 2005a, for a discussion on this subject]. Moreover, our results show that sampling along

valley bottoms does not allow resolving accurately the thermal parameters. Sampling along elevation profiles helps constraining the geothermal gradient as suggested by *Gallagher et al.* [2005a], pointing out that even though numerical modelling allows to infer exhumation histories from complex spatial sampling, age-elevation relationships are still necessary for interpreting thermochronology data. The ability of age-elevation profiles in constraining both the exhumation history and thermal parameters comes from the altitudinal samples repartition, the slope of the age-elevation relationship providing an estimate of the apparent exhumation rate [*e.g.*, *Hurford*, 1991], while the age-window of the dataset may help to constrain the near-surface geothermal gradient [*Gallagher et al.*, 2005a]. Surprisingly, the *Transect* sampling provided the best estimates on thermal parameters, which can be explained by the simultaneous spatial and altitudinal data coverage allowed by this sampling scheme (Figure II.4.2b). It thus might be used not only for spectral analysis [*Braun*, 2002b] but also, like elevation profiles, to constrain the geothermal gradient.

The inversion results using different model grid resolutions show that coarse-grid models (*i.e.*, pixel size larger than ~1 km) result in a loss of both accuracy and precision on denudation and relief change predictions. This finding may be important for modelling wide areas, for which degrading the model topography could decrease computation time, but may also reduce the ability of the models to quantitatively constrain denudation and relief histories from thermochronology data. On the contrary, our results clearly demonstrate that increasing the model grid resolution beyond a threshold (~750-m resolution in our case) does not improve inversion predictions, illustrating that both denudation and relief information are best recorded by thermochronology data at specific topographic wavelengths below which no supplementary resolution can be gained.

Our study was initially designed to determine to which extent sampling and modelling strategies can help in constraining relief evolution from low-temperature thermochronology datasets. Following *Valla et al.* [2010b], we have shown here that age-elevation relationships do not resolve relief changes if relief development does not induce an additional spatially variable exhumation rate that is at least two times higher than the regional denudation rate. We demonstrate that spatially dense sampling a long transect, several elevation profiles or even better along valley bottoms only or combined with an elevation profile can lead to better predictions concerning relief evolution. The main problem of only sampling along valley bottoms is the loss of information concerning the near-surface thermal structure. However,

using higher-temperature thermochronometers may provide supplementary constraints on thermal parameters. *Glotzbach et al.* [submitted] recently used a dense thermochronology dataset combining both low- and high-temperature thermochronometers along elevation profiles and tunnel data to constrain the exhumation history of the Mont-Blanc massif (Western European Alps). Their modelling results resolved recent relief increase whereas other recent studies using only low-temperature data along a single age-elevation profile could not manage to resolve the recent relief evolution [*Vernon et al.*, 2009; *van der Beek et al.*, 2010].

To conclude, we have shown that the 3D thermal-kinematic model *Pecube* can be used to interpret thermochronology data in terms of denudation and relief histories. Based on synthetic data produced under an imposed exhumation and relief scenario, we tested different sampling strategies to best derive quantitative estimates on denudation rates, timing and relief change. Our results show that dense spatial sampling combining valley bottom samples and elevation profiles, as well as long transect may help improving quantification of complex exhumation histories. Moreover, we highlighted that modelling approach concerning thermal parameters or model topography resolution could have an important effect on output predictions for denudation and relief evolution. Although age-elevation profiles may be a useful and most direct way to interpret thermochronology data, sampling strategies may be rethought in the light of recent numerical modelling developments. We thus suggest to put less emphasis on elevation profiles when designing thermochronology studies but rather favour spatially distributed sampling and different thermochronometers (high- and low-temperature systems) for constraining both denudation rates, topographic relief changes and near-surface thermal structure.

Acknowledgments

This study is supported by INSU-CNRS through the European Science Foundation Eurocores Topo-Europe programme 07-TOPO-EUROPE-FP-023 “Coupled climatic/tectonic forcing of European topography revealed through thermochronometry (Thermo-Europe)” and the Agence Nationale de la Recherche project No. ANR-08-BLAN-0303-01 “Erosion and Relief Development in the Western Alps”. It forms part of PV's PhD project at Université Joseph Fourier, supported by the French Ministry for Research and Higher Education. Computations were performed on Brutus, the high performance computing facilities at ETH Zurich. The codes are available at http://svn-geo.ethz.ch after registering at this site.

Chapter III :

Late Neogene exhumation and Quaternary relief development of the Western European Alps using apatite $^{4}He/^{3}He$ and (U-Th-Sm)/He thermochronometry

III.1 - Chapter III overview (Présentation du Chapitre III)

III.1.1 - Introduction

Dans le chapitre précédent, nous avons exploré les capacités et les limites de données thermochronologiques "classiques" à fournir des informations quantitatives sur les histoires d'exhumation et d'évolution du relief. Dans ce chapitre, je présente l'acquisition et l'utilisation de données thermochronologiques basse température (essentiellement (U-Th-Sm)/He sur apatite) couplée à la thermochronométrie $^{4}He/^{3}He$ sur apatite [*e.g.*, *Shuster and Farley*, 2005] afin de contraindre l'exhumation récente dans les Alpes suisses (vallée du Rhône, région du Valais).

Dans une première partie, je présente un manuscrit soumis à *Nature Geoscience* [*Valla et al.*, submitted, a] décrivant l'acquisition de données inédites $^{4}He/^{3}He$, couplées à des données (U-Th-Sm)/He sur apatite, afin de contraindre l'histoire d'exhumation tardive et notamment l'évolution de la topographie en lien avec la mise en place des glaciations Quaternaires. Notre étude s'inscrit dans un débat actuel autour de l'action effective des glaciers sur l'évolution du relief; il s'agit notamment de savoir si la mise en place de périodes glaciaires récurrentes depuis le Pliocène-Quaternaire a potentiellement engendré une augmentation [*e.g.*, *Molnar and England*, 1990; *Montgomery*, 2002; *Shuster et al.*, 2005] ou au contraire une diminution nette [*e.g.*, *Whipple et al.*, 1999; *Egholm et al.*, 2009] du relief dans les chaînes de montagne. Nos résultats démontrent clairement que, dans le cas des Alpes suisses, les glaciations Quaternaires ont mené à une augmentation majeure du relief local, d'une part par le creusement préférentiel des vallées (~1-1.5 km durant le Quaternaire), et d'autre part par la protection des crêtes et sommets. Ce changement de relief est probablement initié lors du changement climatique Mi-Pléistocène (~1-1.2 Ma; *Lisiecki*, 2010) marquant la transition depuis des cycles glaciaire/interglaciaire symétriques de 40 ka vers des cycles fortement asymétriques de 100 ka.

Dans une deuxième partie, j'utilise mes données personnelles, ainsi que des données thermochronologiques basse température disponibles dans la littérature, afin de contraindre l'exhumation Néogène et récente d'une partie des Alpes suisses. Cette étude est présentée sous la forme d'un article prêt à être soumis [*Valla et al.*, submitted, b], et combine, d'une part l'interprétation de données thermochronologiques "classiques" selon une approche

numérique inverse (développée au cours du Chapitre II), et d'autre part l'interprétation de données $^{4}He/^{3}He$ sur apatite, afin de contraindre respectivement l'exhumation Néogène et le creusement de la vallée du Rhône au cours du Quaternaire. Nos résultats montrent une exhumation contrastée des Alpes suisses, en accord avec la chapitre précédent [*van der Beek et al.*, 2010] ainsi que d'autres études au sein des Alpes occidentales [*e.g.*, *Glotzbach et al.*, 2008; 2010; *Vernon et al.*, 2009]. L'évolution de la topographie est, également en accord avec les études précédentes, plus difficile à quantifier; cependant nos modèles inverses apportent des contraintes vis à vis d'un développement du relief assez récent (Pliocène-Quaternaire) pour cette région, en accord avec l'interprétation des données $^{4}He/^{3}He$. Enfin, l'étude comparée de données thermochronologiques "classiques" et de la thermochronométrie $^{4}He/^{3}He$ montre clairement l'efficacité de cette nouvelle technique et sa meilleure résolution dans la quantification de l'évolution récente du relief.

Dans une troisième partie, je présente un travail de reconstruction géomorphologique concernant la topographie pré-glaciaire (*i.e.*, antérieure à la mise en place des glaciations Quaternaires) de la vallée du Rhône (Valais suisse). Cette étude est également présentée sous la forme d'un article prêt à être soumis et est basée sur la quantification du creusement local de la vallée du Rhône (partie précédente, *Valla et al.*, submitted, b) comme contrainte vis-à-vis de la topographie pré-glaciaire. Ces données sont par la suite extrapolées numériquement afin de reconstruire la morphologie pré-glaciaire sur l'ensemble du bassin versant du Rhône. Nos résultats montrent que, contrairement au relief local le long de la vallée du Rhône [*Valla et al.*, submitted, a], le relief moyen sur l'ensemble du bassin n'a que très peu été affecté par les glaciations Quaternaires [*Whipple et al.*, 1999]. Par ailleurs, notre étude démontre que les vitesses d'érosion post-glaciaires [*Hinderer*, 2001] et moyennées sur le Quaternaire sont du même ordre de grandeur, illustrant une érosion moyenne constante tout au long du Quaternaire et vraisemblablement du même ordre de grandeur durant les périodes glaciaires et interglaciaires. Enfin, nous avons quantifié, grâce à un modèle de rebond flexural, la réponse isostatique à l'érosion Quaternaire qui, d'après nos résultats, n'explique qu'en partie les vitesses de soulèvement géodésiques mesurées aujourd'hui.

II.1.2 - Presentations at international meetings

- December 2009, American Geophysical Union, Fall meeting, San Francisco (USA):

Valla, P.G., Shuster, D.L., van der Beek, P.A., Balco, G., Herman, F., Braun, J. Tectonically-controlled exhumation versus climatically driven relief development in the Valais area (Western European Alps) revealed by apatite (U-Th-Sm)/He and $^{4}He/^{3}He$ thermochronometry. *Eos Trans. AGU, 90*(52), Fall Meet. Suppl., Abstract V52C-08.

- **May, 2010**, European Geosciences Union, General assembly, Vienna (Austria):

Valla, P.G., Shuster, D.L., van der Beek, P.A., Herman, F., Braun, J. Neogene relief development in the Western European Alps revealed by apatite (U-Th-Sm)/He and $^{4}He/^{3}He$ thermochronometry. *Geophysical Research Abstracts*, Vol. 12, EGU2010-10346.

- **August 2010**, Thermo2010, 12th International conference on thermochronology, Glasgow (United Kingdom):

Valla, P.G., Shuster, D.L., van der Beek, P.A. Quaternary Alpine landscape evolution from apatite (U-Th-Sm)/He, $^{4}He/^{3}He$ thermochronometry and numerical modelling, Western European Alps. *Extended Abstract Volume*, *p.305*.

III.1.3 - Publications and contributors to Chapter III

This chapter presents one paper submitted to *Nature Geoscience* (August 26th 2010) and two manuscripts ready to be submitted (to *Journal of Geophysical Research* and *Geology*, respectively). D. Shuster, P. van der Beek and I designed the study of the 1st paper. I personally collected and processed the samples, and I participated in the data analyses at the Berkeley Geochronology Center (collaboration D. Shuster, L. Hedges and B. Lum). I produced all the results presented in the 2nd and 3rd manuscripts. The new (U-Th)/He code (originally developed by C. Gautheron and L. Tassan-Got, *Gautheron et al.*, 2009) used in this study has been modified by L. Tassan-Got and myself to be implemented into the *Pecube* model (collaboration J. Braun and F. Herman). M. Rahn kindly shared unpublished apatite fission-track data that I used for numerical modelling.

III.2 - Major increase in relief of the European Alps during Mid-Pleistocene glaciations recorded by apatite $^{4}He/^{3}He$ thermochronometry

Pierre G. Valla [1], David L. Shuster [2,3], and Peter A. van der Beek [1]

[1] *ISTerre-OSUG, Université de Grenoble, CNRS, BP 53, F-38041 Grenoble, France*

[2] *Berkeley Geochronology Center, 2455 Ridge Road, CA-94709 Berkeley, USA*

[3] *Department of Earth and Planetary Science, U.C. Berkeley, CA-94709 Berkeley, USA*

Abstract

Some of the highest relief observed at the Earth's surface occurs where glacial processes act upon uplifted bedrock [*Meigs and Sauber*, 2000; *Brocklehurst and Whipple*, 2007], providing what has long been interpreted as a spectacular record of the Pleistocene climate imprint upon high-latitude landscapes [*Penck*, 1905; *Molnar and England*, 1990]. However, the net effect of glacial erosion on mountain belt relief remains disputed, with studies arguing for both positive [*Small and Anderson*, 1995; *Montgomery*, 2002] and negative [*Brozovic et al.*, 1997; *Whipple et al.*, 1999; *Egholm et al.*, 2009] coupling between increased glacial erosion and relief development. Testing these hypotheses requires observational constraints on relief evolution over ~1 km and ~1 million year (Ma) scales, which have proven remarkably elusive. Here we report $^{4}He/^{3}He$ thermochronometry [*Shuster and Farley*, 2004] and thermal-kinematic models, which reveal that an approximately 2-fold increase in local topographic relief associated with 1-1.5 km deepening of the Rhône valley (Swiss Alps) occurred over the last 1 Ma. Therefore, the main effect of glaciation in this region was to significantly increase local relief while lowering the mean elevation through valley incision. The onset timing of valley incision is likely linked to the Mid-Pleistocene transition from symmetric 41,000-year to asymmetric 100,000-year glacial/interglacial oscillations [*Ruddiman et al.*, 1986; *Lisiecki*, 2010], which triggered large, long-lived and strongly erosive alpine glaciers.

III.2.1 - Introduction

Alpine landscapes result from the interactions between fluvial, glacial and hillslope processes. Understanding how the topographic relief of mountains develops and what controls this evolution requires quantifying the relative efficiency of these surface processes. Recent

studies have suggested that glacial erosion efficiently shapes mountain-belt topography through glacial valley carving and cirque retreat [*Montgomery*, 2002; *Brocklehurst and Whipple*, 2007; *Naylor and Gabet*, 2007], leading to significant relief development and mountain-peak uplift in response to late Cenozoic climate cooling [*Molnar and England*, 1990]. However, others have proposed that, because glacial erosion is most efficient around the Equilibrium Line Altitude (ELA), it should limit mountain height and therefore reduce topographic relief [*Brozovic et al.*, 1997; *Whipple et al.*, 1999; *Egholm et al.*, 2009]. Therefore, understanding how mountain topography develops in response to climatic forcing, and to assess whether present-day relief primarily reflects continuous orogenic processes or climate-induced processes at the Pliocene-Quaternary onset of global glacial conditions, requires detailed quantitative information on the spatial and temporal patterns of erosion over ~10^6 year timescales.

III.2.2 - Methods

In this study, we combine apatite (U-Th-Sm)/He dating [*Farley*, 2002] with $^4He/^3He$ thermochronometry [*Shuster and Farley*, 2004] to constrain the timing and rate of glacial incision of the Rhône valley in the European Alps. The radiometric (U-Th-Sm)/He system in apatite (AHe) is sensitive to bedrock cooling through ~80 °C and therefore records bedrock exhumation through the uppermost 2-4 km beneath the topographic surface. Apatite $^4He/^3He$ thermochronometry constrains the spatial distribution of ^4He within individual apatite crystals and therefore the cooling history of specific locations within an evolving thermal field (see section III.2.6 for details). The resulting detailed exhumation histories may be compared at different locations to test cooling scenarios predicted by models of evolving topography [*Shuster et al.*, 2005; *Valla et al.*, 2010b].

III.2.3 - Geomorphic setting

We focus on the upper Rhône valley (Switzerland), one of the major drainage systems of the western European Alps (Figure III.2.1a). The upper Rhône drainage basin features ~3 km of topographic relief and several of the highest peaks of the Alps, with elevations at and above 4000 m. It has been extensively glaciated during Quaternary glaciations [*Kelly et al.*, 2004].

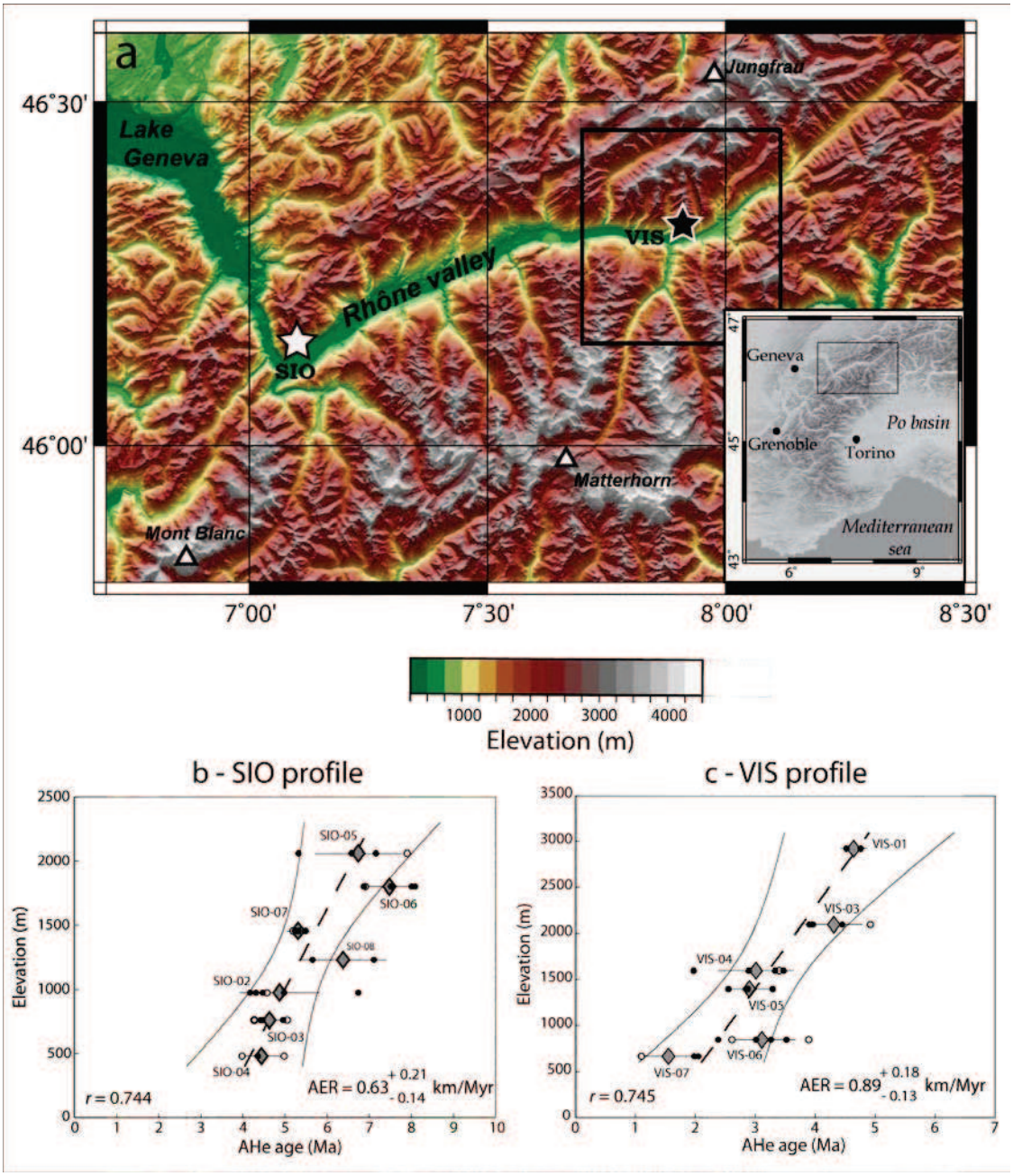

Figure III.2.1. *Topography, sample locations and apatite (U-Th-Sm)/He (AHe) age elevation relationships. (a) Shaded relief map of the studied area in the European Alps. Stars represent SIO (white) and VIS (black) sampling transects along the Rhône Valley. Major summits are also indicated (Jungfrau: 4160 m, Mattherhorn: 4480 m, Mont Blanc: 4810 m). The large black box outlines the model domain shown in Fig. III.2.4. Inset shows location of the study area within the European Alps. (b-c) Martigny-Sion (SIO) and Visp (VIS) AHe age-elevation profiles. Grey diamonds are mean AHe ages with standard deviation, circles show single crystal AHe ages (filled: conventional AHe ages; open: AHe ages derived from $^{4}He/^{3}He$ measurements). Dashed straight line is weighted linear regression; envelopes show 95% confidence limits on age-elevation relationship; r: Pearson correlation coefficient; AER: apparent exhumation rate calculated from the weighted linear regression.*

The present-day morphology of the upper Rhône valley is typical of glacially-influenced landscapes with U-shaped cross-profiles of 2-4 km width, a stepped longitudinal profile and major glacial overdeepenings [*Norton et al.*, 2010a]. We studied bedrock samples from two elevation transects (SIO and VIS profiles, Figure III.2.1a) along the Rhône valley (see section III.2.7 for details), on the southern flanks of the Aiguilles Rouges and Aar massifs, respectively. These are two of the so-called "External Crystalline Massifs" [*Schmid et al.*, 2004] of the Alps; uplifted blocks of European crystalline basement characterized by high topography and relief, as well as a strong glacial imprint on landscape morphology. Previous studies have identified exhumation pulses within the External Crystalline Massifs during the late Neogene [*Glotzbach et al.*, 2008; *Vernon et al.*, 2009; *van der Beek et al.*, 2010]. However, the exhumation and relief history throughout the Pliocene-Quaternary remains unclear.

III.2.4 - Apatite (U-Th-Sm)/He and $^{4}He/^{3}He$ results

Apatite (U-Th-Sm)/He ages range from 4.4±0.5 to 7.5±0.6 Ma for the SIO profile and from 1.6 ±0.5 to 4.6 ±0.2 Ma for the VIS profile; ages are positively correlated with elevation in both profiles (Figure III.2.1b, c). Apparent exhumation rates derived from both age-elevation relationships are similar at ~0.6-0.9 km Ma^{-1}, despite differences in the apparent time interval. The (U-Th-Sm)/He data alone do not clearly constrain the recent exhumation and relief history of the area. Moreover, AHe ages of valley bottom samples disagree (4.4 ±0.5 Ma for SIO-04 versus 1.6 ±0.5 Ma for VIS-07), which may suggest different recent exhumation histories between the two locations. Alternatively, the age difference between SIO and VIS samples may be explained by differences in U-content as the U concentrations of the former are significantly higher (see section III.2.7), implying higher closure temperatures [*Flowers et al.*, 2009].

$^{4}He/^{3}He$ thermochronometry of a subset of samples from both profiles (see sections III.2.6 and III.2.7) constrains each sample's cooling history below ~80 °C and highlights spatio-temporal variations in recent exhumation. For instance, SIO-04 records a much more diffusive ^{4}He-distribution pattern than SIO-06 and -07 (Figure III.2.2). This requires that the valley-bottom sample SIO-04 recently experienced more rapid cooling than the two samples at higher elevations [*Shuster and Farley*, 2004].

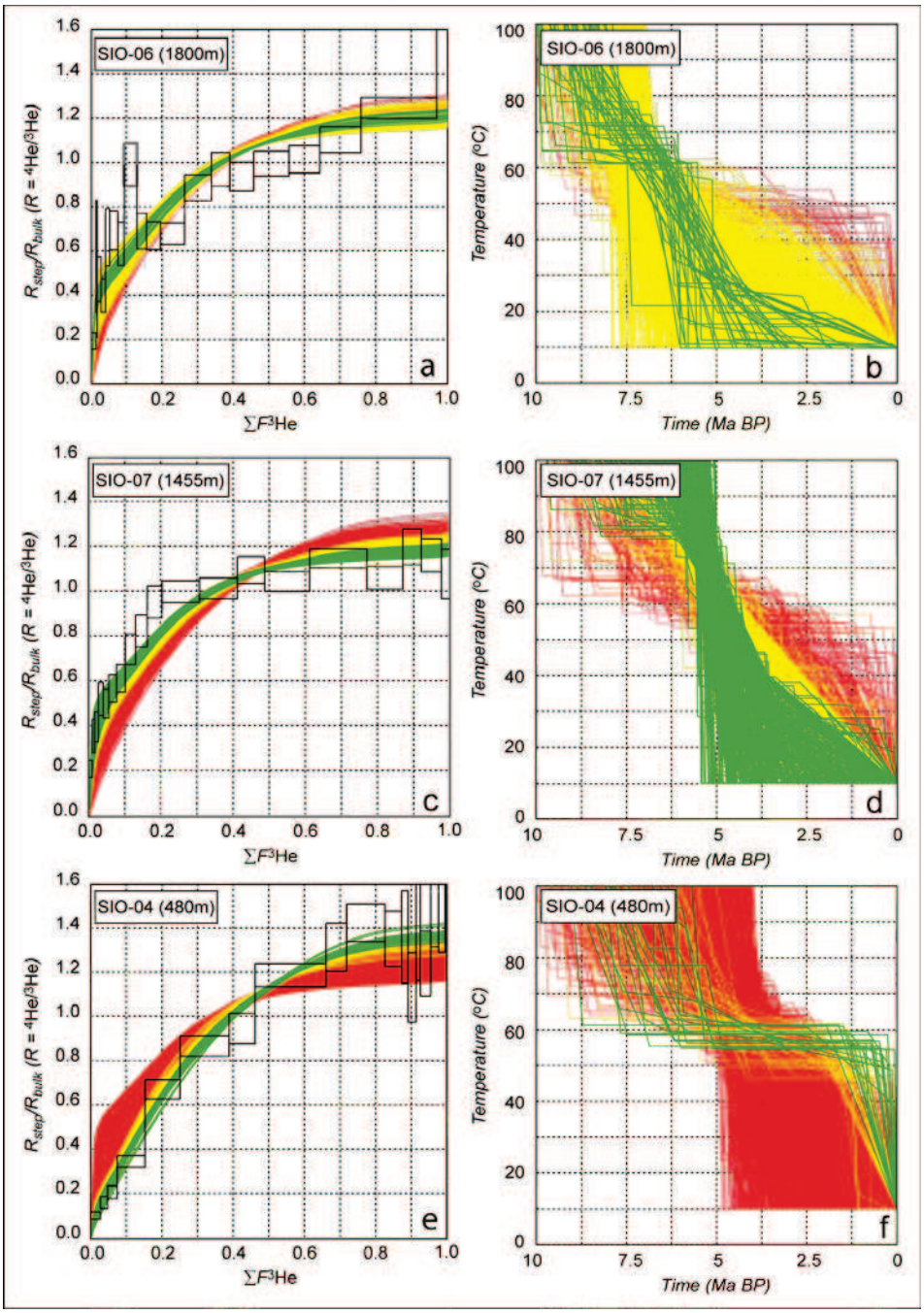

Figure III.2.2. *$^4He/^3He$ thermochronometry of SIO samples. Observed $^4He/^3He$ ratio evolution diagrams and model cooling paths for SIO-06 (1800 m, a-b), SIO-07 (1455 m, c-d) and SIO-04 (480 m, e-f). The measured $^4He/^3He$ ratios of each degassing step (R_{step}) are normalized to the bulk ratio (R_{bulk}) and plotted versus the cumulative ^3He release fraction ($\sum F\,^3He$). Open black boxes indicate 1 standard error (vertical) and integration steps (horizontal); open grey boxes show released steps that were excluded from the misfit calculation (see section III.2.6 for discussion). Colored lines show the predicted $^4He/^3He$ ratio evolution diagrams (a, c, e) for arbitrary cooling paths (b, d, f), each of which predicts the observed (U-Th-Sm)/He age of each sample within analytical uncertainty (±1σ standard deviation). Cooling paths shown in red and yellow are excluded by the $^4He/^3He$ data, whereas the green cooling paths are permitted (see sections III.2.6 and III.2.7).*

We use a numerical model (see section III.2.6 and *Schildgen et al.*, 2010) to constrain cooling paths from the observed $^{4}He/^{3}He$ data. All SIO samples indicate rapid cooling from >6-7 Ma before present (BP) until around 5 Ma BP (Figure III.2.2). However, cooling histories clearly differ since 5 Ma BP. The high-elevation sample SIO-06 (Figure III.2.2b) requires <10 °C cooling since 5 Ma BP and the mid-profile sample SIO-07 (Figure III.2.2d) permits only limited cooling (<25 °C) over the last 5 Ma. However, the valley-floor sample SIO-04 (Figure III.2.2e) clearly requires a different cooling history: 4-5 Ma of residence within the partial retention zone (*i.e.*, 60-80 °C) prior to rapid cooling to surface temperatures initiating ~1 Ma ago.

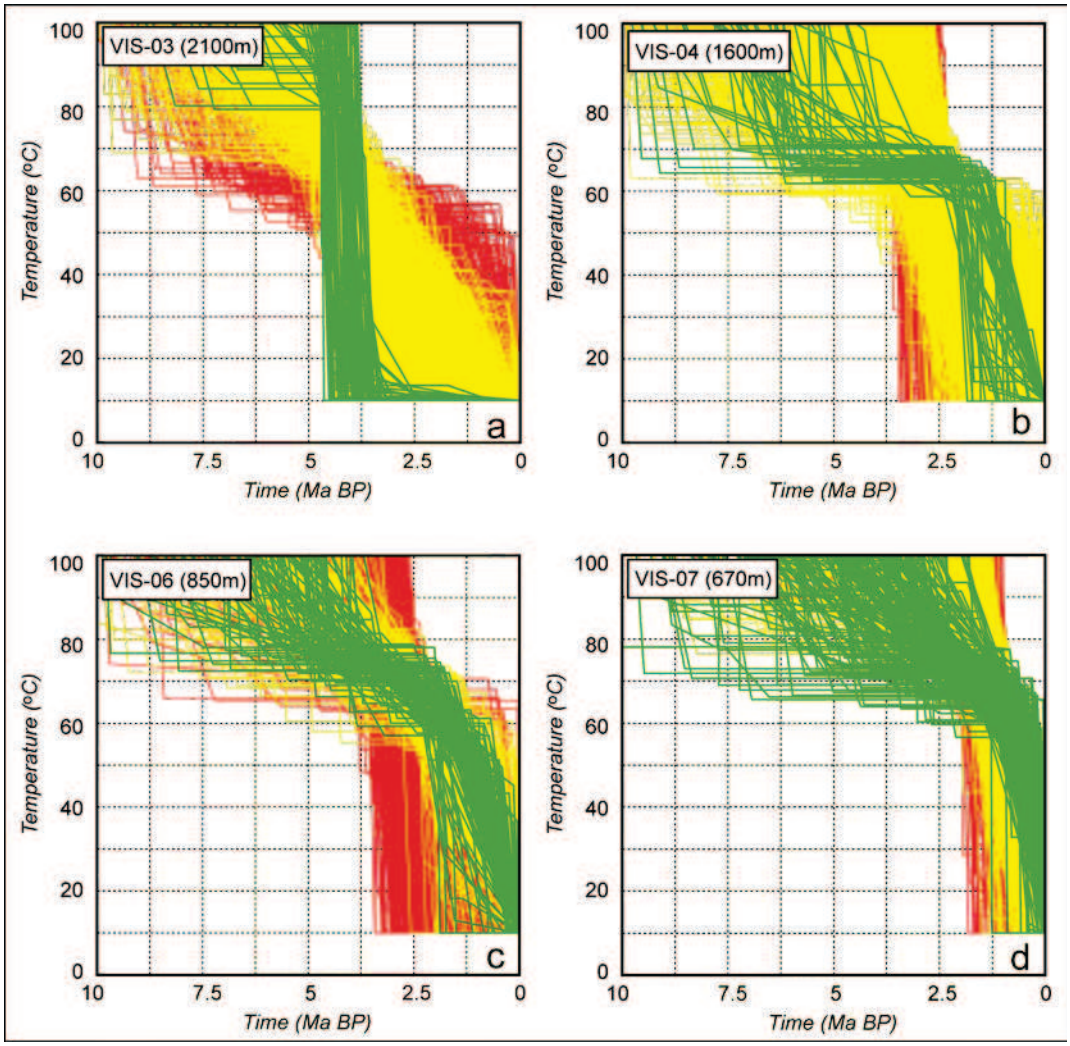

Figure III.2.3. *Modelled cooling paths for VIS samples. Each plot shows cooling paths for VIS-03 (a, 2100 m), -04 (b, 1600 m), -06 (c, 850 m) and -07 (d, 670 m) samples. Curve colors are as in Fig. III.2.2 (see Fig. III.2.5 for $^{4}He/^{3}He$ ratio evolution diagrams of these samples).*

VIS samples also record rapid cooling ~6-4 Ma ago (Figure III.2.3), although this initial cooling phase is less resolved than for SIO samples due to younger (U-Th-Sm)/He ages. However the spatial pattern of cooling trends is similar : whereas the high-elevation sample VIS-03 (Figure III.2.3a) had cooled to surface temperatures by ~4 Ma BP, the lower-elevation samples VIS-04, -06 and -07 (Figure III.2.3b-d) all require significant cooling since 1 Ma BP from successively higher temperatures with decreasing sample elevation.

Thus, despite different (U-Th-Sm)/He ages, the $^{4}He/^{3}He$ thermochronometry results indicate that both transects within the Rhône valley experienced similar exhumation histories during late Miocene to Quaternary: a rapid phase of exhumation recorded by summit samples between 6-7 and ~4-5 Ma BP, followed by a quiescent phase until ~1 Ma BP when low-elevation samples record a recent episode of rapid cooling. Because the thermal histories constrained by $^{4}He/^{3}He$ data incorporate the effect of U-concentration on He diffusion (see section III.2.6 and *Flowers et al.*, 2009), we thus conclude that the absolute age difference between the two transects reflects the influence of radiation damage.

III.2.5 - Discussion and conclusions

This exhumation history of the Rhône valley corroborates a late Miocene phase of exhumation in the External Crystalline Massifs of the Alps inferred from modelling thermochronological age-elevation profiles [*Glotzbach et al.*, 2008; *Vernon et al.*, 2009; *van der Beek et al.*, 2010]. However, no unequivocal evidence for recent relief development was inferred from those previous studies. In contrast, the $^{4}He/^{3}He$ results clearly reveal substantial local exhumation beginning ~1 Ma ago within the Rhône valley in both transect locations, and minimal exhumation since ~5 Ma ago for high-elevation samples.

To constrain background rock uplift and potential relief changes from the sample cooling paths we use the thermal-kinematic model *Pecube* [*Braun*, 2003; *Valla et al.*, 2010b]. We test 3 different exhumation scenarios and compare modelled cooling paths with the $^{4}He/^{3}He$ data for summit and valley-floor samples: (1) continuous steady-state exhumation, (2) temporally varying exhumation under steady-state topography and (3) relief increase through valley incision since 1 Ma BP (Figure III.2.4; although only the model for the VIS profile is shown here, modelling of the SIO profile leads to similar results).

Models 1 and 2, which include steady-state topography, cannot explain simultaneous rapid cooling of the valley floor over the last 1 Ma (VIS-07, Figure III.2.4d) and constant near-surface thermal conditions for the high-elevation sample (VIS-03, Figure III.2.4c). The contrast between summit and valley floor samples clearly requires significant relief increase in both VIS and SIO locations (model 3). The combined $^{4}He/^{3}He$ data and *Pecube* modelling results therefore indicate that the depth of the Rhône valley has increased by 1-1.5 km since 1 Ma BP; a roughly two-fold increase in local topographic relief (Figure III.2.4a, b).

While widespread glacial morphologic features qualitatively suggest that the present-day relief of the Alps resulted from intense glacial erosion, gradual cooling of Northern Hemisphere climate initiated ~3.5 Ma BP [*Mudelsee et al.*, 2005] and the earliest alpine glaciers within the European Alps date from the late Pliocene [*Schlüchter*, 1986]. This global climate transition clearly predates major valley incision ~1 Ma BP inferred from our $^{4}He/^{3}He$ results. However, the data are consistent with evidence for 1-km incision of the Aar valley, ~100 km to the NE of our study area, from cosmogenic nuclide abundances [*Haeuselmann et al.*, 2007] and onset of major glacial sediment flux to the Po foreland basin [*Muttoni et al.*, 2003], both dated at 0.8-1.0 Ma ago. Intense glaciation and topographic relief development within the European Alps thus corresponds to the global Mid-Pleistocene climatic transition from symmetric 41,000-year to strongly asymmetric 100,000-year glacial/interglacial oscillations [*Ruddiman et al.*, 1986; *Lisiecki*, 2010]. This major climatic change may have enhanced glacial conditions by permitting larger, more erosive and longer-lived alpine glaciers to develop. Moreover, the onset of asymmetric high-amplitude climate oscillations has enhanced erosion and topographic relief development by both promoting transient landscapes and preventing fluvial processes from reaching steady state conditions [*Norton et al.*, 2010a].

Apatite $^{4}He/^{3}He$ thermochronometry from the western European Alps reveals a ~100% increase in relief since 1 Ma BP. Glacial valley lowering clearly outpaced erosion rates affecting high-elevation regions of the landscape around or above the ELA (both present-day and Last Glacial Maximum conditions). Thus, glaciation of the Alps has led to significant relief increase, which in turn contributes to isostatic rock uplift in response to increased local erosion [*Champagnac et al.*, 2007]. The present-day topographic relief of the European Alps thus results from recent climate forcing which enhanced landscape disequilibrium and promoted valley incision through both glacial and fluvial processes.

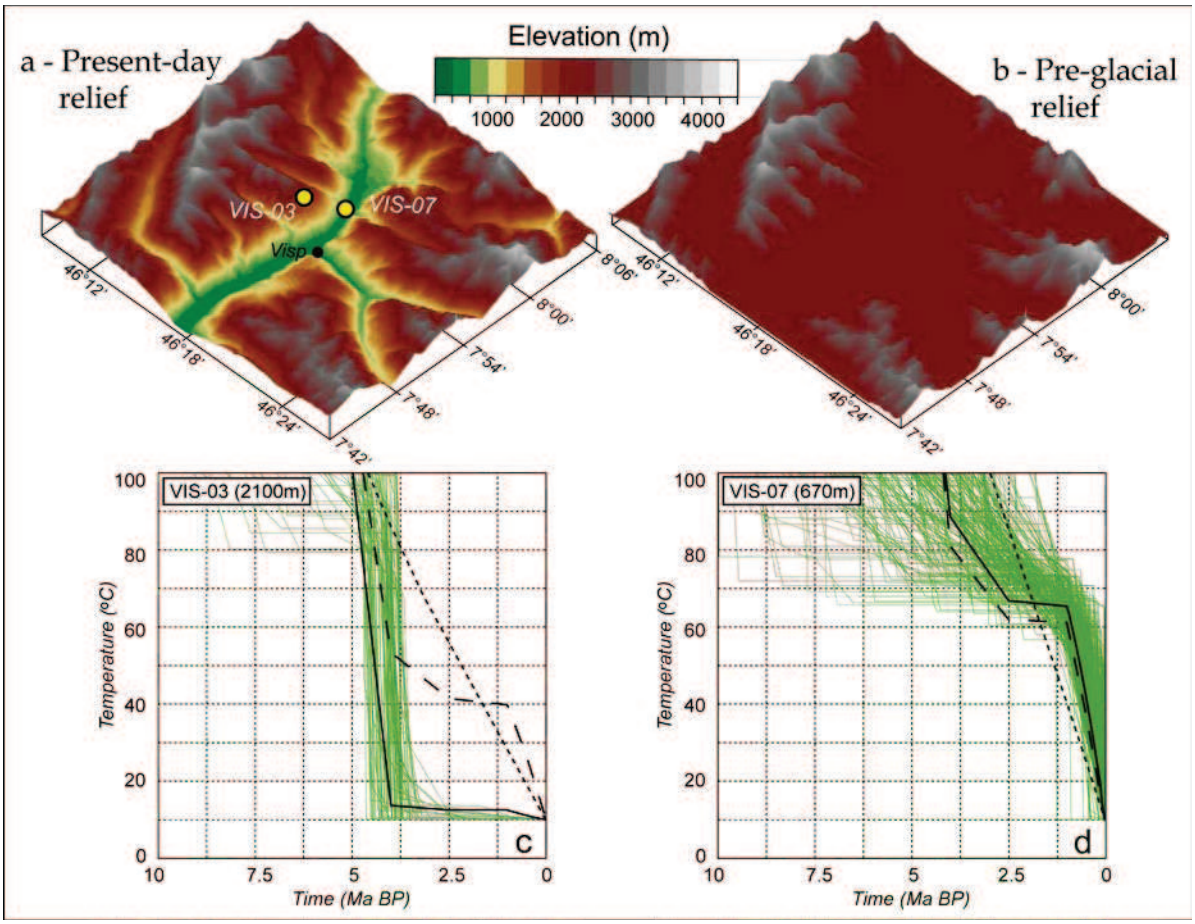

Figure III.2.4. *Predicted cooling paths for three exhumation / relief scenarios. (a) Present-day topography of the Visp area at 500-m resolution, derived from SRTM 90-m digital elevation model and (b) 50% of the present-day relief (i.e., summits are at the same elevation whereas valley bottoms are set to ~2100 m elevation) ascribed to pre-glacial time. VIS-03 and VIS-07 sample locations are indicated in (a) (also see Fig. III.2.1). (c, d) Predicted cooling paths (black lines) using a 3D thermal-kinematic model [Braun, 2003] compared to the best-fitting cooling paths (green lines) constrained by $^{4}He/^{3}He$ data for VIS-03 (c) and VIS-07 (d). The model parameters include: Crustal thickness is 40 km; temperatures at the surface and base of the domain are 10 °C and 600 °C, respectively; and thermal diffusivity is 25 km² Ma^{-1}. The models include three variable phases over the last 10 Ma according to the $^{4}He/^{3}He$ results of Figs. III.2.2 and III.2.3, with the aim to test effects of a recent increase in the background rock-uplift rate versus local relief development. The rock-uplift scenario (dashed lines) shows the effect of a time-variable but spatially uniform exhumation rate with constant relief equivalent to the present-day. The exhumation rate is 1.5 km Ma^{-1} from 10 Ma BP to 4 Ma BP, 0.001 km Ma^{-1} from 4 Ma BP to 1 Ma BP, and 1 km Ma^{-1} from 1 Ma BP to present-day. The relief-change scenario (solid black lines) ascribes the same transition in exhumation at 4 Ma BP (1.5 to 0.001 km Ma^{-1}); however the background exhumation rate is held at 0.001 km Ma^{-1} until present while imposing a 100% increase in local relief starting at 1 Ma BP (i.e, linear transition from relief shown in (b) to (a) over the last 1 Ma). Also shown (dotted lines) are the cooling paths predicted for constant regional exhumation (0.6 km Ma^{-1}) and constant relief over the last 10 Ma. Only the relief-change scenario can satisfactorily reproduce the thermal histories of both the top- and bottom samples.*

Acknowledgements

We thank J.-D. Champagnac for field assistance, F. Cœur, B.K. Lum and F. Senebier for help during sample preparation. The staff of the Caltech Noble Gas Laboratory is acknowledged for conducting conventional (U-Th-Sm)/He analyses. We thank G. Balco for development of the $^4He/^3He$ thermochronometry search algorithm, and F. Chirouze and R. Delunel for fruitful discussions. Financial support for this work was provided by the French Agence Nationale de la Recherche (ANR-08-BLAN-0303-01 grant to PAvdB), European Science Fundation Topo-Europe Eurocores programme, France-Berkeley Fund, U.S. National Science Foundation grant EAR-0720225 (to DLS) and the Ann and Gordon Getty Foundation.

III.2.6 - Methods details

III.2.6.1 - (U-Th-Sm)/He thermochronometry

Apatites were extracted from bedrock samples using standard magnetic and heavy liquid separation techniques. Preparation included selection of grains for euhedral shape, uniform size and absence of inclusions. Conventional (U-Th-Sm)/He thermochronometry was performed at the Caltech Noble Gas Laboratory, Pasadena, USA. Single-crystal aliquots of apatite were wrapped in Pt foils and degassed by laser heating. ^4He abundances were measured using ^3He isotope dilution and quadrupole mass spectrometry. Degassed aliquots were dissolved and U, Th and Sm concentrations were measured by isotope dilution using ICP-MS. An α-ejection correction was applied to calculate the (U-Th-Sm)/He age following *Farley et al.* [1996].

III.2.6.2 - $^4He/^3He$ thermochronometry

In $^4He/^3He$ thermochronometry [*Shuster and Farley*, 2004], the natural spatial distribution of radiogenic ^4He is constrained by stepwise degassing and $^4He/^3He$ analysis of a sample containing synthetic, homogeneous, proton-induced ^3He [*Shuster et al.*, 2004]. Approximately 50 mg of separated apatite grains were packaged into Sn foil and exposed to $\sim 5 \times 10^{15}$ protons/cm^2 with incident energy ~220 MeV over a continuous 7 hour period at The Francis H. Burr Proton Therapy Center, Boston, USA. Euhedral crystals free of visible mineral inclusions were selected using the above criteria; crystal dimensions were measured using a calibrated binocular microscope. Individual crystals were then sequentially heated in multiple steps under ultra-high vacuum while in contact with a thermocouple using a feedback-

controlled 70 W diode laser at the BGC Noble Gas Thermochronometry Lab. The molar ^{3}He abundance and the $^{4}He/^{3}He$ ratio were measured for each heating step using calibrated pulse-counting sector-field mass spectrometry and corrected for blank contributions to ^{3}He and ^{4}He (uncertainties in blank corrections are propagated into ratio uncertainties). Following the stepped $^{4}He/^{3}He$ analysis, U, Th, and Sm concentrations were measured as described above at Caltech; the (U-Th-Sm)/He age was then calculated from these molar abundances and the total molar ^{4}He abundance summed from the incremental heating steps.

III.2.6.3 - Thermal modelling and inversion method

We used a recently developed numerical model to predict the (U-Th)/He age and the evolution of the $^{4}He/^{3}He$ ratio during a step-degassing analysis [*Schildgen et al.*, 2010]. Input parameters are characteristics of the analyzed crystal (apatite size, U/Th-content) and a cooling history. All cooling histories began at 150 °C and ended after 10 Ma at the modern mean surface temperature (~10 °C). The model generates random time-temperature (*t-T*) paths defined by 3 to 10 points to ensure extensive exploration of the *t-T* space and predicts an evolving spatial distribution of ^{4}He along each cooling path, assuming a uniform spatial distribution of U and Th (defined by U and Th concentration measurements) and an effective spherical diffusion geometry with surface/volume equivalent to the analyzed grain. Apatite diffusion kinetics is quantified from the radiation damage and annealing model (RDAAM, *Flowers et al.*, 2009). Following each randomly-generated cooling history, the model first calculates a (U-Th)/He age that is compared to the measured age. If the predicted age is within 1 standard error of the mean measured age, a model $^{4}He/^{3}He$ ratio evolution is calculated using the same analytical heating schedule as the sample and compared to observed ratios.

This approach allows a random-search scheme to identify cooling histories that are incompatible with the observations based on the computation of misfit statistics (M; mean of squared residuals weighted by the individual uncertainties in the ratio measurements, *Schildgen et al.*, 2010). We set a misfit limit M~2, which corresponds to the 99% confidence level. Thermal histories yielding M>4 (red in Figures III.2.2, III.2.3 and III.2.5) are excluded by the data, 2<M<4 are marginally acceptable (yellow), and M<2 are good fits to the data.
A few heating steps yielded $^{4}He/^{3}He$ ratios that plot well outside analytical uncertainty relative to contiguous heating steps and therefore result in evolving ratios that do not monotonically increase over the course of certain stepped heating analyses. For example, the

$^4He/^3He$ analysis of sample VIS-06 (Figure III.2.5c) contains "excess scatter" that is not well understood, particularly in the first steps for $0 < \sum F^3He < 0.3$. Potential explanations for these anomalous ratios include: (i) inaccuracy in the ^4He blank correction for a particular heating step, (ii) small cracks within the crystal that were not visible via optical microscopy, and (iii) significant U and/or Th spatial heterogeneity within the crystal. Although we cannot *a priori* exclude these scenarios, we note that U or Th zonation could not easily produce the non-monotonic $^4He/^3He$ pattern observed in VIS-06, particularly that from $0<\sum F\ ^3He<0.3$. In attempt to minimize the influence of anomalous $^4He/^3He$ ratios and simultaneously place some constraint on the most likely cooling scenarios, several data (shown as open grey boxes in Figures III.2.2 and III.2.5) were excluded from the calculation of misfit statistics. Inclusion of these data would result in somewhat lower levels of confidence in the excluded cooling paths (shown in red), with most of the constraint therefore derived from the (U-Th)/He age alone. For these reasons, we consider the permissible cooling paths for VIS-06 shown in Figure III.2.5c to be somewhat tentative and not directly comparable with the others.

III.2.7 - Supplementary information

This section reports one supplementary figure (Figure III.2.5) showing $^4He/^3He$ data for samples VIS-03, -04, -06 and -07 (see Figure III.2.3 for associated modelled *t-T* cooling paths). We also provide four supplementary tables for sample locations (Table III.2.1), (U-Th-Sm)/He data (Tables III.2.2 and III.2.3), and stepwise $^4He/^3He$ data (Table III.2.4).

Sample	Longitude (°E)	Latitude (°N)	Elevation (m)	Lithology
Martigny Samples:				
SIO-05	7.10163	46.16485	2060	Orthogneiss
SIO-06	7.10810	46.16192	1800	Orthogneiss
SIO-07	7.10680	46.15813	1455	Paragneiss
SIO-08	7.10825	46.15562	1230	Orthogneiss
SIO-02	7.12653	46.15828	975	Granitoid
SIO-03	7.11595	46.14895	760	Granitoid
SIO-04	7.08645	46.12603	480	Orthogneiss
Visp Samples:				
VIS-01	7.91668	46.3439	2925	Orthogneiss
VIS-03	7.91910	46.32732	2100	Micaschist
VIS-04	7.92398	46.31507	1600	Paragneiss
VIS-05	7.93781	46.31788	1400	Orthogneiss
VIS-06	7.98339	46.33000	850	Paragneiss
VIS-07	7.95333	46.30967	670	Orthogneiss

Table III.2.1. *Sample locations and details for SIO and VIS sampling sites.*

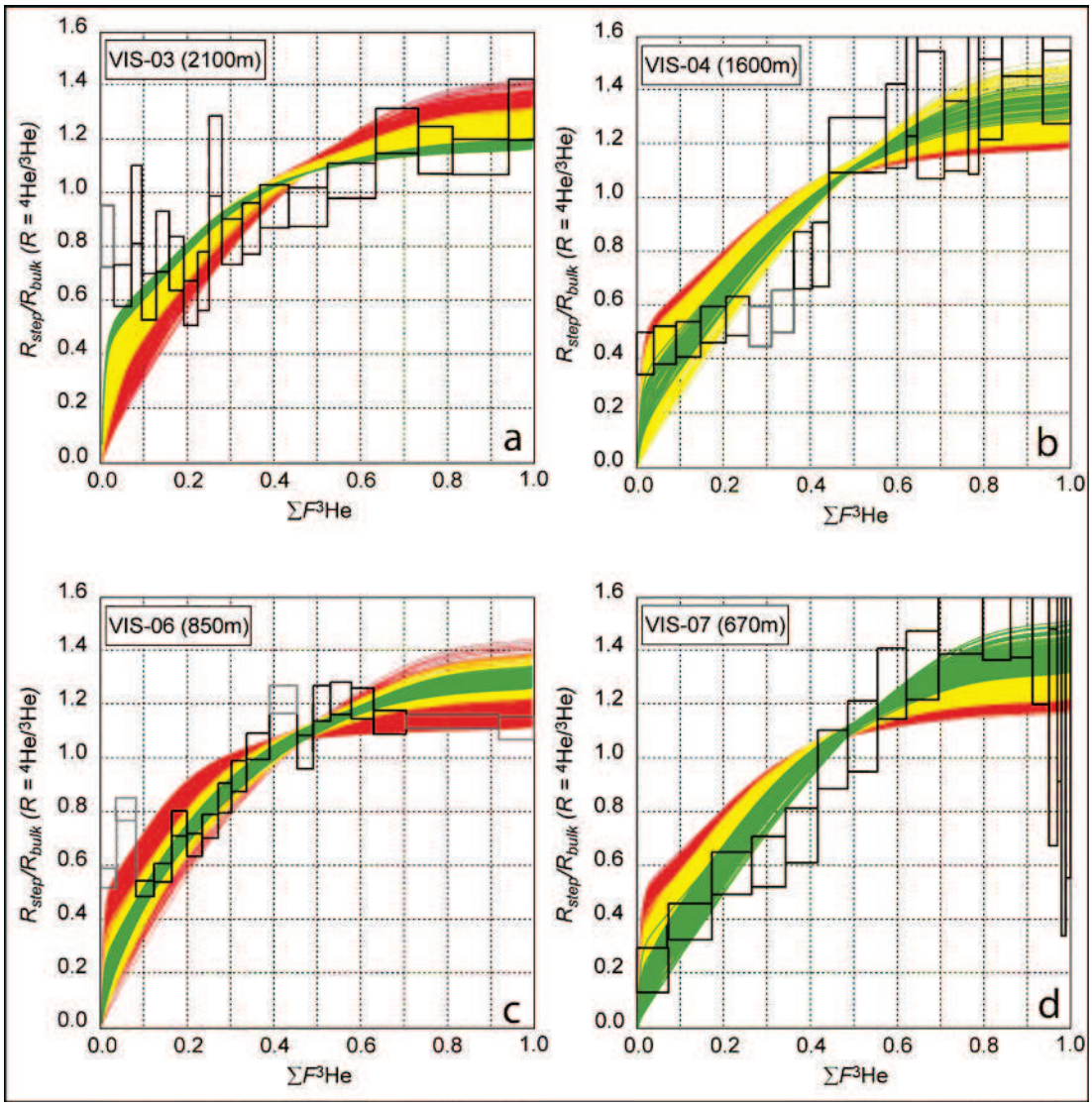

Figure III.2.5. *Observed $^4He/^3He$ ratios of VIS-03 (a), -04 (b), -06 (c) -07 (d). The measured $^4He/^3He$ ratios of each released step (R_{step}) are normalised to the bulk ratio (R_{bulk}) and plotted versus the cumulative ^3He release fraction ($\sum F\,^3He$). Open black boxes indicate 1 standard error (vertical) and integration steps (horizontal); open grey boxes show released steps that were excluded from the misfit calculation (see section III.2.6 for discussion). Colored lines show the predicted $^4He/^3He$ ratio evolution diagrams. Models shown in red and yellow are excluded by the $^4He/^3He$ data, whereas the green cooling paths are permitted.*

Sample	Mass (µg)	U (ppm)	Th (ppm)	Sm (ppm)	^{4}He (nmol g^{-1})	Raw Age (Ma)	Ft	Corrected Age (Ma)
SIO-04_a	4.1	56.1	2.4	152.6	1.2	3.9	0.78	5.0
SIO-04_c	6.8	89.7	1.4	130.0	1.6	3.2	0.81	4.0
SIO-04_o	5.5	177.8	11.5	258.0	4.9	5.0	0.76	6.6
SIO-04_s	4.6	111.9	15.7	333.8	3.7	5.9	0.73	8.2
SIO-04_x	5.8	162.4	11.0	223.0	5.1	5.7	0.77	7.3
SIO-04_y	4.0	147.3	9.2	223.8	3.8	4.7	0.74	6.3
SIO-04_z	11.1	157.3	5.1	206.9	3.0	3.5	0.81	4.3
SIO-04								**4.44 ± 0.51**
SIO-03_a	13.5	113.8	4.0	135.1	2.6	4.2	0.84	5.0
SIO-03_b	29.6	118.9	1.1	95.2	2.4	3.7	0.87	4.3
SIO-03_o	3.4	206.7	13.1	326.1	3.6	3.2	0.71	4.5
SIO-03_x	7.8	199.7	6.3	183.1	3.8	3.5	0.79	4.4
SIO-03_z	9.3	273.4	10.8	248.4	6.0	4.0	0.80	5.0
SIO-03								**4.63 ± 0.35**
SIO-02_a	4.4	67.7	3.2	202.5	1.3	3.6	0.79	4.6
SIO-02_o	7.2	43.2	4.4	211.9	1.3	5.3	0.79	6.7
SIO-02_s	2.1	170.5	14.1	228.1	2.9	3.1	0.71	4.3
SIO-02_x	4.5	72.3	7.1	219.9	1.4	3.3	0.75	4.5
SIO-02_y	13.2	97.2	8.3	135.9	1.9	3.4	0.82	4.2
SIO-02_z	3.4	149.6	11.9	243.2	3.1	3.7	0.74	5.0
SIO-02								**4.87 ± 0.95**
SIO-08_x	5.8	164.2	11.8	249.8	5.0	5.5	0.77	7.1
SIO-08_y	4.8	256.8	12.5	230.5	6.0	4.3	0.76	5.7
SIO-08								**6.38 ± 1.03**
SIO-07_a	17.3	129.3	1.9	122.8	3.1	4.4	0.85	5.2
SIO-07_o	4.8	169.4	8.7	227.1	3.8	4.1	0.75	5.5
SIO-07_x	3.9	156.5	10.0	210.8	3.4	4.0	0.74	5.3
SIO-07_y	7.1	143.8	6.8	193.4	3.2	4.1	0.78	5.2
SIO-07								**5.31 ± 0.27**
SIO-06_a	11.9	111.1	1.8	111.9	3.5	5.8	0.85	6.9
SIO-06_o	5.9	193.2	8.0	181.2	6.7	6.3	0.78	8.1
SIO-06_s	12.2	70.4	8.7	179.9	2.6	6.6	0.82	8.0
SIO-06_x	10.9	168.3	3.5	138.2	5.6	6.1	0.81	7.5
SIO-06_z	3.4	194.4	12.9	253.6	5.4	5.0	0.73	6.9
SIO-06								**7.48 ± 0.58**
SIO-05_a	13.5	56.2	1.1	109.6	2.1	6.7	0.85	7.9
SIO-05_o	6.1	51.6	5.2	239.1	1.5	5.1	0.78	6.6
SIO-05_x	10.0	196.5	3.9	158.7	6.2	5.8	0.81	7.2
SIO-05_z	8.9	29.4	3.6	117.4	0.7	4.3	0.80	5.3
SIO-05								**6.74 ± 1.09**

Tables III.2.2. *Apatite (U-Th-Sm)/He thermochronometry for Martigny profile. We report replicates (standard (U-Th-Sm)/He ages labelled as x/y/o/s, and ages derived from ^{4}He/^{3}He measurements labelled a/b/c/e) U-Th-Sm concentrations, ^{4}He measurements, raw age as well as FT corrections and corrected age. Samples mean age and 1σ standard deviation error are also given. Bold numbers are mean ages calculated from the replicates; 1σ error for mean ages is maximum value between standard deviation of replicate ages and estimated minimum reproducibility from Durango measurements (± 5%). Analytical uncertainties are <1, ~3 and ~2% for respectively U, Th and Sm measurements; and <1% for ^{4}He measurements. Samples labels o/s/x/y/z correspond to standard (U-Th-Sm)/He ages measurements, whereas labels a/b/c correspond to (U-Th-Sm)/He ages derived from ^{4}He/^{3}He analyses. Note that for SIO-04, replicates o/s/x/y were not considered into the calculation of the mean He age. These outliers have ages that were far from the rest of the population of grains analyzed and also compared to other samples. This problem can come from different reasons, such as non-visible microscopic inclusions, strong zoning in U, Th or Sm, He-implantation from adjacent minerals, etc...*

Sample	Mass (µg)	U (ppm)	Th (ppm)	Sm (ppm)	^{4}He (nmol g^{-1})	Raw Age (Ma)	Ft	Corrected Age (Ma)
VIS-07_e	10.6	20.9	39.9	55.8	0.2	0.9	0.86	1.1
VIS-07_x	9.7	38.8	59.3	128.2	0.5	1.6	0.79	2.0
VIS-07_y	5.2	29.9	43.3	87.5	0.2	0.8	0.75	1.1
VIS-07_z	5.1	18.2	39.9	65.6	0.2	1.5	0.74	2.0
VIS-07								**1.55 ± 0.53**
VIS-06_a	28.0	42.1	30.3	77.3	0.6	2.3	0.90	2.6
VIS-06_b	15.6	45.7	56.2	121.9	1.1	3.4	0.87	3.9
VIS-06_s	11.4	74.7	81.7	300.4	1.3	2.4	0.81	3.0
VIS-06_x	24.5	98.2	60.8	168.7	1.7	2.8	0.85	3.3
VIS-06_y	19.6	123.4	67.9	202.5	1.5	2.0	0.84	2.4
VIS-06_z	5.4	42.4	37.1	272.1	0.8	2.7	0.77	3.5
VIS-06								**3.11 ± 0.56**
VIS-05_x	7.2	26.7	30.5	225.1	0.5	2.5	0.76	3.3
VIS-05_y	9.9	19.3	24.9	196.6	0.3	2.3	0.80	2.9
VIS-05_z	8.3	13.2	15.8	226.1	0.2	2.0	0.77	2.6
VIS-05								**2.90 ± 0.37**
VIS-04_c	10.9	17.6	18.2	74.2	0.4	2.9	0.86	3.4
VIS-04_s	7.2	12.2	20.6	68.7	0.1	1.5	0.77	2.0
VIS-04_x	6.8	22.0	25.7	94.3	0.4	2.6	0.77	3.3
VIS-04_y	6.3	17.7	17.0	72.5	0.3	2.5	0.73	3.5
VIS-04_z	11.2	45.2	42.0	181.7	0.8	2.3	0.80	2.9
VIS-04								**3.01 ± 0.63**
VIS-03_a	8.5	20.8	5.5	190.7	0.5	4.1	0.84	4.9
VIS-03_s	7.6	61.0	15.0	297.2	1.1	3.0	0.78	3.9
VIS-03_x	10.7	48.2	17.1	313.6	1.0	3.6	0.81	4.4
VIS-03_z	5.3	99.8	42.0	543.2	1.8	3.0	0.75	4.0
VIS-03								**4.31 ± 0.48**
VIS-01_x	4.5	51.1	28.4	293.2	1.1	3.5	0.73	4.8
VIS-01_z	4.8	38.0	19.1	262.0	0.8	3.3	0.73	4.5
VIS-01								**4.64 ± 0.23**

Tables III.2.3. *Apatite (U-Th-Sm)/He thermochronometry for Visp profile. We report replicates (standard (U-Th-Sm)/He ages labelled as x/y/o/s, and ages derived from ^{4}He/^{3}He measurements labelled a/b/c/e) U-Th-Sm concentrations, ^{4}He measurements, raw age as well as FT corrections and corrected age. Samples mean age and 1σ standard deviation error are also given. Ft = age correction factor. Bold numbers are mean ages calculated from the replicates; 1σ error for mean ages is maximum value between standard deviation of replicate ages and estimated minimum reproducibility from Durango measurements (± 5%). Analytical uncertainties are ~1-2% for U, Th and Sm measurements; and <1% for ^{4}He measurements. Samples labels o/s/x/y/z correspond to standard (U-Th-Sm)/He ages measurements, whereas labels a/b/c/e correspond to (U-Th-Sm)/He ages derived from ^{4}He/^{3}He analyses.*

SIO-04b (480m)

Step	Temp (°C)	Duration (hours)	^{3}He (x 10^6 atoms)	(+/-) (x 10^6 atoms)	^{4}He/^{3}He	(+/-)
1	260	0.38	0.099	0.013	495	80
2	275	0.38	0.072	0.011	766	129
3	290	0.51	0.099	0.013	989	134
4	300	0.66	0.281	0.022	1638	119
5	310	0.66	0.353	0.025	3167	202
6	330	0.46	0.497	0.030	4082	216
7	340	0.45	0.264	0.022	4449	324
8	350	0.48	0.716	0.036	5585	245
9	350	0.66	0.206	0.019	6176	510
10	370	0.53	0.388	0.026	6690	397
11	400	0.48	0.170	0.017	6351	582
12	410	0.63	0.065	0.010	6389	980
13	420	0.50	0.079	0.012	5323	734
14	440	0.50	0.044	0.008	6779	1314
15	475	0.50	0.105	0.013	5828	689
16	500	0.50	0.080	0.012	7160	980
17	550	0.50	0.066	0.010	7146	1082
18	700	0.50	0.016	0.005	9536	3467
19	900	0.50	0.003	0.001	2353	3118
20	950	0.50	0.000	0.000	8154	71738

Effective model : a = 97 µm, U = 101.1 ppm, Th = 3.0 ppm,
Replicates : (U-Th)/He age = 4.44 +/- 0.51 Ma (no age for SIO-04b); dated grains a = 76.1 µm

SIO-07a (1455m)

Step	Temp (°C)	Duration (hours)	^{3}He (x 10^6 atoms)	(+/-) (x 10^6 atoms)	^{4}He/^{3}He	(+/-)
1	260	0.38	0.063	0.010	1272	222
2	275	0.38	0.041	0.008	2096	428
3	290	0.51	0.063	0.010	2321	374
4	300	0.66	0.082	0.012	3027	412
5	310	0.66	0.099	0.013	2907	359
6	330	0.46	0.131	0.015	3288	346
7	340	0.45	0.154	0.016	3544	343
8	350	0.48	0.178	0.018	4267	381
9	350	0.66	0.200	0.019	4736	398
10	370	0.53	0.256	0.021	5457	402
11	400	0.48	0.648	0.034	5726	265
12	410	0.63	0.654	0.034	5798	265
13	420	0.50	0.475	0.029	6261	337
14	440	0.50	0.778	0.037	5966	249
15	475	0.50	0.990	0.042	6551	242
16	500	0.50	0.617	0.033	6059	284
17	550	0.50	0.322	0.024	6843	448
18	700	0.50	0.350	0.025	6627	416
19	900	0.50	0.138	0.016	6157	624

Effective model : a = 101 µm, U = 149.8 ppm, Th = 6.8 ppm,
Replicates : (U-Th)/He age = 5.31 +/- 0.27 Ma (SIO-07a : 5.20 Ma); dated grains a = 71.6 µm

SIO-06a (1800m)

Step	Temp (°C)	Duration (hours)	^{3}He (x 10^6 atoms)	(+/-) (x 10^6 atoms)	^{4}He/^{3}He	(+/-)
1	260	0.38	0.058	0.010	1708	311
2	275	0.38	0.016	0.005	4823	2062
3	290	0.51	0.048	0.009	3981	820
4	300	0.66	0.057	0.010	3374	603
5	310	0.66	0.052	0.009	5521	1041
6	330	0.46	0.105	0.013	5765	707
7	340	0.45	0.076	0.011	5286	791
8	350	0.48	0.163	0.017	8181	784
9	350	0.66	0.121	0.014	5744	651
10	370	0.53	0.177	0.018	5581	511
11	400	0.48	0.305	0.023	5656	389
12	410	0.63	0.336	0.024	7337	476
13	420	0.50	0.235	0.020	8009	628
14	440	0.50	0.300	0.023	7743	533
15	475	0.50	0.447	0.028	8219	460
16	500	0.50	0.391	0.026	8382	501
17	550	0.50	0.518	0.030	9099	468
18	700	0.50	0.958	0.042	10265	386
19	900	0.50	0.150	0.016	15355	1532

Effective model : a = 98 µm, U = 147.5 ppm, Th = 7.0 ppm,
Replicates : (U-Th)/He age = 7.48 +/- 0.58 Ma (SIO-06a : 6.90 Ma); dated grains a = 79.3 µm

VIS-07e (670m)

Step	Temp (°C)	Duration (hours)	^{3}He (x 10^6 atoms)	(+/-) (x 10^6 atoms)	^{4}He/^{3}He	(+/-)
1	260	0.38	0.358	0.025	61	22
2	290	0.51	0.488	0.030	109	18
3	300	0.66	0.451	0.028	157	21
4	310	0.66	0.380	0.026	168	25
5	330	0.46	0.365	0.025	194	27
6	340	0.45	0.338	0.025	269	29
7	350	0.48	0.335	0.024	292	35
8	350	0.66	0.326	0.024	344	35
9	370	0.53	0.363	0.025	362	34
10	400	0.48	0.499	0.030	404	30
11	410	0.50	0.314	0.024	414	46
12	420	0.56	0.246	0.021	433	63
13	440	0.63	0.187	0.018	391	67
14	475	0.50	0.092	0.012	291	107
15	500	0.50	0.050	0.009	455	207
16	550	0.50	0.046	0.008	405	310
17	700	0.50	0.055	0.009	371	219

Effective model : a = 90 µm, U = 27.0 ppm, Th = 45.6 ppm,
Replicates : (U-Th)/He age = 1.55 +/- 0.53 Ma (VIS-07e : 1.10 Ma); dated grains a = 71.3 µm

VIS-06a (850m)

Step	Temp (°C)	Duration (hours)	^{3}He (x 10^6 atoms)	(+/-) (x 10^6 atoms)	^{4}He/^{3}He	(+/-)
1	260	0.38	0.472	0.029	568	36
2	290	0.51	0.630	0.034	827	43
3	300	0.66	0.566	0.032	528	30
4	310	0.66	0.551	0.031	588	35
5	330	0.46	0.473	0.029	774	47
6	340	0.45	0.477	0.029	693	43
7	350	0.48	0.499	0.030	763	45
8	350	0.66	0.414	0.027	870	56
9	370	0.53	0.466	0.029	952	58
10	400	0.48	0.720	0.036	1065	50
11	410	0.50	0.869	0.039	1241	53
12	420	0.56	0.496	0.030	1043	63
13	440	0.63	0.536	0.031	1227	67
14	475	0.50	0.653	0.034	1246	61
15	500	0.50	0.690	0.035	1226	58
16	550	0.50	1.025	0.043	1155	45
17	700	0.50	2.876	0.072	1158	26
18	900	0.50	1.105	0.045	1133	43

Effective model : a = 149 µm, U = 71.1 ppm, Th = 55.7 ppm,
Replicates : (U-Th)/He age = 3.11 +/- 0.56 Ma (VIS-06a : 2.61 Ma); dated grains a = 101.3 µm

VIS-04c (1600m)

Step	Temp (°C)	Duration (hours)	^{3}He (x 10^6 atoms)	(+/-) (x 10^6 atoms)	^{4}He/^{3}He	(+/-)
1	260	0.38	0.162	0.015	234	42
2	290	0.51	0.213	0.018	250	38
3	300	0.66	0.234	0.019	262	35
4	310	0.66	0.239	0.019	291	36
5	330	0.46	0.222	0.018	308	39
6	340	0.45	0.211	0.017	287	40
7	350	0.48	0.212	0.018	318	42
8	350	0.66	0.177	0.016	419	57
9	370	0.53	0.159	0.015	431	64
10	400	0.48	0.540	0.030	649	55
11	410	0.50	0.194	0.017	687	84
12	420	0.56	0.103	0.011	814	147
13	440	0.63	0.259	0.020	709	127
14	475	0.50	0.227	0.018	667	70
15	500	0.50	0.098	0.011	734	143
16	550	0.50	0.222	0.018	740	80
17	700	0.50	0.387	0.025	848	61
18	900	0.50	0.264	0.020	765	73

Effective model : a = 82 µm, U = 22.9 ppm, Th = 24.7 ppm,
Replicates : (U-Th)/He age = 3.01 +/- 0.63 Ma (VIS-04c : 3.40 Ma); dated grains a = 70.4 µm

VIS-03a (2100m)

Step	Temp (°C)	Duration (hours)	^{3}He (x 10^{6} atoms)	(+/-) (x 10^{6} atoms)	$^{4}He/^{3}He$	(+/-)
1	260	0.38	0.111	0.013	922	124
2	290	0.51	0.151	0.016	724	83
3	300	0.66	0.089	0.012	1050	157
4	310	0.66	0.122	0.014	680	93
5	330	0.46	0.112	0.014	901	122
6	340	0.45	0.125	0.014	813	108
7	350	0.48	0.121	0.014	654	89
8	350	0.66	0.095	0.012	742	118
9	370	0.53	0.110	0.013	1244	161
10	400	0.48	0.175	0.017	900	91
11	410	0.50	0.153	0.016	953	103
12	420	0.56	0.247	0.021	1043	86
13	440	0.63	0.331	0.024	1039	78
14	475	0.50	0.415	0.027	1145	70
15	500	0.50	0.364	0.025	1345	90
16	550	0.50	0.295	0.023	1268	95
17	700	0.50	0.479	0.029	1241	71
18	900	0.50	0.219	0.019	1430	122

Effective model : a = 91 µm, U = 57.4 ppm, Th = 19.9 ppm,
Replicates : (U-Th)/He age = 4.31 +/- 0.48 Ma (VIS-03a : 4.92 Ma); dated grains a = 74.2 µm

Table III.2.4. *Stepwise $^{4}He/^{3}He$ data for SIO and VIS samples.*

III.3 - Late Neogene exhumation and relief development of the Aar and Aiguilles Rouges massifs (Swiss Alps) from low-temperature thermochronology modeling and $^{4}He/^{3}He$ thermochronometry

Pierre G. Valla [1], Peter A. van der Beek [1], David L. Shuster [2,3], Jean Braun [1], Frédéric Herman [4], Laurent Tassan-Got [5], and Cécile Gautheron [6]

[1] *ISTerre-OSUG, University of Grenoble, CNRS, BP 53, F-38041 Grenoble, France*

[2] *Berkeley Geochronology Center, 2455 Ridge Road, CA-94709 Berkeley, USA*

[3] *Department of Earth and Planetary Science, U.C. Berkeley, CA-94709 Berkeley, USA*

[4] *Geologisches Institut, ETH Zürich, 8092 Zürich, Switzerland*

[5] *Institut de Physique Nucléaire, CNRS/IN2P3, Université Paris Sud, 91405 Orsay, France*

[6] *Interactions et Dynamique des Environnements de Surface - CNRS, Université Paris Sud, 91405 Orsay, France*

Abstract

The late Neogene to Pliocene-Quaternary exhumation history of the European Alps is the subject of controversial findings and interpretations, with several thermochronological studies arguing for long-term steady-state exhumation rates, while others have pointed to late Miocene-Pliocene exhumation pulses associated with tectonic and/or climatic changes. Here, we perform inverse thermal-kinematic modeling on dense thermochronological datasets combining literature apatite fission-track data (AFT) from the literature and recently published apatite (U-Th-Sm)/He data (AHe) along the upper Rhône valley (Aar and Aiguilles Rouges massifs, Swiss Alps), in order to find best-fitting exhumation scenarios and to derive precise estimates on denudation and relief histories. We then apply forward numerical modeling to interpret cooling paths quantified from apatite $^{4}He/^{3}He$ data in terms of denudation and relief development scenarios. Our modeling results highlight the complementarities between AFT/AHe thermochronology data and $^{4}He/^{3}He$ thermochronometry in quantitatively providing denudation and relief information. Modeling results suggest a late-Miocene exhumation pulse lasting until ~8-10 Ma, consistent with recently proposed exhumation histories for other parts of the European Alps, and followed by moderate (~0.3-0.5 km Ma^{-1}) denudation rates during the late Miocene/Pliocene. Both inverse modeling and $^{4}He/^{3}He$ data reveal that the late-stage exhumation of these studied massifs can

be explained by a significant increase (~85-100%) in local topographic relief through efficient glacial valley incision. Modeling results quantitatively constrain Rhône valley carving to ~1-1.5 km since ~1 Ma. We postulate that recent relief development within this part of the Swiss Alps is climatically-driven by the Mid-Pleistocene climate transition and the onset of major Alpine glaciations.

III.3.1 Introduction

Understanding the long-term evolution of active mountain belts requires precise identification and quantification of the complex couplings between tectonics, climate and erosion [*e.g.*, *Beaumont et al.*, 1992; *Willett*, 1999; *Whipple and Meade*, 2006; *Whipple*, 2009]. One key illustration of this problem is the ongoing debate on the potential links between the late Cenozoic increase in global sediment budgets [*e.g.*, *Hay et al.*, 1988; *Zhang et al.*, 2001; *Molnar*, 2004], which has, however, recently been questioned [*Schumer and Jerolmack*, 2009; *Willenbring and von Blanckenburg*, 2010], and Pliocene-Quaternary climate or tectonic changes enhancing mountain-belt denudation [*Molnar and England*, 1990; *Raymo and Ruddiman*, 1992; *Zhang et al.*, 2001].

A similar increase in foreland sedimentation rates has been reported for the European Alps since the Miocene-Pliocene transition [*Kuhlemann et al.*, 2002; *Willett et al.*, 2006], in concordance with the initiation of exhumation in the northern alpine foreland basin [*Cederbom et al.*, 2004; in press], cessation of Jura folding [*Becker*, 2000] and possibly re-activation of deformation in the internal part of the orogen [*Willett et al.*, 2006]. A compilation of thermochronology data within the western and central Alps also evidenced an exhumation pulse of the Alpine crystalline massifs [*Schmid et al.*, 1996; 2004] since the Pliocene [*Vernon et al.*, 2008]. Many studies have interpreted this major exhumation change within the Alpine orogen as an erosional response to the establishment of more humid climatic conditions during the Pliocene [*Cederbom et al.*, 2004; *Willett et al.*, 2006] and the onset of glacial/interglacial oscillations in the late Pliocene-Quaternary [*e.g.*, *Haeuselmann et al.*, 2007; *Glotzbach et al.*, 2008; submitted; *Valla et al.*, submitted, a].

However, the timing of both sedimentation and exhumation pulses appears to be spatially diachronous for the western and central Alps; sedimentation-rate increases occurred at around 5 and 1 Ma [*Kuhlemann et al.*, 2002], while accelerations in denudation rates started between

6.5 and 2.5 Ma for the different crystalline massifs [*Vernon et al.*, 2008]. Similarly, local studies using *in-situ* thermochronology data have led to contrasting conclusions regarding timing and rates for Neogene exhumation histories with no or inconsistent exhumation pulses evidenced in the western and central Alps [*e.g.*, *Wagner et al.*, 1977; *Hurford*, 1986; 1991; *Bigot-Cormier et al.*, 2006; *Glotzbach et al.*, 2008; *Reinecker et al.*, 2008; *Vernon et al.*, 2009; *van der Beek et al.*, 2010; *Glotzbach et al.*, submitted]. Moreover, detrital thermochronology results suggest constant orogen-scale exhumation rates in the western European Alps since 10-15 Ma [*Bernet et al.*, 2001; 2009; *Glotzbach et al.*, 2011].

It thus appears necessary to provide tighter quantitative constrains on the late Neogene exhumation of the Alpine massifs in order to : (1) better understand this spatial heterogeneity in exhumation histories, and (2) identify the potential climatic and/or tectonic forcing for accelerations in exhumation within the western and central Alps. The nature of exhumation triggers for the late Neogene evolution of the Alps has been widely discussed in the literature, with contrasting interpretations. On the one hand, *Persaud and Pfiffner* [2004] have linked a Pliocene acceleration in denudation rates to ongoing compression in the Swiss central Alps, while *Reinecker et al.* [2008] attributed Mid-Pliocene tectonic denudation in the same area to orogen-perpendicular extension. On the other hand, the Pliocene increase in both exhumation and sedimentation rates has been interpreted as a response to major climatic changes, associated with gradual climate cooling in the Pliocene [*e.g.*, *Zhang et al.*, 2001; *Haug et al.*, 2005] and transition toward wetter conditions [*Driscoll and Haug*, 1998] that could have enhanced mountain belt denudation [*e.g.*, *Molnar and England*, 1990]. Moreover, recent studies have suggested that topographic relief development following the onset of Quaternary glaciations [*e.g.*, *Haug et al.*, 2005; *Lisiecki*, 2010] may have contributed to the late stage exhumation of the Alpine massifs [*e.g.*, *Haeuselmann et al.*, 2007; *Glotzbach et al.*, submitted; *Valla et al.*, submitted, a].

Here, we combine low-temperature thermochronology data (apatite fission-track (AFT) and apatite (U-Th-Sm)/He data (AHe)) with apatite $^{4}He/^{3}He$ thermochronometry [*Shuster and Farley*, 2005] to constrain the late-Neogene exhumation history of the central Alps (Aiguilles Rouges and Aar massifs) and to assess the impact of Pliocene climate change and/or Quaternary glaciations on the late-stage exhumation of these massifs. We use a recently developed method coupling thermal-kinematic modeling (*Pecube* model; *Braun*, 2003) with an iterative inverse approach [*Sambridge*, 1999a, b] to quantitatively extract information on

both exhumation and relief histories from thermochronology data [*e.g.*, *Herman et al.*, 2007; 2010a; *Valla et al.*, 2010b; *van der Beek et al.*, 2010; *Glotzbach et al.*, submitted], implementing the control of alpha-recoil damage on He diffusion kinetics in apatite [*Shuster et al.*, 2006; *Flowers et al.*, 2009; *Gautheron et al.*, 2009].

We compile apatite fission-track data from the literature [*Wagner et al.*, 1997; *Rahn*, 1994; *Reinecker et al.*, 2008] with recent apatite (U-Th-Sm)/He data [*Valla et al.*, submitted, a]. We then interpret cooling histories quantified from apatite $^{4}He/^{3}He$ data [*Valla et al.*, submitted, a] in terms of exhumation and relief scenarios using forward thermal-kinematic modeling (*Pecube* model). We finally compare the results from the two approaches to assess how to provide best constraints on both the regional late-Neogene exhumation history and potential local relief development during Pliocene-Quaternary times.

In the following, we first present the study area, and discuss the selected thermochronology data and their qualitative interpretation in terms of apparent exhumation rates. We then summarize our modeling approach and show the predictions for the Neogene-Quaternary exhumation histories of the Aiguilles Rouges and Aar massifs. Finally, we assess whether late Pliocene-Quaternary glaciations have led to significant topographic relief development and attempt to precisely quantify both the timing and amplitude of the topographic change, using recently published and new $^{4}He/^{3}He$ data.

III.3.2 Geological and geomorphic setting

The Aar and Aiguilles Rouges massifs (Figure III.3.1a) belong to the Alpine external crystalline massifs (ECMs): blocks of European crystalline basement that are exposed in an orogen-parallel string of massifs [*e.g.*, *Schmid et al.*, 2004]. The Aar and Aiguilles Rouges massifs comprise Pre-Variscan and Variscan crystalline units and Paleozoic to Tertiary sedimentary series [*e.g.*, *von Raumer and Neubauer*, 1993] that have been buried and metamorphosed by overthrusting of the Helvetic and Penninic nappes during the Alpine collision [*Abrecht*, 1994; *Frey and Ferreiro Maehlmann*, 1999]. Ongoing collision resulted in Oligocene-Miocene exhumation of the ECMs from ~15 km depth [*e.g.*, *Schmid and Kissling*, 2000; *Leloup et al.*, 2005] along major crustal-scale faults (*e.g.*, the Penninic frontal thrust; *Schmid et al.*, 1996; 2004).

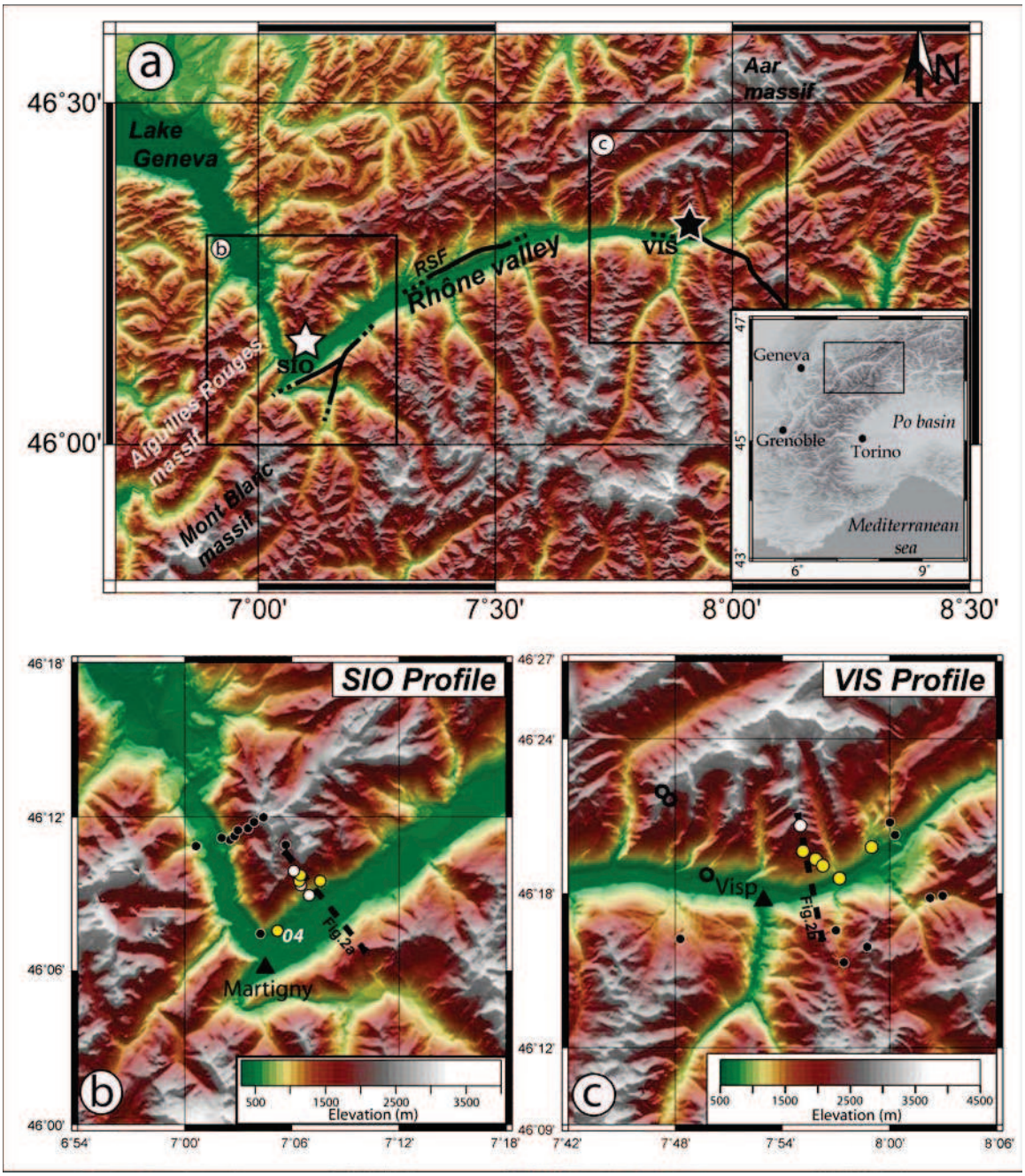

Figure III.3.1. *Topography and sample locations. (a) Relief map of the studied area in the Swiss Alps. Stars represent SIO (white) and VIS (black) sampling sites along the Rhône valley. The black boxes outline the model domains shown in Figures III.3.1b and c. Black lines indicate the location of the Rhône-Simplon fault (RSF) along the Rhône valley [Mancktelow, 1985; 1992; Seward and Mancktelow, 1994]. Inset shows location of the study area within the European Alps. (b-c) Sample locations for SIO (b) and VIS (c) sites (yellow circles: AHe and* $^{4}He/^{3}He$ *data, white circles: AHe data only, black circles : AFT data from the literature [b: black circles from Rahn, 1994; c: open circles from Reinecker et al., 2008, and black circles from Wagner et al., 1977], see Figure III.3.2 and Tables III.3.1 and III.3.2 for details). Cross profiles shown in Figure III.3.2 are also indicated (dashed lines in b and c).*

The Neogene tectonic evolution of the area is related to the activity of the Rhône-Simplon fault (Figure III.3.1a), a low-angle detachment fault [*e.g.*, *Mancktelow*, 1985; 1992; *Seward and Mancktelow*, 1994] accommodating tectonic denudation since the early Miocene until Pliocene to recent times [*Reinecker et al.*, 2008; *Campani et al.*, 2010]. However, the late Neogene activity of this tectonic structure is subject of discussion, with studies arguing for a Pliocene acceleration of tectonic denudation [*Soom*, 1990; *Reinecker et al.*, 2008], while others suggested a decrease in Rhône-Simplon fault activity during the late Neogene [*e.g.*, *Mancktelow*, 1992; *Campani et al.*, 2010]. The present-day kinematics of the area reveals no active compression [*Calais et al.*, 2002; *Nocquet and Calais*, 2004] and orogen-perpendicular extension [*e.g.*, *Champagnac et al.*, 2004; *Sue et al.*, 2007]; in contrast, geodetic measurements record significant present-day rock uplift rates > 1 mm a^{-1} within the Swiss Alps [*Kahle et al.*, 1997; *Schlatter et al.*, 2005].

Published thermochronology data include zircon fission track (ZFT) ages >100 Ma for the Aiguilles Rouges massif [*Rahn*, 1994] and from 10 to ~100 Ma for the Aar massif [*Michalski and Soom*, 1990; *Glotzbach et al.*, 2010]. The ZFT thermochronometric system has thus been only partially reset during Alpine collision, which constrains the Cenozoic exhumation of the area to ≤~8-9 km (adopting a ZFT closure temperature of ~210-240 °C, *Brandon et al.*, 1998; *Bernet*, 2009). Apatite fission-track (AFT) and (U-Th)/He (AHe) ages range from ~2 to 10 Ma in the Aar massif [*Wagner et al.*, 1977; *Michalski and Soom*, 1990; *Soom*, 1990; *Reinecker et al.*, 2008; *Vernon et al.*, 2009; *Glotzbach et al.*, 2010], similar to AFT ages for the Aiguilles Rouges massif [*Soom*, 1990; *Rahn*, 1994; *Seward and Mancktelow*, 1994].

Age-elevation relationships [*Wagner et al.*, 1977; *Hurford*, 1986; 1991; *Reinecker et al.*, 2008] and numerical thermal modeling [*Vernon et al.*, 2009; *Glotzbach et al.*, 2010] both suggest fairly constant exhumation rates of ~0.3-0.7 km Ma^{-1} through the late Neogene, with a potential acceleration during the late Pliocene [*Reinecker et al.*, 2008; *Glotzbach et al.*, 2010; *Pignalosa et al.*, 2010]. However, these studies (except for *Vernon et al.*, 2009) have not considered the effects of potential topographic relief change [*Braun*, 2002a; *Foeken et al.*, 2007] on the Neogene exhumation, and the relief history has not been studied in detail for these two massifs.

The topography of the Swiss Alps presents high relief with peaks reaching up to 4000 m and valley bottoms lying at ~400-700 m elevation (Figure III.3.1a). Both the drainage pattern and

the first-order relief organization are strongly controlled by lithological and tectonic structures [*Kühni and Pfiffner*, 2001a, b]; however, the present-day landscape reveals a strong imprint of late Quaternary glaciations with typical U-shaped valleys (Figure III.3.2a, b) and major overdeepenings within the upper Rhône catchment [*Finkh and Frey*, 1991; *Pfiffner et al.*, 1997; *Rosseli and Olivier*, 2003] that have been carved by thick, large and erosive glaciers [*e.g.*, *Kelly et al.*, 2004]. The amount of relief development following Quaternary glaciations has mostly been evaluated from the massif-scale geophysical relief [*e.g.*, *Small and Anderson*, 1998; *Brocklehurst and Whipple*, 2002]. Recent studies have proposed a maximum of ~1-1.5 km Quaternary relief production in the western and central Alps [*Champagnac et al.*, 2007; *van der Beek and Bourbon*, 2008], in agreement with quantitative constraints on local Quaternary valley carving [*Haeuselmann et al.*, 2007; *Valla et al.*, submitted, a].

The present-day landscape also shows evidence for efficient post-glacial relief rejuvenation [*Schlunegger and Hinderer*, 2003; *Norton et al.*, 2010a] by hillslope and fluvial processes [*e.g.*, *Korup and Schlunegger*, 2007; *Delunel et al.*, 2010a; *Valla et al.*, 2010c]. Moreover, late Pleistocene to Holocene sediment fluxes [*Hinderer*, 2001; *Schlunegger and Hinderer*, 2001] and catchment integrated denudation rates from cosmogenic ^{10}Be [*Wittmann et al.*, 2007] closely correlate with geodetic rock-uplift rates [*Schlatter et al.*, 2005], suggesting a potential coupling between erosion and uplift for late Quaternary to recent times. Several studies have proposed that modern rock uplift measured within the western and central Alps at least partly results from isostatic response to Quaternary erosional unloading [*Champagnac et al.*, 2007; 2009] as well as late-glacial to Holocene glacier retreat [*Gudmundsson*, 1994; *Barletta et al.*, 2006].

III.3.3 Numerical modeling of thermochronology data

III.3.3.1 AHe and AFT thermochronology

The AHe and AFT systems are characterized by closure temperatures (T_c) ranging from 60-80 °C to 100-120 °C, respectively [*Gallagher et al.*, 1998; *Farley*, 2002]. However, recent studies have shown that He diffusivity and consequently the AHe closure temperature are linked to the amount of alpha-recoil damage [*Shuster et al.*, 2006; *Flowers et al.*, 2009; *Gautheron et al.*, 2009], which itself depends on effective U-content (creating the lattice damages by both U and Th alpha-decay) and the thermal history (damages can be thermally

annealed; see *Flowers et al.*, 2009; *Gautheron et al.*, 2009; *Shuster and Farley*, 2009). As an example, different effective Uranium concentrations (eU = [U] + 0.24 [Th], which weights each parent nuclide by its α production) of 10, 50, 100, 150 and 200 ppm, for a 10 °C Ma^{-1} cooling rate and 60 μm grain radius, will lead to *Tc* values of ~74, 80, 83, 86, and 87 °C, respectively [*Gautheron et al.*, 2009], significantly different from the *Tc* obtained for standard diffusion parameters ($T_c \approx 74$ °C; *Farley*, 2000).

Recent numerical algorithms have been developed to simulate the radiation-damage effect on He retention [*Flowers et al.*, 2009; *Gautheron et al.*, 2009]. *Valla et al.* [submitted, a] used the RDAAM algorithm (Radiation Damage Accumulation and Annealing Model; *Flowers et al.*, 2009) to interpret $^4He/^3He$ and AHe data in terms of *t-T* paths.

Here, we combine a similar numerical approach [*Gautheron and Tassan-Got, 2010*] with the *Pecube* model for AHe age predictions. Both models are very similar and use the effective U concentration, U/Th ratio, and the sphere-equivalent radius (respectively eU, UTh and a, Tables III.3.1 and III.3.2) as well as a *t-T* history as input parameters [*Flowers et al.*, 2009; *Gautheron et al.*, 2009]. The main difference between the codes concerns the assumed dependence between radiation damage defects and He retention within the crystal lattice. *Flowers et al.* [2009] adopted a cubic form from empirical data [*Shuster et al.*, 2006], while *Gautheron et al.* [2009] used a physically-derived linear dependence between the creation of lattice defects and the amount of trapped He.

III.3.3.2 Thermochronology data compilation

In this study, we combine apatite (U-Th-Sm)/He (AHe) data sampled along two elevation profiles (*VIS* and *SIO* sites, see Figures III.3.1, III.3.2 and *Valla et al.*, submitted, a) with apatite fission-track (AFT) data from the literature [*Wagner et al.*, 1977; *Rahn*, 1994; *Reinecker et al.*, 2008]. We define two specific areas for thermal-kinematic modeling (Figure III.3.1a): (1) a first area centered on the *VIS* sampling profile (*VIS* area, Figure III.3.1c) within the Aar massif (upper Rhône valley); and (2) a second area for the *SIO* elevation profile (*SIO* area, Figure III.3.1b) covering the Aiguilles Rouges massif (~50 km downstream in the Rhône valley).

Sample	Longitude (°E)	Latitude (°N)	Elevation (m)	Tectonic unit	AFT Age ±1σ (Ma)	AHe Age ±1σ (Ma)	eU / a / UTh (ppm / µm)	Source
VIS-01	7.91668	46.3439	2925	Aar massif	/	4.6 ± 0.2	45 / 58.0 / 1.9	*Valla et al.*, subm.
VIS-03	7.91910	46.32732	2100	Aar massif	/	4.3 ± 0.5	60 / 74.2 / 2.9	*Valla et al.*, subm.
VIS-04	7.93106	46.32198	1700	Aar massif	/	3.0 ± 0.6	24 / 70.4 / 0.9	*Valla et al.*, subm.
VIS-05	7.93781	46.31788	1400	Aar massif	/	2.9 ± 0.4	23 / 68.5 / 0.8	*Valla et al.*, subm.
VIS-06	7.98339	46.33000	850	Aar massif	/	3.1 ± 0.6	86 / 101.3 / 1.3	*Valla et al.*, subm.
VIS-07	7.95333	46.30967	670	Aar massif	/	1.6 ± 0.5	38 / 71.3 / 0.6	*Valla et al.*, subm.
KAW-0400	7.95168	46.27076	1480	Monte Leone nappe	3.4 ±0.3	/	/	*Wagner et al.*, 1977
KAW-0401	7.80704	46.27132	2300	Monte Leone nappe	5.6 ±0.6	/	/	*Wagner et al.*, 1977
KAW-0399	7.95348	46.25546	1720	Monte Leone nappe	3.5 ±0.4	/	/	*Wagner et al.*, 1977
KAW-0409	7.98467	46.26251	2600	Monte Leone nappe	6.7 ±0.7	/	/	*Wagner et al.*, 1977
KAW-0164	8.04940	46.29771	1410	Berisal series	4.2 ±0.4	/	/	*Wagner et al.*, 1977
KAW-0165	8.04265	46.29766	1390	Berisal series	4.4 ±0.4	/	/	*Wagner et al.*, 1977
KAW-0315	8.00583	46.33651	900	Aar massif	3.0 ±0.3	/	/	*Wagner et al.*, 1977
KAW-0360	8.00365	46.34158	900	Aar massif	3.4 ±0.3	/	/	*Wagner et al.*, 1977
LBS-17	7.78339	46.34588	2700	Aar massif	7.5 ±0.5	/	/	*Reinecker et al.*, 2008
LBS-18	7.78909	46.34325	2280	Aar massif	5.9 ±0.6	/	/	*Reinecker et al.*, 2008
LB-12	7.82646	46.31151	645	Aar massif	3.5 ±0.5	/	/	*Reinecker et al.*, 2008

Table III.3.1. *Apatite fission track (AFT) and (U-Th-Sm)/He (AHe) data [Wagner et al., 1977; Reinecker et al., 2008; Valla et al., submitted, a] for VIS modeling. Effective uranium concentration (eU), equivalent sphere radius (a) and U/Th ratio (UTh) are used for AHe age predictions using the alpha-damage and annealing model [Gautheron et al., 2009].*

Sample	Longitude (°E)	Latitude (°N)	Elevation (m)	Tectonic unit	AFT Age ±1σ (Ma)	MTL ±1σ (µm)	AHe Age ±1σ (Ma)	eU / a / UTh (ppm / µm)	Source
SIO-05	7.10163	46.16485	2060	Aiguilles Rouges Massif	/	/	6.7 ± 1.1	85 / 80.3 / 24.1	*Valla et al.*, subm.
SIO-06	7.10810	46.16192	1800	Aiguilles Rouges Massif	/	/	7.5 ± 0.6	157 / 79.3 / 21.1	*Valla et al.*, subm.
SIO-07	7.10680	46.15813	1455	Aiguilles Rouges Massif	/	/	5.3 ± 0.3	145 / 71.6 / 22.0	*Valla et al.*, subm.
SIO-08	7.10825	46.15562	1230	Aiguilles Rouges Massif	/	/	6.4 ± 1.0	192 / 63.4 / 17.4	*Valla et al.*, subm.
SIO-02	7.12653	46.15828	975	Aiguilles Rouges Massif	/	/	4.9 ± 1.0	109 / 66.1 / 12.2	*Valla et al.*, subm.
SIO-03	7.11595	46.14895	760	Aiguilles Rouges Massif	/	/	4.6 ± 0.4	179 / 80.7 / 25.9	*Valla et al.*, subm.
SIO-04	7.08645	46.12603	480	Aiguilles Rouges Massif	/	/	4.4 ± 0.5	126 / 76.1 / 34.3	*Valla et al.*, subm.
MRP-012	7.04576	46.19298	1175	Aiguilles Rouges Massif	5.5 ±0.4	13.90 ±0.16	/	/	*Rahn*, 1994
MRP-013	7.04197	46.18918	930	Aiguilles Rouges Massif	4.4 ± 0.3	13.32 ±0.18	/	/	*Rahn*, 1994
MRP-014	7.03862	46.18652	740	Aiguilles Rouges Massif	4.6 ±0.4	13.59 ±0.21	/	/	*Rahn*, 1994
MRP-022	7.06062	46.19770	2055	Morcles Nappe	6.6 ±0.7	14.26 ±0.18	/	/	*Rahn*, 1994
MRP-071	7.05488	46.19427	1675	Arpille massif	5.9 ±0.4	/	/	/	*Rahn*, 1994
MRP-200	7.01489	46.18225	560	Aiguilles Rouges Massif	5.0 ±0.3	13.80 ±0.18	/	/	*Rahn*, 1994
MRP-015	7.03428	46.18592	450	Aiguilles Rouges Massif	4.2 ±0.3	14.08 ±0.24	/	/	*Rahn*, 1994
MRP-208	7.06969	46.12082	460	Arpille massif	5.4 ±0.5	13.67 ±0.16	/	/	*Rahn*, 1994
MWeil-1	7.09480	46.18104	2130	Dorénaz Syncline	6.2 ±0.4	14.02 ±0.18	/	/	*Rahn*, 1994
MRP-021	7.06599	46.19988	2420	Morcles Nappe	8.9 ±0.4	14.63 ±0.13	/	/	*Rahn*, 1994

Table III.3.2. *Apatite fission track (AFT), (U-Th-Sm)/He (AHe) and mean track-lengths (MTL) data [Rahn, 1994; Valla et al., submitted, a] for SIO modeling. Effective uranium concentration (eU), equivalent sphere radius (a) and U/Th ratio (UTh) are used for AHe age predictions using the alpha-damage and annealing model [Gautheron et al., 2009].*

For the *VIS* area (Table III.3.1), we compile 6 apatite (U-Th-Sm)/He ages (Figures III.3.1c and III.3.2b, d; see *Valla et al.*, submitted, a, for details on data acquisition) and apatite fission track ages from *Reinecker et al.* [2008] and *Wagner et al.* [1977] (respectively 3 and 8 AFT ages, Figures III.3.1c and III.3.2d). AHe ages range from 1.6 to 4.6 Ma (Figures III.3.2b, d) and their age-elevation relationship suggests an apparent exhumation rate of 0.9 ±0.2 km Ma^{-1} (Pearson's coefficient r = 0.74; *Valla et al.*, submitted, a). AFT data are spatially distributed within the studied area (Figure III.3.1c) and have not been collected following an age-elevation sampling strategy; however, vertically projected AFT ages ranging from ~3 to 8 Ma (Figure III.3.2d) yield an apparent exhumation rate of 0.5 ±0.1 km Ma^{-1} (r = 0.83). One-dimensional interpretation of the *VIS* data thus suggests an increasing apparent exhumation rate around the Miocene-Pliocene transition (~4-5 Ma, Figure III.3.2d). Although we choose, for simplicity, not to incorporate ZFT data into our thermal-kinematic modeling, ZFT ages close to the studied area show partial to total Alpine resetting, with most ZFT ages ~10 Ma [*Soom*, 1990; *Glotzbach et al.*, 2010], suggesting ≥8 km of exhumation of the Aar massif since this time.

SIO data (Table III.3.2) combine 7 apatite (U-Th-Sm)/He ages collected along an elevation profile (Figures III.3.1b and III.3.2a, c; see *Valla et al.*, submitted, a, for details) with 10 AFT ages [*Rahn*, 1994] mostly collected along a second elevation profile downstream in the Rhône valley (Figure III.3.1b). AHe and AFT ages overlap and range from ~4 to 8 Ma (Figure III.3.2c). One dimensional interpretation of the age-elevation relationships suggest apparent exhumation rates of 0.6 ±0.2 km Ma^{-1} (r = 0.74; *Valla et al.*, submitted, a) and ~0.6 ±0.1 km Ma^{-1} (r = 0.76), for AHe and AFT data, respectively. Most AFT ages are associated with mean track lengths [*Rahn*, 1994] that show a positive correlation with elevation (Figure III.3.2c). *Rahn* [1994] also reported ZFT ages that have only been partially reset during the Alpine collision (ZFT ages≥ ~100 Ma), limiting the total Cenozoic exhumation to ≤8 km for the area. Other studies have also reported AFT data from this area [*Soom*, 1990; *Seward and Mancktelow*, 1994]; however, those AFT ages are extremely young (~1 to 3 Ma) compared to the data of *Rahn* [1994]. These differences may be explained by either poor AFT counting statistics (very few counted grains for some samples; *Soom*, 1990; *Seward and Mancktelow*, 1994) and/or potential local complications such as fluid circulation. We thus choose to only select AFT data from *Rahn* [1994] to avoid problems of non-concordant thermochronological ages during thermal-kinematic modeling.

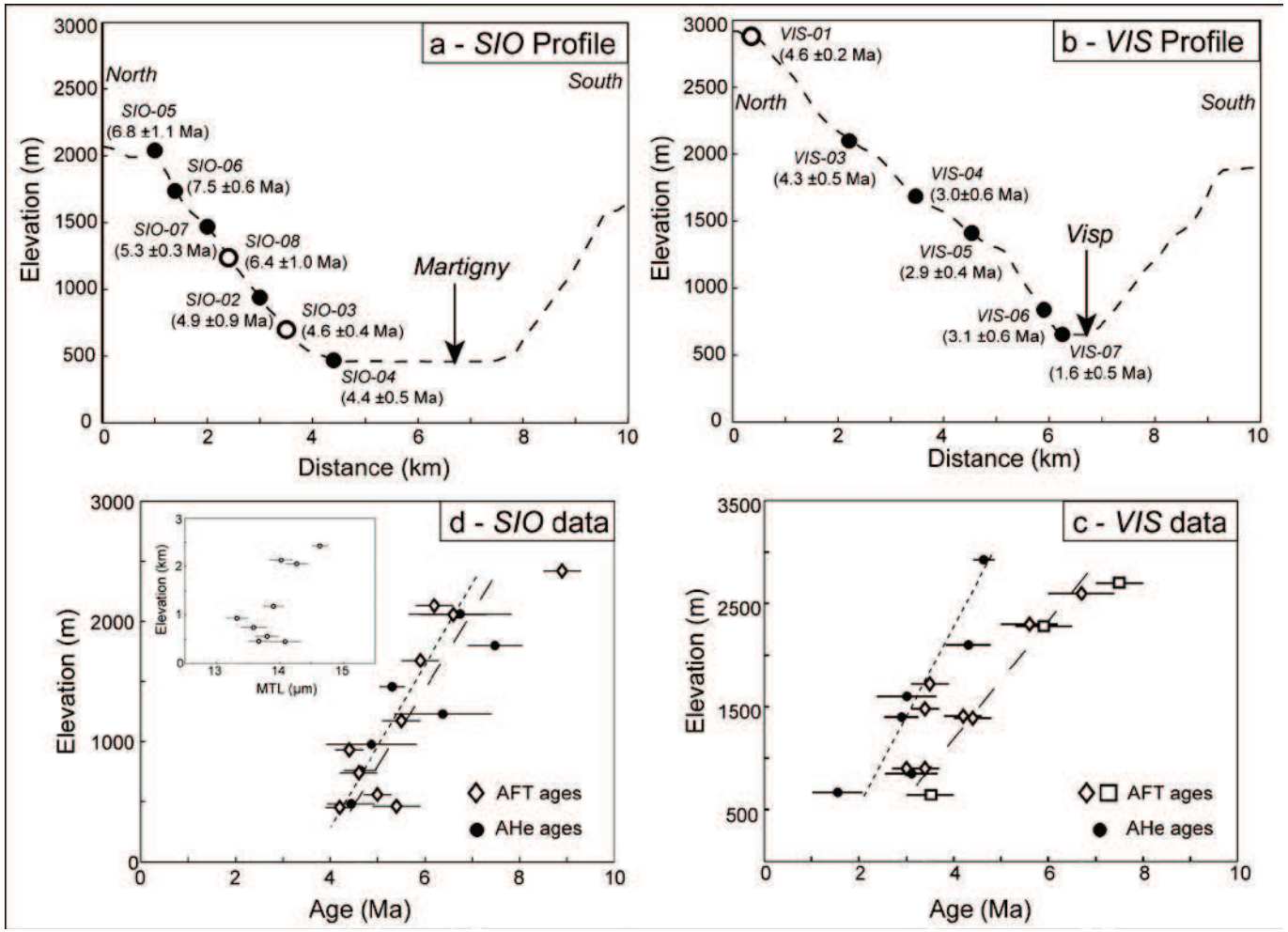

Figure III.3.2. *(a-b) Topographic cross-profiles of the Rhône valley at SIO (a) and VIS (b) sampling sites showing apatite samples from Valla et al., submitted, a (black: AHe + $^{4}He/^{3}He$ data; open: AHe data only). (c-d) Thermochronological data for VIS and SIO sampling sites. (c) SIO age-elevation profiles for AHe (black circles) and AFT data (open diamonds: Rahn, 1994). Inset shows mean fission track-lengths of AFT samples [Rahn, 1994]. (d) VIS age-elevation profiles for AHe (black circles) and AFT data (open squares: Reinecker et al., 2008; open diamonds: Wagner et al., 1977). Regression lines show weighted linear fits to the data (dotted line : AHe ages; dashed line : AFT ages). See Tables III.3.1 and III.3.2 for sample details.*

Qualitative interpretation of the two datasets suggests apparent differences in the late Miocene-Pliocene exhumation histories of the Aar (*VIS* area) and Aiguilles Rouges (*SIO* area) massifs. While AFT data are similar and suggest late Neogene exhumation rates around 0.5-0.6 km Ma^{-1}, AHe ages clearly differ, with much younger ages and a much higher (~50%) apparent exhumation rate for the *VIS* AHe data (Figures III.3.2a, b; *Valla et al.*, submitted, a). The *VIS* data show an apparent acceleration in exhumation by a factor of two between closure of the AFT and AHe systems that should have occurred during the Pliocene (~4-5 Ma, Figure III.3.2d). In contrast, AFT and AHe ages clearly overlap in the *SIO* region (Figure III.3.2c), suggesting synchronous cooling (at ~0.6 km Ma^{-1}) through both the AFT and AHe closure temperatures during the late Miocene/early Pliocene, in agreement with relatively long mean track lengths (Figure III.3.2c; *Rahn*, 1994). Alternatively, a potential explanation for the apparent disagreement between the *SIO* and *VIS* AHe data may be the observed differences in apatite U-Th content (Tables III.3.1 and III.3.2). Effective U concentrations in these apatites range from ~20 to 90 ppm (Table III.3.1) for *VIS* samples, whereas *SIO* samples show much higher eU of ~ 90 to 190 ppm (Table III.3.2) and thus have potentially higher AHe closure temperatures (see section III.3.3.1).

In addition to low-temperature thermochronometric ages, we also report cooling histories for the *VIS* and *SIO* samples quantified from apatite $^4He/^3He$ data [*Valla et al.*, submitted, a]. Apatite $^4He/^3He$ thermochronometry [*Shuster and Farley*, 2004; 2005] reflects the radiogenic ^4He concentration within an apatite crystal using proton-induced ^3He production [*Shuster et al.*, 2004] and step-degassing experiments [*Shuster and Farley*, 2004; 2005]. This method thus enables deriving quantitative constraints on the cooling history from ~90 °C, where ^4He starts to accumulate within the apatite crystal, down to surface temperatures (~20-30 °C). Quantitative interpretation of apatite $^4He/^3He$ data [*Shuster and Farley*, 2005] requires numerical thermal modeling to identify the sets of time-temperature (*t-T*) histories that are consistent with $^4He/^3He$ observations [*Schildgen et al.*, 2010]. The model generates random time-temperature (*t-T*) histories and predicts an evolving spatial distribution of ^4He for each cooling path, assuming a uniform spatial distribution of U and Th and an effective spherical diffusion geometry with surface/volume ratio equivalent to the analyzed grain [*Schildgen et al.*, 2010]. Following each randomly-generated cooling history, the model first calculates a (U-Th)/He age that is compared to the measured age (using the RDAAM algorithm to take into account the alpha-recoil damage effects on He retention; *Flowers et al.*, 2009); and a model $^4He/^3He$ ratio evolution is calculated using the same analytical heating schedule as the

sample and compared to observed ratios [*Shuster et al.*, 2005; *Schildgen et al.*, 2010; *Valla et al.*, submitted, a]. Here, we report cooling histories from *VIS* and *SIO* ^{4}He/^{3}He data previously published by *Valla et al.* [submitted, a], and add two supplementary samples to the existing dataset (VIS-05 and SIO-02, Supplementary Figure III.3.10). Qualitative interpretation of *t-T* histories reveals rapid cooling of both *VIS* and *SIO* samples from ≥7-6 until 5-4 Ma (see VIS-03 and SIO-06, -07, respectively Figures III.3.7a and III.3.8a, b) and a late stage exhumation pulse around 1 Ma that is recorded only by low and mid-elevation samples. *Valla et al.* [submitted, a] interpreted this recent exhumation as being linked to significant relief development through glacial valley carving since ~1 Ma. Here, we aim to provide tighter constraints on the timing and magnitude of this late exhumation; we wish to assess whether it resulted from a massif-scale denudation event or by local relief development, and in the latter case to quantify the amount of local relief increase associated with Rhône valley deepening at both the *VIS* and *SIO* sampling sites.

III.3.3.3 Modeling approach

We aim to quantitatively interpret low-temperature thermochronology data and cooling *t-T* paths from ^{4}He/^{3}He thermochronometry in terms of both denudation and relief histories. This requires defining denudation and relief scenarios, *i.e*, timing and rates for both denudation history and relief evolution that we constrain using a numerical approach. We employ the finite-element thermal-kinematic code *Pecube* [*Braun*, 2003] which solves the heat-transfer equation [*Carslaw and Jaeger*, 1959] to determine the 3D thermal structure within an exhuming crustal block:

$$\rho c \left(\frac{\partial T}{\partial t} + E \frac{\partial T}{\partial z}\right) = \frac{\partial}{\partial x} k \frac{\partial T}{\partial x} + \frac{\partial}{\partial y} k \frac{\partial T}{\partial y} + \frac{\partial}{\partial z} k \frac{\partial T}{\partial z} + H \qquad \text{(III.3.1)}$$

where $T(x,y,z,t)$ is the time-varying thermal field (°C), ρ is rock density (kg m^{-3}), c is the heat capacity (J kg^{-1} K^{-1}), k is the rock conductivity (W m^{-1} K^{-1}), E is the vertical velocity of rocks with respect to the base of the model (m a^{-1}, *i.e.*, the rock-uplift rate, which is equal to the exhumation rate for steady-state topography; *England and Molnar*, 1990; *Willett and Brandon*, 2002); and H is the crustal radioactive heat production (W m^{-3}).

Pecube enables numerical modeling of exhumation under either steady-state or time-varying topography, and thus allows to address the potential effects of transient topographic relief on crustal isotherms [*Mancktelow and Grasseman*, 1997; *Foeken et al.*, 2007] and consequently on thermochronology data [*Braun*, 2002a]. Relief evolution has been incorporated into *Pecube* following different ways. Most recent studies have used the concept of the relief ratio between past and present-day topographies to address massif-scale relief changes [*e.g.*, *Herman et al.*, 2010b; *Valla et al.*, 2010b; *van der Beek et al.*, 2010; *Glotzbach et al.*, submitted], while *Braun and van der Beek* [2004] and *Herman et al.* [2010a] coupled *Pecube* with a surface-process model to physically simulate topographic evolution. Here, we choose a different and simplified approach for predicting relief evolution in *Pecube* simulations. Since our study area encompasses only one major valley, we assume in our modeling that relief development is promoted by efficient valley carving and relative peak preservation; paleo-relief is thus similar to the present-day topography except that valley bottoms are filled up to account for recent valley carving [*Valla et al.*, submitted, a].

Thermal-kinematic modeling using *Pecube* requires geometric and thermal parameterization of the numerical problem [*Braun*, 2003]. First, we assume that rock exhumation is mostly achieved by uniform block uplift. Although we previously pointed out the potential activity of the Rhône-Simplon fault during the late Neogene [*e.g.*, *Mancktelow*, 1992; *Reinecker et al.*, 2008; *Campani et al.*, 2010], the main dip-slip strand of this fault is located outside our studied area, along the Simplon shear zone [*Campani et al.*, 2010]. Moreover, the thermochronology data from the *VIS* area (Figure III.3.1c), although close to the fault zone, do not present any age differences between the two sides of the Rhône valley (Figure III.3.2d), suggesting that the vertical component of the Rhône-Simplon fault in this area is negligible during the late Neogene. This spatially uniform rock uplift is combined with additional isostatic uplift simulating the flexural response to erosional unloading. Following many studies on the flexural parameters for the European Alps [*Stewart and Watts*, 1997; *Burkhard and Sommaruga*, 1998; *Pfiffner et al.*, 2002], we choose an equivalent elastic thickness of 25 km (Table III.3.3) to simulate moderate isostatic rebound [*van der Beek et al.*, 2010].

Parameter (unit)	*Value*
Grid Resolution (m)	750
Crustal thickness (km)	40
Crustal density (kg m^{-3})	2700
Sublithospheric mantle density (kg m^{-3})	3200
Young's modulus (Pa)	1.10^{11}
Poisson ratio	0.25
Equivalent elastic thickness (km)	25
Thermal diffusivity (km^2 Ma^{-1})	25
Basal crustal temperature (°C)	600
Crustal heat production (°C Ma^{-1})	0.8 (2.3)
Sea-level temperature (°C)	10
Atmospheric lapse rate (°C km)	6 (0)

Table III.3.3. *Thermal-kinematic and elastic parameters used in Pecube. Crustal thickness, basal temperature and crustal heat production are set to obtain a geothermal gradient of ~25 °C km^{-1} (~35 °C km^{-1} for $^4He/^3He$ Pecube forward models, see thermal parameter values in brackets). Poisson ratio, Young's modulus and equivalent elastic thickness are used for calculating the isostatic rebound in response to relief change.*

We use *a priori* information from geophysical studies [*e.g.*, *Stampfli et al.*, 1998; *Tesauro et al.*, 2008] to fix the crustal thickness to 40 km (lower boundary of the crustal block, Table III.3.3) and the basal crustal temperature to 600 °C [*e.g.*, *Bousquet et al.*, 1997], in agreement with Moho-temperature estimates of 500-800 °C [*Vigano and Martin*, 2007]. Estimates for the geothermal gradient [*e.g.*, *Vuattaz et al.*, 1993; *Bianchetti*, 1994; *Sonney and Vuattaz*, 2009; *Pignalosa et al.*, 2010] suggest strong spatial variations along the Rhône valley and within the neighboring massifs, with mean values between 20 and 40 °C km^{-1}. Constraining both the geothermal gradient and the exhumation history from thermochronology data requires both low- and high-temperature thermochronometers [*Glotzbach et al.*, submitted]. Previous studies [*Vernon et al.*, 2009; *van der Beek et al.*, 2010] have proposed a fixed geothermal gradient of ~20-25 °C km^{-1}, although *Glotzbach et al.* [submitted] proposed higher values of ~30-40 °C km^{-1}. Preliminary tests reveal that, in our case, setting the geothermal gradient to ~25-35 °C km^{-1} does not significantly influence the inversion predictions. We thus decide to fix the initial geothermal gradient to 25 °C km^{-1} (Table III.3.3) for inverse modeling. Surface temperatures are computed using a mean sea-level temperature of 10 °C and a lapse rate of 6 °C km^{-1} (Table III.3.3). We adopted a different approach to interpret *t-T* histories from $^4He/^3He$ data using forward thermal-kinematic modeling. *Valla et al.* [submitted, a] arbitrarily fixed the present-day surface temperature to the modern mean

surface temperature of the area for all samples (~10 °C), and set a 35 °C km^{-1} geothermal gradient for interpreting *VIS* and *SIO* cooling histories (Table III.3.3). Local geothermal gradients may be much higher than massif-scale estimates [*Bianchetti*, 1993; 1994; *Sonney and Vuattaz*, 2009], thus following the study of *Valla et al.* [submitted, a], we adopt similar thermal parameters for forward *Pecube* models (Table III.3.3).

Thermochronological ages are predicted from thermal histories using different numerical algorithms [*e.g.*, *Braun*, 2003]. AFT ages and associated mean track lengths (MTL) are calculated using a forward model for AFT annealing [*Green et al.*, 1989; *Stephenson et al.*, 2006]. We choose this approach rather than more elaborate models taking variable annealing kinetics into account [*e.g.*, *Ketcham*, 2005] because no kinetic indicators are available for the literature AFT data. AHe ages are computed using a simple forward model for He production-diffusion-ejection [*Wolf et al.*, 1998; *Meesters and Dunai*, 2002]. However, as previously explained, radiation-damage defects caused by U-Th alpha-decay [*e.g.*, *Shuster et al.*, 2006] may influence the AHe closure temperature, potentially explaining the AHe-age differences observed between the *VIS* and *SIO* profiles (Figure III.3.2). Previous studies in the European Alps that interpreted thermochronology data using numerical modeling [*Vernon et al.*, 2009; *van der Beek et al.*, 2010; *Glotzbach et al.*, submitted] did not consider this effect and only used the simple forward model for AHe age predictions [*Wolf et al.*, 1998; *Meesters and Dunai*, 2002], assuming that both low [eU] and relatively rapid cooling during the Neogene exhumation of the external crystalline massifs limits the influence of radiation damage on AHe ages [*e.g.*, *Glotzbach et al.*, submitted]. Although our samples may also have been exhumed quite rapidly during the Neogene Alpine history, we want to compare the potential differences in denudation and relief predictions when considering the radiation damage effect on AHe ages (section III.3.3.1), especially for the *SIO* samples with high eU concentration (90-190 ppm, Table III.3.2). We therefore included the radiation-damage model of *Gautheron et al.* [2009] in *Pecube* and use this alternative model to predict AHe ages.

In the following, we first describe our numerical inversion procedure for extracting denudation and relief scenarios from "classic" low-temperature thermochronology, and then present the forward thermal-kinematic modeling to interpret *t-T* paths deduced from $^{4}He/^{3}He$ data.

Inverse modeling has been performed using a recently developed approach [*e.g.*, *Braun and Robert*, 2005; *Herman et al.*, 2007, 2010a, b; *Valla et al.*, 2010b; *van der Beek et al.*, 2010] combining the thermal-kinematic code *Pecube* [*Braun*, 2003] with a two-step inverse method *NA* (*Neighbourhood Algorithm*; *Sambridge*, 1999a, b) to: (1) extract best-fitting denudation and relief scenarios from thermochronology data; and (2) derive quantitative estimates of the precision with which denudation rates, timing and relief evolution are resolved. The *NA* approach has been fully described in previous studies [*Herman et al.*, 2010a; *Valla et al.*, 2010b; *Glotzbach et al.*, submitted]. In summary, the first stage (*NA* sampling stage; *Sambridge*, 1999a) iteratively explores the multi-dimensional parameter space to find optimal parameter combinations that minimize the misfit function. The multi-dimensional space is divided into Voronoi cells, each of them being sampled for forward *Pecube* modeling to construct misfit surfaces following the log-likelihood function (*Ln(L)*) :

$$Ln(L) = -0.5\sum_{i=1}^{N}\sum_{j=1}^{M}\frac{({}^{i}\alpha_{j,\mathrm{mod}} - {}^{i}\alpha_{j,dat})^2}{{}^{i}\sigma_{j}{}^{2}} \qquad \text{(III.3.2)}$$

where N is the number of datasets (AFT, AHe, and/or MTL data), M is the number of samples in each dataset (Tables III.3.1 and III.3.2), ${}^{\mathrm{i}}\alpha_{j,\mathrm{mod}}$ and ${}^{\mathrm{i}}\alpha_{j,dat}$ are predicted and observed values for AFT/AHe ages or MTL data respectively, and ${}^{\mathrm{i}}\sigma_{j}$ is the uncertainty on the data. The calculated misfit surface is then used to concentrate subsequent sampling of the parameter space and ensures numerical convergence towards an optimal set of parameters. As explained in detail by *Glotzbach et al.* [submitted], the *NA* sampling stage is mainly controlled by three parameters: (1) the number of iterative samplings of the parameter space, (2) the number of forward *Pecube* models generated at each iteration, and (3) the number of Voronoi cells re-sampled after each misfit surface calculation. In this study, we perform ~8500 models for each inversion distributed in 55 iterations, with 95% re-sampling at each iteration.

The second stage (*NA* appraisal stage) uses the ensemble of generated models from the sampling stage to derive Bayesian estimates on parameter values, *i.e.*, a marginal probability density function (PDF) from the likelihood function defined above [*Sambridge*, 1999b]. Modeling results are then represented both as scatter plots for different parameter combinations (*NA* sampling stage) and 1D marginal PDFs of individual parameters (*NA* appraisal stage).

One main unknown in inverse theory is the appropriate dimensionality of the problem [*e.g.*, *Akaike*, 1974; *Schwartz*, 1978] compared to the intrinsic resolution of the data. In our case, we have to define the number of denudation/relief phases in our model (*i.e.*, the number of *t-T* points in the cooling history to be constrained by the thermochronology data; *e.g.*, *Gallagher et al.*, 2005a; *Glotzbach et al.*, submitted) and associated denudation rates, timing, and relief parameters. We thus need to find a balance between satisfactorily fitting the thermochronology data and over-interpreting them with too complex and unrealistic models. We use the Bayesian Information Criterion (*BIC*; *Schwartz*, 1978) to assess the appropriate number of exhumation phases allowed by our data resolution:

$$BIC = -2Ln(L) + k\ln(n) \qquad \text{(III.3.3)}$$

where *Ln(L)* is the log-likelihood function (Eq. (III.3.2)), and *k* and *n* are the number of free parameters (denudation rates, timing and relief parameters) and observations (thermochronology data, *i.e.*, AFT/AHe ages and MTL data), respectively. The appropriate model will thus be defined by: (1) best-fitting exhumation scenarios matching the input thermochronology data; (2) lowest *BIC* values, avoiding highly complex models [*Glotzbach et al.*, submitted].

We do not perform similar inverse modeling to interpret ^{4}He/^{3}He derived *t-T* paths but rather use forward thermal-kinematic modeling. This approach does not require any numerical algorithms to predict thermochronology data from output thermal histories; we directly compare *t-T* paths derived from the ^{4}He/^{3}He data with *Pecube* models [*e.g.*, *Schildgen et al.*, 2010]. Following *Valla et al.* [submitted, a] and the outcome of our inversions (see below), we define a three-phase exhumation history: (1) late Neogene rapid denudation of both the *VIS* and *SIO* areas, followed by (2) a quiescent phase, and (3) a late-stage exhumation pulse. We first put qualitative constraints on the late-Neogene exhumation of *VIS*/*SIO* samples, especially on denudation rates and the ending time of this exhumation phase. We then quantitatively assess whether the late-stage exhumation pulse observed in the ^{4}He/^{3}He data is due to regional denudation or local relief development and attempt to constrain the timing and rate of this final exhumation pulse.

III.3.4 Modeling results

III.3.4.1 Inverse modeling of thermochronology data

For both the *VIS* and *SIO* datasets, we define a set of inversions with various degrees of model complexity (*i.e.*, number of inverted parameters, Tables III.3.4 and III.3.5). All inversions are run over 15 Ma. We define one-, two- and three-phase denudation scenarios with associated denudation rates (E_1, E_2 and E_3, range: 0-4 km Ma^{-1}) and transition times between each phase ($T_{E1\text{-}2}$, $T_{E2\text{-}3}$, range: 1-10 Ma). Exhumation scenarios include either a steady-state (present-day topography) or time-varying topography (onset time of relief development T_R, range: 1-14 Ma) with paleo-valley bottoms at higher elevation compared to present-day conditions (H_{limit}, *i.e.*, minimum paleo-valley floor elevation, range: 600-3900 m and 400-3200 m for *VIS* and *SIO* modeling areas, respectively). All inverted parameters and their respective ranges are listed in Tables III.3.4 and III.3.5 (for *VIS* and *SIO* inversions, respectively), together with the best-fitting (maximum log-likelihood) parameter values, resulting *BIC* value and associated uncertainties. Inversion outputs are also reported as scatter plots showing parameter combinations (*NA* sampling stage, Figures III.3.3 and III.3.5) and one-dimensional marginal PDFs of individual parameters (*NA* appraisal stage, Figures III.3.4 and III.3.6). We first present modeling results for *VIS* data and then describe inversion outputs for *SIO* data.

For the *VIS* area, we define 3 steady-state topography inversions with either one (*VIS_1*), two (*VIS_2*) or three (*VIS_4*) denudation phases. Inversion results (Table III.3.4) show that we both maximize the likelihood (*Ln(L)* from -33.5 to -24.8) and optimize the *BIC* (from 70.0 to 63.7) by adding successive denudation phases. Inversions simulating time-varying topography (*VIS_3* and *VIS_5*) led to best log-likelihood predictions (-21.4 and -22.7 respectively); however, *BIC* values show that the best exhumation scenario combines two denudation phases with a phase of relief development (*VIS_3*, *BIC* = 56.9, >10% lower than other *BIC* values); the three-phase denudation scenario under evolving relief leading to a higher *BIC* value (*VIS_5*, *BIC* = 65.3). Output predictions for inversion *VIS_3* are reported as scatter plots in Figure III.3.3 to allow qualitative interpretation of the inversion results. Denudation rates during the second phase ($E_2 \approx$ 0.2-0.8 km Ma^{-1}, Figure III.3.3a) appear to be much tighter constrained than those of the first phase ($E_1 \approx$ 1-4 km Ma^{-1}, Figure III.3.3a); the transition between these two denudation phases may have occurred between 7 and 10 Ma ($T_{E1\text{-}2}$, Figure III.3.3b).

Parameter (unit)	***E_1 (km Ma^{-1})***	***$T_{E_{1-2}}$ (Ma)***	***E_2 (km Ma^{-1})***	***$T_{E_{2-3}}$ (Ma)***	***E_3 (km Ma^{-1})***	***T_R (Ma)***	***H_{limit} (m)***	***Log-likelihood***	***BIC***
Range	0-4	1-10	0-4	1-10	0-4	1-14	600-3900	*Ln(L)*	
***Inv.* (param./obs.)**									
VIS_1 (1 / 17)	0.80 ±0.01	-	-	-	-	-	-	-33.6	70.0
VIS_2 (3 / 17)	3.9 ±0.7	9.0 +1.0/-2.8	0.70 ±0.01	-	-	-	-	-30.8	70.1
VIS_3 (5 / 17)	3.9 +0.2/-0.4	7.9 ±0.6	0.4 ±0.1	-	-	2.1 ±0.8	2800 ±400	-21.4	56.9
VIS_4 (5 /17)	3.8 +0.3/-0.9	8.1 ±0.7	0.3 ±0.1	4.1 ±2.1	0.8 ±0.2	-	-	-24.8	63.7
VIS_5 (7 / 17)	3.4 ±0.4	8.1 ±1.1	2.8 ±1.2	6.7 ±1.6	0.1 +0.5/-0.1	3.1 ±1.1	3400 ±400	-22.7	65.3
*VIS_3** (5 / 17)	3.4 +0.7/-1.5	9.9 +0.1/-1.7	0.5 ±0.2	-	-	1.2 +1.6/-0.2	3000 ±400	-21.5	57.2

Table III.3.4. *VIS Inversions: Bayesian estimates after the NA appraisal stage for parameters E_1, E_2, E_3, T_{E1-2}, T_{E2-3}, T_R and H_{limit} (optimal values (mode) and estimated uncertainties of parameters, see text for description and discussion). Each inversion is characterised by respectively a number of free parameters to be inverted (param.) and a number of observations (obs., i.e., thermochronological data). Almost all inversions (VIS_1 to VIS_5) use the He production-diffusion-ejection model [Wolf et al., 1998; Meesters and Dunai, 2002] for AHe age predictions, and inversion VIS_03* uses the alpha-damage and annealing model [Gautheron et al., 2009] for AHe age calculations.*

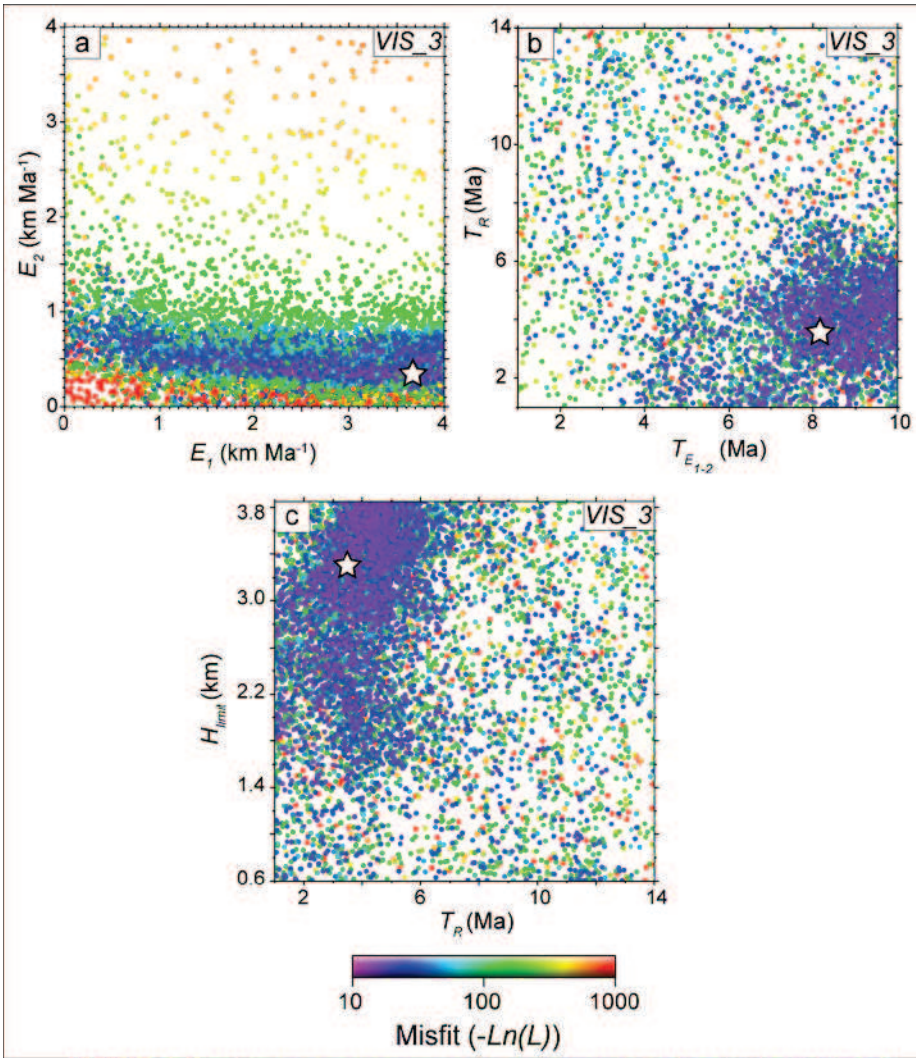

Figure III.3.3. *Scatter diagrams for best-fitting VIS inversion (VIS_3, see Table III.3.4 for details). Each dot corresponds to a forward model; its colour is proportional to the misfit value between predictions and data (-Ln(L)). Each diagram is the projection onto a plane defined by two of the five parameters. (a): denudation rates E_1 and E_2; (b): denudation and relief transition times, respectively $T_{E1\text{-}2}$ and T_R; and (c) relief increase onset T_R and relief amplification H_{limit}; horizontal and vertical axes define the parameter space. White stars indicate the best-fitting model.*

Timing estimates for relief development suggest a Pliocene initiation of valley incision ($T_R \approx$ 2-6 Ma, Figure III.3.3c) and relief predictions set some constraints on the paleo-valley floor elevations; between 2.0 and 3.9 km (H_{limit}, Figure III.3.3c). The *NA* appraisal stage allows to derive quantitative estimates on inverted parameters (Figure III.3.4 and Table III.3.4). One-dimensional marginal PDFs confirm that relatively high denudation rates (E_1 = 3.9 +0.2/-0.4 km Ma^{-1}, Figure III.3.4a) are followed by moderate denudation (E_2 = 0.4 ±0.1 km Ma^{-1}, Figure III.3.4a); moreover, Figure III.3.4a confirms that E_2 is better constrained than E_1. The transition time between the two denudation phases is well constrained (Figure III.3.4b) and may have occurred during the late Miocene ($T_{E1\text{-}2}$ = 7.9 ±0.6 Ma, Table III.3.4).

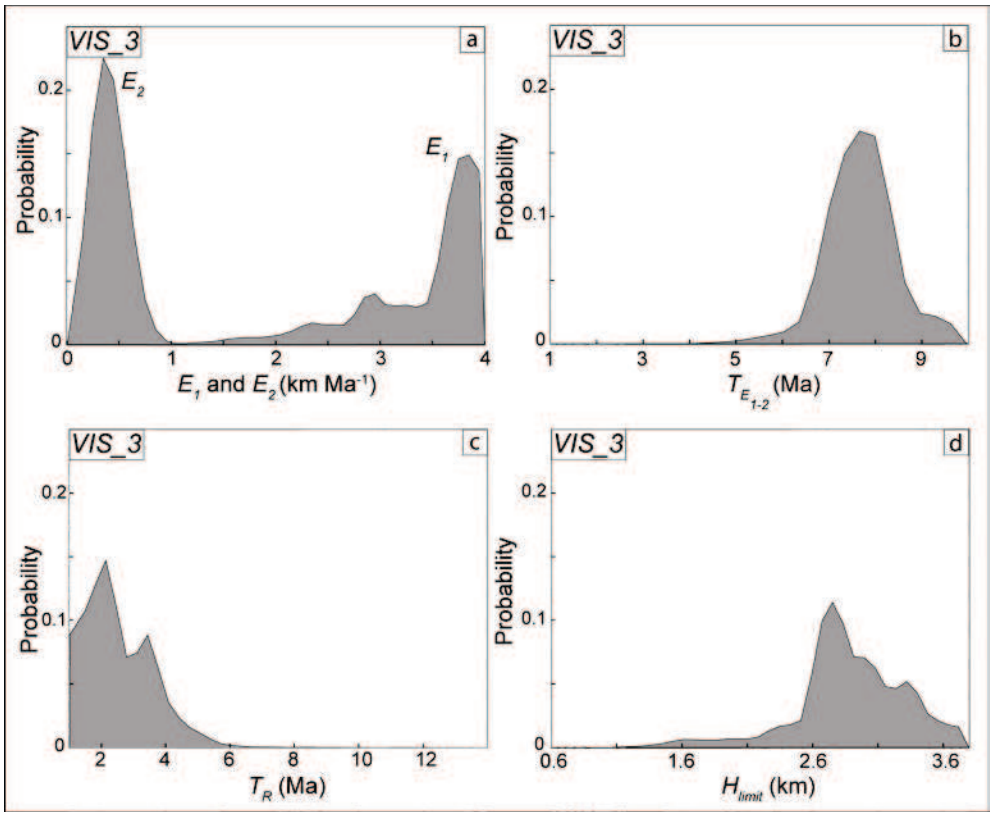

Figure III.3.4. *1D posterior PDFs for best-fitting VIS inversion (VIS_3, Figure III.3.3 and Table III.3.4) after the NA appraisal stage : (a) denudation rates E_1 and E_2; (b) denudation transition time $T_{E1\text{-}2}$; (c) relief increase onset T_R; and (d) relief amplification H_{limit}. Horizontal axes define each parameter space.*

Timing predictions concerning relief development are less tight (Figure III.3.4c); however, they suggest a late-Pliocene initiation of relief carving (T_R = 2.1 ±0.8 Ma, Table III.3.4) and a paleo-valley bottom at much higher elevations (H_{limit} = 2800 ±400 m, Figure III.3.4d) than present-day conditions (valley bottoms at ~600-800 m elevation, Figure III.3.1c). We previously reported relatively low to moderate eU concentrations for *VIS* samples (~20-90 ppm, Table III.3.1). Here, we compare the influence of including radiation-damage effects in the AHe age calculations [*Gautheron et al.*, 2009] for resulting constraints on denudation and relief predictions. We thus perform a similar inversion to *VIS_3* with two denudation phases and relief development (*VIS_3**, Table III.3.4) but using a radiation-damage model to predict AHe ages. Inversion results provide similar log-likelihood and *BIC* values (-21.4/-21.5 and 56.9/57.21 for *VIS_3* and *VIS_3** respectively, Table III.3.4). Optimal parameter values are also quite similar (Table III.3.4), although, in detail, *VIS_3** suggest lower (E_1 = 3.4 +0.7/-1.5 km Ma^{-1}) and higher (E_2 = 0.5 ±0.2 km Ma^{-1}) rates for the first and second denudation phases, respectively; and a somewhat older transition between the two phases ($T_{E1\text{-}2}$ = 9.9 +0.1/-1.7 Ma). Relief predictions also differ somewhat; *VIS_03** suggesting both younger (T_R = 1.2

+1.6/-0.2 Ma) and stronger (H_{limit} = 3000 ±400 m) valley carving (Table III.3.4). However, all optimal parameter values overlap withon their 1σ uncertainty.

We adopt the same approach for *SIO* inversions (Table III.3.5); however, output results clearly differ from *VIS*-model predictions. Both log-likelihood and *BIC* values are much higher (-86.7 to -56.5 and 135.1 to 176.7 for *Ln(L)* and *BIC* results, respectively), and except for *SIO_1*, which provided the highest *BIC* value (176.7), all inversions yield very similar *BIC* estimates (135.7-143.6, less than 6% differences between all *BIC* values) so we cannot quantitatively assess what scenario best explains the *SIO* data. We interpret this somewhat disappointing outcome to be due to the strong overlap between AFT and AHe ages (Figure III.3.2c) and the incapacity of the *Pecube* model to satisfactorily predict the observed similar AFT and AHe ages. However, using a radiation damage and annealing model to calculate AHe ages (*SIO_3** and *SIO_5**) does not improve the misfit to the observed data (*Ln(L)* ~-60 and *BIC* values ~140, Table III.3.5). Another potential explanation may be the distribution of *SIO* samples, with AFT and AHe data located along two profiles, whereas *VIS* samples are more widely distributed spatially.

The *SIO* and *VIS* areas are geographically very close (Figure III.3.1) and are not separated by major tectonic structures; we can thus reasonably assume that their exhumation history, at least for the late Neogene, and their relief development are similar. We consequently consider the two-denudation phases with relief evolution scenario as being representative of the *SIO* exhumation history (*SIO_3* and *SIO_03**, Table III.3.5) to derive optimal estimates on denudation and relief parameters. We also include the effect of radiation damage defects on AHe ages (*SIO_3**, Table III.3.5) as *SIO* samples present much higher apatite eU concentration (~90-190 ppm, Table III.3.2) than *VIS* samples. The main difference between the two inversions is the prediction for the onset time of relief development (T_R); although both inversions predict similar amplitudes of relief development (H_{limit} = 1600 ±500 and 1500 ±400 m for *SIO_3* and *SIO_3**, respectively, Table III.3.5). *SIO_3* (no radiation damage effect for AHe age calculation) suggests a late Miocene onset of valley carving (T_R = 6.6 ±0.6 Ma, Table III.3.5), while *SIO_3** predicts a much later initiation, during the late Pliocene (T_R = 2.5 ±0.5 Ma, Table III.3.5 and Figure III.3.6), in closer agreement with *VIS* predictions (T_R ≈ 1.2-2.1 Ma, Table III.3.4). This result clearly highlights the advantage of including the radiation damage effect for AHe age predictions [*Gautheron et al.*, 2009] in *Pecube* simulations to best explain the *SIO* data [*Valla et al.*, submitted, a].

Parameter (unit)	***E_1 (km Ma^{-1})***	***$T_{E_{1-2}}$ (Ma)***	***E_2 (km Ma^{-1})***	***$T_{E_{2-3}}$ (Ma)***	***E_3 (km Ma^{-1})***	***T_R (Ma)***	***H_{limit} (m)***	***Log-likelihood***	***BIC***
Range	0-4	1-10	0-4	1-10	0-4	1-14	400-3200	*Ln(L)*	
***Inv.* (param./obs.)**									
SIO_1 (1 / 26)	0.65 ±0.01	-	-	-	-	-	-	-86.7	176.7
SIO_2 (3 / 26)	2.7 ±1.0	5.4 ±0.1	0.25 ±0.01	-	-	-	-	-62.8	135.4
SIO_3 (5 / 26)	3.9 +0.1/-0.2	5.7 ±0.2	0.25 ±0.06	-	-	6.6 ±0.6	1600 ±500	-59.8	136.0
SIO_4 (5 /26)	2.6 ±0.4	5.8 ±3.4	0.1 +0.3/-0.1	4.5 +3.9/-3.5	0.15 ±0.06	-	-	-59.4	135.1
SIO_5 (7 / 26)	3.9 +0.1/-0.4	6.3 ±0.4	0.9 ±0.2	3.8 ±0.4	0.1 +0.1/-0.1	8.3 ±1.5	2500 ±100	-56.5	135.8
*SIO_3** (5 / 26)	2.6 ±0.3	6.7 ±0.3	0.25 ±0.08	-	-	2.5 ±0.5	1500 ±400	-61.6	139.5
*SIO_5** (7 / 26)	2.5 ±0.9	5.8 ±1.0	1.0 +1.2/-1.0	4.5 ±1.1	0.1 +0.3/-0.1	6.0 ±2.8	1600 ±800	-60.4	143.6

Table III.3.5. *SIO Inversions: Bayesian estimates after the NA appraisal stage for parameters E_1, E_2, E_3, T_{E1-2}, T_{E2-3}, T_R and H_{limit} (optimal values (mode) and estimated uncertainties of parameters, see text for description and discussion). Each inversion is characterised by respectively a number of free parameters to be inverted (param.) and a number of observations (obs., i.e., thermochronological data). Almost all inversions (SIO_1 to SIO_5) use the He production-diffusion-ejection model [Wolf et al., 1998; Meesters and Dunai, 2002] for AHe age predictions, and inversions SIO_03* and SIO_05* uses the alpha-damage and annealing model [Gautheron et al., 2009] for AHe age calculations.*

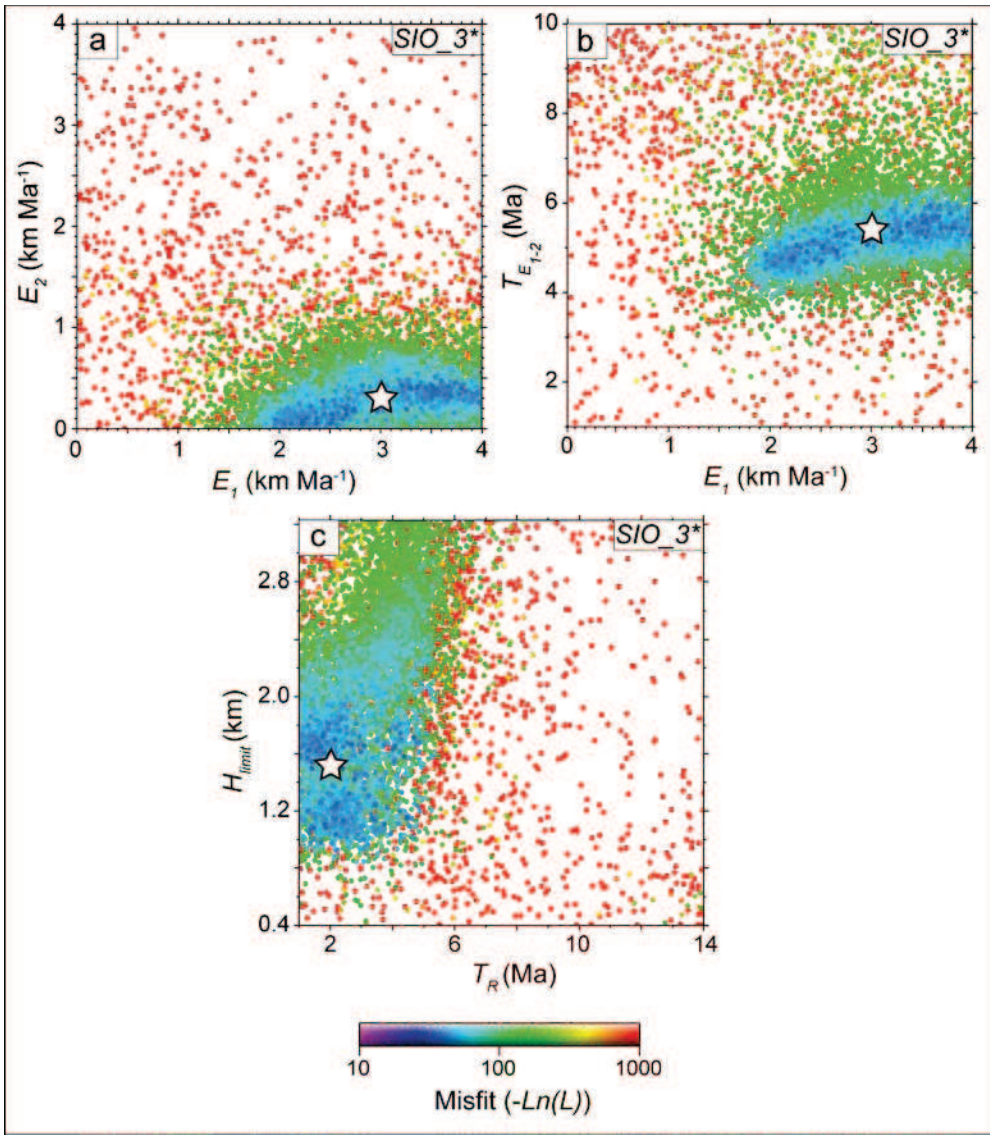

Figure III.3.5. *Scatter diagrams for best-fitting SIO inversion (SIO_3*, see Table III.3.5 for details). Each dot corresponds to a forward model; its colour is proportional to the misfit value between predictions and data (-Ln(L)). Each diagram is the projection onto a plane defined by two of the five parameters. (a): denudation rates E_1 and E_2; (b): denudation transition time and first denudation phase rate, respectively T_{E1-2} and E_1; and (c) relief increase timing T_R and relief amplification H_{limit}; horizontal and vertical axes define the parameter space. White stars indicate the best-fitting model.*

Results for inversion *SIO_3** are reported in Figures III.3.5 and III.3.6 and confirm the contrasted denudation history previously revealed by *VIS* results: a rapid denudation phase (E_1 ≈ 2-4 km Ma^{-1}, Figure III.3.5a) until the Miocene-Pliocene transition (T_{E1-2} ≈ 4-6 Ma, Figure III.3.5b) is followed by much lower denudation rates (E_2 ≈ 0-0.4 km Ma^{-1}, Figure III.3.5a). As previously discussed, relief-development predictions suggest a Pliocene onset of valley carving (T_R ≈ 1-5 Ma, Figure III.3.5c) with a paleo-valley bottom at ~1-2.2 km elevation

(Figure III.3.5c). One-dimensional PDFs (Figure III.3.6) provide quantitative estimates for these parameters (Table III.3.5). Similar to *VIS* results, the denudation rate of the most recent phase is tightly constrained (E_2 = 0.25 ±0.08 km Ma^{-1}, Figure III.3.6a) while estimates of the first denudation rate are less precise (E_1 = 2.6 ±0.4 km Ma^{-1}, the PDF is bimodal with peaks at ~2.5 and ~3 km Ma^{-1}, Figure III.3.6a). The transition time between the two denudation phases may have occurred in the late Miocene ($T_{E1\text{-}2}$ = 6.7 ±0.3 Ma, Figure III.3.6b), in agreement with estimates for the *VIS* area ($T_{E1\text{-}2}$ ≈ 7-10 Ma, Table III.3.4). Relief predictions are less constrained (Figures III.3.6c, d) and suggest moderate valley carving (H_{limit} = 1500 ±400 m, a bimodal PDF with peaks at ~1.1 and ~1.5 km, Figure III.3.6d) occurring in the Pliocene (T_R = 2.5 ±0.5 Ma, a main peak in the PDF at ~2.5 Ma and a minor peak at ~4.5 Ma, Figure III.3.6c).

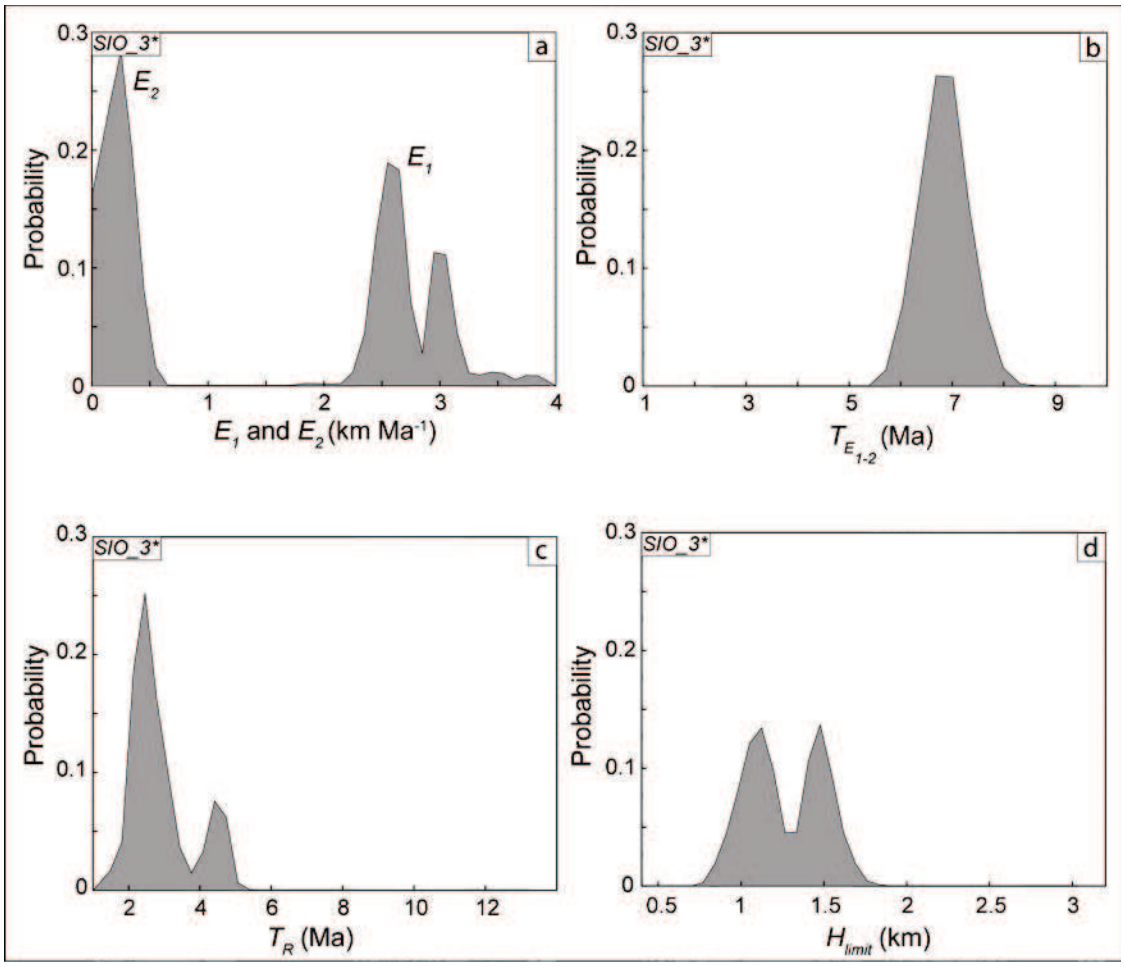

Figure III.3.6. *1D posterior PDFs for best-fitting SIO inversion (SIO_3*, Figure III.3.5 and Table III.3.5) after the NA appraisal stage : (a) denudation rates E_1 and E_2; (b) denudation transition time $T_{E1\text{-}2}$; (c) relief increase timing T_R; and (d) relief amplification H_{limit}. Horizontal axes define each parameter space.*

III.3.4.2 Forward modeling of $^{4}He/^{3}He$ data

We now present results of *Pecube* forward models with the aim to further constrain Pliocene exhumation histories for the *VIS* and *SIO* samples from AHe and $^{4}He/^{3}He$ data [*Valla et al.*, submitted, a]. As previously explained, we ran 3-phase exhumation scenarios over 15 Ma, in agreement with sample cooling paths quantified from $^{4}He/^{3}He$ data and the above inversion outcomes (Figures III.3.7 and III.3.8). However, apatite $^{4}He/^{3}He$ data only provide constraints on the cooling history since the onset of He retention (*i.e.*, for temperatures close to the AHe closure temperature; *Shuster and Farley*, 2005); thus constraints on late Miocene exhumation (denudation rates and timing) cannot be precisely extracted from the *VIS* and *SIO* $^{4}He/^{3}He$ data, as most samples have AHe ages younger than ~5-6 Ma (Figures III.3.2a, b). The late Miocene exhumation signal is best recorded by summit samples which experienced only little cooling in the Pliocene (VIS-03, SIO-06 and -07; Figures III.3.7a and III.3.8a, b, respectively).

The $^{4}He/^{3}He$-derived cooling paths for VIS-03 suggest rapid denudation (~1-1.5 km Ma^{-1}), which ended at ~3-4 Ma (Figure III.3.7a). Other *VIS* samples do not have sufficient resolution to constrain the late Neogene exhumation, although most suggest a deceleration in exhumation rates at around 3-5 Ma (Figure III.3.7b-e). We thus choose to impose for *VIS* models an initial denudation phase at ~1.5 km Ma^{-1}, ending at 3.5 Ma and followed by very slow denudation at ~0.001 km Ma^{-1}.

SIO samples have older AHe ages (Figure III.3.2a) than the *VIS* samples and consequently provide more constraints on the late Neogene exhumation history. Qualitative interpretation of *SIO* cooling paths also reveals a rapid exhumation phase that ended at ~5-6 Ma [*Valla et al.*, submitted, a]. Forward modeling for SIO-06 and -07 (summit samples, Figure III.3.8a, b) suggests rapid denudation (~0.75-1.5 km Ma^{-1}) until ~5.5-5 Ma and followed by low exhumation (~0.001 km Ma^{-1}). In the following, we impose an initial denudation phase (~1 km Ma^{-1}) ending at 5 Ma for *SIO* modeling.

Figures III.3.7 and III.3.8 clearly show that mid- to low-elevation *SIO* and *VIS* samples record a late-stage exhumation pulse at ~1-2 Ma, in contrast to high-elevation samples that have remained at surface temperatures for the last 3-5 Ma. This contrast led *Valla et al.* [submitted, a] to interpret this late exhumation signal as reflecting major relief increase through Rhône valley carving, instead of a regional denudation pulse within the Swiss Alps. Here, we

quantitatively test this interpretation by defining various denudation (0.5 to 1.5 km Ma^{-1}, Supplementary Figures III.3.11 and III.3.12) and relief (80-105% of relief increase, Figures III.3.7 and III.3.8) scenarios for the last ~1 Ma and compare resulting *t-T* paths predicted by *Pecube* with those recorded by the $^{4}He/^{3}He$ data.

We first present output results for the recent denudation pulse hypothesis (Supplementary Figures III.3.11 and III.3.12). The *VIS* summit sample (VIS-03, Supplementary Figure III.3.11a) only allows recent denudation rates <0.25 km Ma^{-1}, while both mid- and low-elevation samples (SIO-04, -05, -06 and -07, Supplementary Figure III.3.11b-e) require denudation rates of ~1-1.25 km Ma^{-1} to explain their cooling histories. Modeling results are more similar for *SIO* samples; summit and high-elevation samples requiring denudation rates of ~0.25-0.5 km Ma^{-1} (SIO-06, Supplementary Figure III.3.12a) and ~0.25-0.75 km Ma^{-1} (SIO-07, Supplementary Figure III.3.12b), respectively. The mid-profile sample (SIO-02, Supplementary Figure III.3.12c) yields denudation rate estimates between 0.75 and 1.25 km Ma^{-1}, and final cooling of the valley bottom sample (SIO-04) is only explained by a denudation rate of ~1 km Ma^{-1} (Supplementary Figure III.3.12d). In summary, our *Pecube* modeling results clearly highlight that progressively increasing denudation rates are required to explain the late-stage exhumation of summit to valley bottom samples (Supplementary Figure III.3.12), in both the *SIO* and *VIS* profiles (Supplementary Figure III.3.11). We thus quantitatively confirm that explaining the late Pliocene exhumation pulse of both *VIS* and *SIO* samples requires spatially contrasted exhumation histories, implying a significant increase in the valley's relief [*Valla et al.*, submitted, a].

We now aim to quantitatively constrain this topographic change by focusing on the Rhône paleo-valley floor changes allowed by both *VIS* and *SIO* $^{4}He/^{3}He$ data. We test six different relief scenarios for the *VIS* samples, with paleo-valley bottom elevations (H_{limit}) ranging between 1900 and 2400 m (associated paleo-relief between 45 and 55% of the present-day relief, Figure III.3.7). The summit sample (VIS-03) sets upper limits on the predicted relief development, excluding the 105% relief increase scenario (H_{limit} = 2400 m, Figure III.3.7a), similar to VIS-06 results (Figure III.3.7d). Mid-elevation samples (Figure III.3.7b, c) allow to discard low relief increase scenarios (~80 and 85% of relief increase, H_{limit} = 1900-2000 m). Finally, the valley bottom sample (VIS-07, Figure III.3.7e) does not provide significant resolving power between the different relief scenarios. In summary, we propose that the *VIS* paleo-valley floor elevation may have been between 2100 and 2300 m before Rhône valley carving, resulting in a ~90-100% increase in local relief (Figure III.3.7).

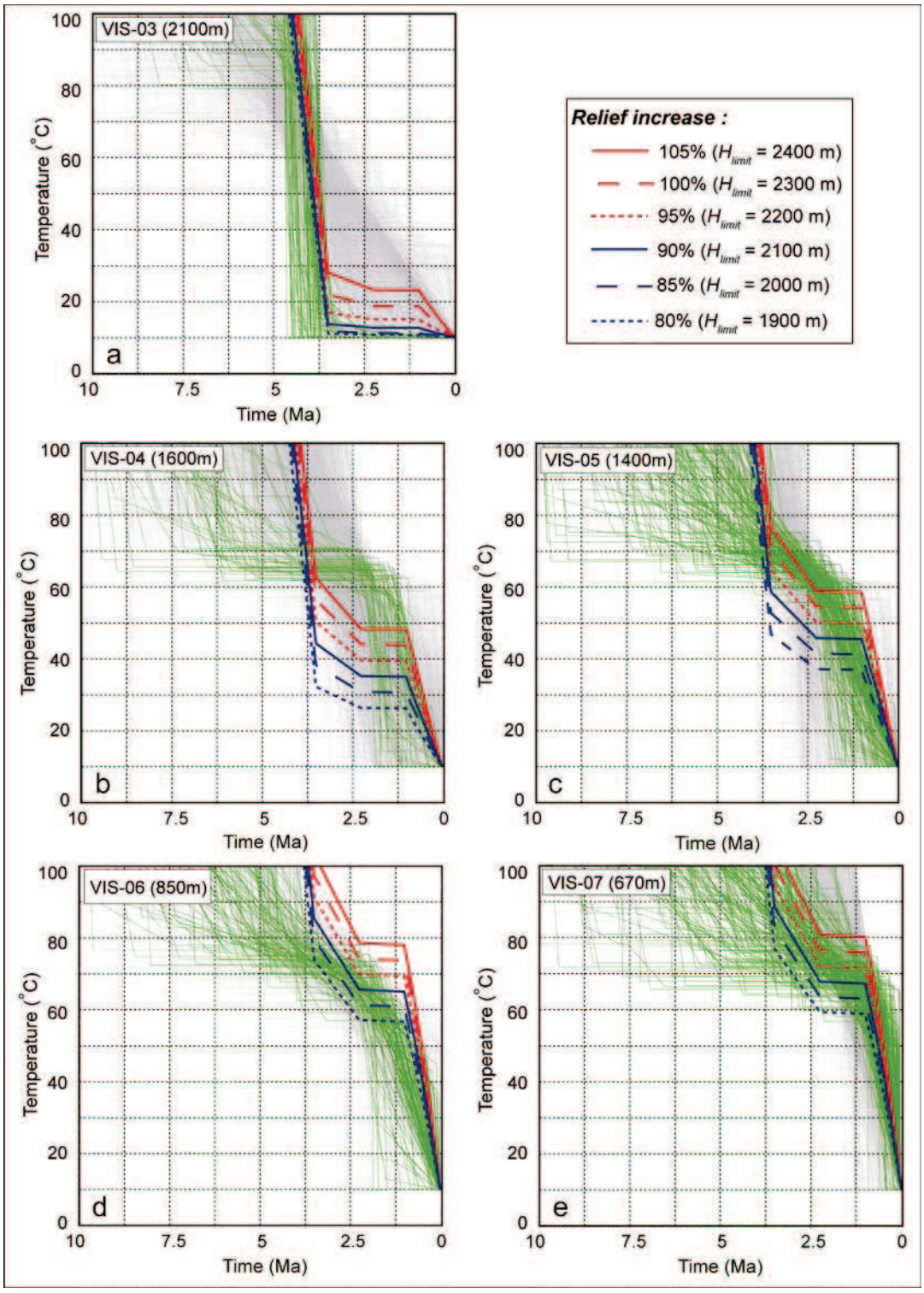

Figure III.3.7. *Cooling paths for VIS samples inferred from $^{4}He/^{3}He$ and Pecube models (see Figures III.3.1 and III.3.2 for sample locations). Green/grey lines show respectively good and acceptable $^{4}He/^{3}He$ modeled cooling paths for VIS-03 (a), -04 (b), -05 (c), -06 (d) and -07 (e) [Valla et al., submitted, a]. Thick coloured lines (blue and red) show modeled cooling paths simulating relief development carving of various amplitudes (80 to 105% relief increase, see legend for colours code) since ~1 Ma. See text for other parameters.*

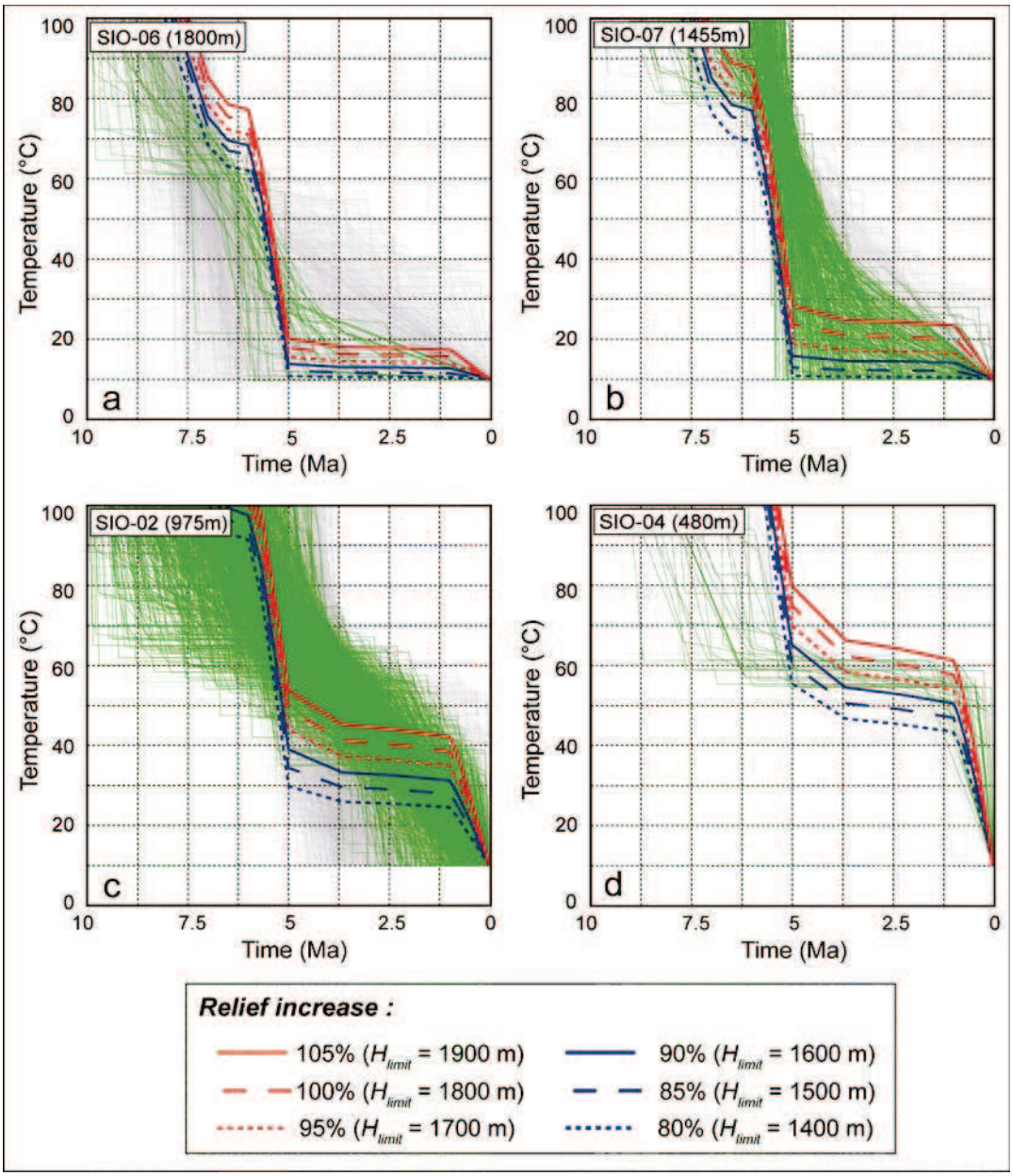

Figure III.3.8. *Cooling paths for SIO samples inferred from $^{4}He/^{3}He$ and Pecube models (see Figures III.3.1 and III.3.2 for sample locations). Green/grey lines show respectively good and acceptable $^{4}He/^{3}He$ modeled cooling paths for SIO-06 (a), -07 (b), -02 (c) and -04 (d) [Valla et al., submitted, a]. Thick coloured lines (blue and red) show Pecube modeled cooling paths simulating relief development carving of various amplitudes (80 to 100% relief increase, see legend for colours code) since ~1 Ma. See text for other parameters.*

We adopt the same approach for *SIO* samples, with six paleo-relief scenarios ranging between ~45 and 55% of the present-day relief (~80 to 105% relief increase, associated Rhône paleo-valley floor at 1400-1900 m elevation, Figure III.3.8). The summit samples (SIO-06 and -07) do not provide any constraint on the paleo-valley floor elevation; all relief scenarios agree

with the $^{4}He/^{3}He$ cooling paths (Figure III.3.8a, b). Quantitative constraints on valley deepening primarily come from the mid- and low-elevation samples (Figure III.3.8c, d); both SIO-02 and -04 exclude the lowest amplitude relief change (~80% relief increase, H_{limit} = 1400 m) while SIO-04 discards the 105% relief increase scenario (H_{limit} = 1900 m, Figure III.3.8d). Paleo-valley floor predictions from *SIO* samples thus suggest a ~85-100% increase in local relief (H_{limit} = 1500-1800 m).

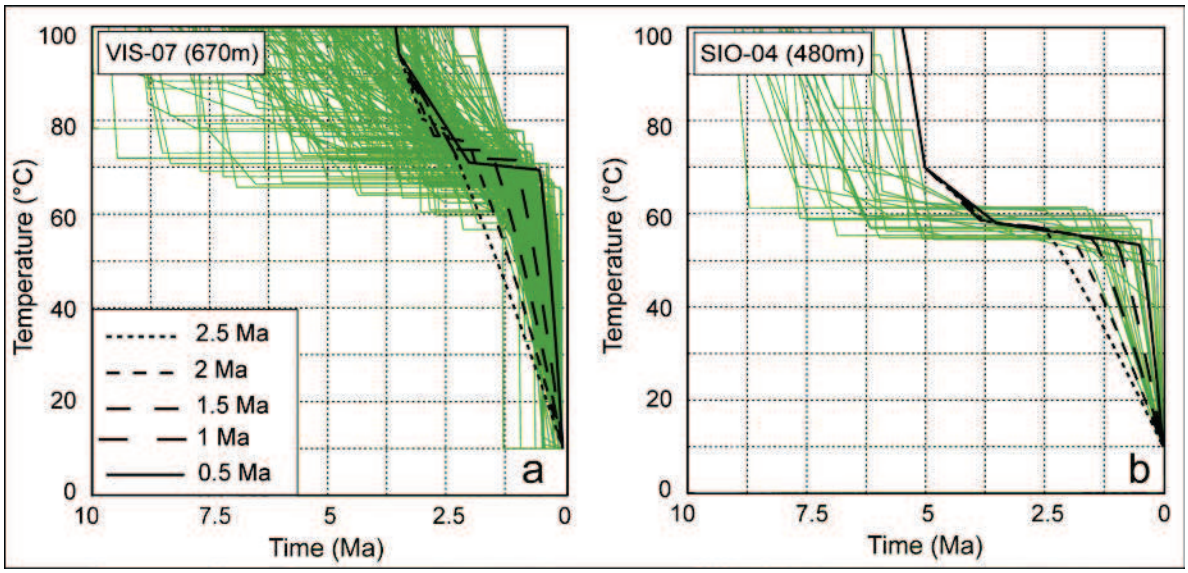

Figure III.3.9. *Timing of the recent exhumation pulse for VIS (a) and SIO (b) valley bottom samples (VIS-07 and SIO-04, respectively). Green lines show $^{4}He/^{3}He$ modeled cooling paths for respectively VIS-07 (a) and SIO-04 (b), and black lines represent modeled cooling histories simulating a relief increase initiating between 2.5 and 0.5 Ma (see text for details).*

We finally assess whether we can derive more precise constraints on the timing of relief increase from the $^{4}He/^{3}He$ data, by using relief scenarios with mean paleo-valley floor estimates (H_{limit} = 2100 and 1650 m for *VIS* and *SIO* areas, respectively) and varying the timing of onset of valley carving (0.5-2.5 Ma). We only use valley bottom samples (VIS-07 and SIO-04) as they provide the strongest constraints on the late-stage exhumation.

Output results (Figure III.3.9) show that although we cannot discriminate between recent scenarios (0.5-1.5 Ma), an onset of final exhumation ≥2 Ma predicts a poorer match to the $^{4}He/^{3}He$ cooling paths. We thus propose that the late-stage exhumation pulse triggered by local relief development may have been initiated at 1.0 ±0.5 Ma (Figure III.3.9).

III.3.5 Discussion

III.3.5.1 Exhumation and relief histories from thermochronology data

We have derived quantitative constraints on both exhumation and relief histories using thermochronology and numerical thermal-kinematic modeling. We show that combining inverse modeling [*e.g.*, *Valla et al.*, 2010b] of low-temperature thermochronologic (AFT and AHe) ages with quantitative interpretation of $^{4}He/^{3}He$ cooling paths [*Shuster et al.*, 2005; *Schildgen et al.*, 2010; *Valla et al.*, submitted, a] provides complementary constraints on denudation history and relief development. On the one hand, AFT and AHe data constrain late Miocene and Pliocene exhumation of the *VIS* and *SIO* areas by providing quantitative estimates on denudation rates and timing of changes in these rates. On the other hand, $^{4}He/^{3}He$ data and associated *t-T* histories provide tight constraints on late-stage exhumation through valley carving.

Inverse models produce contrasted results for both areas, with statistically better constrained exhumation scenarios for the *VIS* samples, implying a two-phase denudation history and a significant relief change (Table III.3.4, Figures III.3.3 and III.3.4). *SIO* data do not provide such well-constrained output results, and inverse modeling does not allow discriminating between the different exhumation scenarios (Table III.3.5). We thus choose a similar denudation history (two-phase denudation scenario with a phase of relief change) for both *VIS* and *SIO* areas as they are spatially very close. Moreover, the relief histories for both areas must have been tightly connected as they encompass the same major valley (*i.e.*, the Rhône valley, Figure III.3.1). We thus suggest that using a statistical criterion (*BIC*; *Schwartz,* 1978) may allow to quantitatively assess the adequate complexity of the inverse model [*e.g.*, *Gallagher et al.*, 2005a; *Glotzbach et al.*, submitted]; however, small (<10%) differences in the *BIC* values, as for our *SIO* data, do not permit to define an appropriate exhumation scenario without external constraints from adjacent areas (in this case the *VIS* data).

As previously explained, differences between *SIO* and *VIS* model results are due in part to the spatial distribution of thermochronologic data (Figure III.3.1b, c). *SIO* data are distributed along two separate profiles (either AHe or AFT data, Figure III.3.1b), while *VIS* data are more broadly distributed (especially the AFT data, Figure III.3.1c). These results are in close agreement with findings of *Valla et al.* [2010b] and *van der Beek et al.* [2010], which suggest

that sampling along age-elevation profiles only may not be the most appropriate way to infer both exhumation and relief histories. Another potential explanation previously proposed is the overlap between AFT and AHe ages for *SIO* samples (Figure III.3.2c), preventing the *NA* inverse model to converge towards best-fitting exhumation scenarios matching both the AHe and AFT data. We thus use a model [*Gautheron et al.*, 2009] that takes into account radiation-damage effects on apatite He retention to predict AHe ages. We show that including this model does not make significant difference as compared to the standard kinetics for *VIS* predictions; however, output results for *SIO* samples are clearly influenced by the radiation-damage effects. Although this model helps to improve the *BIC* contrast between different exhumation scenarios (*SIO_3**/*SIO_5** compared to *SIO_3*/*SIO_5*, Table III.3.5), we still have to rely on *VIS* modeling outputs to constrain the *SIO* exhumation history. Our modeling results also highlight that, even though *SIO* samples have AHe ages ranging between 4 and 8 Ma (Table III.3.2), and have experienced rapid cooling [*Valla et al.*, submitted, a], they have such high eU content (>100 ppm, Table III.3.2) that radiation damage effects must be incorporated into their numerical interpretation [*Shuster et al.*, 2006; *Flowers et al.*, 2009; *Gautheron et al.*, 2009].

In the following, we first discuss our modeling results for the late Miocene and Pliocene exhumation of both *VIS* and *SIO* areas, and then set some quantitative constraints on the late-stage relief development associated with deepening of the Rhône valley.

III.3.5.2 Late Miocene-Pliocene exhumation of the Aar-Aiguilles Rouges massifs

VIS modeling results provide a two-phase denudation history (*VIS_3* and *VIS_3**, Table III.3.4), with relatively rapid denudation rates (~2-4 km Ma^{-1}, Table III.3.4) until 8-10 Ma followed by moderate denudation rates of ~0.4-0.5 km Ma^{-1}. Pliocene denudation results are similar to those inferred by previous studies in the adjacent Aar and Gothard areas [*Reinecker et al.*, 2008; *Vernon et al.*, 2009; *Glotzbach et al.*, 2010; *Campani et al.*, 2010], which all predicted denudation rates of ~0.3-0.5 km Ma^{-1} for late Miocene to Pliocene times.

Moreover, a late Neogene exhumation pulse (~1-2 km Ma^{-1}) lasting until ~5-6 Ma has been suggested for the Mont-Blanc [*Glotzbach et al.*, submitted] and the Ecrins-Pelvoux [*van der Beek et al.*, 2010] massifs. *Vernon et al.* [2009] and *Glotzbach et al.* [2010] also pointed out a phase of rapid exhumation between ~10 and 7 Ma for the Aar and Gothard massifs,

respectively, although they report much lower denudation rates (~0.7 km Ma^{-1}) than our modeling results (~2-4 km Ma^{-1}, Table III.3.4). Thermochronological ages from the *VIS* profile (Table III.3.1 and Figure III.3.2d) are younger than this exhumation event and cannot provide precise constraint on this exhumation period; thus predicted denudation estimates have to be interpreted with caution. Moreover, ZFT data from adjacent areas [*Soom*, 1990; *Glotzbach et al.*, 2010] are ~10-12 Ma and would limit the duration of this pulse to 2-4 Ma (*i.e.*, maximum of 8-9 km exhumation). We thus propose that predicted denudation rates could be overestimated as we did not include higher-temperature constraints for this 10-8 Ma time-window period. Constraining the early denudation history of the area would have required high-temperature data as in the Ecrins-Pelvoux massif (*e.g.*, ZFT data, *van der Beek et al.*, 2010). However, these results are in agreement with other studies [*Vernon et al.*, 2009; *Glotzbach et al.*, 2010], and suggest a late Miocene transition from rapid to moderate denudation rates at ~8-10 Ma.

VIS AHe ages are too young to have recorded the late Neogene exhumation pulse; however, they suggest a different Pliocene denudation history than our inverse modeling. One-dimensional AHe age-elevation relationship suggests rapid apparent exhumation rates (~0.9 km Ma^{-1}, Figure III.3.2d) between 2-4 Ma, in agreement with $^4He/^3He$ *t-T* paths from the *VIS* summit sample (~1-1.5 km Ma^{-1} until ~3-4 Ma, and followed by only little exhumation, Figure III.3.7a). We previously explained that $^4He/^3He$ data may not have enough resolution to quantitatively constrain the late Miocene to early Pliocene exhumation history; however, this Pliocene exhumation pulse (recorded by $^4He/^3He$ data but not evidenced by our numerical modeling) may potentially result from a short denudation event [*Reinecker et al.*, 2008; *Pignalosa et al.*, 2010] that cannot be easily extracted from low-temperature thermochronology ages alone, but clearly appears in the $^4He/^3He$ data. This event may potentially have been smeared out in the inversion to overall moderate exhumation rates (~0.4 km Ma^{-1}) over the late Neogene.

Inverse modeling results for *SIO* are in closer agreement with $^4He/^3He$ cooling paths for the late Miocene and Pliocene. Model *SIO_3** (Table III.3.5) reveals rapid late Miocene denudation (~2.5 km Ma^{-1}, Figures III.3.5 and III.3.6) until ~6-7 Ma (somewhat later than for the Aar massif, but not statistically different), followed by moderate denudation rates during the Pliocene (~0.25 km Ma^{-1}, Figures III.3.5 and III.3.6), while $^4He/^3He$ data (Figure III.3.8) suggest quite lower denudation rates (~0.75-1.5 km Ma^{-1}) until 5-5.5 Ma followed by very

little exhumation (<0.1 km Ma^{-1}, Figure III.3.8a). In summary, even though timing and rates may differ slightly, both inverse modeling results and $^{4}He/^{3}He$ data evidence rapid late Miocene denudation followed by lower denudation rates during the Pliocene. ZFT data [*Rahn*, 1994] reveal only partial Alpine resetting (ZFT ages≥100 Ma), suggesting that predicted denudation rate estimates, similar to *VIS* results, cannot be sustained more than 3 to 5 Ma during the late Miocene. *Glotzbach et al.* [submitted] reported similar denudation rates and timing predictions for the Mont-Blanc exhumation history, with a relatively rapid denudation phase (~0.7-0.8 km Ma^{-1}) until ~5-6 Ma followed by lower exhumation rates (~0.4 km Ma^{-1}).

This coeval late Miocene decrease in exhumation rates observed within most of the ECMs [*Bigot-Cormier et al.*, 2006; *Glotzbach et al.*, 2008; *Vernon et al.*, 2009; *Glotzbach et al.*, 2010; *van der Beek et al.*, 2010; *Glotzbach et al.*, submitted] may have different potential explanations such as a global climate change during the Messinian [*e.g.*, *Willett et al.*, 2006] and/or potential tectonic controls (*e.g.*, lowering of convergence rates; *Schmid et al.*, 1996). However, this decrease in overall exhumation rates around the Miocene-Pliocene transition is not consistent with the ~5 Ma onset of Alpine foreland basin exhumation [*Cederbom et al.*, 2004; in press] and an increase in sediment flux [*Kuhleman et al.*, 2002] that have been interpreted as reflecting increase in erosional efficiency within the Alpine orogen [*Vernon et al.*, 2008]. One alternative explanation, recently proposed by *Glotzbach et al.* [submitted], connects the observed drop in the exhumation rates of the ECMs to widespread late Miocene exposure of crystalline basement rocks that are less erodible than the overlying Mezosoic sedimentary cover units.

III.3.5.3 Pleistocene relief development

Forward modeling permitted quantitative interpretation of late-stage $^{4}He/^{3}He$-derived cooling paths for *VIS* and *SIO* samples. Our modeling results clearly confirm that final exhumation of these samples cannot be related to tectonic activity [*Reinecker et al.*, 2008], which would have influenced massif-scale denudation (Supplementary Figures III.3.11 and III.3.12) but is rather associated with recent relief development through valley carving [*Valla et al.*, submitted, a]. Valley deepening induced additional exhumation only for mid- to low-elevation samples (Figures III.3.7 and III.3.8). Using numerical thermal-kinematic modeling, we can use the $^{4}He/^{3}He$-derived *t-T* paths to place quantitative constraints on the pre-glacial Rhône valley floor elevation: 2100 ±100 m (*VIS*, Figure III.3.7) and 1650 ±150 m (*SIO*, Figure III.3.8),

implying a ~85-100% increase in local relief during the last 1.0 ±0.5 Ma (Figure III.3.9). Note that these paleo-elevation estimates do not take the isostatic response to valley carving into account.

Our inverse modeling results also provided quantitative predictions for late-Pliocene relief development. *VIS* modeling results (Table III.3.4) suggest that paleo-valley floor elevations may have been at ~2700-3000 ±400 m elevation (*i.e.*, an overestimation of relief increase compared to $^{4}He/^{3}He$ predictions), and predict an onset of valley carving between ~1 and 3 Ma (*VIS_3* and *VIS_3** inversions, Table III.3.4). *SIO* relief predictions (*SIO_3**, Table III.3.5) confirm $^{4}He/^{3}He$ estimates of paleo-valley floor elevation (1500 ±400 m, Figure III.3.6d) and provide similar timing constraints as the *VIS* data (~2-3 Ma, Figure III.3.6c). As previously explained, inverse modeling of AFT and AHe thermochronologic data does not provide as much resolution on late-stage exhumation as the $^{4}He/^{3}He$ data [*Valla et al.*, submitted, a], consequently leading to less precise timing and relief growth estimates. However, even though the timing and rate predictions differ slightly, both inverse modeling results and $^{4}He/^{3}He$ cooling *t-T* paths suggest that the topographic relief of the Rhône valley has roughly doubled [*Valla et al.*, submitted, a] since ~1-2 Ma.

Thermochronologic studies from adjacent areas report a significant increase in exhumation rates (up to ~1 km Ma^{-1}) since ~2-3 Ma [*Glotzbach et al.*, 2008; *Campani et al.*, 2010; *Glotzbach et al.*, 2010; *Pignalosa et al.*, 2010]; however, these studies did not interpret this exhumation pulse as being linked to relief development but rather to enhanced massif-scale denudation. *Glotzbach et al.* [submitted] did manage to extract precise relief information by performing inverse modeling of thermochronology data from the Mont-Blanc area. Their results suggest an approximate doubling in topographic relief since ~1 Ma, in close agreement with our relief estimates from $^{4}He/^{3}He$ data. Relief predictions from our thermochronologic data are also consistent with ~1 km of incision of the Aar valley, dated at ~0.8-1.0 Ma from cosmogenic burial dating of cave sediments [*Haeuselmann et al.*, 2007].

Both the existing literature data and our own results thus point towards a significant impact of Alpine Quaternary glaciations on topographic relief growth [*e.g.*, *Valla et al.*, submitted, a]; however, timing predictions suggest that relief development within the core of the Alpine orogen postdated both the onset of the Northern-Hemisphere glaciations at ~3.5-2.7 Ma [*Haug et al.*, 2005; *Lisiecki and Raymo*, 2005; *Mudelsee and Raymo*, 2005] and evidence of

late Pliocene glaciers within the European Alps [*Schlüchter*, 1986; *Jeannin*, 1991; *Zuccoli*, 2000]. We thus speculate, in agreement with *Haeuselamnn et al.* [2007] and *Valla et al.* [submitted, a], that major valley carving within the Swiss Alps may be linked to the Mid-Pleistocene climate transition from 41-kyr to 100-kyr glacial/interglacial oscillations [*e.g.*, *Lisiecki*, 2010] and the onset of widespread major Alpine glaciations [*Muttoni et al.*, 2003]. Periodic oscillations between glacial and interglacial conditions may have promoted transient landscapes [*Norton et al.*, 2010a] and favoured alpine relief development from Mid-Pleistocene to present-day times (Figure III.3.9, *Glotzbach et al.*, submitted), inducing an isostatic response to Quaternary erosional unloading [*Molnar and England*, 1990; *Champagnac et al.*, 2007; 2008; *van der Beek and Bourbon*, 2008] that partly contributes to modern rock uplift [*Schlatter et al.*, 2005].

III.3.6 Conclusions

Based on thermal-kinematic modeling of both low-temperature thermochronologic ages and $^{4}He/^{3}He$ stepped-heating results, we derive quantitative constraints on the late Miocene and Pliocene exhumation history of the Aar and Aiguilles Rouges massifs (Swiss Alps). Modeling results highlight the complementarities between AFT/AHe data and $^{4}He/^{3}He$ thermochronometry in quantifying both denudation and relief evolution. Inverse modeling of AFT and AHe data reveals that numerically interpreting thermochronology data first requires assessing the appropriate model complexity, as well as constraining thermal parameters using high-temperature thermochronometers and/or external constraints.

Moreover, our results highlight the potential problem of interpreting AHe ages without taking into account the effects of radiation damage on apatite He retention even in relatively young samples that cooled rapidly. We use two different numerical codes [*Flowers et al.*, 2009; *Gautheron et al.*, 2009] to include theses effects in AHe ages prediction and our results show that, for our study, both codes provide similar outcomes. Modeling results suggest a late Miocene exhumation pulse until ~5-8 Ma, consistent with recent thermochronological outcomes from adjacent areas and the exhumation histories inferred for other ECMs. This exhumation event is followed by moderate (~0.3-0.5 km Ma^{-1}) and apparently steady-state denudation rates during the Pliocene, contrasting with the inferred ~5 Ma increase in sediment flux out of the orogen.

Extracting relief information from thermochronological observations has remained elusive and age-elevation sampling strategies do not necessarily provide precise estimates of relief development. However, we have showed that using spatially distributed samples may help to provide quantitative information on topographic relief changes, although best predictions are given by methods that are sensitive to lower temperatures, such as $^{4}He/^{3}He$ thermochronometry. Our modeling results, in agreement with other thermochronological studies, allow for interpretation of the late-stage exhumation of the Swiss Alps as being caused by a doubling in local topographic relief through glacial valley carving (~1-1.5 km of Rhône valley incision). We postulate that this massif-scale relief change may have been initiated at ~1 Ma, triggered by the Mid-Pleistocene climate transition and the enhancement of transient landscape conditions by glacial/interglacial oscillations.

Acknowledgments

This study is supported by INSU-CNRS through the European Science Foundation Eurocores Topo-Europe programme 07-TOPO-EUROPE-FP-023 “Coupled climatic/tectonic forcing of European topography revealed through thermochronometry (Thermo-Europe)” (to PAvdB), the Agence Nationale de la Recherche project No. ANR-08-BLAN-0303-01 “Erosion and Relief Development in the Western Alps” (to PAvdB), U.S. National Science Foundation grant EAR-0720225 (to DLS), the ANR-06-JCJC-0079 (to CG), and the Ann and Gordon Getty Foundation. It forms part of PV's PhD project at Université Joseph Fourier, supported by the French Ministry for Research and Higher Education. We thank M. Rahn who kindly shared his unpublished fission-track data. Computations were performed on Brutus, the high performance computing facilities at ETH Zurich. The codes are available at http://svn-geo.ethz.ch after registering at this site.

III.3.7 Auxiliary material

This section reports one supplementary figure (Figure III.3.10) showing $^{4}He/^{3}He$ data for samples SIO-03 and VIS-05 (see Tables III.3.1 and III.3.2 for description). We also provide two supplementary figures showing comparisons between *VIS*/*SIO* $^{4}He/^{3}He$-derived *t-T* paths and *Pecube* forward models simulating a late-stage regional denudation pulse since ~1 Ma (Figures III.3.11 and III.3.12, respectively).

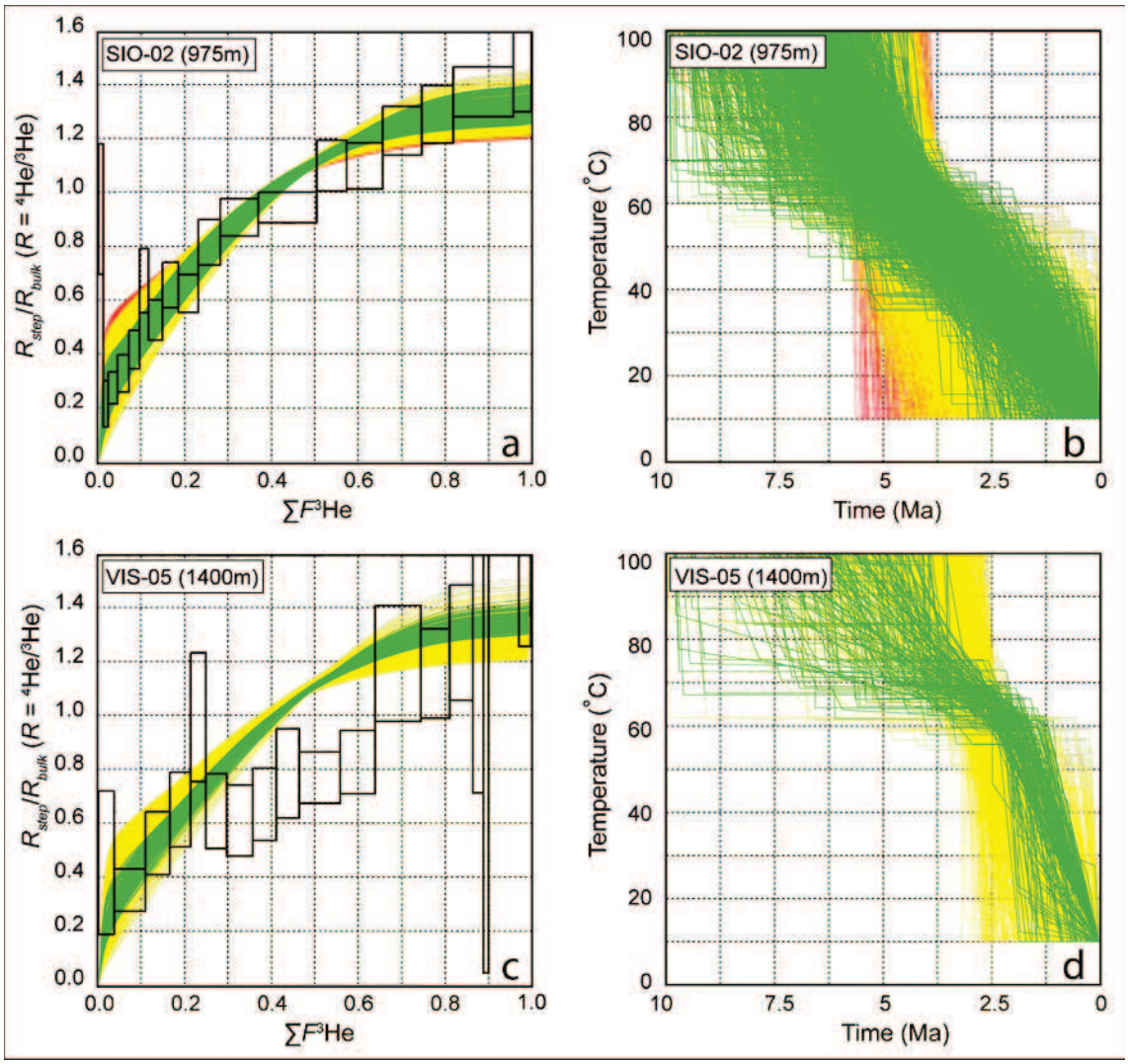

Figure III.3.10. *$^4He/^3He$ thermochronometry of samples SIO-02 and VIS-05 (for other VIS and SIO samples; see Valla et al., submitted, a). Observed $^4He/^3He$ ratio evolution diagrams and model cooling paths for SIO-02 (a-b) and VIS-05 (c-d). The measured $^4He/^3He$ ratios of each degassing step (R_{step}) are normalized to the bulk ratio (R_{bulk}) and plotted versus the cumulative ^3He release fraction ($\sum F^3He$). Open black boxes indicate 1 standard error (vertical) and integration steps (horizontal). Colored lines show the predicted $^4He/^3He$ ratio evolution diagrams (a, c) for arbitrary cooling paths (b, d), each of which predicts the observed (U-Th-Sm)/He age of each sample to within analytical uncertainty (±1σ standard deviation). Cooling paths shown in red and yellow are excluded by the $^4He/^3He$ data, whereas the green cooling paths are permitted (see Valla et al., submitted, a, for details on numerical thermal modeling).*

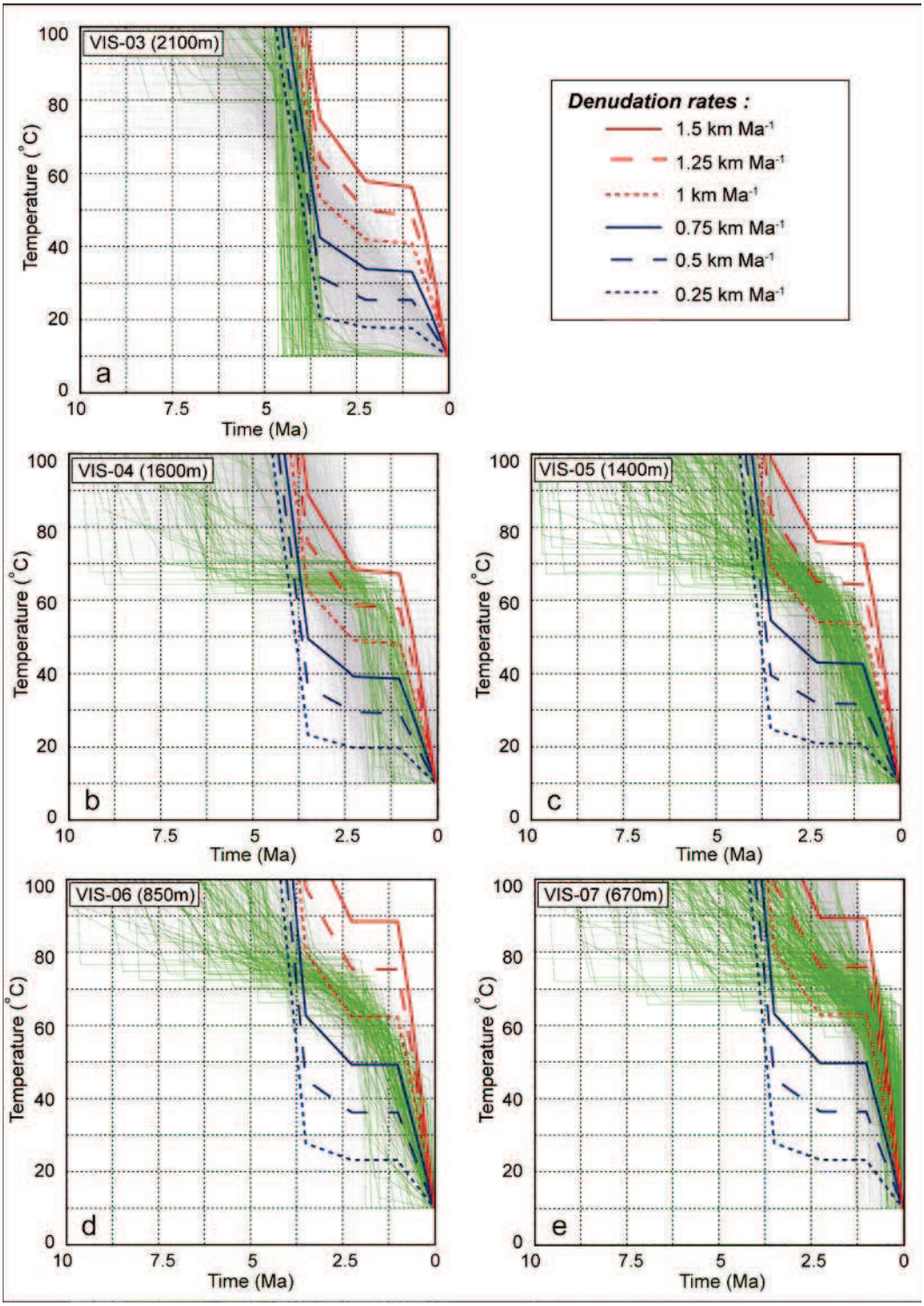

Figure III.3.11. *Cooling paths for VIS samples inferred from $^{4}He/^{3}He$ and Pecube models (see Figures III.3.1 and III.3.2 for sample locations). Green/grey lines show respectively good and acceptable $^{4}He/^{3}He$ modeled cooling paths for VIS-03 (a), -04 (b), -05 (c), -06 (d) and -07 (e) [Valla et al., submitted, a]. Thick coloured lines (blue and red) show modeled cooling paths for a late-stage regional denudation pulse since ~1 Ma at various rates (0.25 to 1.5 km Ma^{-1}, see legend for colours code). See text for other parameters.*

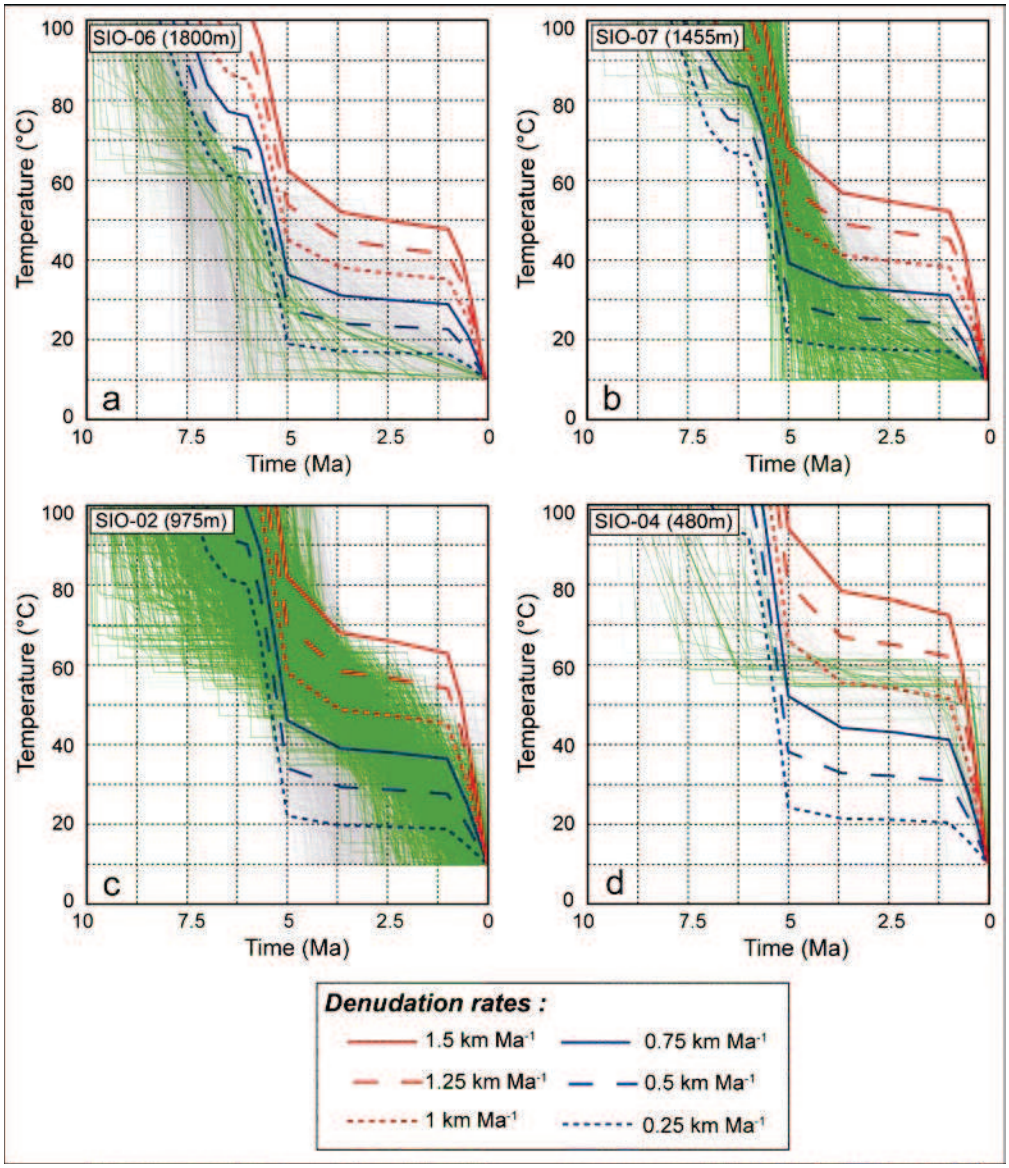

Figure III.3.12. *Cooling paths for SIO samples inferred from $^{4}He/^{3}He$ and Pecube models (see Figures III.3.1 and III.3.2 for sample locations). Green/grey lines show respectively good and acceptable $^{4}He/^{3}He$ modeled cooling paths for SIO-06 (a), -07 (b), -02 (c) and -04 (d) [Valla et al., submitted, a]. Thick coloured lines (blue and red) show modeled cooling paths for a late-stage regional denudation pulse since ~1 Ma at various rates (0.25 to 1.5 km Ma^{-1}, see legend for colours code). See text for other parameters.*

III.4 - Alpine pre-glacial topography and Quaternary relief development, Swiss Alps

Pierre G. Valla [1], Peter A. van der Beek [1], Jean Braun [1], and David L. Shuster [2,3]

[1] *ISTerre-OSUG, Université de Grenoble, CNRS, BP 53, F-38041 Grenoble, France*

[2] *Berkeley Geochronology Center, 2455 Ridge Road, CA-94709 Berkeley, USA*

[3] *Department of Earth and Planetary Science, U.C. Berkeley, CA-94709 Berkeley, USA*

Abstract

Evaluating the net effect of glacial erosion on mountain belt topography requires quantitative estimates of relief evolution. Recent studies have shown that Quaternary glaciations led to relief development at the valley scale; however, basin-scale mean elevation and relief changes have remained poorly constrained. Here, we use a new approach to reconstruct the pre-glacial topography of the Rhône basin (Swiss Alps) from local $^{4}He/^{3}He$ thermochronometry data. Our results show that the net effect of Quaternary glaciations has been to both deepen and steepen alpine valleys, leading to strong local relief increase. However, at the basin scale, we infer that while producing a net decrease in the mean topographic elevation, Quaternary glaciations have not significantly modified the mean relief. Finally, we suggest that basin-scale erosion rates have been nearly constant over the last ~1 Ma and show that the isostatic response to Quaternary erosional unloading only partly explains present-day rock-uplift rates within the Swiss Alps.

III.4.1 - Introduction

Present-day alpine topography presents glacially-influenced high local relief that has been interpreted to result from Pliocene climate change and onset of widespread Quaternary glaciations [*Molnar and England*, 1990]. However, the net effect of glacial erosion on topography is still debated, with studies arguing for glacial enhancement of mountain relief by efficient valley carving [*Small and Anderson*, 1998; *Brocklehurst and Whipple*, 2002; *Montgomery*, 2002]; while others have suggested that glaciations limit topography above the Equilibrium Line Altitude (ELA) and thus reduce topographic relief [*Brozovic et al.*, 1997; *Whipple et al.*, 1999; *Egholm et al.*, 2009]. Recent studies have shown that local topographic

relief has dramatically increased since the onset of Quaternary glaciations [*Haeuselmann et al.*, 2007; *Valla et al.*, submitted, a]; however, assessing relief amplification at the basin scale (mean basin value of ridge line to valley bottom relief calculated within in a specified radius; *Brocklehurst and Whipple*, 2002) is more challenging and has essentially been inferred from topographic interpolations such as the analysis of "geophysical relief" [*Small and Anderson*, 1998; *Champagnac et al.*, 2007; van *der Beek and Bourbon*, 2008]. Assessing the net effects of glacial erosion on topographic relief and the associated isostatic response requires quantitative constraints on basin-scale paleo-topography.

Here, we show that the net effect of Quaternary glaciations in the Swiss Alps has been first to deepen major valleys such as the Rhône valley (Figure III.4.1) and steepen river profiles by focusing glacial erosion close to the ELA and at major glacier confluences. Second, based on a pre-glacial basin topography reconstruction inferred from high-resolution $^{4}He/^{3}He$ thermochronology, we derive topographic metrics that reveal a decrease in mean elevation of the Rhône basin through the Quaternary, while valley carving and peak preservation have lead to a significant increase in local topographic relief. However, we show that the mean basin relief only slightly increased during this same period. Finally, we argue that the present-day rock uplift observed in the Swiss Alps, although correlated with Quaternary incision along the Rhône valley, is only partly explained by the isostatic response to Quaternary erosional unloading.

III.4.2 - Geomorphic setting

The European Alps are a doubly vergent orogen that formed during the continental collision between European and African plates [*Schmid et al.*, 2004]. This study focuses on the upper Rhône basin (Swiss Alps, Figure III.4.1) that drains both crystalline (Aar and Aiguilles Rouges massifs) and sedimentary (Helvetic nappes) units. The current drainage pattern has been inherited from tectonic structures [*Kühni and Pfiffner*, 2001a] associated with the exhumation of the External Crystalline Massifs since Oligocene-early Miocene times [*Schmid et al.*, 2004]. The current kinematics of the Swiss Alps shows no active convergence [*Nocquet and Calais*, 2004] and evidence for large-scale extension [*e.g.*, *Champagnac et al.*, 2004].

The morphology of the Rhône basin reflects a classic glacial imprint upon an alpine landscape [*e.g.*, *Kelly et al.*, 2004]. Valleys show U-shaped cross-profiles, flat-and-step longitudinal river profiles and major glacial overdeepenings (*Norton et al.*, 2010a, Figure III.4.2).

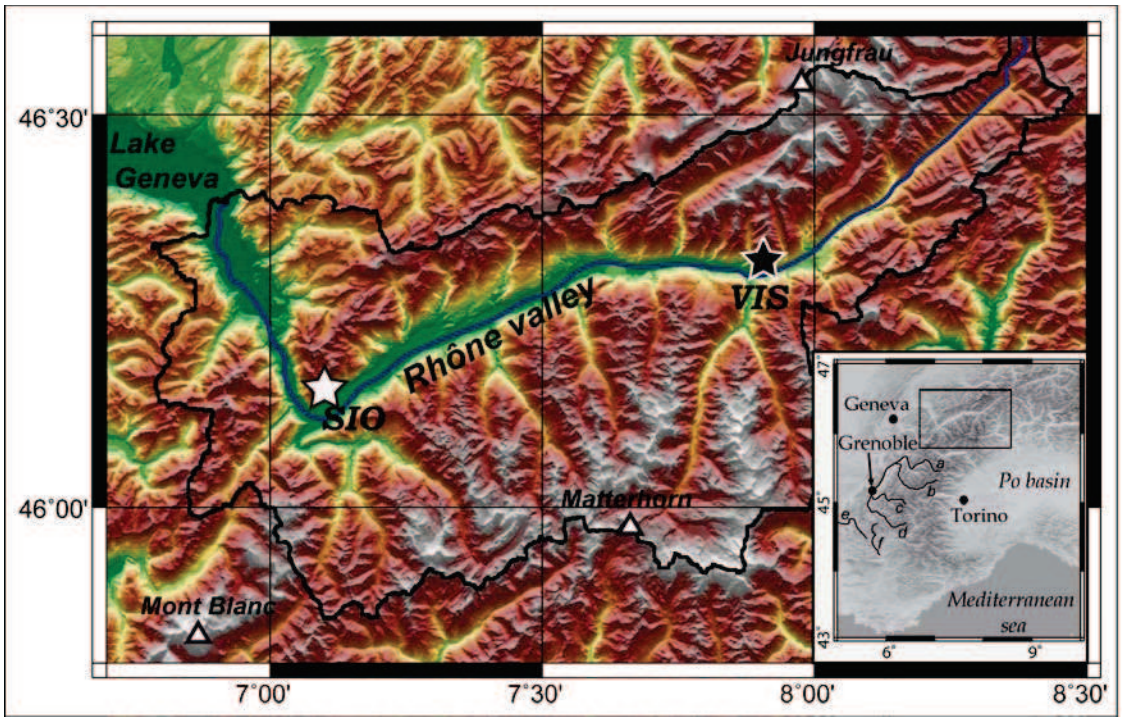

Figure III.4.1. *Digital Elevation Model of the studied area in the European Alps. Stars represent SIO (white) and VIS (black) sampling sites for $^{4}He/^{3}He$ thermochronology data along the Rhône Valley [Valla et al., submitted, a]. Major summits are also indicated (Jungfrau: 4160 m, Mattherhorn: 4480 m, Mont Blanc: 4810 m). Blue and black lines indicate the Rhône river and watershed limit, respectively, upstream of Lake Geneva. Inset shows location of the study area within the European Alps (black lines represent studied drainage systems: (a) Arc, (b) Isère, (c) Romanche, (d) Drac, (e) Drôme and (f) Buëch, section III.4.6.1).*

The development of large and erosive alpine glaciers since ~1 Ma [*Muttoni et al.*, 2003] has led to significant valley deepening [*Haeuselmann et al.*, 2007; *Valla et al.*, submitted, a]. The Rhône valley (Figure III.4.2) exhibits a longitudinal profile that is highly perturbed by late-Quaternary glacial erosion [*Finkh and Frey*, 1991; *Rosselli and Olivier*, 2003] and post-glacial sediment filling [*Hinderer*, 2001]. Holocene erosion rates from ^{10}Be concentrations in stream sediments [*Wittmann et al.*, 2007] and modern sediment yields [*Hinderer*, 2001] indicate efficient post-glacial fluvial and hillslope erosion [*Norton et al.*, 2010a]. Furthermore, modern erosion patterns [*Wittmann et al.*, 2007; *Champagnac et al.*, 2009] closely correlate with present-day rock uplift as measured by geodesy in the Swiss Alps [*Schlatter et al.*, 2005]. Recent studies using geophysical relief as a proxy for erosion rates during the Quaternary [*Champagnac et al.*, 2007; *van der Beek and Bourbon*, 2008] and Holocene/present-day [*Champagnac et al.*, 2009] proposed that about half of the modern rock uplift can be explained by flexural isostatic response to erosional unloading.

III.4.3 - Methods

In this study, our objectives are: (1) to constrain the present-day profile concavity of the Rhône valley (Figure III.4.2) for comparison with fluvial and formerly glaciated rivers within the Western Alps (see Figure III.4.1 for locations and section III.4.6.1 for details); and (2) to reconstruct the pre-glacial Rhône basin topography based on local topographic evolution constraints.

At topographic steady-state, bedrock rivers typically have longitudinal profiles with upward concavity [*e.g.*, *Whipple*, 2004], relating local channel gradient S to upstream drainage area A [*Flint*, 1974; *Whipple and Tucker*, 1999] :

$$S = k_s \, A^{-\theta} \tag{III.4.1}$$

where k_s and θ are termed the steepness and concavity indexes, respectively. Present-day k_s and θ indexes are obtained by fitting a "steady-state" profile (Eq. (III.4.1)) to the observed longitudinal profile extracted from a 90-m resolution digital elevation model. Assuming fixed outlet and source elevations, we derive both k_s and θ values for each selected river (see section III.4.6, Figures III.4.6 and III.4.7) to assess the potential differences between fluvial (no evidence of any glacial imprint on the landscape) and glacially-influenced (formerly glaciated) valleys.

Pre-Quaternary profile reconstruction of the Rhône valley is based on recently published constraints on valley deepening from $^4He/^3He$ thermochronometry data [*Valla et al.*, submitted, a, b] along two elevation profiles (SIO and VIS profiles, Figure III.4.1). Thermal-kinematic modeling [*Braun*, 2003] allowed us to convert sample cooling histories into quantitative constraints on relief development [*Valla et al.*, submitted, a, b]. The results imply a two-fold deepening of the Rhône valley through the Quaternary (~1 Ma) and therefore constrain the pre-glacial Rhône valley floor elevation to be ~1.2 ±0.15 km (SIO) and 1.4 ±0.1 km (VIS) above the present-day valley floor. Assuming no elevation change for the Rhône channel head, we use these two local constraints along the Rhône valley to numerically reconstruct a pre-glacial "steady-state" profile and calculate the associated pre-glacial concavity index, θ_p (Figure III.4.2).

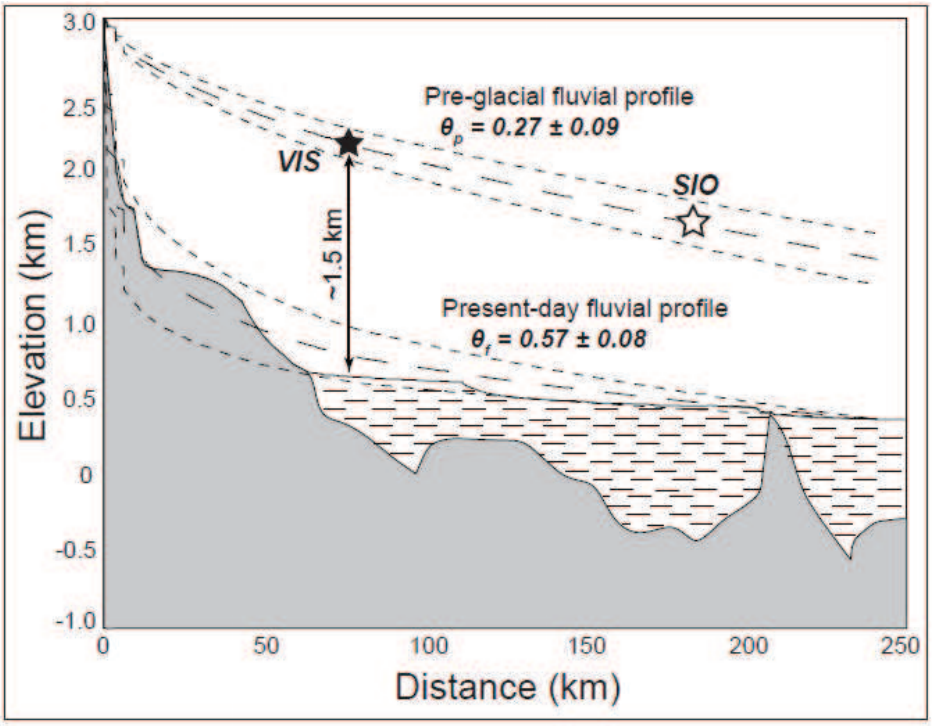

Figure III.4.2. *Present-day profile and pre-glacial reconstruction of the Rhône valley. Black lines show observed present-day (SRTM 90-m resolution) and bedrock glacial (seismic and gravity data; Finckh and Frey, 1991; Rosselli and Olivier, 2003) profiles; post-glacial sediment filling (grey dashes) of the Rhône valley is also shown [Hinderer, 2001]. Dashed lines correspond to best-fits and associated 1σ uncertainties (θ_f = 0.57 ±0.08 for present-day "steady-state" profile and θ_p = 0.27 ±0.09 for pre-glacial reconstruction).*

Based on the pre-Quaternary Rhône profile reconstruction (Figure III.4.2), we constrain the pre-glacial longitudinal profile of major tributaries within the Rhône watershed (section III.4.6.1; *Mathes*, 1930). Finally, we reconstruct the pre-Quaternary hillslope relief assuming a spatially uniform local slope gradient of ~25° (see section III.4.6.2 for full details on the fluvial and hillslope topographic reconstructions).

We then extract topographic metrics (mean basin elevation and relief; *Brocklehurst and Whipple*, 2002), using standard GIS methods (section III.4.6.2), of both the pre-glacial topographic reconstruction and present-day topography (Figure III.4.3) to assess the net geomorphic effect of Quaternary glaciations on the landscape.

Finally, we directly compare the distribution of Quaternary incision along the Rhône valley to the present-day rock-uplift pattern [*Schlatter et al.*, 2005]. We then calculate the proportion of the modern rock uplift attributable to the isostatic response to erosion by performing 2D

flexural rebound modelling [*Champagnac et al.*, 2007; 2009]. In this calculation, we use the Quaternary Rhône basin incision (Figure III.4.3C) as a quantitative proxy for Quaternary erosional unloading and simulate the associated flexural isostatic response (section III.4.6.3).

III.4.4 - Quaternary relief production and isostatic response

The pre-glacial profile reconstruction reveals ~1-1.5 km of Quaternary incision along the Rhône valley (Figure III.4.2), corresponding to the ~80-100% increase in local relief proposed by *Valla et al.* [submitted, a, b]. Moreover, our results show that the Rhône valley has been significantly steepened following the onset of glacial conditions, with a modern concavity index (θ_f = 0.57 ±0.08 for present-day fluvial profile and 0.49 ±0.11 when considering the glacial bedrock profile, Figures III.4.2 and III.4.6) around twice that of the pre-glacial conditions (Figure III.4.2, θ_p = 0.27 ±0.09). This difference is confirmed by present-day concavity constraints from glacially-influenced (Isère, Drac, Romanche and Arc) and typical fluvial (Drôme and Büech) drainage systems within the Western Alps (Figure III.4.7). Present-day river profiles show that glacially-influenced streams tend to exhibit higher θ values ($\theta \approx$ 0.46-0.79) than fluvial ones ($\theta \approx$ 0.28-0.33), in agreement with our predictions for the Rhône valley. Similar outcomes are found concerning the steepness index k_s; both present-day Rhône and other glacially-influenced alpine rivers showing k_s values 2-3 orders of magnitude higher than pre-glacial Rhône valley and alpine fluvial profiles (section III.4.6.1).

Pre-glacial Rhône topographic reconstruction permits quantification of basin-integrated Quaternary incision (from 0 to ~2.1 km), yielding a mean basin incision of ~0.7 ±0.4 km (Figure III.4.3C) through the Quaternary. Moreover, our results predict a ~25% decrease in the mean basin elevation during the Quaternary (mean basin elevation of ~2.7 ±0.3 km and 2.1 ±0.8 km for pre-glacial and present-day topographies, respectively). However, the mean basin relief has only increased by ~5-10%, essentially through incision of local valleys and cirques (Figures III.4.3C and III.4.9).

Assuming a linear Quaternary incision over the last ~1 Ma and an immediate isostatic response to erosional unloading, both inferred incision rates along the Rhône valley and modeled flexural isostatic rebound within the Rhône basin closely correlates with the modern rock uplift pattern, even though the isostatic response to Quaternary erosional unloading only accounts for ~30-50% of the modern geodetic rock uplift (Figure III.4.4A, B).

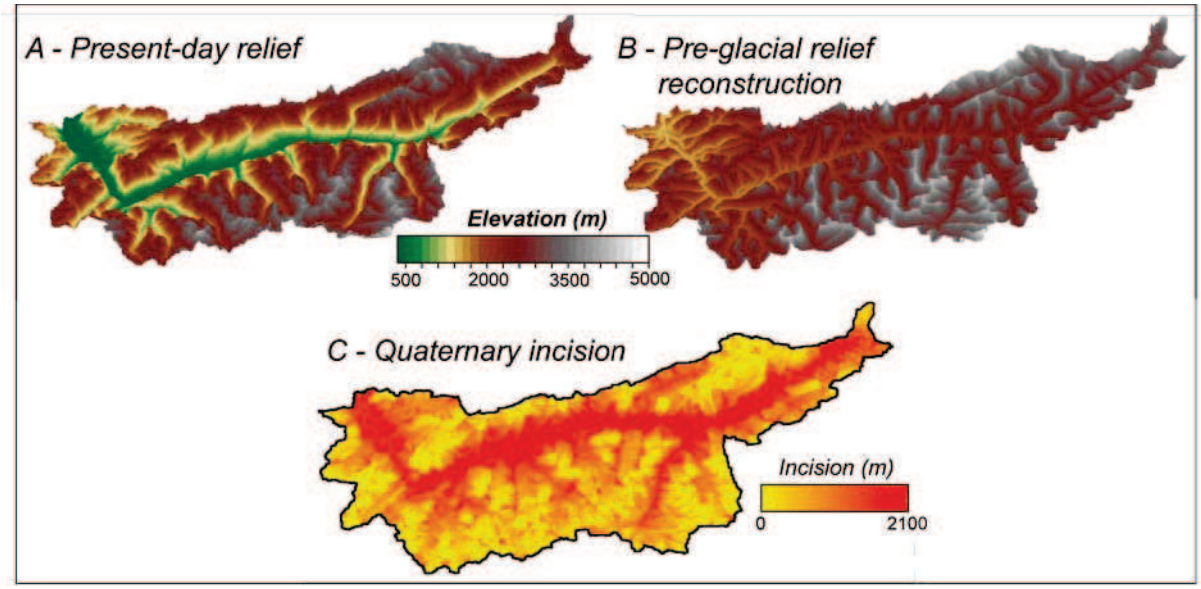

Figure III.4.3. *(A) Present-day topography of the Rhône basin (90-m SRTM) and (B) pre-glacial topography reconstruction (section III.4.6.2). (C) Incision map of the Rhône basin integrated over the Quaternary.*

III.4.5 - Discussion and conclusions

Our topographic reconstruction relies on several assumptions. First, applying Eq. (III.4.1) requires that river profiles are in topographic steady-state over timescales of climate and tectonic forcings; however, the present-day Alpine landscape is clearly transient [*e.g.*, *Norton et al.*, 2010a] and there is no clear evidence for pre-Quaternary topographic steady-state in the Swiss Alps. Moreover, our pre-glacial river reconstruction assumes no major drainage pattern modification (no evidence for any Quaternary river capture event) and minor elevation change of channel heads (peak preservation by frozen ice and/or reduced periglacial processes). Second, we assume that parameters deduced from the Rhône pre-glacial reconstruction also apply to all tributaries (similar range of concavity index values), in agreement with similar concavity index ranges found for other alpine rivers (Figure III.4.7). Finally, we choose a constant hisllsope gradient (over both space and time) for the Rhône pre-glacial basin; data from the Rhône area show similar slope gradients for various lithological units [*Kühni and Pfiffner*, 2001b] and we find no evidence of significant hillslope gradient change following the onset of glaciations (section III.4.6.2).

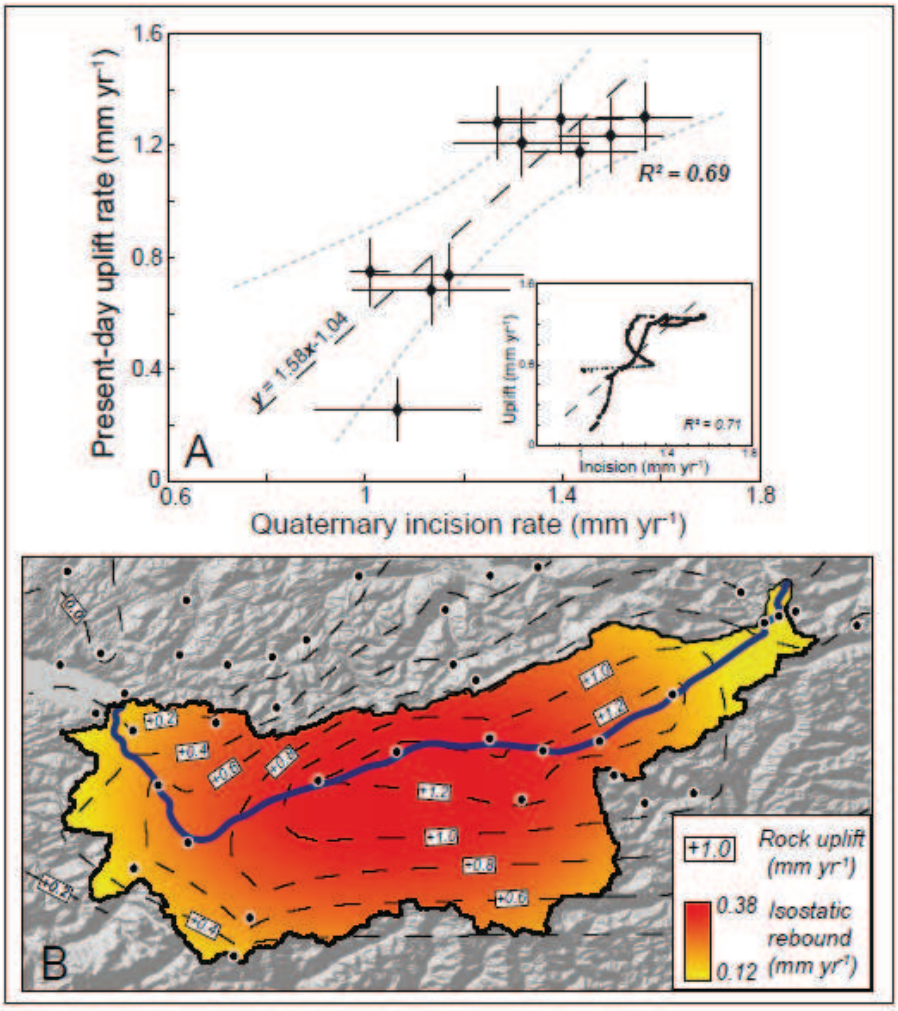

Figure III.4.4. *(A) Quaternary incision rates (onset of valley carving at ~1 Ma) with respect to modern rock-uplift measurements [Schlatter et al., 2005] along the Rhône valley. Dashed line shows linear regression (Pearson's coefficient of 0.744, regression slope of 1.58 ±0.31 and vertical axis-intercept of -1.04 ±0.38 mm yr^{-1}), and dotted lines represent the 95% confidence interval error envelopes. Inset shows correlation between incision and uplift rates when considering data interpolation along the Rhône valley. (B) Geodetic measurements locations (black circles) and interpolated rock-uplift rates (dashed contour lines) with respect to Aarburg [Schlatter et al., 2005] for the Rhône watershed (basin contour: black line; Rhône river: blue line). Colours indicate modeled 2D flexural isostatic rebound using the total Rhône basin incision (Fig. III.4.3C) as a proxy for the Quaternary erosional unloading (section III.4.6.3).*

Under this set of assumptions, our pre-glacial Rhône profile reconstruction suggests a mean valley incision rate of ~1.3 ±0.2 km Ma^{-1} (~1.7 ±0.3 km Ma^{-1} when considering the present-day glacial bedrock profile). Recent studies estimated similar valley deepening rates using geophysical relief constraints [*Champagnac et al.*, 2007; *van der Beek and Bourbon*, 2008] or direct quantification of valley deepening [*Haeuselmann et al.*, 2007]. Our results also suggest

that the Quaternary glaciations resulted in significant increases in both concavity and steepness indexes of major alpine rivers (Figures III.4.2 and III.4.7), in agreement with recent estimates for post-glacial Himalayan rivers [*Hobley et al.*, 2010]. However, our findings contrast with previous results of *Norton et al.* [2010a] and *Whipple et al.* [1999] that proposed no significant difference or a net decrease in the concavity index between non-glaciated and glacially-influenced rivers. *Norton et al.* [2010a] found similar river concavities between glaciated and small "non-glaciated" basins (Swiss Alps); however, all these basins are close to Quaternary glaciated areas and must have been influenced by glacial and/or periglacial processes. *Whipple et al.* [1999] reported low concavity values for rivers in the Sierra Nevada; however, Quaternary glacial erosion was less efficient and more localised around the ELA [*Brocklehurst and Whipple*, 2002] than in the European Alps. We suggest that the Rhône valley concavity index increased through the Quaternary due to intense glacial incision near the ELA and at major confluences with tributaries [*Kelly et al.*, 2004; *Norton et al.*, 2010a] associated with relative preservation of the river headwaters.

Comparison of the reconstructed pre-glacial topography to the modern relief (Figure III.4.3) reveals that the net effect of Quaternary glaciations in the Swiss Alps has been to significantly reduce the mean basin elevation, which supports the glacial "buzz-saw" hypothesis [*Egholm et al.*, 2009]. Moreover, glacial erosion focused local relief development along major valleys and tributaries (Figures III.4.3C and III.4.9), but induced only a minor increase in the mean basin relief [*Whipple et al.*, 1999]. *Schlunegger and Hinderer* [2003] proposed similar observation of a moderate basin relief increase since the late-Pleistocene/Holocene transition.

We estimate a basin-scale sediment production rate for the Quaternary by adding a constant "background denudation rate" of ~0.15 km Ma^{-1} [*Kuhlemann et al.*, 2006] to our Rhône basin incision reconstruction (Figure III.4.3C). The mean Quaternary denudation rate for the Rhône basin is estimated at ~0.85 km Ma^{-1}, in agreement with post-glacial sediment flux estimates (~0.95 km Ma^{-1}, *Hinderer*, 2001), and reflects that the Rhône basin evolution and sediment production integrate both glacial and interglacial periods [*Hinderer*, 2001].

Quaternary incision rates along the Rhône valley correlate positively with modern uplift rates (Figure III.4.4A), even though the isostatic response to incision slightly underestimates (Rhône valley headwaters) or overestimates (Geneva Lake outlet) modern rock uplift. These differences may be due to the isostatic contribution of glacier melting to modern uplift in the

Rhône valley headwaters [*Barletta et al.*, 2006], and to Holocene lake sediment loading in the downstream part of the valley [*Champagnac et al.*, 2009].

Modeled flexural isostatic rebound closely matches, but underestimates, the modern rock-uplift pattern (Figure III.4.4B; *Champagnac et al.*, 2007), especially for the Rhône valley headwaters. Note that we first imposed no change in elevation of the Rhône channel heads for the pre-glacial reconstruction, and did not consider any isostatic contribution from the adjacent watersheds in our flexural model. Moreover, as mentioned above, the Quaternary erosional unloading (Figure III.4.3C) includes only the non-steady component of the total Rhône basin denudation, and does not consider the subsequent post-glacial sediment filling of glacial valley overdeepenings (Figure III.4.2). These limitations may partly explain our relatively low isostatic rebound predictions compared to present-day rock-uplift rates [*Champagnac et al.*, 2007; 2009].

We presented a new approach to quantitatively reconstruct the pre-glacial topography of the Rhône basin. Our results show that the net effect of Quaternary glaciations has been to both deepen and steepen alpine valleys, leading to major relief development at the local scale and a net decrease in the mean topographic elevation. However, in concordance with previous studies, we propose that glacial/interglacial oscillations do not significantly modify the mean basin-scale relief. Similarly, mean basin erosion rates through the Quaternary are in good agreement with post-glacial sediment filling estimates and suggest that erosion rates have been nearly constant over the last ~1 Ma. Finally, isostatic response to Quaternary erosional unloading only partly explains present-day rock-uplift rates within the Swiss Alps. Isostatic effects of glacier retreat or regional geodynamic processes [*e.g.*, *Champagnac et al.*, 2008] may explain these differences.

Acknowledgements

We thank F. Chirouze and R. Delunel for fruitful discussions. Financial support for this work was provided by the French Agence Nationale de la Recherche (ANR-08-BLAN-0303-01), the European Science Foundation Topo-Europe Eurocores program and the Ann and Gordon Getty Foundation.

III.4.6 - Data repository

III.4.6.1 - "Steady-state" river profile reconstruction, θ and k_s indexes

"Steady-state" river profile reconstruction is based on the "Slope-Area" relationship (see Eq. (III.4.1) in main text; *Flint*, 1974; *Whipple and Tucker*, 1999) and requires several assumptions and iterative steps described in the following. First, the total elevation drop (H) between the river source ($z_{source} = z_n$) and its outlet ($z_{outlet} = z_1$) can be approximated by the integral of local channel gradients S_i at each discrete river node i following:

$$H = z_{source} - z_{outlet} = \sum_{i=1}^{n} S_i \, d_i \tag{III.4.2}$$

where d_i (m) is the spacing (not necessarily uniform) between river nodes (n nodes in total). Combining Eq. (III.4.1) and (III.4.2) allows deriving the steepness index k_s from:

$$H = \sum_{i=1}^{n} S_i \, d_i = \sum_{i=1}^{n} k_s \, A_i^{-\theta} \, d_i \quad \longrightarrow \quad k_s = \frac{H}{\sum_{i=1}^{n} A_i^{-\theta} \, d_i} \tag{III.4.3}$$

A topographic "steady-state" profile is then iteratively calculated for fixed outlet and source elevations by integrating each river node elevation (z_i) from the outlet ($z_{outlet} = z_1$) to the source [*van der Beek and Bourbon*, 2008; *Willett*, 2010a], as presented below:

$$z_i = z_{i-1} + S_i \, d_i \quad \longrightarrow \quad z_i = z_{i-1} + \frac{H}{\sum_{j=1}^{n} A_j^{-\theta} \, d_j} A_i^{-\theta} \, d_i \tag{III.4.4}$$

Following Eq. (III.4.4), the concavity index θ can be constrained by an iterative fitting procedure calculating the root-mean-square (RMS) deviation between reconstructed (z_{pred}) and observed (z_{obs}) river profiles:

$$RMS = \sqrt{\frac{\sum_{i=1}^{n} \left(z_{obs}^{i} - z_{pred}^{i} \right)^2}{n}} \tag{III.4.5}$$

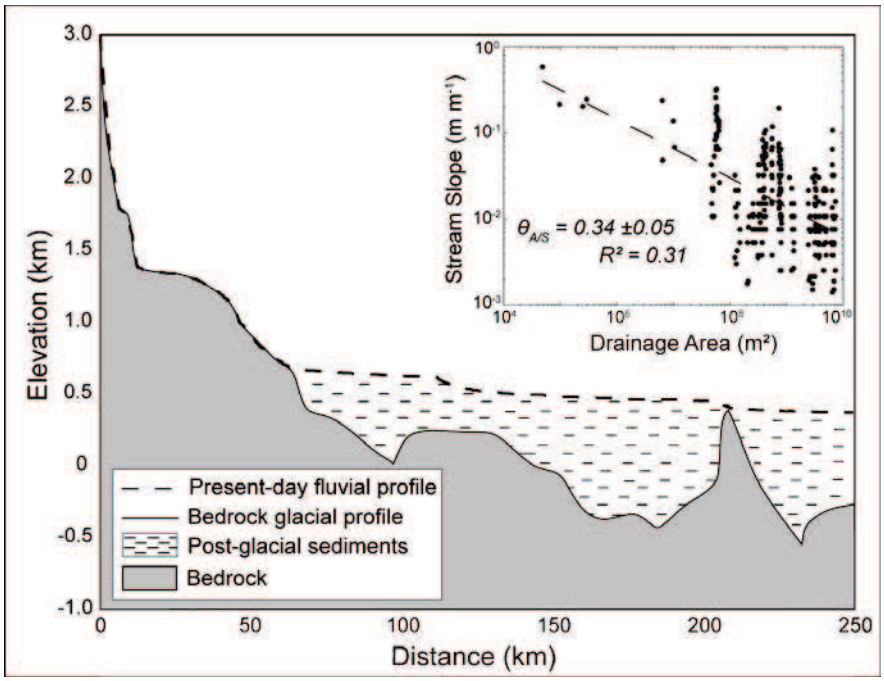

Figure III.4.5. *Longitudinal present-day profile (dashed line) of the Rhône valley derived from SRTM 90-m resolution. Bedrock glacial profile (black line) has been reconstructed using seismic and gravity data [Finkh and Frey, 1991; Rosselli and Olivier, 2003], post-glacial sediment filling of the Rhône valley is also shown [Hinderer, 2001]. Inset shows Slope/Area plot (concavity index* $\theta_{A/S} \approx 0.34 \pm 0.05$; $R^2 = 0.31$*).*

"Steady-state" fits to the Rhône present-day (θ_f) and bedrock glacial (θ_g) profiles are shown in Figure III.4.6. Best-fitting θ_f and θ_g values are derived by minimizing the *RMS* deviation (Eq. (III.4.5)), and associated 1σ uncertainties are arbitrarily chosen for *RMS* values twice higher than the minimum *RMS* deviation (see insets in Figures III.4.6A and B). Note that we also reconstruct the present-day Rhône profile based on the concavity index $\theta_{A/S}$ deduced from the Slope/Area relationship (Figures III.4.5 and III.4.6A), providing relative high *RMS* deviation compared to the observed Rhône profile. The present-day Rhône concavity estimate (θ_f = 0.57±0.08, Figure III.4.2) clearly differs from the concavity value provided by the direct Slope/Area relationship ($\theta_{A/S} \approx 0.34 \pm 0.05$, Figure III.4.5). Figure III.4.5 shows that the downstream part of the Rhône profile is highly perturbed by local steps [*Norton et al.*, 2010a] which potentially add some noise to the Slope/Area plot, explaining the underestimate of the true profile concavity. Finally, we evaluate mean steepness indexes k_s (Eq. (III.4.3)) for the Rhône present-day ($k_s \sim 800$) and bedrock glacial ($k_s \sim 250$) profiles. These indexes are two orders of magnitude higher than the k_s value obtained for the pre-glacial Rhône reconstruction ($k_s \sim 2$, see Figure III.4.2 in main text).

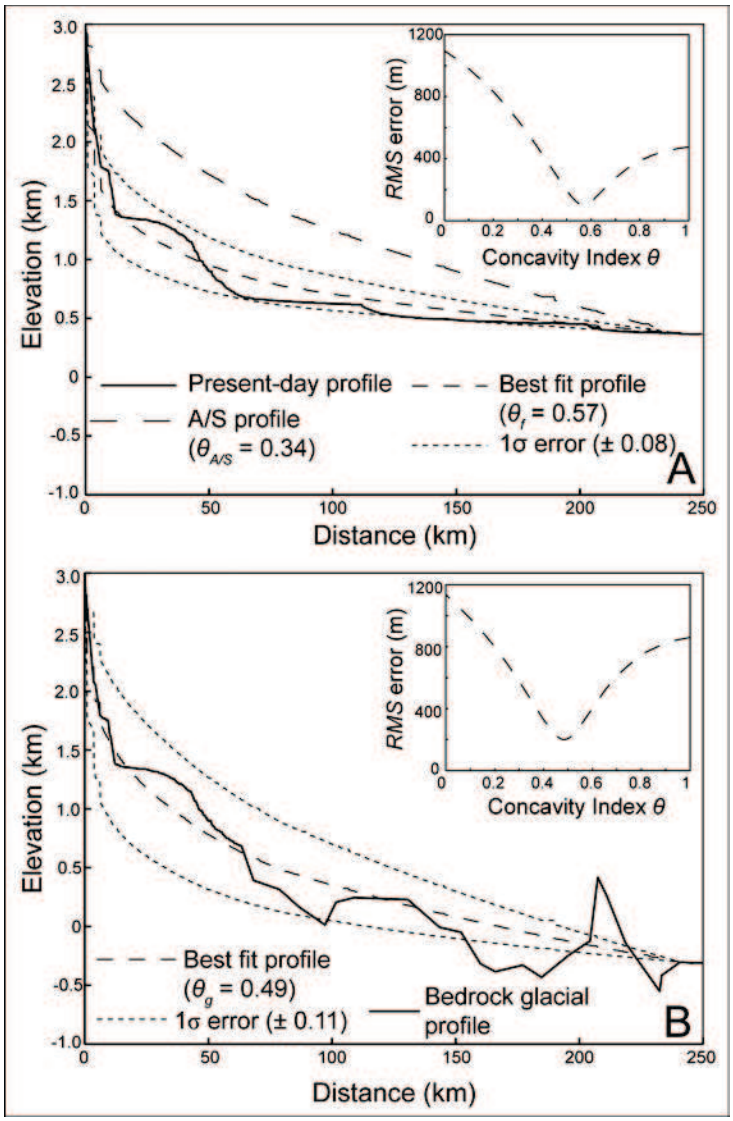

Figure III.4.6. *Rhône present-day (A) and bedrock glacial (B) observed profiles and "steady-state" reconstructions. Continuous lines show observed present-day and bedrock glacial profiles; dashed lines correspond to best-fits and associated 1σ uncertainties (concavity index θ_f = 0.57 ±0.08 for present-day and θ_g = 0.49 ±0.11 for bedrock glacial profiles, see insets for illustration of the sensitivity analysis). Also shown in (A) is the profile reconstruction (dotted-dashed line) when using the concavity value deduced from the Slope/Area relationship (Fig. III.4.5, $\theta_{A/S}$ = 0.34).*

We then compare our results with "steady-state" profile reconstructions for several glacially-influenced and typical fluvial rivers within the Western Alps (see Figure III.4.1 in main text for locations). River profiles and drainage areas have been extracted from the 90-m resolution SRTM digital elevation model (same GIS procedure as for the Rhône basin). Results show that glacially-influenced rivers (Isère, Romanche, Drac and Arc, respectively Figures III.4.7A, B, C and D) have relatively high concavity indexes θ ranging from 0.46 to 0.79, while typical fluvial valleys (Drôme and Büech, respectively Figures III.4.7E and F) present statistically

significantly lower θ values (between 0.28 and 0.33). Calculation of k_s indexes also provides high steepness values for glacially-influenced rivers (k_s ranging from ~200 up to 10^5 for the Isère stream) compared to fluvial profiles (k_s ~2-5).

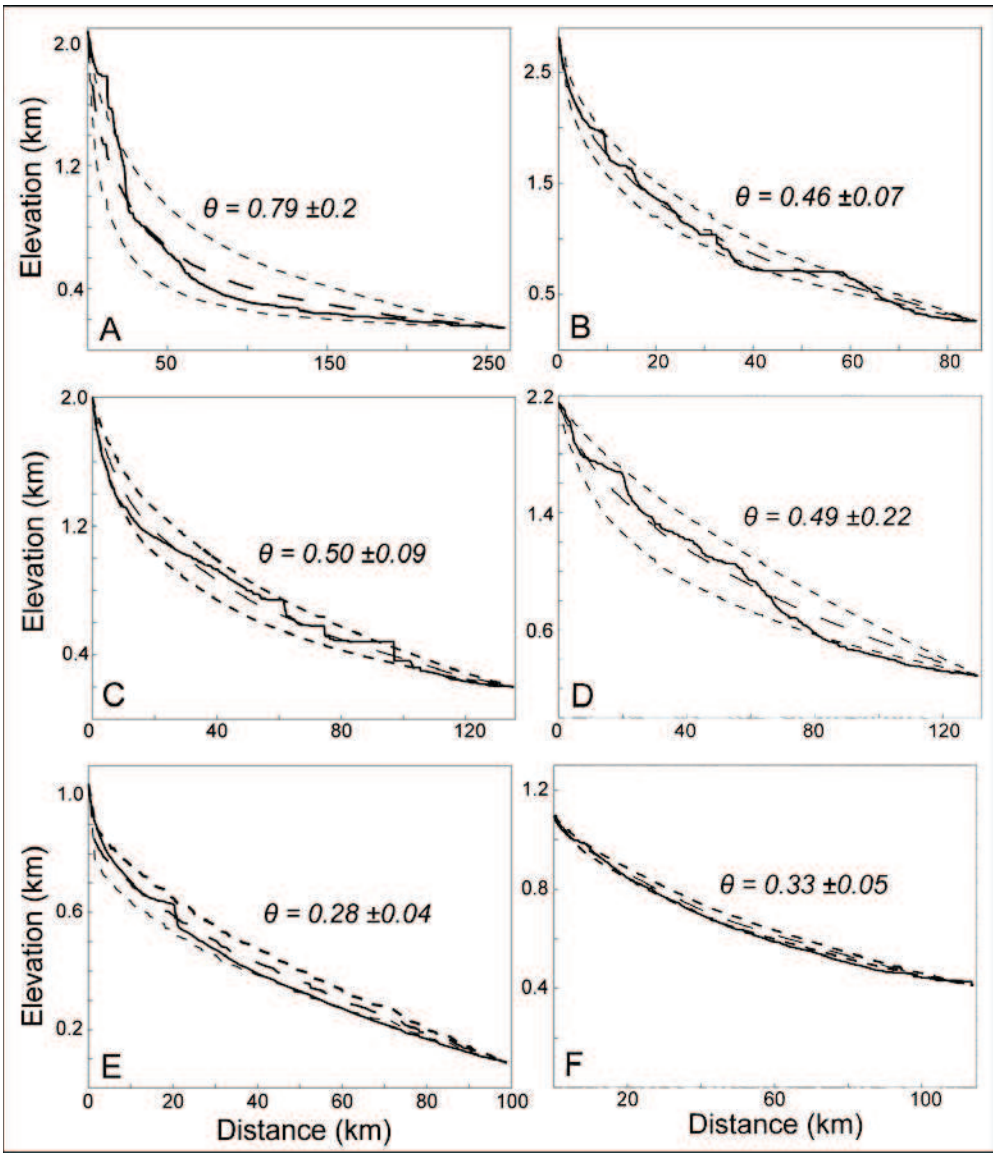

Figure III.4.7. *Longitudinal profile reconstructions for major Western Alps rivers. Dashed lines show best-fit profile "steady-state" reconstructions (associated 1σ uncertainties are represented by dotted lines) and solid lines are present-day river profiles for glacially-influenced streams (A: Isere, B: Romanche, C: Drac, D: Arc, Montjuvent, 1974; 1978) and typical fluvial streams (E: Drôme, F: Buëch, Brocard and van der Beek, 2006).*

III.4.6.2 - "Steady-state" basin topography reconstruction, and topographic metrics

We first reconstruct the pre-glacial profile of the Rhône valley using thermochronology constraints at 2 different sites (SIO and VIS, see main text and Figures III.4.1 and III.4.2 for details). We assume no major elevation change of the Rhône channel heads (*i.e.*, preservation by cold-based ice and/or minor periglacial erosion during Quaternary times) and use both site constraints on the Rhône paleo-valley floor (respectively ~1.2 ±0.2 km and 1.4 ±0.1 km above the present-day valley floor for SIO and VIS profiles; *Valla et al.*, submitted, a, b) to reconstruct the pre-glacial Rhône profile (Figure III.4.2) and derive the pre-glacial concavity index (θ_p = 0.27 ±0.09).

As the Rhône river is the trunk valley of the basin, it fully integrates the hypsometry of the watershed and contains all primary confluences with the main tributaries. We thus determine main tributaries and smaller streams within the Rhône basin using GIS applications and restrict our analysis to drainage areas higher than ~10 km², without considering final channel heads (*i.e.*, colluvial channels with drainage areas <2 km², *Lague and Davy*, 2003; *Willett*, 2010a). We extract ~180 tributary streams within the Rhône basin (Figure III.4.8) that we classify according to stream order (*i.e.*, ranging from main tributaries connecting to the Rhône river to smaller streams within tributary sub-catchments).

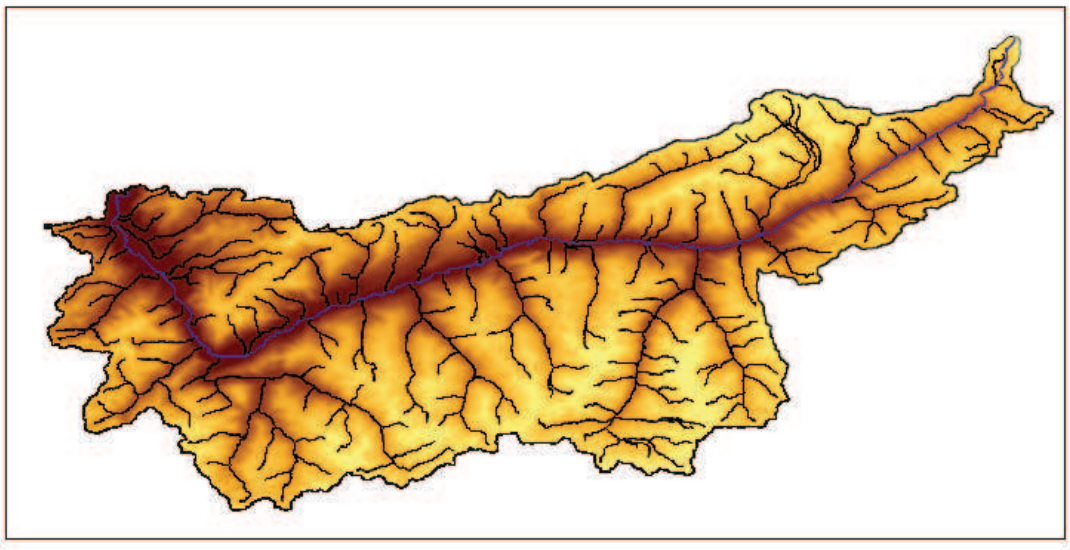

Figure III.4.8. *Rhône watershed and drainage network (black lines ~180 streams) used for tributaries profile reconstruction. Blue line represents the Rhône stream.*

We reconstruct each tributary profile based on Eq. (III.4.2) to (III.4.4), starting from streams connecting to the Rhône valley and progressively integrating the pre-glacial reconstruction within all tributary watersheds. For each tributary stream, the pre-glacial concavity index θ is allowed to vary between 0.27 ±0.18 (*i.e.*, the Rhône pre-glacial concavity index with 2σ uncertainties, as tributary morphology may differ from the trunk stream). We allow tributaries to be either more or less concave than the Rhône pre-glacial stream but we assume that all streams (except for channel heads) must have experienced incision during the Quaternary (*i.e.*, each node of the pre-glacial reconstruction must be at higher or at least the same elevation than the observed present-day profile). All profile reconstructions start with θ equals 0.45 (*i.e.*, maximum value of the allowed range), and the concavity index θ is progressively lowered during iterative calculations until either all nodes of the pre-glacial profile are at higher elevation than the present-day one, or until we reach the minimum θ value of 0.09 (if few nodes of the pre-glacial profile are still below the present-day observed elevation, we arbitrary impose the node present-day elevation for the pre-glacial reconstruction).

Hillslope topography has been reconstructed assuming a spatially uniform slope gradient. Pixels next to fluvial streams have been first modified and the reconstruction is iteratively propagated through the entire basin. Present-day mean basin slope is ~25.8 ±11.7° (ArcGis calculation, in agreement with *Kühni and Pfiffner*, 2001b) and we arbitrary choose to impose a similar slope gradient for the pre-glacial hillslope topography (~25.7 ±8.5°, Table III.4.1). The net impact of fluvial to glacial landscape transition on hillslope topography is poorly known, some studies arguing that valley-side slopes have been significantly steepened by glacial erosion [*e.g.*, *Montgomery*, 2002; *Amerson et al.*, 2008] while others have shown that cirques erosion has led to a net reduction in local slope gradients [*e.g.*, *Brozovic et al.*, 1997; *Naylor and Gabet*, 2007]. At the basin scale, no clear evidence of hillslope gradient change following the onset of glaciations has been demonstrated and conceptual models suggest that mean basin hillslope gradients may not significantly differ between fluvial and glacial landscapes [*Burbank*, 2002]. To justify this assumption, we analyze hillslope gradients in the purely fluvial Drôme basin (see Figure III.4.1 for location; *Brocard and van der Beek*, 2006) which is mainly composed of Mesozoic marly and limestones formations, and reveals a mean basin slope of ~19.5 ±9.5° (ArcGis calculation). Similar lithologies within the strongly glacially-influenced Ecrins-Pelvoux massif (south-east of Grenoble, see Figure III.4.1 for location) display mean slope gradients of ~21-24 ±15° [*van der Beek and Bourbon*, 2008] that are not statistically different from the Drôme basin. Following these results, we choose to

keep the present-day mean basin slope gradient for reconstructing the pre-glacial hillslope topography of the Rhône basin.

	Present-day topography	*Pre-glacial topography*
Mean Basin Slope (°)	25.9 ±11.7	25.7 ± 8.5
Basin Elevation (m)		
Mean ±1σ	2080 ±810	2710 ± 290
Min./Max.	340/4500	1310/4910
Mean Incision (Max.) (m)	/	665 ± 420 (2100)
Mean Basin relief (Max.) (m)		
1-km radius	680 ±270 (2070)	660 ±200 (1720)
2.5-km radius	1270 ±440 (3050)	1200 ±365 (2390)
5-km radius	1760 ±600 (3450)	1560 ±450 (2500)

Table III.4.1. *Relief statistics between present-day and pre-glacial Rhône topographies.*

Topographic metrics have been extracted for both present-day and pre-glacial Rhône basin topographies using GIS techniques [*Brocklehurst and Whipple*, 2002]. The mean basin relief has been calculated at different scales using the average estimate within a sliding window (radius between 1-km and 5-km, Table III.4.1 and Figure III.4.9).

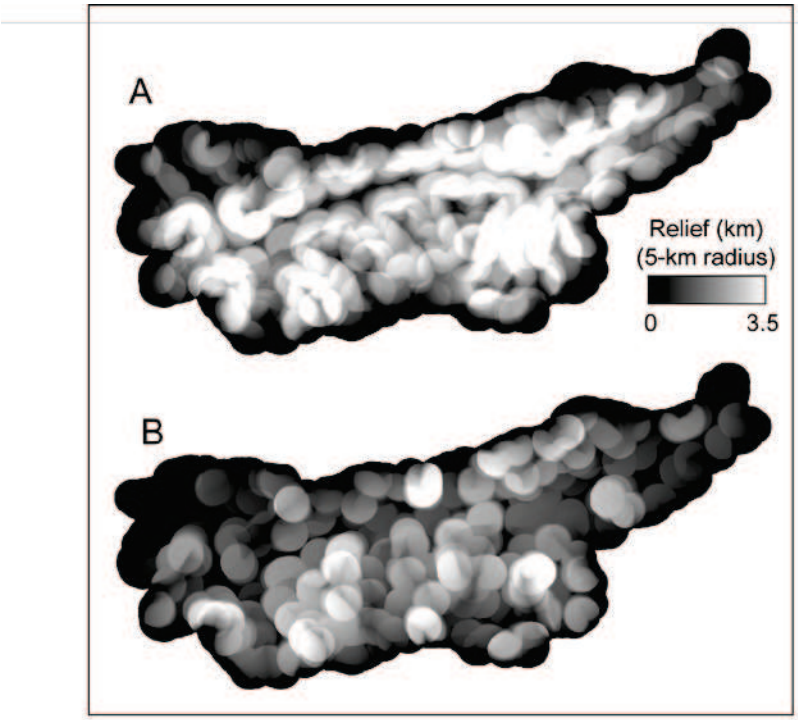

Figure III.4.9. *Rhône basin relief (ridge line to valley bottom relief) calculated using a 5-km radius for both present-day (A, R_{max} = 3.5 km and R_{mean} = ~1.8 ±0.6 km) and pre-glacial (B, R_{max} = 2.5 km and R_{mean} = ~1.6 ±0.5 km) topographies.*

III.4.6.3 - Flexural isostatic rebound model and geodetic rock-uplift data

We evaluate the flexural isostatic rebound triggered by Quaternary erosional unloading within the Rhône basin using a 2D numerical model based on the flexure equation [*Watts*, 2001]:

$$D \nabla^4 w_{(x,y)} = I_{(x,y)} \rho_c - \rho_m g w_{(x,y)} \quad \text{(III.4.6)}$$

where D is the flexural rigidity, w is the flexural deflection of the topography (in the x and y coordinates), I is the amount of eroded material at each pixel of the Rhône basin (see Figure III.4.3C in main text), ρ_c (2800 kg m^{-3}) and ρ_m (3300 kg m^{-3}) are crustal and mantle densities respectively, and g (9.8 m s^{-2}) is the acceleration of gravity. The 2D flexure of an elastic plate can be solved in the frequency domain [*Nunn and Aires*, 1988; *Watts*, 2001; *van der Beek and Bourbon*, 2008] after Fourier transformation of the spatial unloading (I) and inverse Fourier transformation of the flexural deflection (w):

$$w_{(k)} = \frac{\rho_c I_{(k)}}{\rho_m g (1 + C)} \quad \text{(III.4.7)}$$

where k is the wave number (2D frequency domain of x and y coordinates), and $C = Dk^4/\rho_m$. The main unknown in this calculation is the flexural rigidity of the crustal block:

$$D = \frac{Y T_e^3}{12 (1 - \nu^2)} \quad \text{(III.4.8)}$$

where Y is the Young's modulus (10^{11} N m^{-2}), T_e is the equivalent elastic thickness of the lithosphere (km), and ν is the Poisson's ratio (0.25). Estimating the equivalent elastic thickness is problematic as literature estimates are highly variable for the European Alps (~10-30 km; *e.g.*, *Stewart and Watts*, 1997; *Pfiffner et al.*, 2002). Following recent studies within the western Alps, we use an equivalent elastic thickness T_e of 10 km [*Champagnac et al.*, 2007; *van der Beek and Bourbon*, 2008].

Assuming linear Quaternary incision over the last ~1 Myr and an immediate isostatic response to erosional unloading, both Quaternary incision rates along the Rhône valley and basin-scale 2D flexural isostatic rebound have been compared to modern geodetic rock-uplift rates. Modern uplift rates have been interpolated from relative vertical movements with respect to Aarburg (provided by *Swisstopo*; *Schlatter et al.*, 2005) with the natural neighbor method (using ArcGis software), and exported to a 90-m resolution grid (Figure III.4.4 in main text).

Chapter IV :

Alpine landscape response to glacial and interglacial climatic conditions: insights from surface process numerical modelling

IV.1 - Chapter IV overview (Présentation du Chapitre IV)

IV.1.1 - Introduction

Dans les chapitres précédents (chapitres II et III), j'ai apporté des contraintes quantitatives via la thermochronologie basse-température sur l'évolution du relief Alpin et son lien avec les glaciations Pléistocènes. Dans ce chapitre, je propose une étude focalisée sur la dynamique de l'érosion fluviale et glaciaire, afin d'appréhender en termes de processus la problématique liée à l'évolution de la topographie dans les chaînes de montagne.

Dans une première partie, je présente les résultats préliminaires de mon travail portant sur la compréhension de l'impact des glaciations Pléistocènes sur le relief Alpin via la modélisation numérique de la dynamique glaciaire [*e.g.*, *Tomkin and Braun*, 2002; *Herman and Braun*, 2008; *Egholm et al.*, 2009]. Dans cette partie, j'utilise le modèle numérique 2D SPMIce [*Egholm et al.*, 2009; *Egholm and Nielsen*, 2010] afin d'une part, de simuler la dynamique glaciaire et l'extension passée des glaciers dans les Alpes occidentales, et d'autre part de mieux appréhender la distribution spatiale et temporelle de l'érosion glaciaire durant les multiples oscillations entre périodes glaciaires et interglaciaires au cours du Pléistocène.

Dans un premier temps, j'ai travaillé sur l'optimisation de la modélisation du bilan de masse glaciaire en surface dans le modèle SPMIce, afin de pouvoir prédire de façon réaliste l'extension glaciaire actuelle dans le massif du Mont-Blanc à partir des données climatiques issues de la littérature. Nos résultats montrent la nécessité de modéliser le bilan de masse en surface directement à partir de l'estimation de la ligne d'équilibre glaciaire (Equilibrium Line Altitude en anglais, *ELA*; *e.g.*, *Porter*, 2000), et de calibrer le bilan de masse glaciaire dans les zones d'accumulation et d'ablation. Plusieurs simulations tests ont par la suite été réalisées dans le massif du Mont-Blanc pour lequel les données climatiques actuelles [*e.g.*, *Glacioclim*, 2009], ainsi que les reconstructions paléo-géographiques d'extensions glaciaires [*e.g.*, *Coutterand and Nicoud*, 2005; *Coutterand*, 2010] existent dans la littérature. Les simulations d'extension glaciaire depuis le Dernier Maximum Glaciaire (~20-21 ka, *e.g.*, *Ivy-Ochs et al.*, 2006) sont en accord avec les reconstructions paléo-géographiques, même si dans le détail les prédictions numériques peuvent quelque peu différer des observations géomorphologiques et des estimations de paléo-*ELA*s associées. Cet exercice préliminaire m'a par conséquent permis d'évaluer les variations de la *ELA* depuis le Dernier Maximum Glaciaire et de

confirmer les reconstructions paléo-géographiques à partir d'un modèle numérique 2D (SPMIce). Par ailleurs, les simulations réalisées dans le massif du Mont-Blanc ont mis en évidence les limites actuelles de cette version du modèle SPMIce, notamment dans la gestion des processus d'avalanches neigeuses et par conséquent de la redistribution de neige dans les zones d'accumulation (pas de nunataks prédits par les simulations numériques), la gestion de gradients spatiaux de températures et/ou de précipitations (effets orographiques et climatiques locaux…), ou encore la gestion des conditions limites dans la prédiction des vitesses d'écoulement des glaciers. Ces problèmes potentiels, inhérents à l'approche numérique et à la détermination de la complexité adéquate des algorithmes de calcul du bilan de masse glaciaire et de la dynamique d'écoulement du glacier, sont en cours de développement et devraient aboutir à une nouvelle version du modèle SPMIce (collaboration avec D. Egholm, Aarhus University). Enfin, nos simulations numériques mettent en avant la question de l'utilisation des méthodes traditionnelles dans la détermination de paléo-*ELA*s à partir des extensions glaciaires passées [*e.g.*, *Porter*, 2000]; ces méthodes étant calibrées sur des glaciers actuellement en retrait et en situation de fort déséquilibre vis-à-vis des conditions climatiques actuelles.

J'ai également abordé, à partir de quelques simulations numériques et d'une réflexion plus conceptuelle, la question de l'impact des glaciations Pléistocènes sur le relief Alpin et notamment du changement climatique Mi-Pléistocène sur la dynamique glaciaire et le développement de la topographie [*Valla et al.*, submitted, a]. Les simulations numériques mettent en évidence une distribution spatiale complexe des vitesses d'écoulement glaciaire (et par conséquent de l'érosion) au cours des différentes étapes d'un cycle glaciaire/interglaciaire, suggérant une part importante des phases d'englacement et de retrait glaciaire dans le bilan final d'érosion, ainsi que l'existence de fortes disparités spatiales en terme de vitesses d'écoulement des glaciers (et donc des taux d'érosion) observées dans la zone étudiée (région du Valais, Alpes suisses).

Cependant, les simulations réalisées comportent des simplifications importantes, comme l'utilisation d'une topographie initiale basée sur le relief actuel (tandis que les données obtenues dans le chapitre III démontrent clairement une évolution majeure de la topographie au cours du Pléistocène), l'hypothèse d'une lithologie (et donc une érodabilité des roches) uniforme, ou encore la modélisation d'un soulèvement isostatique uniquement relié à la

décharge érosive ou à la dynamique glaciaire (sans prendre en compte un éventuel soulèvement tectonique local ou plus régional).

Enfin, l'analyse des cycles glaciaires/interglaciaires de 40 ka et 100 ka [*Lisiecki and Raymo*, 2005] révèle des différences marquées non seulement dans la durée et la symétrie/asymétrie des cycles, mais également dans l'amplitude climatique propre à chaque oscillation. Ainsi, il semblerait que les cycles symétriques de 40 ka soient non seulement plus courts concernant la durée de la période glaciaire, mais également moins importants en termes de dépression de la *ELA*, et par conséquent de l'extension glaciaire associée, que les cycles de 100 ka. Ainsi, le développement du relief observé dans la vallée du Rhône [*Valla et al.*, submitted, a], associé à la mise en place de glaciations majeures dans les Alpes [*Muttoni et al.*, 2003], serait potentiellement expliqué par le changement climatique Mi-Pléistocène et la transition depuis des cycles de 40 ka vers des cycles de 100 ka.

Dans une deuxième partie, je présente les résultats d'un travail portant sur l'évolution post-glaciaire du massif des Ecrins-Pelvoux (Alpes françaises). Cette étude, débutée au cours de mon Master 2ème année et poursuivie au cours de ma 1ère année de Thèse, se focalise sur l'évolution des gorges de raccordement, objets géomorphologiques abondants dans le massif des Ecrins-Pelvoux et illustrant la réponse post-glaciaire d'un relief préalablement englacé et fortement modelé par les processus d'érosion glaciaire/périglaciaire. Ces résultats on fait l'objet de deux publications, respectivement dans les revues *Journal of Geophysical Research-Earth Surface* [*Valla et al.*, 2010c] et *Terra Nova* [*Valla et al.*, 2010a].

Dans un premier temps, je rapporte les résultats d'une étude portant sur ~30 gorges de raccordement au sein du bassin versant de la Romanche [*Valla et al.*, 2010c]. Les gorges de raccordement sont des marqueurs de l'incision fluviale et se trouvent principalement au niveau de gradins de confluence entre la vallée principale et ses tributaires; elles sont caractérisées par un profil en long convexe ainsi que par la présence de ruptures de pente majeures (appelées "knickpoints" par la suite) dans la limite supérieure de la gorge.

Afin de quantifier l'incision fluviale à l'origine de ces gorges, nous avons tout d'abord essayé de contraindre l'origine des gradins de confluence. L'analyse morphométrique démontre une corrélation positive entre la hauteur du gradin de confluence et le ratio entre les aires drainées de la vallée suspendue et de la vallée principale, en accord avec une origine glaciaire

(différence d'érosion des flux de glace provenant de la vallée principale et du bassin tributaire; *MacGregor et al.*, 2000; *Anderson et al.*, 2006) dans la formation des vallées suspendues. Pour chaque gorge de raccordement, nous avons reconstruit un profil initial glaciaire à partir de morphologies glaciaires avoisinantes.

L'analyse morphométrique des profils actuels révèle une forte corrélation négative entre la pente moyenne de la gorge et l'aire drainée du bassin versant amont, cette relation étant modulée par la lithologie. De plus, une analyse plus détaillée le long de trois rivières (Diable, Gâ et Etages) montre une corrélation inverse entre la pente locale et la largeur de la gorge (également dépendante de l'aire drainée totale du bassin versant), illustrant une adaptation de la géométrie hydraulique du chenal au cours de l'évolution de la gorge. La comparaison des profils en long initiaux et actuels a mis en évidence une forte dépendance du retrait des knickpoints vis-à-vis de l'aire drainée du bassin versant amont, cette corrélation étant également modulée par la lithologie. De plus, nos résultats, en faisant l'hypothèse d'une évolution synchrone et post-glaciaire de l'ensemble des gorges, rapportent des vitesses d'incision fluviale (0.5 à 16 mm an^{-1}) et de retrait des knickpoints (1 à 200 mm an^{-1}) élevées mais cohérentes avec des études similaires [*Whipple et al.*, 2000b; *Bishop et al.*, 2005; *Lamb et al.*, 2007].

Afin de mieux appréhender les mécanismes opérant dans l'évolution de ces gorges, nous avons utilisé différents modèles numériques 1D permettant de simuler l'incision fluviale des gorges du Diable, du Gâ et des Etages. Nos résultats montrent que les modèles où l'incision est limitée par le détachement (detachment-limited models; *Whipple and Tucker*, 2002) ne permettent pas de reproduire convenablement l'évolution post-glaciaire des gorges étudiées; tandis que les modèles pour lesquels l'incision est limitée par le transport de sédiments (transport-limited models; *Whipple and Tucker*, 2002) prédisent une évolution en accord avec les profils observés. Cette première conclusion peut paraître quelque peu paradoxale aux vues des observations réalisées au sein des gorges : morphologies fluviales typiques de processus d'incision limitée par le détachement [*Whipple et al.*, 2000a], et faible abondance de dépôts sédimentaires le long de la gorge. Par la suite, nous avons utilisé un modèle d'incision fluviale plus élaboré [*Lague*, 2010] prenant en considération à la fois l'ajustement dynamique de la largeur du chenal, un seuil critique dans l'incision fluviale, une répartition stochastique des débits, mais également la dépendance des taux d'incision vis-à-vis du transport sédimentaire (effet de couverture statique et dynamique). Cette approche permet de simuler d'une part,

l'évolution 1D du profil en long, mais également l'évolution temporelle de la largeur du chenal tout au long du profil. Ce modèle de couverture sédimentaire prédit une évolution des gorges de raccordement similaire à celle obtenue via le modèle où l'incision est limitée par le transport sédimentaire (transport-limited model).

Nos résultats illustrent également un comportement hybride des gorges de raccordement, leur évolution récente suggérant une prédominance des processus d'incision limitée par le détachement, tandis que leur évolution long-terme est illustrée par une incision limitée par la nécessité de transporter les sédiments érodés. De plus, la dynamique des gorges de raccordement semble caractérisée par un fort couplage entre l'incision de la gorge et les processus d'éboulement rocheux associés, ces derniers produisant un fort apport de sédiments et par conséquent une inhibition transitoire de l'incision du socle rocheux.

Dans un second temps, nous nous sommes focalisés sur la Gorge du Diable [*Valla et al.*, 2010a] afin d'essayer de dater l'initiation de l'incision fluviale, et d'en quantifier les vitesses Holocènes et actuelles. Nous avons échantillonné deux profils verticaux le long de la gorge, ainsi que plusieurs sites dans le lit actif de la rivière, afin de mesurer la concentration en nucléides cosmogéniques produits *in-situ* (^{10}Be) et d'en dériver à la fois des âges d'exposition (le long des parois de la gorge) et des vitesses d'incision actuelles (dans le lit actif de la gorge).

Les âges d'exposition obtenus au sommet des profils révèlent un âge tardi-Holocène (~5 ka) d'initiation de l'incision, postérieure aux données régionales datant le retrait glaciaire aux alentours de 11-13 ka [*Delunel*, 2010]. Cette différence suggère un délai temporel entre le retrait glaciaire et l'incision de la gorge, une explication alternative impliquant un enfouissement de la gorge durant l'Holocène.

La distribution des âges d'exposition le long des profils permet de calculer des vitesses d'incision allant de 6.5 à 13 mm an^{-1} au cours de l'Holocène, tandis que les échantillons prélevés dans le lit actif de la gorge prédisent des vitesses d'incision actuelles de l'ordre de 0.5 à 3 mm an^{-1}. Nos résultats démontrent, en accord avec l'étude précédente [*Valla et al.*, 2010c], que des vitesses d'incision de l'ordre du cm an^{-1} peuvent être rencontrées localement en réponse aux transitions climatiques glaciaires/interglaciaires.

IV.1.2 - Presentations at international meetings

- **April, 2008**, European Geosciences Union, General assembly, Vienna (Austria):
  Valla, P.G., van der Beek, P.A., Lague, D. Bedrock gorges incising glacial hanging valleys: insights from morphometric analysis and numerical modelling. *Geophysical Research Abstracts*, Vol. 10, EGU2008-A-03381.

- **April, 2009**, European Geosciences Union, General assembly, Vienna (Austria):
  Valla, P.G., Herman, F., Champagnac, J.-D., van der Beek, P.A. Lithological and structural controls for glacial valley development in the Valais, Swiss Alps. *Geophysical Research Abstracts*, Vol. 11, EGU2009-3404-1.

- **May, 2010**, European Geosciences Union, General assembly, Vienna (Austria):
  Valla, P.G., van der Beek, P.A., Lague, D., Carcaillet, J. Bedrock gorges incising glacial hanging valleys (Western Alps, France): results from morphometric analysis, numerical modeling and ^{10}Be cosmogenic dating. *Geophysical Research Abstracts*, Vol. 12, EGU2010-5947.

IV.1.3 - Publications and contributors to Chapter IV

This chapter first comprises preliminary results on glacial numerical modelling. The second part of the chapter presents two papers published respectively in *Journal of Geophysical Research-Earth Surface* (2010, Vol. 115, F02010, doi:10.1029/2008JF001079; submitted May 21st 2008, accepted November 23rd 2009) and *Terra Nova* (2010, Vol. 22, 18-25; submitted March 18th 2009, accepted September 8th 2009).

The first part of this chapter is based on a 2D glacial numerical code developed by D. Egholm [*Egholm et al.*, 2009]. I personally performed all the numerical simulations presented here (collaboration D. Egholm and F. Herman). For the 1st paper [*Valla et al.*, 2010c], I personally realised the morphometric analysis mainly during my Master thesis under the supervision of P. van der Beek (January-June 2007), and I performed fluvial incision numerical modelling based on codes originally developed by P. van der Beek [*van der Beek and Bishop*, 2003] and D. Lague [*Lague*, 2010]. The 2nd paper [*Valla et al.*, 2010a] reports *in-situ* cosmogenic ^{10}Be data that I personally produced (collaboration R. Delunel and X. Robert for sampling, R. Braucher and J. Carcaillet for chemical preparation and sample measurements).

IV.2 - Modeling ice dynamics and the impact of glaciations on topographic evolution

In this section, I present some preliminary results on modeling ice dynamics in order to discuss the impact of Pleistocene glaciations on Alpine topographic evolution and potential ways to quantitatively assess this impact using numerical modeling. This work arises from the thermochronological constraints obtained in chapter III and pointing toward a temporal agreement between the development of topographic relief within the Swiss Alps and Mid-Pleistocene glaciations [*Valla et al.*, submitted, a, b]. Moreover, this section introduces the next part of the manuscript which will report quantification of the postglacial landscape response during the Late-Glacial and Holocene (section IV.3).

In the following, I will briefly discuss the ice model (SPMIce, see section I.2.3.2 for details) and expose how the code was parameterized for studying ice dynamics within the western and central Alps. I will then present two case studies (Figure IV.2.1) of modeling experiments to: (1) simulate Late-Glacial to present-day ice extent within the Mont-Blanc massif; and (2) explore potential ways to assess the impact of Pleistocene glaciations on relief evolution in the Valais area (Swiss Alps), and discuss the influence of Mid-Pleistocene climate change on glacial erosion and landscape development.

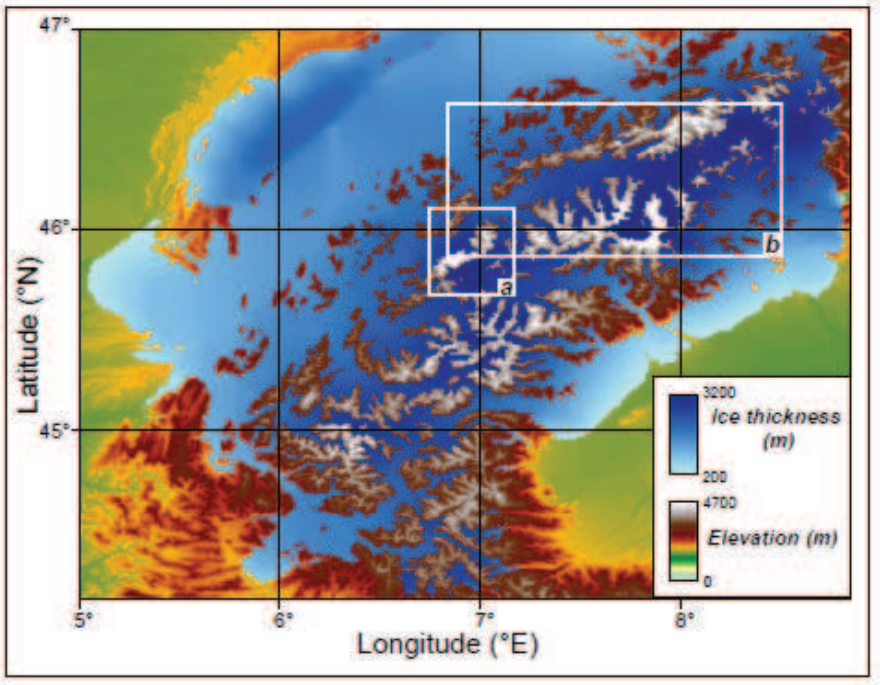

Figure IV.2.1. *Topography and ice extent during the Last Glacial Maximum (~21 ka) of the western and central Alps [Ehlers and Gibbard, 2004]. Locations (open white boxes) of the Mont-Blanc massif (a) and the Valais area (b) are also shown.*

IV.2.1 - Ice model description and parameterization

All ice dynamics simulations described in this chapter have been performed using the 2D ice model SPMIce, originally developed by *Egholm et al.* [2009], which solves the second order shallow ice approximation (SOSIA) on an irregular grid [*Egholm and Nielsen*, 2010]. All algorithm developments and specificities of the SOSIA approach (section I.2.2.3) have been developed in detail by *Egholm et al.* [2009] and *Egholm and Nielsen* [2010]. Here, I will review the main characteristics of the code concerning the physics of ice dynamics, the climatic input parameters and the way glacial erosion is implemented.

The ice dynamics is governed by the temporal and spatial evolution of ice thickness [*Paterson*, 1994], which can be solved using the mass-conservation equation of the ice:

$$\frac{\partial H}{\partial t} = \nabla q + M \quad ; \quad q = Hu \quad \text{and} \quad M = M_s + M_b \tag{IV.2.1}$$

where H is ice thickness (m), q is depth-averaged ice flux ($m^2\ yr^{-1}$), and M is mass balance ($m\ yr^{-1}$). The average ice flux (q) is the product of ice thickness (H) and vertically integrated horizontal ice velocity (u, $m\ yr^{-1}$). The mass balance (M) is the sum of both surface (M_s) and basal (M_b) components.

The horizontal velocity of glaciers is a combination of two terms: the ice-deformation velocity (u_d) calculated following Glen's law [*e.g.*, *Hooke*, 1981], and the ice-sliding velocity (u_s) defined by Weertman's law [*Paterson*, 1994]. The internal deformation velocity (u_d) is calculated by relating components of the strain-rate tensor (ε_{ij}) to the stress tensor (τ_{ij}):

$$\varepsilon_{ij} = A \tau_e^{n-1} \tau_{ij} \tag{IV.2.2}$$

where τ_e is effective stress (Pa, *Baral et al.*, 2001), n is Glen's law exponent (commonly set between 1 and 3, fixed here to 3) and A is ice-flow law parameter ($Pa^{-n}\ yr^{-1}$). The SOSIA computation of vertically integrated deformation velocity is performed following the equation:

$$u_{d\,x,y} = 2A \tau_e^{n-1} \left(-\frac{1}{3} \frac{\partial (H+z)}{\partial x, y} H^2 + \Theta_{x,y} + \Omega_{x,y}\right) - \Lambda_{x,y} \tag{IV.2.3}$$

where H (m) is ice thickness, z (m) is bedrock elevation, and $\Theta_{x,y}$, $\Omega_{x,y}$ and $\Lambda_{x,y}$ are supplementary correction terms [*Egholm et al.*, 2009] to take into account steep ice-surface gradients, longitudinal/transverse stress gradients and vertical movements of the ice [*Egholm and Nielsen*, 2010] for optimal computation of the internal deformation velocity.

The sliding velocity (u_s) is only calculated where the base of the glacier is at the melting point (the computation of the basal temperature is described in detail by *Tomkin and Braun*, 2002 and *Herman and Braun*, 2008) following the equation:

$$u_s = \frac{B_s \tau_b^n}{P_e^r} \tag{IV.2.4}$$

where τ_b (Pa) is basal stress, P_e is effective pressure (Pa) with exponent r (which I choose equal to 1), and B_s is sliding constant (m $Pa^{-(n-r)}$ an^{-1}).

The calibration of A (~5.2 10^{-17} Pa^{-3} yr^{-1}) and B_s (~7.1 10^{-10} m Pa^{-2} yr^{-1}) parameters is based on values reported by *Le Meur and Vincent* [2003] and *Schaefer* [2007]. The computation of ice thickness and velocities assumes open boundary conditions [*Egholm and Nielsen*, 2010], which can pose potential problems for estimating the velocity pattern where the glacier reaches the model margins (see next section for illustration). The erosion-law calculation follows the same approach as *Herman and Braun* [2008] and *Eghom et al.* [2009], where the glacial erosion rate is simply a function of the ice-sliding velocity at the glacier-bedrock interface [*Hallet*, 1979]. Finally, the SPMIce model also computes the flexural response due to both ice loading/unloading and topographic evolution following glacial erosion.

The main contribution of the present work is related to the treatment of the surface mass balance in the SPMIce model. The basal mass balance (M_b, Eq. (IV.2.1)) is calculated following the description of *Egholm et al.* [2009] and is dependent on both basal temperature and ice thickness [*Tomkin and Braun*, 2002; *Herman and Braun*, 2008].

The surface mass balance (M_s, Eq. (IV.2.1)) is often assumed to be directly dependent on surface temperature [*Tomkin and Braun*, 2002; *Herman and Braun*, 2008; *Egholm et al.*, 2009], following the equation:

$$M_s = -\Delta m_s(T_s) \quad ; \quad T_s = T_0 - \alpha(H + z) \tag{IV.2.5}$$

where Δm_s is mass-balance gradient (m yr^{-1} $°C^{-1}$), T_s is surface temperature (°C), α is lapse rate (°C km^{-1}) and T_0 is sea-level temperature (°C). This approach assumes that the Equilibrium Line Altitude (*ELA*, *i.e.*, the elevation at which the annual mass balance is null) is concordant with the 0 °C isotherm. In order to test this assumption, I have compiled annually-averaged temperature measurements (Figure IV.2.2) within the Swiss (data from *the Federal Office of Meteorology and Climatology MeteoSwiss*) and French [*Delunel et al., 2010b*] Alps. Temperature data provide a sea-level temperature of ~12.4 °C and a lapse rate of ~4.5 °C km^{-1} that I will use in following SPMIce simulations to model the spatial variations in temperature. Moreover, using these temperature parameters and Eq. (IV.2.5) allows deriving an apparent present-day *ELA* at around 2750 m for the French and Swiss Alps.

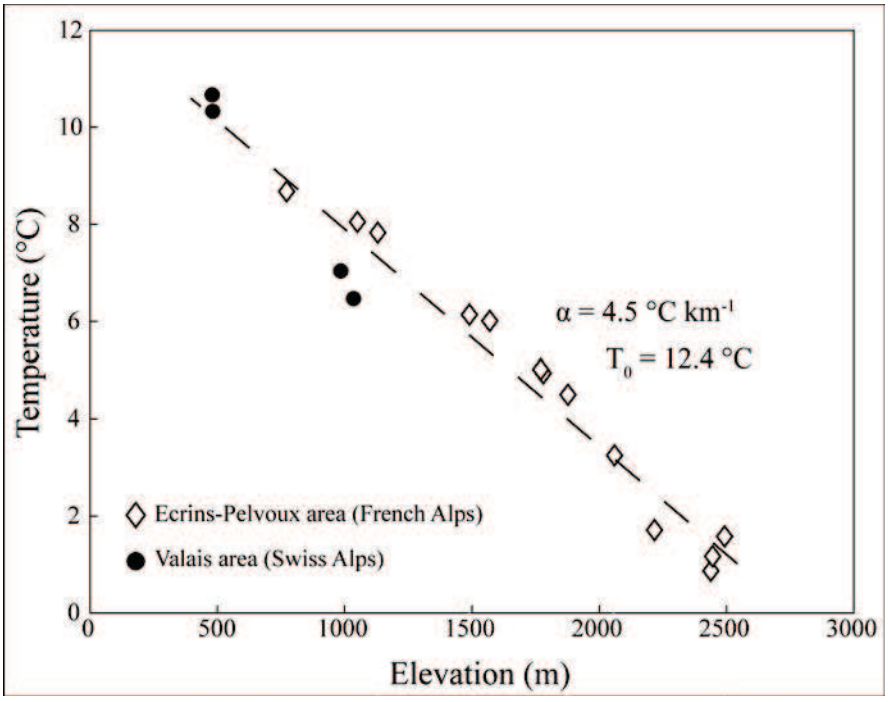

Figure IV.2.2. *Annual temperature measurements in the French and Swiss Alps. Data for the French Alps [Delunel et al., 2010b] are averaged over the last ~30 years (Electricité de France); while Swiss data (Federal Office of Meteorology and Climatology MeteoSwiss) are averaged over the last century.*

Comparing this present-day *ELA* estimate with direct measurements on several glaciers [*WGMS*, 1998; 2005; 2008] within the western and central Alps (Table IV.2.1) shows that *ELA* estimates are significantly higher than the temperature-derived value (Figure IV.2.2); they reveal a mean *ELA* value of 2990 ±160m for the European Alps, with significant disparity between the different glaciers (Table IV.2.1). I thus propose that calibrating the surface mass balance from direct temperature measurements may be problematic, as the *ELA*

position depends not only on air temperature, but also on the exposition of the glacier to solar radiation or the annual distribution of precipitation. Using temperature records at face value as a proxy for estimating the *ELA* position may result in erroneous numerical reconstructions of ice extent.

Glacier Name	Localisation Lat. (°N)/Long. (°E)	Elevation (m) Min/Max/Median	Temporal coverage (years)	ELA (m) (± 1σ)
Switzerland				
Basodino	46.42/8.48	2540/3230/2880	1995-2004	2960 ±150
Gries	46.44/8.34	2410/3370/2920	1995-2004	2780 ±180
Silvretta	46.85/10.08	2470/2780/3160	1995-2004	2830 ±150
Mean value				**2860 ±100**
France				
Argentière	45.95/6.99	1500/3500/2600	2000-2005	2860 ±200
Gebroulaz	45.30/6.83	2600/3400/3000	2000-2005	3100 ±130
Mer de Glace	45.88/6.93	1480/3600/3000	1994-2007	2870 ±70
Saint-Sorlin	45.17/6.15	2850/3150/3000	2000-2004	3110 ±190
Mean value				**2990 ±140**
Austria				
Goldberg	47.03/12.07	2310/3080/2680	2000-2005	2920 ±30
Hintereis	46.80/10.77	2400/3730/3010	1991-2005	3100 ±70
Kesselwand	46.84/10.79	2700/3490/3180	1991-2005	3140 ±50
Kleinfleiss	47.05/12.95	2510/3080/2840	2000-2005	2920 ±130
Ochsentaler	46.85/10.10	2290/3160/2910	1990-1999	2910 ±60
Jamtal	46.87/10.17	2370/3120/2780	1992-2002	2880 ±110
Sonnblick	47.13/12.60	2500/3050/2780	1991-2005	2850 ±100
Vermunt	46.85/10.13	2430/3130/2790	1990-1999	2970 ±90
Vernagt	46.88/10.82	2770/3630/3140	1991-2005	2950 ±60
Wurten	47.03/13.01	2380/3120/2680	1990-2005	3010 ±80
Mean value				**2960 ±90**
Italy				
Calderone	42.47/13.62	2630/2830/2730	2000-2005	2710 ±50
Careser	46.45/10.70	2860/3310/3090	1990-2002	3390 ±180
Ciardoney	45.52/7.39	2850/3170/3000	1991-2002	3070 ±70
Fontana Bianca	46.48/10.77	2880/3360/3120	1991-2001	3360 ±190
Malavalle	46.95/11.20	2520/3470/2950	2001-2005	3050 ±50
Pendente	46.96/11.23	2620/3110/2820	1999-2001	2940 ±110
Sfrozellina	46.33/10.50	2790/3120/2930	1990-2000	3010 ±30
Mean value				**3070 ±240**
Mean ELA				***2990 ±160***

Table IV.2.1. *Equilibrium Line Altitude (ELA) values for different glaciers in the western and central European Alps. Average ELA estimates have been provided by annual measurements on individual glaciers [WGMS, 1998; 2005; 2008].*

An alternative approach [*e.g.*, *Kessler et al.*, 2006] is to directly model the *ELA* position in SPMIce simulations to adequately predict the surface mass balance:

$$M_s = \Delta m_s[(z + H) - ELA] \tag{IV.2.6}$$

This approach ensures appropriate surface mass balance predictions for present-day conditions as we can reasonably estimate the *ELA* position (Table IV.2.1). However, it is

more problematic for past periods [*e.g.*, *Norton and Hampel*, 2010], for which the climatic record is mostly constituted of paleo-temperature and paleo-precipitation estimates [*e.g.*, *Peyron et al.*, 1998; *Fauquette et al.*, 1999]. Investigations on the *ELA* sensitivity to climatic variations show that a temperature change of ±1 °C (or a precipitation change of ±25-30%) would result in an *ELA* variation between ±60-70 m [*Vincent*, 2002] and ±100-140 m [*Maisch*, 2000; *Zemp et al.*, 2007], so translating temperature records into *ELA* variations may prove to be difficult. On the contrary, one may use *ELA* variations reported from ice-extent reconstructions based on moraine and/or trimline mapping [*e.g.*, *Kelly et al.*, 2004; *Ivy-Ochs et al.*, 2006; *van der Beek and Bourbon,* 2008; *Coutterand*, 2010; *Norton and Hampel*, 2010] to avoid the necessity of converting climatic records into paleo-*ELA* values.

One supplementary problem in calibrating the surface mass balance arises from the mass-balance gradient (Δm_s) determination, which defines the spatial distribution of ice ablation/accumulation. Most glacier simulations have used constant values for modeling ice ablation and accumulation [*Tomkin and Braun*, 2002; *Kessler et al.*, 2006; *Herman and Braun*, 2008], although *Egholm et al.* [2009] recently proposed different arbitrary mass-balance gradient values for ice accumulation and ablation.

Here, I attempt to quantify the difference in mass-balance gradients for the accumulation and ablation areas by compiling mass-balance measurements for present-day glaciers within the European Alps (Table IV.2.2). These estimates reveal that the mean accumulation gradient is around 2.5 times lower than the mean ablation gradient (Table IV.2.2). I illustrate these differences in ice-accumulation and ablation dynamics by reporting mass-balance measurements on the Mer de Glace glacier (Mont-Blanc massif, western Alps) between 1994 and 2007 (Figure IV.2.3). Figure IV.2.3 clearly shows that the ablation gradient is much higher (~2-3 times) than the accumulation gradient. Thus numerical simulations considering a similar gradient for accumulation and ablation areas would lead to erroneous predictions of ice extent for an assumed *ELA* value.

Finally, ice-dynamics simulations require defining a maximum ice-accumulation parameter, in order to limit the ice-accumulation rate and prevent incoherent ice thicknesses for high elevations [*e.g.*, *Herman and Braun*, 2008; *Egholm et al.*, 2009]. However, all previously cited studies have considered this parameter to be spatially constant and did not take into account the large disparity in precipitation that is encountered in mountainous environments due to orographic effects [*Roe et al.*, 2002; *Kessler et al.*, 2006].

Glacier Name	Localisation Lat. (°N)/Long. (°E)	Elevation (m) Max./Min/Median	Temporal coverage (years)	Max. accumulation (m yr^{-1})	Max. ablation (m yr^{-1})	Accumulation gradient (±1σ) (m yr^{-1} km^{-1})	Ablation gradient (±1σ) (m yr^{-1} km^{-1})
Switzerland							
Basodino	46.42/8.48	2540/3230/2880	1993-2005	1.54	3.70	3.8 ±1.8	7.3 ±2.2
Gries	46.44/8.34	2410/3370/2920	1962-2005	3.07	5.89	2.5 ±2.1	6.5 ±1.6
Silvretta	46.85/10.08	2470/3160/2780	1960-2005	2.66	5.84	3.1 ±1.8	10.8 ±4.8
Mean value						3.1 ±0.7	8.2 ±2.3
France							
Argentière	45.95/6.99	1500/3500/2600	1976-2007	3.85	9.60	2.7 ±1.4	7.0 ±1.5
Gebroulaz	45.3/6.63	2600/3400/3000	1995-2007	2.57	4.54	3.1 ±1.0	5.3 ±1.9
Mer de Glace	45.88/6.93	1480/3600/3000	1994-2007	3.19	11.92	1.8 ±0.8	7.3 ±1.4
Sarennes	45.14/6.14	2850/3150/3000	1994-2007	0.96	4.32	1.7 ±0.2	6.7 ±6.0
Saint-Sorlin	45.17/6.15	2600/3400/2900	1994-2006	2.40	4.41	2.0 ±1.9	7.3 ±2.0
Mean value						2.3 ±0.6	6.7 ±0.8
Austria							
Hintereis	46.8/10.77	2400/3730/3010	1991-2005	0.87	7.28	1.8 ±0.4	10.1 ±1.1
Jamtal	46.87/10.17	2370/3120/3780	1991-2005	0.53	5.66	1.0 ±0.5	5.8 ±1.2
Kesselwand	46.84/10.79	2700/3490/3180	1991-2005	1.27	6.40	3.1 ±0.8	11.6 ±2.4
Kleinfleiss	47.05/12.95	2510/3080/2840	2001-2005	1.23	3.22	3.5 ±0.7	8.2 ±5.7
Ochsentaler	46.85/10.10	2290/3160/2910	1991-1997	0.79	5.00	2.4 ±0.8	6.8 ±1.0
Vermunt	46.85/10.13	2430/3130/2790	1991-1998	0.38	3.49	0.9 ±0.4	5.8 ±0.8
Vernagt	46.88/10.82	2770/3630/3140	1991-2005	0.70	5.20	0.6 ±0.4	8.7 ±1.9
Wurten	47.03/13.01	2380/3120/2680	1983-2005	1.19	4.33	2.5 ±2.1	3.7 ±0.9
Mean value						2.0 ±1.1	7.6 ±2.6
Italy							
Careser	46.45/10.70	2860/3310/3090	1991-2005	0.54	4.21	5.7 ±1.2	4.5 ±1.2
Calderone	42.47/13.63	2630/2830/2730	2001-2005	0.97	2.17	/	4.8 ±1.6
Ciardoney	45.52/7.39	2850/3170/3000	2001-2005	0.50	3.57	2.4 ±1.1	4.7 ±0.5
Fontana Bianca	46.48/10.77	2880/3360/3120	1996-2005	0.69	3.30	/	2.8 ±0.8
Malavalle	46.95/11.20	2520/3470/2950	2002-2005	2.12	3.79	2.7 ±1.5	6.8 ±1.4
Pendente	46.96/11.23	2620/3110/2820	1996-2005	1.05	3.89	0.8 ±0.7	6.7 ±2.6
Mean value						2.9 ±2.1	5.1 ±1.5
Mean Acc./Abl. gradients						***2.4 ±1.2***	***6.8 ±2.2***

Table IV.2.2. *Mass-balance gradients for present-day glaciers within the western and central European Alps. Accumulation and ablation gradients are calculated from annual ablation/accumulation measurements within specific glaciers [WGMS, 1998; 2005; 2008].*

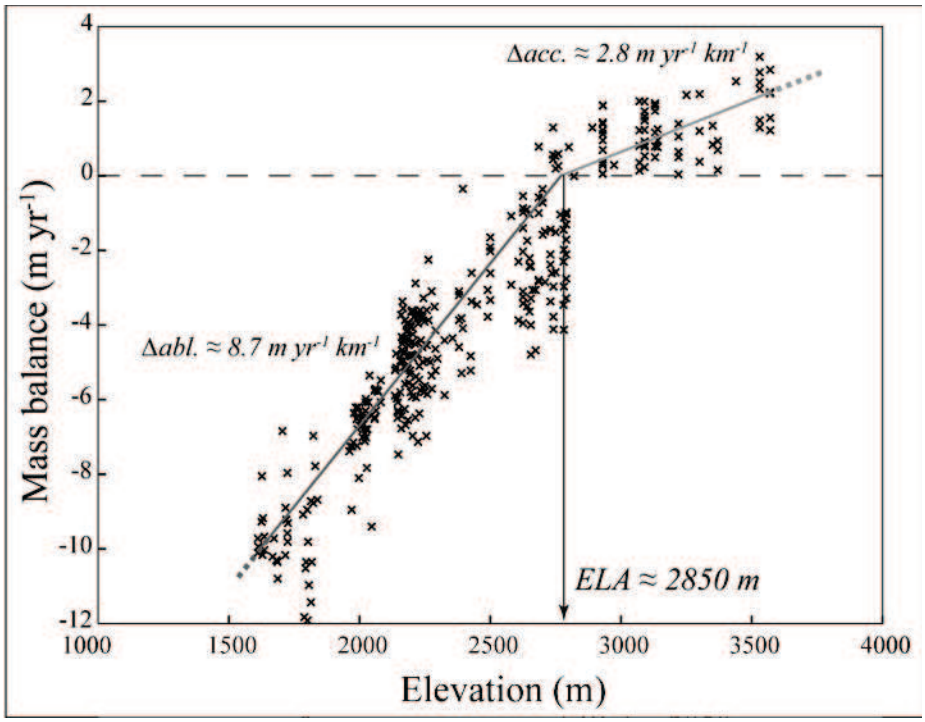

Figure IV.2.3. *Mass-balance measurements (black crosses) for the Mer de Glace glacier (Mont-Blanc massif) between 1994 and 2007 [Glacioclim, 2009]. Linear fits to the data yield ablation and accumulation gradients of ~8.7 and 2.8 m yr^{-1} km^{-1}, respectively (overestimated values compared to annually averaged data, Table IV.2.2), as well as an averaged ELA of ~2850 m (similar to the annually-averaged value of 2870 ±70m, Table IV.2.1).*

Here, I use average precipitation data (1971-1990 temporal coverage; *Frei and Schär*, 1998; *Schwarb et al.*, 2001) as a proxy for the maximum ice-accumulation rate. This first-order approach does not take into account the seasonal distribution or phase of precipitation; however, it allows to model orographic and more local effects on ice-accumulation dynamics. I illustrate this effect by presenting precipitation maps of the two study areas, the Mont-Blanc massif (Figure IV.2.4) and the Valais area (Figure IV.2.5), respectively. Figure IV.2.4 shows that the orographic effect does not seem to strongly influence the spatial distribution of annual precipitation in the Mont-Blanc massif, although precipitation is strongly correlated to elevation. However, Figure IV.2.5 clearly shows that the Valais area presents local climatic singularities with reduced precipitations in the southern part of the area, reducing the annual ice-accumulation rate in these massifs.

Furthermore, the mass-balance calculation in the SPMIce model does not include local ice redistribution by snow avalanches [*e.g.*, *Kessler et al.*, 2006; *MacGregor et al.*, 2009] or other effects related to atmospheric processes. Consequently, the current version of SPMIce does not allow predicting nunataks (*i.e.*, ice-free peaks).

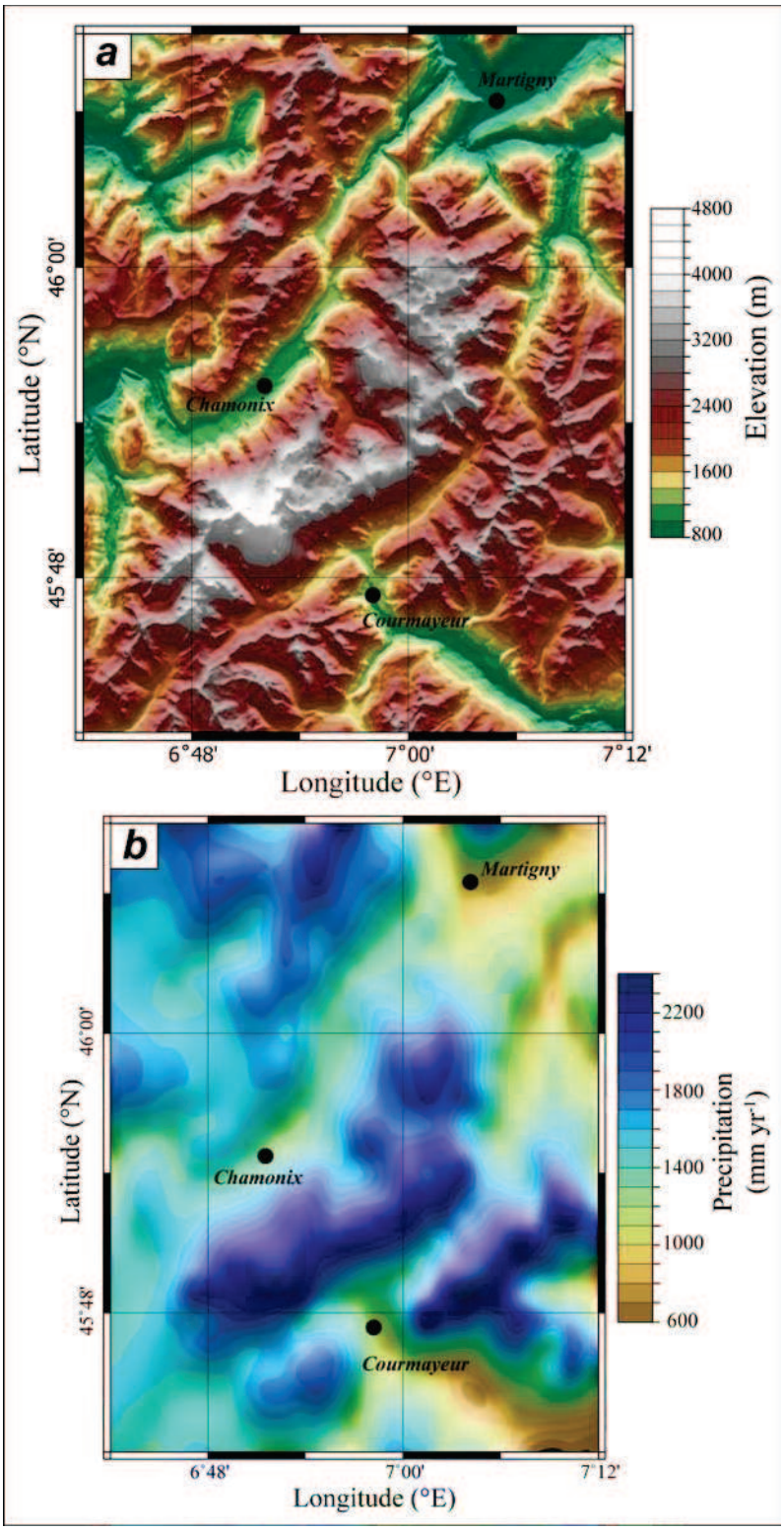

Figure IV.2.4. *Topography and precipitation maps of the Mont-Blanc massif. The topographic relief map (a) is derived from the SRTM 90-m resolution DEM, and precipitation data (b) are from Schwarb et al. [2001], interpolated onto a 2-km resolution grid using the model of Daly et al. [1994], which takes into account the orographic control on precipitation (see Frei and Schär, 1998, for meteorological stations location).*

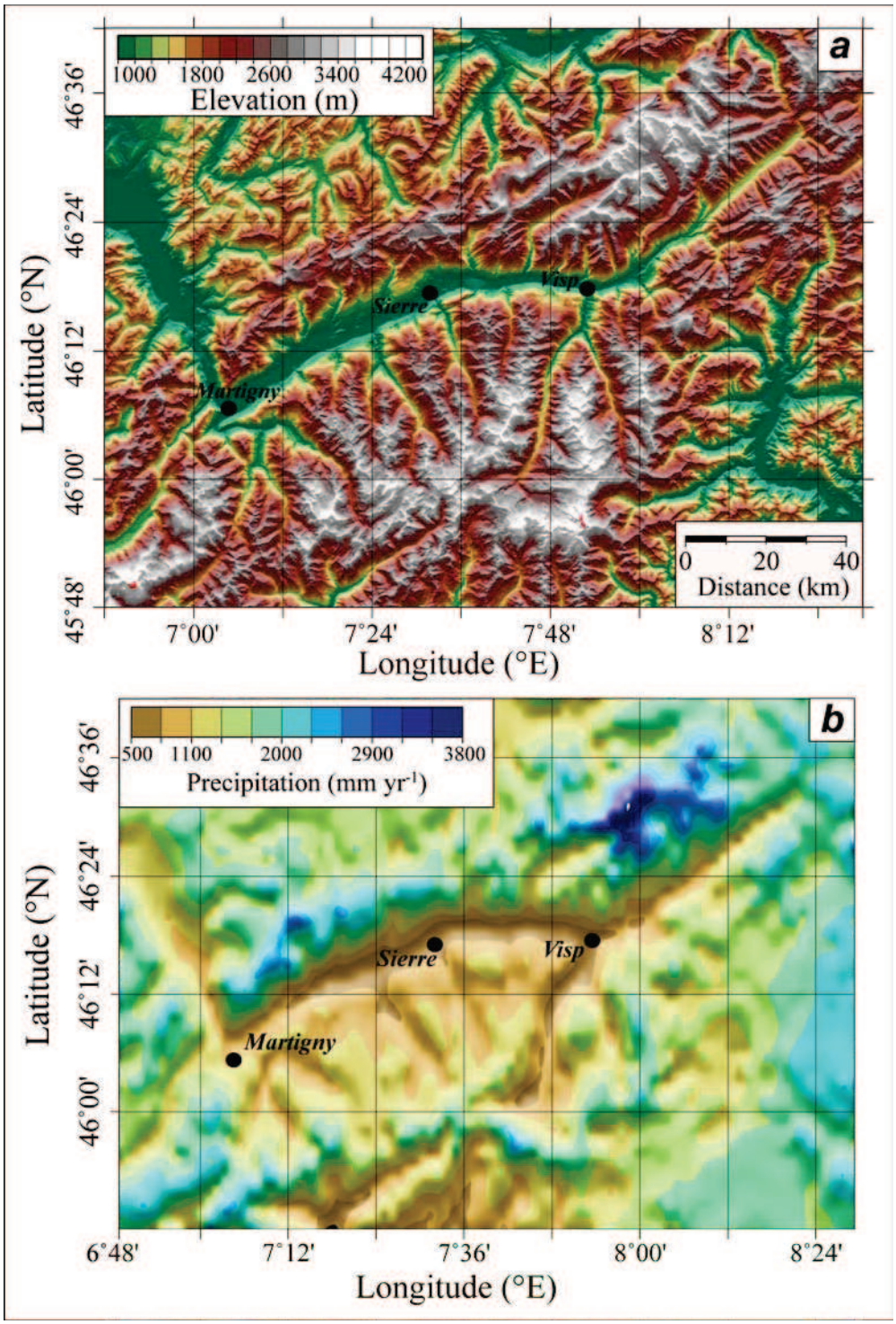

Figure IV.2.5. *Topography and precipitation maps of the Valais area (Swiss Alps). The topographic relief map (a) is derived from the SRTM 90-m resolution DEM, and precipitation data (b) are from Schwarb et al. [2001], interpolated onto a 2-km resolution grid using the model of Daly et al. [1994], which takes into account the orographic control on precipitation (see Frei and Schär, 1998, for meteorological stations location).*

IV.2.2 - Reconstructing the ice extent since the Last Glacial Maximum (Mont-Blanc massif, western Alps)

Here, I present ice-dynamics simulations for different ice-extent conditions (and associated *ELA* positions) in the Mont-Blanc massif (western Alps, Figures IV.2.4 and IV.2.6). I choose this massif as it is currently extensively monitored [*Glacioclim*, 2009] in terms of present-day glacier dynamics and climatic records (Tables IV.2.1 and IV.2.2, Figure IV.2.3). Moreover, the spatial organization of the massif is relatively simple with two main valleys: the Arve valley to the north-west and the Baltée valley to the south-east (Figure IV.2.6). The glacial retreat history of these two valleys since the Last Glacial Maximum (LGM, dated at ~20-21 ka; *Ivy-Ochs et al.*, 2006) has been documented by several geomorphic studies [*e.g.*, *Porter and Orombelli*, 1982; *Dorthe-Monachon*, 1986; *Coutterand and Nicoud*, 2005; *Gianotti et al.*, 2008].

In this section, I aim to assess to which extent both the present-day (Figure IV.2.6a) and paleo-ice extents of the Mont-Blanc glaciers can be reconstructed based on climate- or geomorphology-derived *ELA* positions [*e.g.*, *Coutterand and Nicoud*, 2005, and references therein]. I first consider the present-day climatic conditions to test whether modeling the surface mass balance with either temperature (Eq. (IV.2.5)) or direct *ELA* (Eq. (IV.2.6)) measurements provide optimal ice-extent reconstructions. I then consider different glacial stages (from the LGM to the Younger Dryas event) to explore the ability of the SPMIce model to correctly match ice-extent reconstructions inferred from geomorphological evidence [*Coutterand and Nicoud*, 2005].

I use a 90-m resolution SRTM Digital Elevation Model (Figure IV.2.4a) that I interpolate on a 300-m resolution irregular mesh (Figure IV.2.6b). The surface-temperature prediction is based on observed data (sea-level temperature of ~12.4 °C and lapse rate of ~4.5 °C km^{-1}, Figure IV.2.2), while the maximum ice-accumulation rate is derived from 2-km resolution precipitation data (Figure IV.2.5b). Ice-extent simulations are run for ~1-2 kyr at fixed *ELA* positions to ensure that the modeled glaciers are at steady-state regarding the input climatic conditions.

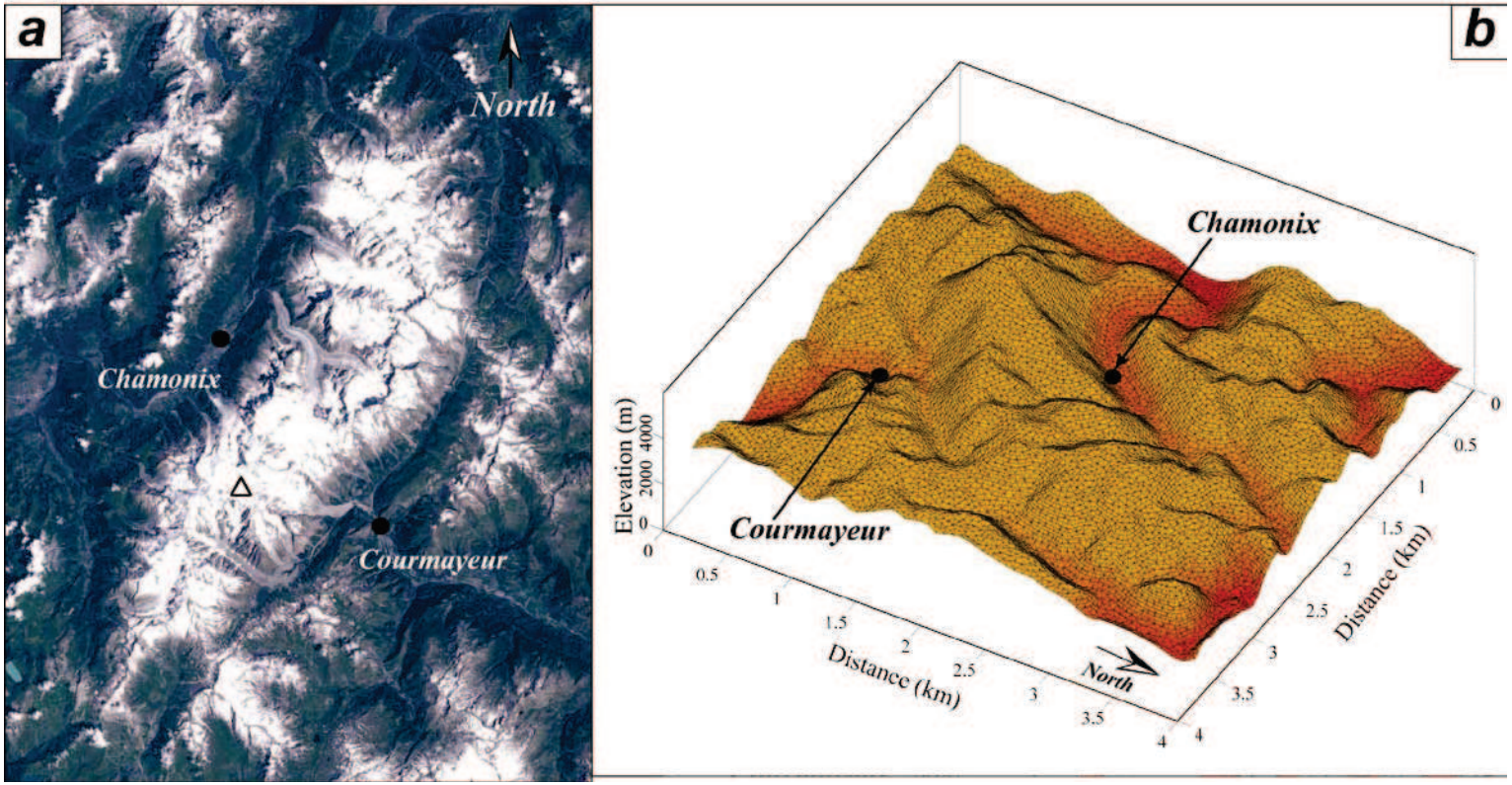

Figure IV.2.6. *Mont-Blanc massif topography and model grid. (a) Satellite view (SPOT5 image, courtesy of CNES) of the Mont-Blanc massif (Mont-Blanc peak indicated by black triangle), illustrating the present-day ice extent (end of summer/beginning of fall). Locations of the towns of Chamonix (Arve valley) and Courmayeur (Baltée valley) are also reported. (b) Irregular mesh (Voronoi cells, Egholm and Nielsen, 2010) used for ice-extent simulations (grid resolution of ~300 m).*

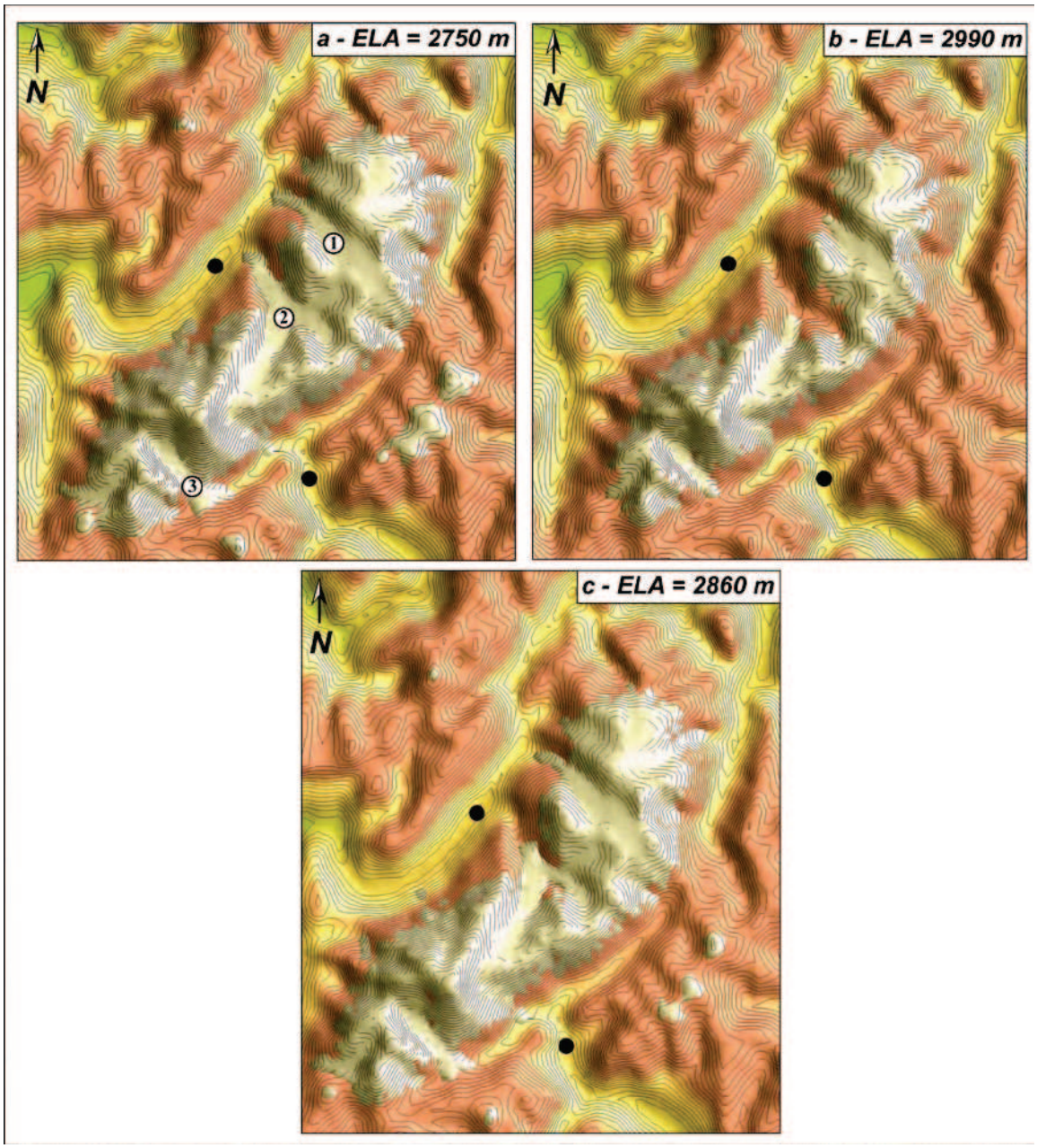

Figure IV.2.7. *Ice-extent modeling for present-day conditions with input ELA values derived from: (a) temperature data, (b) averaged ELA from different Alpine glaciers (Table IV.2.1), and (c) specific ELA value for the Mer de Glace and Argentière glaciers (1: Argentière glacier, 2: Mer de Glace glacier, 3: Miage glacier).*

Predicted present-day ice extents are shown in Figure IV.2.7. Note that assuming a temperature-based *ELA* (Eq. (IV.2.5)) results in overestimating the ice extent (Figure IV.2.7a) compared to present-day glaciers (Figure IV.2.6a), especially for the major glaciers of the Mont-Blanc massif (Argentière and Mer de Glace glaciers on the north side of the massif, and Miage glacier on the south side). Modeled glaciers reach the Arve valley (Figure IV.2.7a), in

agreement with Little Ice Age conditions (17^{th}-19^{th} centuries; *e.g.*, *Nesje and Dahl*, 2003) and an associated *ELA* shift of ~-100 m [*Casty et al.*, 2005; *Vincent et al.*, 2005].

On the contrary, imposing a present-day *ELA* of ~2990 m (averaged estimate derived from a compilation of glaciers in the European Alps, Table IV.2.1) results in underestimating ice extents (Figure IV.2.7b); the modeled glaciers terminating far upstream in the inner valleys. These results clearly show that the present-day glaciers are highly sensitive to small *ELA* shifts, and that the averaged Alpine *ELA* estimate (Table IV.2.1) may not apply to individual glaciers within the Mont-Blanc massif.

I thus perform a supplementary simulation in which I apply the present-day *ELA* estimate (~2860 m, Figure IV.2.7c) reported for specific glaciers within the Mont-Blanc massif (Argentière and Mer de Glace glaciers, Table IV.2.1). This numerical experiment provides an accurate prediction of the present-day glacier extent, except the Mer de Glace glacier for which the predicted glacier extent is smaller than the observed extent (Figure IV.2.7c). These differences may be explained by the current transient state of the Mer de Glace glacier, which is retreating rapidly compared to other glaciers in the Mont-Blanc massif [*Glacioclim*, 2009]; thus the present-day *ELA* position may not reflect the observed extent of the Mer de Glace glacier. This result also points out that ice-dynamics modeling might be used to predict future glacier evolution for either present-day climatic conditions or any imposed climate-change scenario [*e.g.*, *Le Meur et al.*, 2007]. In the following, I will adopt the ~2860 m *ELA* estimate as a proxy for present-day climatic conditions within the Mont-Blanc massif.

One can also extract the horizontal ice-velocity pattern predicted by the SPMIce model and compare it to observed values for the Mer de Glace and Argentière glaciers (Figure IV.2.8). Figure IV.2.8 shows that the predicted ice-velocity pattern is roughly in agreement with data derived from correlation of optical satellite images [*Berthier*, 2005], even though modeled velocities are lower than observed values, especially for the accumulation area of the Mer de Glace glacier (Figure IV.2.8a). On the contrary, predicted velocities are in good agreement with observed values for the Argentière glacier derived from optical satellite imagery (Figure IV.2.8a) and local ice-velocity measurements [*Glacioclim*, 2009].

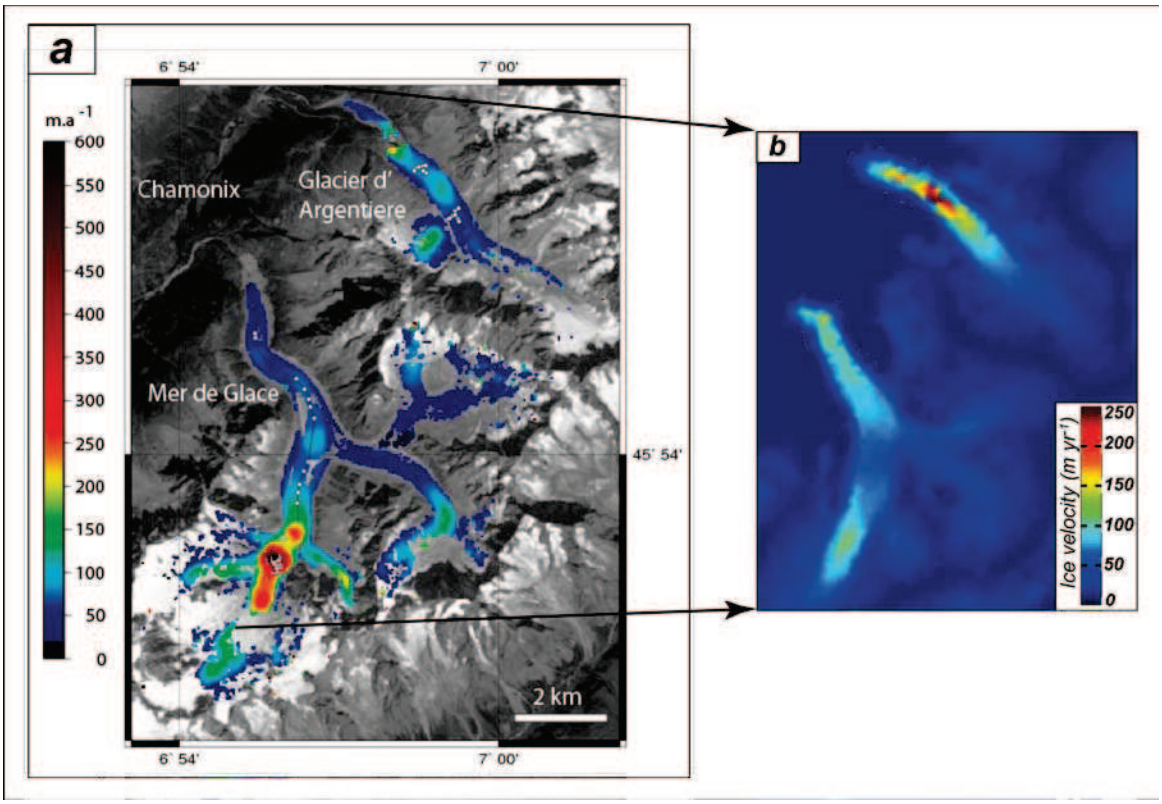

Figure IV.2.8. *Optical satellite imagery-derived and modeled ice-velocity patterns in the Mont-Blanc massif. (a) Optical satellite imagery-derived ice-velocity pattern during August 2003 [Berthier, 2005]; and (b) SPMIce modeled ice-velocity pattern for present-day climatic conditions (Figure IV.2.7c).*

The observed differences for the Mer de Glace glacier may be explained by the grid resolution used for ice modeling (~300 m, Figure IV.2.6b), which does not allow to predict high ice velocities for steep bedrock-gradient areas (as observed in the accumulation area of the Mer de Glace glacier, Figure IV.2.8a). An alternative explanation is the temporal difference between steady-state annually averaged ice velocities predicted by the model (Figure IV.2.8a) and the observed velocities on a short time period (summer 2003, *Berthier*, 2005). In summary, I show that modeled horizontal ice velocities are in good agreement, at first order, with observed values [*Berthier*, 2005; *Glacioclim*, 2009], illustrating that the SOSIA computation is sufficiently accurate in predicting glacier dynamics for alpine glaciers at reasonable grid resolution, and allows capturing both glaciological and geomorphic processes [*e.g.*, *Egholm et al.*, 2009].

I now present experiments of ice-extent modeling for different glacier-retreat stages [*Coutterand and Nicoud*, 2005] to assess whether one can rely on geomorphologically-derived paleo-*ELA*s to constrain paleo-ice extents.

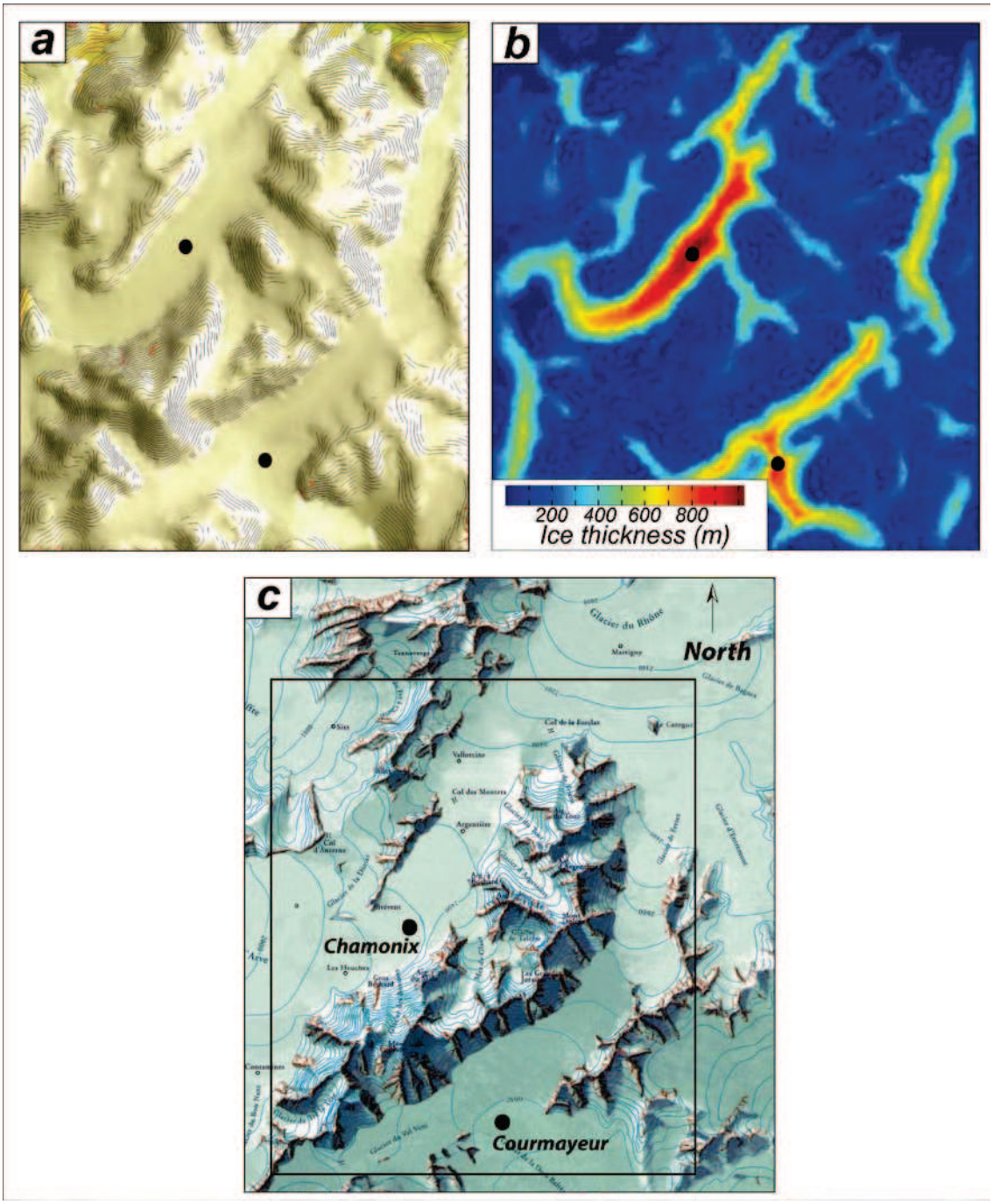

Figure IV.2.9. *Last Glacial Maximum (LGM ~20-21 ka) ice reconstructions. (a) Ice-extent simulation using the SPMIce model with an input ELA shift of -1280 m [Ivy-Ochs et al., 2006; van der Beek and Bourbon, 2008; Coutterand, 2010; Norton and Hampel, 2010], (b) associated ice-thickness pattern, and (c) ice-extent reconstruction (box indicates model extent) based on trimline distribution [Coutterand and Buoncristiani, 2006].*

I first present a simulation for LGM climatic conditions (~21-20 ka, *Ivy-Ochs et al.*, 2006), for which an extensive geomorphic database of paleo-glacier extent suggests a mean *ELA* shift of around -1280 m compared to present-day conditions [*Kelly et al.*, 2004; *Ivy-Ochs et al.*, 2006;

van der Beek and Bourbon, 2008; *Coutterand*, 2010; *Norton and Hampel*, 2010]. Figure IV.2.9 shows that both modeled ice extent (Figure IV.2.9a) and glacier thickness (Figure IV.2.9b) are in close agreement with paleo-geographical reconstructions (Figure IV.2.9c; *Coutterand and Buoncristiani*, 2006). The main difference is the absence of nunataks in model outputs (Figure IV.2.9a), due to the non-implementation of snow-avalanche processes [*e.g.*, *MacGregor et al.*, 2009] in this version of the SPMIce model.

Although some constraints exist for glacier retreat during early post-LGM times, the ice-extent limits for these periods are well outside our study area (as for the LGM conditions), and ice-extent simulations would result in similar predictions as for LGM conditions (Figure IV.2.9a). Paleo-*ELA* shifts derived from paleo-geographical reconstructions [*Dorthe-Monachon*, 1986; *Coutterand and Nicoud*, 2005] are approximately -1180 m and -925 m at around 19-20 ka and ~18 ka, respectively, in agreement with paleo-climatic data [*Peyron et al.*, 1998].

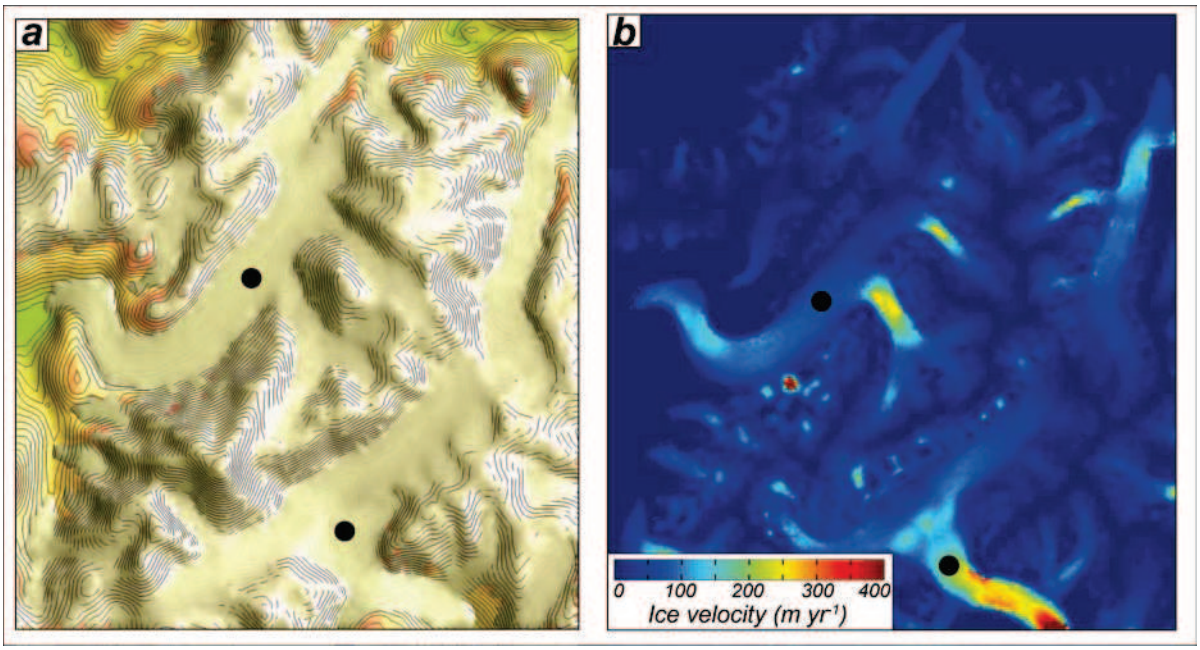

Figure IV.2.10. *Late-Glacial (~16-17 ka) ice-extent reconstruction and predicted ice velocities. (a) Ice-extent modeling with an input ELA shift of -800 m [Dorthe-Monachon, 1986; Coutterand and Nicoud, 2005; Norton and Hampel, 2010], showing the progressive glacier retreat within the Arve and Baltée valleys, and (b) predicted horizontal ice velocities (see text for discussion). Dots indicate location of towns of Chamonix and Courmayeur.*

The first significant glacier retreat within our study area is observed at around 16-17 ka when the Arve glacier retreated upstream into the Chamonix valley (Figure IV.2.10a; *Coutterand and Nicoud*, 2005). Paleo-*ELA* estimates suggest a shift of around -800 m for that period [*Dorthe-Monachon*, 1986; *Coutterand and Nicoud*, 2005; *Norton and Hampel*, 2010], and ice-extent reconstructions [*Coutterand*, 2010] are in close agreement with our model predictions (Figure IV.2.10a) for such an *ELA* value.

Predicted horizontal ice velocities for this simulation (Figure IV.2.10b) permit to discuss the predicted velocity pattern and consequently the expected distribution of glacial erosion within the massif. Figure IV.2.10b, however, illustrates the numerical limitation of the current version of the SPMIce model where the ice reaches the model boundaries (such as in the Baltée valley, south of Courmayeur in Figure IV.2.10b). The open boundary conditions result in steep ice gradients for these configurations, and consequently high velocities that may influence the numerical solution well upstream in the Baltée valley (Figure IV.2.10b). Consequently, the ice-velocity pattern (and associated predicted glacial erosion) is not driven by glaciological processes but rather by local numerical instabilities. Other numerical instabilities may also appear where bedrock gradients are very high (Figure IV.2.10b, south-west of Chamonix in the Arve valley), resulting in locally high and inaccurate ice velocities. These potential effects have to be taken into account when interpreting the predicted glacial erosion pattern.

Keeping these limitations in mind, Figure IV.2.10b shows that the maximum ice velocity is not encountered for the highest ice thicknesses (Figure IV.2.9b), but rather at valley confluences ("outlet" of the Argentière and Mer de Glace glaciers in the Arve valley, or valley confluence just upstream of Courmayeur), at local valley constrictions (downstream of the Arve valley), or at the glacier front (Arve valley). These results have important implications for the spatial and temporal glacial erosion patterns during a glacial/interglacial cycle, with relatively high erosion rates during glacier-advance or -retreat episodes, whereas erosion is restricted to ice confluences or local valley constrictions during full glacial conditions [*Tomkin and Braun*, 2002; *Herman and Braun*, 2008].

I finally present simulations for the Younger Dryas event (~11-13 ka), the latest episode of significant post-LGM glacier advance recorded within the European Alps [*e.g.*, *Kerschner and Ivy-Ochs*, 2008; *Ivy-Ochs et al.*, 2009; *Norton and Hampel*, 2010] for which the *ELA* shift

is estimated to be around -425 m compared to present-day conditions [*Coutterand and Nicoud*, 2005; *Kerschner and Ivy-Ochs*, 2008; *Norton and Hampel*, 2010]. Model results show quite a good agreement between the predicted ice extent (Figure IV.2.11b) and paleo-geographical reconstructions (Figure IV.2.11a; *Coutterand*, 2010), except for the Arve valley downstream of Chamonix where the SPMIce model does not predict as much ice as proposed based on geomorphic evidence [*Coutterand*, 2010]. The model does predict correctly the glacier termination at Chamonix; however, downstream glaciers do not reach the valley bottom as inferred from geomorphologic data [*Coutterand*, 2010]. An other difference concerns the predicted ice extent in the Baltée valley, compared to paleo-geographical reconstructions (Figure IV.2.11). Here, the SPMIce model appears to predict much larger glaciers than those inferred from geomorphic reconstructions during Late-Glacial episodes (*i.e.*, later than ~16-17 ka).

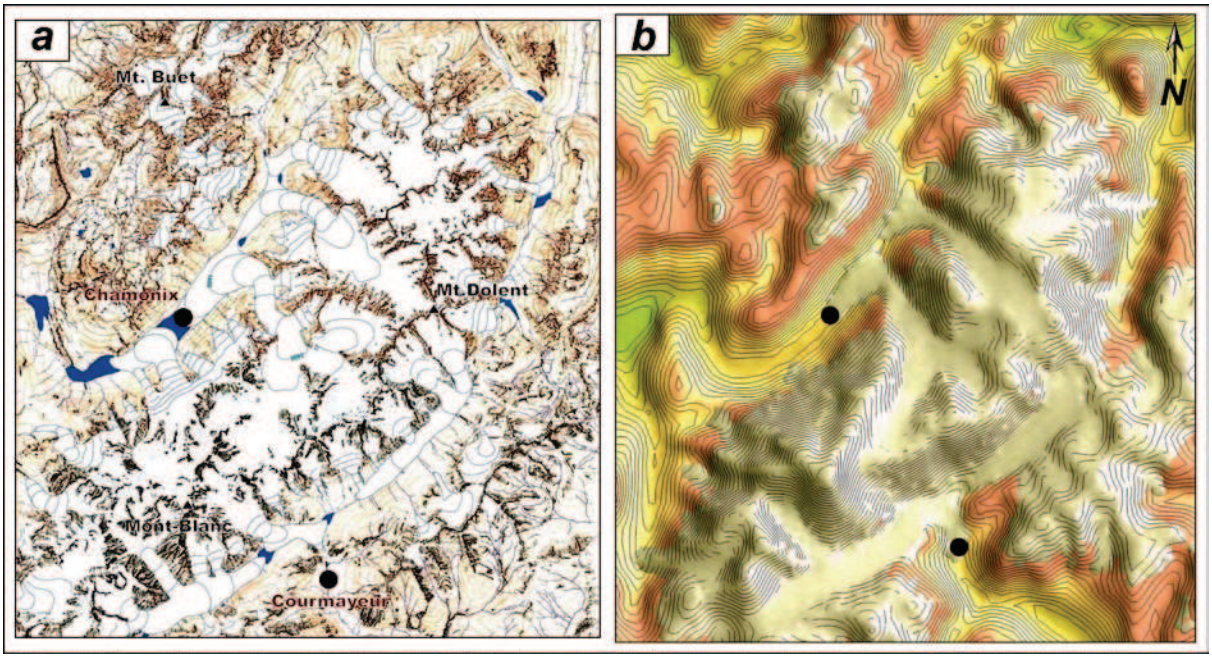

Figure IV.2.11. *Younger Dryas (~11-13 ka) ice-extent reconstructions from: (a) location of frontal moraines [Coutterand, 2010], and (b) SPMIce simulation with an ELA shift of -425 m [Coutterand and Nicoud, 2005; Kerschner and Ivy-Ochs, 2008; Norton and Hampel, 2010].*

These differences may have two potential explanations. First, our climatic model only considers an altitudinal temperature dependence (Eq. (IV.2.5)); thus temperature predictions for the Baltée valley are lower than those inferred for the Arve valley because of its ~200 m higher elevation. This temperature distribution around the Mont-Blanc massif does not include any local climatic effects; however, temperature measurements over the last decades

strongly suggest that annual temperatures are ~1 °C higher in Courmayeur than in Chamonix, even though its elevation is ~200 m higher [*Vartanian-Traynard*, 1969]. Second, the glacier retreat history for the Baltée valley is not as well constrained as for the Arve valley, with contradicting geochronological records of glacier retreat [*e.g.*, *Porter and Orombelli*, 1982; *Gianotti et al.*, 2008, and references therein]. Thus, the paleo-geographical reconstruction of the Younger Dryas glacier extent [*Coutterand*, 2010] might be quite inconsistent for the Baltée valley.

In summary, in this section I have compiled literature data and derived Late-Glacial paleo-*ELA* positions with respect to present-day climatic conditions. These paleo-*ELA* estimates will be used in the next section to discuss in more detail the differences between 100-kyr and 40-kyr glacial/interglacial cycles and propose potential ways to test their influence on relief development.

Moreover, those simulation results evidence the current limitations of numerical ice modeling in predicting ice velocities (steep local gradients, open boundary predictions) or defining the adequate complexity of the climatic input model to accurately predict the surface mass balance (snow-avalanche processes, spatial distribution of temperature and precipitation).

One potential limitation in the adopted approach concerns the validity of extrapolating *ELA* determination methods (calibrated from present-day glaciers) for paleo-ice extent conditions. Traditional methods (THAR or AAR methods; *e.g.*, *Porter*, 2000 and references therein) to derive paleo-*ELA*s from ice-extent reconstructions [*e.g.*, *van der Beek and Bourbon*, 2008; *Coutterand*, 2010] consider present-day empirical calibrations (AAR ~0.67, THAR ~0.5-06; *e.g.*, *Coutterand*, 2010) as being representative for past glacial periods. However, present-day empirical calibrations for these methods have been realized on transient glaciers that are currently retreating very rapidly due to climate change. One may wonder whether these calibrations are also valid for advancing glaciers, or eventually for close to steady-state glaciers as was the case during the LGM. This question may have important implications, as paleo-*ELA*s are widely used as direct proxies of past climate changes.

IV.2.3 - Pleistocene glaciations and topographic evolution (Valais, Swiss Alps)

In this section, I explore potential ways of using ice-dynamics modeling to quantify the impact of Pleistocene glaciations, and especially the Mid-Pleistocene climate transition, on Alpine landscape development. My initial aim was to simulate a full glacial/interglacial cycle (both 40-kyr and 100-kyr cycles) on the Valais area (Swiss Alps, Figure IV.2.5) and quantify the glacial erosional response and associated impact on landscape evolution. I chose the Valais area as I have previously obtained quantitative estimates on basin-scale relief evolution in the upper Rhône catchment using low-temperature thermochronology (chapter III).

Unfortunately, I lacked the time to develop this quantitative modeling approach, which would have required first to properly model glacial (and fluvial/hillslope) processes over a glacial/interglacial cycle, and second to fully explore the differences between the 100-kyr and 40-kyr cycles in terms of climate variability and of impact on landscape evolution. I thus only present here preliminary simulations of ice-extent reconstructions and associated ice-velocity patterns in the Valais area, to qualitatively discuss the spatial and temporal distribution of glacial erosion during an episode of glacier advance. I finally propose potential ways to quantitatively discuss the role of the Mid-Pleistocene climate transition in the development of Alpine topographic relief.

I first perform an ice-extent simulation with input LGM climatic conditions (paleo-*ELA* shift of -1280 m, see previous section) and run the model until glacier extent is at steady-state regarding the climatic conditions (~1.5 kyr simulation). I then extract both the final ice extent (and associated ice-thickness pattern, Figure IV.2.12) and different snapshots during the glacier advance for which I present the ice-extent and velocity predictions (Figure IV.2.13).

Figure IV.2.12 shows good agreement between the ice-model predictions (Figure IV.2.12a) and the paleogeographical reconstructions of ice extent (Figure IV.2.12b; *Kelly et al.*, 2004; *Coutterand*, 2010), although the open boundary conditions in the SPMIce model do not allow to accurately predict ice extent at the outlet of the Rhône basin (Figure IV.2.12a). However, ice-thickness predictions (Figure IV.2.12c) are much higher than trimline-based reconstructions (Figure IV.2.12b; *Kelly et al.*, 2004; *Coutterand*, 2010). Potential explanations for these observed differences might be the non-implementation of snow avalanches into the SPMIce model (see previous section) or an underestimation of the ice-velocity parameters (*A*

and B_s, see section IV.2.1). However, the Mont-Blanc results (section IV.2.2) were in reasonable agreement with observed ice-velocity patterns (Figure IV.2.8), and the simplifications in the surface mass-balance modeling (no snow avalanches) might not explain such high differences in ice thicknesses (~100-500 m). An alternative explanation would imply that observed trimlines only represent the elevation limit of the "erosive" part of the glacier [*Beaudevin*, 2000; *van der Beek and Bourbon*, 2008; *Coutterand*, 2010], the ice thickness thus being higher than suggested by the paleogeographical reconstructions [*Kelly et al.*, 2004; *Coutterand*, 2010] as it has been suggested for ice sheets [*e.g.*, *Li et al.*, 2005]. Further ice modeling in well calibrated areas (as the Mont-Blanc or Valais areas) might be a potential way to quantitatively test this hypothesis and assess the significance of the trimline for ice-extent reconstructions.

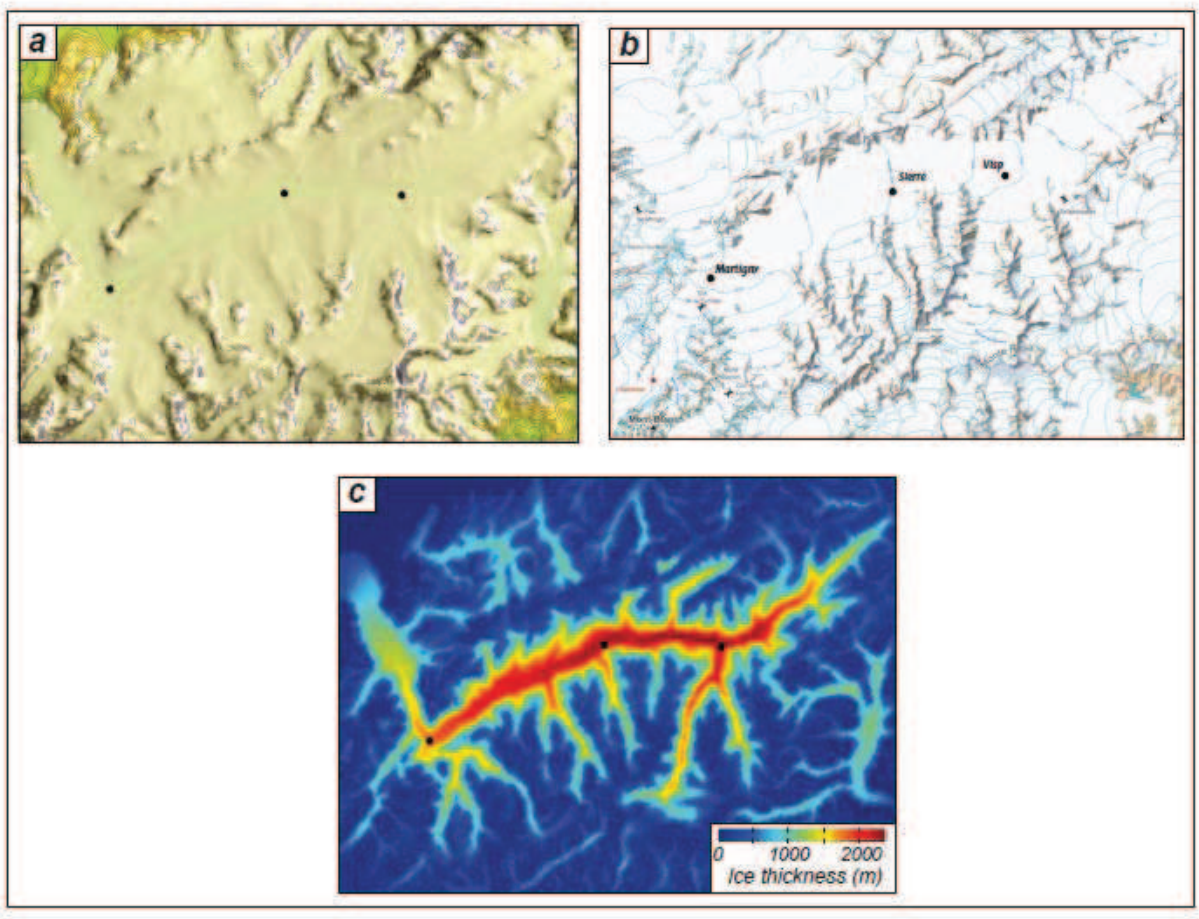

Figure IV.2.12. *Last Glacial Maximum (LGM ~20-21 ka) reconstruction of ice extent in the Valais area (Swiss Alps, see Figure IV.2.1 for location). (a) Ice-extent reconstruction using the SPMIce model with an input ELA shift of -1280 m, (b) ice-extent reconstruction based on trimlines and moraines distribution [Kelly et al., 2004; Coutterand, 2010], and (c) predicted ice-thickness pattern using the SPMIce model.*

Although I did not include glacial erosion in the SPMIce simulations, snapshots of the progressive advance of the Rhône glacier (Figure IV.2.13) provide qualitative insights into the expected spatial and temporal patterns of erosion.

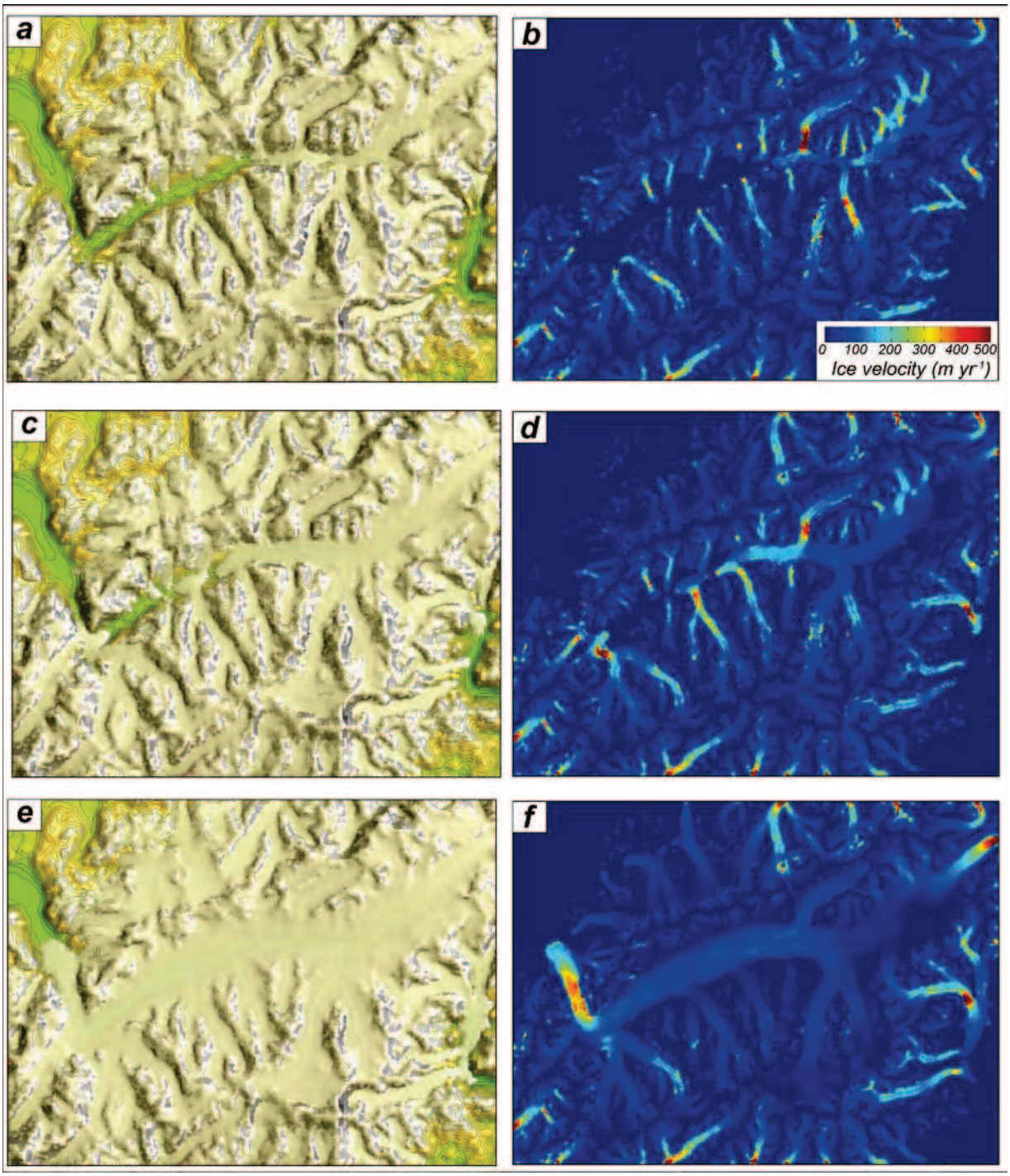

Figure IV.2.13. *Snapshot views of different ice extents (a, c, e) and associated ice-velocity patterns (b, d, f) during the Rhône glacier advance towards LGM conditions (Figure IV.2.12).*

Figure IV.2.13 shows that during the early glacial stages (Figures IV.2.13a, b and IV.2.13c, d), maximum ice velocities are encountered in tributary valleys and at glacier confluences, while the ice-velocity pattern constantly evolves through time (see Figures IV.2.13b and IV.2.13d). The mature glacial stage (Figure IV.2.13e, f) reveals a completely different ice-velocity pattern, with low ice velocities within most of the basin, except for the Rhône glacier front where the ice is moving rapidly (Figure IV.2.13f). These preliminary results, although not reflecting the complex glacial erosion pattern during a glacial/interglacial cycle (fluvial and hillslope processes are not included), provides some qualitative expectations on the spatial and temporal distribution of glacial erosion during an episode of glacier advance [*Herman and Braun*, 2008; *Egholm et al.*, 2009].

However, these numerical results have been inferred from simulating LGM ice-extent conditions on the present-day topography, and may not directly reflect the glacial erosion patterns for different initial topographies that must have existed throughout the Pleistocene or before the onset of Pleistocene glaciations (chapter III, section III.4). Present-day topography has been efficiently shaped by the last glacial periods [*e.g.*, *Kelly et al.*, 2004; *Coutterand*, 2010; *Delunel*, 2010] and might be in a "quasi-equilibrium" state regarding LGM conditions, which explains the low ice-velocity pattern predicted by the SPMIce simulation (Figure IV.2.13f).

Output results might be very different when using a different topography, such as a typical fluvial landscape generated after applying a surface process model (fluvial and hillsope processes) on the present-day topography for several thousands of years (Figure IV.2.14a). An interesting test would be to use the "pre-glacial" reconstructed topography of the Rhône basin estimated from low-temperature thermochronology (section III.4 and Figure IV.2.14b) as the initial input topography for quantifying landscape response to glacial processes over a full glacial/interglacial cycle.

Finally, estimating the glacial erosion pattern from predicted ice velocities (Figure IV.2.13) implicitly assumes that the glacial erosional efficiency is spatially uniform, although strong spatial variations in lithology (and associated erosional resistance) exist in the Valais area (Figure IV.2.15; *e.g.*, *Kühni and Pfiffner*, 2001b]; potentially implying that glacial erosion patterns strongly differ from ice-velocity predictions. Evidence of lithological and structural effects on glacial erosion have been reported in the literature [*Glasser and Ghiglione*, 2009;

Dühnforth et al., 2010]; one interesting illustration of these potential effects in the glacial landscape evolution of the Valais area is shown in Figure IV.2.13f: while ice velocities are relatively low along most of the Rhône valley (except for the Rhône glacier front), high ice velocities are predicted by the SPMIce model just downstream of the town of Martigny (see Figure IV.2.14a for location), where the orientation of the Rhône valley changes from roughly east-west to south-north.

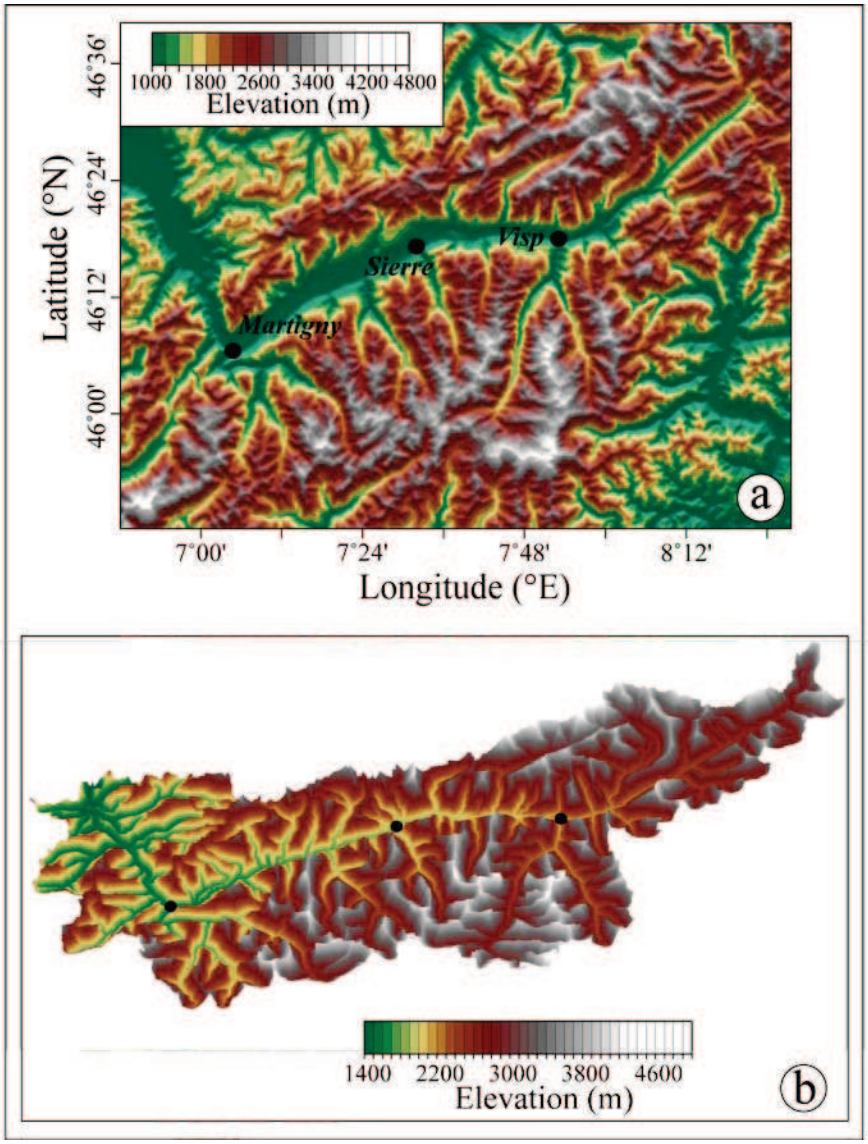

Figure IV.2.14. *Pre-glacial topography of the Valais area. (a) Synthetic fluvial topography of the Valais area obtained using Cascade surface process model [e.g., Braun and Sambridge, 1997] over 20-kyr simulation of fluvial and hillslope processes and 1 mm yr^{-1} of rock-uplift rate; and (b) pre-glacial topography reconstruction of the Rhône basin from low-temperature thermochronology data (section III.4).*

Moreover, this orientation change is associated with strong narrowing of the Rhône valley, leading to the predicted high ice velocities (that may be associated with relatively high erosion rates) in order to maintain a constant ice flux. However, both geomorphological and geophysical evidence [*e.g.*, *Finckh and Frey*, 1991; *Rosseli and Olivier*, 2003] do not reveal any strong overdeepening of the Rhône valley at this specific location, while Figure IV.2.15 shows that narrowing of the Rhône valley is spatially concordant with highly resistant lithologies (*i.e.*, the Aiguilles Rouges crystalline massif). Resistant lithologies may explain both the narrowing of the Rhône valley and the high ice velocities needed to sustain uniform valley deepening rates, evidencing the potential control of lithology on glacial erosion.

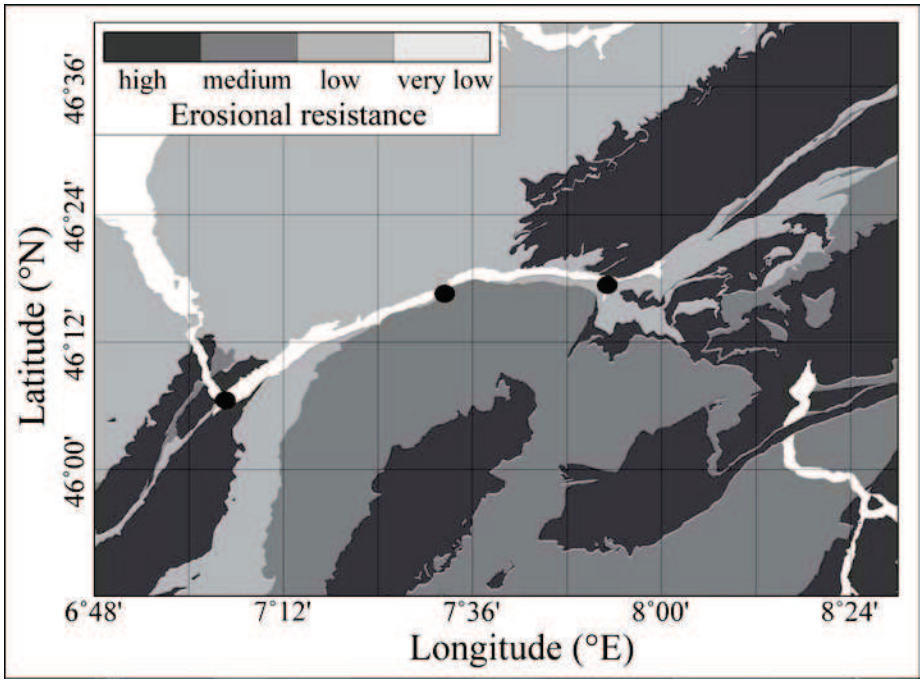

Figure IV.2.15. *Simplified spatial distribution of lithologies in the Valais area, illustrating the spatial variability in erosional resistance [Kühni and Pfiffner, 2001b; Schlunegger and Hinderer, 2001; Norton et al., 2010a].*

Simulating a full glacial/interglacial cycle would require quantitative constraints on the climate variability, *i.e.*, both the climatic amplitude and the asymmetry between glacial and interglacial periods. $\delta^{18}O$ isotopic records from ice cores (*e.g.*, Greenland or Antarctic ice sheets; *Petit et al.*, 1997; 1999; *NGRIP members*, 2004) could be used as proxies for quantifying paleo-ice volumes, mimicking the first order climatic variability between glacial and interglacial periods. Figure IV.2.16 shows $\delta^{18}O$ measurements from NGRIP (North GReenland Ice core Project) over the last ~120 kyr [*NGRIP members*, 2004] and reveals the

strong asymmetry of the last glacial/interglacial cycle, with a glacier-advance episode of ~80 kyr until the Last Glacial Maximum (~20 ka; *Ivy-Ochs et al.*, 2006), followed by a much more rapid glacier retreat over the last ~20 kyr.

I attempt to compare the $\delta^{18}O$ variability from these ice-core records with paleo-*ELA*s inferred from paleogeographical ice-extent reconstructions (section IV.2.2), in order to assess to what extent ice-core $\delta^{18}O$ records may be used as proxies for the paleo-ice extent variations within the European Alps. I thus calculate 1-kyr averaged $\delta^{18}O$ NGRIP values and compare these with paleo-*ELA* estimates (Figure IV.2.16). The results show a reasonably good agreement between averaged $\delta^{18}O$ values and paleo-*ELA* estimates (see inset in Figure IV.2.16).

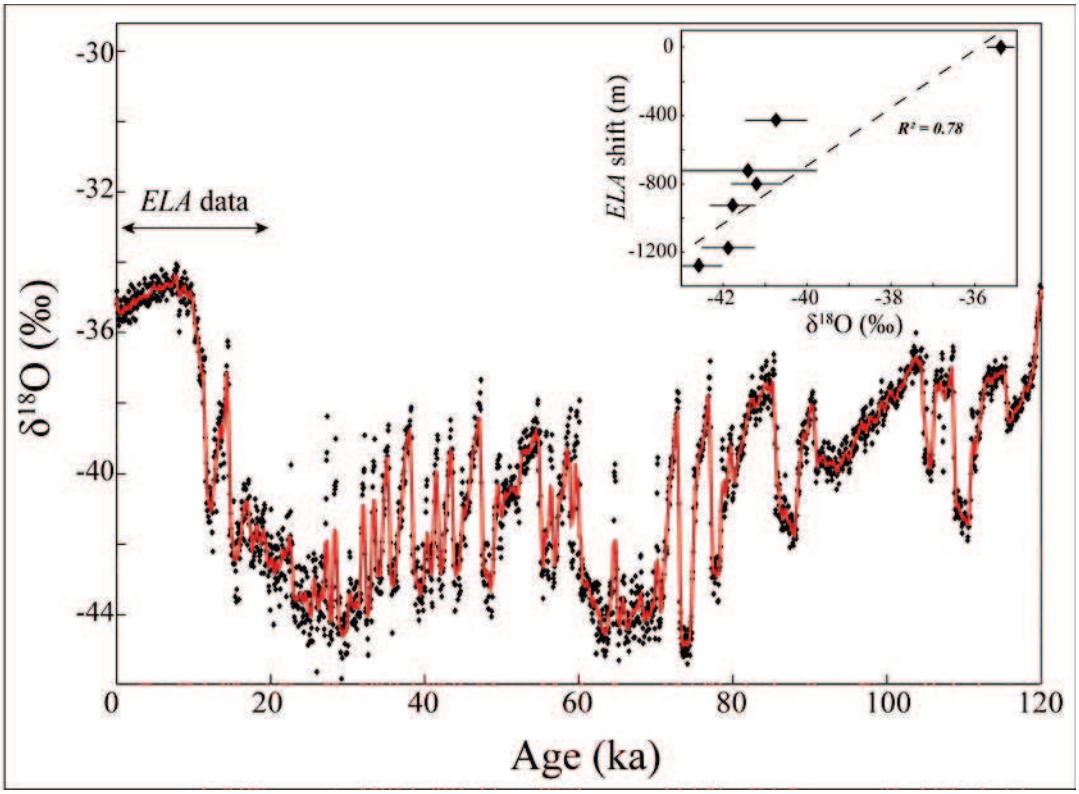

Figure IV.2.16. *$\delta^{18}O$ records from NGRIP project ice core [NGRIP members, 2004], illustrating the climate variability over the last glacial/interglacial cycle. Inset shows a tentative linear correlation between inferred paleo-ELA shifts relative to present-day (section IV.2.2) and 1-kyr averaged $\delta^{18}O$ values since the LGM (see text for discussion).*

However, this approach has some limitations as paleo-*ELA*s are only available since the Last Glacial Maximum (Figure IV.2.16) and may not correctly reflect the glacier-advance period. Moreover, paleo-*ELA* estimates are well constrained from LGM conditions (~20-21 ka) to the Younger Dryas event (~11-13 ka) as geomorphological records (moraines) are abundant

within the Alps [*e.g.*, *Ivy-Ochs et al.*, 2006; *Coutterand*, 2010 and references therein] for that time, but *ELA* variations during the Holocene are much less constrained, except in specific locations [*e.g.*, *Ivy-Ochs et al.*, 2009; *Norton and Hampel*, 2010]. The inferred correlation between $\delta^{18}O$ values and paleo-*ELA* estimates (Figure IV.2.16) thus does not consider Holocene times, and the resolution of the dataset does not allow assessing whether the correlation is linear (Figure IV.2.16) or rather follows a power-law (or any other relationship). These limitations thus imply several assumptions in order to use post-LGM *ELA* estimates as proxies for simulating a full glacial/interglacial cycle.

Assessing the differences in the 40-kyr and 100-kyr glacial/interglacial cycles requires temporal coverage of the climate variability that is beyond the resolution of ice-core records, which only allow constraining the late Pleistocene glacial/interglacial oscillations [*Petit et al.*, 1997; 1999; *NGRIP members*, 2004]. Benthic $\delta^{18}O$ records might be used to obtain constraints on climatic variability over longer time-periods such as the Pliocene [*Lisiecki and Raymo*, 2005] or even throughout the Cenozoic [*e.g.*, *Zachos et al.*, 2001]. However, using benthic $\delta^{18}O$ records to constrain paleo-ice extents is less straightforward than ice-core $\delta^{18}O$ measurements, as the benthic record does not directly reflect paleo-ice volumes but also depends on sea-water temperature [*Zachos et al.*, 2001 and references therein]. In the following, I present a benthic $\delta^{18}O$ record compilation from *Lisiecki and Raymo* [2005] over the Pleistocene that I assume to be relevant as a proxy for discussing the differences between 40-kyr and 100-kyr glacial/interglacial cycles (Figure IV.2.17).

Figure IV.2.17 clearly shows the Mid-Pleistocene climate transition that occurred at around 1-1.2 Ma [*e.g.*, *Lisiecki*, 2010], associated with the onset of 100-kyr cycles (92 ±15 kyr, Figure IV.2.17), while 40-kyr cycles (41 ±8 kyr, Figure IV.2.17) were present during the early Pleistocene period. Moreover, the data highlight the strong asymmetry of the 100-kyr cycles with glacial periods of ~70-80 kyr followed by very rapid glacier retreat (~10-20 kyr, Figure IV.2.17). On the contrary, benthic $\delta^{18}O$ records show that the 40-kyr cycles were symmetric [*e.g.*, *Lisiecki*, 2010 and references therein] with glacial and interglacial periods of the order of 20 kyr (22 ±7 kyr and 19 ±6 kyr, respectively). The onset of 100-kyr asymmetric cycles would thus have promoted long-lived glaciers, potentially explaining the initiation of major and widespread Alpine glaciations at ~1 Ma [*Muttoni et al.*, 2003].

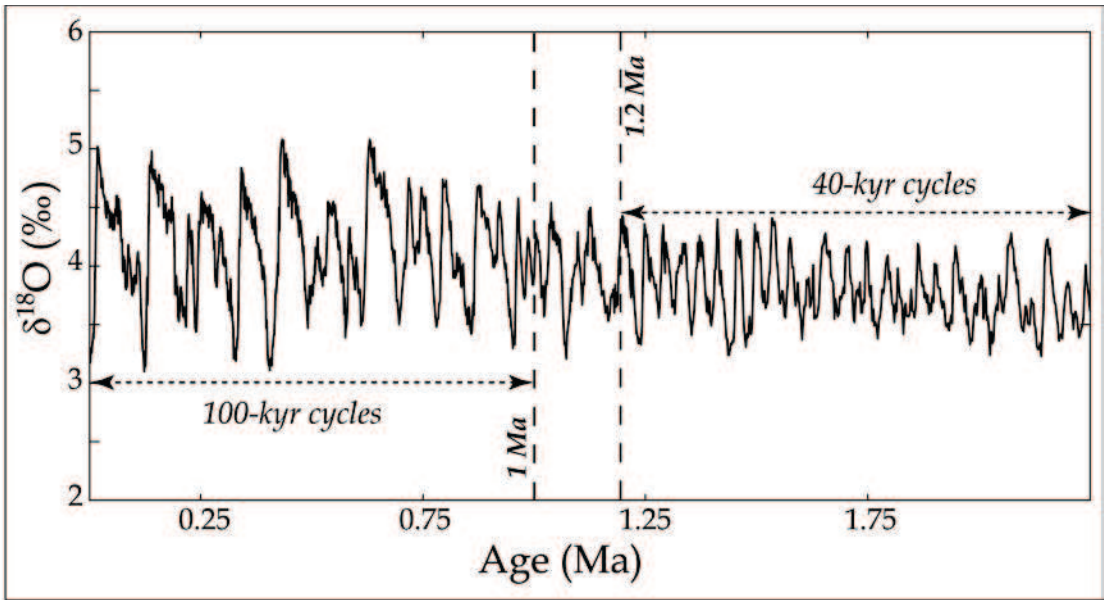

Figure IV.2.17. *Benthic $\delta^{18}O$ records [Lisiecki and Raymo, 2005] over the Pleistocene (~2.5 Ma to present-day), showing the glacial/interglacial climatic oscillations and the transition from symmetric 40-kyr to asymmetric 100-kyr cycles at around 1-1.2 Ma [e.g., Lisiecki, 2010].*

Figure IV.2.17 also shows that the 40-kyr and 100-kyr cycles differ not only in total and glacial versus interglacial time-extents, but they are also clearly different regarding climatic amplitudes. Averaged glacial/interglacial climatic variability in benthic $\delta^{18}O$ values is 1.4 ±0.3 and 0.7 ±0.2 ‰ for the 100-kyr and 40-kyr cycles, respectively. Moreover, $\delta^{18}O$ values (Figure IV.2.17) suggest that 40-kyr and 100-kyr interglacial periods were on average similar in terms of climatic conditions (3.4 ±0.1 and 3.4 ±0.2 ‰, respectively), while glacial periods clearly differ (4.1 ±0.2 and 4.8 ±0.2 ‰ for the 40-kyr and 100-kyr cycles, respectively). Consequently, the onset of 100-kyr cycles would have promoted both long-lived and larger glacier extents [*e.g.*, *Muttoni et al.*, 2003]. Considering the benthic $\delta^{18}O$ records to be representative at first order of the Alpine *ELA* variations, these results may imply maximum paleo-*ELA* shifts that were twice lower during the 40-kyr cycles compared to late Pleistocene glacial/interglacial oscillations; this difference can explain the observed Alpine relief development [*Haeuselmann et al.*, 2007; *Valla et al.*, submitted, a] associated with the initiation of larger ice extents during 100-kyr cycles. Further investigations combining climatic, geochronological and erosion constraints with ice-dynamics numerical modeling would help to quantitatively assess this hypothesis.

IV.3 - Post-glacial fluvial erosion in the Ecrins-Pelvoux massif (Western Alps)

IV.3.1 - Fluvial incision into bedrock: insights from morphometric analysis and numerical modeling of gorges incising glacial hanging valleys (western Alps)

Pierre G. Valla [1], Peter A. van der Beek [1], and Dimitri Lague [2]

[1] *LGCA-OSUG, Université de Grenoble, CNRS, BP 53, F-38041 Grenoble, France*

[2] *Géosciences Rennes, Université Rennes 1, Campus de Beaulieu, 35042 Rennes, France*

Abstract

Bedrock gorges incising glacial hanging valleys potentially allow measurements of fluvial bedrock incision in mountainous relief. Using digital elevation models, topographic maps and field reconnaissance, we identified and characterized 30 tributary hanging valleys incised by gorges near their confluence with trunk streams in the Romanche watershed, French Western Alps. Longitudinal profiles of these tributaries are all convex and have abrupt knickpoints at the upper limit of oversteepened gorge reaches. We reconstructed initial glacial profiles from glacially polished bedrock knobs surrounding the gorges in order to quantify the amount of fluvial incision and knickpoint retreat. From morphometric analyses, we find that mean channel gradients and widths, as well as knickpoint retreat rates, display a drainage-area dependence modulated by bedrock lithology. However, there appears to be no relation between horizontal retreat and vertical downwearing of knickpoints. Assuming a post-glacial origin of these gorges, our results imply high post-glacial fluvial incision (0.5-15 mm y^{-1}) and knickpoint retreat (1-200 mm y^{-1}) rates that are, however, consistent with previous estimates. Numerical modeling was used to test the capacity of different fluvial incision models to predict the inferred evolution of the gorges. Results from simple end-member models suggest transport-limited behavior of the bedrock gorges. A more sophisticated model including dynamic width adjustment and sediment-dependent incision rates predicts present-day channel geometry only if a significant supply of sediment from the gorge sidewalls (~10 mm y^{-1}) is triggered by gorge deepening, combined with pronounced inhibition of bedrock incision by sediment transport and deposition.

IV.3.1.1 - Introduction

The relative efficiency of glacial, fluvial and hillslope processes operating in orogens remains poorly constrained and improved empirical as well as physically-based models are needed [*e.g.*, *Hallet*, 1996; *Whipple et al.*, 2000a] to better constrain the role of surface processes in relief development. During Quaternary times, most mountain belts have experienced glaciations; transitions between glacial and interglacial periods have led to landscape disequilibrium governed by both glacial and fluvial processes. In this context, it appears difficult to assess clearly which processes most strongly control the current transient landforms, as few authors have studied the relative efficacy of glacial versus fluvial erosion [*Whipple et al.*, 1999; *Brocklehurst and Whipple*, 2002; *Montgomery*, 2002; *Naylor and Gabet*, 2007, *Amerson et al.*, 2008; *Koppes and Montgomery*, 2009].

Bedrock gorges are frequent features in fluvial and post-glacial landscapes [*e.g.*, *Weissel and Seidl,* 1998; *Crosby and Whipple,* 2006; *Korup and Schlunegger,* 2007], illustrating the potential of fluvial or subglacial erosion in relief evolution. Such gorges are commonly interpreted as transient features [*Schlunegger and Schneider*, 2005]; their origin and evolution can be explained by different processes. Bedrock gorges can be formed by fluvial incision in response to base level change [*Loget et al.*, 2006; *Harkins et al.*, 2007], multiple climate oscillations leading to transience between glacially and fluvially dominated landscapes [*Schlunegger and Schneider*, 2005], or by subglacial erosion [*Alley et al.*, 2003]. These processes are all active in mountain areas and quantitative landscape analysis is required to identify their relative importance and topographic signatures [*Brocklehurst and Whipple*, 2002] as well as the timing of gorge initiation and evolution.

In this paper, we study bedrock gorges incising glacial hanging valleys in the French Western Alps, with the aim to quantify gorge incision. Hanging valleys are found in many fluvial or glacial contexts and occur at tributary junctions with the trunk valley [*e.g.*, *Anderson et al.*, 2006; *Wobus et al.*, 2006a]. In fluvial landscapes, they occur mainly in actively uplifting areas and reflect contrasts in discharge and sediment flux between trunk and tributary channels, although contrasting views have been expressed concerning their formation [*Wobus et al.*, 2006a, *Crosby et al.*, 2007; *Lamb et al.*, 2008a; *Goode and Burbank*, 2009]. In glacial contexts, hanging valleys are explained by the dependence of glacial erosion rates on ice flux (and thus glacial drainage area) and reflect the relative incision capacity between the trunk

and tributary glaciers [*MacGregor et al.*, 2000; *Amundsson and Iverson*, 2006]. The origin of hanging valleys in the western Alps is generally considered to be glacial. Steep bedrock gorges incise these hanging valleys, some of which are associated with waterfalls and others with step-pool morphology [as defined by *Montgomery and Buffington*, 1997; *Wohl and Merritt*, 2001].

Both the origin and longevity of such gorges throughout Quaternary times are still poorly constrained. They can be seen as old landscape elements the incision of which was initiated at the beginning of glacial-interglacial cycles; or they may result from post-glacial incision [*Valla et al.*, 2010a] since ice retreat after the Last Glacial Maximum at ~20 ky. *Korup and Schlunegger* [2007] have tackled this issue by quantifying the role of bedrock landsliding in inner gorge incision. Their results show strong hillslope-channel coupling during the evolution of inner gorges; these authors conclude that a pre-glacial origin for at least some of the gorges is plausible, but that post-glacial rejuvenation affected most of the gorges. *Valla et al.* [2010a] recently reported cosmogenic data that imply Holocene (<10 ky) incision for a single bedrock gorge (the Diable gorge, also studied here), supporting the hypothesis of a post-glacial origin.

Here, we focus on incision processes of fluvial gorges into glacial hanging valleys. Longitudinal profiles of these valleys reveal abrupt breaks in slope (*i.e.*, knickpoints) and well developed oversteepened reaches. The geomorphic setting of these knickzones allows reconstruction of initial knickpoint position and height constraining bedrock incision in response to base-level fall by quantifying knickpoint behavior [*e.g.*, *Bishop et al.*, 2005; *Loget et al*., 2006; *Harkins et al.*, 2007].

In the following, we characterize fluvial incision of these gorges through morphometric analysis, in particular by studying knickpoint form and valley slope and width adjustments accommodating gorge incision. We then test the ability of different 1-D fluvial incision models to predict present-day gorge profile and channel geometry. Our results suggest that multiple processes are associated with gorge evolution and show that predictions of fluvial incision models should be considered with caution. Finally, we discuss the implications of our results for gorge incision and landscape evolution and review potential research needs to better constrain the origin of these gorges.

IV.3.1.2 - Study area

IV.3.1.2.1 - Geological and structural context

We focus on the Ecrins-Pelvoux, Belledonne, Taillefer, and Grandes Rousses massifs, which belong to the "external crystalline massifs" of the French Western Alps (Figure IV.3.1). They consist of European crystalline basement blocks that were exhumed along crustal-scale faults [*Ford*, 1996; *Dumont et al*., 2008] and are separated by remnants of inverted Jurassic extensional basins. The external massifs contain some of the highest peaks in the Alpine orogen, with several summits close to or higher than 4000 m (Figure IV.3.1). Although their exhumation started during Oligocene-Early Miocene times [*Leloup et al*., 2005] several kilometers of denudation have occurred since the Pliocene [*Vernon et al.*, 2008 and references therein] and present-day rock uplift rates reach up to 1 mm y^{-1} [*Jouanne et al.*, 1995; *Kahle et al.,* 1997]. Several authors have argued that rock uplift may be due to isostatic rebound in response to deglaciation [*Gudmundsson*, 1994] or high erosion rates during Pliocene-Quaternary times [*Cederbom et al.*, 2004; *Champagnac et al.*, 2007]; this question, however, remains debated.

The massifs studied here are bordered by major valleys that separate basement areas from “subalpine” massifs consisting of Mesozoic sedimentary sequences. In our study area, crystalline massifs are limited to the north by the Isère (or Grésivaudan) valley, to the west by the Drac valley, and to the south-east by the Durance valley. The studied massifs are separated from each other by deeply incised valleys (Romanche, Eau d’Olle and Vénéon), the planform drainage network of which appears to be controlled by structural and lithological trends.

IV.3.1.2.2 - Geomorphic setting

Present-day landscape features reveal that the French Western Alps were extensively glaciated during Quaternary times and the landscape is currently affected by efficient post-glacial fluvial erosion [*e.g.*, *Brocard et al.*, 2003]. Major valleys (*e.g.*, Grésivaudan and Durance) surrounding the crystalline massifs were occupied by large valley glaciers, which have widened and overdeepened them [*Montjuvent*, 1978]. Glacial overdeepenings were subsequently filled by late-glacial and post-glacial lake sediments [*Hinderer*, 2001; *Nicoud et*

al., 2002]. Valleys within the major massifs are much narrower but also reflect a strong glacial imprint. Their longitudinal profiles show a succession of characteristic valley steps and flats [*Montjuvent*, 1978] and create a high-relief landscape, with valley bottoms at around ~1000 m and summits over 4000 m elevation. The main trunk valleys show characteristic glacial U-shapes for the central part of the Romanche Valley (Bourg d'Oisans trough) and the lower Vénéon and Eau d'Olle valleys. Tributary hanging valleys also show a glacial U-shaped morphology (Figure IV.3.2-a, c) with polished surfaces ("roches moutonnées"). Hanging valley terminations are commonly marked by a bedrock gorge that indicates substantial incision, although smaller hanging tributary valleys may terminate in free-falling waterfalls (Figure IV.3.2).

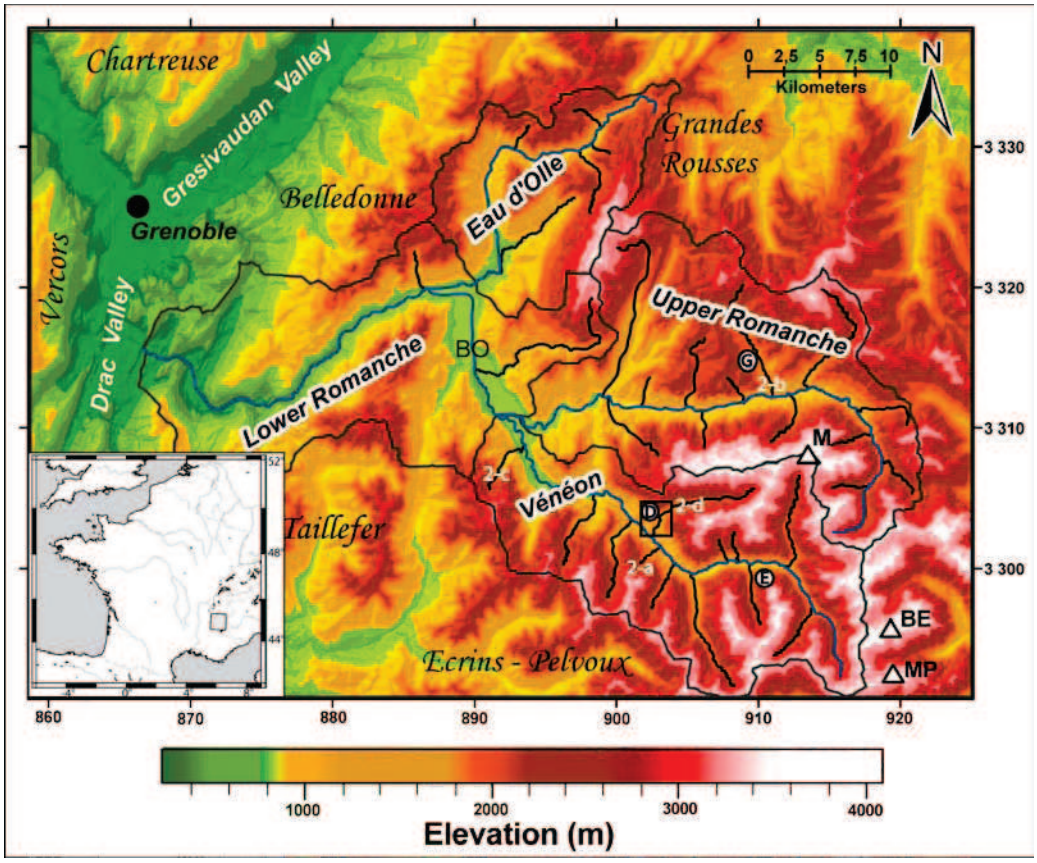

Figure IV.3.1. *Digital Elevation Model (Institut Géographique National, 50-m resolution) of the study area showing different major watersheds and selected tributaries, regional massifs and major summits (M: La Meije - 3983 m; BE: Barre des Ecrins - 4102 m; MP: Mont Pelvoux - 3943 m). Blue lines: trunk streams; thin black lines: tributary streams with gorges and knickpoints used in this analysis; thick gray lines: catchment boundaries. Locations of views shown in Fig. IV.3.2 (2-a, 2-b, 2-c and 2-d) and of Diable (D), Etages (E) and Gâ (G) streams are indicated. Small box indicates location of Fig. IV.3.4-b. B.O.: Bourg d'Oisans glacial trough. Eastings and northings are according to the IGN Lambert-III grid, in kilometers. Inset shows location within France with latitude and longitude.*

For our morphological analysis, we focused on the Romanche watershed (~1200 km²) which mainly drains the Ecrins-Pelvoux massif, but also the Taillefer, Grandes Rousses and Belledonne massifs in its lower part and via its tributaries. The Romanche watershed has been divided into four catchments (Figure IV.3.1): Upper Romanche (~360 km²), Vénéon (~320 km²), Eau d'Olle (~170 km²) and Lower Romanche (~350 km²). The Romanche river, the main river of the region, is ~85 km long and drains all previously cited crystalline massifs before connecting to the Drac river just south of Grenoble. The Vénéon river mainly drains the Ecrins-Pelvoux massif; the glacially overdeepened Bourg d'Oisans trough has formed immediately downstream of its confluence with the Romanche river. The Eau d'Olle river drains parts of the Belledonne and Grandes Rousses massifs and joins the Romanche river at the northern end of the Bourg d'Oisans trough. Although bedrock gorges also occur in surrounding areas like the Drac watershed, the Gresivaudan valley or the Vercors and Chartreuse massifs, we restrict our study to the Romanche watershed in order to maintain a homogeneous lithological and geomorphic setting, and thus avoid local complexities, such as differences in tectonic and glacial histories, in our analysis.

IV.3.1.3 - Data and methods

We used a 50-m resolution Digital Elevation Model (DEM) acquired from the *Institut Géographique National* to perform morphometric analyses on the Romanche watershed (Figure IV.3.1). First, we extracted the drainage pattern and longitudinal profiles for trunk valleys and their tributaries using TAS [*Lindsay*, 2005] and ArcMap GIS applications. We restricted our analysis to tributaries with characteristic glacial features and with drainage areas >1 km² to avoid potential complications for smaller catchments which mainly evolve through processes such as debris flows [*e.g.*, *Stock and Dietrich*, 2003], local mass movements or waterfall erosion.

Around thirty gorges were identified, mainly located in the Vénéon and Upper Romanche catchments because these constitute the most elevated parts of the Romanche watershed, but some also occur in the Eau d'Olle and Lower Romanche catchments (Figure IV.3.1).

Figure IV.3.2. *Field photos showing bedrock gorge morphologies (locations in Fig. IV.3.1). (a) View of a small glaciated catchment with a glacial hanging valley that ends in a waterfall (Cascade de la Pisse, Vénéon valley). (b) Detail of a gorge waterfall incising the sidewall of the trunk glacial valley (Saut de la Pucelle, Gâ gorge, Upper Romanche valley). (c) Confluence between hanging and trunk valley showing incised U-shaped glacial hanging valley form (Vallon stream, Vénéon valley). (d) Bedrock gorge channel, filled with meter-scale blocks, exhibiting step-pool morphology (Diable gorge, Vénéon valley).*

We followed several steps to extract morphometric information about gorge morphology. Due to the low resolution of the DEM (50 m) relative to gorge size (typical widths around 10 to 30 m), longitudinal profiles extracted from the DEM contain errors in channel locations and elevations, especially for the gorge location where several cells provide spurious values that strongly overestimate real channel elevations. We tried to correct these errors using topographic maps (10-m contour intervals). Although the maps may contain interpolation

errors, smoothing effects are much smaller than for the 50-m DEM; moreover extracted profiles are coherent with our field (handheld GPS) data on channel locations and elevations. River profiles show the same morphological pattern: a concave upper reach with a succession of steps and flats characteristic of a glacially-perturbed profile, followed by a convex and steep lower gorge reach (Figure IV.3.3). The two reaches are separated by clearly defined knickpoints.

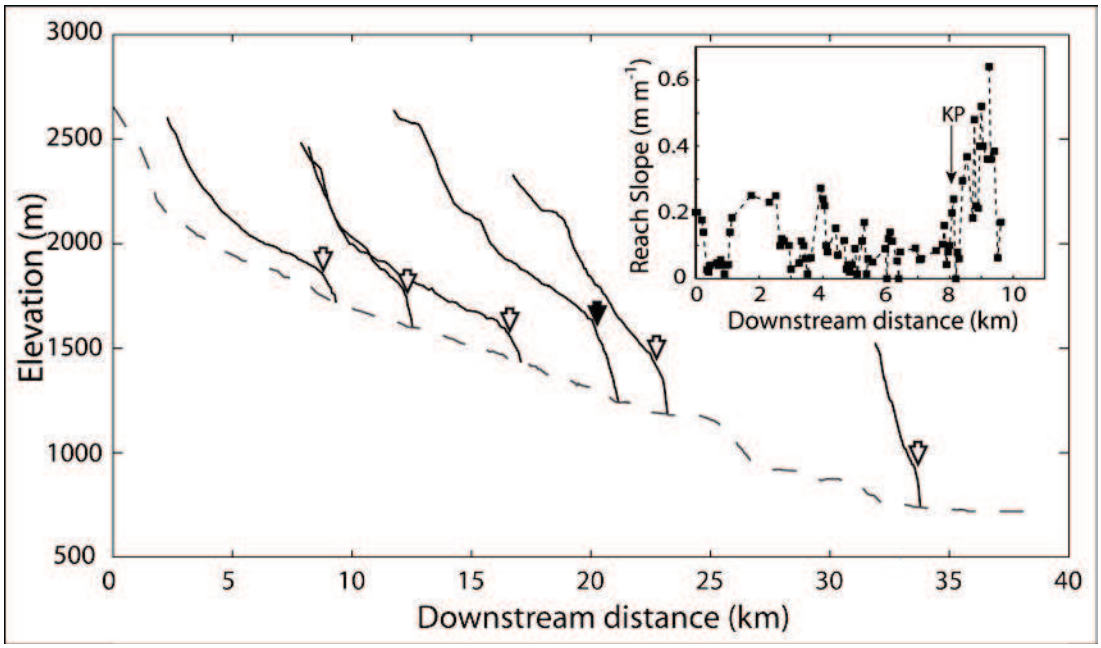

Figure IV.3.3. *Longitudinal profiles of main tributaries (continuous curves) and the Vénéon trunk stream (dashed curve). Arrows mark locations of knickpoints at upstream ends of gorges. Inset shows slope-distance plot with knickpoint (KP) marking the upper limit of the oversteepened gorge reach for the Diable stream (marked by the black arrow on the main frame).*

We pinpointed knickpoint locations and oversteepened (gorge) reaches as accurately as possible on each river profile. To achieve this, we used logarithmic slope-distance diagrams for each tributary. Such plots provide similar information as more generally used slope-area plots; however we chose to use this kind of diagram for more direct comparison with the long profiles. Knickpoint locations and total gorge lengths can easily be obtained from this kind of plot [*Brocard et al.,* 2003; *Bishop et al.,* 2005; *Goldrick and Bishop,* 2007].

As an example, Figure IV.3.3 shows a slope-distance diagram for the Diable stream in the Vénéon catchment. The gorge reach is not marked by a single knickpoint; rather, the gorge profile shows several knickpoints that mark a well-developed oversteepened reach. We thus

identify for each tributary the location of the first major knickpoint, *i.e.*, the beginning of the oversteepened gorge reach (Figure IV.3.3). This knickpoint location will be used as the reference for quantifying stream profile evolution during gorge incision, for which we quantify lateral retreat and potential vertical downwearing of the knickpoint (Figure IV.3.4-a).

We completed our morphological study with direct channel observations. For three accessible streams (Etages, Diable and Gâ; see Figure IV.3.1 for locations), we measured gorge widths (10-15 measurements) along the stream profile using a laser-range distance-meter so as to detect possible adjustments in channel geometry accompanying gorge incision [*Duvall et al*., 2004; *Finnegan et al.*, 2005; *Whittaker et al.,* 2007]. We measured channel width directly both upstream and downstream of the gorge reaches. Access to the gorges themselves was much more difficult due to steep sidewalls. Consequently, most width measurements were performed at the tops of the gorges, except for a few locations along the Diable stream where direct access to the gorge channel was possible.

Potential errors in our measurements need to be considered. For drainage areas, we quantified the perimeter/area ratio for studied watersheds and expect errors to be less than 5%. Profiles contain errors that cannot easily be quantified but may strongly influence our morphometric results and thus our interpretation.

We expect errors to be less than ±50 m for horizontal locations (*i.e.*, the DEM resolution).However, elevation errors may be important because grid cells of the DEM are larger than gorge widths and may not fall within the gorge. Expected elevation errors can be quite high (*i.e.*, ±30 m, which can be important compared to gorge depth). Gradient estimates were obtained by different methods. We calculated the mean slope of each gorge by averaging slope along the entire gorge profiles. Local slope estimations were determined for each location where we made channel width measurements. For these estimations, we calculate the finite difference for one DEM-cell upstream and downstream of the location and obtained an average value of the local slope. For both slope estimations, we expect errors to be around 20% due to the combined errors in locations and elevations. We made multiple acquisitions for each width measurement and obtained variations less than 0.5 m. Our acquisition method combined with the relatively high resolution of the laser-range distance-meter lead us to assume maximum errors of ±1 m on width measurements.

For each studied tributary, we reconstructed "initial" profiles that define the landscape before fluvial incision; these are crucial for constraining the initial glacial knickpoint position, and consequently the amount of fluvial incision and knickpoint retreat since gorge initiation. For the upper reach of the tributary, we took the present valley floor as a proxy for the initial profile and extrapolated it by fitting a power law to the profile of the upper reach data. The upper "glacial" reaches generally contain several minor knickpoints; for this reason we fitted our power law regression to the first concave reach upstream of the gorge only (Figure IV.3.4-a). We implicitly assume an "equilibrium" profile for these reaches (several hundred meters to kilometers in length depending the tributary), which may provide an objective proxy for the initial glacial valley floor.

Topography close to the gorge has been strongly influenced by gorge deepening and cannot be taken as a reference for the initial glacial profile. Therefore, the downstream ends of the initial profiles were reconstructed using glacially polished bedrock knobs surrounding the gorges (recognized from aerial photographs and field reconnaissance; Figure IV.3.4-b), assuming that these glacial landforms have not been eroded since the last glacial retreat. The very abrupt break in slope in the glacial profile is in agreement with observed profiles of recently deglaciated hanging tributaries [see, for instance, Figure 1 in *MacGregor et al.*, 2000].

These reconstructions assume that trunk stream profiles have not been significantly modified since the last glacier retreat. Trunk streams have typically perturbed transient profiles (see Figure IV.3.3) with numerous flats and steps. However, except for some steps where significant incision has occurred, most trunk valleys contain braided streams with an alluvial cover, suggesting they have experienced significant sediment infill (with up to 100 meters of sediment thickness in some reaches) since the last glacier retreat. Trunk valley floors currently appear to be mostly characterized by sedimentation and transport. However, without additional geophysical data we are unable to accurately map this sediment infill of trunk valleys except for some locations. Thus, boundary conditions for gorge deepening (*i.e.*, the base level of trunk streams) may have varied by an unknown amount since deglaciation. This may add an error to the determination of the tributary hang height and can also be important for our numerical modeling, as we consider the tributary outlet as fixed (see section IV.3.5.2).

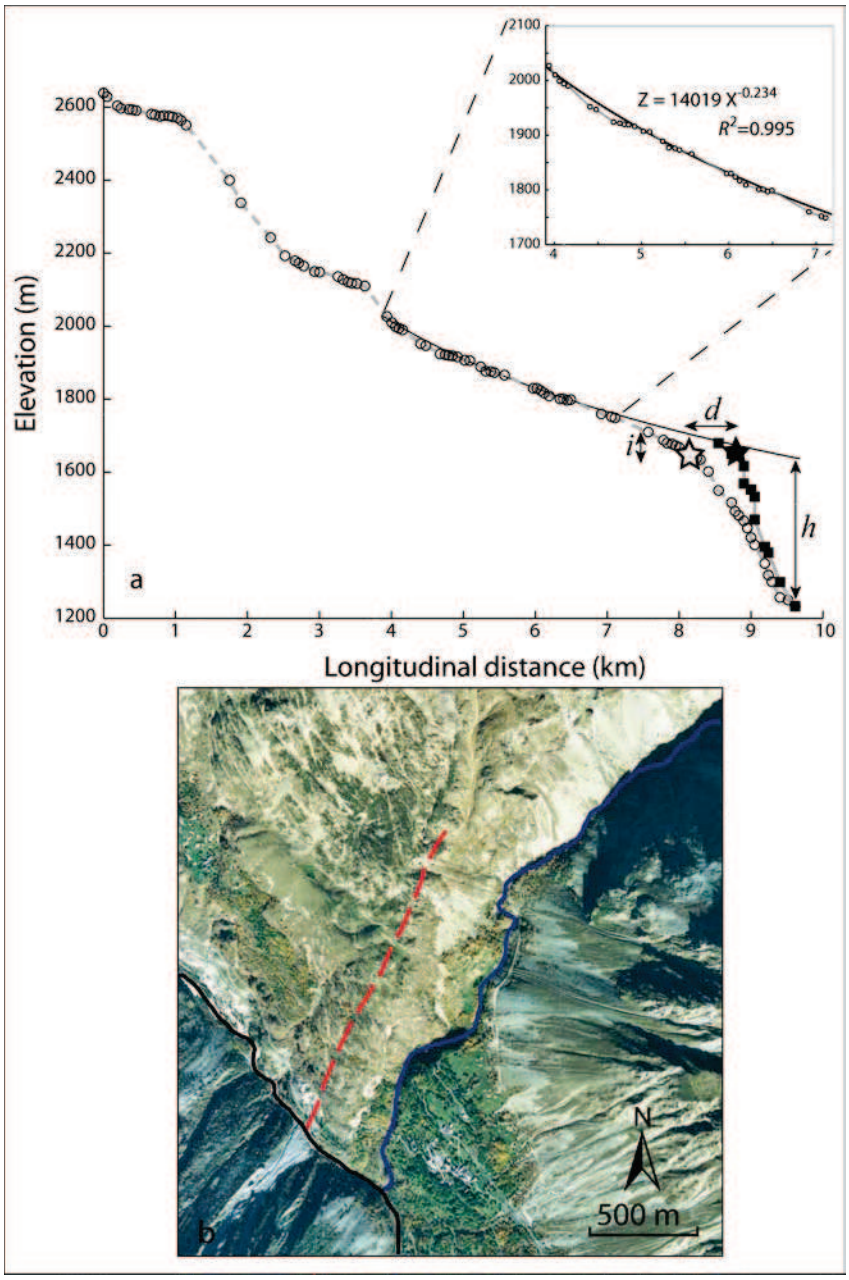

Figure IV.3.4. *Longitudinal profiles and aerial photograph illustrating reconstruction method for the initial conditions and morphometric data used in our analysis (d: knickpoint retreat; h: height of tributary valley hang; i: knickpoint downwearing). a) Diable stream profile (open circles and grey dashed curve) and present-day knickpoint (white star) extracted from DEM and topographic map (see Fig. IV.3.2 for location). Inset shows extrapolated glacial valley floor (black solid curve) obtained by power law fit on "equilibrium" reach immediately upstream of gorge ($Z = 14019\ X^{-0.234}$, $R^2=0.995$). Glacial profile end (black squares and grey curve) and initial glacial knickpoint (black star) are also shown. b) Aerial photograph (Institut Geographique National) of the Diable stream (blue curve) and glacial morphology (red dashed curve) used to reconstruct the initial glacial profile. Black line indicates Vénéon trunk stream. See text for discussion.*

IV.3.1.4 - Morphometric analysis of bedrock gorges

IV.3.1.4.1 - Knickpoint origin

We assumed in our introduction that all knickpoints have a glacial origin through the formation of glacial hanging valleys. We based this statement on qualitative field evidence of glacial morphology. Here, we use morphometric analyses to support this inference, by comparing hanging valley heights (*i.e.*, the elevation difference between tributary and trunk valley bottoms) with the contrast in glacial erosion capacity of the trunk and tributary valleys [*MacGregor et al.*, 2000]. Glacial erosion rates are partly controlled by ice discharge [*Anderson et al.,* 2006], which can be approximated to a first order by drainage area [*Amundson and Iverson*, 2006]. We use the reconstructed initial knickpoint elevation with respect to the trunk valley floor as a proxy for the tributary valley hang height. Figure IV.3.5 shows that for all catchments (occurring both in sedimentary and crystalline lithologies), tributary hang heights appear to be correlated with the ratio of trunk/tributary drainage areas (all correlations except for Eau d'Olle are statistically significant at the 95% confidence level). This analysis supports the glacial origin of gorge knickpoints. It also suggests that lithology may influence the dependence of hang height on the ratio of drainage areas, as the power law exponent on the hang-height/drainage-area ratio relationship appears to be higher for valleys incising sedimentary rocks (0.36 ±0.19 (standard deviation) for the Romanche and 0.32 ±0.10 for the Eau d'Olle, Figure IV.3.5-b) than for valleys on crystalline basement (0.20 ±0.07 for the Romanche and 0.23 ±0.16 for the Vénéon, Figure IV.3.5-a). Although these ranges overlap because uncertainties in the hang heights are large (±60 m) and the number of data points is relatively low, they provide some support to the notion that glacial erosion is dependent on bedrock resistance [*Harbor*, 1995].

IV.3.1.4.2 - Bedrock gorge channels

Gorges represent highly incised and steep bedrock channels with scarce sediment deposits (see Figures IV.3.2-b, d). In their upper reaches, some channels have an alluvial cover inherited from sediment filling after glacial retreat, but this sediment cover rapidly disappears at the upstream entrance of the gorge. However, meter-scale blocks derived from the gorge sidewalls by major rockfalls are frequent in the channel (see Figure IV.3.2-d) and may partially protect bedrock from stream incision.

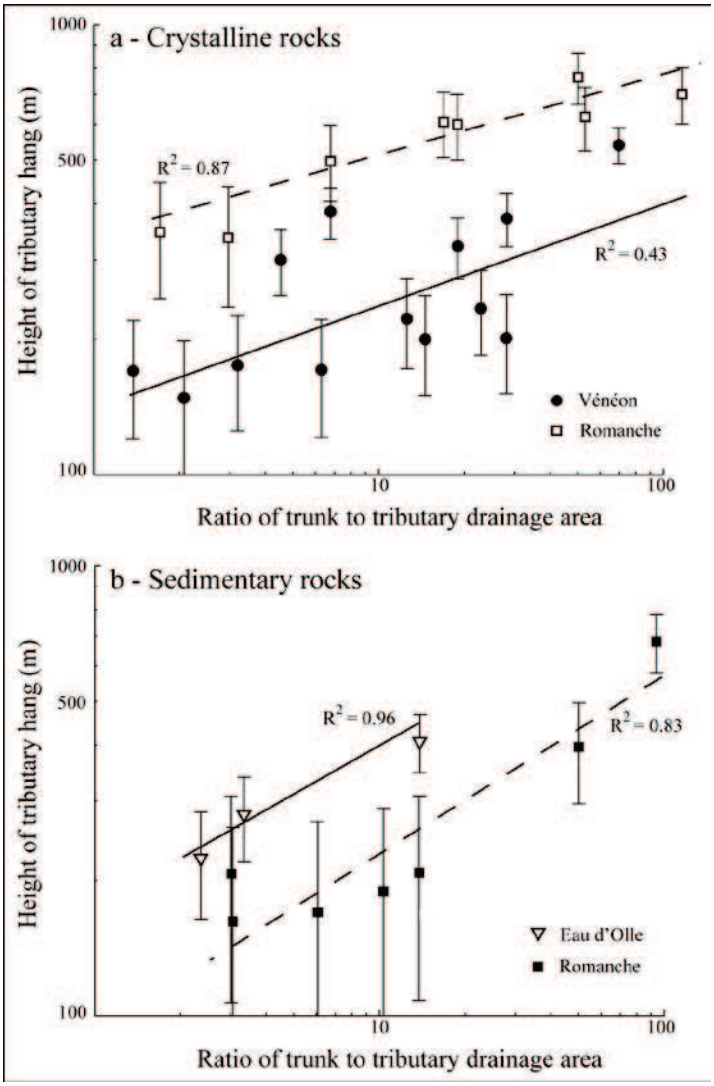

Figure IV.3.5. *Logarithmic plot showing height of tributary valley hang as a function of ratio of tributary to trunk drainage area for a) tributaries on crystalline basement (power law exponent of 0.20 ±0.07 for Romanche and 0.23 ±0.16 for Vénéon); b) tributaries draining sedimentary lithologies (power law exponent of 0.36 ±0.19 for Romanche; 0.32 ±0.10 for Eau d'Olle). Errors on tributary heights (±60 m) are indicated.*

Active gorge channels show typical bed morphologies with step-pools, boulder cascades (*e.g.*, Figure IV.3.2-d), and fluvial abrasion features such as smooth and polished bedrock surfaces, ripples and potholes [*e.g.*, *Whipple et al.*, 2000a]. For gorges incising crystalline lithologies, these morphological features are well developed and remnants of ancient potholes can be seen along gorge sidewalls. Local gorge gradients suggest that bedrock incision can also occur during debris flows [*e.g.*, *Stock and Dietrich*, 2003]. However, field observations suggest that these are not the main process operating as fluvial abrasion forms are preserved in the active channel and debris-flow remnants are rare. Finally, amplified erosion due to flow acceleration

[*Haviv et al.*, 2006] or waterfall free-fall incision [*Lamb et al.*, 2007] may occur in gorge formation, but free-falling waterfalls currently occur only at the outlet of the smallest tributaries, where the glacial knickpoint has hardly retreated because the upstream drainage area is quite small. We thus suggest that this process might be restricted to the early stages of the gorge incision or to small tributaries.

Because the studied gorges are located at the confluence between glacial hanging and trunk valleys, the gorge morphology can be influenced by either trunk or tributary valley dynamics such as fluvial aggradation/incision or slope processes. Figure IV.3.6 shows that, although we study tributaries from different catchments, there is a clear correlation between tributary drainage area and mean gorge gradient; hanging valleys with large drainage areas exhibit gentler averaged gorge gradients than smaller tributaries (the correlations are significant at the 95% confidence level). In contrast, we do not find any correlation between trunk drainage area and gorge gradient, which suggests that mean gorge gradients do not show any influence of the trunk valley; however they reflect the greater erosional capacity of larger tributaries [*Wobus et al.*, 2006a].

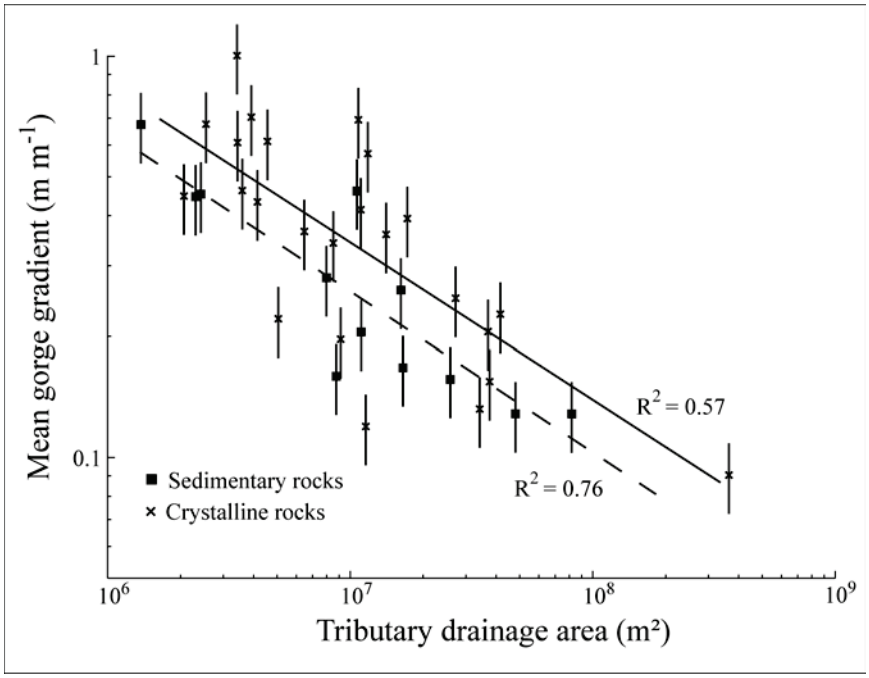

Figure IV.3.6. *Logarithmic plot showing the relation between mean gorge gradient and tributary drainage area. Note that for similar drainage areas crystalline lithologies (crosses and black curve) present higher gradients than sedimentary lithologies (squares and dashed curve) even though the slope exponent of the correlation is the same (Crystalline: -0.40 ±0.14; Sedimentary: -0.41 ±0.15). Errors of ±20% for averaged gorge slope are indicated.*

Figure IV.3.6 also shows lithological effects on gorge gradient; although all gorges follow the same inverse correlation between mean gradient and tributary drainage area (the power law exponent is -0.40 ±0.14 for crystalline lithologies and -0.41 ±0.15 for sedimentary rocks), gorges incising sedimentary rocks have lower mean slopes than those in crystalline basement for similar upstream drainage area. This observation might suggest that gorge gradients are modulated by lithology, although this difference is not statistically significant as the two datasets overlap. The link between gorge gradient and trunk drainage area may also reflect conditions inherited from glaciations during which larger tributaries acquired smaller hang height because of more similar glacial erosion with the trunk valley. This difference may have been enhanced by post-glacial fluvial processes since deglaciation, the larger tributaries reflecting faster knickpoint retreat than smaller ones (see section IV.3.4.3 and Figure IV.3.8).

Measured local width variations (Etages, Diable and Gâ, Figure IV.3.7) indicate an inverse correlation between channel widths and estimated local slopes. For all three streams, largest widths were encountered in the upstream reaches of the profiles (the glacial valley floor), characterized by very gentle slopes (<0.01 m m^{-1}). Here, the streams incise fluvio-glacial sediments and braid across the valley floor. When entering the gorges, the streams start incising bedrock; channel widths are greatly reduced (up to 10 times) and are associated with higher slopes. Width measurements were easier for the upper reaches of the profiles because channel banks are clearly marked by sediment terraces in these reaches. Measurements within the gorge were much more difficult to make, as previously discussed. When measuring gorge width from the top of the gorges, we assume that active channel widths are close to the top widths, *i.e.*, gorge sidewalls are close to vertical and the channel fills the gorge floor. Keeping these methodological limitations in mind, we show that the three streams exhibit the same trend between local slope and channel width (Figure IV.3.7).

Moreover, the data suggests that regression slopes are modulated by drainage area. For the Etages, which is the smallest basin (14 km²), the slope coefficient is higher in absolute value (1.23 ±0.36) than for the Diable (0.59 ±0.21) and the Gâ (0.23 ±0.09), which have larger drainage areas (20 and 42 km², respectively). Channel width thus appears to be both influenced by local slope variations and dependent on the stream discharge, illustrating dynamic channel evolution along the gorge to sustain incision [*Finnegan et al.,* 2005; *Wobus et al.*, 2006b]. We suggest that these channel adaptations accompanying fluvial incision have strong implications for water and sediment flow through the gorge and thus have consequences for gorge deepening.

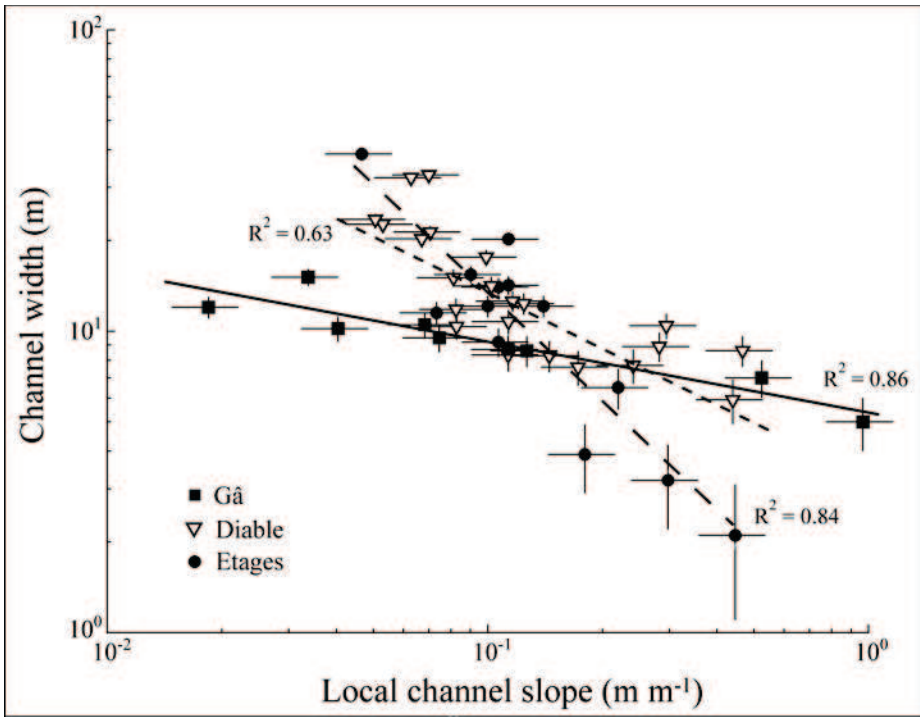

Figure IV.3.7. *Channel width and slope variations (logarithmic plot) for the Etages (circles and dashed curve), Diable (inverted triangles and dot curve) and Gâ (squares and solid curve) streams. Note that the exponent of the power-law correlation between local gradient and channel width (Etages: -1.23 ±0.36; Diable: -0.59 ±0.21; Gâ: -0.23 ±0.09) appears to be modulated by tributary drainage area (Etages: 14 km²; Diable: 20 km²; Gâ: 42 km²). Errors on slope (±20%) and width (±1 m) values are indicated.*

IV.3.1.4.3 - Knickpoint distribution and characteristics

Knickpoint evolution can operate through different ways depending on climatic and tectonic context or basement lithology [see *Gardner*, 1983 and *Frankel et al.*, 2007 for detailed discussions]. In our introduction, we have assumed coeval knickpoint evolution for all studied tributaries, *i.e.*, that glacial retreat has been rapid and synchronous on the scale of the Romanche watershed. Here, we interpret knickpoint evolution to start from an abrupt glacial knickpoint that wears back by fluvial processes (Figure IV.3.4-a). Our morphometric analysis indicates that both vertical downwearing and horizontal retreat of knickpoints take place during gorge incision.

The amount of knickpoint retreat is correlated with tributary drainage area (Figure IV.3.8). This dependence has been described in other fluvial settings [*Hayakawa and Matsukura*, 2003; *Bishop et al.*, 2005; *Crosby and Whipple*, 2006; *Berlin and Anderson*, 2007; *Lamb et*

al., 2007] and is consistent with fluvial incision models in which incision and knickpoint retreat rates are dependent on drainage area [*e.g.*, *Whipple and Tucker*, 1999]. The relationships shown in Figure IV.3.8 also suggest that the regression slope is the same for sedimentary and crystalline lithologies (0.83 ±0.17 for crystalline basement and 0.79 ±0.39 for sedimentary rocks). Moreover, assuming a coeval knickpoint evolution, it appears that knickpoint retreat rates are higher in sedimentary lithologies than in crystalline rocks for similar drainage areas (Figure IV.3.8); this difference is statistically significant at the 95% confidence level.

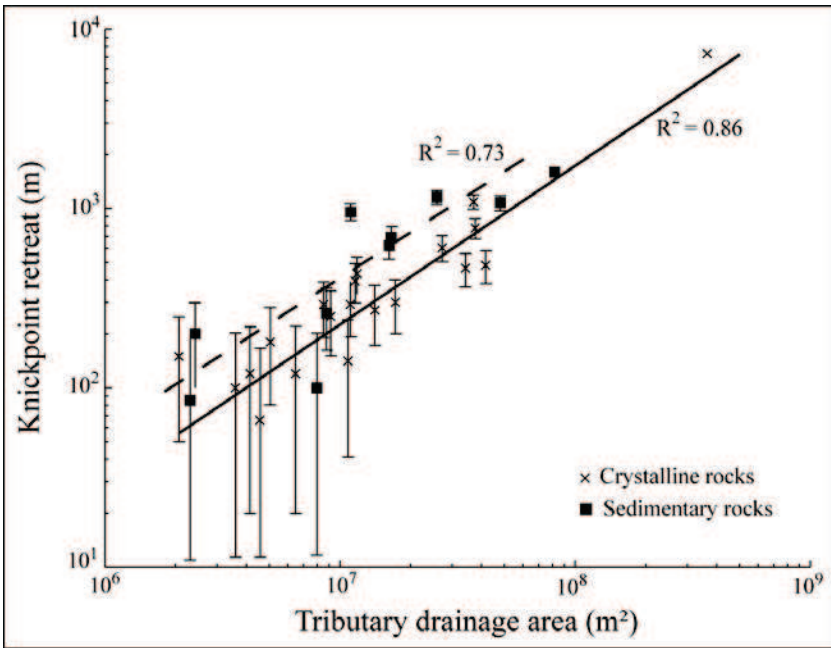

Figure IV.3.8. *Logarithmic plot of knickpoint retreat versus tributary drainage area for all selected gorges. Note that for similar drainage areas, knickpoint retreat is less in crystalline lithologies (crosses and solid curve) than in sedimentary lithologies (squares and dashed curve), even though the exponent of the power-law correlation is the same (Crystalline: 0.83 ±0.17; Sedimentary: 0.79 ±0.39). Single very large catchment (2×10^8 m²) is upper Romanche River and Infernet gorge upstream of junction with Vénéon (cf. Fig.IV.3.1). Errors on knickpoint retreat (±100 m) are indicated.*

As previously noted, vertical downwearing of knickpoints is more ambiguous due to large errors on elevations (see section IV.3.3) and cannot be directly related to parameters describing either the trunk or the tributary valleys (Figures IV.3.9a-b).

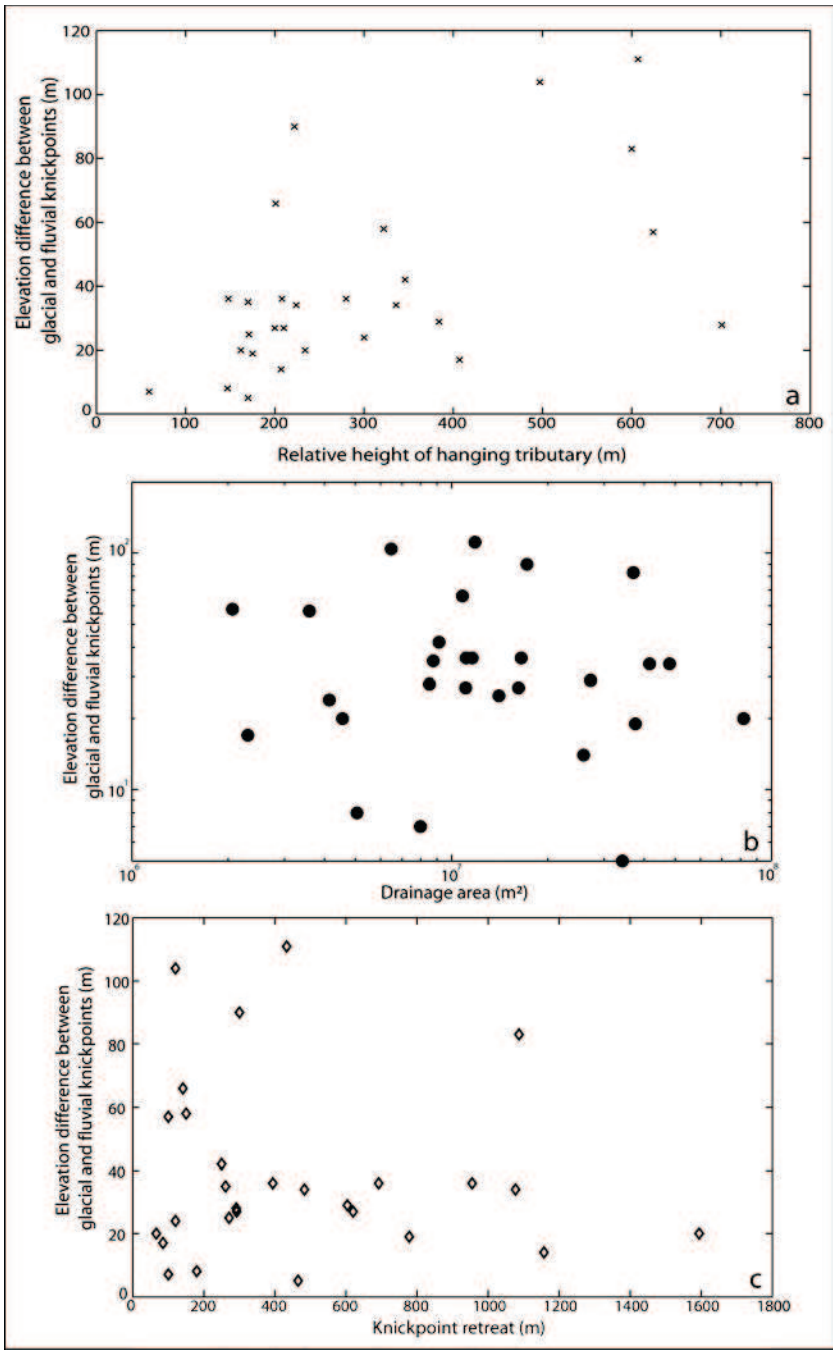

Figure IV.3.9. *Vertical lowering of tributary knickpoints versus (a) height of the tributary hang, (b) tributary drainage area and (c) knickpoint retreat. No clear correlations appear (see text for discussion). Note that elevation differences are between 0 and 120 m and thus relatively close to data resolution (±30 m).*

We suggest that this absence of correlation for vertical knickpoint evolution is due to two opposing controls: the initial knickpoint is higher for smaller tributaries (larger ratio of trunk/tributary drainage areas) but the erosion capacity of the tributary stream is higher for larger drainage areas. Moreover, no correlation is observed between vertical downwearing and horizontal retreat of knickpoints (Figure IV.3.9c). *Niemann et al.* [2001] suggested that

knickpoint elevations may be comparable for tributaries experiencing the same wave of incision from the trunk stream [*Harkins et al.*, 2007]. However, this is not the case for hanging valleys where gorge incision occurs in response to both the relative height difference between tributary and trunk streams and the tributary drainage area; we thus suggest that in these settings knickpoint elevation and its evolution cannot be used directly to quantify processes associated with gorge deepening [*Wobus et al.*, 2006a].

IV.3.1.5 - Constraints from fluvial incision modeling

In this section, we employ 1-D numerical modeling to test different fluvial erosion algorithms for gorge incision. We do not exhaustively review all existing fluvial incision models because this has already been done by several authors [*e.g.*, *Tomkin et al.*, 2003; *van der Beek and Bishop*, 2003]; we instead focus our study on three formulations that describe different processes for bedrock incision.

IV.3.1.5.1 - Fluvial incision models

Fluvial incision algorithms abound in the literature and are widely used for landscape evolution modeling. The most general models are based on the hypothesis that incision rate should be proportional to either total stream power, unit stream power, or basal shear stress [*Howard et al.*, 1994; *Whipple and Tucker*, 1999]. These formulations can be written using slope and drainage-area power laws as proxies for stream power, leading to the well-known "stream power law" for fluvial incision:

$$\dot{E} = K A^m S^n \qquad \text{(IV.3.1)}$$

where $\dot{E}$ is fluvial incision rate (m y^{-1}), K is a dimensional constant reflecting the resistance of the substrate to incision ($m^{(1-2m)}$ y^{-1}), S is local stream gradient (m m^{-1}), A is drainage area (m^2), and n and m are dimensionless exponents supposedly reflecting the physics behind the models [for further details, see *van der Beek and Bishop*, 2003], but possibly dependent on other factors such as discharge variability [*Lague et al.,* 2005]. For these models, width variations are assumed to be dependent on drainage area only ($W \sim A^{0.5}$) and are consequently implicitly incorporated in the incision algorithm. In their simplest form, stream power law models do not take into account sediment transport; bedrock incision rates are only limited by the stream power of the river and they are referred to as “detachment-limited” models [see *Whipple and Tucker*, 2002 for a discussion].

An alternative formulation for fluvial incision argues that bedrock incision rates could be limited by the river's capacity to transport and export eroded materials [*e.g.*, *Willgoose et al.*, 1991; *Tucker and Whipple*, 2002]. Such "transport-limited" models take sediments into account as a limiting factor for bedrock incision because stream power is expended in sediment transport. These models are based on the transport capacity Q_{eq} of the river, which is taken as a function of stream power:

$$Q_{eq} = K_s A^{m_s} S^{n_s} \qquad \text{(IV.3.2)}$$

where again K_s is a dimensional constant ($m^{(3-2m_s)}$ y^{-1}), and n_s and m_s are dimensionless exponents. This formulation assumes that the river is always at carrying capacity; spatial variations in the carrying capacity lead to incision or deposition. Incision rates are thus calculated by combining equation (IV.3.2) with the continuity equation:

$$\dot{E} = \frac{1}{W}\frac{\delta Q_s}{\delta \vec{x}} \quad ; \quad Q_s = Q_{eq} \qquad \text{(IV.3.3)}$$

where $\vec{x}$ is the flow direction and W the channel width (m). Unlike detachment-limited models, transport-limited models may take width variations and sediment transport along the stream explicitly into account. In our modeling, we include width variations by assuming that the slope-width relation currently observed along the gorge (Figure IV.3.7) is valid during the entire episode of gorge deepening.

Although the detachment- and transport-limited models are most generally used for landscape evolution modeling [*e.g.*, *Anderson,* 1994; *Willet*, 1999], they ignore several potentially important controls on fluvial incision, including thresholds and stochastic distributions of discharge [*e.g.*, *Tucker*, 2004, *Lague et al.*, 2005], dynamic adaptation of channel geometry [*e.g.*, *Finnegan et al.*, 2005; *Turowski et al.*, 2006; *Wobus et al.*, 2006b] and the interaction between sediment and bedrock [*e.g.*, *Sklar and Dietrich,* 1998, 2006; *Johnson et al.*, 2009]. Sediment supply and transport by the river can influence bedrock incision in two different ways: at low sediment fluxes, sediments impact the bedrock, providing efficient "tools" for erosion and increasing the incision capacity of the stream; large amounts of sediments, in contrast, partially cover and protect the bed from erosion [*e.g.*, *Sklar and Dietrich*, 2004].

We investigate these potential controls by using a new fluvial incision algorithm described extensively in *Lague* [2010]. As opposed to the simple end-member detachment- and transport-limited models, this model factors in various elements of the complexity of bedrock incision, including a stochastic variation of discharge and sediment flux at daily timescales, a separate calculation of bed and bank incision rate allowing width and slope to vary dynamically, and tracking of sediment transport and deposition in the channel to compute static and/or dynamic cover effects. Our objective in using this model is not to deliver a perfectly calibrated set of parameters, but rather to show the effect of taking into account these important but ill-understood controls on stream incision. As discussed in *Lague* [2010], many elementary ingredients of the numerical model are still only partially understood or are built on empirically derived laws (hydraulics, sediment transport, incision laws, mode and timing of sediment supply from hillslopes…). Yet, even with these limitations, we show that only a limited set of conditions of hillslope/channel coupling lead to the present-day profile geometry (slope, width and sediment thickness). We summarize the main features of the numerical model (referred to in the following as the "cover" model) and the boundary conditions used for gorge incision modeling in the Appendix (section IV.3.1.8). Details of the numerical procedure and the justification of chosen elementary laws of incision and transport are given in *Lague* [2010].

In the following, we assess these three different models in terms of their capability of adequately reproducing the present-day river longitudinal profiles and channel geometry of the studied gorges.

IV.3.1.5.2 - Modeling approach

We model three tributary streams (Diable, Etages and Gâ) for which we have both profile and width data. The starting condition for all numerical simulations is given by the reconstructed initial profile (see Figure IV.3.4-a); the present fluvial profile is taken as a reference to test the ability of our models to predict present-day gorge geometry. Both profiles are linearly interpolated to a uniform 5-m horizontal spacing. The variation of drainage area along the stream profiles is included using Hack's law ($A \sim k X^a$, where A is drainage area, X is distance from the divide, and k and a are fit constants). The fit constants in Hack's law were estimated for each stream using TAS [*Lindsay*, 2005]. This method assumes that the tributary drainage pattern has not changed since gorge initiation; this assumption seems reasonable for these

relatively small valleys that are delimited by high ridges and that are not joined by tributaries within the gorge.

For the transport-limited model, channel widths evolve through the width/slope relationship that was deduced from field observations (Figure IV.3.7); whereas in the cover model, the evolution of channel width is a model prediction for which initial conditions are those measured in the field just upstream of the gorge, assuming that they are proxies for the immediate post-glacial channel widths. Best-fit values for the controlling detachment-limited (K, n and m) and transport-limited (K_s, n_s and m_s) models are searched by comparing predicted and observed fluvial profiles. In the cover model, the parameters K_{ref}, K_{bank}, K_{sed}, ξ, v and Q_{wall} are set as free parameters during our modeling. Detachment- and transport-limited models are thus three-parameter models, whereas the cover model is a two-parameter model for calculating incision (K_{ref}, K_{bank}) when sediment effects are neglected, but for which we add four more degrees of freedom for sediment supply (from gorge sidewalls and surrounding hillslopes) and transport. Note however, that we have additional constraints for the cover model compared to the detachment- and transport-limited models, which only consider channel profile: cover model predictions compared to observed data include along-stream channel width and mean sediment thickness on the bed.

Numerical simulations are achieved by integrating the fluvial incision algorithms through time using a finite-difference technique with adaptive time stepping [*Press et al.,* 1992] for the detachment- and transport-limited models, and constant time step of 1 day for the cover model. The downstream boundary condition was fixed at the elevation of the tributary junction with the trunk stream throughout the model run. As discussed in section IV.3.3, this is a simplification as the trunk valleys may have been glacially overdeepened and filled by an unknown amount of post-glacial sediment. However, at all three tributary junctions, the trunk valley is relatively narrow and bedrock is widely exposed (cf. Figure IV.3.4-b for the Diable example). We thus believe that the fixed base-level assumption does not introduce major errors into our analysis. We assume for numerical modeling that bedrock gorges are purely post-LGM features based on recent cosmogenic data for one gorge [*Valla et al.*, 2010a]; all models are run for 20 ky, which is a rough estimate for the onset of glacial retreat in the Alps [*Hinderer*, 2001; *Ivy-Ochs et al.*, 2004]. However, the exact timing of onset of gorge incision is not critical for our simulations, as incision rates are linearly dependent on a dimensional constant in all models (K, K_s or K_{bank}/K_{ref}). Varying these constants leads to exactly the same

evolution of the gorges but at a different rate, except for the cover model where incision is more complex due to the incision threshold and sediment cover effect. We test model performance by calculating the root-mean-square (*RMS*) deviation between predicted and observed fluvial profile elevation (and thus stream incision) at the end of the simulations:

$$RMS = \sqrt{\frac{\sum_{i=1}^{n}\left(h_{obs,i} - h_{\mathrm{mod},i}\right)^2}{n}} \qquad \text{(IV.3.4)}$$

where n is the number of data along the profiles and h_{obs} and h_{mod} are observed and modeled present-day streambed elevations, respectively. A parameter search was performed for all models through a systematic trial-and-error process.

IV.3.1.5.3 - Model results and implications for gorge dynamics

We first report results for the stream power models as they constitute simple end-member fluvial incision laws before presenting modeling results for the cover model. For each model, we ran numerous trial-and-error simulations to constrain acceptable values of m and n (or m_s and n_s). For the detachment-limited model, m and n values characteristic for abrasion processes can be found in the literature [*Whipple et al.*, 2000a] and are expected to depend on the physical theory of the stream power law [see *van der Beek and Bishop*, 2003 for more details]. We thus chose to restrict m and n variations between [0.3;1.0] and [0.7;1.0] respectively which are the most common values for stream power models, although some studies [*e.g.*, *Stock and Montgomery*, 1999; *Kirby and Whipple*, 2001] have come up with m and n ranges that were much larger than theoretical predictions. The exponents m_s and n_s for the transport limited model are more difficult to constrain and for simplicity many studies have chosen unity values for m_s and n_s [*e.g.*, *Kooi and Beaumont*, 1994]. Following previous studies [*van der Beek and Bishop*, 2003], we chose to vary m_s and n_s between [1.0;1.3] and [0.4;1.0], respectively.

Although we tested several m and n combinations, differences between various m/n values are small (Figure IV.3.10-a) and relatively small misfits are found for values close to unity (m=n=1).

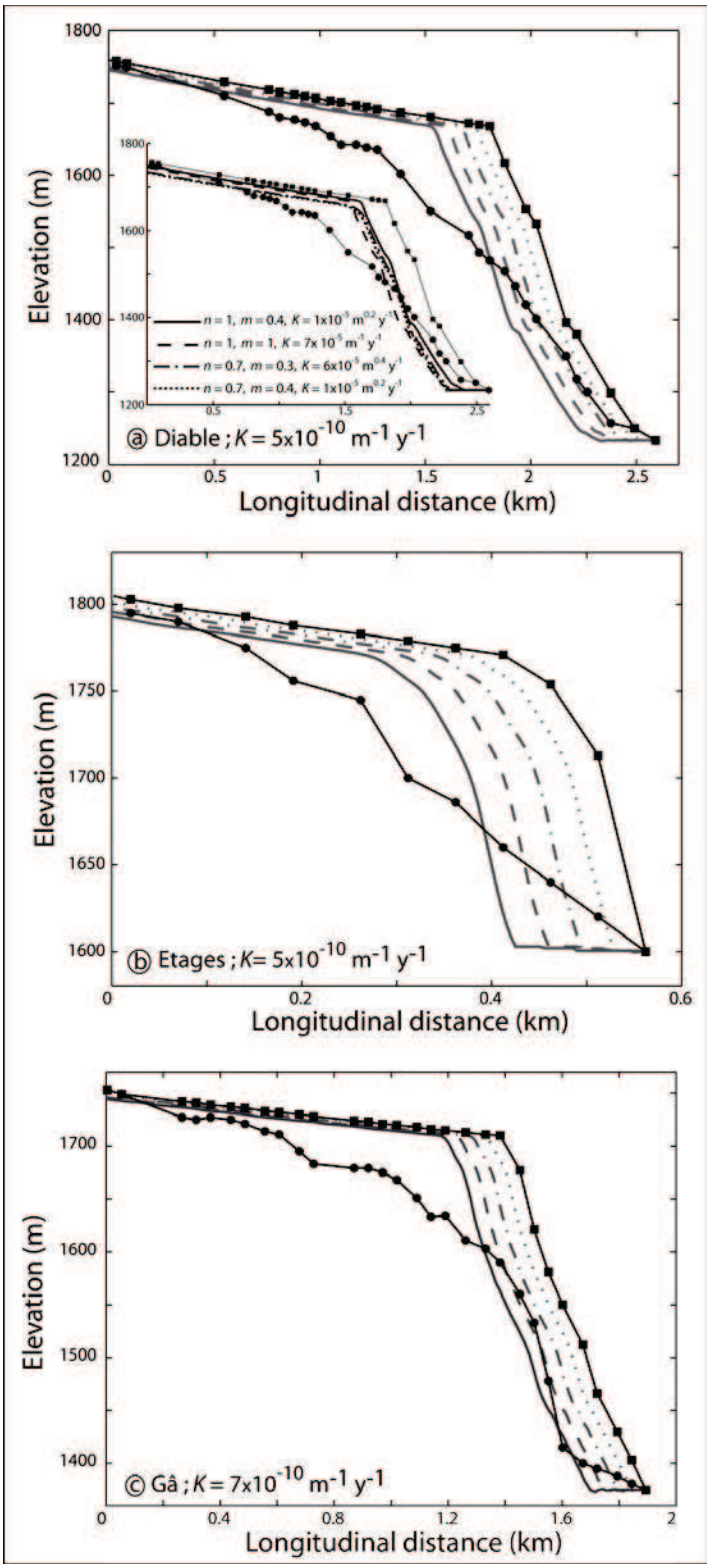

Figure IV.3.10. *Initial glacial (squares) and present-day fluvial (circles) profiles for (a) Diable, (b) Etages and (c) Gâ streams; and profile evolution predicted by the best-fit detachment-limited model (m = n = 1; K as indicated in the plots). Thick lines show profiles at 5-ky intervals during the model run (dotted: 5 ky; dashed-dotted: 10 ky; dashed: 15 ky and solid: 20 ky). Inset in (a) shows dependence of predicted present-day profile on choice of m and n exponents.*

This unusual result (when compared, for instance, to *Stock and Montgomery*, 1999; *Tomkin et al*., 2003 or *van der Beek and Bishop*, 2003) can be attributed to the specific evolution of channel width, which decreases downstream in the gorges. We thus report results for the linear stream power model in Figure IV.3.10. Values for K range between 5 and 7×10^{-10} m^{-1} y^{-1} for the three rivers; even best-fit models, however, retain high *RMS* misfit values (41 m for Diable, 23 m for Etages and 30 m for Gâ; cf. Figure IV.3.10).

Linear detachment-limited models predict parallel retreat of knickpoints without downwearing or any diffusive component [*e.g.*, *Howard et al*., 1994]. Some studies [*e.g.*, *Tucker and Whipple*, 2002] have modeled diffusive profile steps using values of $n < 1$. We tested these conditions for the three rivers; although we managed to predict some knickpoint lip diffusion, *RMS* misfit values are comparable to the linear model. These results are explained by the mostly advective behavior of the knickpoint, which leads to excess incision of the lower profile reach (Figures IV.3.10 and IV.3.12). Detachment-limited conditions thus do not predict the observed evolution of glacial knickpoints by "replacement" [*Gardner*, 1983; *Frankel et al.*, 2007], highlighting their inability to predict long-term fluvial dynamics of gorge deepening in our specific case.

We adopt the same approach for the transport-limited model; again m_s and n_s variations provide best-fit results for the linear model, with K_s values ranging from 2×10^{-6} to 3×10^{-5} m y^{-1}. Transport-limited simulations, including explicit width variations in space and time, provide much better fits (*RMS* misfits of 14 m for Diable, 4 m for Etages and 20 m for Gâ) between predicted and observed profiles (Figure IV.3.11) than the detachment-limited model. This is mainly because the transport-limited algorithm includes a diffusive component in the incision formulation; numerical simulations thus reproduce knickpoint evolution by replacement. The difference between the two models shows up most clearly when looking at the distribution of incision along the longitudinal profiles (Figure IV.3.12). Although both models correctly reproduce fluvial deepening for the most upstream part of the profile, detachment-limited models strongly underestimate knickzone incision and overestimate fluvial incision for lowest part of the profiles due to the strong advective component of these models. In contrast, transport-limited models provide realistic predictions of gorge incision except for the lowest profile reach. We believe the misfit in this reach may be due to efficient sediment entrainment in this area resulting from interactions with the trunk stream, as well as potential transient base-level effects, which are both not included in our models.

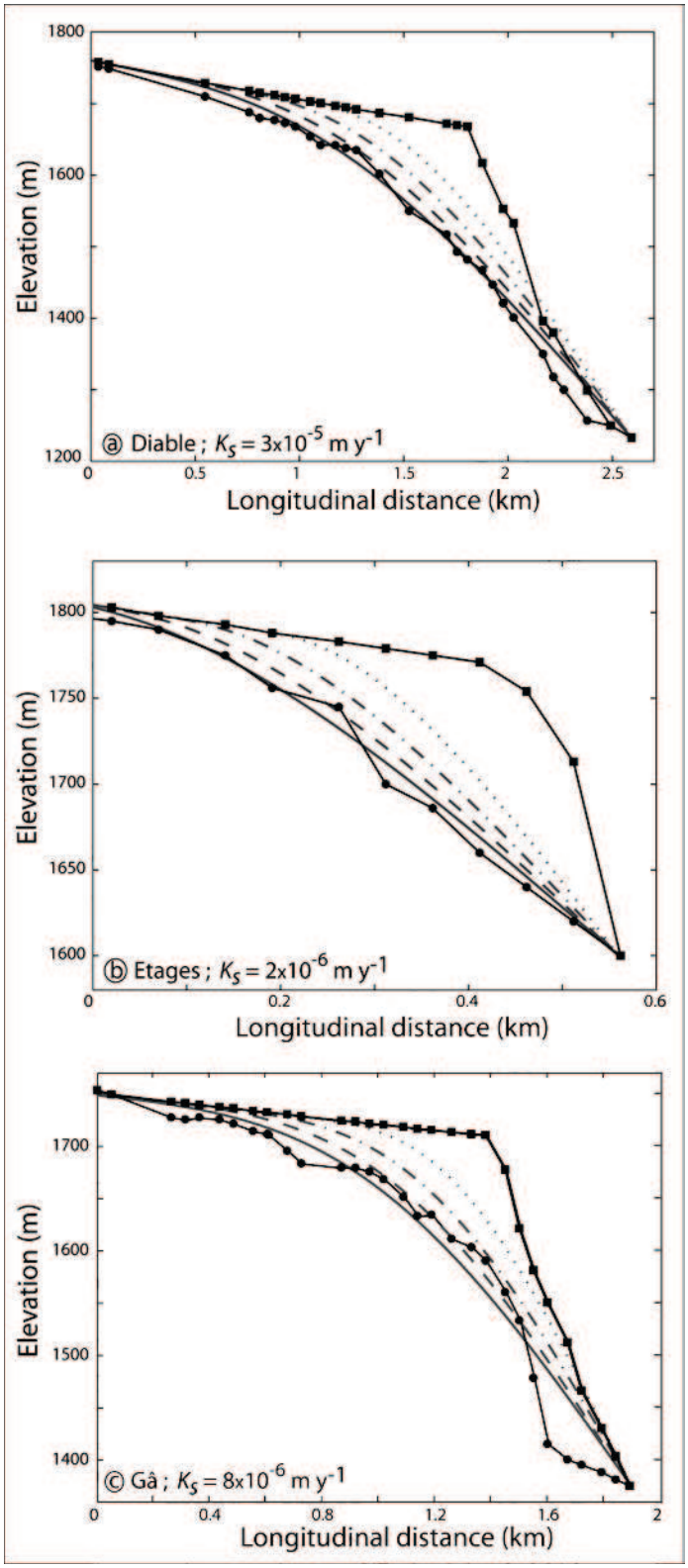

Figure IV.3.11. *Initial glacial (squares) and present-day fluvial (circles) profiles for (a) Diable, (b) Etages and (c) Gâ streams; and profile evolution predicted by the best-fit transport-limited model ($m_s = n_s = 1$; K_s as indicated in the plots). Thick lines show profiles at 5-ky intervals during the model run (dotted: 5 ky; dashed-dotted: 10 ky; dashed: 15 ky and solid: 20 ky).*

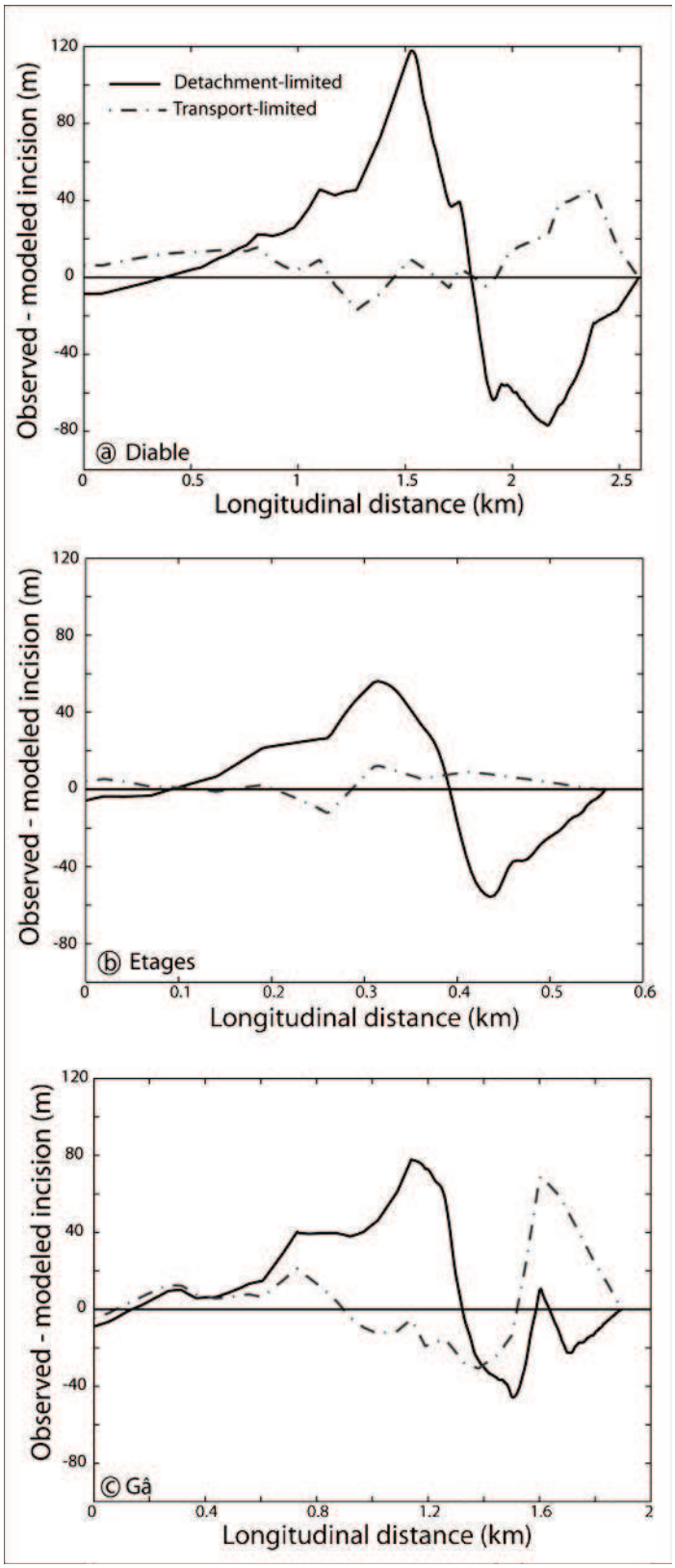

Figure IV.3.12. *Difference between observed and modeled incision as a function of longitudinal distance for the transport- (dashed line) and detachment-limited (continuous line) models for (a) Diable, (b) Etages and (c) Gâ streams.*

These initial results show that transport-limited models provide much better predictions for stream profile evolution in these gorges than detachment-limited models. This outcome is surprising in the light of field indications for present-day incision dynamics: the gorge walls and floor show smooth polished bedrock surfaces characteristic of incision by abrasion and plucking in a detachment-limited setting [*Whipple et al.*, 2000a]. Moreover, except for meter-scale blocks in some reaches, sediment deposits are scarce along the gorges and sediment transport does not appear to be the limiting incision process during recent times.

The above paradox between the morphological evidence for current gorge dynamics and the long-term numerical predictions for stream-profile evolution suggests that simple end-member models may not be appropriate to model gorge evolution, or that the field evidence pertains only to present-day channel conditions. We therefore attempt to model gorge evolution using the more elaborate cover model. However, this model requires more information about stream dynamics and sediments (bank angle, D_{50}, bedload proportion, mean discharge and discharge variability, see Table IV.3.1) than the end-member models.

Input parameters	Diable River (Cover)	Diable River (without Cover)
Dynamic Cover effect, ν	15	0
Static Cover effect, ξ	0.4	0
Bank Angle (°)	75	75
Manning Coefficient	0.08	0.08
Bedload Proportion (%)	50	/
Median Grain Size D_{50} (m)	0.5	0.5
Bed Erosion Factor K_{ref} (m^2 s kg^{-1})	1.6×10^{-11}	9.0×10^{-12}
Bed and Wall Critical Shield Stress	0.04	0.04
Wall Erosion Factor K_{bank} (m^2 s kg^{-1})	8.0×10^{-11}	5.0×10^{-12}
Sediment Transport Coeff. K_{sed} ($m^{5/2}$ s^2 $kg^{-3/2}$)	1.4×10^{-7}	/
Sediment Supply Rate Coeff. Q_{wall} (mm y^{-1})	9	/
Mean Runoff, r (m y^{-1})	1	1
Discharge Variability Parameter, k*	1	1

Table IV.3.1. *Parameter values for Diable stream using the cover model with and without the sediment effect; *See Lague et al. [2005] and particularly Equation 3 for details.*

We did not have access to the active channel of the Gâ and Etages gorges and thus could not estimate these parameters. Moreover, initial results with end-members models indicate that the Diable, Etages, and Gâ streams are governed by similar long term dynamics as K or K_s

values are similar for the three streams (even if the nature and importance of incision processes might be different in the three gorges). Thus, we decided to limit simulations using the cover model to the Diable stream, because this is the only gorge for which we managed to estimate the channel morphology and sediment properties.

Initial runs with the cover model do not include a dependence of incision rate on sediment cover, as we wanted to first verify the ability of a more realistic detachment-limited model, including an incision threshold, stochastic discharge distribution and dynamic width adjustment, to predict gorge deepening. We constrain the K_{ref} and K_{bank} parameters, which are the key for setting gorge incision. If bank erosion is too low compared to bed erosion, gorge incision will be extremely efficient and will lead to very narrow and deep channels. On the contrary, if bank erosion is too high compared with bed erosion, the gorge channel will widen and consequently decrease shear stress and incision of its bed. These two incision parameters thus have to be correctly adjusted to predict realistic present-day stream profiles and channel widths that match the field and morphometric observations.

Best-fit runs for the model without the cover effect predict widths of 20-25 m and gentle slopes (0 to 0.01 m m^{-1}) above the knickpoint and close to the confluence with the trunk valley, contrasting to narrow predicted widths (5-10 m, Figure IV.3.13a) and high slopes (0.25 to 1 m m^{-1}) for the gorge reach. These results compare favorably to measured values for the Diable gorge (see Figures IV.3.7 and IV.3.13a). However, numerical simulations lead to a relatively high misfit between predicted and observed stream profiles; the *RMS* misfit of ~25 m is much lower than the basic detachment-limited model but is still larger than results from transport-limited models (Figure IV.3.13a).

In essence, the behavior remains mostly advective, with parallel retreat of the gorge. The downstream part of the gorge is less steep than in the detachment-limited model because of the inclusion of a critical threshold of incision. Thus, taking into account spatial and temporal variations in channel geometry and a realistic discharge distribution combined with a threshold of erosion has improved numerical predictions of gorge incision, even though this appears not to be sufficient to predict gorge deepening with a simple detachment-limited formulation.

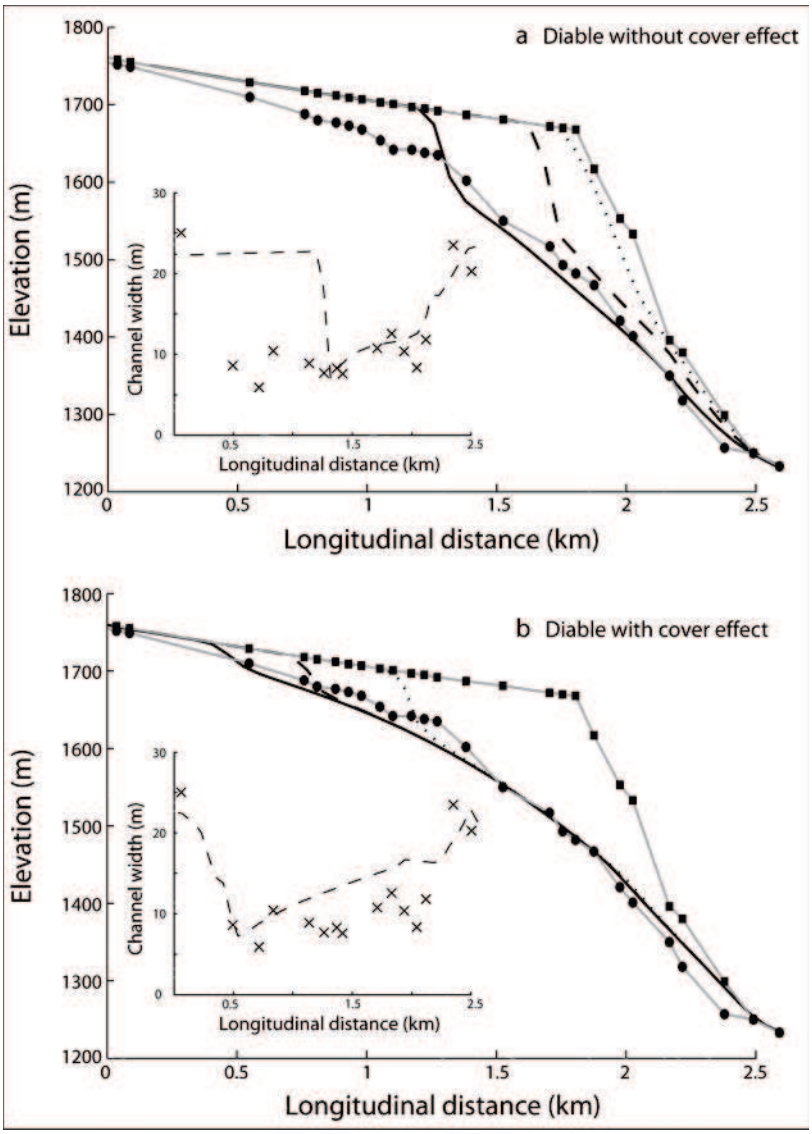

Figure IV.3.13. *Initial glacial (squares) and present-day fluvial (circles) profiles for the Diable stream and predicted profile evolution for the cover model without (a) and with (b) the sediment cover effect. Lines show profiles at different times during the model run (dotted: 5 ky; dashed: 10 ky and solid: 20 ky). Insets show predicted (dashed line) and observed (crosses) channel widths for present-day configuration.*

When sediment effects are taken into account, if the transport capacity (Q_{eq}, which depends on K_{sed} parameter) of the channel is too high, or the sediment supply (q_{lat}, which depends on Q_{wall} parameter) too low, the sediment does not significantly limit downstream of knickpoint incision, and the profile evolution is similar to the detachment- limited models. On the contrary, if the sediment supply is too large with respect to transport capacity, the channel is rapidly filled with sediment and cannot incise vertically anymore. Hence, as the present-day channel does not have a significant cover of sediment (less than 1 m in the gorge, even though

this is a value largely variable in time and not representative of long-term values; *Lague*, 2010), this places an upper boundary on the ratio q_{lat}/Q_{eq} above which the model predicts too much sediment deposited in the channel. A large q_{lat} would also imply extremely rapid erosion of the gorge sidewalls and hillslopes. We found that a value of $Q_{wall} \sim 9$ mm y^{-1}, combined with a value of $K_{sed} = 1.4\ 10^{-7}$ $m^{5/2}$ s^2 $kg^{-3/2}$ provided realistic predictions of mean sediment thickness in the gorge (see Table IV.3.1 and section IV.3.1.8 for details). This would suggest an erosion of the gorge sidewall and surrounding hillslopes of ~180 m since the LGM on both sides, which is roughly consistent with the present day topography of the Diable gorge. Given the blocky nature of the supply in the gorge, we suppose that 50 % of the volume of lateral sediment supply consists of bedload material. Assuming that 90 % of the volume contributes to bedload would require gorge sidewall and hillslope erosion Q_{wall} of only 5 mm y^{-1}.

Preliminary simulations in which the lateral supply of sediment was spatially homogeneous led to unrealistic sedimentation (> 30 m of sediment) upstream of the knickpoint. This led us to introduce Q_{wall} (see section IV.3.1.8, equation IV.3.10) to dynamically couple gorge incision and lateral sediment supply by gorge sidewall erosion. In this way, sediment supply increases in time, and varies spatially. We note that the resulting present-day pattern of sediment supply is in accord with the present-day pattern of in-channel deposits, which are more frequent in the gorge reach compared to the upstream reach of the stream. A difference arises at the lower reaches near the outlet where some of the rockfalls directly enter the trunk stream. This may explain the slight overprediction of mean sediment thickness (~5 m) in this location compared to the present-day configuration. As for the transport-limited model, this might also be due to the model not taking interactions with the trunk stream into account.

The final part of the calibration requires finding the correct values for K_{ref}, K_{bank}, ξ and v. The ratio of K_{ref} and K_{bank} strongly controls the predicted channel width, as well as the propagation rate of the knickpoint. ξ and v will mostly control how incision is attenuated downstream of the knickpoint. By trial and error, we find an optimal configuration (Figure IV.3.13b) leading to a low misfit between observed and predicted present day stream profiles ($RMS \sim 14.8$ m) comparable to what we obtain with the transport-limited model. We note that final predicted widths and slopes are also realistic and range from a very steep (0.25-0.35 m m^{-1}) and narrow (around 10 m wide) channel in the gorge to a wider (15-20 m) channel with gentle slopes (0-0.01 m m^{-1}) upstream and downstream. This result requires both static and dynamic cover

effects (ξ = 0.4, v=15) to operate. The static cover effect is always more pronounced than the dynamic cover effect, representing in average 75 % of bedrock incision inhibition at 2 ky and up to 100 % at the end of the simulation. A relatively strong to almost complete inhibition of incision by sediment transport downstream of the knickpoint is necessary to obtain satisfactory results, especially during the early stages of evolution. How exactly this inhibition operates is not clear. *Lague* [2010] shows that the variability of discharge and sediment supply significantly affects the long-term cover effect. The parameters related to this effect (variability of discharge, non-linearity of the sediment supply law, see section IV.3.1.8, equation IV.3.9) are not well constrained for the type of small alpine gorge we are studying. Also, the assumption of a single representative grain size may not well average the dynamics of an extremely skewed distribution of grain sizes. Hence we cannot rule out that the necessity to impose a relatively strong dynamic cover effect arises from incorrect parameterization of the sediment supply, transport and static cover effect.

Despite the uncertainties on the nature of the inhibiting effect of sediment in the gorge, our numerical simulations support the notion that sediments play an important role in gorge deepening. The predicted profile evolution through time shows that gorges exhibit behavior that is close to that predicted by transport-limited models (Figure IV.3.13b) and that sediment flux from sidewalls has a major influence on fluvial incision dynamics [*Crosby et al.*, 2007; *Gasparini et al.*, 2007]. There are, however, two notable differences in the evolution of the transport-limited model and the cover model in terms of knickpoint propagation and present-day erosion rates. The cover model predicts the migration of a well defined knickpoint (Figure IV.3.13b) delimiting an upstream zone with no erosion, while the transport-limited model shows widespread erosion typical of diffusion behavior even at early stages, without a clearly defined knickpoint. We note that the transport-limited model does not predict the propagation of knickpoints, whereas these are observed in the upper reaches of the gorge. Another difference is that in the present-day configuration, incision is close to zero in the cover model (because of significant inhibition by sediment), while it is still ongoing in the transport limited model. In the cover model for instance, the first km of the gorge reaches a constant bedrock profile within 2-3 ky, after which incision is inhibited by the sediment supply derived from upstream (Figure IV.3.13b). This difference in timing may have important implications for gorge evolution and sediment delivery to the trunk stream, and may help in differentiating which of the cover or transport-limited model governs post-glacial gorge incision.

IV.3.1.6 - Discussion

Our combined field, morphometric and numerical modeling approach provides insights into the fluvial evolution of bedrock gorges incising glacial hanging valleys. Based on field evidence, we show that these gorges mainly evolve by knickpoint diffusion through fluvial processes, starting from an abrupt glacial knickpoint. We quantified the glacial imprint on hanging valleys by studying the dependence of glacial hang heights on the ratio between tributary and trunk stream drainage area (Figure IV.3.5). This observation is consistent with the hypothesis that in glacial landscapes, hanging valleys mark the relative erosion capacities of the trunk and tributary glaciers [*MacGregor et al.*, 2000; *Amundson and Iverson*, 2006; *Anderson et al*., 2006].

Present-day gorge profiles were used to quantify fluvial incision processes. Field measurements highlight that gorge deepening is associated with channel narrowing and steep slopes (Figure IV.3.7). This observation suggests that high fluvial incision rates are accommodated by variations in both local gradients and channel geometry, especially channel width [*Turowski et al.*, 2006; *Wobus et al.*, 2006b; *Whittaker et al.,* 2007; *Snyder and Krammer*, 2008]. Mean gorge gradients (Figure IV.3.6) may reflect the incision and sediment-transport capacity of tributary streams [*Wobus et al.*, 2006a] although inherited glacial controls on gorge gradients could not be excluded; subglacial controls have probably provided "initial" gorge gradients that further evolved through fluvial processes. By comparing glacial and present-day gorge profiles, we have made a first-order estimate of the maximum fluvial incision of these gorges (Figure IV.3.4). We have focused on knickpoint form and quantified the amount of knickpoint retreat for all gorges. Our results show that this retreat is correlated with the tributary drainage area (Figure IV.3.8), consistent with previous studies on knickpoint dynamics [*Bishop et al.*, 2005; *Crosby and Whipple*, 2006]. However, in contrast to *Crosby and Whipple* [2006], we have no indication that a threshold drainage area plays a role in maintaining knickpoint position, and in contrast to *Bishop et al.* [2005], who argued that this dependence implies detachment-limited incision, our modeling results indicate this not to be the case here.

Our results show that knickpoint evolution takes place through “replacement-like” dynamics in which knickpoints evolve through horizontal retreat and vertical downwearing. *Gardner* [1983] suggests that this kind of evolution operates in a homogeneous substrate of

intermediate resistance, where shear stress at the stream bed is only slightly larger than the critical shear stress required for incision. In our case, lithologies vary from sedimentary cover rocks (marls and limestones) to crystalline bedrock (granites, gneisses and amphibolites). Morphometric results suggest that rates of gorge evolution may vary with lithology, although fluvial incision takes place by the same process of knickpoint replacement independent of lithology. The most striking lithological controls are observed for mean gorge gradients and knickpoint retreat rates. Bedrock gorges incising the more easily erodible sedimentary rocks are characterized by lower mean gradients and higher knickpoint retreat rates than gorges occurring in basement lithologies (Figures IV.3.6 and IV.3.8). A simple explanation could be that lower slopes correspond to a higher rate of overall gorge downwearing in the sedimentary rocks.

Resolving the timing of onset of gorge incision has important implications for landscape evolution in response to glacial/interglacial conditions [*Korup and Schlunegger*, 2007]. Morphological evidence suggests that fluvial abrasion is one of the main processes operating in present-day gorge incision. This abrasion could potentially take place in either fluvial or subglacial conditions during glacial episodes. Moreover, field observations of inner gorges in the Swiss Alps revealed some evidence for periodic sediment infill during glacial stages [*Korup and Schlunegger*, 2007], supporting an older origin of bedrock gorges. On the contrary, *Valla et al.* [2010a] recently reported cosmogenic data supporting Holocene post-glacial incision of bedrock gorges; however this study focuses on a single bedrock gorge (the Diable) and others should be investigated to produce more data and better understand the post-glacial evolution of these transient features.

Assuming a coeval post-glacial initiation of the gorges (*i.e.*, younger than 20 ky), estimated long-term incision rates from our morphometric results range between a minimum of 0.5 mm y^{-1} and a maximum of 15 mm y^{-1}. Such rates are high for fluvial processes in this lithological (sedimentary and crystalline rocks) and tectonic (the European Alps) setting. However, incision rates up to cm y^{-1} have been inferred for transient fluvial reaches [*Whipple et al.*, 2000b] and have been reported for post-glacial incision in the Western Alps from cosmogenic dating of fluvial terraces [*Brocard et al.*, 2003] and bedrock gorge sidewalls [*Valla et al.*, 2010a]. Assuming a post-glacial onset, temporally-averaged knickpoint retreat rates lie between 2-200 mm y^{-1} depending on drainage area; in agreement with values proposed in other fluvial settings [*Hayakawa and Matsukura*, 2003; *Bishop et al.*, 2005; *Lamb et al.*,

2007]. These studies and our results suggest that high fluvial incision rates can be encountered in disequilibrium contexts such as induced by glacial/interglacial climate oscillations.

Numerical modeling has provided insights into the processes driving gorge deepening. We have shown that detachment-limited models, which consider incision rates to be limited by the incision capacity of the stream only, are not able to predict the observed gorge evolution. In contrast, transport-limited models, which consider that incision rates are limited by the capacity of the stream to carry sediments, predict the patterns of gorge deepening well, with relatively small misfits between modeled and observed profiles. Even though transport-limited models do not appear to be consistent with the relatively "resistant" lithologies and persistent knickpoints at timescales of 10^4 years [*e.g.*, *Bishop and Goldrick*, 2000; *Bishop et al*., 2005], the long term behavior of bedrock gorges requires (close to) transport-limited conditions. A similar conclusion was reached by *Loget et al*. [2006] for knickpoints on much larger catchments. An alternative explanation for convex stream profiles associated with knickpoints was provided by *Haviv et al*. [2006], who suggest that they result from amplified erosion due to flow acceleration above waterfalls [*Berlin and Anderson*, 2009]. Although such a mechanism could explain the early evolution of the gorges we studied, when the glacial knickpoint is expressed as a free-falling waterfall (Figures IV.3.2a, b), most present-day gorges are not associated with waterfalls and drawdown of the knickpoint lip through this mechanism thus appears minimal or present only at a local step-pool scale.

Detachment-limited models do not satisfactorily predict gorge evolution as their simple formulation does not take into account the evolution of channel geometry or sediment supply and transport. This supports the notion that even if present-day gorge incision appears to take place under detachment-limited conditions, the long term dynamics differ and suggest high oscillations in sediment supply and thus sediment cover effect during gorge deepening [*Lague*, 2010]. Long-term gorge evolution thus depends on hillslope processes such as rockfalls, which can explain the diffusive component of knickpoint evolution and the presence of meter-scale blocks within the gorges. Moreover, debris-flow incision may have occurred during gorge deepening, especially shortly after glacier retreat when sediment supply could have been important; morphological evidence does not suggest such processes for the recent gorge evolution, however.

Transport-limited models do include potential sediment controls on bedrock incision; however the interaction between sediment transport and bedrock incision is included in a relatively simplistic manner. The use of more elaborate models thus appears required to fully explore the dynamics of stream incision. Such models should include a stochastic representation of stream discharges [*Tucker*, 2004; *Lague et al.*, 2005] as well as a full description of channel geometry [*Turowski et al.*, 2006; *Wobus et al.,* 2006b], and have to take into account the role of sediments in both limiting or increasing bedrock incision [*Sklar and Dietrich*, 2004; 2006; *Turowski et al.*, 2007]. However, the use of such models presupposes that all climatic, tectonic and hydraulic parameters controlling channel geometry and evolution can be estimated, which is clearly not the case in most situations.

We have used the cover model to explore fluvial incision dynamics in more detail; this has highlighted the important role of an incision threshold, dynamic width adjustment and lateral sediment flux into the gorge. Slope failure events on the gorge sidewalls are required to provide relatively large amounts of sediment (up to 5-10 mm y^{-1}) to the gorge stream. Meter-scale blocks are observed in the gorges (Figure IV.3.2d), suggesting that mass-wasting mechanisms are active along gorge sidewalls and contribute significantly to lateral sediment supply into the river. Consequently, bedrock is partially protected from stream incision, reducing gorge deepening rates in a manner analogous to larger-scale examples described by *Korup et al*. [2006] and *Ouimet et al*. [2007]. Moreover, the hanging valleys we studied have small sizes (maximum drainage area of 40 km²) and field evidence suggests that many large blocks have long residence times, as they are fluvially sculpted and differ from more recently produced and angular blocks. We thus suggest that present-day gorge incision mainly occurs during floods in spring (due to snow melt) or summer (storms) that are capable of carrying and eroding such large blocks, thus leading to bedrock erosion. Similar to the dynamics exhibited in the modeling of *Lague* [2010], these frequent fluctuations of sediment supply and discharge entrain the system alternatively between detachment-limited behavior (when sediment deposits are negligible) and net-deposition of sediment. At longer time scales, this propagates into a regime that can be close to a detachment-limited model if mean sediment supply is low or a transport-limited model if mean sediment supply is high [*Lague*, 2010].

The ability of transport-limited and cover models to predict gorge evolution is also enhanced because they explicitly include spatial variations in channel geometry and its evolution through time (*e.g.*, *Whittaker et al.*, 2007; *Snyder and Kammer*, 2008; Figures IV.3.7 and

IV.3.13) even though width evolution is empirically imposed from field measurements for the transport-limited models. The advantage of the cover model compared to transport-limited models is that it not only predicts vertical incision, but also potential width adjustments and sediment cover on the channel bed. Cover model simulations allow modeled and observed outcomes to be additionally tested using channel width and sediment thickness. They thereby allow further constraints on incision to be established.

IV.3.1.7 - Conclusions

We conclude from our study that morphometric data combined with numerical fluvial incision models provides insights into gorge incision processes. Longitudinal profile reconstructions for both initial and present-day states allowed us to extract information on the formation of glacial hanging valleys and the incision of bedrock gorges. Our morphometric results support field evidence pointing to present-day fluvial incision of a formerly glaciated landscape. Field observations on active gorge channels suggest that fluvial abrasion is one of the main incision processes; however hillslope processes, in particular rockfalls from gorge sidewalls may provide substantial amounts of sediment to the gorge. Other processes such as subglacial abrasion, debris flows or incision during large floods cannot be excluded by our field observations. Assuming a post-glacial initiation of gorge incision, we infer incision and knickpoint retreat rates that are not unrealistic compared to literature data. However, we cannot exclude an older origin of bedrock gorges in the light of morphological evidence and morphometric results.

Numerical results clearly indicate that the long-term evolution of bedrock gorges cannot be caused by detachment-limited mechanisms alone. Numerical predictions suggest an important role for sediment supply and transport, but also for evolving channel geometry during gorge incision. We conclude from our numerical modeling that gorge incision can be modeled either by a simple transport-limited model, or by a complex model involving channel width evolution, discharge variability, strong inhibition by sediment transport and deposition downstream and tight coupling between gorge incision and sediment production from sidewall gorges and/or hillslopes. These results suggest that more detailed treatment of both channel geometry and sediment-bedrock interaction is required to capture the kinematics of gorge deepening. However, this requires detailed knowledge of past and present-day dynamics that is generally difficult to constrain. Our numerical results provide some insights

into gorge incision process; however they do not clearly constrain the potential mechanisms acting in gorge incision and in bedrock incision inhibition by sediment transport. We thus conclude that morphometric data and/or numerical modeling have to be used with caution to quantify erosion rates and landscape evolution; they must be combined with detailed field observations and absolute dating to capture the dynamics and timing of erosion processes and landscape evolution.

Acknowledgments

This study represent P. Valla's MSc and PhD project at Université Joseph Fourier and forms part of 2 projects on Quaternary relief development and denudation rates in the western Alps (P. van der Beek) and drainage network dynamics (D. Lague) funded by the INSU-CNRS *Reliefs de la Terre* program. We thank reviewers Simon Brocklehurst, Oliver Korup, Michael Lamb and an anonymous reviewer, and associate editor Brian MacArdell for thorough and constructive reviews that helped to significantly improve the manuscript.

IV.3.1.8 - Appendix: description of the cover model

The exact nature of the so-called cover effect and the adequate way to model it is still debated (see *Lague* [2010] for a review). Two types of modeling approach have been proposed : one in which the cover effect is expressed as a function of the ratio between the flux of bedload sediment Q_s and the bedload transport capacity Q_{eq} [*Beaumont et al.*, 1992; *Tucker and Slingerland*, 1994; *Sklar and Dietrich*, 2004; *Gasparini et al.*, 2007; *Turowski et al.*, 2007; *Chatanantavet and Parker*, 2008], and one in which the cover effect is expressed as a function of the mean thickness of sediment deposited on the bed [*Howard*, 1998; *Hancock and Anderson*, 2002; *Lague*, 2010]. It is not clear at present if these formulations represent different physical mechanisms of inhibition, and how they factor in elements of the complexity of the coupling between sediment transport, deposition and hydraulics (via roughness modifications). The effect of immobile alluvial deposits (called a static cover effect) on the bed has been demonstrated experimentally [*Sklar and Dietrich*, 2001; *Johnson and Whipple*, 2007], and is expected to translate into a dependence of the cover effect on the mean thickness of immobile sediment deposited on the bed [*Howard*, 1998; *Hancock and Anderson*, 2002; *Lague*, 2010]. The formulation of the cover effect using Q_s/Q_{eq} inherently fails to take into account any previous history of sediment stored on the bed [*Goode and*

Burbank, 2009; *Lague*, 2010] and cannot be used at daily to yearly timescales alone. It can emerge as a long-term cover effect law when discharge and sediment supply stochasticity are factored in [*Lague*, 2010]; but it has also been advocated to model a so-called dynamic cover effect [*Turowski et al.*, 2007], in which mobile patches of sediment and increased near-bed sediment concentration reduces the bedrock surface exposed to incision at the timescales of single floods. This effect could be superimposed on the effect of immobile bed patches due to the presence of bedforms or different grain sizes.

The cover model divides the stream channel into series of trapezoidal cross-sections of fixed bank angle θ, linked together as in *Stark* [2006]. In contrast to *Stark* [2006], we do not account for meandering effects as they are negligible in the study area. The model is driven by daily runoff events picked randomly from a probability distribution [*Lague et al.*, 2005] mimicking natural river flow variability at a daily timescale. In each section, daily discharge is equal to drainage area times daily runoff. As we do not have hydrological data for these gorges, we used mean runoff and variability typical of mountain environments (mean runoff r = 1 m yr^{-1}, discharge variability parameter k = 1; *Lague et al.*, 2005). For a given discharge and at each section, water depth is calculated using a Manning friction law, and corresponding mean bed and bank shear stresses (τ_{bed} and τ_{bank}, respectively) are computed using an experimentally derived law [*Knight et al.*, 1984; *Flintham and Carling*, 1988]. Corresponding mean bed incision and mean bank incision are computed using a simple shear stress incision law [*e.g.*, *Howard and Kerby*, 1983; *Lave and Avouac*, 2001]:

$$\dot{E}_x = K_x(\tau_x - \tau_{cx}), \text{ if } \tau_x > \tau_{cx}, \text{ else } \dot{E}_x = 0 \qquad \text{(IV.3.5)}$$

In equation (IV.3.5) the subscript x refers to bed or bank, and τ_{cx} corresponds to a critical shear stress (that we assume equal to the critical shear stress for incipient motion, see discussion in *Lague*, 2010). On the bed, K_{bed} in equation (IV.3.5) can be decreased by a static and/or a dynamic cover effect. According to the formulations used in *Lague* [2010], the resulting expression for K_{bed} is:

$$K_{bed} = K_{ref} \exp(-\upsilon \frac{Q_s}{Q_{eq}}) \exp(-\frac{h_s}{\xi D_{50}}) \qquad \text{(IV.3.6)}$$

where K_{ref} is a constant, v is a dynamic cover factor, h_s is the mean sediment thickness on the bed, D_{50} is the median grain diameter (estimated from field evidence), and ξ is a static cover factor. Given the very complex bed morphology of the gorges and the lack of a physical basis to set realistic values, we left ξ and v as free parameters in our simulations. Note that the exact expression for static and dynamic cover effects in equation (IV.3.6) does not change the overall dynamics of the model (see also *Lague*, 2010); although it would change the value of parameters inferred from modeling results (K_{ref} for instance). Using linearly decreasing laws (*e.g.*, *Sklar and Dietrich*, 2004) would predict a similar channel evolution.

The numerical model explicitly tracks the volume of sediment $Vol(x)$ deposited between two sections using the following equation:

$$\frac{dVol(x)}{dt} = Q_s(x-dx,t) + \beta q_{lat}(x,t)dx - Q_s(x,t) \qquad \text{(IV.3.7)}$$

where t is time, β is the bedload fraction of the sediment supply, $q_{lat}(x,t)$ is the lateral supply of sediment per unit length of channel between x and x-dx (see Figure 2 in *Lague*, 2010), dx is the distance between sections and $Q_s(x,t)$ is the total volumetric bedload flux at a distance x (x positive in the downstream direction). The volume of sediment stored is translated into a mean sediment thickness h_s assuming a packing density of 0.7. In equation (IV.3.7), $Q_s(x,t)$ can be limited by the transport capacity $Q_{eq}(x)$ of the section, estimated using a typical bedload sediment transport capacity law :

$$Q_{eq} = WK_{sed}(\tau_{bed} - \tau_{cbed})^{1.5}, \text{ if } \tau_{bed} > \tau_{cbed}, \text{ else } Q_{eq}=0 \qquad \text{(IV.3.8)}$$

where W is the flow width and K_{sed} a transport efficiency coefficient. In equation (IV.3.8) the asymptotic scaling of transport capacity with shear stress is robust, and is predicted theoretically [*e.g.*, *Bagnold*, 1977] and experimentally [*e.g.*, *Meyer-Peter and Muller*, 1948; *Fernandez-Luque and van Beek*, 1976] in plane bed conditions (although a slightly higher exponent of 1.6 has been obtained by *Wong and Parker*, 2006). On the contrary, the value of K_{sed} and τ_{cbed} (or more commonly the critical shield stress τ^*_{cbed}) is not universal. In steep gorges with significant protruding blocks and bedform roughness, the prediction of K_{sed} and τ^*_{cbed} is challenging and does not yield universal parameters [*Yager et al.*, 2007; *Lamb et al.*, 2008b]. Hence we allow K_{sed} to be significantly smaller than the typical value predicted by the

Wong and Parker [2006] law ($K_{sed} \sim 5.10^{-6}$ $m^{5/2}$ s^2 $kg^{-3/2}$ in that case) while we arbitrarily fix $\tau^*_{cbed} = 0.04$. The median grain size D_{50} is set to 50 cm, which is close to the median size of sediments found in the gorges (including meter scale blocks).

In these simulations, sediment is supplied to the river at each cross-section by lateral supply $q_{lat}(x)$ from gorge wall and hillslope erosion. As in *Lague* [2010] this supply of sediment varies stochastically with the daily variation of runoff according to a one to one relationship:

$$q_{lat}(x,t) = k_{\sup}(x,t)Q^*(t)^m \tag{IV.3.9}$$

in which $k_{sup}(x)$ can vary longitudinally and $Q^*(t)$ is the normalized runoff (*i.e.*, the daily runoff divided by mean annual runoff). We use $m=2$, although we do not have any constraint on this parameter. As discussed in the text, it rapidly became clear that a realistic profile evolution required the supply of sediment to vary along the stream. We basically interpret this effect as wall collapse and erosion due to gorge incision. To factor in this effect, we couple lateral sediment supply to the total local incision since the beginning of the simulation:

$$k_{\sup}(x,t) = 2(h(x,t) - h(x,0))Q_{wall} \tag{IV.3.10}$$

where $h(x,t)$ is the local bed elevation at time t and Q_{wall} is the mean sidewall erosion rate. Equation (IV.3.10) mimics parallel retreat of the two sidewalls of the gorge leading to higher sediment supply where the channel is incising most rapidly. Slope stability modeling [*Korup and Schlunegger*, 2007] supports this approach: the higher the gorge sidewalls, the less stable they are and the more sediment they produce. We acknowledge that equation (IV.3.10) is likely oversimplified and could be for instance more non-linear, but it does dynamically couple gorge deepening and sidewall erosion with only one parameter.

Finally, channel geometry is altered at daily time steps as a function of mean bed and bank incision, keeping the bank angle fixed. For instance, if $E_{\text{bank}} > E_{\text{bed}} \cos\theta$, the channel widens, whereas if $E_{\text{bank}} = E_{\text{bed}} \cos\theta$ the channel width is not modified. As demonstrated in *Stark* [2006], this simple model allows for a dynamic (and implicit) variation of channel width.

IV.3.2 - Dating bedrock gorge incision in the French Western Alps (Ecrins-Pelvoux massif) using cosmogenic ^{10}Be

Pierre G. Valla [1], Peter A. van der Beek [1], and Julien Carcaillet[1]

[1] *LGCA-OSUG, Université de Grenoble, CNRS, BP 53, F-38041 Grenoble, France*

Abstract

We report *in-situ* produced ^{10}Be data from the Gorge du Diable (French Western Alps) to date and quantify bedrock gorge incision into a glacial hanging valley. We sampled gorge sidewalls and the active channel bed to derive both long-term and present-day incision rates. ^{10}Be ages of sidewall profiles reveal rapid incision through the late Holocene (ca 5 ka) at rates ranging from 6.5 to 13 mm yr^{-1}. Present-day incision rates are significantly lower and vary from 0.5 to 3 mm yr^{-1} within the gorge. Our data imply either delayed initiation of gorge incision after final ice retreat from internal Alpine valleys at ~12 ka, or post-glacial surface reburial of the gorge. Our results suggest that fluvial incision rates >1 cm yr^{-1} into crystalline bedrock may be encountered in transient landscape features induced by glacial/interglacial transitions.

IV.3.2.1 - Introduction

Present-day landscapes result from the integrated effect of past and current geomorphic processes and are generally in a transient state, as opposed to the ideal "steady state" [*e.g.*, *Whipple*, 2001] in which surface processes have reached an equilibrium with respect to tectonic and climate forcing. Quaternary climate cooling [*e.g.*, *Raymo*, 1994] and fluctuations between glacial and interglacial periods have led to significant landscape changes governed by both glacial and fluvial processes, the relative efficiencies of which are currently poorly quantified [*e.g.*, *Whipple et al.*, 1999; *Brocklehurst and Whipple*, 2002; *Montgomery*, 2002]. In mountainous regions, the conjunctive occurrence of both glacial features that were formed during glaciations and fluvial markers of post-glacial processes raises the question of the landscape response time to climate oscillations. Studies of late Quaternary valley fills [*e.g.*, *Hinderer,* 2001] or post-glacial fluvial incision rates [*Brocard et al.*, 2003] imply that relief rejuvenation has been significant since the last glaciation. In this context, inner gorges [*Korup*

and Schlunegger, 2007] or smaller bedrock gorges incising glacial valleys [*Montjuvent*, 1978] can be used as markers of fluvial incision in relief development. Such gorges have commonly been interpreted as transient features [*Schlunegger and Schneider*, 2005] but their origin and evolution remain debated. One of the major questions concerns the origin and persistence of such gorges throughout Quaternary times [*Korup and Schlunegger*, 2007]. One hypothesis argues that bedrock gorges are post-glacial features and their incision started after the last glacier retreat. An alternative hypothesis suggests that gorges are much older landscape elements and that their incision was initiated at the onset of the Quaternary glacial-interglacial cycles [*e.g.*, *Montjuvent*, 1978]. Assuming a postglacial origin of these gorges implies long-term gorge incision rates of several mm to cm yr^{-1} through crystalline bedrock [*e.g.*, *Korup and Schlunegger*, 2007; *Valla et al.*, 2010c]. Such high rates may be realistic in a context of landscape rejuvenation in response to deglaciation [*Hinderer*, 2001]; however an older origin of bedrock gorges cannot be excluded and absolute dating of gorge deepening is needed to resolve this debate.

Here, we report *in-situ* produced ^{10}Be data in order to date the incision of a bedrock gorge (Gorge du Diable, Ecrins-Pelvoux massif, French western Alps; Figure IV.3.14). We collected samples both on vertical gorge sidewalls and along the present-day active channel (Figure IV.3.15). We selected the Diable stream because it presents one of the few gorges in the area allowing direct access to gorge sidewalls and to the active channel. Moreover, the initial glacial valley can be relatively precisely reconstructed [*Valla et al.*, 2010c]. Cosmic ray exposure (CRE) ages for vertical profiles provide insights into long-term gorge incision [*Schaller et al.*, 2005; *Ouimet et al.*, 2008], which can be compared to present-day incision rates calculated from samples collected along the active channel [*Seidl et al.*, 1997; *Weissel and Seidl*, 1998]. We discuss our results on long-term and present-day incision rates of bedrock gorges in terms of their implications for relief inheritance, rejuvenation and landscape response time.

IV.3.2.2 - Geological and geomorphic setting

The Ecrins-Pelvoux massif is one of the "External Crystalline Massifs" (ECM) of the Western Alps. It consists of blocks of European crystalline basement that were exhumed along crustal-scale faults [*Ford*, 1996; *Dumont et al.*, 2008] and are separated by remnants of inverted Jurassic extensional basins. Present-day rock-uplift rates in the Western Alps show local

maxima within the ECM, reaching up to 1 mm yr^{-1} [*Jouanne et al.*, 1995; *Kahle et al.,* 1997]. It has been argued that a significant part of the present-day rock-uplift signal may be due to isostatic rebound induced by deglaciation [*Gudmundsson*, 1994] and/or increased erosion rates during Pliocene-Quaternary times [*Cederbom et al.*, 2004; *Champagnac et al.*, 2007; 2009]. The Ecrins-Pelvoux massif comprises high Alpine relief, with several peaks around 4000 m and valley bottoms at ~1000 m. The massif was extensively glaciated during Quaternary times. Major valleys were occupied by large valley glaciers, which have widened and overdeepened them [*Montjuvent*, 1974; 1978; *van der Beek and Bourbon,* 2008]. Glacial overdeepenings such as the Bourg d'Oisans trough (Figure IV.3.14) were subsequently filled by late-glacial and post-glacial lake sediments [*Hinderer*, 2001; *Nicoud et al.*, 2002], and present-day longitudinal valley profiles show a succession of characteristic valley steps and flats [*Montjuvent*, 1974; 1978].

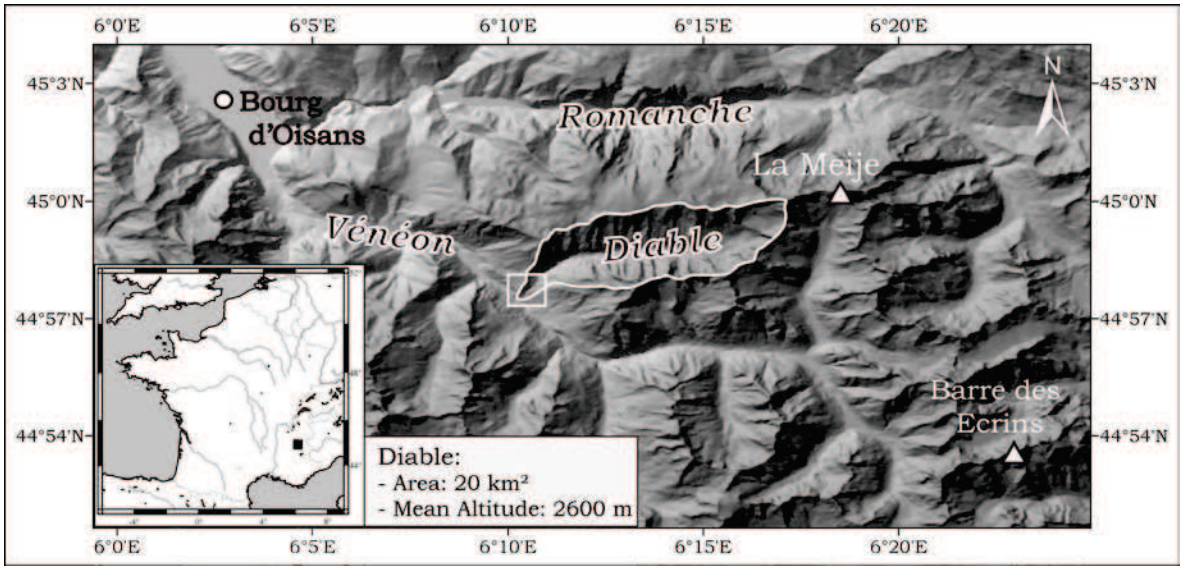

Figure IV.3.14. *Digital Elevation Model (Institut Geographique National, 50-m resolution) of the study area, showing major summits (La Meije: 3983 m; Barre des Ecrins: 4102 m) and valleys (Romanche and Vénéon). Box indicates location of Figure IV.3.15a. Eastings and northings are WGS 84 longitude and latitude, in degrees. Inset shows location within France.*

Glacial hanging valleys occur at tributary junctions with the trunk valley [*e.g.*, *Anderson et al.*, 2006] and their terminations are commonly marked by waterfalls or bedrock gorges that indicate substantial incision. Gorges present highly incised, narrow and steep bedrock channels with dominant step-pool and boulder-cascade bed morphologies. The present-day active channels display fluvial abrasion features (Figure IV.3.16c), such as smooth and

polished bedrock surfaces, ripples and potholes [*e.g.*, *Whipple et al*., 2000a]. Meter-scale blocks derived from the gorge sidewalls (Figure IV.3.18a) or surrounding hillslopes are frequent and suggest important hillslope-channel coupling [*Korup and Schlunegger,* 2007; *Valla et al*., 2010c].

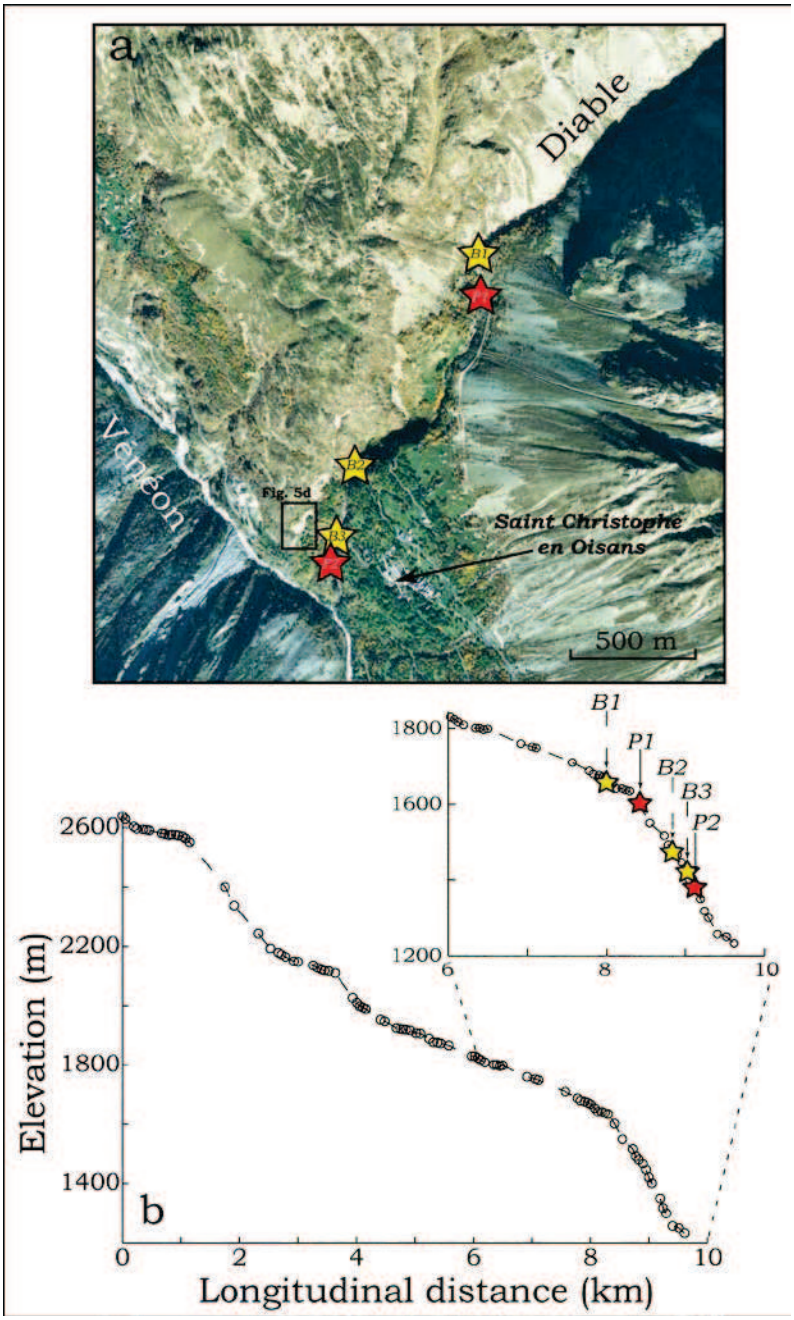

Figure IV.3.15. *Aerial photograph and longitudinal profile of the Diable stream showing sampling sites. a) Aerial photograph (Institut Geographique National) of the lower Diable catchment with sampling locations; black box indicates location of Figure IV.3.18d. b) Diable stream profile (open circles and dashed curve). Inset shows zoom on the gorge reach with locations of the two vertical profiles (P1, P2; red stars) and active bed sampling sites (B1, B2 and B3; yellow stars). See text and Figure IV.3.16 for details.*

IV.3.2.3 - Sampling methodology and preparation

We have sampled active channel sites located both upstream from and within the gorge (*B1*, *B2* and *B3*, Figure IV.3.15b), choosing well-developed and polished abrasion forms (Figure IV.3.16c) as targets to ensure that our samples record present-day stream incision with minimum passive exposure. Because we are unable to estimate the thickness and duration of temporary sediment cover in the active channel, we assume permanent bedrock exposure to fluvial incision when calculating erosion rates.

Vertical profiles along gorge sidewalls were chosen in the upper gorge reach (*P1*, Figure IV.3.16a, b) and just upstream of the confluence with the Vénéon trunk valley (*P2*, Figure IV.3.16d). We collected 4 to 5 samples along ~30 m of wall profiles (Figure IV.3.16b, d). Abraded and polished surfaces along gorge sidewalls suggest that they have not experienced subsequent erosion and allow calculating minimum CRE ages. Samples collected at the bottom of our profiles (*VAM-01* and *VAV-01*; Table IV.3.2) have been used to derive both erosion rates and apparent exposure ages.

Extraction of *in-situ* produced ^{10}Be followed procedures described by *Brown et al.* [1991]. Measurements were performed at the ASTER AMS Facility in Aix-en-Provence, France. The data were calibrated directly against NIST standard reference material 4325 using a ^{10}Be/^{9}Be ratio of 2.79 $\pm 0.03 \times 10^{-11}$ and ^{10}Be half-life ($T_{1/2}$) of 1.36 $\pm 0.07 \times 10^{6}$ years, as recently determined by *Nishiizumi et al.* [2007]. ^{10}Be production rates were calculated with a modern high-latitude sea-level value of 4.5 ±0.3 atoms g^{-1}(quartz) yr^{-1} [*Balco et al.*, 2008].

For each sample, we adjusted production rates for latitude and elevation using the *Stone* [2000] polynomials, took in account cosmic-ray attenuation induced by sample thickness (<5 cm) [*Balco et al.*, 2008] and calculated the geomorphic scaling factor [*Dunne et al.,* 1999] to account for the shielding effect of both surrounding topography and gorge geometry on incoming cosmic rays. Because CRE ages are younger than ~5 ka, we neglected potential geomagnetic effects on time-integrated cosmogenic nuclide production; CRE ages are thus given in ^{10}Be-ka.

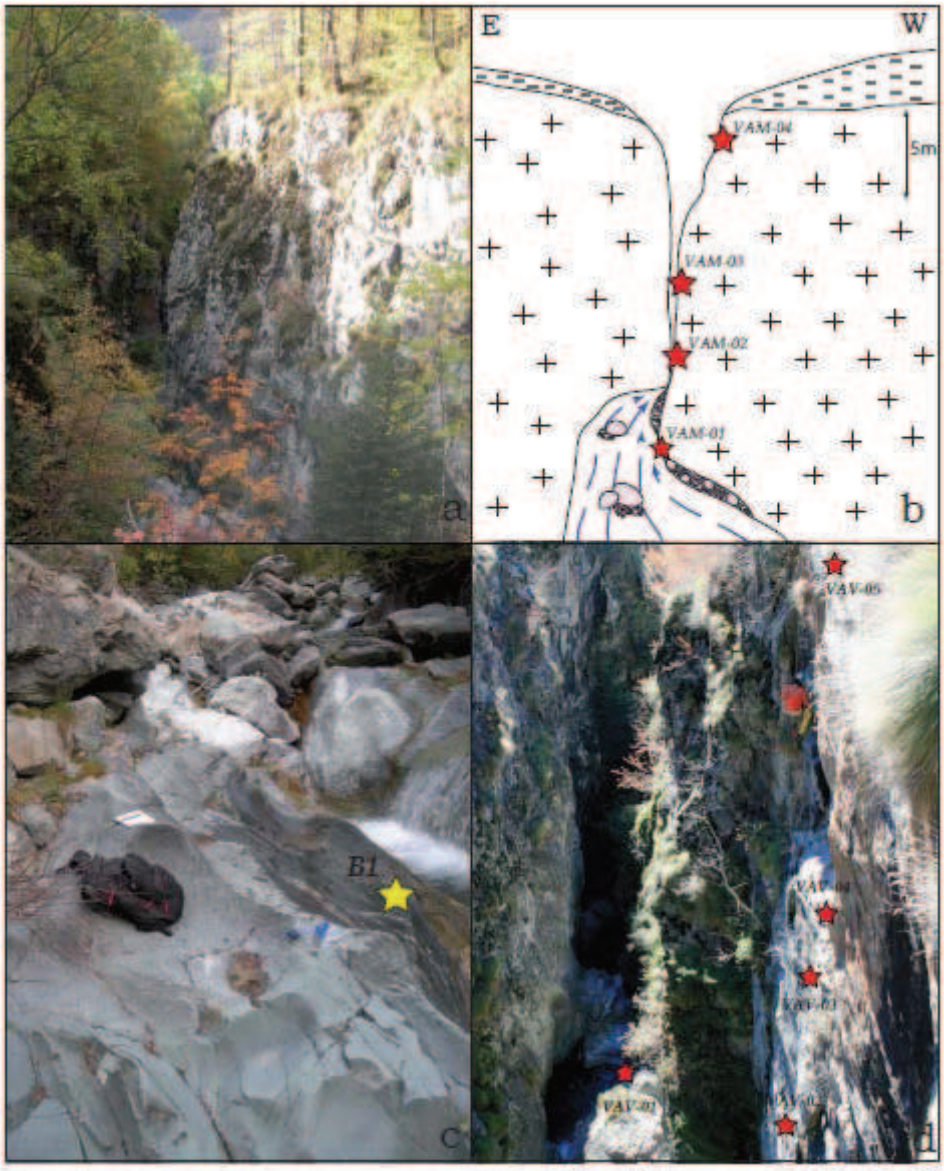

Figure IV.3.16. *Field photographs showing bedrock gorge morphologies and sampling strategy. a) View of the Gorge du Diable at sampling site P1. b) Schematic sketch illustrating Diable stream, gorge sidewalls (black crosses and gray dashes), active channel and sediments, and sampling sites along the gorge sidewall (red stars). c) Abrasion forms of the active channel at sampling site B1 (yellow star). d) Sampling along gorge sidewall at site P2 (sampling sites indicated by red stars).*

IV.3.2.4 - Results

^{10}Be concentrations range from 1.94 ±0.87 to 50.6 ±22.2×10^{3} atoms per gram quartz (at g^{-1}; Table IV.3.2). These low concentrations suggest recent exposure of the gorge sidewalls and/or strong shielding of incoming rays into the steep gorge. Samples collected from the top of the profiles (*VAM-04* and *VAV-05*) were taken sufficiently deep below the gorge surface to not be

subject to significant production from cosmic rays passing through the upper rock layer. Due to the steep gorge sidewalls (55 to 85°), incoming cosmic radiation is significantly attenuated: topographic scaling factors vary from 0.23 to 0.92 (Table IV.3.2), implying an important control of topographic shielding on the computed CRE ages and incision rates. The calculation of these scaling factors is affected by the complex geometry of the sidewalls; we thus add a ±5° uncertainty to our geomorphic shielding measurements, leading to uncertainties in the computed scaling factors that range from 5 to 30% (Table IV.3.2). These have been included in the calculations of CRE ages and incision rates, leading to an increase in the associated uncertainties of 0.5 to 15%.

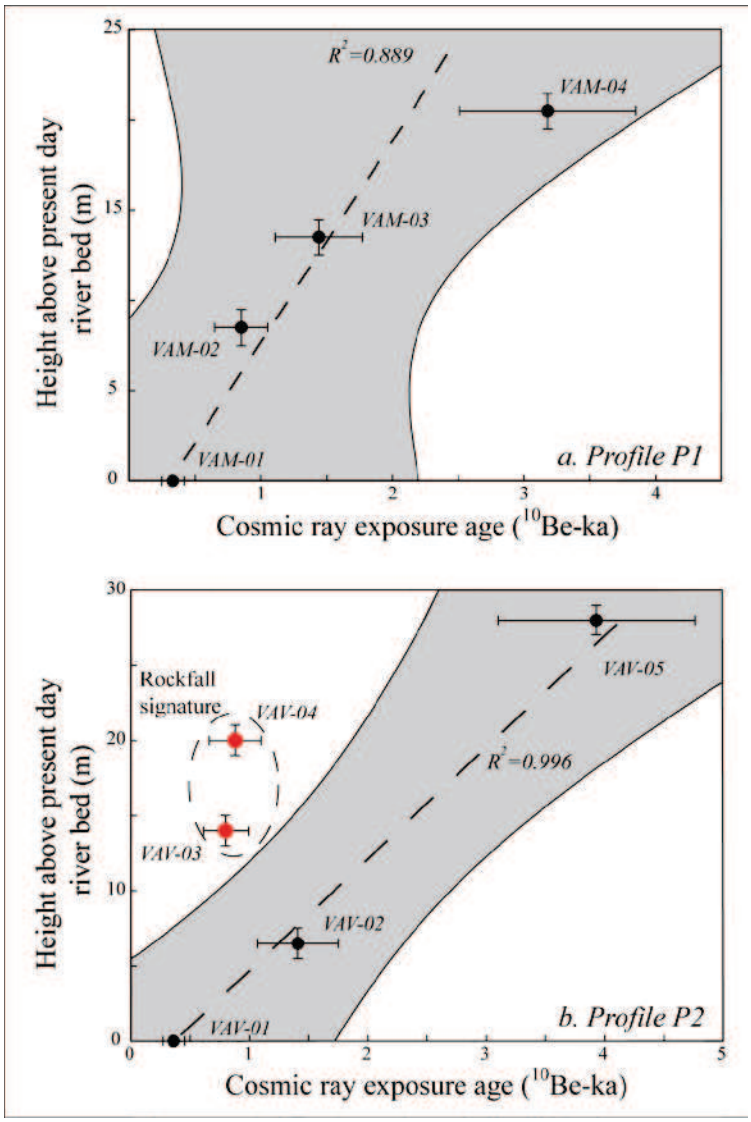

Figure IV.3.17. *Vertical profiles P1 (a) and P2 (b) (see Figure IV.3.15 for locations) and calculated CRE ages. Errors on height measurements (±1 m) and CRE ages (see Table IV.3.2) are given. Best linear fits (dashed line, a: Slope = 11 ±2 m ka^{-1}; R^2 = 0.889; b: Slope = 7.5 ±1.5 m ka^{-1}; R^2 = 0.996) and 95% confidence interval (grey zone) are also shown.*

Sample – Elevation (m) WGS 84 Latitude (°N) WGS 84 Longitude (°E)	Height above present day river bed (m)	Surface production rate*	Geomorphic scaling factor†	Corrected production rate‡	^{10}Be concentration (10^3) atoms g^{-1} quartz§		Exposure ages (^{10}Be-ka)		Present-day estimated erosion rates (mm yr^{-1})	
					Value	Uncertainty	Value	Uncertainty	Value	Uncertainty
Site P1 (1630 m)										
44°57′50″/6°10′40″										
VAM-01	0	17.15	0.56 ± 0.08	9.18 ± 1.33	3.04	0.73	0.33	0.10	2.81	0.91
VAM-02	8.5	17.15	0.63 ± 0.07	10.42 ± 1.14	8.84	2.01	0.85	0.22	–	–
VAM-03	13.5	17.15	0.72 ± 0.06	11.92 ± 1.03	17.16	3.77	1.44	0.35	–	–
VAM-04	20.5	17.15	0.75 ± 0.06	12.43 ± 1.01	39.47	7.89	3.18	0.72	–	–
Site P2 (1390 m)										
44°57′28″/6°10′22″										
VAV-01	0	14.31	0.38 ± 0.08	5.35 ± 1.09	1.94	0.47	0.36	0.12	3.07	0.89
VAV-02	6.5	14.31	0.28 ± 0.07	3.90 ± 0.97	5.51	1.28	1.41	0.49	–	–
VAV-03	14	14.31	0.39 ± 0.07	5.51 ± 1.01	4.41	0.99	0.80	0.24	–	–
VAV-04	20	14.31	0.58 ± 0.06	8.12 ± 0.78	7.16	1.72	0.88	0.24	–	–
VAV-05	28	14.31	0.92 ± 0.04	12.88 ± 0.58	50.58	10.01	3.93	0.84	–	–
Site B1 (1640 m)										
44°57′55″/6°10′44″	0	17.28	0.67 ± 0.09	11.12 ± 1.43	16.58	5.43	–	–	0.68	0.24
Site B2 (1450 m)										
44°57′36″/6°10′25″	0	14.99	0.23 ± 0.07	3.26 ± 1.04	3.59	0.78	–	–	0.92	0.36
Site B3 (1400 m)										
44°57′29″/6°10′22″	0	14.40	0.35 ± 0.08	4.87 ± 1.15	10.39	2.93	–	–	0.47	0.18

Table IV.3.2. *Cosmogenic nuclide data. (a) Surface production rates (atoms g^{-1}quartz yr^{-1}) scaled for latitudinal and altitudinal effects from Stone [2000]. (b) Geomorphic scaling factors have been calculated following the method of Dunne et al. [1999] with a ±5° uncertainty to our geomorphic shielding measurements. (c) Sample production rate (atoms g^{-1}quartz yr^{-1}) corrected for sample location within the gorge (geomorphic scaling factor) and sample thickness. (d) Analytical uncertainties are based on counting statistics, a conservative estimate of 3% instrumental variability and a ~20% uncertainty in the chemical blank correction.*

The four CRE ages of profile *P1* range from 0.33 ±0.10 ^{10}Be-ka (*VAM-01*) at the bottom (in accordance with the evidence for recent fluvial abrasion) to 3.18 ±0.72 ^{10}Be-ka (*VAM-04*) at the top of the gorge. The linear relation between sample height and CRE age implies that gorge incision rates have been constant at 11 ±2 mm yr^{-1} since the last ~4 kyr (Figure IV.3.17a). Profile *P2* shows similar trends, with CRE ages ranging from 0.36 ±0.12 ^{10}Be-ka (*VAV-01*) at the bottom to 3.93 ±0.84 ^{10}Be-ka (*VAV-05*) at the top of the gorge. However, two samples of profile *P2* (*VAV-03* and *VAV-04*) show very similar CRE ages (0.80 ±0.24 and 0.88 ±0.24 ^{10}Be-ka, respectively) that are significantly younger than the age-trend defined by the other three samples (Figure IV.3.17b). Excluding these outliers, profile *P2* also shows a linear relation between sample height and CRE age, suggesting a gorge deepening rate of 7.5 ±1.5 mm yr^{-1} (Figure IV.3.17b).

Present-day erosion rates measured in the active gorge channel are lower. For the upper reach of the stream, where gorge deepening has just started (Figures IV.3.15b and IV.3.16c), sample *B1* records an incision rate of 0.7 ±0.2 mm yr^{-1}. Samples collected within the gorge show variable incision. *VAV-01* and *VAM-01* samples provide incision rates of ~3 mm yr^{-1} (Table IV.3.2) whereas samples *B2* and *B3* record more moderate incision rates of 0.9 ±0.4 and 0.5 ±0.2 mm yr^{-1}, respectively.

IV.3.2.5 - Discussion and conclusions

All CRE ages are post-glacial, suggesting that the present-day Gorge du Diable results from Holocene fluvial incision. Top profile samples (*VAM-04* and *VAV-05*) provide ages younger than 5 ka. *VAM-04* was collected on the gorge sidewall and thus reflects continuous fluvial incision of the gorge. *VAV-05*, however, was sampled close to the glacial surface at the top of the gorge. Its CRE age of 3.9 ±0.8 ^{10}Be-ka is much younger than the age of glacial retreat from the alpine piedmonts, dated at ~20 ka [*Ivy-Ochs et al.*, 2004], or even final ice retreat from internal Alpine valleys dated to the end of the Younger Dryas event at ~12 ka [*Ivy-Ochs et al*., 1996; *Kelly et al*., 2006]. This time lag can be interpreted either as resulting from post-glacial surface reburial, leading to an underestimation of the retreat age, or as implying delayed initiation of gorge incision during the late Holocene. Topography nearby the gorge reveals high cliffs and scree deposits formed by abundant rock-falls (Figure IV.3.18d). These features argue for potential burial of the gorge during the Holocene. Some of these blocks

coming from surrounding cliffs may be encountered in the present-day active channel of the gorge (Figure IV.3.18a).

Figure IV.3.18. *Field photographs showing geomorphic configuration of the gorge. a) View of active channel at sampling site P2 showing meter-scale blocks derived from both surrounding topography and gorge sidewalls. b) Profile P2 showing potential rock-fall scar (red star corresponds to VAV-04 sample). c) Planar surface at sampling site B3 (yellow star) above a pool. d) Photograph of surrounding topography close to the gorge (<100m, see Figure IV.3.15a for location) showing a high rock cliff and scree-slope deposits resulting from abundant rock-fall events.*

Along the profiles, our sampling strategy was to collect fluvial abrasion remnants. However, these morphologies may be difficult to differentiate from rock-fall scars and some sampled surfaces (*e.g.*, sample locations *VAV-03* and *VAV-04*) may record rock-fall events (Figure IV.3.18b). Moreover, at the location of profile *P2*, meter-scale blocks are abundant in the active channel, suggesting that rock-fall events are recurrent and may imply large amounts of material (Figure IV.3.18a). We thus interpret the similar CRE ages of *VAV-03* and *VAV-04* as

recording a rock-fall that occurred around 0.8 ka, supposing no prior production. Excluding these two outliers, best fits on age-elevation profiles (Figure IV.3.17a, b) suggest constant incision rates between 6 and 13 mm yr^{-1}. These local Holocene rates are more than an order of magnitude higher than million-year scale denudation rates (0.2-0.7 km myr^{-1}) inferred for the surrounding massifs [*e.g.*, *Seward et al.*, 1999; *Vernon et al.*, 2008]. They are also significantly higher than late Quaternary erosion rates (~0.2-1.0 mm yr^{-1}) inferred from sedimentation in Alpine lakes [*Hinderer*, 2001]. However, these high local incision rates are similar to values measured in other settings of transient landscape response to climatic or tectonic forcing, where incision rates may reach up to cm yr^{-1} [*e.g.*, *Whipple et al.*, 2000b, *Schaller et al., 2005*; *Ouimet et al.*, 2008]. For the Drac watershed, which is close to the Vénéon area, *Brocard et al.* [2003] reported incision rates in fluvial terraces and calcareous bedrock that exceed cm yr^{-1} since the last glacier retreat.

In the active channel of the gorge, present-day incision rates range from 0.5 to 3 mm yr^{-1}. This spatial difference may be explained by stream configurations at the different sampling sites. Samples *B2* and *B3* were collected on a planar surface in a pool ~1 m above the present-day stream (Figure IV.3.18c). This configuration suggests that the sampled surface may have been episodically protected from fluvial abrasion, which would explain its relatively long exposure and thus low apparent erosion rates (0.9 ±0.4 and 0.5 ±0.2 mm.yr^{-1} respectively). Samples *VAV-01* and *VAM-01* have been sampled directly in the present-day stream and reveal higher erosion rates (3.1 ±0.9 and 2.8 ±0.9 mm yr^{-1}, respectively). Sample *B1* (upstream reach where incision has just begun) has also been collected from present-day stream (Figure IV.3.16c) but reports much lower erosion rate (0.7 ±0.2 mm yr^{-1}). These spatial variations are consistent with an "incision wave" in which knickpoints propagate upstream along the catchment [*e.g.*, *Weissel and Seidl*, 1998; *Whipple and Tucker*, 1999].

Present-day gorge incision rates are 2-5 times lower than long-term gorge deepening and are in close agreement with catchment-scale denudation rates ranging between 0.3 and 1.5 mm yr^{-1} in the Ecrins-Pelvoux massif [*Delunel et al.*, 2008] or in the Swiss Alps [*Wittmann et al.*, 2007; *Norton et al.*, 2008]. This difference may result from recent human activities such as intense deforestation, which led to an increase in sediment production in mountainous areas [*e.g.*, *Noël et al.*, 2001]. This increased sediment flux is transported from the catchment to the trunk stream via the gorge, and sediment storage may episodically and partially protect the

present-day bed from fluvial abrasion and thus reduce incision rates [*Korup and Schlunegger*, 2007; *Valla et al.*, 2010c].

Our data show that ~30 m of local relief was carved during the last 3-5 kyr in the Gorge du Diable with incision rates >1 cm yr^{-1}, in agreement with morphometric [*Korup and Schlunegger*, 2007] and numerical modeling [*Valla et al.*, 2010c] studies. We infer that bedrock gorges incising glacial hanging valleys respond rapidly to glacial/interglacial cycles and can be used as markers of recent post-glacial processes.

Although this study focuses on a single bedrock gorge and other gorges should be investigated to produce more data and better understand the post-glacial evolution of these transient features, our first results show that the Gorge du Diable is post-glacial in origin and that high incision rates of up to cm y^{-1} may occur locally in transient landscapes.

Acknowledgments

This study is part of PV's PhD project at Université Joseph Fourier in the framework of the *ERD-Alps* project funded by the *Agence Nationale de la Recherche* (project N° ANR-08-BLAN-0303-01 awarded to PvdB). We thank R. Delunel and X. Robert for invaluable field assistance and R. Braucher for help during sample preparation. The staff of the ASTER AMS facility is acknowledged for technical assistance during ^{10}Be measurements. We thank reviewers Stefano Andreucci, Jo De Waele and Fritz Schlunegger and associate editor Vincenzo Pascucci for constructive reviews that helped to improve the manuscript.

Chapter V :

Synthèse et perspectives

Mon travail de thèse s'est organisé autour de la problématique associée à la compréhension et la quantification de l'évolution du relief Alpin, ainsi que son lien avec l'histoire d'exhumation tardi-Néogène et Quaternaire des Alpes occidentales. Dans cette optique, j'ai développé différentes approches basées sur : (1) l'utilisation de la modélisation numérique afin d'extraire des informations quantitatives et indépendantes sur les histoires d'exhumation et l'évolution du relief à partir de données thermochronologiques [*Valla et al.*, 2010b; *van der Beek et al.*, 2010]; (2) l'application d'un nouvel outil thermochronométrique, l'$^{4}He/^{3}He$ sur apatite [*Valla et al.*, submitted, a, b], afin de contraindre l'exhumation terminale et le développement du relief local associés à l'initiation Mi-Pléistocène du creusement de la vallée du Rhône (Alpes suisses); et (3) la modélisation numérique de l'action des processus d'érosion glaciaire (partie IV.2) et fluviale [*Valla et al.*, 2010c] associée à la quantification des vitesses d'incision fluviale post-glaciaire à partir de la mesure des concentrations en ^{10}Be *in-situ* [*Valla et al.*, 2010a]. Ce chapitre de discussion synthétise l'ensemble des résultats obtenus lors de cette étude, ainsi que leurs interprétations et les implications qui en découlent vis-à-vis de la quantification de l'exhumation et de l'évolution du relief des Alpes occidentales, mais pouvant être étendues à d'autres contextes orogéniques, avant de proposer des perspectives potentielles de recherche afin de compléter ce travail et répondre aux nombreuses questions soulevées ou restées en suspens.

V.1 - Quantification de l'exhumation et de l'évolution du relief via la thermochronologie

Interprétation quantitative de données thermochronologiques

Le développement des méthodes thermochronométriques, initié lors des dernières décennies [*e.g.*, *Wagner and Reimer*, 1972 *Zeitler et al.*, 1987; *Hurford*, 1991; *Gallagher et al.*, 1998; *Farley*, 2002; *Shuster and Farley*, 2005], a permis l'application d'outils quantitatifs que sont les différents thermochronomètres (hautes- et basses-températures) afin de contraindre les histoires d'exhumation dans les chaînes de montagne [*Wagner and Reimer*, 1972; *Hurford*, 1991; *Gallagher et al.*, 1998; *Ehlers and Farley*, 2003]. La définition d'une température de fermeture [*Dodson*, 1973], propre à un système thermochronométrique et à un minéral, permet certes de quantifier l'âge de franchissement d'une isotherme spécifique (en posant

quelques hypothèses simplificatrices, partie I.2.1), mais elle ne donne que très peu d'informations sur les détails de l'histoire de refroidissement d'une roche.

Différentes stratégies d'échantillonnage permettent d'optimiser l'utilisation des outils thermochronométriques dans la quantification de l'histoire d'exhumation d'un échantillon. Ainsi, la mesure des longueurs de trace de fission [*e.g.*, *Gleadow et al.*, 1986; *Green et al.*, 1986; *Lasslet et al.*, 1987], combinée à la modélisation numérique [*Gallagher et al.*, 2005a, *Ketcham*, 2005], apporte des contraintes sur l'histoire thermique d'un échantillon; cependant, les approches développées considèrent chaque échantillon individuellement et ne permettent pas d'exploiter la cohérence spatiale existant dans une série d'échantillons. Par ailleurs, l'apport des longueurs de trace de fission n'est pas toujours discriminatoire quant à la détermination du chemin de refroidissement d'un échantillon [*Gallagher et al.*, 1998; *Kohn et al.*, 2005].

Une autre approche dans la quantification de l'histoire d'exhumation consiste à adopter une une stratégie multi-échantillons et/ou multi-thermochronomètres, avec notamment l'échantillonnage de données thermochronologiques réparties le long d'un profil altitudinal [*e.g.*, *Wagner and Reimer*, 1972; *Hurford*, 1991; *Fitzgerald et al.*, 1995; 1999; *House et al.*, 1997; *Reiners et al.*, 2002]. L'analyse de la relation âge-altitude à partir de ces données permet d'une part de s'affranchir de toute hypothèse sur le gradient géothermique (sauf pour le stade final d'exhumation), et d'autre part elle permet de déduire une vitesse d'exhumation apparente et moyennée sur la fenêtre temporelle couverte par les échantillons. De plus, l'analyse de la relation âge-altitude peut dans certains cas mettre en évidence l'exhumation d'une zone de recuit partiel pour les traces de fission (PAZ), ou zone de rétention partielle pour le système (U-Th-Sm)/He (PRZ), signal d'un événement d'exhumation rapide suite à une période de stabilité [*Fitzgerald et al.*, 1995; 2006]. Néanmoins, dans la plupart des cas d'étude, cette approche ne permet pas de contraindre des changements temporels dans les vitesses d'exhumation, la relation âge-altitude ne donnant accès qu'à une vitesse d'exhumation moyenne. Par ailleurs, l'approche unidimensionnelle de la relation âge-altitude ne prend pas en compte l'influence de la topographie sur les isothermes crustales [*Stüwe et al.*, 1994; *Mancktelow and Grasseman*, 1997].

L'utilisation d'outils thermochronométriques basses-températures tel le système (U-Th-Sm)/He sur apatite (température de fermeture $T_c \approx 70 \pm 15$ °C; *Farley*, 2000) a ouvert de

nouveaux horizons quant aux applications de la thermochronologie à des problèmes géodynamiques et notamment vis-à-vis de la quantification de l'évolution du relief [*House et al.*, 1998; *Braun*, 2002a; *Ehlers and Farley*, 2003; *Clarke et al.*, 2005; *Foeken et al.*, 2007]. *Braun* [2002a, b] a en effet montré que l'évolution de la topographie au cours du temps avait une influence non-négligeable sur l'organisation des isothermes sous-jacentes, et par conséquent sur l'enregistrement thermochronologique lors de l'exhumation des roches. Ainsi, l'utilisation de données thermochronologiques permet, en théorie, de pourvoir des informations complémentaires à la fois sur les vitesses d'exhumation et sur l'évolution du relief topographique.

Le développement du modèle numérique *Pecube* [*Braun*, 2003] a été entrepris afin de répondre à ces nouvelles attentes. L'utilisation de *Pecube* permet de résoudre l'équation de la chaleur en 3D et ainsi de prédire des histoires *t-T* (éventuellement converties en données thermochronologiques diverses, voir partie I.2.2.2) à partir de scénarios d'exhumation combinant une vitesse de dénudation régionale (spatialement homogène ou non) à une exhumation additionnelle et variable résultant de l'évolution de la topographie (et éventuellement de la réponse isostatique associée; *Braun*, 2003).

Mon approche, similaire à celle développée par des travaux antérieurs [*Braun and van der Beek*, 2004; *Braun and Robert*, 2005; *Herman et al.*, 2007] a été de coupler le modèle numérique *Pecube* à un algorithme d'inversion (*Neighbourhood Algorithm*; *Sambridge*, 1999a, b), permettant une analyse multidimensionnelle et la recherche de scénarios d'exhumation et d'évolution du relief compatibles avec les données thermochronologiques observées. Cependant, à la différence des études citées ci-dessus, je ne me suis pas limité à une recherche du meilleur scénario d'exhumation vis-à-vis des données [*Sambridge*, 1999a] mais j'ai utilisé l'ensemble des modèles *Pecube* générés lors de la recherche multidimensionnelle afin de contraindre quantitativement quelle était la résolution (fonction de densité de probabilité; *Sambridge*, 1999b) des données thermochronologiques vis-à-vis de la quantification des histoires d'exhumation et de relief [*Herman et al.*, 2010a, b; *Valla et al*., 2010b; *van der Beek et al.*, 2010; *Glotzbach et al.*, submitted]. Mon étude, aussi bien synthétique (parties II.2 et II.4; *Valla et al.*, 2010b) que lors de l'application de la méthode à un jeu de données réelles dans le massif des Ecrins-Pelvoux (partie II.3; *van der Beek et al.*, 2010) a montré la nécessité d'inclure cette étape statistique *a posteriori* afin d'expliciter dans

quelle mesure les données thermochronologiques peuvent fournir des informations quantitatives sur les scénarios d'exhumation et d'évolution du relief.

Par ailleurs, un problème récurrent à l'étude menée et propre à l'approche numérique inverse concerne la détermination de la dimensionnalité adéquate du problème inverse [*e.g.*, *Akaike*, 1974; *Schwartz*, 1978]. En effet, la complexité du modèle numérique utilisé, définie à partir des divers degrés de liberté dans les scénarios d'exhumation (nombre de phases d'exhumation et de développement de la topographie, *i.e.*, nombre de points *t-T* le long de l'histoire de refroidissement; *Gallagher et al.*, 2005a), ainsi que les contraintes imposées ou non sur les paramètres thermiques et élastiques utilisés dans *Pecube*, est liée à la résolution du jeu de données thermochronologiques disponibles. Ainsi, l'utilisation d'un critère statistique, le Bayesian Information Criterion (*BIC*; Schwartz, 1978), permet de limiter la complexité du modèle utilisé au regard des données thermochronologiques incoporées à ce modèle. Le critère *BIC*, déjà proposé par *Gallagher et al.* [2005a] pour l'inversion de données thermochronologiques, a été incorporé dans mon approche couplant le modèle *Pecube* avec l'algorithme d'inversion *NA* afin de déterminer l'exhumation tardi-Néogène et l'évolution du relief dans la région du Valais suisse (partie III.3, *Valla et al.*, submitted, b). Mes résultats, ainsi qu'une étude similaire récemment proposée par *Glotzbach et al.* [submitted] dans le massif voisin du Mont-Blanc, démontrent l'utilité d'utiliser un tel critère statistique afin d'évaluer la complexité optimale du modèle à utiliser et de ne pas sur-interpréter les données à disposition par un modèle dont la complexité dépasse leur résolution.

Mon travail étant centré sur la quantification de l'évolution du relief au cours de l'histoire tardi-Néogène des Alpes françaises et suisses, je me suis par conséquent intéressé à comprendre dans quelle mesure et sous quelle(s) configuration(s) l'histoire d'exhumation d'une chaîne de montagne et son évolution topographique pouvaient être quantifiées à partir de l'utilisation de données thermochronologiques (essentiellement des thermochronomètres basses-températures) couplée à l'approche numérique exposée ci-dessus.

Une première étude synthétique (partie II.2, *Valla et al.*, 2010b) est basée sur l'utilisation de données thermochronologiques basses-températures spatialement réparties selon une relation âge-altitude (profil altitudinal). Nos résultats démontrent clairement que pour cette configuration d'échantillonnage, l'histoire d'exhumation peut être quantitativement résolue à condition de combiner plusieurs thermochronomètres. Au contraire, l'évolution du relief reste

difficile à évaluer et ne peut être quantitativement prédite que dans les conditions où le développement de la topographie induit une exhumation locale deux à trois fois supérieure à la vitesse de dénudation régionale [*Valla et al.*, 2010b].

Ces résultats sont confirmés par l'application de la méthode d'inversion à un jeu de données thermochronologiques (combinant traces de fission et (U-Th)/He, à la fois sur apatite et zircon) collectées le long d'un profil altitudinal dans massif des Ecrins-Pelvoux (Alpes françaises, *van der Beek et al.*, 2010). Notre étude montre que, même si l'histoire d'exhumation peut être assez précisément déterminée, l'évolution du relief reste difficile à quantifier malgré la combinaison de plusieurs thermochronomètres. *Vernon et al.* [2009] ont utilisé une approche similaire le long de deux profils altitudinaux dans les Alpes centrales et arrivent à la même conclusion concernant la non-prédiction de l'évolution du relief. A contrario, *Glotzbach et al.* [submitted] ont clairement mis en évidence une augmentation récente du relief dans le massif du Mont-Blanc à partir de la même approche; cependant ces derniers ont utilisé des données collectées à la fois le long de profils altitudinaux, mais également le long d'un tunnel traversant le massif étudié [*Glotzbach et al.*, 2008]. Deux hypothèses sont alors envisageables afin d'expliquer ces différences : (1) soit la topographie actuelle du massif du Mont-Blanc a effectivement été acquise au cours du Pliocène-Quaternaire, tandis que le relief dans le massif des Ecrins-Pelvoux et les Alpes centrales est resté plus ou moins stationnaire durant le tardi-Néogène ou n'a pas connu une augmentation suffisamment importante pour avoir été enregistrée par la thermochronologie, (2) soit la stratégie d'échantillonnage proposée par *Glotzbach et al.* [2008; submitted] a permis de quantifier un développement récent du relief, tandis que les données de *Vernon et al.* [2009] et *van der Beek et al.* [2010] collectées uniquement le long de profils altitudinaux ne présentent pas une résolution suffisante pour identifier cet épisode récent. Les trois zones d'étude présentent un relief topographique similaire, fortement influencé par les glaciations Quaternaires [*Montjuvent*, 1974; 1978; *Delunel*, 2010; *Valla et al.*, 2010c], laissant penser que leur histoire en termes d'évolution du relief est assez concordante, à l'encontre de l'hypothèse (1). Ainsi, les différences dans la prédiction ou non d'un développement récent du relief au sein des Alpes occidentales et centrales pourraient provenir des stratégies d'échantillonnage selon lesquelles sont collectées les données thermochronologiques (hypothèse (2)).

Afin d'évaluer dans quelle mesure les stratégies d'échantillonnage de données thermochronologiques peuvent influencer les prédictions concernant les histoires

d'exhumation et de relief, j'ai développé une seconde étude synthétique (partie II.4) similaire au travail exposé ci-dessus [*Valla et al.*, 2010b]. Ainsi j'ai défini, à partir d'une topographie réelle haute résolution, un jeu de données thermochronologiques basses-températures synthétiques prédites via le modèle numérique *Pecube* pour un scénario impliquant une augmentation récente du relief topographique associée à une vitesse de dénudation régionale constante.

A partir de ce jeu de données, et de l'approche inverse développée auparavant (*Pecube* + *NA*), j'ai exploré la résolution intrinsèque de différentes stratégies d'échantillonnage combinant profil(s) altitudinal(aux), fonds de vallées, et/ou profil collecté à travers un massif montagneux, dans la quantification des histoires d'exhumation et la prédiction de l'évolution du relief. Mes résultats confirment l'hypothèse avancée ci-dessus selon laquelle la stratégie d'acquisition de données thermochronologiques uniquement le long d'un profil altitudinal n'apparait pas comme la plus optimale dans l'optique de quantifier l'évolution du relief. La combinaison de plusieurs stratégies d'échantillonnage, favorisant la distribution spatiale des données thermochronologiques, apporte de bien meilleures contraintes quant à la prédiction de l'évolution du relief. Ces résultats sont par ailleurs confirmés par l'étude menée dans le Valais suisse (partie III.3, *Valla et al.*, submitted, b), pour laquelle l'interprétation numérique de diverses données thermochronologiques distribuées le long de la vallée du Rhône a permis de quantifier un développement récent du relief; tandis que *Vernon et al.* [2009], utilisant des données similaires mais réparties le long d'un profil altitudinal unique, n'avaient pas pu conclure quant à un changement récent du relief pour la même zone d'étude. Nos résultats impliquent la nécessité de repenser *a priori* la stratégie d'échantillonnage à mettre en place en fonction du contexte géodynamique, mais également du signal d'exhumation que l'on cherche à identifier et quantifier via la thermochronologie.

Enfin, j'ai également profité de cette étude synthétique pour explorer la problématique liée à la supposition *a priori* du gradient géothermique lors des modélisations thermo-cinématiques *Pecube*. En effet, ce paramètre reste extrêmement difficile à évaluer, pourtant son influence sur la prédiction des données thermochronologiques est non négligeable [*Braun*, 2002a; *Gallagher et al.*, 2005a]. J'ai par conséquent déterminé dans quelle mesure les diverses stratégies d'échantillonnage, évoquées ci-dessus, pouvaient apporter des contraintes non seulement sur les histoires d'exhumation et du relief, mais également sur la structure thermique de la croûte supérieure. Notre étude montre l'intérêt de continuer à utiliser les

relations âge-altitude; ces dernières, tout comme l'utilisation de données collectées le long de profils à travers un massif, présentant la meilleure résolution quant à la prédiction du gradient géothermique. Cependant, comme l'ont démontré récemment *Glotzbach et al.* [submitted], plus important que la stratégie d'échantillonnage, c'est la combinaison de thermochronomètres hautes- et basses-températures qui permet l'obtention de prédictions optimales quant à la structure thermique de la croûte supérieure.

Enfin, il apparait nécessaire d'aborder dans cette section un dernier point concernant la façon quelque peu simpliste selon laquelle sont implémentés les changements du relief topographique dans les modélisations thermo-cinématiques *Pecube*. En effet, la plupart des modélisations réalisées jusqu'à ce jour ont utilisé un paramètre géométrique (*R*) afin de simuler les changements de relief [*e.g.*, *Herman et al.*, 2007; *Vernon et al.*, 2009; *Herman et al.*, 2010b; *Valla et al.*, 2010b; *van der Beek et al.*, 2010; *Glotzbach et al.*, submitted]. Ce paramètre *R* (voir partie II.1, *Valla et al.*, 2010b) est défini par le rapport entre le paléo-relief à une période donnée et le relief actuel, et permet de modéliser d'une façon simplifiée mais assez efficace (en terme de coût de calcul et de complexité) une augmentation ou diminution du relief topographique. Cependant, cette approche simpliste ne rend pas compte de la complexité liée au processus d'évolution de la topographie (cf. partie I.2.3) comme l'évolution en plan du réseau de drainage ou encore un développement local ou spatialement non-homogène du relief.

Lors de cette étude, j'ai été amené à réfléchir sur la façon optimale de simuler le changement de relief induit par la mise en place des glaciations Quaternaires (parties III.2. et III.3, *Valla et al., submitted*, a, b]. Une méthode, certes encore très simpliste au regard de la complexité des processus glaciaires et péri-glaciaires, a été de considérer l'augmentation du relief comme étant uniquement liée au creusement des vallées par l'action érosive des glaciers. Ainsi, mon approche intègre le relief actuel comme un proxy du paléo-relief (*i.e.*, antérieur à la mise en place des glaciations Quaternaires) tout en "ré-haussant" le fonds des vallées principales afin de tenir compte, d'une part, du creusement important des vallées par les glaciers, et d'autre part de la préservation des zones de haute altitude de par l'action réduite des processus péri-glaciaires et/ou la protection de ces zones par des glaciers à base froide. Cette approche, validée dans le cas des Alpes suisses, n'est pas facilement exportable dans d'autres contextes géodynamiques où l'impact des glaciations sur le relief topographique est opérée suivant des

modalités variables [*Brozovic et al.*, 1997; *Whipple et al.*, 1999; *Mitchell and Montgomery*, 2006; *Egholm et al.*, 2009; *Thompson et al.*, 2010; *Shuster et al.*, in press].

Enfin, l'approche optimale dans la simulation des changements de reliefs lors de modélisations thermo-cinématiques *Pecube* serait de coupler dynamiquement *Pecube* avec des algorithmes simulant l'action des processus de surface, le transfert de sédiments et l'évolution de la topographie [*e.g.*, *Braun and Sambridge.*, 1997; *Crave and Davy*, 2001; *Tucker et al.*, *2001*; *Herman and Braun*, 2008; *Egholm et al.*, 2009]. Ce couplage entre simulations thermo-cinématiques et modèles d'évolution des paysages a déjà été effectué avec succès dans la modélisation de l'évolution d'escarpements de marges passives [*Braun and van der Beek*, 2004], l'évolution de la topographie en Himalaya [*Herman et al.*, 2010a], ou encore la réponse topographique à la transition depuis un système d'érosion fluviale à glaciaire [*Pedersen et al.*, 2010]. Cependant, cette approche couplée pose potentiellement un problème d'échelles spatiales et temporelles, souvent différentes entre les modélisations thermo-cinématiques (échelles spatiales et temporelles assez grandes) et la modélisation des processus de surface (échelles spatiales extrêmement variables mais échelles de temps souvent plus courtes).

De plus, nos résultats synthétiques (partie II.4) démontrent clairement que, si l'utilisation d'une grille basse-résolution lors des modélisations thermo-cinématiques *Pecube* peut entrainer une perte non négligeable des informations relatives aux histoires d'exhumation et d'évolution du relief, l'utilisation d'une grille à très haute résolution (souvent mise en place pour simuler les processus de surface) n'apporte pas d'information supplémentaire à partir d'un certain seuil topographique (~750-1000 m de résolution). Ainsi, la méthode de couplage entre les prédictions des modèles simulant les processus de surface et les codes thermo-cinématiques tel *Pecube* nécessite une réflexion *a priori* sur l'approche optimale à employer, notamment vis-à-vis de l'interpolation des grilles topographiques prédites par les modèles d'évolution du paysage et utilisées comme paramètres d'entrée dans les modélisations thermo-cinématiques *Pecube*.

Apports et spécificités de la thermochronométrie $^{4}He/^{3}He$

Au cours de ma thèse, j'ai eu la possibilité d'utiliser la thermochronométrie $^{4}He/^{3}He$ sur apatite (en collaboration avec D. Shuster du Berkeley Geochronology Center). Cet outil thermochronométrique, récemment développé [*Shuster and Farley*, 2004; 2005], apporte des contraintes complémentaires au thermochronomètre (U-Th-Sm)/He sur apatite à partir de la quantification de la distribution de l'^{4}He radiogénique au sein d'un minéral d'apatite. Ainsi, la thermochronométrie $^{4}He/^{3}He$ permet de poser des contraintes sur le chemin de refroidissement d'un échantillon depuis ~90 °C (température à laquelle la rétention de l'^{4}He devient effective) jusqu'à des températures de surface (~20-30 °C).

D'un point de vue analytique, la thermochronométrie $^{4}He/^{3}He$ est certes plus contraignante que la détermination d'un âge (U-Th-Sm)/He (voir partie I.2.1.1). En effet, les échantillons analysés doivent dans un premier temps contenir des apatites en proportion suffisante, car ~50 mg d'apatites doivent être isolés et préparés avant d'être exposés à une irradiation protonique (production synthétique d'^{3}He). Cette étape nécessite également un temps d'attente de ~2 à 3 mois [*Shuster et al.*, 2004] avant de pouvoir manipuler et analyser les échantillons irradiés. De plus, la sélection du grain d'apatite est plus restrictive que pour la détermination d'un âge He. Outre la sélection d'apatites ne présentant pas d'inclusion apparente (microscope binoculaire à polariseur), l'analyse par dégazage de la distribution spatiale du rapport $^{4}He/^{3}He$ nécessite la sélection d'une apatite non brisée et ne présentant pas de signe d'abrasion. En effet, l'utilisation d'un grain d'apatite non entier (terminaisons du grain brisées) peut être corrigée *a posteriori* dans la détermination d'un âge He, la détermination des concentrations en U-Th-Sm et He étant associée à la mesure de la taille du grain. Au contraire, cette configuration peut potentiellement résulter dans la perte d'information quantitative sur la distribution de l'^{4}He radiogénique dans le grain d'apatite (notamment pour la surface du grain), et ne peut que difficilement être corrigée dans l'approche thermochronométrique $^{4}He/^{3}He$. Par ailleurs, les problèmes, récurrents pour la thermochronométrie (U-Th-Sm)/He sur apatite [*Farley*, 2002], de zonations spatiales potentielles dans la répartition des isotopes parents (U-Th-Sm), ainsi que la présence d'inclusions non visibles lors de l'étape de sélection, peuvent être identifiés suite à l'expérience de dégazage par paliers successifs, ces configurations amenant à des rapports $^{4}He/^{3}He$ anormaux vis-à-vis des prédictions théoriques [*Farley et al.*, 2010] et permettant d'écarter *a posteriori* l'analyse.

Enfin, l'analyse du rapport $^4He/^3He$, par dégazage et suivant des paliers temps/température successifs, nécessite des concentrations en ^4He suffisantes afin de dépasser le seuil de détection analytique pour chacun des paliers de dégazage, limitant potentiellement l'applicabilité de la méthode thermochronométrique $^4He/^3He$ pour des échantillons pauvres en U-Th-Sm et/ou ayant des âges He relativement jeunes [*Shuster and Farley*, 2005].

En dépit des limites potentielles inhérentes à la thermochronométrie $^4He/^3He$, notre étude a clairement démontré son avantage vis-à-vis des méthodes thermochronométriques "classiques" (traces de fission et (U-Th-Sm)/He sur apatite) dans la quantification de l'exhumation terminale d'un échantillon (partie III.2, *Valla et al.*, submitted, a). Cependant, il est important de préciser que la résolution avec laquelle ce stade terminal d'exhumation peut être déterminé reste fortement dépendante de l'âge He de l'échantillon, et donc du contexte géodynamique régional. En effet, le travail de *Schildgen et al.* [2010] apporte des contraintes sur l'initiation du creusement d'un canyon autour de ~8-13 Ma à partir de données $^4He/^3He$, la résolution sur ces données étant limitée de par la gamme des âges He (~10-20 Ma). Au contraire, *Shuster et al.* [in press] rapportent des âges beaucoup plus jeunes en Nouvelle-Zélande (âges He ~1-2 Ma) et proposent par conséquent des contraintes beaucoup plus précises sur l'exhumation finale de leurs échantillons durant le tardi-Pléistocène. Dans notre cas, tout comme pour l'étude menée par *Shuster et al.* [2005] en Colombie Britannique, nos échantillons présentent des âges He entre ~2 et 8 Ma [*Valla et al.*, submitted, a], et les données $^4He/^3He$ associées mettent en évidence une exhumation terminale datée à ~1 Ma, en lien avec la transition climatique Mi-Pléistocène.

De plus, l'intérêt de la thermochronométrie $^4He/^3He$ est renforcé par la capacité de quantifier une histoire de refroidissement individuellement pour chaque échantillon [*Shuster and Farley*, 2004; 2005]. Ainsi, l'analyse comparée d'échantillons spatialement répartis (par exemple, le long d'un profil altitudinal) autorise la mise en évidence de différences dans leurs histoires *t-T* et ainsi une interprétation en termes d'évolution du relief [*Shuster et al.*, 2005; *Schildgen et al.*, 2010; *Shuster et al.*, in press; *Valla et al.*, submitted, a]. L'analyse d'échantillons collectés le long de deux profils altitudinaux dans la vallée du Rhône [*Valla et al.*, submitted, a] révèle en effet un fort contraste entre les échantillons de fond de vallée, présentant un refroidissement terminal récent, et ceux collectés à plus hautes altitudes, qui ne présentent pas d'indice d'une exhumation récente. Ce contraste, non révélé par les âges He mais mis en évidence à partir des données $^4He/^3He$, nous a permis d'interpréter l'histoire d'exhumation

récente de ces échantillons comme étant associée au creusement glaciaire de la vallée du Rhône durant le Pléistocène [*Valla et al.*, submitted, a].

Une des limites actuelles dans l'interprétation des données $^4He/^3He$ concerne la conversion de ces données en termes d'histoires thermiques uniquement [*e.g.*, *Shuster et al.*, 2005]; cette approche ne facilitant pas la quantification des processus d'exhumation tectoniques et/ou géomorphologiques associés à ces histoires *t-T*. Une alternative, développée lors de mes travaux [*Valla et al.*, submitted, a, b] et initialement proposée par *Schildgen et al.* [2010], consiste à comparer les histoires de refroidissement déduites des données $^4He/^3He$ avec les résultats de modélisations thermo-cinématiques *Pecube*. Cependant, l'approche optimale pour l'interprétation des données $^4He/^3He$, associées aux autres données thermochronologiques "classiques", serait de coupler directement l'approche numérique développée par *Schildgen et al.* [2010] avec le modèle *Pecube*, permettant ainsi de tester directement les prédictions issues de scénarios d'exhumation et/ou d'évolution du relief avec les données observées.

L'utilisation de la thermochronométrie $^4He/^3He$ dans la quantification de l'histoire d'exhumation tardi-Néogène et le développement du relief Pléistocène dans le Valais suisse [*Valla et al.*, submitted, a, b] met en évidence l'apport complémentaire de cette technique vis-à-vis du thermochronomètre (U-Th-Sm)/He, mais également des thermochronomètres plus hautes-températures telle la méthode des traces de fission sur apatite. De plus, la thermochronométrie $^4He/^3He$ permet d'établir un lien entre les données thermochronologiques "classiques" et les datations par mesure des isotopes cosmogéniques produits *in-situ* [*e.g.*, *Gosse and Philips*, 2001]. Cependant, nos données $^4He/^3He$ obtenues dans le Valais suisse, même si elles mettent en évidence une exhumation Pléistocène associée au creusement des vallées, ne possèdent pas une résolution suffisante pour contraindre dans le détail l'histoire d'exhumation tardi-Pléistocène, et notamment la réponse topographique spécifique à chacune des oscillations périodiques glaciaires/interglaciaires. De plus, les datations à partir de la mesure des nucléides cosmogéniques produits *in-situ* apportent uniquement des contraintes sur la dynamique de déglaciation tardi-Pléistocène et Holocène des Alpes occidentales [*Ivy-Ochs et al.*, 2006; 2009; *Delunel*, 2010] et ne permettent pas de remonter au-delà de la dernière période glaciaire. Ainsi, les données $^4He/^3He$ ne peuvent pas directement être mises en correspondance avec les données issues de la mesure des nucléides cosmogéniques, aucune des deux méthodologies ne semblant, dans le cas des Alpes Européennes, pouvoir apporter des informations quantitatives quant à l'évolution du relief à une échelle temporelle

intermédiaire de l'ordre du cycle glaciaire/interglaciaire (~100 ka). Le développement d'un nouveau thermochronomètre basé sur la luminescence stimulée optiquement (Optically Stimulated Luminescence, OSL) pourrait apporter des contraintes complémentaires aux données $^{4}He/^{3}He$, ce thermochronomètre ayant potentiellement une température de fermeture de l'ordre de ~30-35 °C [*Herman et al.*, 2010b] et pouvant être appliqué sur des échelles de temps de l'ordre du cycle glaciaire/interglaciaire [*Herman et al.*, 2009; 2010b].

Problèmes potentiels et développements liés au système (U-Th-Sm)/He sur apatite

J'aimerais terminer cette discussion sur l'utilisation des méthodes thermochronomètriques par l'exposition des problèmes inhérents au thermochronomètre (U-Th-Sm)/He sur apatite, ainsi que les développements analytiques et numériques potentiellement applicables afin d'identifier ces biais et de quantifier leur influence sur la significativité d'un âge He.

Les données (U-Th-Sm)/He sur apatite obtenues dans le massif des Ecrins-Pelvoux (partie II.3, *van der Beek et al.*, 2010; *Beucher et al.*, submitted) et le massif des Aiguilles Rouges (partie III.2, *Valla et al.*, submitted, a) présentent, pour certains échantillons, une faible reproductibilité entre les différents réplicas [*Vernon et al.*, 2009], ainsi que des âges He pouvant être plus vieux que les âges traces de fission associés. Plusieurs biais peuvent expliquer ces complications dans la détermination et l'interprétation de données (U-Th-Sm)/He sur apatite [*e.g.*, *Farley*, 2002]. En effet, comme proposées précédemment, la présence d'inclusions microscopiques (zircon, monazite…), l'implantation d'^{4}He radiogénique depuis des minéraux voisins ou encore une répartition non homogène des isotopes parents (U-Th-Sm) peuvent engendrer des incohérences dans la détermination des âges He [*Spiegel et al.*, 2009; *Farley et al.*, 2010].

Plusieurs moyens analytiques permettent d'appréhender ce type de biais, comme la préparation et l'observation de lame mince pour chaque échantillon, afin d'évaluer le voisinage minéral autour des apatites et d'écarter ainsi les échantillons présentant des potentialités d'implantation d'^{4}He radiogénique. De plus, l'analyse des populations d'apatites au moyen de la microscopie électronique à balayage, ou de procédés impliquant la cathodoluminescence [*Gautheron et al.*, 2009], permet d'identifier de potentielles zonations spatiales dans la répartition des éléments U-Th-Sm, mais également la présence d'inclusions microscopiques au sein d'un grain d'apatite [*Gautheron et al.*, 2009]. *Spiegel et al.* [2009] ont

proposé un procédé d'abrasion de la surface (~20 µm) des grains d'apatite afin de s'affranchir des effets liés à l'implantation d'^{4}He radiogénique depuis les minéraux voisins. Néanmoins, cette méthode résulte dans la perte d'information sur la distribution spatiale de l'^{4}He radiogénique et peut potentiellement entrainer un biais dans le calcul de l'âge He. Une méthode alternative dans la prévention de ces complications est l'analyse de la distribution de l'^{4}He radiogénique dans le grain d'apatite à partir de la méthode de dégazage ^{4}He/^{3}He. En effet, l'ensemble des biais évoqués ci-dessus influence fortement la répartition spatiale de l'^{4}He radiogénique au sein du minéral, résultant dans la mesure de rapports ^{4}He/^{3}He déviant significativement des prédictions théoriques [*Farley et al.*, 2010].

Enfin, j'ai exposé, lors de la présentation de la méthodologie (U-Th-Sm)/He sur apatite (partie I.2.1), l'influence potentielle des dommages cristallins créés par les désintégrations alpha (U-Th "α-decay") sur la rétention de l'He au sein du réseau [*Shuster et al.*, 2006; *Shuster and Farley*, 2009]. Cet effet, dépendant d'une part de la concentration en éléments U-Th dans un grain d'apatite, et d'autre part de l'histoire thermique propre à l'échantillon, peut avoir une influence non négligeable sur la température de fermeture du système et par conséquent sur l'âge He obtenu [*Flowers et al.*, 2009; *Gautheron et al.*, 2009].

Une partie des échantillons récoltés dans le Valais suisse (parties III.2 et III.3, *Valla et al.*, submitted, a, b) présentent des âges He plus vieux que les âges traces de fission sur apatite avoisinants, ainsi que de très fortes teneurs en U-Th. L'utilisation de modèles numériques simulant la création et le recuit des dommages alpha, ainsi que leur influence sur la rétention d'He au sein du réseau cristallin [*Flowers et al.*, 2009; *Gautheron et al.*, 2009], a permis d'interpréter ces données en termes d'exhumation et d'évolution du relief, les prédictions étant en accord avec des données avoisinantes mais ne présentant pas ce type de complication [*Valla et al.*, submitted, b]. Ces résultats indiquent clairement la nécessité de prendre en compte et de quantifier l'influence des dommages alpha sur la température de fermeture du système (U-Th-Sm)/He et par conséquent dans l'interprétation d'âges He, aussi bien pour des échantillons ayant une histoire d'exhumation ancienne et potentiellement complexe [*Flowers et al.*, 2009; *Gautheron et al.*, 2009] que pour des échantillons relativement "jeunes" ayant enregistré une exhumation plutôt rapide mais étant riches en U-Th [*Valla et al.*, submitted, b].

V.2 - Histoire Néogène-Pléistocène des Alpes occidentales et centrales

Les contraintes apportées par les données thermochronologiques et leur interprétation via la modélisation numérique (chapitres II et III), ainsi que la quantification des processus d'érosion fluviale et glaciaire en réponse aux oscillations climatiques durant le Pléistocène (chapitre IV), permettent de proposer un cadre pour l'histoire d'exhumation tardi-Néogène et Pléistocène des Alpes occidentales et centrales.

L'évolution des Alpes occidentales et centrales au cours du tardi-Néogène a été et reste un sujet controversé quant aux histoires d'exhumation et de développement du relief topographique [*e.g.*, *Willett*, 2010b], en particulier pour l'évolution des massifs cristallins externes (ECMs, *e.g.*, *Vernon et al.*, 2008). Mon travail apporte de nouvelles contraintes sur l'histoire d'exhumation des massifs des Ecrins-Pelvoux (partie II.3, *van der Beek et al.*, 2010), des Aiguilles Rouges et de l'Aar (partie III.3, *Valla et al.*, submitted, b). Nous avons mis en évidence [*van der Beek et al.*, 2010; *Valla et al.*, submitted, b] l'existence d'un épisode d'exhumation rapide (~1-2 km Ma^{-1}) affectant ces deux zones d'étude au cours du tardi-Miocène (~10 à 5 Ma), cet épisode étant précédé et suivi par des vitesses de dénudation plus modérées (~0.3-0.5 km Ma^{-1}). Nos résultats sont en accord avec d'autres études utilisant la thermochronologie *in-situ* dans les Alpes occidentales et centrales [*Glotzbach et al.*, 2008; *Vernon et al.*, 2009; *Glotzbach et al.*, submitted], et semblent indiquer un épisode d'exhumation rapide généralisé à l'ensemble des ECMs. Cet épisode est grossièrement concordant avec la mise en place de la déformation du Jura autour de ~12 Ma [*Burkhard and Sommaruga*, 1998], et l'évolution tardi-Miocèene du réseau de drainage nord-alpin [*Schlunegger and Willett*, 1999; *Kuhlemann et al.*, 2001; *Glotzbach et al.*, 2011], potentiellement associés à un changement géodynamique dans la nature du sous-plaquage crustal au niveau des ECMs [*Bonnet et al.*, 2007].

De même, la brusque cessation de cet épisode à ~5 Ma est en accord avec la fin de la déformation enregistrée dans le Jura [*Becker*, 2000], et serait potentiellement associée à une transition dans le régime d'érosion, l'exposition de roches cristallines Paléozoïques (socle des ECMs) et moins sensibles à l'érosion que la couverture sédimentaire Mézosoïque entrainant une diminution transitoire des vitesses d'exhumation [*Glotzbach et al.*, submitted]. Cependant, cet épisode d'exhumation rapide, ainsi que les mécanismes proposés pour son

initiation et sa terminaison, contrastent avec la compilation de données thermochronologiques basses-températures [*Vernon et al.*, 2008], les flux sédimentaires vers les bassins périphériques [*Kuhlemann et al.*, 2002] et l'initiation de l'exhumation du bassin d'avant-pays molassique [*Cederbom et al.*, 2004; in press], ces observations suggérant fortmement une augmentation de l'exhumation autour de ~5 Ma.

Glotzbach et al. [submitted] proposent l'hypothèse selon laquelle les flux sédimentaires enregistrés dans les bassins [*Kuhlemann et al.*, 2002] ne refléteraient pas la totalité des sédiments érodés dans la chaîne, une partie non négligeable des sédiments carbonatés étant exportée sous forme dissoute. Ainsi, la brusque augmentation des flux sédimentaires (par ailleurs récemment remise en cause par *Schumer and Jerolmack*, 2009 ainsi que par *Willenbring and von Blanckenburg*, 2010) observée à ~5 Ma [*Kuhlemann et al.*, 2002] serait éventuellement reliée à l'augmentation du ratio entre les sédiments silicatés et les roches carbonatées, expliquant également la diminution des vitesses de dénudation observée au sein des ECMs [*Glotzbach et al.*, submitted]. Cependant, ce phénomène ne permet pas d'expliquer l'arrêt de la déformation dans le Jura [*Becker*, 2000], ainsi que l'exhumation du bassin d'avant-pays molassique [*Cederbom et al.*, 2004; in press]. Une explication alternative, d'origine climatique [*Willett*, 2010b], implique un changement climatique au Messinien [*Rouchy et al.*, 2001; *Willett et al.*, 2006], le refroidissement global du climat autour de ~5 Ma [*Zachos et al.*, 2001; *Zhang et al.*, 2001], ou encore l'initiation de la circulation du Gulf Stream à ~4.6 Ma [*Haug and Tiedemann*, 1998; *Cederbom et al.*, 2004] dans le changement géodynamique observé pour les Alpes Européennes [*Willett et al.*, 2006; *Willett*, 2010b].

La combinaison des processus tectoniques, climatiques, ou encore l'influence de processus régionaux d'origine crustale ou mantellique [*e.g.*, *Lyon-Caen and Molnar*, 1989; *Lippitsch et al.*, 2003; *Lardeaux et al.*, 2006] dans l'évolution tardi-Néogène des Alpes occidentales et centrales, rend le signal d'exhumation déduit de la thermochronologie difficile à interpréter et à relier à l'un ou l'autre des processus mis en jeu [*Willett*, 2010b]. Ainsi, les Alpes Européennes ne semblent pas présenter un cas "idéal" dans l'étude détaillée des couplages entre tectonique, climat et processus de surface [*Whipple*, 2009], de par la diversité et la complexité des processus impliqués durant le Néogène. Dans la perspective d'apporter des contraintes plus précises sur l'évolution tardi-Néogène des Alpes, il serait important de compléter les études thermochronologiques pour l'ensemble des ECMs, et d'essayer ainsi de relier leur histoire d'exhumation respective avec l'enregistrement sédimentaire dans les sous-

bassins périphériques associés [*Kuhlemann*, 2000]. La quantification des flux sédimentaires peut également être complétée par l'ajout de données récentes non incorporées dans les bilans initiaux [*Kuhlemann*, 2000], ainsi qu'une meilleure prise en compte de la part des flux dissous et/ou en suspension dans les bilans globaux. Enfin, il semble important de prendre en considération les données thermochronologiques détritiques mettant en évidence une exhumation quasi-stationnaire à l'échelle de toutes les Alpes occidentales et centrales durant le Néogène [*Bernet et al.*, 2001; 2009; *Glotzbach et al.*, 2011], en désaccord avec les évidences thermochronologiques *in-situ* et les bilans sédimentaires exposés ci-dessus. Une meilleure compréhension du signal thermochronologique détritique apparait nécessaire afin de quantifier dans quelle mesure il permet de retranscrire des épisodes d'exhumation rapide sur une fenêtre temporelle réduite [*Glotzbach et al.*, 2011], et ainsi potentiellement réconcilier les données *in-situ* avec le signal détritique.

Un autre thème abordé dans mon étude concerne l'histoire du relief Alpin tel que nous pouvons l'observer à ce jour, et notamment de savoir si la topographie Alpine actuelle résulte d'une évolution long-terme initiée depuis les premiers stades de la collision orogénique, ou si cette signature topographique a été au contraire acquise durant l'évolution tardive de l'orogène, en lien avec les changements climatiques tardi-Néogène [*Cederbom et al.*, 2004; *Molnar*, 2004] et/ou la mise en place des glaciations Pliocènes-Pléistocènes [*Haug et al.*, 2005; *Lisiecki and Raymo*, 2005]. Les données thermochronologiques récoltées dans le massif des Ecrins-Pelvoux (partie II.3, *van der Beek et al.*, 2010) ne permettent pas d'apporter de contraintes quantitatives sur l'évolution tardi-Néogène du relief, la résolution limitée des données étant potentiellement expliquée par la stratégie d'échantillonnage (voir partie précédente) et le nombre limité de données basses-températures (seulement deux âges (U-Th)/He). L'étude menée dans le Valais suisse (parties III.2 et III.3, *Valla et al.*, submitted, a, b) combine des données thermochronologiques "classiques" (traces de fission et (U-Th-Sm)/He sur apatite) avec des données $^{4}He/^{3}He$. Nos résultats, et notamment la résolution des données thermochronométriques $^{4}He/^{3}He$, indiquent clairement un épisode d'exhumation terminal depuis le Mi-Pléistocène (~1 Ma) associé au creusement de la vallée du Rhône (~1-1.5 km d'incision), et en accord avec l'évolution topographique du massif voisin du Mont-Blanc [*Glotzbach et al.*, submitted], ou encore le creusement de la vallée de l'Aar (~1 km d'incision) dont l'initiation a été datée autour de ~0.8-1 Ma [*Haeuselmann et al.*, 2007]. Cependant, ce développement du relief topographique Alpin est postérieur à l'initiation des glaciations globales dans l'Hémisphère Nord [*Maslin et al.*, 1996; *Haug et al.*, 2005] et les

premières évidences de glaciations dans les Alpes Européennes durant le Pliocène [*Schlüchter*, 1986; *Jeannin*, 1991]. Cet épisode semble plutôt être relié à la transition climatique Mi-Pléistocène depuis des cycles glaciaires/interglaciaires symétriques de 40 ka vers des cycles asymétriques de 100 ka et de plus fortes amplitudes climatiques [*Lisiecki*, 2010]. L'enregistrement sédimentaire du bassin d'avant-pays du Pô confirme également un changement majeur dans la nature des sédiments déposés autour de ~0.8-0.9 Ma [*Muttoni et al.*, 2003] avec la transition depuis des dépôts typiquement fluviaux vers des sédiments plus grossiers d'origine glaciaire [*Scardia et al.*, 2006], confirmant la mise en place de glaciations majeures au sein des Alpes à partir de ~1 Ma.

L'ensemble des résultats exposés ci-dessus suggèrent un fort développement du relief topographique local associé au creusement des vallées principales et la préservation des zones de haute altitude durant les glaciations Mi-Pléistocènes [*Valla et al.*, submitted, a], en accord avec les conclusions de *Shuster et al.* [2005] en Colombie Britannique (Amérique du Nord). Cependant, cette réponse topographique à la mise en place des glaciations diffère de la théorie du "glacial buzzsaw" [*Brozovic et al.*, 1997; *Whipple et al.*, 1999] selon laquelle le relief topographique aurait fortement diminué suite à l'initiation des périodes glaciaires, les glaciers maximisant l'érosion autour de la ligne d'équilibre glaciaire [*Egholm et al.*, 2009]. Une théorie alternative, proposée récemment par *Thompson et al.* [2010], suggère une préservation relative du relief de par la présence de glaciers à base froide comme dans le cas des calottes polaires [*Bo et al.*, 2009].

D'un point de vue géomorphologique, notre étude dans le bassin du Rhône (partie III.4) montre que la mise en place des oscillations périodiques glaciaires/interglaciaires a engendré une augmentation majeure du relief local associée à une diminution de l'élévation moyenne de la topographie [*Whipple et al.*, 1999], en accord avec des données de paléo-altimétrie préliminaires suggérant une paléo-topographie Néogène en moyenne plus élevée (~1 km) que la configuration actuelle [*Mulch et al.*, 2010]. A l'échelle du bassin versant, la reconstruction topographique préglaciaire met cependant en évidence que le relief *moyen* du bassin [*Whipple et al.*, 1999] n'a que très peu augmenté (~5-10 %) depuis la mise en place des glaciations Pléistocènes.

Le lien entre la mise en place des cycles glaciaires/interglaciaires asymétriques de 100 ka et le développement du relief topographique reste une question non totalement élucidée. Une

interprétation personnelle, également proposée par *Norton et al.* [2010a], implique la forte amplitude climatique et l'asymétrie de ces cycles de 100 ka dans la création d'un déséquilibre topographique qui s'amplifie au cours des multiples oscillations Pléistocènes. Ainsi, durant chaque période glaciaire puis interglaciaire, les processus d'érosion tendent à modeler le relief topographique vers un "état d'équilibre" différent selon les processus glaciaires/périglaciaires et les agents d'érosion actifs durant les périodes interglaciaires (processus de pente et fluviaux). Cet état transitoire de la topographie, initié depuis le Mi-Pléistocène, accélère les processus d'érosion et amplifie ainsi le développement du relief. La question relative à l'efficacité des processus d'érosion glaciaire versus fluviale dans la modification de la topographie reste ouverte [*e.g.*, *Hallet et al.*, 1996; *Montgomery*, 2002; *Koppes and Montgomery*, 2009]; cependant, la comparaison des vitesses d'érosion moyennées sur le Pléistocène (intégrant par conséquent de multiples oscillations glaciaires/interglaciaires) et des flux sédimentaires depuis le début de l'interglaciaire actuel [*Hinderer*, 2001] semble suggérer, pour le bassin du Rhône, une certaine constance dans les vitesses d'érosion moyennes depuis le Mi-Pléistocène (partie III.4).

Enfin, les prédictions numériques (partie III.4) concernant la réponse isostatique au développement Pléistocène du relief [*Molnar and England*, 1990; *Champagnac et al.*, 2007; *van der Beek and Bourbon*, 2008] montrent que celle-ci semble être spatialement corrélée avec la distribution des vitesses géodésiques mesurées aujourd'hui dans le Valais suisse [*Schlatter et al.*, 2005]. Cependant, cette décharge isostatique ne peut expliquer à elle seule l'amplitude du soulèvement actuel, impliquant d'autres processus géodynamiques tels que le retrait glaciaire initié depuis le tardi-Pléistocène [*Gudmundsson*, 1994; *Barletta et al.*, 2006], le remplissage sédimentaire des grandes vallées et des lacs alpins [*Champagnac et al.*, 2009], ou encore des processus géodynamiques à plus grande échelle [*e.g.*, *Champagnac et al.*, 2008].

La quantification de l'impact des oscillations entre périodes glaciaires et interglaciaires sur l'évolution de la topographie passe par une meilleure compréhension de la dynamique des processus de surface (fluviaux et glaciaires), notamment via une approche numérique (chapitre IV). En effet, l'utilisation d'un modèle numérique simulant les processus d'érosion glaciaire [*Egholm et al.*, 2009] permet d'apporter des contraintes supplémentaires quant aux différences en termes d'érosion (et donc d'évolution de la topographie) entre les cycles glaciaires/interglaciaires de 40 et 100 ka (partie IV.2). Cependant, les résultats préliminaires

menés dans la modélisation de différents stades d'englacement pour le massif du Mont-Blanc (partie IV.2.2) démontrent la difficulté d'intégrer l'ensemble de la complexité climatique (gradients de températures et de précipitations, bilan radiatif…) dans les modèles numériques glaciaires [*Tomkin and Braun*, 2002; *Kessler et al.*, 2006; *Herman and Braun*, 2008; *Egholm et al.*, 2009]. Ainsi, même si la modélisation de la dynamique glaciaire a été grandement améliorée et permet de simuler de façon plus réaliste l'écoulement des glaciers sur des échelles de temps géologiques [*Herman and Braun*, 2008; *Egholm et al.*, 2009], la gestion des données climatiques, et de leurs variations spatio-temporelles, demande à être perfectionnée afin de modéliser fidèlement, dans un premier temps, les reconstitutions paléogéographiques des extensions glaciaires tardi-Pléistocènes [*Kelly et al.*, 2004; *Coutterand*, 2010 ; *Delunel*, 2010]. Ces perspectives de développement pourront par la suite permettre d'explorer la complexité liée à l'érosion glaciaire [*Hallet*, 1979; 1996], ou encore le transport sédimentaire par les glaciers [*Hagdorn and Boulton*, 2004], et ainsi de quantifier l'impact réel de la mise en place des glaciations sur le relief Alpin [*Herman and Braun*, 2008; *Egholm et al.*, 2009].

Enfin, la réponse topographique liée à la dernière déglaciation a également été abordée lors de mon étude (partie IV.3, *Valla et al.*, 2010a, c). Nos résultats démontrent que l'action des glaciers durant les périodes froides amplifie l'érosion postglaciaire, notamment par l'action des processus fluviaux au niveau de zones de fort déséquilibre telles les gorges de raccordement [*Montjuvent*, 1974; *Korup and Schlunegger*, 2007; *Norton et al.*, 2010a; *Valla et al.*, 2010c], ces objets présentant des vitesses d'érosion Holocènes de l'ordre du cm an^{-1} [*Valla et al.*, 2010a] ainsi qu'un fort couplage avec les processus de pente [*Valla et al.*, 2010c]. Ces processus fluviaux participent à l'évolution du relief topographique local au cours des périodes interglaciaires et sont combinés à la dynamique des processus de pente [*Cossart et al.*, 2008; *Delunel et al.*, 2010a] et périglaciaires, ces derniers étant extrêmement efficaces en période interglaciaire dans la production de sédiments pour les zones de haute altitude [*Delunel et al.*, 2010b]. Ainsi, ces résultats montrent que l'évolution de la topographie durant le Pléistocène n'est pas seulement opérée pendant les périodes glaciaires; en effet le modelé du relief par les glaciers favorise l'action des processus d'érosion durant les stades interglaciaires suivants, et par conséquent une amplification du relief topographique [*Norton et al.*, 2010a].

V.3 - Conclusions générales et perspectives

L'étude présentée dans ce manuscrit apporte de nouvelles contraintes vis-à-vis de la compréhension des interactions entre processus climatiques, tectoniques et de surface dans l'évolution géodynamique et géomorphologique des chaînes de montagne.

Mon travail a mené au développement d'outils numériques quantitatifs afin d'extraire, à partir de données thermochronologiques, des informations indépendantes quant aux histoires d'exhumation et d'évolution du relief, et montre la nécessité de réfléchir *a priori* sur les stratégies d'échantillonnage et d'interprétation numérique des données à mettre en œuvre suivant le contexte géodynamique étudié et la problématique recherchée. Par ailleurs, l'utilisation de la thermochronométrie $^{4}He/^{3}He$ sur apatite apporte une résolution précise sur les derniers stades de l'histoire d'exhumation, permettant de quantifier des changements récents dans la dénudation et/ou l'évolution du relief.

L'application de ces outils quantitatifs dans les Alpes occidentales et centrales m'a permis d'apporter de nouveaux éléments de contrainte quant à l'histoire d'exhumation tardi-Néogène des massifs cristallins externes (massifs des Ecrins-Pelvoux, des Aiguilles Rouges et de l'Aar) et notamment l'existence d'un épisode d'exhumation rapide se terminant aux alentours de la transition Miocène-Pliocène (~5 Ma), celui-ci étant précédé et suivi par une dynamique d'exhumation plus modérée. Enfin, l'histoire d'exhumation Pléistocène des Alpes semble marquée par le développement du relief topographique, associé à la mise en place de glaciations majeures au Mi-Pléistocène.

L'impact des changements climatiques Pliocènes et des glaciations Pléistocènes sur l'évolution du relief reste cependant encore mal contraint et demande à être mieux appréhendé, la réponse topographique à ces forçages climatiques étant apparemment variable suivant les différents contextes géodynamiques. L'étude de ces questions passe par une approche plus globale combinant : (1) l'acquisition de données quantitatives sur les vitesses d'exhumation et d'érosion (thermochronométrie (U-Th-Sm)/He, $^{4}He/^{3}He$ et OSL, nucléides cosmogéniques), (2) le développement de la modélisation numérique couplant les processus de surface aux modèles thermo-cinématiques, et enfin (3) une compréhension plus avancée de la dynamique des processus d'érosion glaciaire et fluviale.

Références bibliographiques

Abrecht, J. (1994). Geologic units of the Aar massif and their pre-Alpine rock associations: a critical review. *Schweitzerische Mineralogische und Petrographische Mitteilungen*, 74, 5-27.

Akaike, H. (1974). A new look at the statistical identification model. *IEEE Transactions in Automatic Control*, 19, 716-723.

Allen, P.A. (2008). Time scales of tectonic landscapes and their sediment routing systems. *Geological Society, London, Special Publications*, 296, 7-28.

Alley, R.B., Lawson, D.E., Larson, G.J., Evenson, E.B., and Baker, G.S. (2003). Stabilizing feedbacks in glacier-bed erosion. *Nature*, 424(6950), 758-760.

Amerson, B., Montgomery, D.R., and Meyer, G. (2008). Relative size of glacial and fluvial valleys in central Idaho, *Geomorphology*, 93, 537-547.

Amundson, J.M., and Iverson, N.R. (2006). Testing a glacial erosion rule using hang heights of hanging valleys, Jasper National Park, Alberta, Canada. *Journal of Geophysical Research*, 111, 10.1029/2005JF000359.

Anderson, R.S. (1994). Evolution of the Santa Cruz Mountains, California, through tectonic growth and geomorphic decay. *Journal of Geophysical Research*, 99, 20,161-20,180.

Anderson, R.S., Molnar, P., and Kessler, M.A. (2006). Features of glacial valley profiles simply explained. *Journal of Geophysical Research,* 111, 10.1029/2005JF000344.

Avouac, J.P., and Burov, E.B. (1996). Erosion as a driving mechanism of intracontinental mountain growth. *Journal of Geophysical Research*, 101, 17747-17769.

Bagnold, R.A. (1977). Bed load transport by natural rivers. *Water Resources Research*, 13, 303-312.

Balco, G., Stone, J.O., Lifton, N.A., and Dunai, T.J. (2008). A complete and easily accessible means of calculating surface exposure ages or erosion rates from ^{10}Be and ^{26}Al measurements. *Quaternary Geochronology*, 3, 174-195.

Balco, G., and Rovey, C.W. (2010). Absolute chronology for major Pleistocene advances of the Laurentide Ice Sheet. *Geology*, 38, 795-798.

Baral, D.R., Hutter, K., and Greve, R. (2001). Asymptotic theories of large-scale motion, temperature, and moisture distribution in land-based polythermal ice sheets: a critical review and new developments. *Applied Mechanics Reviews*, 54, 215-256.

Barbarand, J., Carter, A., Wood, I., and Hurford, A. (2003). Compositional and structural control of fission-track annealing in apatite. *Chemical Geology*, 198, 107-137.

Barletta, V.R., Ferrari, C., Diolaiuti, G., Carnielli, T., Sabadini, R., and Smiraglia, C. (2006). Glacier shrinkage and modeled uplift of the Alps. *Geophysical Research Letters*, 33, L14307, doi:10.1029/2006GL026490.

Beaudevin, C. (2000). Contribution à l'étude de l'altitude atteinte par les glaciers quaternaires dans quelques vallées alpines. *Géologie Alpine*, 76, 83-116.

Beaumont, C., Fullsack, P., and Hamilton, J. (1992). Erosional control of active compressional orogens. In: K. R. McClay (Ed.) *Thrust Tectonics*, Chapman and Hall, London, 1-18.

Beck, C., Deville, E., Blanc, E., Philippe, Y., and Tardy, M. (1998). Horizontal shortening control of Middle Miocene marine siliciclastic accumulation (Upper Marine Molasse) in the southern termination of the Savoy Molasse Basin (northwestern Alps/southern Jura). *in* A. Mascle, C. Puigdefàbregas, H.P. Luterbacher, M. Fernàndez, (Eds), Cenozoic Foreland Basins of Western Europe, *Geological Society of London Special Publications*, 134, 263-278.

Becker, A. (2000). The Jura Mountains - an active foreland fold-and-thrust belt?. *Tectonophysics*, 321, 381-406.

Berlin, M.M., and Anderson, R.S. (2007). Modeling of knickpoint retreat on the Roan Plateau, western Colorado. *Journal of Geophysical Research*, 112, 10.1029/2006JF000553.

Berlin, M.M., and Anderson, R.S. (2009). Steepened channels upstream of knickpoints: Controls on relict landscape response. *Journal of Geophysical Research*, 114, 10.1029/2008JF001148.

Bernet, M., Zattin, M., Garver, J.I., Brandon, M.T., and Vance, J.A. (2001). Steady-state exhumation of the European Alps. *Geology*, 29, 35-38.

Bernet, M. (2009). A field-based estimate of the zircon fission-track closure temperature. *Chemical Geology*, 259, 181-189.

Bernet, M., Brandon, M., Garver, J., Balestieri, M.L., Ventura, B., and Zattin, M. (2009). Exhuming the Alps through time: clues from detrital zircon fission-track thermochronology. *Basin Research*, 21, 781-798.

Berthier, E. (2005). Dynamique et bilan de masse des glaciers de montagne (Alpes, Islande, Himalaya) : contribution de l'imagerie satellitaire. Thèse de Doctorat, Université de Toulouse.

Beucher, R., van der Beek, P.A., and Braun, J. (submitted). Assessing exhumation and relief development in the Pelvoux and Dora-Maira massifs (western Alps) from spectral analysis and inversion of thermochronological age transects. *Journal of Geophysical Reasearch*.

Bianchetti, G. (1993). Hydrogéologie et géothermie des venues d'eau du tunnel du Rawyl (Valais, Suisse). *Bulletin du Centre d'Hydrogéologie de l'Université de Neuchâtel*, 12, 88-109.

Bianchetti, G. (1994). Hydrogéologie et géothermie de la région de Lavey-les-Bains (Vallée du Rhône, Suisse). *Bulletin du Centre d'Hydrogéologie de l'Université de Neuchâtel*, 13, 3-32.

Bierman, P.R. (1994). Using in situ produced cosmogenic isotopes to estimate rates of landscape evolution: A review from the geomorphic perspective. *Journal of Geophysical Research*, 99(13), 885-896.

Bigot-Cormier, F., Sosson, M., Poupeau, G., Stéphan, J.-F., and Labrin, E. (2006). The denudation history of the Argentera Alpine External Crystalline Massif (Western Alps, France- Italy): an overview from the analysis of fission tracks in apatites and zircons. *Geodinamica Acta*, 19, 455-473.

Bini, A., Buoncristiani, J.-F., Couterrand, S., Ellwanger, D., Felber, M., Florineth, D., Graf, H.R., Keller, O., Kelly, M., Schlüchter, C., and Schoeneich, P. (2009). Switzerland during

the Last Maximal, map 1:500 000. *Federal Office of Topography Swisstopo*, 978-3-302-40049-5.

Bishop, P., and Goldrick, G. (2000). Geomorphological evolution of the East Australian continental margin. *in* Geomorphology and Global Tectonics, edited by M. A. Summerfield, pp. 225-254, John Wiley, New York.

Bishop, P., Hoey, T.B., Jansen, J.D., and Artza, I.L. (2005). Knickpoint recession rate and catchment area: the case of uplifted rivers in Eastern Scotland. *Earth Surface Processes and Landforms*, 30(6), 767-778.

Blatter, H. (1995). Velocity and stress fields in grounded glaciers: a simple algorithm for including deviatoric stress gradients. *Journal of Glaciology*, 41(138), 333-344.

Bo, S., Siegert, M.J., Mudd, S.M., Sugden, D., Fujita, S., Xiangbin, C., Yunyun, J., Xueyuan, T., and Yuansheng, L. (2009). The Gamburtsev mountains and the origin and early evolution of the Antarctic Ice Sheet. *Nature*, 459, 690-693.

Bonnet, C., Malavieille, J., and Mosar, J. (2007). Interactions between tectonics, erosion, and sedimentation during the recent evolution of the Alpine orogen: Analogue modeling insights. *Tectonics*, 26, TC6016, doi:10.1029/2006TC002048.

Boulton, G. (1974). Process and patterns of glacial erosion. *in* Glacial Geomorphology, edited by D. R. Coates, State University of New York at Binghamton, Binghamton, pp. 41-87.

Boulton, G. (1979). Processes of glacier erosion on different substrata. *Journal of Glaciology*, 23, 15-8.

Bousquet, R., Goffé, B., Henry, P., Le Pichon, X., and Chopin, C. (1997). Kinematic, thermal and petrological model of the central Alps: Lepontine metamorphism in the upper crust and eclogitisation of the lower crust. *Tectonophysics*, 273, 105-127.

Brandon, M.T., Roden-Tice, M., and Garver, J.I. (1998). Late Cenozoic exhumation of the Cascadia accretionary wedge in the Olympic Mountains, northwest Washington State. *Geological Society American Bulletin*, 110, 985-1009.

Braucher R., Bourlès D.L., Brown E.T., Colin F., Muller J.P., Braun J.J., Delaune M., Lescouet C., Raisbeck G.M., and Yiou F. (2000). Application of in situ-produced cosmogenic ^{10}Be and ^{26}Al to the study of lateritic soil development in tropical forest : Theory and examples from Cameron and Gabon. *Chemical Geology*, 170(1-4), 95-111.

Braucher, R., Brown, E.T., Bourlès, D.L., and Colin, F. (2003). In situ produced ^{10}Be measurements at great depths: implications for production rates by fast muons. *Earth and Planetary Science Letters*, 211, 251-258.

Braun, J., and Sambridge, M. (1997). Modelling landscape evolution on geological time scales: a new method based on irregular spatial discretization. *Basin Research*, 9, 27-52.

Braun, J., Zwartz, D., and Tomkin, J. (1998). A new surface-processes model combining glacial and fluvial erosion. *Annals of Glaciology*, 28, 282-290.

Braun, J. (2002a). Quantifying the effect of recent relief changes on age-elevation relationships. *Earth Planetary Science Letters*, 200, 331-343.

Braun, J. (2002b). Estimating exhumation rate and relief evolution by spectral analysis of age-elevation profiles. *Terra Nova*, 14, 210-214.

Braun, J. (2003). Pecube: A new finite element code to solve the heat transport equation in three dimensions in the Earth's crust including the effects of a time-varying, finite amplitude surface topography. *Computer & Geosciences*, 29, 787-794.

Braun, J., and van der Beek, P.A. (2004). Evolution of passive margin escarpments: What can we learn from low-temperature thermochronology? *Journal of Geophysical Research*, 109, F04009, doi:04010.01029/02004JF000147.

Braun, J. (2005). Quantitative constraints on the rate of landform evolution derived from low-temperature thermochronology. *Reviews in Mineralogy & Geochemistry* 58, 351-374.

Braun, J., and Robert, X. (2005). Constraints on the rate of post-orogenic erosional decay from low-temperature thermochronological data: application to the Dabie Shan, China. *Earth Surface Processes and Landforms*, 30, 1203-1225.

Braun, J., van der Beek, P.A., and Batt, G. (2006). Quantitative Thermochronology: Numerical Methods for the Interpretation of Thermochronological Data. Cambridge University Press, Cambridge, New York, 258 pp.

Braun, J. and members of the Low-T Thermochonology Team (2010). Numerical modeling as an essential tool for the interpretation of thermochronological datasets. Thermo2010, 12th International conference on thermochronology Glasgow, *Extended Abstract Volume p. 213*.

Briner, J.P., Kaufman, D.S., Manley, W.F., Finkel, R.C., and Caffee, M.W. (2005). Cosmogenic exposure dating of late Pleistocene moraine stabilization in Alaska. *Geological Society of America Bulletin*, 117(7), 1108-1120.

Brocard, G. (2002). Origine, variabilité spatio-temporelle et signature morhpologique de l'incision fluviale dans les Alpes Dauphinoises (SE France). Thèse de doctorat, Université Joseph Fourier Grenoble.

Brocard, G.Y., van der Beek, P.A., Bourles, D.L., Siame, L.L., and Mugnier, J.L. (2003). Long-term fluvial incision rates and postglacial river relaxation time in the French Western Alps from ^{10}Be dating of alluvial terraces with assessment of inheritance, soil development and wind ablation effects. *Earth and Planetary Science Letters*, 209(1-2), 197-214.

Brocard, G.Y., and van der Beek, P.A. (2006). Influence of incision rate, rock strength and bedload supply on bedrock river gradients and valley-flat widths: field-based evidence and calibrations from western Alpine rivers (SE France). *in* Willett, S.D., Hovius, N., Brandon, M.T., Fisher, D. (Eds.), Tectonics, Climate and Landscape Evolution. *Geological Society of America Special Publication*, 398, 101-126.

Brocklehurst, S.H., and Whipple, K.X. (2002). Glacial erosion and relief production in the Eastern Sierra Nevada, California. *Geomorphology*, 42(1-2), 1-24.

Brocklehurst, S.H., and Whipple, K.X. (2007). Response of glacial landscapes to spatial variations in rock uplift rate. *Journal of Geophysical Research*, 112, F02035, doi:10.1029/2006JF000667.

Brown, E.T., Edmond, J.M., Raisbeck, G.M., Yiou, F., Kurz, M.D., and Brook, E.D. (1991). Examination of surface exposure ages of moraines in Arena Valley, Antarctica, using in situ produced ^{10}Be and ^{26}Al. *Geochimica et Cosmochimica Acta*, 55, 2269-2283.

Brozovic, N., Burbank, D.W., and Meigs, A.J. (1997). Climatic limits on landscape development in the northwestern Himalaya. *Science*, 276, 571-574.

Buoncristiani, J.-F., and Campy, M. (2004). The palaeogeography of the last two glacial episodes in France: the Alps and Jura. in Extent and Chronology of Glaciations (eds Ehlers J., and Gibbard, P.L.), Elevier, pp.101-110.

Burbank, D.W. (2002). Rates of erosion and their implications for exhumation. *Mineralogical Magazine*, 66, 25-52.

Burkhard, M., and Sommaruga, A. (1998). Evolution of the western Swiss Molasse basin: structural relations with the Alps and the Jura belt. *in* A. Mascle, C. Puigdefàbregas, H.P. Luterbacher, M. Fernàndez, (Eds), Cenozoic Foreland Basins of Western Europe, *Geological Society of London Special Publications*, 134, 279-298.

Calais, E., Nocquet, J.-M., Jouanne, F., and Tardy, M. (2002). Current strain regime in the Western Alps from continuous Global Positioning System measurements, 1996-2001. *Geology*, 30, 651–654.

Campani, M., Herman, F., and Mancktelow, N. (2010). Two- and three-dimensional thermal modeling of a low-angle detachment: Exhumation history of the simplon Fault Zone, central Alps. *Journal of Geophysical Research*, 115, doi:10.1029/2009JB007036.

Carcaillet J. (2003). Modulation de la production atmosphérique du cosmonucléide béryllium-10 lors des excursions et inversions géomagnatiques depuis 1,3 Ma. Thèse de Doctorat, Université d'Aix Marseille III.

Carlson, W.D., Donelick, R.A., and Ketcham, R.A. (1999). Variability of apatite fission-track annealing kinetics: I. Experimental results. *American Mineralogist*, 84, 1213-1223.

Carslaw, H.S., and Jaeger, C.J. (1959). Conduction of Heat in Solids, 3rd Edition. Clarendon Press, Oxford, 510 pp.

Casty, C., Wanner, H., Luterbacher, J., Esper, J., and Böhm, R. (2005). Temperature and precipitation variability in the European Alps since 1500. *International Journal of Climatology*, 25, 1855-1880.

Cederbom, C., Sinclair, H., Schlunegger, F., and Rahn, M. (2004). Climate-induced rebound and exhumation of the European Alps. *Geology*, 32, 709-712.

Cederbom, C.E, van der Beek, P.A., Schlunegger, F., Sinclair, H.D., and Oncken, O. (in press). Rapid extensive erosion of the North Alpine foreland basin at 5-4 Ma: Climatic, tectonic and geodynamic forcing on the European Alps. *Basin Research*.

Champagnac, J.-D., Sue, C., Delacou, B., and Burkhard, M. (2004). Brittle deformation in the inner NW Alps: from early orogen-parallel extrusion to late orogen-perpendicular collapse. *Terra Nova*, 16, 232-242.

Champagnac, J.-D., Molnar, P., Anderson, R.S., Sue, C., and Delacou, B. (2007). Quaternary erosion-induced isostatic rebound in the western Alps. *Geology*, 35, 195-198.

Champagnac, J.-D., van der Beek, P., Diraison, G., and Dauphin, S. (2008). Flexural isostatic response of the Alps to increased Quaternary erosion recorded by foreland basin remnants, SE France. *Terra Nova*, 20, 213-220.

Champagnac J.-D., Schlunegger F., Norton K., von Blanckenburg F., Abbühl L.M., and Schwab M. (2009). Erosion-driven uplift of the modern Central Alps. *Tectonophysics*, 474, 236-249.

Chatanantavet, P., and Parker, G. (2008). Experimental study of bedrock channel alluviation under varied sediment supply and hydraulic conditions. *Water Resource Research*, 44, 10.1029/2007WR006581.

Clark, M.K., Maheo, G., Saleeby, J., and Farley, K.A. (2005). The non-equilibrium landscape of the southern Sierra Nevada, California. *GSA Today*, 15, 4-10.

Codilean, A.T., Bishop, P., Stuart, F.M., Hoey, T.B., Fabel, D., and Freeman, S.P.H.T. (2008). Single-grain cosmogenic ^{21}Ne concentrations in fluvial sediments reveal spatially variable erosion rates. *Geology*, 36(2), 159-162.

Cossart E., Braucher R., Fort M., Bourlès D.L., and Carcaillet J. (2008). Slope instability in relation to glacial debuttressing in alpine areas (Upper Durance catchment, southeastern France): Evidence from field data and ^{10}Be cosmic ray exposure ages. *Geomorphology*, 95, 3-26.

Coutterand S., and Nicoud, G. (2005). Les stades de retrait du glacier de l'Arve entre le verrou de Cluses et l'ombilic de Chamonix au cours du Tardiglaciaire (vallée de l'Arve, Haute Savoie). *Quaternaire*, 16, 85-94.

Coutterand, S., and Buoncristiani, J.-F. (2006). Paléogéographie du dernier maximum glaciaire du pléistocène de la région du massif du Mont-Blanc, France. *Quaternaire*, 17, 35-43.

Coutterand, S. (2010). Etude géomorphologique des flux glaciaires dans les Alpes Nord-Occidentales au Pléistocène récent : du maximum de la dernière glaciation aux premières étapes de la féglaciation. Thèse de Doctorat, Université de Chambéry.

Crave, A., and Davy, P. (2001). A stochastic ''precipiton'' model for simulating erosion/sedimentation dynamics. *Computer & Geosciences*, 27, 815-827.

Crosby, B.T., and Whipple, K.X. (2006). Knickpoint initiation and distribution within fluvial networks: 236 waterfalls in the Waipaoa River, North Island, New Zealand. *Geomorphology*, 82(1-2), 16-38.

Crosby, B.T., Whipple, K.X., Gasparini, N.M., and Wobus, C.W. (2007). Formation of fluvial hanging valleys: Theory and simulation. *Journal of Geophysical Research*, 112, 10.1029/2006JF000566.

Crouzet, C., Menard, G., and Rochette, P. (2001). Cooling history of the Dauphinoise Zone (Western Alps, France) deduced from the thermopaleomagnetic record: geodynamic implications. *Tectonophysics*, 340, 79-93.

Daly, C., Neilson, R.P., and Phillips, D.L. (1994). A statistical-topographic model for mapping climatological precipitation over mountainous terrain. *Journal of Applied Meteorology*, 33, 140-158.

Davies, T.A., Hay, W.W., Southam, J.R., and Worseley, T.R. (1977). Estimates of Cenozoic oceanic sedimentation rates. *Science*, 197, 53-55.

Davis W.M. (1899). The geographical cycle. *Geographical Journal*, 14, 481-504.

Debelmas, J., and Lemoine, M. (1970). The Western Alps: Paleogeography and Structure. *Earth-Science Reviews*, 6, 221-256.

Delacou, B., Sue, C., Champagnac, J.-D., and Burkhard, M. (2004). Present-day geodynamics in the bend of the western and central Alps as constrained by earthquake analysis. *Geophysical Journal International*, 158, 753-774.

Delunel, R., van der Beek, P.A., Bourlès, D.L., and Carcaillet, J. (2008). Frost-shattering processes increase denudation at catchment scales: results from *in-situ* produced ^{10}Be measurement in stream sediments (French Western Alps). *Eos Transactions AGU,* 89(53), Fall Meeting Supplementary Abstract H54D-04.

Delunel, R. (2010). Evolution géomorphologique du massif des Ecrins-Pelvoux depuis le Dernier Maximum Glaciaire. Thèse de Doctorat, Université de Grenoble.

Delunel, R., Hantz, D., Braucher, R., Bourlès, D.L., Schoeneich, P., and Deparis, J. (2010a). Surface exposure dating and geophysical prospecting of the Holocene Lauvitel rock slide (French Alps). *Landslides*, 7, 393-400.

Delunel, R., van der Beek, P.A., Carcaillet, J., Bourlès, D.L., and Valla, P.G. (2010b). Frost-cracking control on catchment denudation rates: Insights from in situ produced ^{10}Be concentrations in stream sediments (Ecrins–Pelvoux massif, French Western Alps). *Earth and Planetary Science Letters*, 293, 72-83.

Delunel, R., Bourlès, D.L., van der Beek, P.A., and Paquet, E. (in preparation). Altitude-dependant cosmic-ray flux attenuation by seasonal snow cover revealed by neutron detector monitoring: implications for cosmic-ray exposure dating in Alpine environments. *Quaternary Geochronology*.

Densmore, M.S., Ehlers, T.A., and Woodsworth, G.J. (2007). Effect of Alpine glaciation on thermochronometer age-elevation profiles. *Geophysical Research Letters*, 34, L02502, doi:10.1029/2006GL028371.

Dobson, K.J., Persano, C., and Stuart, F.M. (2009). Quantitative constraints on mid- to shallow crustal processes using the zircon (U-Th)/He thermochronometer. *in* F. Lisker, B. Ventura and U.A. Glasmacher (Eds), Thermochronological methods: From palaeotemperature constraints to landscape evolution models, *Geological Society of London Special Publications*, 324, 47-56.

Dodson, M.H. (1973). Closure temperature in cooling geochronological and petrological systems. *Contributions to Mineralogy and Petrology*, 40, 259-274.

Donelick, R.A., and Miller, D.S. (1991). Enhanced TINT fission track densities in low spontaneous track density apatites using ^{252}Cf-derived fission fragment tracks: A model and experimental observations. *Nuclear Tracks and Radiation Measurements*, 18, 301-307.

Dorthe-Monachon, C. (1986). Contribution à l'étude de la morphologie glaciaire de la vallée de l'Arve (Haute-Savoie, France). Essai de reconstitution paléogéographique. Thèse de Doctorat, Université de Lausanne.

Dowdeswell, J.A., Ottesen, D., and Rise, L. (2010). Rates of sediment delivery from the Fennoscandian Ice Sheet through an ice age. *Geology*, 38, 3-6.

Driscoll, N.W., and Haug, G.H. (1998). A short circuit in thermohaline circulation: a cause for Northern Hemisphere glaciation?. *Science*, 282, 436-438.

Dühnforth, M., Anderson, R.S., Ward, D., and Stock, G.M. (2010).Bedrock fracture control of glacial erosion processes and rates. *Geology*, 38, 423-426.

Dumont, T., Champagnac, J.-D., Crouzet, C., and Rochat, P. (2008). Multistage Alpine shortening in Central Dauphiné (French Western Alps): implications for pre-Alpine restoration. *Swiss Journal of Geosciences,* 101, 89-110.

Dunne, A., Elmore, D., and Muzikar, P. (1999). Scaling of cosmogenic nuclide production rates for geometric shielding and attenuation at depth on sloped surface. *Geomorphology*, 27, 3-11.

Duvall, A., Kirby, E. and Burbank, D. (2004). Tectonic and lithologic controls on bedrock channel profiles and processes in coastal California. *Journal of Geophysical Research*, 109, 10.1029/2003JF000086.

Egholm, D.L., Nielsen, S.B., Pedersen, V.K., and Lesemann, J.-E. (2009). Glacial effects limiting mountain height. *Nature*, 460, 884-887.

Egholm, D.L., and Nielsen, S.B. (2010). An adaptive finite volume solver for ice sheets and glaciers. *Journal of Geophysical Research*, 115, F01006, doi:10.1029/2009JF001394.

Ehlers J., and Gibbard, P.L. (2004). Extent and chronology of Glaciation. Volume 1: Europe. Elsevier Science, Amsterdam, 488 pp.

Ehlers, T.A., and Farley, K.A. (2003). Apatite (U-Th)/He thermochronometry: methods and applications to problems in tectonic and surface processes. *Earth and Planetary Science Letters*, 206(1-2), 1-14.

Ehlers, T.A., Farley, K.A., Rusmore, M.E., and Woodsworth, G.J. (2006). Apatite (U-Th)/He signal of large-magnitude accelerated glacial erosion, southwest British Columbia. *Geology*, 34, 765-768.

England, P., and Molnar, P. (1990). Surface uplift, uplift of rocks, and exhumation of rocks. *Geology*, 18, 1173-1177.

Farley, K.A., Wolf, R.A., Silver, L.T. (1996). The effects of long alpha-stopping distances on (U-Th)/He ages. *Geochimica et Cosmochimica Acta,* 60, 4223-4229.

Farley, K.A. (2000). Helium diffusion from apatite: General behavior as illustrated by Durango fluorapatite. *Journal of Geophysical Research*, 105, 2903-2914.

Farley, K.A. (2002). (U-Th)/He dating: techniques, calibrations, and applications. In *Reviews in Mineralogy and Geochemistry: Noble Gases in Geochemistry and Cosmochemistry* (eds. Porcelli, D., Ballentine, C. J. & Wieler, R.), 47, 819-844 (Mineralogical Society of America, Washington, DC, 2002).

Farley, K.A., Shuster, D.L., Watson, E.B., Wanser, K.H., and Balco, G. (2010). Numerical investigations of apatite $^{4}He/^{3}He$ thermochronometry. *Geochemistry, Geophysics, Geosystems*, 11, Q10001, doi:10.1029/2010GC003243.

Fauquette, S., Suc, J.-P., Guiot, J., Diniz, F., Feddi, N., Zheng, Z., Bessais, E., and Drivaliari, A. (1999). Climate and biomes in the West Mediterranean area during the Pliocene. *Palaeogeography, Palaeoclimatology, Palaeoecology*,152, 15-36.

Fernandez Luque, R., and van Beek, R. (1976). Erosion and transport of bed-load sediment. *Journal of Hydraulics Research*, 14, 127-144.

Finckh, P., and Frei, W. (1991). Seismic reflection profiling in the Swiss Rhone valley, Part 1: Seismic reflection field work, seismic processing and seismic results of the Roche-Vouvry and Turtmann and Agarn lines, *Eclogae Geologicae Helvetiae*, 84, 345-357.

Finnegan, N.J., Roe, G., Montgomery, D.R., and Hallet, B. (2005). Controls on the channel width of rivers: Implications for modeling fluvial incision of bedrock. *Geology*, 33: 229-232.

Fitzgerald, P.G., Sorkhabi, R.B., Redfield, T.F., and Stump, E. (1995). Uplift and denudation of the central Alaska Range: A case study in the use of apatite fission track thermochronology to determine absolute uplift parameters. *Journal of Geophysical Research*, 100, 20175-20191.

Fitzgerald, P.G., Muñoz, J.A., Coney, P.J., and Baldwin, S.L. (1999). Asymmetric exhumation across the Pyrenean orogen: implications for the tectonic evolution of a collisional orogen. *Earth and Planetary Science Letters*, 173, 157–170.

Fitzgerald, P.G., Baldwin, S.L., Webb, L.E., and O'Sullivan, P.B. (2006). Interpretation of (U-Th)/He single grain ages from slowly cooled crustal terranes: A case study from the Transantarctic Mountains of southern Victoria Land. *Chemical Geology*, 225, 91-120.

Flint, J.J. (1974). Stream gradient as a function of order, magnitude, and discharge. *Water Resources Research*, 10, 969-973.

Flintham, T.P., and Carling, P.A. (1988). The prediction of mean bed and wall boundary shear in uniform and compositely roughened channels. *in* W.P. White, Editors, *International Conference on River Regime*, John Wiley and Sons, Chichester, England: pp. 267-287.

Florineth D., and Schluchter C. (1998). Reconstructing the Last Glacial Maximum (LGM) ice surface geometry and flowlines in the central Swiss Alps. *Eclogae Geologicae Helvetiae*, 91, 391-407.

Flowers, R.M., Ketcham, R.A., Shuster, D.L., and Farley, K.A. (2009). Apatite (U-Th)/He thermochronometry using a radiation damage accumulation and annealing model. *Geochimica et Cosmochimica Acta*, 73, 2347-2365.

Foeken, J.P.T., Stuart, F.M., Dobson, K.J., Persano, C., and Vilbert, D. (2006). A diode laser system for heating minerals for (U-Th)/He chronometry, *Geochemistry Geophysics Geosystems*, 7, Q04015, doi:10.1029/2005GC001190.

Foeken, J.P.T., Persano, C., Stuart, F.M., and ter Voorde, M. (2007). Role of topography in isotherm perturbation: Apatite (U-Th)/He and fission track results from the Malta tunnel, Tauern Window, Austria. *Tectonics*, 26, TC3006, doi:10.1029/2006TC002049.

Ford, M. (1996). Kinematics and geometry of early alpine, basement-involved folds, SW Pelvoux Massif, SE France. *Eclogae Geologicae Helvetiae*, 89, 269-295.

Frankel, K.L., Pazzaglia, F.J., and Vaughn, J.D. (2007). Knickpoint evolution in a vertically bedded substrate, upstream-dipping terraces, and Atlantic slope bedrock channels. *Geological Society of America Bulletin*, 119(3), 476-486.

Frei, C., and Schär, J. (1998). A precipitation climatology of the Alps from high resolution rain gauge observations. *Journal of Climatology*, 18, 873-900.

Frey, M., and Ferreiro Maehlmann, R. (1999). Alpine metamorphism of the Central Alps. *Schweitzerische Mineralogische und Petrographische Mitteilungen*, 79, 135-154.

Galbraith, R.F. (2005). Statistics for Fission Track Analysis. Taylor & Francis/CRC Press.

Gallagher, K., Brown, R., and Johnson, C. (1998). Fission track analysis and its applications to geological problems. *Annual Review of Earth and Planetary Sciences*, 26, 519-572.

Gallagher, K., Stephenson, J., Brown, R., Holmes, C., and Fitzgerald, P. (2005a). Low temperature thermochronology and modeling strategies for multiple samples 1: Vertical profiles. *Earth and Planetary Science Letters*, 237(1-2), 193-208.

Gallagher, K., Stephenson, J., Brown, R., Holmes, C., and Ballester, P. (2005b). Exploiting 3D spatial sampling in inverse modeling of thermochronological data. *in* Reiners, P.W., and Ehlers, T.A., eds., Low-Temperature Thermochronology: Techniques, Interpretations, and Applications, Volume 58, *Reviews in Mineralogy and Geochemistry*, Chantilly, Virginia, Mineralogical Society of America/Geochemical Society, p. 375-387.

Galy, V., France-Lanord, C., Beyssac, O., Faure, P., Kudrass, H., and Palhol, F. (2007). Efficient organic carbon burial in the Bengal fan sustained by the Himalayan erosional system. *Nature*, 450, 407-410.

Gardner, T.W. (1983). Experimental study of knickpoint and longitudinal profile evolution in cohesive, homogeneous material. *Geological Society of America Bulletin*, 94(5), 664-672.

Gasparini, N.M., Whipple, K.X., and Bras, R.L. (2007). Predictions of steady state and transient landscape morphology using sediment-flux-dependent river incision models. *Journal of Geophysical Research*, 112, 10.1029/2006JF000567.

Gautheron, C., Tassan-Got, L., Barbarand, J., and Pagel, M. (2009). Effect of alpha-damage annealing on apatite (U-Th)/He thermochronology. *Chemical Geology*, 266, 157-170.

Gautheron, C., and Tassan-Got, L. (2010). A Monte Carlo approach to diffusion applied to noble gas/helium thermochronology. *Chemical Geology*, 273, 212-224

Gianotti, F., Forno, M.G., Ivy-Ochs, S., and Kubik, P.W. (2008). New chronological and stratigraphical data on the Ivrea amphitheatre (Piedmont, NW Italy). *Quaternary International*, 190, 123-135.

Gibson, M., Sinclair, H.D., Lynn, G.J., and Stuart, F.M. (2007). Late- to post-orogenic exhumation of the Central Pyrenees revealed through combined thermochronological data and modelling. *Basin Research*, 19, 323-334.

Gilbert G.K. (1897). Report on the Geology of the Henry Mountains, Geographical and Geological Survey of the Rock Mountains Region. United States Department of the Interior, Washington DC.

Glacioclim (2009). Les GLACIers, un Observatoire du CLIMat (Alpes, Andes, Antarctique). *http://www-lgge.ujf-grenoble.fr/ServiceObs/*.

Glasser, N.F., and Ghiglione, M.C. (2009). Structural, tectonic and glaciological controls on the evolution of fjord landscapes. *Geomorphology*, 105, 291-302.

Gleadow, A.J.W., and Duddy, I.R. (1981). A natural long-term track annealing experiment for apatite. *Nuclear Tracks and Radiation Measurements*, 5, 169-174.

Gleadow, A.J.W, Duddy, I.R., Green, P.F., and Lovering, J.F. (1986). Confined track lengths in apatite: a diagnostic tool for thermal history analysis. *Contributions to Mineralogy and Petrology*, 94, 405-15.

Gleadow, A.J.W., and Brown, R.W. (2000). Fission-track thermochronology and the long-term denudational response to tectonics. *in* M.A. Summerfield (Ed), *Geomorphology and Global Tectonics*, Wiley, Chichester, 57-76.

Glotzbach, C., Reinecker, J., Danisik, M., Rahn, M., Frisch, W., and Spiegel, C. (2008). Neogene exhumation history of the Mont Blanc massif, western Alps. *Tectonics*, 27, TC4011, doi: 10.1029/2008TC002257.

Glotzbach, C., Reinecker, J., Danisik, M., Rahn, M., Frisch, W., and Spiegel, C. (2010). Thermal history of the central Gotthard and Aar massifs (European Alps): Evidence for steady state, long-term exhumation. *Journal of Geophysical Research*, doi: 10.1029/2009JF001304.

Glotzbach, C., Bernet, M., and van der Beek, P. (2011). Detrital thermochronology records changing source areas and steady exhumation in the Western European Alps. *Geology*, 39, 239-242.

Glotzbach, C., van der Beek, P.A., and Spiegel, C. (submitted). Episodic exhumation of the Mont Blanc massif, Western Alps: constraints from numerical modelling of thermochronology data. *Earth and Planetary Science Letters*.

Goldrick, G., and Bishop, P. (2007). Regional analysis of bedrock stream long profiles: evaluation of Hack's SL form, and formulation and assessment of an alternative (the DS form). *Earth Surface Processes and Landforms*, 32(5), 649-671.

Goode, J.K., and Burbank, D.W. (2009). Numerical study of degradation of fluvial hanging valleys due to climate change. *Journal of Geophysical Research*, 114, 10.1029/2007JF000965.

Gosse, J.C., and Philips, F.M. (2001), Terrestrial in situ cosmogenic nuclides: theory and application, *Quaternary Science Reviews*, 20, 1475-1560.

Granger, D.E., Kirchner, J.W., and Finkel, R. (1996). Spatially averaged long-term erosion rates measured from in situ-produced cosmogenic nuclides in alluvial sediment. *Journal of Geology*, 104, 249-257.

Green, P.F., Duddy, I.R., Gleadow, A.J.W., Tingate, P.R, and Laslett, G.M. (1986). Thermal annealing of fission tracks in apatite, 1. A qualitative description. *Chemical Geology*, 59, 237-53.

Green, P.F., Duddy, I.R., Laslett, G.M., Hegarty, K.A., Gleadow, A.J.W., and Lovering, J.F. (1989). Thermal annealing of fission tracks in apatite IV: Quantitative modelling techniques and extension to geological timescales. *Chemical Geology*, 79, 155-182.

Green, P.F., and Duddy, I.R. (2006). Interpretation of apatite (U-Th)/He ages and fission track ages from cratons. *Earth and Planetary Science*, 244, 541-547.

Green, P.F., Crowhurst, P.V., Duddy, I.R., Japsen, P., and Holford, S.P. (2006). Conflicting (U–Th)/He and fission track ages in apatite: Enhanced He retention, not anomalous annealing behaviour. *Earth and Planetary Science Letters*, 250, 407-427.

Greve, R., and Blatter., H. (2009). Dynamics of Ice Sheets and Glaciers. Springer, Berlin, Germany, pp. 287.

Gudmundsson, G.H. (1994). An order of magnitude estimate of the current uplift rates in Switzerland caused by the Würm alpine deglaciation. *Eclogae Geologicae Helvetiae*, 87, 545-557.

Guenthner, W.R., and Reiners, P.W. (2009). He diffusion in zircon: Observations from (U-Th)/He age suites and ^{4}He diffusion experiments and implications for radiation damage and anisotropic effects. *Eos Transactions AGU*, 90, Fall Meeting Supplementary Abstract V52C-06.

Hack, J. (1957). Studies of longitudinal stream profiles in Virginia and Maryland, U.S. *Geological Survey Professional Paper*, 294 B, 45-94.

Haeuselmann, P., Granger, D.E., Jeannin, P.-Y., and Lauritzen, S.-E. (2007). Abrupt glacial valley incision at 0.8 Ma dated from cave deposits in Switzerland. *Geology*, 35, 143-146.

Hagdorn, M., and Boulton, G. (2004). Simulating Subglacial Sediment Transport using a Semi Lagragian Method. *Geophysical Research Abstracts*, 6, 05153.

Hallet, B. (1979). A theoretical model of glacial abrasion. *Journal of Glaciology*, 17, 209-222.

Hallet, B. (1996). Glacial quarrying: A simple theoretical model. *Annals of Glaciology*, 22, 1-8.

Hallet, B., Hunter, L., and Bogen, J. (1996). Rates of erosion and sediment evacuation by glaciers: a review of field data and their implications. *Global and Planetary Change*, 12, 213–235, doi:10.1016/0921-8181(95)00021-6.

Hancock, G.S., and Anderson, R.S. (2002). Numerical modeling of fluvial terrace formation in response to oscilating climate. *Geological Society of America Bulletin*, 114(9), 1131-1142.

Harbor, J. (1992a). Application of a general sliding law to simulating flow in a glacier cross section. *Journal of Glaciology*, 38, 182-190.

Harbor, J. (1992b). Numerical modelling of the development of U-shaped valleys by glacial erosion. *Geological Society of America Bulletin*, 104, 1364-1375.

Harbor, J.M. (1995). Development of glacial-valley cross sections under conditions of spatially variable resistance to erosion. *Geomorphology*, 14(2), 99-107.

Harkins, N., Kirby, E., Heimsath, A., Robinson, R., and Reiser, U. (2007). Transient fluvial incision in the headwaters of the Yellow River, northeastern Tibet, China. *Journal of Geophysical Research*, 112, 10.1029/2006JF000570.

Haug, G.H., and Tiedemann, R. (1998). Effect of the formation of the Isthmus of Panama on Atlantic Ocean thermohaline circulation, *Nature*, 393, 673-676.

Haug, G.H., Ganopolski, A., Sigman, D.M., Rosell-Mele, A., Swann, G.E.A., Tiedemann, R., Jaccard, S.L., Bollmann, J., Maslin, M.A., Leng, M.J., and Eglinton, G. (2005). North Pacific seasonality and the glaciation of North America 2.7 million years ago. *Nature*, 433, 821-824.

Haviv, I., Enzel, Y., Whipple, K.X., Zilberman, E., Stone, J., Matmon, A., and Fifield, L.K. (2006). Amplified erosion above waterfalls and oversteepened bedrock reaches. *Journal of Geophysical Research*, 111, 10.1029/2006JF000461.

Hay, W.W., Sloan, J.L., and Wold, C.N. (1988). Mass/age distribution and composition of sediments on the ocean floor and the global rate of sediment subduction. *Journal of Geophysical Research*, 93, 14933-14940.

Hayakawa, Y., and Matsukura, Y. (2003). Recession rates of waterfalls in Boso Peninsula, Japan, and a predictive equation. *Earth Surface Processes and Landforms*, 28(6), 675-684.

Herman, F., Braun, J., and Dunlap, W. (2007). Tectono-morphic scenarios in the Southern Alps of New Zealand. *Journal of Geophysical Research*, 112, B04201, doi:10.1029/2004JB003.

Herman F., and Braun, J. (2008). Glacial evolution of the topography of the Southern Alps of New Zealand. *Journal of Geophysical Research*, 113, F02009, doi:10.1029/2007JF00080.

Herman, F., Rhodes, E.J., Jaiswal, M., Schwenninger, J., and Reverman, R. (2009). OSL-thermochronology: introduction, application and limitations. *Eos Transactions AGU*, 90, Fall Meet. Suppl., Abstract V41D-2203.

Herman F., Copeland, P., Avouac, J-P., Bollinger, L., Mahéo, G., Le Fort, P., Rai, S., Foster, D., Pecher, A., Stuwe, K., and Henry, P. (2010a). Exhumation, crustal deformation and thermal structure of the Nepal Himalaya derived from the inversion of thermochronological and thermobarometric data and modeling of the topography. *Journal of Geophysical Research*, 115, B06407, doi:10.1029/2008JB006126.

Herman, F., Rhodes, E.J., Braun, J., and Heiniger, L. (2010b). Uniform erosion rates and relief amplitude during glacial cycles in the Southern Alps of New Zealand, as revealed from OSL-thermochronology. *Earth and Planetary Science Letters*, 297, 183-189.

Hinderer, M. (2001). Late Quaternary denudation of the Alps; valley and lake fillings and modern river loads. *Geodinamica Acta*, 14(4), 231-263.

Hindmarsh, R., and Payne, A. (1996). Time-step limit for stable solutions of the ice-sheet equation. *Annals of Glaciology*, 23, 74-85.

Hobley, D.E.J., Sinclair, H.D., and Cowie, P.A. (2010). Processes, rates, and time scales of fluvial response in an ancient postglacial landscape of the northwest Indian Himalaya. *Geological Society of America Bulletin*, 122, 1569-1584.

Hooke, R.L. (1981). Flow law for polycrystalline ice in glaciers: comparison of theoretical predictions, laboratory data, and field measurements. *Reviews of Geophysics*, 19, 664-672.

Hooke, R.L. (1998). Principles of Glacier Mechanics. Prentice-Hall, Upper Saddle River, pp. 429.

Hourigan, J.K., Reiners, P.W., and Brandon, M.T. (2005). U-Th zonation-dependent alpha-ejection in (U-Th)/He chronometry. *Geochimica et Cosmochimica Acta*, 69, 3349-3365.

House, M.A., Wernicke, B.P., Farley, K.A., and Dumitru, T.A. (1997). Cenozoic thermal evolution of the central Sierra Nevada, California, from (U-Th)/He thermochronometry. *Earth and Planetary Science Letters*, 151, 167-179.

House, M.A., Wernicke, B.P., and Farley, K.A. (1998). Dating topography of the Sierra Nevada, California, using apatite (U-Th)/He ages. *Nature*, 396, 66-69.

House, M.A., Farley, K.A., and Stockli, D. (2000). Helium chronometry of apatite and titanite using Nd-YAG laser heating. *Earth and Planetary Science Letters*, 183, 365-368.

House, M.A., Wernicke, B.P., and Farley, K.A. (2001). Paleo-geomorphology of the Sierra Nevada, California, from (U-Th)/He ages in apatite *American Journal of Science*, 301, 77-102.

Howard, A.D., and Kerby, G. (1983). Channel changes in badlands. *Geological Society of America Bulletin*, 94, 739-752.

Howard, A.D. (1994). A detachment-limited model of drainage basin evolution. *Water Resources Research*, 30(7), 2261-2285.

Howard, A.D., Dietrich, W.E., and Seidl, M.A. (1994). Modeling fluvial erosion on regional to continental scales, *Journal of Geophysical Research*, 99, 13,971-13,986.

Howard, A.D. (1998). Long profile developpement of bedrock channels: interaction of weathering, mass wasting, bed erosion, and sediment transport in *River Over Rocks : Fluvial processes in bedrock channels*, edited by K. J. Tinkler and E. E. Wohl, pp. 297-319, AGU Monograph.

Hurford, A.J. (1986). Cooling and uplift patterns in the Lepontine Alps, south central Switzerland and an age of vertical movement on the Insubric fault line. *Contributions to Mineralogy and Petrology*, 92, 413-427.

Hurford, A.J. (1991). Uplift and cooling pathways derived from fission track analysis and mica dating: a review. *Geologische Rundschau*, 80, 349-368.

Hurley, P.M., Larsen, E.S., and Gottfried, D. (1956). Comparison of radiogenic helium and lead in zircon. *Geochimica et Cosmochimica Acta*, 9, 98-102.

Hutter, K. (1983). Theoretical Glaciology, Reidel, D. Dordrecht, Netherlands, pp. 510.

Ivy-Ochs, S., Schlüchter, C., Kubik, P.W., Synal, H.-A., Beer, J., and Kerschner, H. (1996). The exposure age of an Egesen moraine at Julier Pass, Switzerland, measured with the cosmogenic radionuclides ^{10}Be, ^{26}Al, ^{36}Cl. *Eclogae Geologicae Helvetiae*, 89, 1049-1063.

Ivy-Ochs, S., Schäfer, J., Kubik, P.W., Synal, H.A., and Schlüchter, C. (2004). Timing of deglaciation on the northern Alpine foreland (Switzerland). *Eclogae Geologicae Helvetiae*, 97(1), 47-55.

Ivy Ochs, S., Kerchner, H., Kubik, P.W., and Schlüchter, C. (2006). Glacier response in the European Alps to Heinrich Event 1 cooling: the Gschnitz stadial. *Journal of Quaternary Science*, 21, 115-130.

Ivy-Ochs, S., Kerschner, H., Maisch, M., Christl, M., Kubik, P.W., and Schlüchter, C. (2009). Latest Pleistocene and Holocene glacier variations in the European Alps. *Quaternary Science Reviews*, 28(21-22), 2137-2149.

Jaboyedoff, M. (1999). Modèles thermiques simples de la croûte terrestre : un regard sur les Alpes. *Bulletin de la société vaudoise des sciences naturelles*, 340, 229-271.

Jäckli, A. (1970). Die Schweiz zur letzen Eiszeit. Atlas des Schweiz Blatt 6, Bundesamt für Landestopographie, Wabern-Bern.

Jeannin, P.-Y. (1991). Mise en évidence d'importantes glaciations anciennes par l'étude des remplissages karstiques du Réseau des Siebenhengste (chaîne bordière helvetique). *Eclogae Geologicae Helvetiae*, 84, 207-221.

Joerin U.E., Stocker T.F., and Schlüchter C. (2006). Multicentury glacier fluctuations in the Swiss Alps during the Holocene. *The Holocene*, 16, 697-704.

Johnson, J.P., and Whipple, K.X. (2007). Feedbacks between erosion and sediment transport in experimental bedrock channels. *Earth Surface Processes and Landforms*, 32(7), 1048-1062.

Johnson, J.P.L., Whipple, K.X., Sklar, L.S., and Hanks, T.C. (2009). Transport slopes, sediment cover, and bedrock channel incision in the Henry Mountains, Utah. *Journal of Geophysical Research*, 114, 10.1029/2007JF000862.

Jouanne, F., Ménard, G., and Darmendrail, X. (1995). Present-day vertical displacements in the north-western Alps and southern Jura Mountains: Data from levelling comparisons. *Tectonics*, 14, 606-616.

Kahle H.G., Geiger A., Bürki B., Gubler E., Marti U., Wirth B., Rothacher M., Gurtner W., Beutler G., Bauersima I., and Pfiffner, O.A. (1997). Recent crustal movements, geoid and density distribution: contribution from integrated satellite and terrestrial measurements. Results of the National Research Program. O.A. Pfiffner, Lehner, P., Heitzmann, P., Müller, S., Steck, A. Birkhäuser, Basel, NRP, pp. 251-259.

Kelly, M.A., Buoncristiani, J.F., and Schluchter C. (2004). A reconstruction of the last glacial maximum (LGM) ice-surface geometry in the western Swiss Alps and contiguous Alpine regions in Italy and France. *Eclogae Geologicae Helvetiae*, 97, 57-75.

Kelly, M.A., Ivy Ochs, S., Kubik, P.W., von Blanckenburg, F., and Schlüchter, C. (2006). Chronology of deglaciation based on 10Be dates of glacial erosional features in the Grimsel Pass region, central Swiss Alps. *Boreas*, 35, 635-643.

Kessler, M., Anderson, R., and Stock, G. (2006). Modeling topographic and climatic control of east-west asymmetry in Sierra Nevada glacier length during the Last Glacial Maximum. *Journal of Geophysical Research*, 111, F02002, doi:10.1029/2005JF000365.

Kerschner, H., and Ivy-Ochs, S. (2008). Palaeoclimate from glaciers: examples from the Eastern Alps during the Alpine Lateglacial and early Holocene. *Global and Planetary Change*, 60, 58-71.

Ketcham, R.A. (2005). Forward and inverse modeling of low-temperature thermochronometry data. *Reviews in Mineralogy & Geochemistry,* 58, 275-314.

Kirby, M.J. (1994). Process models and theoretical geomorphology. Chichester, Wiley, 417pp.

Kirby, E., and Whipple, K. (2001). Quantifying differential rock-uplift rates via stream profile analysis. *Geology*, 29 (5), 415-418.

Kirkbride, M., and Matthews, D. (1997). The role of fluvial and glacial erosion in landscape evolution: The Ben Ohau Range, New Zealand. *Earth Surface Processes and Landforms*, 22, 317-327.

Knight, D.W., Demetrious, J.D., and Hamed, M.E. (1984). Boundary shear in smooth rectangular channels. *Journal of Hydraulics, Division ASCE,* 110 (4), 405–422.

Kohn, B.P., Gleadow, A.J.W., Brown, R.W., Gallagher, K., Lorencak, M., and Noble, W.P. (2005). Visualizing thermotectonic and denudation histories using apatite fission track thermochronology. *in* Reiners, P.W., and Ehlers, T.A., eds., Low-Temperature Thermochronology: Techniques, Interpretations, and Applications, 58, *Reviews in Mineralogy and Geochemistry*, Chantilly, Virginia, Mineralogical Society of America/Geochemical Society, pp. 527-565.

Kooi, H., and Beaumont, C. (1994). Escarpment evolution on high-elevation rifted margins – insights derived from a surface processes model that combines diffusion, advection, and reaction. *Journal of Geophysical Research*, 99(B6), 12191-12209.

Kooi, H., and Beaumont, C. (1996). Large-scale geomorphology: classical concepts reconciled and integrated with contemporary ideas via a surface processes model. *Journal of Geophysical Research*, 101 (B2), 3361-3386.

Koons, P.O. (1989). The topographic evolution of collisional mountain belts: a numerical look at the Southern Alps of New Zealand. *American Journal of Sciences*, 289, 1041-1069.

Koppes, M.N. and Montgomery, D.R. (2009). The relative efficacy of fluvial and glacial erosion over modern to orogenic timescales. *Nature Geoscience*, 2, 644-647.

Korup, O., Strom, A.L., and Weidinger, J.T. (2006). Fluvial response to large rock-slope failures - examples from the Himalayas, the Tien Shan, and the Southern Alps in New Zealand. *Geomorphology*, 78, 3-21.

Korup, O., and Schlunegger, F. (2007). Bedrock landsliding, river incision, and transience of geomorphic hillslope-channel coupling: Evidence from inner gorges in the Swiss Alps. *Journal of Geophysical Research*, 112, 10.1029/2006JF000710.

Kuhlemann, J. (2000). Post-collisional sediment budget of circum-Alpine basins (Central Europe). *Memorie di Scienze Geologiche*, 52, 1-91.

Kuhlemann, J., Frisch, W., Dunkl, I., Székely, B., and Spiegel, C. (2001). Miocene shifts of the drainage divide in the Alps and their foreland basin, Zeitschrift für Geomorphologie, 45, 239-265.

Kuhlemann, J., Frisch, W., Székely, B., Dunkl, I., and Kázmér, M. (2002). Post-collisional sediment budget history of the Alps: tectonic versus climatic control. *International Journal of Earth Sciences*, 91, 818-837.

Kuhlemann, J., Dunkl, I., Brugel, A., Spiegel, C., and Frisch, W. (2006). From source terrains of the eastern Alps to the Molasse Basin: Detrital record of non-steady-state exhumation. *Tectonophysics*, 413, 301-316.

Kühni, A., and Pfiffner, O.A. (2001a). Drainage patterns and tectonic forcing: a model study for the Swiss Alps. *Basin Research*, 13, 169-197.

Kühni, A., and Pfiffner, O.A. (2001b). The relief of the Swiss Alps and adjacent areas and its relation to lithology and structure: topographic analysis from a 250-m DEM. *Geomorphology*, 41, 285-307.

Lague, D. (2003). Dynamique de l'érosion continentale aux grandes échelles de temps et d'espace: modélisation expérimentale, numérique et théorique. Thèse de Doctorat, Université de Rennes 1.

Lague, D., and Davy, P. (2003). Constraints on the long-term colluvial erosion law from the analyzis of slope-area relationships at various tectonic uplift rates in the Siwaliks Hills (Nepal). *Journal of Geophysical Research*, 108, 2129, doi:10.1029/2002JB001893.

Lague, D., Hovius, N., and Davy, P. (2005). Discharge, discharge variability, and the bedrock channel profile. *Journal of Geophysical Research*, 110, 10.1029/2004JF000259.

Lague, D. (2010). Reduction of long-term bedrock incision efficiency by short-term alluvial cover intermittency. *Journal of Geophysical Research*, 115, F02011, doi:10.1029/2008JF001210.

Lal, D. (1991). Cosmic ray labelling of erosion surfaces: in situ nuclide production rates and erosion models. *Earth and Planetary Science Letters*, *104*, 424-439.

Lamb, M.P., Howard, A.D., Dietrich, W.E., and Perron, J.T. (2007). Formation of amphitheater-headed valleys by waterfall erosion after large-scale slumping on Hawai'i. *Geological Society of America Bulletin*, 119(7), 805-822.

Lamb, M.P., Dietrich, W.E., and Sklar, L.S. (2008a). A model for fluvial bedrock incision by impacting suspended and bedload sediment. *Journal of Geophysical*, 113, doi:10.1029/2007JF000915.

Lamb, M.P., Dietrich, W.E., and Venditti, J.G. (2008b). Is the critical Shields stress for incipient sediment motion dependent on channel-bed slope?, *Journal of Geophysical Research*, 113, 10.1029/2007JF000831.

Lardeaux, J.M., Schwartz, S., Tricart, P., Paul, A., Guillot, S., Bethoux, N. and Masson, F. (2006). A crustal-scale crosssection of the south-western Alps combining geophysical and geological imagery. *Terra Nova*, 18, 412-422.

Laslett, G.M., Green, P.F., Duddy, I.R., and Gleadow, A.J.W. (1987). Thermal annealing of fission tracks in apatite, 2. A quantitative analysis. *Chemical Geology*, 65, 1-13.

Lavé, J. (1997). Tectonique et erosion: L'apport de la dynamique fluviale à l'étude sismotectonique de l'Himalaya du Népal central. Thèse de Doctorat, Université Paris VII.

Lavé, J., and Avouac, J.P. (2001). Fluvial incision and tectonic uplift across the Himalayas of central Nepal. *Journal of Geophysical Research*, 106, 26561-26591.

Le Meur, E. and Vincent, C. (2003). A two-dimensional shallow ice-flow model of Glacier de Saint-Sorlin, France. *Journal of Glaciology*, 49, 527-538.

Le Meur, E., Gagliardini, O., Zwinger, T., and Ruokolainen, J. (2004). Glacier flow modelling: a comparison of the Shallow Ice Approximation and the full-Stokes solution. *Comptes Rendus de l'Académie des Sciences*, 5(7), 709-722.

Le Meur, E., Gerbaux, M., Schäfer, M., and Vincent, C. (2007). Disappearance of an Alpine glacier over the 21st Century simulated from modeling its future surface mass balance. *Earth and Planetary Science Letters*, 261, 367-374.

Le Roux O., Schwartz S., Gamond J.F., Jongmans D., Bourles D.L., Braucher R., Mahaney W., Carcaillet J., and Leanni L. (2009). CRE dating on the head scarp of a major landslide (Séchilienne, French Alps), age constraints on Holocene kinematics. *Earth and Planetary Science Letters*, 280, 236-245.

Leloup, P.H., Arnaud, N., Sobel, E.R., and Lacassin, R. (2005). Alpine thermal and structural evolution of the highest external crystalline massif: The Mont Blanc. *Tectonics*, 24, TC4002, doi: 4010.1029/2004TC001676.

Li, Y., Harbor, J., Stroeven, A.P., Fabel, D., Kleman, J., Fink, D., Caffee, M., and Elmore, D. (2005). Ice sheet erosion patterns in valley systems in northern Sweden investigated using cosmogenic nuclides. *Earth Surface Processes and Landforms*, 30, 1039-1049.

Lindsay, J.B. (2005). The Terrain Analysis System: a tool for hydro-geomorphic applications. *Hydrological Processes*, 19, 1123-1130.

Lippitsch, R., Kissling, E. and Ansorge, J. (2003). Upper mantle structure beneath the Alpine orogen from high-resolution teleseismic tomography. *Journal of Geophysical Research*, 108, 2376, doi: 2310.1029/2002JB002016.

Lisiecki, L.E, and Raymo, M.E. (2005). A Pliocene-Pleistocene stack of 57 globally distributed benthic $\delta^{18}O$ records. Paleoceanography, 20, PA1003, doi:10.1029/2004PA001071.

Lisiecki, L.E. (2010). Links between eccentricity forcing and the 100,000-year glacial cycle. *Nature Geoscience*, 3, 349-352.

Lliboutry, L. (1994). Monolithologic erosion of hard beds by temperate glaciers. *Journal of Glaciology*, 40, 433-450.

Loget, N., Davy, P., and Van Den Driessche, J. (2006). Mesoscale fluvial erosion parameters deduced from modeling the Mediterranean sea level drop during the Messinian (late Miocene). *Journal of Geophysical Research*, 111, 10.1029/2005JF000387.

Lyon-Caen, H. and Molnar, P. (1989). Constraints on the deep structure and dynamic processes beneath the Alps and adjacent regions from an analysis of gravity anomalies. *Geophysical Journal International*, 99, 19-32.

MacGregor, K.R., Anderson, R.S., Anderson, S.P., and Waddington, E.D. (2000). Numerical simulations of glacial-valley longitudinal profile evolution. *Geology*, 28(11), 1031-1034.

MacGregor, K.R., Anderson, R.S., and Waddington, E.D. (2009). Numerical modeling of glacial erosion and headwall processes in alpine valleys. *Geomorphology*, 103, 189-204.

Maisch, M. (2000). The long-term signal of climate change in the Swiss Alps: glacier retreat since the end of the Little Ice Age and future ice decay scenarios. *Geografia Fisica e Dinamica Quaternaria*, 23, 139-151.

Mancktelow, N. (1985). The Simplon Line: A major displacement zone in the Western Lepontine Alps. *Eclogae Geologicae Helvetiae*, 78, 73-96.

Mancktelow, N.S. (1992). Neogene lateral extension during convergence in the central Alps: Evidence from interrelated faulting and backfolding around the Simplonpass (Switzerland). *Tectonophysics*, 215, 295-317.

Manktelow, N.S., and Grasemann, B. (1997). Time-dependent effects of heat advection and topography on cooling histories during erosion. *Tectonophysics*, 270, 167-195.

Maslin, M.A., Haug, G.H., Sarnthein, M., and Tiedemann, R. (1996). The progressive intensification of northern hemisphere glaciation as seen from the North Pacific. *International Journal of Earth Sciences*, 85, 452-465.

Mathes, F.E. (1930). Geologic history of the Yosemite Valley, U.S. Geological Survey Professional Paper, 160, 137 pp.

McDougall I., and Harrison T.M. (1999). Geochronology and Thermochronology by the $^{40}Ar/^{39}Ar$ method. Oxford University Press, New York, pp. 288.

Meigs, A., and Sauber, J. (2000). Southern Alaska as an example of the long-term consequences of mountain building under the influence of glaciers. *Quaternary Science Reviews*, 19, 1543-1562.

Meesters, A.G.C.A., and Dunai, T.J. (2002). Solving the production-diffusion equation for finite diffusion domains of various shapes: Part I. Implications for low-temperature (U–Th)/He thermochronology. *Chemical Geology*, 186, 333-344.

Métivier F., Gaudemer Y., Tapponnier P., and Klein M. (1999). Mass accumulation rates in Asia during the Cenozoic. *Geophysical Journal International*, 137, 280-318.

Meyer-Peter, E., and Müller, R. (1948). Formulas for bed-load transport. *Proceedings 2nd Meeting*, *IAHR*, Stockholm, Sweden: 39-64.

Michalski, I., and Soom, M. (1990). The Alpine thermo-tectonic evolution of the Aar and Gotthard massifs, Central Switzerland: Fission-Track ages on zircons and apatites and K-Ar mica ages. *Schweizerische Mineralogische und Petrographische Mitteilungen*, 70, 373-387.

Mitchell, S.G., and Montgomery, D.R. (2006). Influence of a glacial buzzsaw on the height and morphology of the Cascade Range in central Washington State, USA. *Quaternary Research*, 65, 96-107.

Molnar, P., and England, P. (1990). Late Cenozoic uplift of mountain ranges and global climate change: chicken or egg? *Nature*, 346, 29-34.

Molnar, P. (2004). Late Cenozoic increase in accumulation rates of terrestrial sediment: How might climate change have affected erosion rates? *Annual Review of Earth and Planetary Sciences*, 32, 67-89.

Montgomery, D.R. (1994). Valley incision and the uplift of mountain peaks. *Journal of Geophysical Research*, 99, 13913-13921.

Montgomery, D.R., and Buffington, J.M. (1997). Channel-reach morphology in mountain drainage basins. *Geological Society of America Bulletin*, 109(5), 596-611.

Montgomery, D.R. (2002). Valley formation by fluvial and glacial erosion. *Geology*, 30, 1047-1050.

Montjuvent, G. (1974). Considérations sur le relief glaciaire à propos des Alpes du Dauphiné. *Revue de Géographie Physique et Géologie Dynamique*, 16, 465-502.

Montjuvent, G. (1978). Le Drac. Morphologie, stratigraphie et chronologie quaternaires d'un bassin alpin. Comité National de la Recherche Scientifique, Paris, 433 pp.

Mudelsee, M., and Raymo, M.E. (2005). Slow dynamics of the Northern Hemisphere. glaciation. *Paleoceanography*, 20, PA4022, doi:10.1029/2005PA001153.

Mulch, A., Mancktelow, N., Zwnigmann, H., and Campani, M. (2010). Topography and rainout in the central European Alps during the late Neogene (8-6 Ma). *Geophysical Research Abstracts*, 12, EGU2010-7067.

Muttoni, G., Carcano, C., Garzanti, E., Ghielmi, M., Piccin, A., Pini, R., Rogledi, S., and Sciunnach, D. (2003). Onset of major Pleistocene glaciations in the Alps. *Geology*, 31, 989-992.

Naylor, S., and Gabet, E.J. (2007). Valley asymmetry and glacial versus nonglacial erosion in the Bitterroot Range, Montana, USA. *Geology*, 35(4), 375-378.

Nesje A., and Dahl S.O. (2003). The 'Little Ice Age' - only temperature? *The Holocene*, 13, 139-145.

Nicoud, G., Royer, G., Corbin, J.-C., Lemeille, F., and Paillet, A. (2002). Glacial erosion and infilling of the Isère valley during the recent Quaternary. New results from borehole GMB1 in the Grenoble area (France). *Geologie de la France,* 4, 39-50.

Niemann, J.D., Gasparini, N.M., Tucker, G.E., and Bras, R.L. (2001). A quantitative evaluation of Playfair's law and its use in testing long-term stream erosion models, *Earth Surfuce Processes and Landforms*, 26, 1317–1332.

Nishiizumi, K., Imamura, M., Caffee, M.W., Southon, J.R., Finkel, R.C., and McAninch, J. (2007). Absolute calibration of ^{10}Be AMS standards. *Nuclear Instruments and Methods in Physics Research B,* 258, 403-413.

Nocquet, J.-M., and Calais, E. (2004). Geodetic measurements of crustal deformation in the Western Mediterranean and Europe. *Pure and Applied Geophysics*, 161 (3), 661-681.

Noël, H., Garbolino, E., Brauer, A., Lallier-Vergès, E., de Beaulieu, J.-L., and Disnar, J.-R. (2001). Human impact and soil erosion during the last 5000 yrs as recorded in lacustrine sedimentary organic matter at Lac d'Annecy, the French Alps. *Journal of Paleolimnology*, 25**,** 229-244.

North Greenland Ice Core Project members (2004). High-resolution record of Northern Hemisphere climate extending into the last interglacial period. *Nature*, 431(7005), 147-151.

Norton, K.P. (2008). Response of the landscape in the Swiss Alps to the late glacial to Holocene climate transition. PhD Thesis, University of Hannover.

Norton, K.P., von Blanckenburg, F., Schlunegger, F., Schwab, M., and Kubik, P.W. (2008). Cosmogenic nuclide-based investigation of spatial erosion and hillslope channel coupling in the transient foreland of the Swiss Alps. *Geomorphology*, 95**,** 474-486.

Norton, K.P., and Hampel, A. (2010). Postglacial rebound promotes glacial re-advances – a case study from the European Alps. *Terra Nova*, 22(4), 297-302.

Norton, K.P., Abbühl, L.M., and Schlunegger, F. (2010a). Glacial conditioning as an erosional driving force in the Central Alps. *Geology*, 38, 655-658.

Norton K.P., von Blanckenburg F., and Kubik, P.W. (2010b). Cosmogenic nuclide-derived rates of diffusive and episodic erosion in the glacially sculpted upper Rhone Valley, Swiss Alps. *Earth Surface Processes and Landforms*, 35, 651-662.

Nunn, J.A., and Aires, J.R. (1988). Gravity anomalies and flexure of the lithosphere at the middle Amazon Basin, Brazil. *Journal of Geophysical Research*, 93, 415-428.

Oerlemans, J. (1984). Numerical experiments on large-scale glacial erosion. *Zeitschrift fur Gletscherkunde und Glazialgeologie*, 20, 107-126.

Oskin, M., and Burbank, D.W. (2005). Alpine landscape evolution dominated by cirque retreat. *Geology*, 33, 933-936.

Ouimet, W.B., Whipple, K.X., Royden, L.H., Sun, Z., and Chen, Z. (2007). The influence of large landslides on river incision in a transient landscape: Eastern margin of the Tibetan Plateau (Sichuan, China). *Geological Society of America Bulletin*, 119(11), 1462-1476.

Ouimet, W.B., Whipple, K.X., Crosby, B.T., Johnson, J.P., and Schildgen, T.F. (2008). Epigenetic gorges in fluvial landscapes. *Earth Surface Processes and Landforms*, 33, 1993-2009.

Paterson, W. (1994). The Physics of Glaciers. 3rd ed., Elsevier, New York, pp. 469.

Pattyn, F. (2003). A new three-dimensional higher-order thermomechanical ice sheet model: Basic sensitivity, ice stream development, and ice flow across subglacial lakes. *Journal of Geophysical Research*, 108(B8), 2382, doi:10.1029/2002JB002329.

Pedersen, V.K., Egholm, D.L., Braun, J., and Nielsen, S.B. (2010).Predicting thermochronological data from a surface process model using *Pecube*. Thermo2010, 12th International conference on thermochronology Glasgow, *Extended Abstract Volume*, p. 267.

Penck, A. (1905). Glacial features in the surface of the Alps. *The Journal of Geology*, 13, 1-19.

Penck W. (1924). Die Morphologische Analyse: Ein Kapital der Physikalischen Geologie. Stuttgart.

Persano, C., Stuart, F.M., Bishop, P., and Barfod, D.N. (2002). Apatite (U-Th)/He age constraints on the development of the Great Escarpment on the southeastern Australian passive margin. *Earth and Planetary Science Letters*, 200, 79-90.

Persaud, M., and Pfiffner, O.A. (2004). Active deformation in the eastern Swiss Alps: post-glacial faults, seismicity and surface uplift. *Tectonophysics*, 385, 59-84.

Petit, J.R., Basile, I., Leruyuet, A., Raynaud, D., Lorius, C., Jouzel, J., Stievenard, M., Lipenkov, V.Y., Barkov, N.I., Kudryashov, B.B., Davis, M., Saltzman, E., and Kotlyakov, V. (1997). Four climate cycles in Vostok ice core. *Nature*, 387, 359-360.

Petit, J.R., Jouzel, J., Raynaud, D., Barkov, N.I., Barnola, J.M., Basile, I., Bender, M., Chappellaz, J., Davis, M., Delaygue, G., Delmotte, M., Kotlyakov, V.M., Legrand, M., Lipenkov, V.Y., Lorius, C., Pepin, L., Ritz, C., Saltzman, E., and Stievenard, M. (1999). Climate and atmospheric history of the past 420,000 years from the Vostok ice core, Antarctica. *Nature*, 399, 429-436.

Peyron O., Guiot J., Cheddadi R., Tarasov P., Reille M., de Beaulieu J.L., Bottema S., and Andrieu V. (1998). Climatic reconstruction in Europe for 18,000 yr B.P. from pollen data. *Quatemary Research,* 49, 183-196.

Pfiffner, O.A., Heitzmann, P., Lehner, P., Frei, W., Pugin, A., and Felber, M. (1997). Incision and backfilling of Alpine valleys: Pliocene, Pleistocene and Holocene processes. i*n* Pfiffner, O.A. (Ed.), Deep structure of the Swiss Alps and results of NRP 20, Birkhäuser-Verlag, Basel, Boston, Berlin, pp. 265-288.

Pfiffner, O.A., Schlunegger, F., and Buiter, S.J.H. (2002). The Swiss Alps and their peripheral foreland basin: stratigraphic response to deep crustal processes. *Tectonics*, 21, doi:10.1029/2000TC900039.

Pignalosa, A., Zattin, M., Massironi, M., and Cavazza, W. (2010). Thermochronological evidence for a late Pliocene climate-induced erosion rate increase in the Alps. *International Journal of Earth Sciences*, doi: 10.1007/s00531-010-0510-9.

Porter, S.C. (1989). Some geological implications of average Quaternary glacial conditions. *Quaternary Research*, 32, 245-261.

Porter S.C., and Orombelli, G. (1982). Late-glacial ice advances in the western Italian Alps. *Boreas*, 11, 125-140.

Press, W.H., Teukolsky, S.A., Vetterling, W.T. and Flannery, B.P. (1992). Numerical Recipes in FORTRAN 77: The Art of Scientific Computing. Cambridge Univ. Press, New York, 921 pp.

Rahn, M.K. (1994). Incipient metamorphism of the Glarus Alps: Petrology of the Taveyanne Greywacke and fission track dating. PhD Thesis, University of Basel, 209 pp.

Rahn, M.K., Brandon, M.T., Batt, G.E., and Garver, J.I. (2004). A zero-damage model for fission-track annealing in zircon. *American Mineralogist*, 89(4), 473.484.

Raymo M.W., and Ruddiman W.F. (1992). Tectonic forcing of late Cenozoic climate. *Nature*, 359, 117-122.

Raymo, M.E. (1994). The initiation of Nothern-Hemisphere glaciation. *Annual Review of Earth and Planetary Sciences*, 22, 353-383.

Reinecker, J., Danišík, M., Schmid, C., Glotzbach, C., Rahn, M., Frisch, W., and Spiegel, C. (2008). Tectonic control on the late stage exhumation of the Aar Massif (Switzerland): Constraints from apatite fission track and (U-Th)/He data. *Tectonics*, 27, TC6009, doi:10.1029/2007TC002247.

Reiners, P.W., Ehlers, T.A., Garver, J.I., Mitchell, S.G., Montgomery, D.R., Vance, J.A., and Nicolescu, S. (2002). Late Miocene exhumation and uplift of the Washington Cascade Range. *Geology*, 30, 767-770.

Reiners, P.W., Spell, T.L., Nicolescu, S., and Zanetti, K.A. (2004). Zircon (U-Th)/He thermochronometry: He diffusion and comparisons with $^{40}Ar/^{39}Ar$ dating. *Geochimica et Cosmochimica Acta*, 68, 1857-1887.

Reiners, P.W., and Ehlers, T.A. (2005). Low-Temperature Thermochronology: Techniques, Interpretations, and Applications, *Reviews in Mineralogy and Geochemistry,* Chantilly, Virginia, Mineralogical Society of America/Geochemical Society, pp. 622.

Reiners, P.W., Ehlers, T.A., and Zeitler, P.K. (2005). Past, present, and future of thermochronology. *in* Reiners, P.W., and Ehlers, T.A., eds., Low-Temperature Thermochronology: Techniques, Interpretations, and Applications, 58, *Reviews in Mineralogy and Geochemistry*, Chantilly, Virginia, Mineralogical Society of America/Geochemical Society, p. 1-18.

Reiners, P.W., and Brandon, M.T. (2006). Using thermochronology to understand orogenic erosion. *Annual Review of Earth and Planetary Sciences*, 34, 419-466.

Reiners, P.W. (2007). Thermochronologic approaches to paleotopography. *Reviews in Mineralogy and Geochemistry*, 66, 243-267.

Richardson, N.J., Densmore, A.L., Seward, D., Wipf, M., and Yong, L. (2010). Eocene incision of the Three Gorges and growth of the Yangtze River. *Geology*, 38, 551-554.

Ritz, C., Rommelaere, V., and Dumas, C. (2001). Modeling the evolution of Antarctic ice sheet over the last 420,000 years: implications for altitude changes in the Vostok region. *Journal of Geophysical Research*, 106(D23), 31943-31964.

Robert, X., van der Beek, P., Braun, J., Perry, C., Dubille, M., and Mugnier, J.-L. (2009). Assessing Quaternary reactivation of the Main Central thrust zone (central Nepal Himalaya): New thermochronologic data and numerical modeling. *Geology*, 37(8), 731-734.

Roe, G.H., Montgomery, D.R., and Hallet, B. (2002), Effects of orographic precipitation variations on the concavity of steady-state river profiles. *Geology*, 30, 143-146.

Roering, J.J., Perron, J.T., and Kirchner, J.W. (2007). Functional relationships between denudation andhillslope form and relief. *Earth and Planetary Science Letters*, 264(1-2), 245-258.

Rosenbaum, G., and Lister, G.S. (2005). The Western Alps from the Jurassic to Oligocene: spatiotemporal constraints and evolutionary reconstructions. *Earth Science Reviews*, 69, 281-306.

Rosselli, A., and Olivier, R. (2003). Modélisation gravimétrique 2.5D et cartes isohypses au 1:100'000 du substratum rocheux de la Vallée du Rhône entre Villeneuve et Brig (Suisse). *Eclogae Geologicae Helvetiae*, 96, 399-423.

Rouchy, J.M., Orszag-Sperber, F., Blanc-Valleron, M.-M., Pierre, C., Riviere, M., Combourieu-Nebout, N., and Panayides, I. (2001). Paleoenvironmental changes at the Messinian-Pliocene boundary in the eastern mediterranean (southern Cyprus basins): significance of the Messinian Lago-Mare. *Sedimentary Geology*, 145, 93-117.

Ruddiman, W.F., Raymo, M., and McIntyre, A. (1986). Matuyama 41,000-year cycles: North Atlantic Ocean and northern hemisphere ice sheets. *Earth and Planetary Science Letters*, 80, 117-129.

Rutt, I.C., Hagdorn, M., Hulton, N.R.J., and Payne, A.J. (2009). The Glimmer community ice sheet model. *Journal of Geophysical Research*, 114, F02004, doi:10.1029/2008JF001015.

Sabil, N. (1995). La datation par traces de fission : aspects méthodologiques et applications thermochronologiques en contextes alpins et de marge continentale. Thèse de Doctorat, Université Joseph Fourier.

Sadler, P. (1981). Sediment Accumulation Rates and the Completeness of Stratigraphic Sections. *The Journal of Geology*, 89, 569-584.

Sambridge, M. (1999a). Geophysical inversion with a neighbourhood algorithm - I. Searching a parameter space. *Geophysical Journal International*, 138, 479-494.

Sambridge, M. (1999b). Geophysical inversion with a neighbourhood algorithm - II. Appraising the ensemble. *Geophysical Journal International,* 138, 727-746.

Sanchez, G., Rolland, Y., Corsini, M., Braucher, R., Bourlès, D., Arnold, M., and Aumaître, G. (2010). Relationships between tectonics, slope instability and climate change: Cosmic ray exposure dating of active faults, landslides and glacial surfaces in the SW Alps. *Geomorphology*, 117, 1-13.

Scardia, G., Muttoni, G., and Sciunnach, D. (2006). Subsurface magnetostratigraphy of Pleistocene sediments from the Po Plain (Italy): Constraints on rates of sedimentation and rock uplift. *Geological Society of America Bulletin*, 118, 1299-1312.

Schäfer, M. (2007). Modélisation de l'écoulement des glaciers tempérés. Thèse de Doctorat, Université Joseph Fourier.

Schaller, M., Hovius, N., Willett, S.D., Ivy-Ochs, S., Synal, H.-A., and Chen, M.-C. (2005). Fluvial bedrock incision in the active mountain belt of Taiwan from *in situ*-produced cosmogenic nuclides. *Earth Surface Processes and Landforms*, 30, 955-971.

Schildgen, T.F., Phillips, W.M., and Purves, R.S. (2005). Simulation of snow shielding corrections for cosmogenic nuclide surface exposure studies. *Geomorphology*, 64, 67-85.

Schildgen, T.F., Ehlers, T.A., Whipp, D.M. Jr., van Soest, M.C., Whipple, K.X., and Hodges, K.V. (2009). Quantifying canyon incision and Andean Plateau surface uplift, southwest Peru: A thermochronometer and numerical modeling approach. *Journal of Geophysical Research*, 114, doi:10.1029/2009jf001305.

Schildgen, T.F., Balco, G., and Shuster, D.L. (2010). Canyon incision and knickpoint propagation recorded by apatite $^{4}He/^{3}He$ thermochronometry. *Earth Planetary Science Letters*, 293, 377-387.

Schlatter, A., Schneider, D., Geiger, A., and Kahle, H.-G. (2005). Recent vertical movements from precise levelling in the vicinity of the city of Basel, Switzerland. *International Journal of Earth Sciences*, 94, 507-514.

Schlüchter, C. (1986). The Quaternary glaciations of Switzerland, with special reference to the Northern alpine foreland. *Quaternary Science Reviews*, 5, 413-419.

Schlunegger, F., Matter, A., Burbank, D.W., Leu, W., Mange, M., Matyas, J. (1997). Sedimentary sequences, seismofacies and evolution of depositional systems of the Oligo/Miocene Lower Freshwater Molasse Group, Switzerland. *Basin Research*, 9, 1-26.

Schlunegger, F., and Willett, S. (1999). Spatial and temporal variations in exhumation of the central Swiss Alps and implications for exhumation mechanisms. *In* Ring, U., Brandon, M.T., Lister, G.S., and Willett, S.D., eds., Exhumation Mechanisms, *Geological Society Special Publication*, 154, 157-179.

Schlunegger F., and Hinderer, M. (2001). Crustal uplift in the Alps: why the drainage pattern matters. *Terra Nova*, 13, 425-432.

Schlunegger F., and Hinderer, M. (2003). Pleistocene/Holocene climate change, reestablishment of fluvial drainage network and increase in relief in the Swiss Alps. *Terra Nova*, 15, 88-95.

Schlunegger, F., and Schneider, H. (2005). Relief-rejuvenation and topographic length scales in a fluvial drainage basin, Napf area, Central Switzerland. *Geomorphology*, 69(1-4), 102-117.

Schmid, S.M., Pfiffner, O.A., Froitzheim, N., Schönborn, G., and Kissling, E. (1996). Geophysical geological transect and tectonic evolution of the Swiss-Italian Alps. *Tectonics*, 15, 1036-1064.

Schmid, S.M., and Kissling, E. (2000). The arc of the western Alps in the light of geophysical data on deep crustal structure. *Tectonics*, 19, 62-85.

Schmid, S.M., Fügenshuh, B., Kissling, E., and Schuster, R. (2004). Tectonic map and overall architecture of the Alpine orogen. *Eclogae Geologicae Helvetiae*, 97, 93-117.

Schumer, R., and Jerolmack, D.J. (2009). Real and apparent changes in sediment deposition rates through time. *Journal of Geophysical Research*, 114, F00A06, doi:10.1029/2009JF001266.

Schwarb, M., Daly, C., Frei, C., and Schär, C. (2001). Mean annual and seasonal precipitation in the European Alps 1971-1990; Hydrological atlas of Switzerland: Berne, Switzerland, Institute of Geography of the University of Berne, Plates 2.6 and 2.7.

Schwartz, G. (1978). Estimating the dimension of a model. *Annals of Statistics*, 6, 461-646.

Seidl, M.A., Finkel, R.C., Caffee, M.W., Hudson, G.B., and Dietrich, W.E. (1997). Cosmogenic isotope analysis applied to river longitudinal profile evolution: Problems and interpretations. *Earth Surface Processes and Landforms*, 22, 195-209.

Seward, D., and Mancktelow, N.S. (1994). Neogene kinematics of the central and Western Alps: Evidence from fission-track dating. *Geology*, 22, 803-806.

Seward, D., Ford, M., Bürgisser, J, Lickorish, H., Williams, E.A., and Meckel III, L.D. (1999). Preliminary results of fission-track analyses in the southern Pelvoux area, SE France. *in* G. Gosso, F. Jadoul, M. Sella, M.I. Spalla, (Eds), 3rd Workshop on Alpine Geological Studies, Biella-Oropa September 29 -October 1, 1997, *Memorie di Scienze Geologische*, 51, 25-31.

Shuster, D.L., and Farley, K.A. (2004). $^{4}He/^{3}He$ thermochronometry. *Earth Planetary Science Letters,* 217, 1-17.

Shuster, D.L., Farley, K.A., Sisterson, J.M., and Burnett, D.S. (2004). Quantifying the diffusion kinetics and spatial distributions of radiogenic ^{4}He in minerals containing proton-induced ^{3}He. *Earth and Planetary Science Letters*, 217, 19-32.

Shuster, D.L., and Farley, K.A. (2005). $^{4}He/^{3}He$ thermochronometry: Theory, practice, and potential complications. *in* Reiners, P.W., and Ehlers, T.A., eds., Low-Temperature Thermochronology: Techniques, Interpretations, and Applications, 58, *Reviews in Mineralogy and Geochemistry*, Chantilly, Virginia, Mineralogical Society of America/Geochemical Society, pp. 181-203.

Shuster, D.L., Ehlers, T.A., Rusmore, M.E., and Farley, K.A. (2005). Rapid glacial erosion at 1.8 Ma revealed by $^{4}He/^{3}He$ thermochronometry. *Science*, 310, 1668-1670.

Shuster, D.L., Flowers, R.M., and Farley, K.A. (2006). The influence of natural radiation damage on helium diffusion kinetics in apatite. *Earth Planetary Science Letters*, 249, 148-161.

Shuster, D.L., and Farley, K.A. (2009). The influence of artificial radiation damage and thermal annealing on helium diffusion kinetics in apatite. *Geochimica et Cosmochimica Acta,* 73, 183-196.

Shuster, D.L., Cuffey, K.M., Sanders, J.M., and Balco, G. (in press). Thermochronometry reveals headward propagation of erosion in an alpine landscape. *Science*.

Simon-Labric, T., Rolland, Y., Dumont, T., Heymes, T., Authemayou, C., Corsini, M., and Fornari, M. (2009). $^{40}Ar/^{39}Ar$ dating of Penninic Front tectonic displacement (W Alps) during the Lower Oligocene (31-34 Ma), *Terra Nova*, 21, 127-136.

Sklar, L.S., and Dietrich, W.E. (1998). River longitudinal profiles and bedrock incision models: Stream power and the influence of sediment supply. In *Rivers over Rock: Fluvial Processes in Bedrock Channels*, edited by K. J. Tinkler and E. E. Wohl, pp. 237-260, American Geophysical Union.

Sklar, L.S., and Dietrich, W.E. (2001). Sediment and rock strength controls on river incision into bedrock. *Geology*, 29(12), 1087-1090.

Sklar, L.S., and Dietrich, W.E. (2004). A mechanistic model for river incision into bedrock by saltating bed load. *Water Resources Research*, 40(6), 10.1029/2003WR002496.

Sklar, L., and Dietrich, W.E. (2006). The role of sediment in controlling steady state bedrock channel slope: Implications of the saltation-abrasion incision model. *Geomorphology*, 82, 58-83.

Small, E., and Anderson, R.S. (1995). Geomorphically driven late Cenozoic rock uplift in the Sierra Nevada, California. *Science*, 270, 277-280.

Small, E.E., Anderson, R.S., Repka, J.L., and Finkel, R. (1997). Erosion rates of alpine bedrock summit surfaces deduced from in situ Be-10 and Al-26. *Earth and Planetary Science Letters*, 150, 413-425.

Small, E., and Anderson, R.S. (1998). Pleistocene relief production in Laramide mountain ranges, western Unites States. *Geology*, 26, 123-126.

Snyder, N.P., and Kammer, L.L. (2008). Dynamic adjustments in channel width in response to a forced diversion: Gower Gulch, Death Valley National Park, California. *Geology*, 36(2), 187-190.

Sonney, R., and Vuattaz, F.-D. (2009). Numerical modelling of Alpine deep flow systems: a management and prediction tool for an exploited geothermal reservoir (Lavey-les-Bains, Switzerland). *Hydrogeology Journal*, 17, 601-616.

Soom, M.A. (1990). Abkühlungs- und Hebungsgeschichte der Externmassive und der penninischen Decken beidseits der Simplon-Rhone-Linie seit dem Oligozän: Spaltspurdatierung an Apatit/Zirkon und K-Ar-Datierungen an Biotit/Muskovit (westliche Zentralalpen). PhD Thesis, University of Bern, Switzerland, 64 pp.

Spiegel, C., Kohn, B., Belton, D., Berner, Z., Gleadow, A. (2009). Apatite (U-Th-Sm)/He thermochronology of rapidly cooled samples: The effect of He implantation. *Earth and Planetary Science Letters*, 285(1-2), 105-114.

Stampfli, G.M., Mosar, J., Marquer, D., Marchant, R., Baudin, T. and Borel, G. (1998). Subduction and obduction processes in the Swiss Alps. *Tectonophysics*, 296, 159-204.

Stark, C.P. (2006). A self-regulating model of bedrock river channel geometry. *Geophysical Research Letters*, 33, 10.1029/2005GL023193.

Stephenson, J., Gallagher, K., and Holmes, C.C. (2006). A Bayesian approach to calibrating apatite fission track annealing models for laboratory and geological timescales. *Geochimica & Cosmochimica Acta*, 70, 5183-5200.

Stewart, J., and Watts, A.B. (1997). Gravity anomalies and spatial variation of flexural rigidity at mountain ranges. *Journal of Geophysical Research*, 102, 5327-5352, doi: 10.1029/96JB03664.

Stewart, R.J., and Brandon, M.T. (2004). Detrital-zircon fission-track ages for the "Hoh Formation": Implications for late Cenozoic evolution of the Cascadia subduction wedge. *Geological Society of America Bulletin*, 116, 60-75.

Stock, J.D., and Montgomery, D.R. (1999). Geologic constraints on bedrock river incision using the stream power law. *Journal of Geophysical Research*, 104(B3), 4983-4993.

Stock, J.D., and Dietrich, W.E. (2003) Valley incision by debris flows: Evidence of a topographic signature. *Water Resources Research*, 39 (1089),10.1029/2001WR001057.

Stone, J.O. (2000). Air pressure and cosmogenic isotope production. *Journal of Geophysical Research*, 105, 23753-23759.

Stroeven, A.P., Fabel, D., Hättestrand, C., and Harbor, J. (2002). A relict landscape in the centre of Fennoscandian glaciation: cosmogenic radionuclide evidence of tors preserved through multiple glacial cycles. *Geomorphology*, 44, 145-154.

Stüwe, K., White, L., and Brown, R.W. (1994). The influence of eroding topography on steady-state isotherms. Application to fission track analysis. *Earth Planetary Science Letters*, 124, 63-74.

Sue C., Delacou B., Champagnac J.D., Allanic C., Tricart P., and Burkhard M. (2007). Extensional neotectonics around the bend of the Western/Central Alps: an overview. *International Journal of Earth Sciences*. 96, 1101-1129.

Summerfield, M.A. (2000). Geomorphology and Global Tectonics, Wiley, Chichester, 367pp.

Svennson, H. (1958). Is the cross-section of a glacial valley a parabola?. *Journal of Glaciology,* 3, 362-363.

Tagami, T., Galbraith, R.F., Yamada, R., and Laslett, G.M. (1998). Revised annealing kinetics of fission tracks in zircon and geological implications. In: P. Van den haute and F. De Corte (Editors), Advances in Fission-Track Geochronology. Kluwer Academic Publishers, Dordrecht, Netherlands, pp. 99-112.

Tarantola, A. (2005). Inverse Problem Theory and Model Parameter Estimation. *Society for Industrial and Applied Mathematics*, Philadelphia, pp. 358.

Tesauro, M., Kaban, M.K., and Cloetingh S.A.P.L. (2008). EuCRUST-07: A new reference model for the European crust. *Geophysical Research Letters*, 35, L05313, doi:10.1029/2007GL032244.

Thomson, S.N., Brandon, M.T., Tomkin, J.H., Reiners, P.W., Vasquez, S., and Wilson, N.J. (2010). Glaciation as a destructive and constructive control on mountain building. *Nature*, 467, 313-317.

Thorp P.W. (1981). A trimline method for defining the upper limit of the Loch Lomond Advance glaciers: examples from the Coch Levan and Glencoe area. *Scotish Journal of Geology*, 17, 49-64.

Thouvenot, F., Frechet, J., Jenatton, L., and Gamond, J.-F. (2003). The Belledonne Border Fault: identification of an active seismic strike-slip fault in the western Alps. *Geophysical Journal International*, 155, 174-192.

Tomkin, J.H., and Braun, J. (2002). The effect glaciation has on the relief of a fast growing orogen: A numerical modelling study. *American Journal of Science*, 302, 169-190.

Tomkin, J.H., Brandon, M.T., Pazzaglia, F.J., Barbour, J.R., and Willett, S.D. (2003). Quantitative testing of bedrock incision models for the Clearwater River, NW Washington State. *Journal of Geophysical Research*, 108(B6), 2308, doi:10.1029/2001JB000862.

Tricart J., and Cailleux A. (1965). Traité de Géomorphologie. Paris.

Tricart, P., van der Beek, P., Schwartz, S., and Labrin, E. (2007). Diachronous late-stage exhumation across the western Alpine arc: Constraints from apatite fission-track thermochronology between the Pelvoux and Dora-Maira massifs. *Journal of Geological Society of London*, 164, 163-174.

Tucker, G.E., and Slingerland, R.L. (1994). Erosional dynamics, flexural isostasy, and long-lived escarpments: a numerical modeling study. *Journal of Geophysical Research*, 99, 12,229-212,243.

Tucker, G.E., Lancaster, S.T., Gasparini, N.M., and Bras, R.L. (2001). The Channel-Hillslope Integrated Landscape Development (CHILD) Model. in *Landscape Erosion and Evolution Modeling,* edited by R. S. Harmon and W. W. Doe III, Kluwer Academic/Plenum Publishers, pp. 349-388.

Tucker, G.E., and Whipple, K.X. (2002). Topographic outcomes predicted by stream erosion models: Sensitivity analysis and intermodel comparison. *Journal of Geophysical Research*, 107, 2179, doi:10.1029/2001JB000162.

Tucker, G.E. (2004). Drainage basin sensitivity to tectonic and climatic forcing: implications of a stochastic model for the role of entrainment and erosion thresholds. *Earth Surface Processes and Landforms*, 29(2), 185-205.

Turowski, J.M., Lague, D., Crave, A., and Hovius, N. (2006). Experimental channel response to tectonic uplift. *Journal of Geophysical Research*, 111, 10.1029/2005JF000306.

Turowski, J.M., Lague, D., and Hovius, N. (2007). Cover effect in bedrock abrasion: A new derivation and its implications for the modeling of bedrock channel morphology. *Journal of Geophysical Research*, 112, F04006, 10.1029/2006JF000697.

Valla, P.G., van der Beek, P.A., and Carcaillet, J. (2010a). Dating bedrock gorge incision in the French Western Alps (Ecrins-Pelvoux massif) using cosmogenic ^{10}Be. *Terra Nova*, 22, 18-25.

Valla, P.G., Herman, F., van der Beek, P.A, and Braun, J. (2010b). Inversion of thermochronological age-elevation profiles to extract independent estimates of denudation and relief history - I: Theory and conceptual model. *Earth and Planetary Science Letters,* 295, 511-522.

Valla, P.G., van der Beek, P.A., and Lague, D. (2010c). Fluvial incision into bedrock: Insights from morphometric analysis and numerical modeling of gorges incising glacial hanging valleys (Western Alps, France). *Journal of Geophysical Research*, 115(F2), F02010, doi: 10.1029/2008jf001079.

Valla, P.G., Shuster, D.L., and van der Beek, P.A. (submitted, a). Major increase in relief of the European Alps during Mid-Pleistocene glaciations recorded by apatite ^{4}He/^{3}He thermochronometry. *Nature Geoscience*.

Valla, P.G., van der Beek, P.A., Shuster, D.L., Braun, J., Herman, F., Tassan-Got, L., and Gautheron, C. (submitted, b). Late Neogene exhumation and relief development of the Swiss Alps using low-temperature thermochronology modeling and ^{4}He/^{3}He thermochronometry. *Journal of Geophysical Research*.

van der Beek, P., Summerfield, M.A., Braun, J., Brown, R.W., and Fleming, A. (2002). Modeling postbreakup landscape development and denudational history across the southeast African (Drakensberg Escarpment) margin. *Journal of Geophysical Research*, 107(B12), 2351, doi:10.1029/2001JB000744.

van der Beek P., and Bishop, P. (2003). Cenozoic river profile development in the Upper Lachlan catchment (SE Australia) as a test of quantitative fluvial incision models. *Journal of Geophysical Research*, 108, 2309, 10.1029/2002JB002125.

van der Beek, P.A., and Bourbon, P. (2008). A quantification of the glacial imprint on relief development in the French Western Alps. *Geomorphology*, 97, 52-72.

van der Beek, P.A., Valla, P.G., Herman, F., Braun, J., Persano, C., Dobson, K.J., and Labrin, E. (2010). Inversion of thermochronological age-elevation profiles to extract independent estimates of denudation and relief history - II: Application to the French Western Alps. *Earth and Planetary Science Letters*, 296, 9-22.

Vartanian-Traynard, C. (1969). Les premières conséquences économiques et humaines du percement du tunnel du Mont-Blanc. *Revue de géographie alpine*, 57, 707-728.

Vernon, A.J., van der Beek, P.A., Sinclair, H.D., and Rahn, M.K. (2008). Increase in late Neogene denudation of the European Alps confirmed by analysis of a fission track thermochronology database. *Earth and Planetary Science Letters,* 270, 316-329.

Vernon, A.J., van der Beek, P.A., Sinclair, H.D., Persano, C., Foeken, J., and Stuart, F.M. (2009). Variable late Neogene exhumation of the central European Alps: Low-temperature thermochronology from the Aar Massif, Switzerland, and the Lepontine Dome, Italy. *Tectonics*, 28, TC5004, doi:10.1029/2008TC002387.

Vigano, A., and Martin, S. (2007). Thermorheological model for the European Central Alps: brittle-ductile transition and lithospheric strength. *Terra Nova*, 19(5), 309-316.

Vincent, C. (2002). Influence of climate change over the 20th Century on four French glacier mass balances. *Journal of Geophysical Research*, 107, D19(4375), doi:10.1029/2001JD000832.

Vincent C., Le Meur E., Six D., and Funk M. (2005). Solving the paradox of the end of the Little Ice Age in the Alps. *Geophysical Research Letters*, 32, L09706, doi:10.1029/2005GL022552.

von Blanckenburg, F., and Davies, J.H. (1995). Slab breakoff: A model for magmatism and tectonics in the Alps. *Tectonics*, 14, 120-131.

von Blanckenburg, F. (2006). The control mechanisms of erosion and weathering at basin scale from cosmogenic nuclides in river sediment. *Earth and Planetary Science Letters*, 242, 223-239.

von Raumer, J.F., and Neubauer, F. (1993). Pre-Mesozoic Geology in the Alps. *Springer*, New York, 677 pp.

von Raumer, J., Abrecht, J., Bussy, F., Lombardo, B., Menot, R.P., and Schaltegger, U. (1999). The Palaeozoic metamorphic evolution of the Alpine External Massifs. *Schweitzerische Mineralogische und Petrographische Mitteilungen*, 79, 5-22.

Vuattaz, F.-D., Rouiller, J.-D., Dubois, J.-D., Bianchetti, G., and Besson, O. (1993). Programme Géothermoval : résultats d'une prospection des ressources géothermiques du Valais, Suisse. *Bulletin du Centre d'Hydrogéologie de l'Université de Neuchâtel*, 12, 1-37.

Wagner, G.A., and Reimer, G.M. (1972). Fission track tectonics: The tectonic interpretation of fission track apatite ages. *Earth and Planetary Science Letters*, 14, 263-268.

Wagner, G.A., Reimer, G.M., and Jäger, E. (1977). Cooling ages derived by apatite fission track, mica Rb-Sr and K-Ar dating: the uplift and cooling history of the Central Alps: *Memorie di Scienze Geologiche*, 30, 1-27.

Watts, A.B. (2001). Isostasy and Flexure of the Lithosphere. Cambridge University Press, 458pp.

Weissel, J.K., and Seidl, M.A. (1998). Inland propagation of erosional escarpments and river profile evolution across the southeast Australian passive continental margin. *in Rivers over Rock: Fluvial Processes in Bedrock Channels*, edited by K. J. Tinkler and E. E. Wohl, pp. 189-206, American Geophysical Union.

WGMS (1998). Fluctuations of Glaciers 1990-1995. Volume VII, IAHS/UNESCO. World Glacier Monitoring Service, Zurich, Switzerland.

WGMS (2005). Fluctuations of Glaciers 1995-2000, Volume VIII. IUGG (CCS)-UNEP-UNESCO. World Glacier Monitoring Service, Zurich.

WGMS (2008): Fluctuations of Glaciers 2000-2005, Volume IX. Haeberli, W., Zemp, M., Kääb, A., Paul, F. and Hoelzle, M. (eds.), ICSU(FAGS)/IUGG(IACS)/UNEP/UNESCO/ WMO, World Glacier Monitoring Service, Zurich, Switzerland.

Whipp, D.M., and Ehlers, T.A. (2007). Influence of groundwater flow on thermochronometer-derived exhumation rates in the central Nepalese Himalaya. *Geology*, 35, 851-854.

Whipp, D.M., Ehlers, T.A., Blythe, A.E., Huntington, K.W., Hodges, K.V., and Burbank, D.W. (2007). Plio-Quaternary exhumation history of the central Nepalese Himalaya: 2. Thermo-kinematic and thermochronometer age prediction model. *Tectonics*, 26, doi: 10.1029/2006TC001991.

Whipp, D.M., Ehlers, T.A., Braun, J., and Spath, C.D. (2009). Effects of exhumation kinematics and topographic evolution on detrital thermochronometer data. *Journal of Geophysical Research*, 114, doi:10.1029/2008JF001195.

Whipple, K.X., and Tucker, G.E. (1999). Dynamics of the stream-power river incision model: Implications for height limits of mountain ranges, landscape response timescales, and research needs. *Journal of Geophysical Research*, 104, 17,661-17,674.

Whipple, K.X., Kirby, E., and Brocklehurst, S.H. (1999). Geomorphic limits to climate-induced increases in topographic relief. *Nature*, 401, 39-43.

Whipple, K.X., Hancock, G.S., and Anderson, R.S. (2000a). River incision into bedrock: Mechanics and relative efficacy of plucking, abrasion, and cavitation. *Geological Society of America Bulletin*, 112(3), 490-503.

Whipple, K.X., Snyder, N.P., and Dollenmayer, K. (2000b). Rates and processes of bedrock incision by the Upper Ukak River since the 1912 Novarupta ash flow in the Valley of Ten Thousand Smokes, Alaska. *Geology*, 28, 835-838.

Whipple, K.X. (2001). Fluvial landscape response time: How plausible is steady-state denudation? *American Journal of Science*, 301, 313-325.

Whipple, K.X., and Tucker, G.E. (2002). Implications of sediment-flux-dependent river incision models for landscape evolution. *Journal of Geophysical Research*, 107, 10.1029/2000JB000044.

Whipple, K.X. (2004). Bedrock rivers and the geomorphology of active orogens. *Annual Review of Earth and Planetary Sciences*, 32, 151-185.

Whipple, K.X., and Meade, B.J. (2006). Orogen response to changes in climatic and tectonic forcing. *Earth and Planetary Science Letters*, 243, 218-228.

Whipple, K.X. (2009). The influence of climate on the tectonic evolution of mountain belts. *Nature Geosci*ence, 2, 97-104.

Whittaker, A.C., Cowie, P.A., Attal, M., Tucker, G.E., and Roberts, G.P. (2007). Bedrock channel adjustment to tectonic forcing: Implications for predicting river incision rates. *Geology*, 35(2), 103-106.

Willenbring, J.K., and von Blanckenburg, F. (2010). Long-term stability of global erosion rates and weathering during late-Cenozoic cooling. Nature, 465, 211-214.

Willett, S.D. (1999). Orogeny and orography: The effects of erosion on the structure of mountain belts, *Journal of Geophysical Research*, 104:,28 957- 28 981.

Willett, S.D., and Brandon, M.T (2002). On steady states in mountain belts. *Geology*, 30, 175-178.

Willett, S.D., Schlunegger, F., and Picotti, V. (2006). Messinian climate change and erosional destruction of the central European Alps. *Geology*, 34, 613-616.

Willett, S.D. (2010a). Erosion on a line. *Tectonophysics*, 484, 168-180.

Willett, S.D. (2010b). Late Neogene Erosion of the Alps: A Climate Driver? *Annual Review of Earth and Planetary Sciences*, 38, 411-437.

Willgoose, G.R., Bras R.L., and Rodriguez-Iturbe, I. (1991). A physically based coupled network growth and hillslope evolution model: 1, Theory. *Water Resources Research*, 27, 1671-1684.

Williamson, J.H. (1968). Least squares fitting of a straight line. *Canadian Journal of Physics*, 46, 1845-1847.

Wittmann, H., von Blanckenburg, F., Kruesmann, T., Norton, K.P., and Kubik, P.W. (2007). Relation between rock uplift and denudation from cosmogenic nuclides in river sediment in the Central Alps of Switzerland. *Journal of Geophysical Research*, 112, F04010, 10.1029/2006JF000729.

Wobus, C.W., Crosby, B.T., and Whipple, K.X. (2006a). Hanging valleys in fluvial systems: Controls on occurrence and implications for landscape evolution. *Journal of Geophysical Research*, 111, 10.1029/2005JF000406.

Wobus, C.W., Tucker G.E., and Anderson, R.S. (2006b). Self-formed bedrock channels. *Geophysical Research Letters*, 33(18), 10.1029/2006GL027182.

Wohl, E.E., and Merritt, D.M. (2001). Bedrock channel morphology. *Geological Society of America Bulletin*, 113(9), 1205-1212.

Wolf, R.A., Farley, K.A., and Silver, L.T. (1996). Helium diffusion and low-temperature thermochronometry of apatite. *Geochemica et Cosmochimica Acta*, 60, 4231-4240.

Wolf, R.A., Farley, K.A., and Kass, D.M. (1998). Modeling of the temperature sensitivity of the apatite (U-Th)/He thermochronometer. *Chemical Geology*, 148, 105-114.

Wong, M., and Parker, G. (2006). Reanalysis and correction of bed-load relation of Meyer-Peter and Müller using their own database. *Journal of Hydraulic Engineering*, 132 (11), 1159-1168.

Yager, E.M., Kirchner, J.W., and Dietrich, W.E. (2007). Calculating bed load transport in steep boulder bed channels. *Water Resource Research*, 43, 10.1029/2006WR005432.

Zachos, J., Pagani, M., Sloan, L., Thomas,E., and Billups, K. (2001). Trends, Rhythms, and Aberrations in Global Climate 65 Ma to Present. *Science*, 292, 686-693.

Zeitler, P.K., Herczig, A.L., McDougall, I., and Honda, M. (1987). U-Th-He dating of apatite: A potential thermochronometer. *Geochimica et Cosmochimica Acta*, 51, 2865-2868.

Zeitler, P.K., Meltzer, A.S., Koons, P.O., Craw, D., Hallet, B., Chamberlain, C.P., Kidd, W.S.F., Park, S.K., Seeber, L., Bishop, M., and Shroder, J. (2001). Erosion, Himalayan geodynamics, and the geomorphology of metamorphism. *GSA Today*, 11, 4-9.

Zemp, M., Hoelzle, M., and Haeberli, W. (2007). Distributed modelling of the regional climatic equilibrium line altitude of glaciers in the European Alps. *Global and Planetary Change*, 56, 83-100.

Zhang, P., Molnar, P., and Downs W.R. (2001). Increased sedimentation rates and grain sizes 2-4 Myr ago due to the influence of climate change on erosion rates. *Nature*, 410, 891-897.

Ziegler, J.F. (1977). Helium: Stopping powers and ranges in all elemental matter. Pergamon Press, New York, pp. 362.

Zuccoli, L. (2000). Geology of the high plains of Castelseprio and Tradate (Northern Italy). *Italian Journal of Quaternary Science*, 13, 57-80.

Abstract

The topographic evolution of mountain belts results from complex couplings between tectonics, climate and surface processes. Quantifying landscape evolution requires methodological tools to constrain forcing processes over temporal (10^3-10^6 years) and spatial (1-100 km) scales characteristic of orogenic systems. This thesis investigates the Neogene and Quaternary relief evolution of the European Alps using *in situ* low-temperature thermochronometry (mostly apatite (U-Th-Sm)/He and ^{4}He/^{3}He) and numerical modeling.

A novel numerical approach combining thermal-kinematic modeling (*Pecube*) with an inversion scheme (*Neighbourhood Algorithm*) allows extracting quantitative information on exhumation and relief histories from thermochronological datasets. Quantifying relief evolution remains problematic, however, and strongly depends on the geomorphic setting. Our results show that both thermochronology data sampling and modeling strategies have to be considered *a priori*, in function of the geomorphic setting and the spatial/temporal scale of the exhumation signal to be constrained. This approach has been applied on a thermochronological dataset collected in the Ecrins-Pelvoux massif (French Alps). The results show a pulse of rapid exhumation until ~5-6 Ma, preceded and followed by more moderate rates of exhumation. However, the data cannot resolve the late-Neogene relief evolution in the Ecrins-Pelvoux massif.

New ^{4}He/^{3}He thermochronometry data from the Rhône valley (Swiss Alps), combined with thermochronological data from the literature, also point out an episode of rapid exhumation until ~5-7 Ma, and reveal a major increase in local topographic relief (~1-1.5 km) linked to valley carving by large mountain glaciers. The onset of this phase of relief carving corresponds to the Mid-Pleistocene transition from symmetric 40-ka to asymmetric and high amplitude 100-ka glacial/interglacial oscillations. The new data also permit to reconstruct the pre-glacial topography of the Rhône basin, and to evaluate the net effect of Pleistocene glaciations on relief evolution at the basin scale.

Preliminary results from numerical modeling of glacial dynamics highlight the potential opportunity of using such an approach to quantitatively assess the impact of the Mid-Pleistocene climate transition on Alpine relief development, leading to new research avenues. Finally, the post-glacial topographic evolution of the Ecrins-Pelvoux massif has been studied using numerical modeling and *in situ* cosmogenic ^{10}Be analyses. The results suggest efficient fluvial incision at rates of cm yr^{-1}, illustrating the efficient landscape response to late-Pleistocene/Holocene climate change.

Résumé

L'évolution topographique des chaînes de montagne résulte d'interactions complexes entre la tectonique et le climat via l'action des processus de surface. La quantification de l'évolution du relief passe par le développement d'outils méthodologiques permettant d'identifier les processus mis en jeu pour des échelles de temps (10^3-10^6 années) et d'espace (1-100 km) caractéristiques de contextes orogéniques. Dans cette étude, l'évolution Néogène et Quaternaire du relief des Alpes Européennes est abordée à partir d'une approche couplant la thermochronométrie basse-température *in-situ* (essentiellement (U-Th-Sm)/He et $^4He/^3He$ sur apatite) et la modélisation numérique.

Le développement d'une méthode numérique associant la modélisation thermo-cinématique (*Pecube*) à un algorithme d'inversion (*Neighbourhood Algorithm*) permet l'interprétation quantitative de données thermochronologiques en termes d'histoires d'exhumation et d'évolution du relief. La quantification de l'évolution du relief reste néanmoins problématique et fortement dépendante du contexte géomorphologique étudié. Cette étude implique la nécessité de repenser *a priori* la stratégie d'échantillonnage et d'interprétation des données suivant le contexte géomorphologique considéré et le signal d'exhumation que l'on cherche à quantifier via la thermochronologie. Enfin, l'application de cette approche à un jeu de données thermochronologiques échantillonnées dans le massif des Ecrins-Pelvoux (Alpes françaises) révèle l'existence d'un épisode d'exhumation rapide cessant autour de ~5-6 Ma, encadré par des taux d'exhumation plus modérés. Cependant, les données ne permettent pas de conclure quant à l'évolution tardi-Néogène du relief dans le massif des Ecrins-Pelvoux.

L'application de la thermochronométrie $^4He/^3He$ dans la vallée du Rhône (Alpes suisses), couplée à des données thermochronologiques issues de la littérature, confirme un épisode d'exhumation rapide jusqu'à ~5-7 Ma, et révèle une augmentation majeure du relief local (~1-1.5 km) associée au creusement des vallées par d'importants appareils glaciaires. Le début de cette phase de creusement correspond à la transition climatique Mi-Pléistocène (~1 Ma) depuis des cycles glaciaires symétriques de 40 ka vers des cycles asymétriques (100 ka) de plus forte amplitude. Ces données permettent également de reconstruire la topographie pré-glaciaire du bassin versant du Rhône, et ainsi d'évaluer, à une échelle plus globale, l'impact des glaciations Pléistocènes sur l'évolution du relief.

Des résultats préliminaires issus de la modélisation numérique des processus glaciaires mettent en évidence le potentiel d'une telle approche afin de tester quantitativement l'influence de la transition climatique Mi-Pléistocène sur le développement du relief alpin, ouvrant de nouvelles perspectives de recherche. Enfin, l'étude de l'évolution topographique post-glaciaire dans le massif des Ecrins-Pelvoux (modélisation numérique et utilisation du ^{10}Be cosmogénique produit *in-situ*) met en évidence une dynamique d'érosion fluviale pouvant atteindre localement des vitesses de l'ordre du cm an^{-1}, illustrant l'évolution géomorphologique rapide en réponse à la transition climatique entre le tardi-Pléistocène et l'Holocène.